Recent Results in Cancer Research
P.M. Schlag · H.-J. Senn *Series Editors*

Otmar Schober
Burkhard Riemann *Editors*

Molecular Imaging in Oncology

Indexed in PubMed/Medline

Springer

Recent Results in Cancer Research

Volume 187

For further volumes:
http://www.springer.com/series/392

Otmar Schober · Burkhard Riemann
Editors

Molecular Imaging in Oncology

Springer

Editors
Otmar Schober
Klinik für Nuklearmedizin
Universitätsklinikum Münster
Münster
Germany

Burkhard Riemann
Klinik für Nuklearmedizin
Universitätsklinikum Münster
Münster
Germany

ISSN 0080-0015
ISBN 978-3-642-10852-5 ISBN 978-3-642-10853-2 (eBook)
DOI 10.1007/978-3-642-10853-2
Springer Heidelberg New York Dordrecht London

Library of Congress Control Number: 2012942712

Printed on acid-free paper

Springer is part of Springer Science+Business Media (www.springer.com)

Preface

What does "molecular imaging" mean? There are several definitions in the literature. The term "molecular imaging" was formed in the early twenty-first century as a discipline at the intersection of molecular biology and in vivo imaging. It is defined as the visualization, characterization, and quantification of biologic processes at the cellular and molecular levels in living organisms. With the help of molecular imaging procedures cellular and molecular pathways and mechanisms of disease can be studied in their own physiologically authentic environment in order to reveal their molecular abnormalities that form the basis of disease. This is a really innovative conception which is in deep contrast to the classical form of diagnostic imaging where documented findings show the end effects of molecular alterations which are typically verified by well-established methods of pathology.

Molecular imaging includes diagnostic methods of nuclear medicine along with various other different strategies to yield imaging signals. Nuclear medicine uses radiolabeled molecules (tracers) that produce signals by means of radioactive decay. Other methods of molecular imaging can lead to images via means of sound (ultrasound), magnetism (MR), or light (OI, optical techniques of bioluminescence and fluorescence) as well as other emerging techniques.

Nuclear medicine has been playing a crucial role in the development of molecular imaging over the past few decades, with other technologies (e.g., OI, MR) being adapted for molecular imaging by developing different types of molecular probes.

These molecular imaging procedures offer numerous potentialities in the field of diagnosis as well as therapeutic methods for diseases, such as cancer, and neurological and cardiovascular diseases. The description of the human genome may show a new direction via genomics and proteomics to the molecular and functional imaging methods.

Out of the increasing number of publications comprising all fields of molecular imaging this handbook focuses on the increasing impact of molecular imaging in the field of oncology. The development of molecular imaging in the twenty-first

century will and has to go ahead to multimodality imaging. Therefore, hybrid devices like SPECT/CT, PET/CT, and PET/MR which can cover the whole spectrum of preclinical and clinical imaging will become more and more relevant in the future. Prospects and challenges of these innovative techniques will be presented in detail in this handbook. In the field of clinical SPECT/CT applications we decided not to replicate the numerous literature and refer to the corresponding recent issues in Seminars in Nuclear Medicine (Delbeke et al. 2009; Even-Sapir et al. 2009). In addition, optical tomographic hybrid approaches such as fluorescence molecular tomography–X-ray computer tomography (FMT-XCT) systems or multi-spectral optoacoustic tomography (MSOT) systems offer unprecedented levels of performance (Condeelis and Weissleder 2010). These innovative multimodality imaging systems require the competency and accreditation of scientists from different disciplines. Therefore, molecular imaging in oncology in the twenty-first century is not possible without close interdisciplinary and interfaculty collaborations.

This handbook highlights the immense potential this reintegration of different disciplines will offer in the future. It provides updated information about molecular imaging in oncology for nuclear physicians as well as radiologists, oncologists, chemists, mathematicians, computer scientists, and physicists. A careful selection of experts in the different fields of molecular imaging was made to outline the major trends and challenges of molecular imaging in oncology bridging the gap between basic research and clinical applications in a unique way. With respect to the distinct profiles of expertise, each chapter is self-contained.

In view of this background the handbook was structured according to the single steps of molecular imaging, i.e. from probe design to clinical applications. Accordingly, the following chapters were defined:

- Technology and Probe Design
- Preclinical Studies
- Clinical Applications
- Future Challenges

We are very grateful that the handbook has assembled exceptionally comprehensive and stimulating contributions from outstanding stakeholders in molecular imaging in oncology from America and Europe.

References

Condeelis J, Weissleder R (2010) In vivo imaging in cancer. Cold Spring Harb Perspect Biol 2:a003848

Delbeke D, Schöder H, Martin WH, Wahl RL (2009) Hybrid imaging (SPECT/CT and PET/CT): improving therapeutic decisions. Sem Nucl Med 39:308–340

Even-Sapir E, Keidar Z, Bar-Shalom R (2009) Hybrid imaging (SPECT/CT and PET/CT): improving the diagnostic accuracy of functional/metabolic and anatomic imaging. Sem Nucl Med 39:264–275

Münster, Germany

Otmar Schober
Burkhard Riemann

Contents

Part III Clinical Applications

Part I
Technology and Probe Design

Computed Tomography and Magnetic Resonance Imaging

Monique R. Bernsen, Alessandro Ruggiero, Marcel van Straten, Gynla Kotek, Joost C. Haeck, Piotr A. Wielopolski and Gabriel P. Krestin

Abstract

Imaging in Oncology is rapidly moving from the detection and size measurement of a lesion to the quantitative assessment of metabolic processes and cellular and molecular interactions. Increasing insights into cancer as a complex disease with involvement of the tumor stroma in tumor pathobiological processes have made it clear that for successful control of cancer, treatment strategies should not only be directed at the tumor cells but also targeted at the tumor microenvironment. This requires understanding of the complex molecular and cellular interactions in cancer tissue. Recent developments in imaging technology have increased the possibility to image various pathobiological processes in cancer development and response to treatment. For computed tomography (CT) and magnetic resonance imaging (MRI) various improvements in hardware, software, and imaging probes have lifted these modalities from classical anatomical imaging techniques to techniques suitable to image and quantify various physiological processes and molecular and cellular interactions. Next to a more general overview of possible imaging targets in oncology this chapter provides an overview of the various developments in CT and MRI technology and some specific applications.

M. R. Bernsen (✉) · A. Ruggiero · M. van Straten · G. Kotek · J. C. Haeck · P. A. Wielopolski · G. P. Krestin
Department of Radiology, Erasmus MC-University Medical Center Rotterdam, Dr. Molewaterplein 50, 3015 GE , Rotterdam, The Netherlands
e-mail: m.bernsen@erasmusmc.nl

O. Schober and B. Riemann (eds.), *Molecular Imaging in Oncology*, Recent Results in Cancer Research 187, DOI: 10.1007/978-3-642-10853-2_1,

Contents

1 Imaging Targets in Cancer

1.1 Introduction

Classically, imaging is used in clinical response assessment of anticancer therapies through measurements of tumor size from cross-sectional anatomical images obtained by CT or MRI (Eisenhauer et al. 2009; World Health Organization 1979; Therasse et al. 2000). While these measurements can be readily and widely performed, they suffer from a number of limitations. Quantification is fairly crude and not suitable for diffuse and/or multiple tumor lesions and changes in tumor size do not always accurately reflect response to treatment (Wahl et al. 2009). Therefore, significant effort is put into the development and validation of new imaging techniques and imaging biomarkers. These include techniques aimed at the quantitative visualization of metabolic processes and of cellular and molecular

interactions. Such approaches are not only valuable for monitoring treatment responses, but also offer opportunities in studies regarding elucidation of mechanisms involved in cancer pathophysiology, identification of (new) targets for treatment, in drug development, for selection of patients likely to respond to the treatment at hand, and for monitoring of drug delivery efficacy.

In this respect it is important to consider that the view on tumor formation and tumor progression has changed considerably over the past two decades. Until the realization that the microenvironment of tumors plays a crucial role in a variety of oncogenic processes (Hanahan and Weinberg 2000), cancer was considered to be a disease mainly arising from transformed cells that, through successive oncogenic mutations, acquire autonomous resistance to cell death and enhanced proliferative and invasive capacities (Renan 1993). Instead of this cancer cell-focused view, it is now recognized that the tumor stroma plays a crucial role in oncogenesis. Tumor stroma consists of a variety of nonmalignant cells and extracellular matrix (Fig. 1). The various cell types within the tumor stroma comprise fibroblasts, immune cells, and endothelial cells; they are in principle nonmalignant but they do have an altered phenotype and function when compared to normal tissue. Through cell–cell interactions and the production of cytokines these tumor stroma cells actively contribute to tumor formation, progression and metastasis, and resistance to treatment. This paradigm shift has led to the realization that for successful control of cancer, treatment strategies should not only be directed at the tumor cells but also targeted at the tumor microenvironment, for which a understanding of the complex molecular and cellular interactions in cancer tissue is paramount. Therefore, imaging techniques are becoming increasingly important in the development, design, and monitoring of cancer drugs and treatment strategies.

1.2 Physiological Imaging Targets

Tumors are known to have an aberrant vascular network and microcirculation. Tumor vasculature is typically highly disorganized with many structural and functional irregularities, such as: incomplete endothelial lining, endothelial fenestrations, arteriovenous shunts, absence of flow regulation, increased vascular permeability, aberrant flow conditions, and inadequate lymphatic drainage. In addition interstitial fibrosis is often also a hallmark of tumors. These irregularities are responsible for various pathophysiological conditions within tumors, such as interstitial hypertension, hypoxia, and acidosis that contribute to the malignant phenotype and resistance to various treatments (Vaupel 2009c, b). Plasma flow aberrations and high interstitial fluid pressure in tumors can severely hamper drug delivery efficiency through inadequate perfusion and convection within the tumor; hypoxic conditions negatively affect radiation and cytostatic drug efficacy through reduced production of free radicals and altered cell cycle kinetics. Tumor blood volume, tumor perfusion, tumor oxygenation levels, interstitial acidosis, and fibrosis are therefore valuable imaging biomarkers in oncology. They can be used

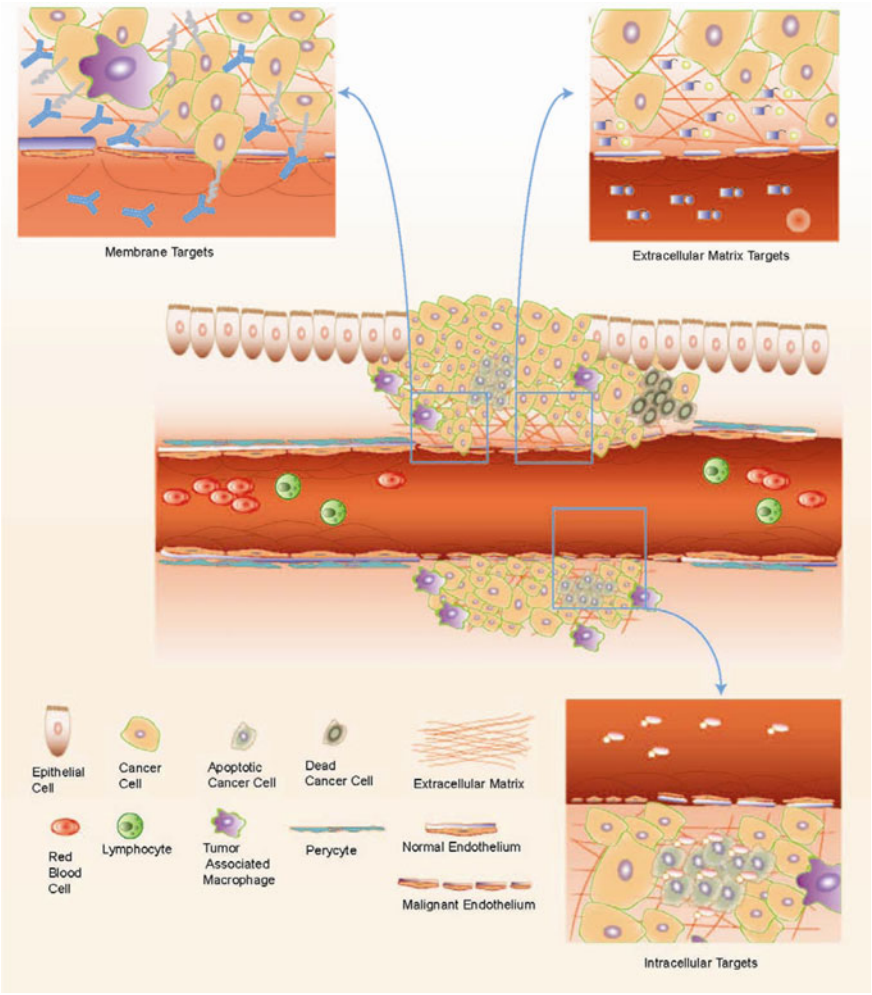

Fig. 1 Schematic representation of the complex composition of a tumor. Various cellular and stromal components can function as targets for therapy and imaging

as either prognostic/predictive indicators or as treatment response parameters (Charnley et al. 2009; DeClerck and Elble 2010; Dhermain et al. 2010; Krohn et al. 2008; Vaupel 2009a; Zhang et al. 2010). Within this pathophysiological environment, tumor cells also display altered energy metabolism as reflected in increased glucose uptake and shifted balances in metabolic products. Metabolic fingerprinting of tumors by imaging techniques is therefore also a widely pursued approach in cancer management (Allen-Auerbach and Weber 2009; Beloueche-Babari et al. 2010; Bohndiek and Brindle 2010; Haberkorn et al. 2007; Plathow and Weber 2008).

Another aspect of tumor physiology considered to be of value as a quantifiable imaging target is tissue cellularity. Depending on the type of tissue, tissue cellularity can be higher or lower in malignant tumors compared to normal tissue. For instance in edematous tumors, cellularity is typically lower compared to normal tissue. In contrast, in breast tumors cellularity is often higher compared to normal tissue that typically has a high fat content (Abdel Razek et al. 2010; Wilson et al. 1992). Cellularity can be determined by imaging based on water diffusion kinetics and in pretreatment situations used for staging and as a prognostic indicator. Cellularity measurements can also be used as an early marker in treatment response assessment (Nilsen et al. 2010).

1.3 Molecular Targets

Imaging of molecular targets commonly comprises the assessment of the presence and/or activity of a specific molecule. Various strategies can be employed, including the use of: imaging probes functionalized by a specific ligand, imaging probes that contain a substrate specific for the molecular function of the target molecule, or reporter gene technology. Imaging probes functionalized by conjugation to a ligand (e.g. antibody, peptide, aptamer, amino acid, or lectine) are generally aimed at molecules expressed on the cell surface, such as somatostatin receptors (Lewis et al. 1999), HER-2 (Smith 2010), VEGF-receptors (Blankenberg et al. 2010), and integrins (Winter et al. 2010). These surface molecules can be involved in tumor cell proliferation, migration, drug resistance, and can thus be used as an imaging biomarker in diagnostics, prognostics, and treatment response assessment.

Imaging probes that contain a substrate specific for the molecular function of the target molecule are often referred to as “smart probes”, “activatable probes”, or “responsive probes”. Characteristic for these probes is that they are largely undetectable in their native state, but following interaction with their target undergo a physiochemical change creating a detectable signal. Typical targets for these imaging probes are enzymes, such as MMPs (Watkins et al. 2009), Cathepsins (Ntziachristos et al. 2002), lipases (Himmelreich et al. 2006), and peroxidases (Tsourkas et al. 2005). However, responsive probes are more and more also being designed to interrogate physicochemical conditions, such as pH, temperature, oxygen pressure, and redox potential in the tumor microenvironment in vivo (Gao et al. 2010; Kobayashi et al. 2009; Aime et al. 2000; Raghunand et al. 2006).

Reporter gene imaging is based on the introduction of specific gene construct into the cells of interest whereby the reporter gene encodes for a receptor, a transporter, or an enzyme resulting in the binding, accumulation, or physicochemical modulation of and injectable probe or a naturally occurring substrate with inherent signal properties such as iron. Reporter gene technology can be used to interrogate the activity of specific signaling pathways, for monitoring of gene therapy, and to track migration and fate of specific cells in vivo (see below) (Kang and Chung 2008; Serganova et al. 2008).

1.4 Cellular Targets

Cellular imaging has applications in diagnosis, prognosis, and treatment monitoring in oncology. Main goals in such approaches are directed at the assessment of the presence, distribution, or fate of a specific cell population. Generally this involves the incorporation of an imaging probe by the cells of interest, either by labeling of the cells with exogenous probes or by reporter gene technology. Examples of cellular imaging applications that can serve diagnostic, prognostic as well as response monitoring purposes can be found in liver and lymph node imaging with intravascularly injected imaging probes. In these applications the selective uptake characteristics of imaging probes by liver parenchymal cells or cells of the reticuloendothelial system are exploited by which presence of tumor (metastatic) lesions can be monitored (Kweon et al. 2010; Lee et al. 2009; Wu et al. 2010). A cellular imaging application that has elicited a wide interest in the past decade is in the field of cell-based therapies. Cell-based therapies are considered to offer unique benefits in cancer treatment. Cells as drug or drug carriers offer potentially favorable targeting and biocompatibility properties, e.g. crossing of the blood–brain barrier, compared to many synthetic drugs (carriers). In vivo cell tracking techniques by which the fate and function of transplanted cells can be monitored are of major importance in developing and improving of such treatment strategies (Helfer et al. 2010; Hong et al. 2010; Tang et al. 2010; Ponomarev 2009). Cellular imaging techniques are also widely used for cancer cell imaging to follow tumor development, tumor cell migration, and metastatic activity in vivo (So et al. 2010; Wang et al. 2009; Zumsteg et al. 2010).

1.5 Image-Guided Drug Delivery

The many developments in imaging techniques have also created exciting possibilities for image-guided drug delivery. In pharmaceutical research, the drug development is a slow, high risk, and costly process. Despite that the specifics and duration of each step depends on the drug class and target indication, overall the introduction of a new drug into clinical development generally takes 10 years (Willmann et al. 2008).

Molecular imaging guidance plays an increasing role in many aspects of pharmaceutical research, providing important advantages over conventional readouts. High spatial and temporal resolution of imaging approaches allows for quantitative, uniform, and potentially high-throughput studies on the same living subject at different time points, increasing the statistical power, and reducing the number of animals and relative costs. Especially in the early stages of drug research and development imaging allows for rapid, noninvasive longitudinal assessment of a drugs pharmacokinetics and pharmacodynamics (Deng and Exner 2010) aiding the selection of lead successful candidates and excluding or deprioritizing others. Therefore, image-guided approaches have the potential to expedite the research and clinical approval of novel imaging and therapeutics probes.

By far, the oncology field benefited most of the recent advancement in molecular imaging. Several targeting moieties (antibodies, peptides, aptamers) specifically directed to molecular targets on malignant cells are currently available. These allow the design of specific probes suitable for the early detection of molecular events that precede the macroscopic development of a disease. Similarly, probes can be designed to perform a therapeutic effect (chemotherapy or radiotherapy) or to be activated in the specific site of interest (ph, thermal, enzymatic activation).

2 Recent Technological Developments in X-ray Computed Tomography of Cancer

2.1 Basics of Multi-Slice Spiral Computed Tomography

2.1.1 Brief History

The history of multi-slice spiral computed tomography (CT) starts in Germany in 1895 when Wilhelm Conrad Röntgen (1845–1923) discovered a new type of radiation, which he called X-rays. This type of electromagnetic radiation, which has a shorter wavelength than visible light and the ability to penetrate matter, was immediately used to image the inner human body. The images thus obtained showed a two-dimensional (2D) projection of the inner structures. The contrast in the images was based on the differences in X-ray attenuation coefficients and in the thickness of the various tissues. For decades the principle of observing the inner human body by looking at projection images in the form of photographs ('X-rays') or fluoroscopic images did not really change. In these images the depth information was lost and details were obscured by overprojection of other structures. Several attempts were made to image only a certain plane of the inner human body, a technique that became known as tomography.

After initial work by Allan M. Cormack (1924–1998), the principle of reconstructing cross-sections was introduced into the medical world by the British engineer Godfrey Newbold Hounsfield (1919–2004). In 1972 he presented the first full-scale CT-scanner (EMI Mark I, EMI Ltd., London, United Kingdom) and the first picture of a patient's head (Ambrose and Hounsfield 1973; Hounsfield 1973). This image represented a cross-section with a thickness of 13 mm and consisted of a matrix of 80 by 80 pixels, which showed the anatomical structure of the brain. Compared to a plain X-ray image, the CT image showed remarkable contrast between tissues with small differences in X-ray attenuation coefficient. A survey of American physicians showed that the invention of CT, together with magnetic resonance imaging (MRI), is seen as the most important medical innovation in the last three decades of the twentieth century (Fuchs and Sox 2001).

After the introduction in 1972, CT-scanners and reconstruction algorithms were improved greatly. The time to obtain the information for reconstructing a cross-section was reduced to the order of one second, and the spatial resolution was improved substantially. Most CT scanners utilized the fan beam geometry, in

which the X-ray tube rotates around the patient and attenuation measurements are obtained with an array of detectors, which also rotates. After data are acquired for one rotation of the X-ray tube, the scanner table is moved and the next slice is scanned. For nearly two decades this scanning technique, which is called the sequential technique, basically remained the same.

Based on new ideas and technical improvements the German physicist Willi A. Kalender (*1949) developed the spiral CT technique and reported the first clinical examinations with spiral CT at the 1998 annual meeting of the Radiological Society of North America. With spiral CT, the patient is moved through the CT scanner, with simultaneous acquisition of projection data of the continuously rotating X-ray source and detector array.

The performance of the spiral CT-scanner was further improved by the introduction of scanners which measured multiple fans simultaneously. With multi-slice spiral CT multiple *fan* measurements are made and an arbitrary number of *slices* can be reconstructed. In literature a number of alternative terms can be found, like multisection, multichannel, and volumetric CT. In 1998 most CT manufacturers introduced a CT system that was able to acquire four fans simultaneously. This innovation reduced the time that was needed for a CT-scan, without necessarily decreasing the spatial resolution. Since then, the technical developments in multi-slice spiral CT were primarily focused on increasing the number of fans. Currently, CT scanners are available which acquire up to 320 fans simultaneously.

The overview given above of the history of multi-slice spiral CT is of course far from complete. For a more extensive overview the reader is referred to a book on CT by W.A. Kalender (Kalender 2005).

2.1.2 Data Acquisition

A CT scanner basically consists of a patient table and a gantry. The patient, who lies on the table, can be moved through the gantry. The table moves in a direction parallel to the z-axis. The gantry accommodates an X-ray tube and a detector array, which rotate around the patient (Fig. 2).

The width of the detectors in the axial plane influences the spatial resolution in the x, y-direction. This width, which generally cannot be chosen by the user, is in the order of 0.5–0.7 mm when scaled to the center of the field-of-view, depending on the CT scanner used. The width of the detector array in the z-direction influences the z-resolution or effective slice thickness. The width of the detector array generally can be varied between 0.5 and 10 mm, scaled to the center of the gantry.

For one complete rotation, the projection data are acquired for approximately 1000 X-ray tube angles. At sequential CT, the data are acquired while the patient table does not move. These data can be used to reconstruct cross-sectional images in the region covered by the X-ray (cone) beam. After data acquisition the patient can be translated in the z-direction for the next region to be covered. State-of-the-art multi-slice CT scanners with 256 or more detector arrays can cover the complete region of interest within a single rotation without movement of the patient at all.

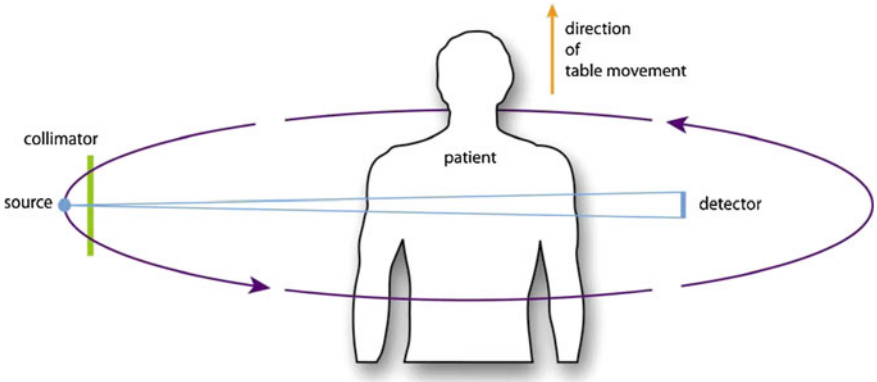

Fig. 2 Schematic drawing of a clinical fan-beam CT scanner. The gantry accommodates an X-ray source, beam collimator, and detector array, which rotate around the patient. The patient lies on a table which can be moved through the gantry during data acquisition

At spiral CT, the projection data are acquired while the patient is moved through the scanner gantry. The ratio of the table translation or table feed per 360° rotation of the X-ray tube and the total width of the detector arrays, is called the pitch value of a spiral scan. The quality of the sampling varies with the pitch. Low pitch spiral scans provide better image quality at the cost of a longer scan time.

Motion of the patient during data acquisition, other than the enforced translation in the z-direction, may lead to inconsistencies in the projection data and to artifacts in the reconstructed images. Therefore, the patient is instructed to lie still and normally to hold his or her breath during data acquisition. This limits the scan time to approximately 30 s. Other motions, for example due to heart beat and vessel pulsation, cannot be suppressed. The influence of these motions can be reduced by using only projection measurements that are made during a particular part of the cardiac cycle in which the motion is minimal (Kachelriess et al. 2000). For this purpose the electrocardiogram (ECG) can be recorded during data acquisition. The temporal resolution of a CT scanner can be defined by the width of the part of the cardiac cycle used for reconstruction. This width is—at the isocenter of the axial plane—equal to half the rotation time. Nowadays, scanners are available with two X-ray tubes instead of one. Each tube acquires half of the data needed for image reconstruction. This way, the temporal resolution is improved by a factor of two for these dual-source CT scanners (Flohr et al. 2006).

Normally, there is virtually no difference in attenuation coefficient between blood and surrounding tissue. Consequently, blood vessels are not visible on CT images. When the vessels have to be visualized, a contrast agent, which increases the attenuation coefficient of blood, is administered intravenously. Most contrast agents contain iodine which has a relatively high atomic number compared to soft tissue and blood.

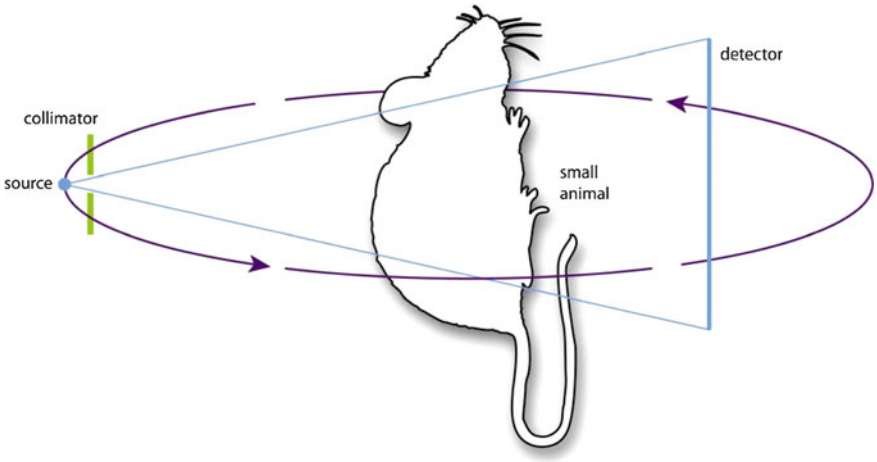

Fig. 3 Schematic drawing of a preclinical cone-beam CT scanner. The gantry accommodates an X-ray source, beam collimator, and detector array, which rotate around the small animal. The cone-beam geometry allows for imaging a relatively large volume without moving the animal during data acquisition

2.1.3 Image Reconstruction

In CT, the attenuation coefficient μ is reconstructed with the aid of the measured intensity of the attenuated X-rays along lines through the human body. Cross-sectional images are generally reconstructed with the filtered backprojection technique (Kak ACaS 1988). Reconstructions are made at a large number of (equidistant) z-positions to obtain a volumetric data set. With the introduction of multi-slice CT, the scanning geometry transformed from fan-beam geometries to cone-beam geometries. The reconstruction algorithms used in fan-beam geometries were not suited for cone-beam geometries. In non-clinical CT, the cone-beam geometry was already more common (Fig. 3) and accompanying reconstruction techniques were developed as well (Paulus et al. 2000). These techniques appeared to be useful in preclinical CT (see below) and later on in multi-slice cone-beam CT as well.

The spatial resolution is primarily determined by the size of the focal spot of the X-ray tube, the dimensions of the detectors, the sampling distance, and the reconstruction kernel used in the filtered backprojection. The choice of this kernel determines the trade-off between the in-plane spatial resolution and the noise level. The relatively sharp filters are mostly used for special purposes, for instance when detail in bony structures is required. They enhance, however, the noise level and may emphasize reconstruction artifacts.

The linear attenuation coefficient μ is not used directly in CT imaging. A value, which represents the attenuation coefficient relative to the attenuation coefficient of water, is used instead. In honor of the inventor of CT this value is specified in Hounsfield units (HU). By definition the CT value of water is 0 HU, and that of air virtually −1000 HU. The maximum CT value on a scanner can be in the order of a

few thousands HU. A transfer function is used to convert these CT values to different shades of gray on a screen. The human observer can only discern a limited number of gray levels. Therefore usually a reduced range of CT values is displayed, which depict only a part of the complete information available in the image. CT values below and above this range are represented by black and white, respectively. The user defined range is specified by the CT values of the level (center of the range) and window (width of the range).

2.1.4 Radiation Dose

Ionizing radiation, including X-rays, is potentially harmful to the human body. To reduce the risk of a CT examination the radiation dose should therefore be "as low as reasonably achievable" (ALARA principle). The possible damage of radiation to the human tissue is in the first place related to the absorbed dose in that tissue. The absorbed dose, in Gray (Gy), is by definition the absorbed energy in Joule (J) per unit of mass (kg). Above a certain threshold for the absorbed dose, ionizing radiation may induce so-called deterministic effects, for example, induction of erythema or cataract. In general, the absorbed dose due to clinical CT examinations is far below this threshold.

Besides deterministic effects the exposure to X-rays may induce stochastic effects, i.e., the induction of cancer, or genetic damage when the reproductive organs are exposed. It is generally assumed that—for a CT examination of a certain part of the human body—the danger of X-rays is proportional to the total amount of energy absorbed in that part of the body. However, the risk for a given absorbed dose is not equal for all organs and tissues. Furthermore, the absorbed dose is not the same for all organs and tissues when a CT scan is made. Therefore an additional quantity, the effective dose, in Sievert (Sv), has been introduced to take these aspects into account. This quantity is a measure for the total damage due to radiation for an average member of a reference population. The effective dose depends on the part of the human body which is scanned, the design of the CT-scanner, and the scanning parameters.

The effective dose of an examination can be translated to an estimated risk to induce cancer. This risk depends on the age of the individual and the part of the human body that is scanned. It is assumed that the absorption of even a small amount of radiation will increase the risk of inducing cancer and genetic defects. It is estimated that an effective dose of 1 mSv corresponds to a risk of the induction of fatal cancer for an average patient of 1:20,000. Generally, the advantages of the information obtained with a CT scan are much greater than the estimated risks, especially for elderly patients.

2.2 Multi-Energy Computed Tomography

CT provides information on the attenuation coefficient μ of a tissue or material via the CT number in Hounsfield Units. Tissue characterization and differentiation are based on differences in attenuation coefficient. Unfortunately, some tissues have virtually

the same attenuation coefficient and cannot be easily discerned. This is for example, the case for iodinated blood vessels and bone tissue. The attenuation coefficient depends on the tissue type, tissue density, but also on the energy of the X-rays.

In multi-energy CT, the energy dependence of the attenuation coefficient is used to discriminate between different tissue types. For this purpose, the X-ray attenuation measurements are performed at different X-ray energies. The measurements should be obtained preferably simultaneously in order to avoid discrepancies between the measurements due to patient or animal movement. Several measurement setups are currently under investigation and available in clinical practice for multi-energy CT. These setups include CT scanners with two X-ray sources operating at different tube voltages (Johnson et al. 2007), CT scanners with an X-ray tube capable of rapidly switching the tube voltage during data acquisition (Kalender et al. 1986), and CT scanners with energy discriminating sandwich detectors (Boll et al. 2008).

In the literature, several (potential) clinical applications of dual-source, dual-energy CT are described. These include the differentiation between iodine and bone in CT angiography (Watanabe et al. 2009), virtual CT colonoscopy approaches (Karcaaltincaba et al. 2009), and for differential diagnosis of adrenal nodules (Gupta et al. 2010). In a preclinical setting, Anderson and colleagues have produced images of mice with the aid of photon-counting detectors that allowed distinguishing between calcium, iodine, and barium (Anderson et al. 2010). They make use of the fact that these materials show a well-defined, up to 10-fold, sharp increase of the attenuation coefficient. This sharp edge in the attenuation profile is called the K-edge and K-edge imaging or K-edge subtraction is one of the advantages of multi-energy imaging.

Which role multi-energy CT will play in the field of molecular imaging in the future has to be observed. In any case, the possibility of this technique to better quantify the density of given materials, contrast agents, and possibly tracers is a valuable contribution to the conventional single-energy CT systems.

2.3 Preclinical Computed Tomography

After the introduction of clinical CT in the 1970s, dedicated imaging of small specimen and animals with CT was introduced in the 1980s (Ritman 2002; Schambach et al. 2010). The principle of preclinical CT is the same as of clinical CT (Fig. 3). The most important difference is the higher spatial resolution required for preclinical CT. Therefore preclinical CT is often also referred to as micro-CT or μCT. The required high resolution has consequences for several components of the scanner. First of all, the X-ray focal spot and the detector elements need to be smaller than that of a clinical CT scanner and the scanner geometry has to be adjusted accordingly. The focal spot size of an X-ray tube in preclinical CT is 1–100 μm, while the focal spot size in clinical CT is typically 300 μm or more. A smaller focal spot size means a better spatial resolution, but it limits the X-ray power that can be applied. With a limited X-ray power, the scanning times can increase considerably to obtain the required image quality, i.e. image noise level.

In state-of-the-art clinical CT, the volume of interest can be scanned within a fraction of a second, while in preclinical CT the scanning time can be reduced to the fraction of a minute, but is in general several minutes long. Preclinical CT-scanners with two X-ray tubes are available which improve the temporal resolution and scan speed by a factor of two like in clinical cardiac CT systems.

The use of ionizing radiation is of concern in preclinical CT as well. In clinical CT, the main focus is on lowering the dose to avoid the long term, stochastic effects. In preclinical CT, the radiation dose is higher. Doses of an imaging series can be in the order of the lethal dose of the animal. Particularly, when one animal is scanned multiple times before being killed, it is important to reduce the dose and assure that the ionizing radiation does not affect the biological processes under investigation (Montet et al. 2007).

Because the size of the animals is much smaller than the patients in clinical CT, the attenuation of the X-rays is much lower. This allows the use of relatively low energies in preclinical CT which has the advantage of a better image contrast when using contrast agents with a high atomic number.

Contrast agents used in clinical CT are less suitable for preclinical CT because in small laboratory animals the contrast agent is largely removed from the blood by the kidneys before the data acquisition can be finished. Therefore, new contrast agents have been developed which act as a blood pool agent with a higher blood-pool half-life and allow for longer acquisition times. Iodinated liposomes proved to be suitable for this purpose. Liposomes are spherical vesicles with a diameter of 100–400 nm (see also further below and Fig. 14). This size limits the passage of the liposomes across the vascular walls. The aqueous core of the liposome can be filled with iodine. Montet et al., for example, have shown that iodinated liposomes are a suitable contrast agent for improved visualization of vessels and hepatic tumors in micro-CT (Montet et al. 2007).

2.4 Dedicated Imaging Systems and New Developments

High resolution or micro-CT imaging systems are mainly used in preclinical research. Although in clinical applications this high resolution is desired as well, it is not generally available because the radiation dose needed for diagnostic image quality at high spatial resolutions would be too high. Moreover, practical considerations like scan time limitations and larger focal spot sizes needed to penetrate the patient play a role. Nevertheless, dedicated high resolution systems are being developed for specific imaging purposes. A good example is the development of a dedicated breast CT scanner. For a breast CT examination, the patients are laid prone with the breast pendant through the table aperture. Each breast is scanned individually and without compression during a breath hold. The X-ray source and the flat-panel detector rotate in the horizontal plane 360° around the patient's breast. High resolution breast CT imaging is expected to improve the sensitivity and specificity of breast cancer screening and diagnosis because it provides the radiologist with 3D cross-sectional images whereas conventional 2D

mammograms of the breast suffer from overprojecting tissue, especially in dense breasts (Lindfors et al. 2008). In radionuclide imaging, improved breast cancer-specific probes are being actively developed. Therefore this field is likely to expand with selective targeting probes that are overexpressed in particular types of breast cancer cells. Since high resolution breast CT is now available, the development of micro-CT probes that target specific molecular changes associated with breast cancer formation is an opportunity for clinical success as well.

Apart from the K-edge subtraction technique mentioned above, other contrast enhancing mechanisms are currently investigated that might result in the development of new molecular imaging techniques using ionizing radiation. These mechanisms include X-ray phase delay, X-ray scatter, X-ray diffraction, and X-ray fluorescence (Ritman 2002). One should realize that imaging techniques based on these mechanisms have been investigated yet in very controlled experimental situations only and that much technological development is needed to make these techniques available for preclinical and clinical CT.

2.5 Multimodality Imaging

X-ray CT by itself is not yet used as a molecular imaging technique in routine clinical practice. It is, however, routinely combined with molecular imaging techniques like single photon emission computed tomography (SPECT) and positron emission tomography (PET) which are covered in detail in subsequent chapters. The integration of an X-ray CT scanner with a SPECT or PET scanner allows for a virtually simultaneous acquisition of detailed anatomical and functional information (Townsend 2008). Moreover, the 3D distribution of the attenuation coefficient μ obtained with CT can be used in the reconstruction of the SPECT and PET images for the correction of the attenuation of the gamma rays originating from the radioactive tracer inside the patient or animal. Still in experimental or developmental stages the use of hybrid systems combining optical imaging techniques with CT are also being explored (Yang et al. 2010).

3 Recent Technological Developments in Magnetic Resonance Imaging of Cancer

3.1 Magnetic Resonance Imaging: Introduction

The ability to view deep within the body without actually cutting it open is a tool of immense importance in medical and biological research. Techniques such as confocal and multi-photon fluorescent microscopy, which allow the researcher to locate fluorescent molecules up to several millimeters deep, have greatly increased our knowledge in a multitude of scientific fields. Yet these techniques only enable the researcher to see labels, not the surrounding structures.

Nuclear Magnetic Resonance, abbreviated NMR, was observed and characterized independently by the groups led by the two Nobel Prize recipients Bloch and Purcell in 1946 (Bloch 1946; Purcell and Pound 1946). Since then, NMR has been used extensively as an analytical tool in Physics and Chemistry for spectral analysis (magnetic resonance spectroscopy, MRS) and the characterization of chemical compounds. NMR techniques have also been exploited to monitor metabolic reactions and have been widely used to elucidate the complex structure of organic molecules.

NMR was introduced in the medical field in the late 1970s, under the name Magnetic Resonance Imaging (MRI). Since then, MRI has provided one of the most exciting imaging techniques and research tools for studying the anatomy and physiology of living tissue.

MRI is based on imaging of hydrogen atoms. Given the natural abundance of water in the body (approximately 70 % of total body weight), it is possible to obtain morphological images with high spatial resolution and with exquisite contrast difference using the diverse magnetization properties of the imaged tissues (intrinsic or modified by the use of contrast agents). On the other hand, MRI can look at more than just the water signal: all nuclei that have an odd number of protons in its core have the properties of magnetic resonance. Therefore, MRI can be tuned to obtain the distribution of other nuclei that are relevant for molecular imaging cancer research such as sodium (^{23}Na) and phosphorus (^{31}P) (Gillies and Morse 2005).

In the past decade, MRI has grown exponentially in the clinical field with a large installation base worldwide. The present generation of MRI systems, while allowing noninvasive, non-harmful examinations, offers the combination of near-cellular (5–40 μm) resolutions and whole-body imaging capabilities to obtain information regarding tissue anatomy and relevant functional information (e.g. perfusion, diffusion, tracer uptake/clearance, and neuronal activation). Some of the basic principles and technological innovations of MRI are highlighted in the following sections.

3.2 MRI Signal Formation and Contrast

The strength of the NMR signal (the magnetization, Mo) is dependent on the polarizing main magnetic field Bo (Fig. 4). Under influence of a magnetic field the nuclear moments of atomic nuclei align themselves along the magnetic field. To generate an NMR signal from the polarized nuclei it is necessary to irradiate or provide energy in the form of a radio-frequency excitation (RF) tuned at the precise frequency of the atomic nucleus of interest. This frequency ωo, the resonance frequency, bears a linear relation with the magnetic field applied (Bo) and the gyromagnetic ratio (γ) of the imaged nuclei (Table 1). The resonance frequency, better known as the Larmor frequency, is given by the relation $\omega o = \gamma$ Bo.

After cessation of RF excitation the disturbed magnetization of the excited nuclei returns back to its equilibrium condition (Fig. 5). Interactions between the protons and the surrounding media (lattice) and between protons themselves (spins) cause the absorbed energy to be dissipated in the lattice.

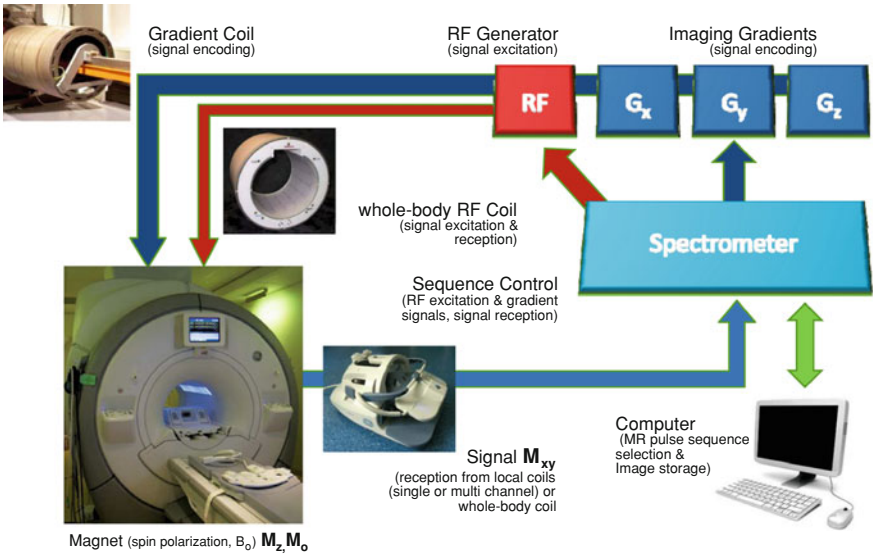

Fig. 4 Diagram of a MRI scanner. The magnet at a field strength Bo provides the spin polarization Mo (or Mz) of protons in the sample. The computer, storing all the MR sequence pulse programs instructs the spectrometer to command the radio frequency excitation (RF) and the imaging gradients for signal selection and image encoding, respectively. A whole-body coil (surrounding the sample) is used for RF excitation (or signal reception, in some cases) to produce the transverse magnetization signal (Mxy) that will be encoded by the same coil or by a local (single or multi-channel coil). The imaging gradient coils (Gx, Gy, Gz), surrounding the sample, provides the magnetic field gradients necessary to provide the spatial encoding of the signal. The computer reconstructs and displays the images after the MR pulse sequence finalizes the measurement

Table 1 Larmor frequency at different magnetic field strengths for hydrogen nuclei

Resonance frequency at various magnetic field strengths for hydrogen nuclei	
Magnet strength B_o (Tesla, T)	Resonance frequency (MHz) $\omega_o = \gamma B_o$ $\gamma = 42.58$ MHz/T
1.5	63.87
3.0	127.74
7.0	298.06
9.4	383.22

The rate at which energy is dissipated in the lattice is characterized by the T1 or spin–lattice relaxation time while T2, or spin–spin relaxation time, governs the disappearance of the transverse magnetization. This emitted energy is the signal

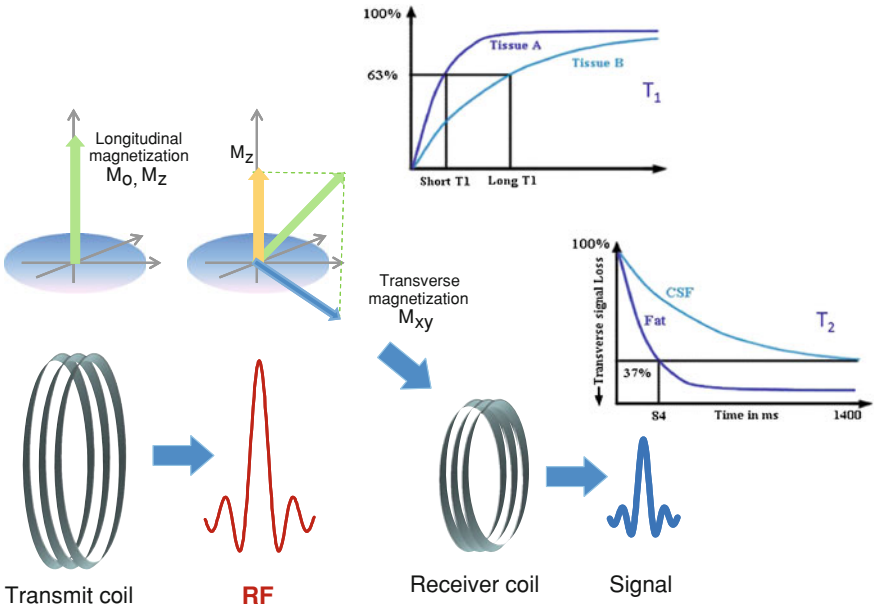

Fig. 5 A transmit coil produces a RF excitation that tilts the magnetization M_o from its equilibrium condition. Part of this magnetization, M_{xy}, the one that can be picked up by a receiver coil is the signal that encodes the final image. After the RF excitation, the signal M_{xy} decays according to the T_2 relaxation constant. In the meanwhile, the magnetization M_z recovers to its equilibrium condition M_o with a time constant T_1

that is received by the MRI equipment using a signal receive coil tuned at the Larmor frequency.

The contrast capabilities of MRI are mainly defined by the proton density and two relaxation times T1 and T2, of the imaged tissues (Figs. 6 and 7). Through MRI pulse sequences contrast characteristics, based on these parameters, can be controlled by changing the timing between the RF irradiation and the time the NMR signal is read during an MRI experiment. Many other mechanisms can provide contrast in biological tissues, such as water diffusion, flow or motion, magnetic field inhomogeneities, and magnetization transfer contrast to better differentiate various tissue types. When magnetic field inhomogeneities are present the decay of the NMR signal is modified, shortening the T2 relaxation time. In these cases, an effective relaxation T2* then dominates the image contrast. This mechanism has been exploited intensively in MRI for molecular imaging applications to provide hypointense signals for cells and tissues.

In the ambit of molecular imaging, in order to fully use the capabilities of MRI it is necessary to have molecular probes and imaging reporter genes that use paramagnetic and superparamagnetic agents (Gd or iron oxide-based constructs) that can dramatically change the T1 and T2 relaxation times of the NMR signal when activated selectively or in response to specific biological events. These types

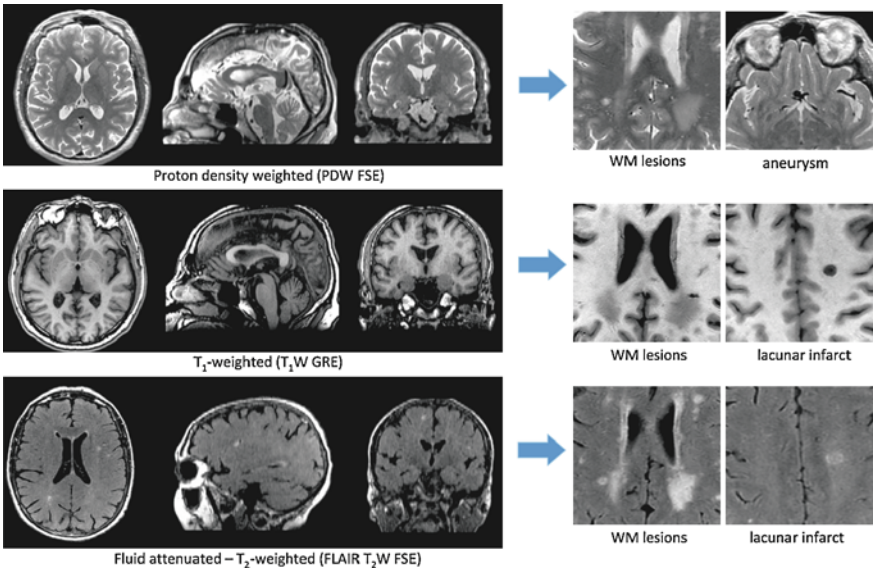

Fig. 6 Contrast capabilities of MRI. Using mainly the proton density and the T_1 and T_2 relaxation times of tissues, it is possible to define an optimal contrast for tissue differentiation. This figure illustrates the volumetric capabilities of MRI and some of the contrast possibilities in the brain of patients with degenerative brain diseases (e.g. dementia, white matter disease). The three panels demonstrate a proton density weighted (PDW), a T_1-weighted and a fluid attenuated T_2-weighted acquisition. On the right side, it is possible to appreciate the different contrasts achieved for white matter (WM) lesion differentiation from healthy WM). FSE refers to fast spin echo and GRE to gradient recalled echo MR pulse sequences used for the acquisition

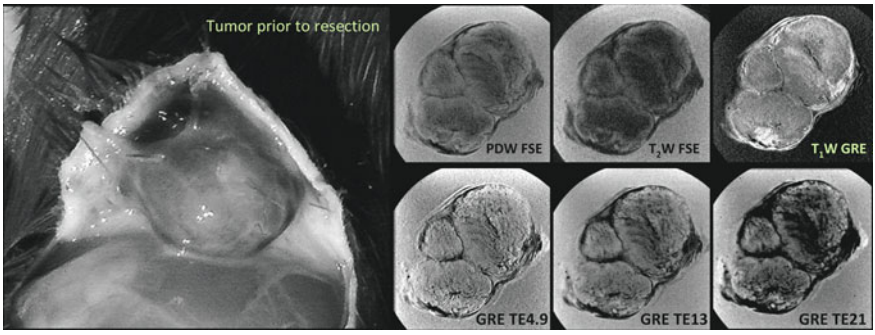

Fig. 7 For cancer research, it is useful to count on a combination of MR pulse sequences and imaging parameters to study different compartments in tumors. The panels show different acquisitions performed on a tumor implanted in a rat limb: a proton density weighted (PDW) fast spin echo (FSE), a more T_2-weighted (T_2W) version, a T_1-weighted (T_1W) gradient recalled acquisition (GRE). To enhance the magnetic susceptibility effects of blood components, it is possible to use a GRE scan with variations in the echo time (TE) to provide more or less weighting (darker structures visualized). The brighter spots in the T_1W GRE scan are correlated with methemoglobin (hemorrhage, blood denaturalization)

Table 2 Comparison of the output of MRI systems of various magnetic field strengths

A comparison of the output of MRI systems of various magnetic field strengths		
Magnet Strength (T, Tesla)	Resolution at a fixed scan time	Scan time at a fixed resolution
1.5	100 μm × 100 μm	3 h
3.0	70 μm × 70 μm	45 min
9.4	40 μm × 40 μm	5 min

of probes are currently being developed and are becoming commercially available in an ever-increasing variety (see further in this chapter).

3.3 Magnetic Field Strength and Signal Sensitivity

Nuclei polarize under any magnetic field strength to provide an effective magnetization in the direction of the applied magnetic field. However, the spatial resolution that can be achieved in a specific measurement time for MRI or MRS depends on the strength of the magnetization achieved. Usually, it is assumed that the strength of the signal received has a linear dependence on the magnetic field strength applied. Table 2 illustrates a comparison on how spatial resolution or imaging times are influenced by the choice of the magnetic field strength, given that the same reception hardware is utilized.

For MRS, not only the spatial resolution but also the spectral resolution of MRS increases with the strength of the magnet. At present, the sensitivity of MRI at molecular levels is less than that of techniques based on radioactive tracers and optical luminescence. Nonetheless, its versatility, the numerous contrast mechanisms and the possibilities for future signal amplification strategies are enormous in comparison, making it possible to build a integrated spectrum of information regarding a particular disease process.

3.4 Imaging Gradients, Signal Encoding, and Signal Reception Chain

The linearity of the Larmor equation has been used extensively to enable spatial encoding of the NMR signal. Spatial encoding is performed using changing magnetic field gradients (known as imaging gradients) that are superimposed over the main magnetic field Bo in order to produce a frequency dispersion that translates into a different resonance frequency at each location in an object, through which the origin of a received signal can be identified (Fig. 4). The larger the frequency dispersion created, the higher the spatial resolution that can be

achieved. These imaging gradients are used in what is known as the MRI pulse sequence and are executed in a specific order during the RF excitation and during the readout to encode the spatial distribution of protons in the imaging volume.

Developments in MRI hardware, specifically the performance of the imaging gradients and receiver hardware, have made it possible to dramatically improve the quality of two-dimensional (2D) and three-dimensional (3D) MRI for molecular imaging protocols. The enhancement in the strength and speed of the imaging gradients provides faster encoding with improved spatial resolution. By today's standards, the imaging gradient subsystem can be regarded as the most influential component of an MRI scanner to produce images with high spatial resolution and large volume coverage. Contemporary clinical MRI units have been equipped with imaging gradients with stronger peak gradient amplitudes (> 30 mT/m) and faster rise times (100–200 mT/m/ms) that enable high quality images. More so, for translational research where molecular imaging protocols in conjunction with MR sensitive probes are developed in animals, newer imaging gradients (e.g. 300 mT/m with rise times > 1000 mT/m/ms) can provide resolutions that are adequate for near-cellular resolution and beyond. Accordingly, the higher resolution is accompanied with large numbers of reception channels to provide higher SNR and decreased acquisition speed. On the signal reception hardware side, the incorporation of increasing numbers of signal reception channels (coils combined in a phased-array configuration) has provided a several-fold improvement in signal-to-noise ratio (SNR) with large field-of-view (FOV) capabilities (Hayes et al. 1991). Both features combined make it possible to reduce imaging time dramatically for highly resolved morphological imaging.

The long standing standard for volume acquisitions in MRI experiments has been a volume coil resonator to provide homogeneous signal reception in the volume of interest. Therefore, at high spatial resolution the only remedy in the past to provide good image quality was to use a stronger main magnetic field Bo (a costly solution) or to make use of multiple excitations (averaging), translating into longer imaging times and more data corruption from physiologic effects. Multi-channel receiver coils have provided a valuable alternative, promoting the use of many MRI sequences to produce different contrasts and encouraging the use of T1, T2, and T2* parametric mapping to produce more quantitative data in more reasonable scanning times. A new technology called parallel imaging can shorten the acquisition speeds by encoding the signal with less RF excitations and using the spatial distribution of the coils in the phased array configuration to reconstruct the missing data; however, generally at the cost of SNR (Heidemann et al. 2003; Blaimer et al. 2004). This has been used extensively in clinical MRI in the past few years but its incorporation into animal MRI scanners has been more recent providing increased benefits for new imaging scenarios for molecular imaging and translational research.

3.5 MRI Pulse Sequences, Parametric Mapping

A receiver coil acquires the MR signal (transverse magnetization) after the protons in tissue are perturbed by a RF excitation. This transverse magnetization can be read either in the form of a spin echo (SE) or a gradient echo (GE). For a simple SE readout, a 90° RF excitation converts all the available magnetization aligned along the main magnetic field (the longitudinal magnetization) to transverse magnetization and is immediately followed by a 180° RF refocusing pulse to produce a spin echo that is read by a signal reception coil (Fig. 8a). A gradient echo readout can collect the MR signal after the application of the 90° RF excitation but it requires that a bipolar readout imaging gradient can be applied to dephase and consequently rephase the transverse magnetization to form an echo (Fig. 8b). SE or GE readouts provide the basis for all the different MRI pulse sequences available. The choice for a particular readout depends on the required contrast and the sensitivity to magnetic field inhomogeneities (e.g. using T2*-weighted with GE scans).

In conventional SE imaging, proton-density, T1- and T2-weighted images are acquired by setting a specific repetition time (TR) and echo time (TE). Proton-density weighting may be acquired by using long TR and short TE. T2 weighting is adjusted by lengthening TE. Intermediate values of TR with short TE produce T1-weighted images. Imaging techniques using GE readouts can modify the RF excitation or flip angle ($\leq 90°$, partial flip angle imaging) to produce optimal signal strength for a specific tissue at a fixed TR value. The flexibility of GE techniques to use partial flip angles provides the possibility to acquire proton density-, T1-, T2-, T2*- and T1/T2-weighted images with short TR settings for faster acquisitions. SE readout variants, referred to as fast SE, make them competitive to GE scans for faster scanning yet with excellent SNR and devoid of magnetic susceptibility weighting. Fast SE techniques make use of multiple refocusing 180° RF pulses after the initial 90° RF excitation to read the signal, making the acquisition more compact and efficient.

Molecular imaging can benefit immensely from using parametric mapping by providing a more quantitative evaluation of tissue properties, e,g, in the relaxation times, especially for longitudinal studies (Baudrexel et al. 2010; Tsien et al. 2010; Yao et al. 2009). Parametric mapping can provide better accuracy in the evaluation of changes as a result of treatment or quantify density parameters of imaging labels that have been incorporated in tissues or cells (e.g. tracking cell density of iron-oxide labeled cells through T2 and T2* effects). Parametric mapping can eliminate the need for coil sensitivity corrections and also the a priori knowledge of the relaxivity effect that contrast material will induce on tissues. Once tissue properties are determined accurately, it is possible to reconstruct synthetically an image with the best contrast possibilities to permit greater tissue differentiation (Deoni et al. 2005, 2008; Warntjes et al. 2007, 2008). In the simplest form of mapping, proton density, T1, and T2 information can be computed directly by acquiring several imaging experiments with changes in TR and TE using SE cans. For T2* mapping, TE is changed using GE techniques.

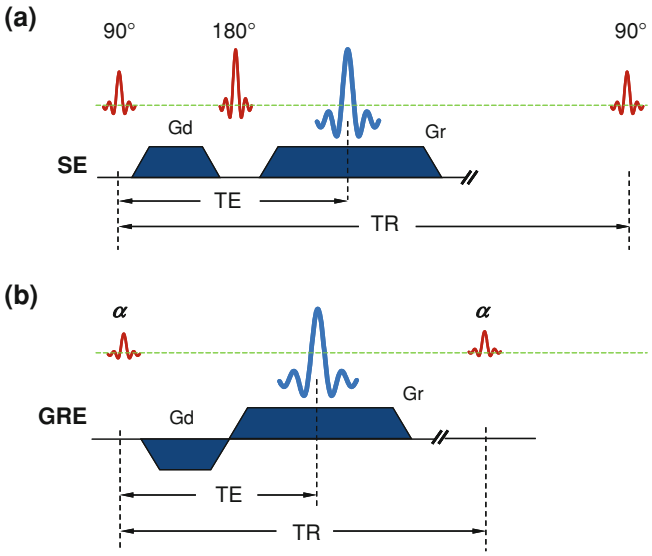

Fig. 8 Proton-density, T_1- and T_2- (and T_2*-) weighted images are acquired by setting a specific repetition time (TR), echo time (TE), RF flip angle α, and the imaging encoding technique: spin-echo (SE) or gradient recalled echo (GRE) readouts. For a SE readout, a 90° RF excitation tips the magnetization M_z to transverse magnetization M_{xy} and is immediately followed by a 180° RF refocusing pulse to produce a spin echo. A positive dephaser gradient (G_d) is applied prior to a 180° RF refocusing pulse and subsequently, a positive rephaser (G_r) is used to spatially encode the signal received. GRE readouts can modify the RF excitation or flip angle ($\leq$ 90°, partial flip angle imaging α and no refocusing 180° RF pulse) to produce optimal signal strength for a specific tissue at a fixed TR value. The signal is produced with opposite polarities of G_d and G_r and no refocusing 180° RF pulse. The flexibility of GRE techniques to use partial flip angles provides the possibility to acquire proton density-, T_1-, T_2-, T_2* -and T_1/T_2-weighted images with short TR settings for faster acquisitions. SE readout variants, referred to as fast SE (FSE), make them competitive to GRE scans for faster scanning yet devoid of magnetic susceptibility weighting. Fast SE techniques make use of multiple refocusing 180° RF pulses after the initial 90° RF excitation to read the signal, making the acquisition more compact and efficient

In cancer research, the combination of more functional parameters besides mapping the inherent T1 and T2 relaxation times, such as maps derived from MRS imaging, diffusion weighted imaging (DWI), and contrast enhanced MRI (CE MRI), especially at higher field strengths, can provide a more precise assessment of the tumor environment and (Kurhanewicz et al. 2008).

3.6 Contrast-Enhanced MRI

In addition to the contrast mechanisms described in the previous sections, tissue contrast can be further manipulated through the use of MRI contrast agents. Based on their contrast effects, MRI contrast agents can be subdivided in so-called T1

and T2 contrast agents. T1 contrast agents are agents that predominantly shorten T1 and T2 contrast agents predominantly shorten T2. With most pulse sequences shortening of T1 results in increases in signal intensity, while shortening of T2 results in reduction of signal intensity, therefore T1 and T2 contrast agents are often also referred to as positive contrast agents and negative contrast agents, respectively. The most prominent examples of T1-agents are paramagnetic gadolinium and manganese-based contrast agents and superparamagnetic iron oxide particles are the most prominent examples of T2 contrast agents. Some more detailed descriptions of MRI contrast agents and recent developments in the use of MRI contrast agents can be found further in this chapter.

4 Imaging Biomarkers in Cancer

4.1 Imaging Biomarkers: X-ray Computed Tomography

The main application of X-ray CT is the detailed depiction of anatomical structures in 3D. In cancer diagnostics, location, size, and specific attenuation values of a lesion before and after contrast are used as diagnostic and prognostic indicators (Lee et al. 2008; Dighe et al. 2008; Forstner 2007). Apart from these structural biomarkers, functional biomarkers are available. The enhancement of a lesion after administration of a contrast agent as a function of time is such a functional biomarker. The corresponding perfusion parameters such as relative blood volume provide physiological correlates for the microscopic changes that occur with tumor angiogenesis (Miles 2002). The measurements can be used to assess the tumor response to drug therapy or to discriminate benign and malignant lesions (Miles 2006).

The biomarkers mentioned above, do not depict processes on a molecular or cellular level. The iodinated contrast agent used in clinical CT contains molecules which are nonspecifically targeted since they cannot be conjugated to most biological components or cancer markers. Moreover, they allow only very short imaging times due to rapid clearance by the kidneys. In preclinical CT, this problem has been solved by the introduction of contrast agents with a higher blood-pool half-life.

First results of molecular imaging biomarkers are presented in the literature for preclinical CT. Wyss et al. showed that the use of a specific molecular contrast agent is able to detect specific molecular markers on activated vessel walls in vivo (Wyss et al. 2009). The contrast agent used consisted of liposomes filled with iodine. Into the membrane of the liposomes a specific targeting moiety was inserted to detect activated endothelial cells with micro-CT. It has been demonstrated in an in vitro study that targeted gold nanoparticles enable molecular CT imaging of head and neck cancer cells (Popovtzer et al. 2008). As gold has a higher atomic number and electron density than iodine, the attenuation coefficient of gold-labeled tracers can be higher than that of iodine-labeled tracers. A higher attenuation coefficient of the label will improve its detectability for a given concentration of the imaging probe.

The major challenge of molecular imaging with CT is to make it more sensitive for small differences in image probe concentrations. This might be achieved by the development of new, highly attenuating imaging probes, or by the development of new X-ray imaging techniques that are not based on the differences in linear attenuation coefficient for the generation of image contrast.

In the future, improved sensitivity of X-ray CT and development of new imaging tracers might result in a more pronounced and independent role of CT in molecular imaging in oncology.

4.2 Imaging Biomarkers: Magnetic Resonance Imaging

Given the wide spectra of questions that may be tackled with MRI, many answers can be found that provide a more complete understanding of the biological processes of interest. In the scope of oncological studies, noninvasive imaging using MRI can promote a greater understanding and provide a unique opportunity to explore a wide variety of scientific questions from macro to molecular levels. To study the tumor microenvironment (TME) and its response to therapy, it is possible to use several biomarkers that can be measured effectively using MRI. These include:

- Angiogenesis and vascular distribution (high resolution MR angiography, MRA)
- Perfusion (dynamic contrast enhancement studies, DCE MRI)
- Oxygenation levels (hypoxia levels using T2*-weighted imaging protocols)
- Diffusion imaging (restriction of movement of water molecules in the extracellular matrix; diffusion weighted imaging, DWI)
- Extracellular pH and hypoxia
- Sodium (intracellular and extracellular concentrations)
- Metabolite concentration (using MRS, e.g. quantifying ratios between choline and citrate concentrations in tumors)

Likewise, tumor monitoring (progression and treatment) can be performed by noninvasively tracking the movement of stromal cells (fibroblasts, immune cells, stem cells, or endothelial progenitor cells in tumors) that have been adequately labeled with an MRI-sensitive contrast agent.

4.2.1 Angiography and Angiogenesis (MRA)

Studies on vascular development and its stimulation or inhibition has become a major field of research in the diagnosis and treatment of cancer. Manipulation of the pathophysiology of a tumor (its vasculature), the inhibition of new vessel formation and the destruction of the tumor associated vasculature can be studied effectively with high resolution vascular MRI (magnetic resonance angiography, MRA) (van Vliet et al. 2005). To provide consistent image quality, contrast agents are usually injected to produce a contrast-enhanced MRA (CE MRA; Figs. 9 and 10). The contrast typically used is Gd-based to provide shortening of T1-

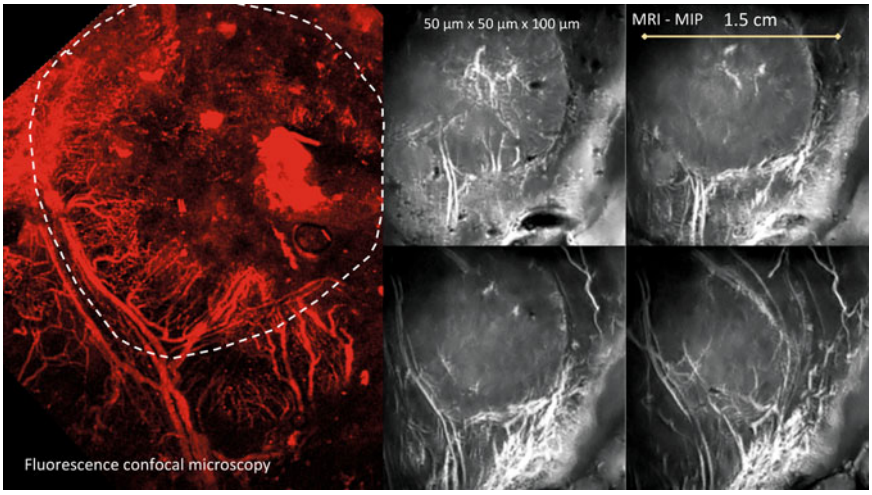

Fig. 9 Magnetic resonance angiography (MRA). A folded skin window model with a BN tumor implanted on a rat was imaged at 8 days post tumor implantation using fluorescence confocal microscopy and MRI. To visualize in vivo the tumor vascular network using MRI, an intravascular contrast agent was used. The MRI panels show thin slice maximum intensity projections (MIP) at four different positions to illustrate the three-dimensionality of the acquisition and the spatial resolution that can be achieved (voxel size of 50 µm× 50 µm× 100 µm) that makes it suitable for comparison to the microscopy image. Acquisition performed at 3.0T using a 3D T_1-weighted GRE technique and a 10 mm surface receiver loop

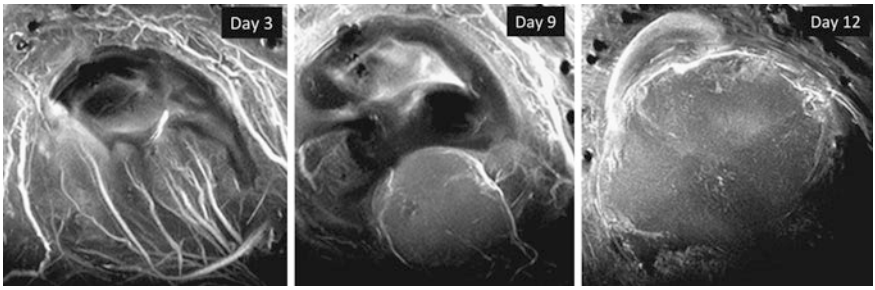

Fig. 10 Another folded skin window model example showing the noninvasive, in vitro longitudinal tracking possibilities with MRI/MRA. The BN tumor vascular network evolution was visualized for several days after tumor implantation. The panels show a MIP from acquisitions performed at days 3, 9, and 12 (voxel size of 80 µm × 80 µm × 100 µm). Acquisition performed at 3.0T using an intravascular contrast agent and a 3D T_1-weighted GRE technique and a 20 mm surface receiver loop

relaxation times and generate high positive contrast between blood vessels and surrounding tissues and therefore, T1-weighted MR sequences are used for acquiring the data. The quantification of tumor vascular morphology is still being researched (Fink et al. 2003).

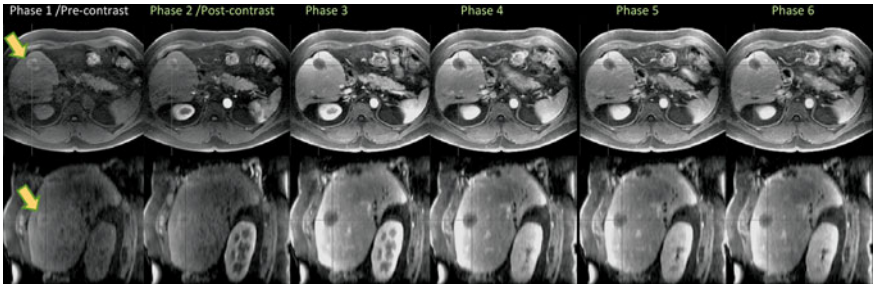

Fig. 11 Contrast-enhanced (CE) MRI. Tissue perfusion can be performed using repeatedly a 3D fat-suppressed T_1-weighted GRE technique after the injection of Gd-DTPA as the enhancement medium. The panels demonstrate both the original axial and the reformatted sagittal views from the MRI perfusion study (Phase 1, pre-contrast, phase 2-6 post-contrast) of a patient that had an intrahepatic cholangiocarcinoma (*arrows*) successfully removed with a RF ablation procedure. Acquisition performed at 1.5T with breath-hold acquisitions of 15 s over a 2 min period and an 8-channel torso coil

4.2.2 Perfusion (DCE MRI)

More detailed and quantitative approaches to dynamic contrast-enhanced (DCE) MRI have been increasingly used to examine tumor perfusion and capillary permeability as an indicator of tumor angiogenesis (Fig. 11). DCE MRI is based on changes in signal intensity in the tumor following injection of contrast material. Functional parameters, such as relative blood volume, perfusion, and vessel permeability can be assessed using T1- and T2*-weighted DCE-MRI. Since antiangiogenic and antivascular agents affect tumor blood vessels, DCE MRI has been employed in numerous trials to monitor the efficacy of these agents (O'Connor et al. 2007). DCE MRI has also been used for the therapeutic evaluation of radiotherapy (Zahra et al. 2007) as tumor perfusion and oxygenation status influence the efficacy of radiotherapy. DCE MRI-derived parameters are also being studied for their ability to predict the delivery of anticancer agents in the interstitium of the tumor (Artemov et al. 2001; van Laarhoven et al. 2007). On a voxel-based level, a significant correlation between presence of MRI contrast agent and drug delivery was found (Artemov et al. 2001). Correlation with histopathology showed the ability of DCE MRI parameters to monitor treatment response by identifying areas of residual viable tumor tissue in, for example, osteosarcoma (Dyke et al. 2003) and soft tissue sarcoma (van Rijswijk et al. 2003).

Different methods are used to quantify DCE MRI scans. Per region of interest, the enhancement of the MR signal over time is quantified. The curves can be described by empirical semi-quantitative parameters, such as the maximal enhancement or the amount of time required for maximal enhancement, or the initial area under the curve. It has been shown that these empirical parameters to some extent correlate with malignancy (Erlemann et al. 1990; Kaiser and Zeitler 1989; Liu et al. 1998). These parameters are relatively simple to calculate. Their clinical value, however, may be limited by the lack of calibration procedures. The

value of these parameters depends on the MRI sequence and the scanner used (Padhani 2002). Therefore, results obtained with different scanners or scanning protocols cannot be compared unless a reliable calibration procedure is used. A further disadvantage of such heuristic parameters is that their correlation with underlying tumor physiology and contrast agent kinetics is not clear.

To overcome these problems, pharmacokinetic models have been introduced in order to quantify the underlying (patho-) physiologic parameters. Different models are described, but generally a two-compartment model, consisting of a vascular and an extracellular/extravascular compartment, is used. The transfer rates of contrast agent between the two compartments and the volumes of the compartments are the key parameters of these models (Brix et al. 1991; Padhani 2002; Tofts et al. 1999).

4.2.3 Blood Oxygenation Level-Dependent Imaging

Aggressive tumors tend to have rapidly growing vasculature and many microhemorrhages. The development of susceptibility-weighted imaging (SWI) or blood oxygenation level-dependent (BOLD) MRI has opened the door for improved contrast in tumor microvasculature and improved detection of hemorrhage, especially at higher magnetic field strengths. The enhanced sensitivity of SWI to blood products leads to better contrast in detecting tumor boundaries and tumor hemorrhage independent of contrast agents. The primary source of contrast is endogenous, paramagnetic deoxyhemoglobin, which decreases the MR transverse relaxation time (T2*) of water in blood and surrounding tissues. With SWI techniques, occult tumors can be detected that do not show on a T1-weighted Gd-DTPA postcontrast scan.

BOLD MRI is also sensitive to oxygen partial pressure (pO_2) in tissues adjacent to perfused vessels. It has been used in revascularization studies in the heart, kidney and brain, and in tumor hypoxia studies of resistance to treatment (Padhani 2005, 2007). SWI or BOLD MRI thus provides information on microvasculature function.

4.2.4 Diffusion Weighted Imaging

In order to develop and optimize a treatment strategy for cancer therapy, quantitative, reproducible, and noninvasive functional parameter determination for the modes of action of specific therapy scenarios are required. New technological developments in Molecular Imaging, such as the characterization of diffusion in tissues allow for the assessment of the microenvironment of a tumor. These techniques are based on assessment of the motility or diffusion of water molecules in intra and extracellular spaces through the use of diffusion weighted imaging (DWI). DWI has been identified as a potential and completely noninvasive and fast MRI methodology for the detection and staging of tumors and the evaluation of therapy.

Water mobility is dependent on both the relative volume of intra- and extracellular spaces and cellular membrane integrity and permeability (Lee et al. 2007). In tumors, quantitative diffusion values are strongly affected by tissue cellularity and extracellular volume (Fig. 12). Recently, DWI has been used as an early response

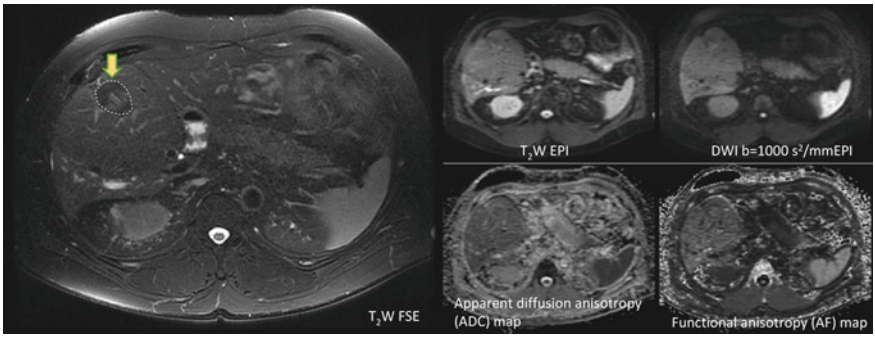

Fig. 12 Diffusion weighted (DWI) MRI. The same patient as in Fig. 11 with a RF-ablated intrahepatic collangiocarcinoma was imaged with a diffusion weighted b-factor of 600 mm^2/s. The left panel shows a respiratory gated 2D T_2-weighted fat-suppressed FSE acquisition. The right panels demonstrate a respiratory gated T_2-weighted echo planar imaging (EPI) acquisition ($b = 0$ mm^2/s) and corresponding isotropic $b = 600$ mm^2/s measurement. The panels below illustrate both the apparent diffusion coefficient (ADC) and the fractional anisotropy (FA) maps. The diffusion values in the ablated tumor shows a successful elimination of tumorous tissue. Acquisition performed at 1.5T using an 8-channel torso coil

parameter in cancer treatment: Treatment-induced loss of tumor cell integrity will result in a local increase in water diffusion, which can be quantified by DWI. Such effects probably occur before macroscopic changes in mass, size, or morphology as removal of cellular debris occurs relatively slowly. Indeed, in preclinical studies, treatment responses could be qualitatively assessed with DWI as early as two days post therapy (Hayashida et al. 2006; Galban et al. 2010; Kharuzhyk et al. 2010). In competition with nuclear medicine (PET and SPECT), a recent concept has received a lot of attention in the medical community: whole-body diffusion imaging for diagnosis and therapy follow-up. Without the need of radioactive tracers and with better spatial resolution and coregistration with high resolution morphological imaging it is possible to provide a high degree of detection sensitivity for tumors and metastatic processes (Fischer et al. 2010; Lin et al. 2010).

4.2.5 Intracellular and Extracellular Sodium Concentrations

Cancer cells have unusually high sodium content. Similarly to mapping ^{1}H diffusion values in tumors, sodium concentration mapping determined by ^{23}Na MRI, can provide dynamic and spatial changes after therapeutic intervention in tumors and could be considered a complementary technique, potentially even more sensitive to subtle changes in tumors (Schepkin et al. 2006). For some time, it was difficult to differentiate intracellular from extracellular sodium unless specific shift reagents were used that remained exclusively extracellular but nonetheless toxic. The Triple Quantum Filtered (TQF) ^{23}Na MRI technique has been proposed as a potential way to monitor alteration of intracellular sodium without the use of shift reagents (Schepkin et al. 1998).

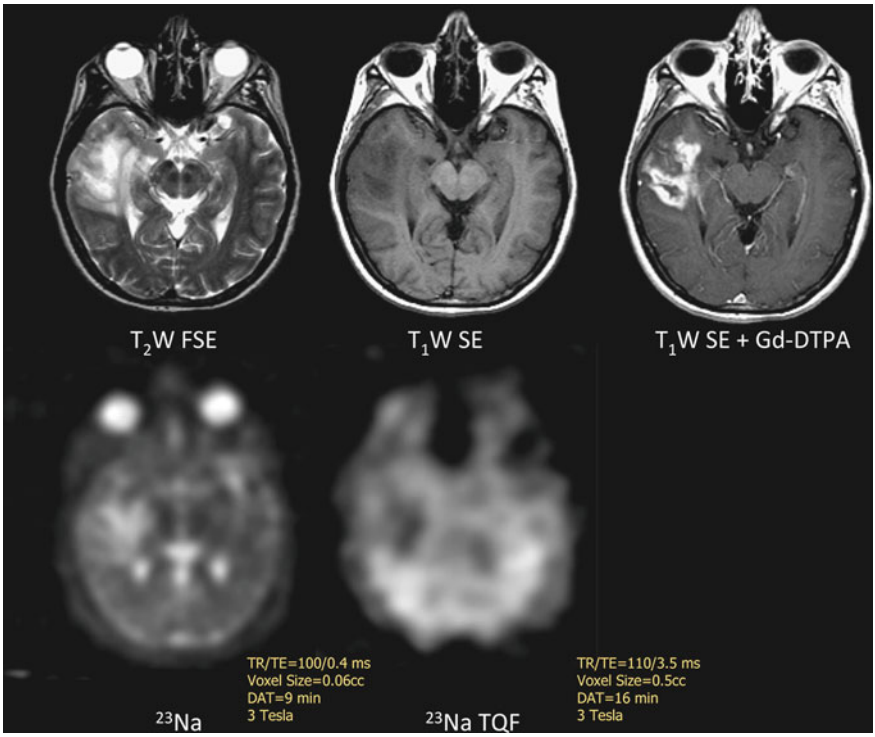

Fig. 13 Sodium (^{23}Na) MRI. ^{23}Na MRI can provide similar dynamic and spatial changes after therapeutic intervention in tumors. Here, a patient with a tumor on the left side of the brain was imaged with a T_2-weighted FSE and pre- and post-contrast acquisition of a T_1-weighted SE scan (enhancement only happens in regions where there is a disruption of the brain–blood barrier, thus showing more clearly the tumor). The triple quantum filtered (TQF) ^{23}Na acquisition permits to monitor the intracellular Na concentration but at much lower resolution (larger voxels) as compared to a ^{23}Na image (which looks similar to a T2-weighted scan). Acquisition performed at 3.0T using a double tuned proton-sodium head coil. Image courtesy of Dr. Fernando Boada (University of Pittsburg, USA)

^{23}Na has much lower spatial resolution than ^{1}H DWI imaging mainly related to the difference in abundance between sodium and proton ions in the body. Nonetheless, clinical systems with higher field strengths ($\geq$ 3T) are providing encouraging results with shorter acquisition times and good spatial resolution (Boada et al. 2004; Qian et al. 2009) (Fig. 13). ^{23}Na measurements are quantitatively more robust in the presence of motion thus giving better access to monitoring therapy in regions affected by cardiac and/or respiratory motion, regions where DWI usually fails. An improved TQF ^{23}Na MRI sequence has been lately developed with better SNR that could provide potentially better resolution with reduced scanning times (Fleysher et al. 2010).

4.2.6 Metabolite Concentration Using MRS

Magnetic Resonance Spectroscopy (MRS), a technique that has progressed in the domain of cancer research for decades allows analysis of functional and metabolic parameters of cells located deep within the living body, again, without resorting to invasive techniques. MRS can categorize specific chemical signatures and measures the regional concentrations of biochemical species. The addition of MRS to obtain metabolic images (spectra) based on the relative concentrations of cellular biochemicals can help to determine more subtle differences in tissue constitution that leads to a better diagnostic of cancer (Kurhanewicz et al. 1996a, b; Parivar et al. 1996). Differences in the behavior of metabolites, such as choline, creatine, and citrate between healthy tissues and tumor can provide a measure of cancer aggressiveness (Kurhanewicz et al. 2000). Studies monitoring the changes in local metabolites after therapy, have indicated that MRS could be effective as an early indicator of cancer response (Meisamy et al. 2004; Beloueche-Babari et al. 2010).

MRS has significantly lower spatial resolution in comparison to MRI. Recent advances using higher magnetic field strengths and MRS pulse sequence developments have promoted 3D measurements of metabolite concentrations with acceptable voxel resolution of 1 cm or less (Bolan et al. 2005).

4.2.7 Extracellular pH and Hypoxia

In order for cells, healthy or cancerous, to live and reproduce it is required that a pH range in the surrounding environment stays between 6.5 and 7.5. While healthy cells maintain a pH around 7.35, cancer cells are more acidic in nature. The extracellular pH is lower in tumors as compared to healthy tissues, degrading the nearby extracellular matrix and facilitating tumor development and invasiveness (Gatenby and Gillies 2004). It has been shown that pH values influences dramatically tumor progression and the efficiency of treatment and can be used as an effective biomarker for MRI and MRS in order to understand better tumor dynamics (Pathak et al. 2004). Nonetheless, this is only possible with the use of specific probes. The introduction of exogenous probes that remain in the extracellular environment, such as imidazol-1-yl-3-ethyoxycarbonylpropionic acid, produce chemical shifts which are pH sensitive and can be seen on ^{1}H spectra and mapped with spectroscopic imaging (Pathak et al. 2004). ^{31}P and fluorine ^{19}F have also been developed that are sensitive to pH. ^{19}F provides a strong NMR signal with minimal background interference and has extreme sensitivity to changes in the tumor microenvironment that can be exploited with varied reporter molecules (Yu et al. 2005).

To measure effectively the oxygen partial pressure pO_2 it is necessary to use sensing molecules that exhibit sensitivity to oxygen concentration levels. Probes that cause a change in T1 relaxation times have been developed for in vivo measurement of pO_2 for both ^{1}H and ^{19}F MRI and MRS (Zhao et al. 2003; Kodibagkar et al. 2006). In the case of ^{19}F, it has been shown that local oxygen tension can be performed using hexafluorobenzene as reporter molecule (Zhao et al. 2003).

5 Magnetic Resonance Imaging Probes in Cancer

5.1 Introduction

Probes for MR application can be divided according to their biodistribution and consequent applications of contrast enhanced MRI that they allow. Nonspecific probes are those that do not interact with any specific type of cells, and include low molecular weight (MW) agents that equilibrate rapidly between the intravascular and interstitial space and undergo a fast kidney clearance and high molecular weight agents, that stay within the intravascular space and are slowly excreted by kidneys and/or the liver. Specific probes are considered those that are passively directed to a particular cell type or those that are actively directed with a targeting moiety to a specific target site on the cell. There are also responsive, smart, or activatable agents, whose contrast is modulated upon activation in presence of specific targets in the tissue of interest.

5.2 Non-Targeted Probes

Although the ultimate goal of molecular imaging is providing tools for the visualization and measurement of molecular targets in living organism, the pathophysiological characteristics of tumor microenvironment allow the design of nanoparticles capable to accumulate within the tumor compartment without any specific targeting agent. In the process of tumor formation, when tumor cells multiply and form aggregates of 2–3 mm, upon the release of pro-angiogenetic factors the development of a tumoral blood supply commences (Folkman 1995). Malignant neovasculature differs greatly from that one in normal tissues. Newly formed vessels are abnormal in form and architecture, lacking a smooth muscle layer and effective lymphatic drainage. Endothelial cells are poorly aligned with wide fenestrations (in most peripheral human tumors ranges from 200 nm to 600 nm in diameter) (Yuan et al. 1995). All these factors lead to abnormal molecular and fluid transport dynamics, resulting in extensive leakage of circulating macromolecules into the tumor tissue. Furthermore, a defective venous and lymphatic system ensures a longer retention of extravasated components within the tumor interstitium. This effect, defined EPR (Enhanced Permeability Effect) known for almost two decades, represent the physiological basis for tumor accumulation of macromolecular drugs within solid tumors (Maeda and Matsumura 1989). It accounts for the accumulation of untargeted nanoparticles and liposomal agents at 10–50 fold higher concentrations than in normal tissue within 1–2 days (Iyer et al. 2006). Importantly, the EPR does apply only to high molecular weight (40 kDa or higher) macromolecules, since low molecular weight substances (described below for the sake of completeness) undergo a faster clearance through a renal route.

5.2.1 Low Molecular Weight Agents

Low molecular weight agents pioneered the improvement of MR contrast. These comprise largely Gd^{3+} chelates of linear or macrocyclic polyaminocarboxylate ligands and are the most important class of MR contrast agents commercially available, e.g. Magnevist®, Dotarem®, Omniscan®, and Prohance®. After being intravenously injected, these agents clear rapidly from the intravascular space through capillaries into the interstitial space with a distribution half-life of about 5 min. Noteworthy, they do not cross the intact blood–brain barrier, and are eliminated through renal route (half-life:1.5 h) with no detectable biotransformation, decomposition, or serum protein binding (Oksendal and Hals 1993; Bellin 2006; Geraldes and Laurent 2009). They can be used for MR angiography (MRA) and provide increased enhancement and visualization of malignant lesions, due to altered permeability. Due to the extravasation to the interstitial space and the rapid elimination from the circulation, the timing for studies is restricted. For MRA the angiogram has to be acquired during the arterial peak enhancement, that is 1–3 min after a bolus injection. After this time window the extravasation of the contrast agent occurs in surrounding tissues, producing artifacts and limiting the use of obtained images. Furthermore, their lower relaxivity, compared to blood pool agents reduces the vessel/to-contrast ratio.

5.2.2 High Molecular Weight Agents

Macromolecular metal-chelate complexes, known also as *blood pool agents* are larger compounds with MW higher than 40 kDa. Their size prevents extravasation through healthy vascular endothelium, prolongs intravascular half-life, and favors the EPR effect in leaky malignant vasculature. Furthermore, because of increased steric hindrance they have higher relaxivity than low molecular weight agents such as Dotarem or Magnevist. Slower molecular tumbling increases rotational correlation time, τ_r, resulting in more enhancement per unit dose of paramagnetic ion (Villaraza et al. 2010a). Moreover, the possibility to append multiple paramagnetic moieties into a macromolecular platform, increases the enhancement and reduces the dose of agent administered (Villaraza et al. 2010b). These agents can be divided in: (a) protein-based MR agents, (b) systems based on liposomes (c) system based on polymers, and (d) systems based on superparamagnetic agents.

5.2.3 Protein-Based MR Agents

In order to increase circulation time and signal enhancement, the approach of using albumin, the most abundant protein in plasma, as a carrier of paramagnetic agents received a lot of attention in the past few years. Albumin-Gd^{3+}-DTPA was first synthesized in 1987 by Ogan et al. In a typical synthesis of paramagnetically labeled albumin 25–35 molecules of Gd^{3+}-DTPA are covalently bound to each albumin molecule, resulting in a molecular weight of 92 kDa with a diameter of 6 nm (Barrett et al. 2006). Prolonged accumulation within neoplastic tissues (> 2 h) was shown to reflect abnormal capillary permeability for macromolecules, associated with neovascularity (Wikstrom et al. 1989). Moreover, quantitative

assays of tumor microvascular characteristics based on albumin-Gd^{3+}-DTPA dynamic MR imaging was shown to correlate with the histopathologic grade in mammary (Daldrup et al. 1998) and prostate (Gossmann et al. 1999) tumors, and with radiation-induced changes in tumor capillary permeability (Schwickert et al. 1996). Despite some successes also several drawbacks were recognized. With plasma half-life of several hours, clearance from the body is slow and incomplete with retention for more than a week. The potential immunogenicity of albumin constitutes another limitation to the clinical translation of albumin-based contrast agents (Barrett et al. 2006).

To overcome these limitations, an agent, MS-325, was introduced that covalently binds to serum albumin (Lauffer et al. 1996). It contains a lipophilic chemical group (diphenylcyclohexyl) that mediates binding to serum albumin. A few preclinical studies have been performed on cancer imaging. In rats bearing chemically induced breast cancer, no significant correlation was found between MS-325-enhanced microvascular assays with either tumor grade or with microvascular density (MVD as opposed to albumin-GD^{3+}-DTPA (Turetschek et al. 2001a). This was probably due to the use of a rodent model. In primates and rabbits, the elimination of MS-325 is relatively long (2–3 h), whereas in rats it is shorter (25 min) and the volume of distribution is 2-fold higher compared to humans (Turetschek et al. 2001a). Furthermore, quantitative issues arise from the impossibility to differentiate the free- from the albumin-bound MS-325 and also from the unknown albumin affinity in the interstitial space, which might be different from that in the plasma.

5.2.4 Lipid-Based Nanoparticles

A wide variety of lipid-based nanoparticles have been proposed and used as candidates for MR contrast agents since the 1980s (Caride et al. 1984). Lipids are naturally occurring amphiphilic molecules that contain a hydrophilic head and a hydrophobic tail. Due to the hydrophobic associative interactions of the tails and the repulsive interactions between the hydrophilic head groups they aggregate and self-assemble in water into well-defined structures, such as micelles, liposomes, and microemulsions. Possible structures are illustrated in Fig. 14. Micelles can be formed from lipids with a relatively large head group, such as lipids with a single fatty acyl chain that constitute the core with their hydrophobic part and the corona with their hydrophilic component. Liposomes are nanosized vesicles used extensively in the biomedical field for many years, both as model system for studying the properties of biological membranes and as drug carriers. They are created from bilayer forming lipids, which are usually comprised of a polar head group and two fatty acyl chains, entrapping an aqueous core. Molecules can be captured in the aqueous core, integrated in the lipid shell or covalently linked to the surface.

The ability of liposomes to generate MR signal enhancement depends and the structure and composition of the lipidic bilayer and also on the specific location of the paramagnetic agent (either in the aqueous lumen or in the lipid bilayer). The first type of liposomes described were liposomes entrapping paramagnetic agents.

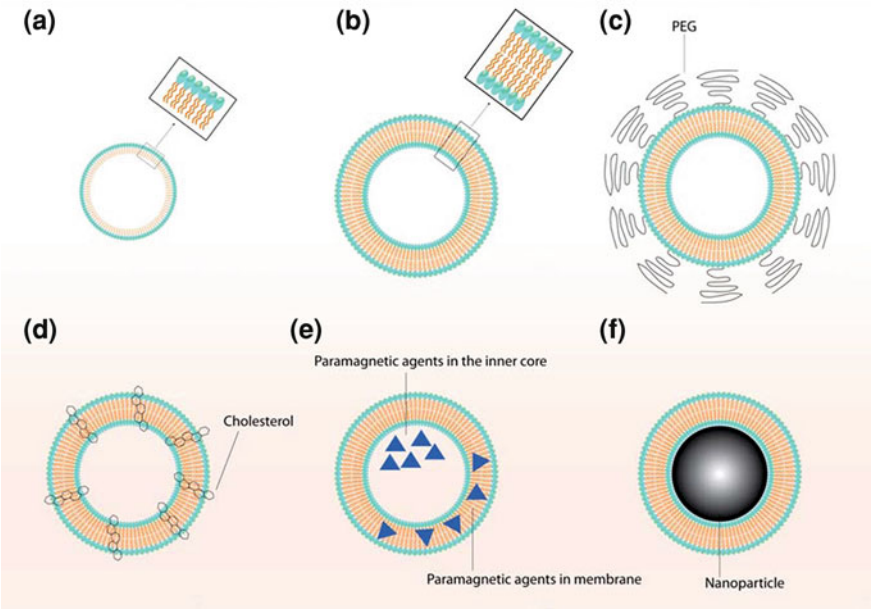

Fig. 14 Illustration of various structures of liposome based contrast agents

Agents, such as $MnCl_2$, Gd-DTPA, Mn-DTPA, Gd-DTPA-BMA, and Gd-HP-DO3A in the aqueous core (Koenig et al. 1988; Caride et al. 1984; Devoisselle et al. 1988; Fossheim et al. 1999). Early studies demonstrated the feasibility of the use of these molecules in mouse models of liver cancer (Unger et al. 1989a) and metastasis (Unger et al. 1989b). However, the main limitation of the loading of paramagnetic agents within the aqueous lumen is the reduced relaxivity, due to the limited exchange of bulk water with the paramagnetic agent. The mayor role in this exchange is played by liposome permeability, which depends on the lipidic composition and can be altered by incorporating cholesterol. Unfortunately, there is a balance between permeability and liposome stability, resulting in more permeable liposomes to be less stable compared to those with a more rigid bilayer. This property has been used to design activatable liposomes to monitor drug/imaging agent release depending on temperature (Frich et al. 2004) or pH (Lokling et al. 2001). In another class of liposomal contrast agents, by using liphophilic chelate such as DTPA-stearate (Schwendener et al. 1990), DTPA-phosphatidyl-ethanolamine (Trubetskoy et al. 1995) or DTPA attached to alkils chains via amide linkers (Kabalka et al. 1991; Bertini et al. 2004), the paramagnetic component can be integrated in the lipidic bilayer (Fig. 15). Higher exchange rate between the contrast agent and the bulk water is obtained with this approach, therefore improved ionic relaxivity of the metal. Liposomes were initially developed for selective imaging of liver and spleen due to their preferential uptake within the Kuppfer cells and the reticuloendothelial system (RES), respectively. By coating

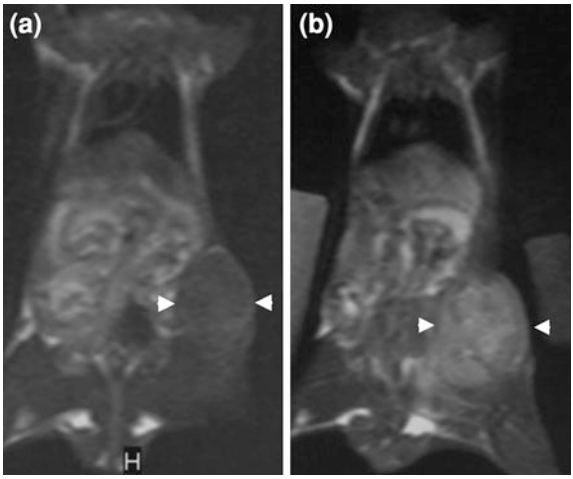

Fig. 15 T1-weighted images of a mouse (**a**) before and (**b**) 20 h after the injection of PEG-stabilized paramagnetic liposomes containing Gd-DMPE-DTPA. (Reprinted by permission from John Wiley and Sons: Bertini etal. 2004)

liposomes with polyethylene glycol (PEG), the RES uptake is greatly reduced, blood circulation and passive tumor targeting is improved ("stealth" liposome).

More recently a new approach of liposome-based imaging have been reported, taking advantage of the chemical exchange saturation transfer (CEST), a method of generating MR contrast that relies on the magnetization transfer that occurs between the bulk water protons and macromolecular protons. By selectively applying a saturation RF pulse at a specific proton frequency (associated with a particular molecule or CEST agent) that is in exchange with surrounding water molecules, the MR signal from the surrounding bulk water molecules is also attenuated. Images obtained with and without the RF saturating pulse reveal the location of the CEST agent. Aime et al. reported the first example of LipoCEST comprised of a Tm^{3+} complex encapsulated within a liposome (Aime et al. 2005). The detection of two different water resonances were reported: intense signal corresponding to the bulk solvent and a less intense peak corresponding to the intraliposomal water in slow exchange with the bulk water through the liposomal bilayer.

A further development of this approach has been reported by using liposomes entrapping the compound Gd^{3+}-HPDO3A. After osmotic induction of liposome shrinking from spheres to oblate vesicles increased relaxivity and shift of the intraliposomal water from the bulk by 7 ppm was reported (Aime et al. 2007). Temperature sensitive liposome have been recently used as lipoCEST agent. By entrapping both Tm^{3+} chelate, as CEST reporter, and NH_4PF_6, as ^{19}F MRS probe Langereis et al. monitored the "activation" (melting) of the liposome. Below the melting temperature the liposome structure is intact and the CEST, effect due to Tm^{3+}, is observed. Above the melting temperature, the liposome content leaks out thus switching off the CEST effect and turning on the ^{19}F resonance (Langereis et al. 2009) (Fig. 16).

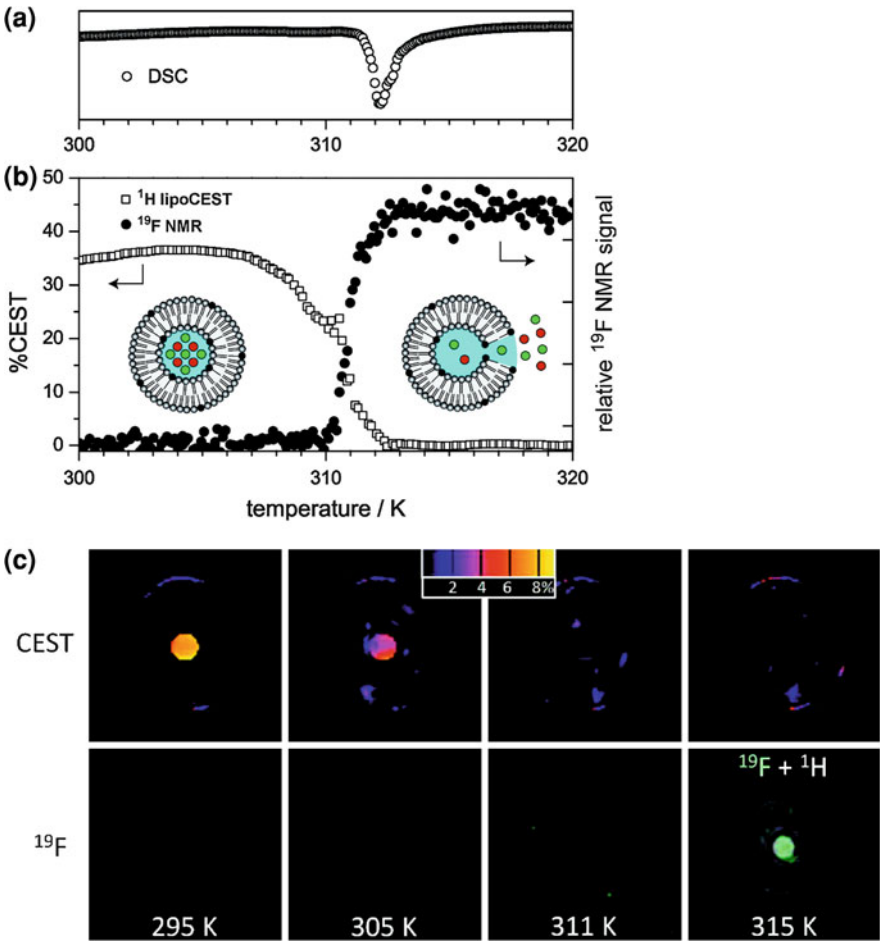

Fig. 16 A temperature sensitive liposomal ^{1}H CEST and ^{19}F contrast agent. **a** DSC thermogram showing the melting temperature of the lipid membrane. **b** The ^{1}H CEST effect and the ^{19}F NMR signal intensity of liposomes containing [Tm(HPDO3A)(H_2O)] and NH_4PF_6 as a function of temperature. **c** MRI images of the liposomal agent. The CEST signal (color scale in percent) vanished at $T \geq 311$ K while the fluorine signal appeared at 315 K (overlay with the 1H image for colocalization and clarity). (Reprinted by permission from American Chemical Society: Langereis et al. 2009)

5.2.5 Dendrimers

Dendrimers (*dendron* in greek, meaning tree) are highly-branched synthetically produced polymers, used for the first time as MR contrast agent in 1994 (Wiener et al. 1994). They have a globular architecture comprising a central core, an interior, and a surface. Two types of dendrimers have been commercially available for a decade and have been studied extensively: polyamidoamine (PAMAM) and poly(propylene imine) (PPI) on a diaminobutane (DAB) core, the former having a an

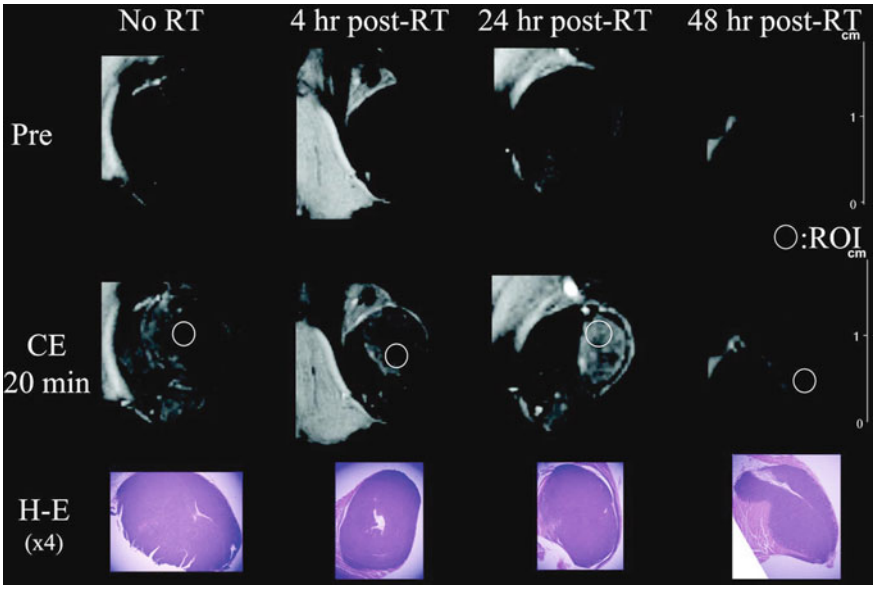

Fig. 17 Representative pre- and postenhanced magnetic resonance images. Magnetic resonance images of the SCCVII tumor are shown at selected time points pre- and postirradiation (15 Gy). Corresponding micrographs of the H&E staining are presented for histologic comparison of the effects on the xenografts (Reprinted by permission fromAmerican Association for Cancer Research, Inc: Kobayashi et al. 2004)

amide functional group core component and the latter a pure aliphatic polyamine core. The synthetic chemistry used to construct them permit to obtain monodisperse products of a specific physical size with consistency and reproducibility. Different "generation" molecules can be synthesized according to their size and molecular weight. Lower generation (2nd and 3rd generation) rapidly leaks from the vasculature into surrounding tissues. Medium-sized dendrimers (5th and 6th generation) with a diameter less than 8 mm are able to selectively extravasate through hyperpermeable tumor vessels. Dendrimers with a diameter higher than 9 nm (6th generation and above) demonstrate good vascular enhancement, but only minimal leakage from the circulation even in the tumors. While dendrimers smaller than 7 nm (generation 5th and below) are excreted via renal route, generation 9th and 10th are generally excreted through the liver, as they are trapped by RES. Linkage to other groups, such as PEG, dramatically alters biodistribution and pharmacokinetic profiles of these constructs. Dendrimer-enhanced MRI has been used to image tumors in mouse models. It has been shown that 8th generation PAMAM-Gd enhanced tumor vasculature, whereas the analogous smaller 6th generation (10 nm) agent provided better delineation of tumor tissue (Yordanov et al. 2003). PAMAM generation 8th have also been used to evaluate malignant permeability after selective irradiation (Kobayashi et al. 2004) (Fig. 17).

Gadomers, developed by Schering, are a class of polylysine dendrimers. Their internal structure comprise aromatic rings, and are simpler and smaller in size compared to PAMAM or DAB. Clearance through glomerular filtration and no long-term accumulation or retention of the nonmetabolized agent in tissues make them promising as blood pool agents. Gadomer-17 (Bayer Schering Pharma, Berlin, Germany) approximates the size of 3rd generation dendrimers and are being successfully used for MR lymphography (Misselwitz et al. 2002) and myocardial perfusion imaging (Gerber et al. 2002). Despite extensive characterization in preclinical studies, gadomers are not clinically available.

5.2.6 Linear Polymers (Polylysine, PEG, and Polysaccharide Complexes)

The wide commercial availability and easy synthesis of monomers and resulting polymers allowed their evaluation as potential contrast agent in MRI. Poly-L-lysine is available in a broad range of molecular weights and is the most studied and used linear polymer. The conjugation to DTPA takes place on the ε-amino group of the lysine. For the macromolecular compound Gd-DTPA-polylysine, relaxivity was three times higher than that of Gd-DTPAGd^{3+} (Schuhmann-Giampieri et al. 1991) independently of the polymer chain length (Spanoghe et al. 1992). Pharmacokinetic studies showed good tolerance in vivo and complete elimination mainly through renal route within 1 day in rat and rabbit. Gd-DTPA-polylysine resulted in higher and sustained enhancement of tumor tissue in rat models of breast and liver cancer compared to Gd-DTPA (Opsahl et al. 1995; Grandin et al. 1995). Polyethylene glycol (PEG) is a nontoxic, biocompatible hydrophilic polymer, and it has been the most likely candidate for use as a macromolecular MR contrast agent. The advantage of using such polymers resides in the ability to manipulate the size and its virtual non-immunogenicity. GD-DTPA-PEG constructs with MW higher than 20 kDa have been shown to provide good blood pool enhancement dynamic and efficient and sustained tumor enhancement in rabbits (Desser et al. 1994). In an attempt to reduce the immunogenicity and improve solubility of polylysine a new class of PEG-polylysine MR macromolecular agent has been designed and tested, by introducing two diverging polylysine cascade amplifiers at each end of a polyethylene glycol (PEG) backbone, followed by substitution of terminal lysine amino groups with Gd-DTPA chelates. These constructs exhibited high water solubility, narrow size polydispersity, and relaxivities 3-fold higher than Gd-DTPA (Fu et al. 2007). MRI assays of vascular endothelial leakiness after injection of these agents demonstrated the ability to visualize and differentiate normal and malignant microvessels in a breast cancer model (Cyran et al. 2008). Polysaccharides, such as dextran, have been used as plasma expander for more than 50 years. The well-known pharmacokinetic and pharmacodynamic profiles, together with their low immunogenic effect and their degradation into small subunits cleared through glomerular filtration raised the interest to use them as a platform for MR contrast agents. Gd-DTPA-dextran compounds have been synthesized and higher (> 2-fold) relaxivities compared to the monomeric chelate

have been reported. Their use as blood pool agents for vascular and tumor imaging in rabbits, demonstrated improved vascular residence time than a conventional Gd chelate and increased tumor rim enhancement.

5.2.7 Iron Oxides

Superparamagnetic iron oxide (SPIO) nanoparticles are a class of contrast agents having a large magnetic moment. They function by acting as magnetic inhomogeneities, locally disturbing the magnetic field. This leads to enhanced dephasing of protons, resulting in decreased signal intensity on T2-weighted and T2*-weighted images. These nanoparticles often consist of a core of iron oxide (magnetite and/or maghemite) with a polymeric or polysaccharide coating such as dextran and PEG. They are considered to be biocompatible, have a limited effect on cell function and can be synthesized to be biodegradable (Thorek et al. 2006; Wang et al. 2001). According to their size, these particles can be classified as monocrystalline iron oxide particles (MION, also called USPIO, ultrasmall superparamagnetic particles 10–30 nm), superparamagnetic iron oxide (SPIO; 60–150 nm), and micron-sized iron oxide particles (MPIO, 0.7–1.6 μm). The pharmacokinetic and biodistribution of SPIO depends on the size and on the physicochemical composition of the coating; however, they are mainly cleared through liver, spleen, and lymph nodes and subsequent incorporation into the body's iron pool.

Ferucarbotran (Resovist) and ferumoxides (Endorem and Feridex) are iron oxide nanoparticles approved by FDA for contrast enhanced MRI imaging of liver tumors (Semelka and Helmberger 2001) and metastatic involvement of lymph nodes. In a normal lymph node with preserved architecture and function, macrophages take up a substantial amount of iron oxides, shortening T2 and T2* relaxation times therefore resulting in decreased signal. Conversely, in malignant lymph nodes, macrophages are replaced by malignant cells therefore the high signal intensity is retained and a heterogeneous signal is displayed (Harisinghani et al. 2003).

USPIO have been used in dynamic contrast enhancement studies to demonstrate angiogenesis in a murine model of breast cancer; a significant correlation has been reported between the dynamic contrast enhancement and microvascular density (Turetschek et al. 2001b). Similarly, USPIO uptake has been correlated to tumor grade (Turetschek et al. 2001c).

In molecular imaging, SPIOs are a prevalent means of labeling cells and to perform cell tracking by MRI. Cell uptake is mediated through the size and electrostatic charge conditions of the SPIO (Thorek and Tsourkas 2008). Further, loading can be augmented through the addition of cell penetrating peptides, electroporation, or transfection agents (Matuszewski et al. 2005; Bernsen et al. 2010). Conventionally, the nanoparticles are believed to have little effect on cell functionality and differentiation (Farrell et al. 2009; Hsiao et al. 2008). The ability of stem cells to specifically home to tumors has suggested their use as delivery for cancer imaging and therapy. The mechanism underlying this process is not

completely understood, although it is thought to involve the release of chemokines and other inflammatory chemoattractants in the tumor pathophysiological environment. Anderson et al. demonstrated the ability to monitor angiogenesis in a glioma model using labeled stem cells injected intravenously. Bone marrow-derived stem cells (Sca+) with phenotypic characteristics of both hematopoietic and endothelial progenitors, were shown to migrate toward the tumor and incorporate in the tumor vasculature, attracted by angiogenic stimuli (Anderson et al. 2005). In another study, SPIO labeled mesenchymal stem cells have been demonstrated to specifically home to lung metastasis as monitored in vivo by MRI and confirmed by histology (Loebinger et al. 2009). A major issue regarding the use of SPIO for cell labeling involves the contrast specificity to the presence of cells. Namely, the hypointense indication is maintained at a site regardless of transplanted cell survival. At longer time points, SPIO were found present not necessarily within implanted stem cells, but rather in phagocytosing monocytes following cell death (Amsalem et al. 2007).

5.2.8 Gadofullerenes and Gadonanotubes

Fullerenes are molecules composed entirely of carbon with their atoms arranged in the form of a closed, endohedral cage, also called buckyballs, or in a cylindrical form called carbon nanotubes. Endohedral gadofullerenes were initially attractive as potential contrast agent for two reasons : the fullerene acts as a perfect chelate, preventing Gd^{3+} leakage in vivo and they demonstrate enhanced relaxivity compared to traditional MR contrast agent (20 times higher than Gd^{3+}-DTPA at 1T) (Bolskar et al. 2003; Mikawa et al. 2001). The anionic Gd@C60[COOH] has been used for labeling mammalian cells close to 100 % efficiency. Gadofullerene-labeled cells have been reported to show a 250 % increase of the T1 signal intensity of labeled cells versus unlabeled cells, suggesting its potential as a probe for in vivo tracking of cells by MRI (Sitharaman et al. 2007). However, low yields and difficult purification steps during synthesis together with high costs of synthesis reduced the practical applicability of gadofullerenes. Another class of carbon structures, defined gadonanotubes outperformed endohedral gadofullerenes and have been suggested as a new platform for molecular imaging (Sitharaman and Wilson 2006). Gd-$^{3+}$-nanotubes are ultrashort carbon structures with an average length of 40 nm, obtained from fluorination and pyrolysis of full length single wall carbon nanotubes. These gadonanotubes have been found to have relaxivities nearly 40 times higher than those of current contrast agents measured at clinical field strength (20–60 MHz) (Sitharaman and Wilson 2006). Moreover, their relaxivity has been found to be pH dependent, exhibiting a dramatic increase when the pH changes from 7.4 to 7.0 suggesting their use as a probe to detect the lower pH environment of malignancies (Hartman et al. 2008).

5.3 Targeted Probes

In targeted imaging various strategies can be employed which can be subdivided in passive targeting strategies and active targeting strategies. Passive targeting strategies include the use of the enhanced permeability and retention (EPR) effect, already described in the previous section, and the selective uptake of nanoparticles by phagocytic cells, such as macrophages and Kupffer cells. Active targeting involves the use of a specific targeting ligand conjugated to the signaling probe. The targeting ligands can consist of antibodies (Olafsen and Wu 2010), antibody fragments (Wu and Yazaki 2000), proteins (Caravan 2009), peptides (Lee et al. 2010b), peptidomimetics (Boutry et al. 2005), aptamers (Hwang do et al. 2010), sugars (van Kasteren et al. 2009), and small molecules (Allen and Meade 2003) and may offer specific advantages or limitations regarding specificity, affinity, availability, immunogenicity, and stability. The various strategies have been used to target surface molecules on tumor cells as well as stromal cells. Examples of successful targeted imaging of such targets by MRI in vivo are listed in the Table 3.

The most direct way to create a targeted imaging probe is by direct conjugation of the ligand to the signaling moiety. For monovalent complexes several limitations are encountered for targeted MRI probes, i.e. limited sensitivity, rapid clearance from the circulation, and low avidity. Strategies to circumvent these limitations involve the use of macromolecular contrast agents and nanoparticles (see also previous sections). Through these approaches higher payloads of the signaling part (Morawski et al. 2004), longer circulation times (van Tilborg et al. 2008), and improved target binding capabilities (Schottelius et al. 2009) can be achieved. Recent technological advances in nanotechnology have even further widened the versatility of targeted imaging probes. The use of nanoparticle platforms do not only offer the earlier mentioned advantages but are now also being developed for the combination of signaling components suitable for imaging with different modalities (Cheon and Lee 2008) and/or the capability to simultaneously function as a carrier for therapeutics, thus combining targeted imaging with targeted drug delivery; an approach referred to as theranostics (or theragnostics) (Shubayev et al. 2009). Several recent studies have already delivered proof of concept for such applications (Grange et al. 2010; Liao et al. 2010; Maeng et al. 2010). While the various strategies in targeted imaging show great promise in improving cancer diagnostics, prognostics, and treatment significant hurdles in application and clinical translation are still faced.

5.4 Responsive Probes

Another exciting development in MR probes is the design of so-called responsive probes. The hallmark of responsive probes is that their signaling properties are dependent on the physicochemical signature of their microenvironment. Typical conditions to which responsive agents can be sensitive to are: pH, temperature, oxygen pressure, enzymatic activity, redox potential, and concentration of a specific ion. Due

Table 3 Examples of targeted imaging applications in oncology

Target	Ligand/probe	Reference
Breast cancer: HER2/neu	Anti-HER2 antibody (Herceptin®)/ Iron oxide nanoparticle	(Chen et al. 2009)
Breast cancer: Somatostatin receptor	Somatostatin peptidomimetic (Octreotide)/ Iron oxide nanoparticle	(Li et al. 2009)
Carcinoma: Folate receptor	Folate/ Gd-dendrimer	(Swanson et al. 2008)
Prostate cancer: Gastrin-releasing peptide receptor	Bombesin peptide/ Iron oxide containing nanoparticle	(Lee et al. 2010a)
Gliosarcoma: Transferrin receptor	Transferrin protein/ Iron oxide nanoparticle	(Hogemann-Savellano et al. 2003)
Pancreatic cancer: Epidermal growth factor receptor	Anti-EGFR antibody fragment/ Iron oxide nanoparticle	(Yang et al. 2009)
Glioma: Inducible nitric oxide synthase	Anti-iNOS antibody Albumin-Gd-DTPA	(Towner et al. 2010b)
Lung cancer/endothelial cells: Alphavbeta3 integrin	Arginine-glycine-aspartic acid (RGD) peptide Iron oxide nanoparticle	(Jiang et al. 2009)
Tumor associated macrophages	Poly-L-glutamic acid/ Gd-DTPA conjugated nanoparticle	(Melancon et al. 2010)
Endothelial cells (Glioma): Vascular endothelial growth factor receptor	Anti-VEGFR2 antibody Iron oxide nanoparticle	(Towner et al. 2010a)

to the underlying mechanisms by which paramagnetic contrast agents exert their signaling properties they are extremely suitable for generating responsive agents. We will only describe the basic concepts of these mechanisms by which agents can be made "responsive". For more detailed explanations of these mechanisms the reader is referred to specific text books or manuscripts on these subjects.

Paramagnetic agents exert their contrast effect by exchange of water molecules. Water molecules linked to a paramagnetic molecule undergo efficient relaxation. Due to the fast exchange of linked molecules with surrounding bulk water molecules (millions per second), paramagnetic agents shorten the relaxation time of their surroundings. The efficiency by which a paramagnetic molecule increases the relaxation speed of their surroundings (relaxivity) is dependent on the molecular structure of the agent. The main molecular characteristics that influence the relaxation properties of paramagnetic agents are: the number of exchangeable

water molecules linked to the agent, the speed by which these molecules can be exchanged and the motion dynamics of the molecule (molecular tumbling rate). Thus by manipulation of the molecular characteristics of paramagnetic agents their relaxivity can be altered and thus probes can be made responsive to their physiological environment (Yoo and Pagel 2008).

The majority of the studies on synthesizing such agents are still limited to concepts or in vitro studies. However, proof of principle has already been obtained in in vivo studies. Garcia-Martin et al. demonstrated the ability to create a pH map in a rat glioma tumor using a Gd-based pH responsive agent (Garcia-Martin et al. 2006). For temperature responsive probes, liposome-based paramagnetic nanoparticles seem to offer major benefits (Langereis et al. 2009; Ponce et al. 2007). Liposome composition can be adapted such that water exchange and molecular diffusion over the liposome membrane can be made temperature-dependent. Through these techniques, hyperthermia-mediated drug delivery can be monitored.

Another application of responsive MRI probes that has shown significant progress is the design of enzyme responsive agents. Various mechanisms can be employed whereby through enzymatic activity either the number or the exchange rate of exchangeable water molecules is manipulated or through manipulation of the tumbling rate of the paramagnetic agent. Moats et al. generated a Gd-based responsive agent sensitive to the activity of β-galactosidase. In this approach, the Gd-ion is "caged" in a sugar moiety preventing water access to the Gd-ions. Upon cleavage of this sugar moiety by β-galactosidase, water exchange is restored and the relaxivity of the agent increases (Louie et al. 2000; Moats et al. 2000). Bogdanov et al. synthesized a peroxidase activatable monomer consisting of a Gd-chelate linked to benzene-1,2-diol. In the presence of peroxide, the monomers are oligomerized, yielding a 3-fold increase in relaxivity due to an increase in molecular tumbling rate (Bogdanov et al. 2002). This principle was used in vivo to monitor myeloperoxidase activity in animal models of aneurism and artherosclerotic plaques (DeLeo et al. 2009; Ronald et al. 2009). Some examples of ongoing studies using MRI responsive agents for monitoring enzyme activity include agents for monitoring activity of : proteases (Jastrzebska et al. 2009), transglutaminase activity (Tei et al. 2010), β-glucuronidase (Duimstra et al. 2005), caspase-3 (Yoo et al. 2007). Many of the presented principles are reported to be adaptable to interrogate the activity of other enzymes.

5.5 Reporter Genes

The convergence of advancements in imaging technology and molecular/cell biology resulted in the mid-1990s in the development of reporter gene techniques for in vivo application. The capability to noninvasively reveal insights into molecular-genetic processes in vivo, the potential use in cell tracking (stem cells, targeted lymphocytes, etc.) and monitoring of gene therapy are areas of major benefit with this approach. Reporter gene approaches has been widely used for in vivo application in

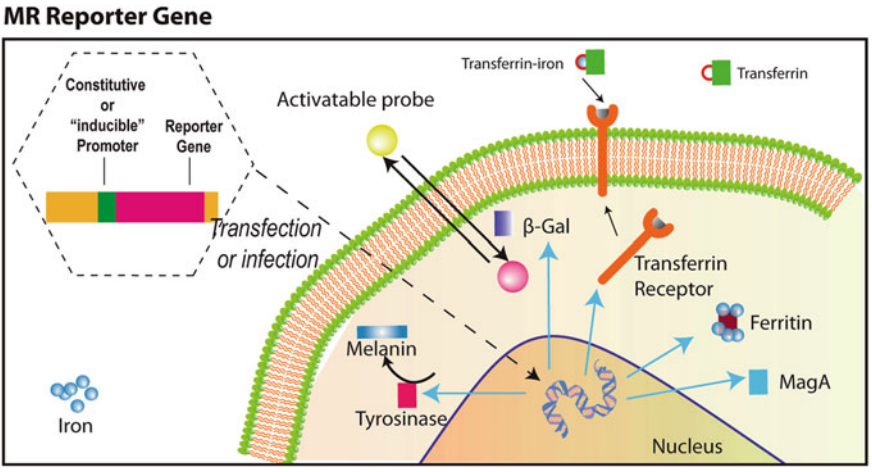

Fig. 18 Illustration of the most common reporter gene for MR and their corresponding probe

bioluminescence imaging (e.g. luciferase), nuclear medicine (e.g. HSV1-*tk*), and recently also for magnetic resonance imaging (MRI) applications.

The reporter gene paradigm requires the appropriate combination of a reporter transgene and a reporter probe, such that the reporter gene product has to interact with an exogenous/endogenous imaging probe (optical, nuclear, magnetic) and following this interaction detection of the signal with the corresponding imaging modality. The first step is to generate a reporter system in the cells. Here, the cDNA expression cassette containing the reporter gene is introduced into the cell of interest through transfection mediated by a vector. While there is a variety of choices for vectors and transfection agents (retrovirus, adenovirus, lentivirus, liposomes, etc.) it should be noted that the ability to image transgene expression is largely independent of the method.

Currently MR reporter genes can be chosen to encode for (a) proteins that are expressed on the cell surface to allow or increase probe uptake (e.g. transferrin receptor); (b) proteins that bind and thus accumulate the probe (e.g. ferritin); (c) enzymes that biochemically activate/modify the probe (e.g. β-galactosidase, tyrosinase); (d) genes that encode for proteins that can be detected directly with imaging techniques (e.g. MagA) (Fig. 18).

5.5.1 Transferrin Receptor Reporter Gene

In the bloodstream, iron is bound to the plasma protein transferrin (Tf) and enters the cells through interaction with the transferrin receptor (TfR). Upon binding, the TfR-Tf complex is internalized, dissociated in acidic endosomes and iron is released. One of the first attempts to use human TfR as a reporter gene was described by Koretsky et al., in this work transfected fibroblasts overexpressing TfR exhibited a 3-fold increase in iron levels, therefore a 20 % reduced MR signal intensity in T2-weighted images (Koretsky et al. 1996). To amplify the MR signal, the overexpression of an

engineered TfR, lacking the feedback down-regulation of receptor expression in response to iron uptake, has been combined with the administration of transferrin covalently conjugated with monocrystalline iron oxide (Tf-MION) as an exogenous probe. In tumors grown from tumor cells transfected with the engineered TfR a significant increase in iron accumulation was obtained. Importantly, the MR signal correlated to the cellular Tf-MION concentrations and to the TfR expression (Weissleder et al. 2000; Moore et al. 2001).

5.5.2 Ferritin Reporter Gene

Ferritin, the major intracellular iron-binding protein that serves as the body's iron depot, has been used as a candidate MRI reporter gene. Ferritin comprises 24 subunits that are heavy (H-ferritin) and light chains (L-Ferritin) and can sequester up to 4000 Fe^{3+} atoms. The feasibility of this approach has been tested in C6 rat glioma (Cohen et al. 2005) by overexpressing H-ferritin under a conditional tetracycline promoter (*tet-hfer*), allowing the expression of the reporter gene to be switched "on" and "off" upon the administration of tetracycline (Fig. 19). H-ferritin overexpression resulted in the up-regulation of the transferrin receptor, increased iron uptake and therefore shortening of T1 and T2 relaxation times. Recently, the generation of a *tet-hfer* transgenic mice in which the overexpression of hemagglutinin-tagged ferritin and EGFP is under tetracycline regulation has been reported (Cohen et al. 2007). These animals, lacking the tetracycline transactivator (tTA) do not express the transgene, however, when mated with mice expressing tTA driven by a promoter of interest, the progeny expresses the reporter gene in those cells in which the promoter is active. By crossing the *tet-hfer* mice with mice expressing tTA under regulation of VE-cadherin or liver associated proteins, overexpression of H-ferritin was detected with MRI in sparse endothelial cells or hepatocytes, respectively (Cohen et al. 2007). Genove et al. reported the use of a replication-defective adenovirus to deliver in vivo the ferritin transgenes (both heavy and light chains). Following focal inoculation of the viral vector into the mouse brain, the reporter activity was measured by time-lapse MRI. Robust contrast in virus-transduced neurons and glia was observed for several weeks (Genove et al. 2005) (Fig. 20). Thereafter, a combined reporter system of TfR overexpression and H-ferritin in a mouse neural stem cell line increased iron accumulation in supplemented iron environment and signal loss on T2-weighted and T2*-weighted images (Deans et al. 2006).

5.5.3 Tyrosinase MR Reporter Gene

Melanotic melanomas, unlike the majority of tumors, appear hyperintense on T1-weighted images. This effect is related to the high affinity and binding capacity of melanin, a polymeric pigment, for metal ions (Enochs et al. 1997). Overexpression of tyrosinase has been considered as a potential approach to increase cellular accumulation of iron to generate contrast for MRI application. Tyrosinase catalyzes the hydroxylation of tyrosine to dioxyphenylalanine (DOPA) and its subsequent oxidation to DOPAquinone. DOPAquinone is then converted to melanin.

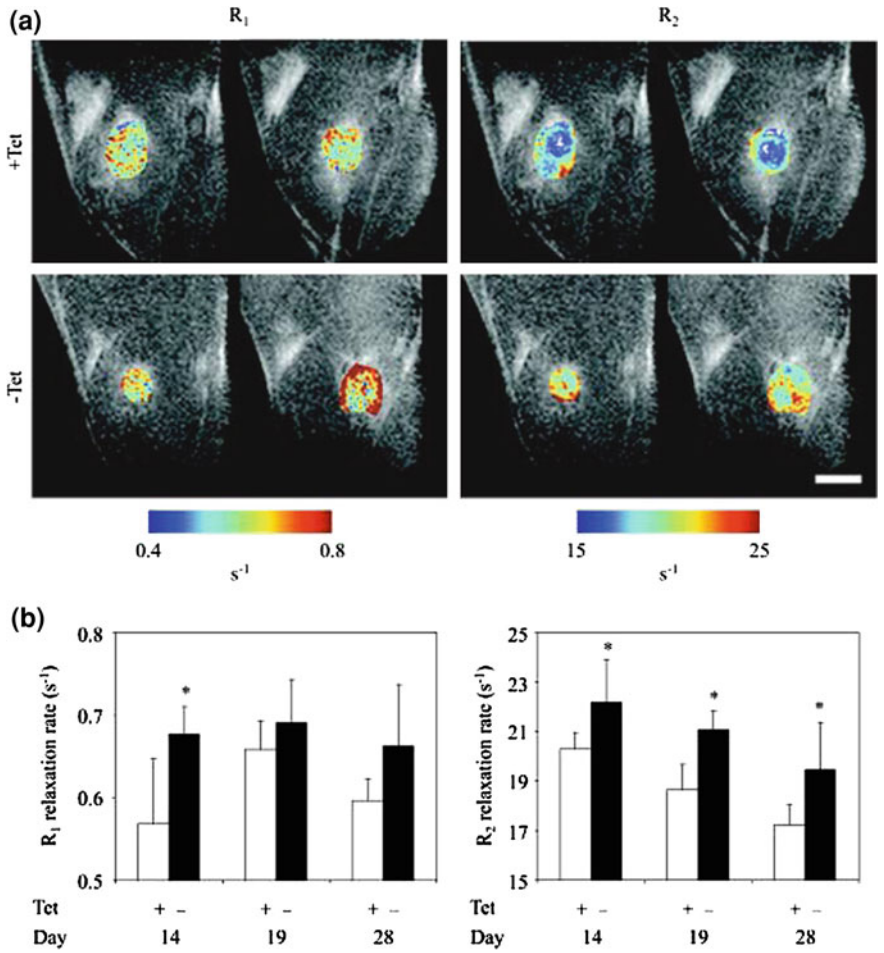

Fig. 19 In vivo detection of ferritin in C6 cells transfected with the "inducible" reporter gene TET-EGFP-ferritin implanted in the hind limb of a nude mice. **a** R_1 and R_2 maps of tumor regions overlaid on the MR images are shown for two representative mice from each group. **b** R_1 and R_2 values (mean ± SD) at the tumor region in the presence (ferritin off) or absence (ferritin on) of TET in drinking water at 14, 19, and 28 days after tumor inoculation. (Reprinted by permission from Neoplasia: Cohen B et al. 2005)

The transfection of mouse fibroblast and human embryonal kidney with a vector encoding for constitutive expression of human tyrosinase gave elevated levels of tyrosinase mRNA, higher melanin production, and higher metal binding capacity, therefore enhanced MR signal intensity (Weissleder et al. 1997).

This approach was further explored in breast cancer cells transfected with a human tyrosinase reporter gene under control of the tetracycline response element which allowed the suppression of gene expression by adding doxycycline to the

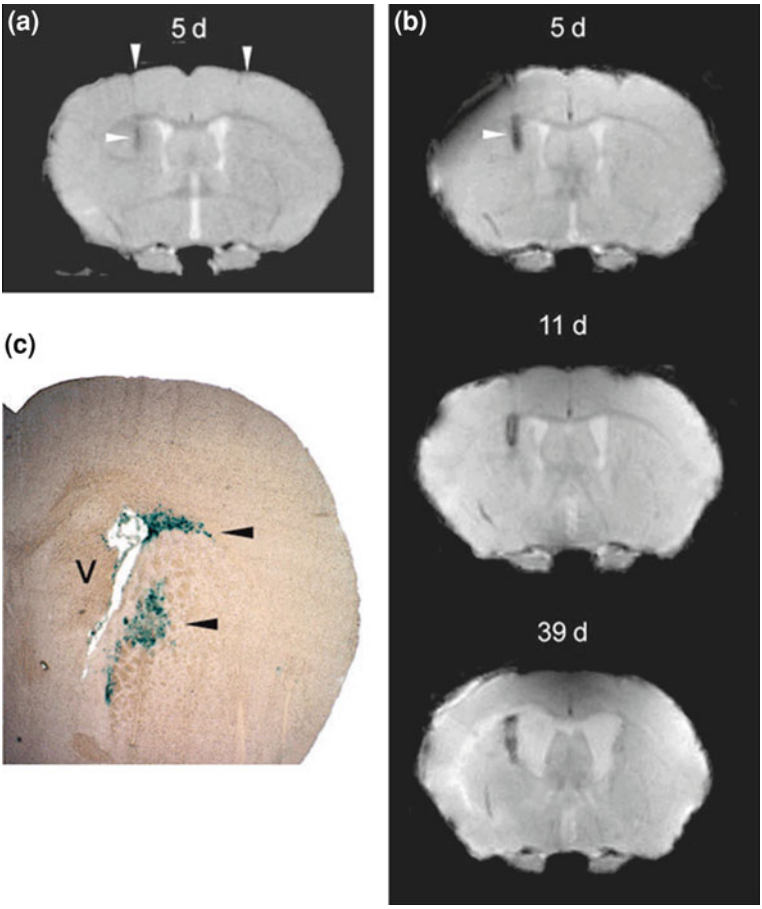

Fig. 20 MRI detection of in vivo delivery of ferritin transgene by using a replication-defective adenovirus. **a** T2-w image 5 days after injection showing the inoculated sites (*left arrows*, MRI reporter; *right arrow*, AdV-lacZ control). **b** X-gal-stained AdV-LacZ transduction pattern at 5 d after inoculation. (Reprinted by permission from Macmillan Publishers Ltd.: Genoveet al. 2005)

medium. Cells cultured with doxycycline showed no background expression of the human tyrosinase gene, whereas withdrawal of doxycycline resulted in detectable tyrosinase messenger RNA expression. Induction of tyrosinase expression resulted in T1 shortening in vitro after culture in iron-enriched medium. Since melanin is a highly stable molecule, MR contrast is preserved for a considerable time interval after switching-off tyrosinase expression (Alfke et al. 2003). However, since melanin and its precursors in catalyzing and binding iron produce reactive oxygen species, this approach may exhibit significant toxic effects and thus limit its application (Gilad et al. 2007b).

5.5.4 β-Galactosidase and MagA Reporter Gene

Another enzyme explored for MR imaging is β-galactosidase (β-gal), the LacZ gene product of *Escherichia Coli* (Juers et al. 2000) responsible for the hydrolysis of lactose and other β-galactosides to monosaccharides. B-gal possesses broad substrate specificity and several colored or fluorescent products are candidates for cleavage, therefore it is a marker frequently used in molecular biology assays and microscopy. The use of β-gal as an MR reporter gene was demonstrated by designing "activatable" gadolinium-based MR contrast agents, such as (1-(2-(β-Galactopyranosyloxy)propyl)-4,7,10-tris(carboxymethyl)-1,4,7,10 tetraazacyclododecane) gadolinium(III) (abbreviated as EgadMe) a modified sugar substrate containing a gadolinium chelate (Louie et al. 2000). It consists of a (1) high affinity chelator that occupies eight of nine coordination sites on Gd^{3+} and (2) a galactopyranose residue positioned to block the remaining coordination site on Gd^{3+} from water access. In the absence of β-Gal, EGadMe is uncleaved and Gd^{3+} is in a water-inaccessible conformation; its T1 relaxivity is low because the primary contribution is only from the outer sphere water. In the presence of β-gal, the galactopyranose is enzymatically cleaved from EGadMe, freeing one coordination site, leading to water's proton increased access to Gd^{3+}, resulting in inner sphere relaxation enhancement and therefore an increase in the T1 relaxivity (higher MR contrast in T1-weighted images). This change in T1 relaxivity can be used for measuring the activity of β-Gal by MRI.

A set of Gram-negative bacteria, defined as magnetotactic, exhibit motility thought to be directed by earth's magnetic field. They naturally synthesize intracellular structures, known as magnetosomes, tiny magnets that can affect the MR signal, similarly to SPIO nanoparticles. It is likely that multiple genes are involved in the production of these magnetosomes. Recently, magA, a gene from *Magnetospirillum Magneticum* known to be involved with iron transport, has been transfected and expressed in a 293FT human cell line, resulting in the production of magnetic, iron oxide nanoparticles and increased transverse relaxivity. This work showed that magnetic particles can be formed in vivo utilizing endogenous iron and can be used to visualize cells positive for magA. This approach generates readily detectable MR contrast, and it has been used as MR reporter in vitro and in vivo (Zurkiya et al. 2008) (Fig. 21).

5.5.5 Alternate Approaches

Also alternate approaches from the ones listed above have been explored. These include reporter genes using contrast mechanisms based Chemical Exchange Saturation Transfer (CEST) and magnetic resonance spectroscopy (MRS).

CEST contrast relies on the magnetization transfer that occurs between the bulk water protons and macromolecular protons. Contrast produced by CEST-agents can be switched on and off by selectively irradiating (saturating) at the exchangeable proton-resonance frequency of the target molecule. Images obtained with and without the RF saturating pulse reveal the location of the specific molecule or CEST agent. Gilad et al. tested the possibility to create a non-metallic

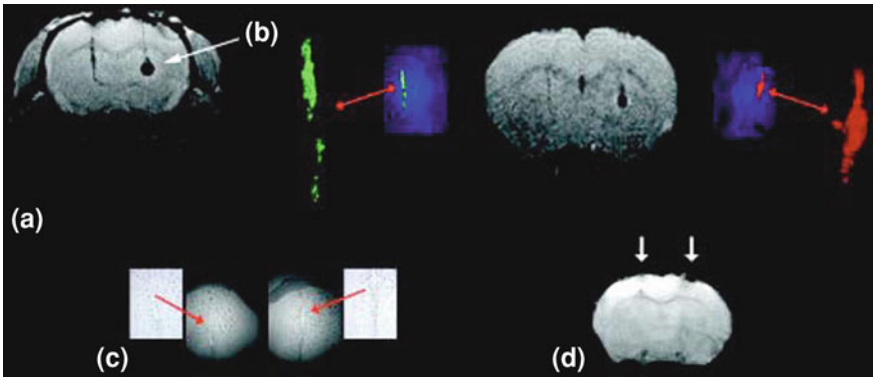

Fig. 21 Detection of the gene MagA in a mouse brain. **a** T2*-weighted image of mouse brain with transplanted magA cells (*white arrow*) (*right*) and GFP control cells (*left*) after 5 d of induction. **a** T2-w image of the same mouse brain showing, although with lower sensitivity, the presence of cells. Histology confirm the presence of control (*green*) and magA positive cells (*red*). (Reprinted by permission from John Wiley and Sons: Zurkiya et al. 2008)

biogradable reporter by constructing a gene encoding for an artificial lysine-rich protein (LRP). The lysine-rich protein functions as a "natural" in vivo CEST-reporter, and was shown to provide excitation frequency dependent contrast in LRP-expressing xenografts in mouse brain (Gilad et al. 2007a). This approach is of particular interest since the contrast properties are switchable and tunable, resulting in elimination of background signals the potential for "multicolor" imaging through the use of reporter gene products having different proton frequencies.

MRS can provide useful information regarding the metabolic state, viability, and also cell localization by using dedicated MRS reporter gene. Creatine kinase (CK) and arginine kinase (AK) are a family of enzymes that catalyze the exchange of phosphate between ATP and creatine (Cr) and arginine (Arg), and therefore are detectable with ^{31}P MRS. In 1989 a reporter gene was investigated for MRS for the first time. CK activity was measured by ^{31}P MRS in Escherichia Coli (Koretsky et al. 1990) and subsequently in the liver of a transgenic mouse (Koretsky et al. 1990).

High concentrations of phosphocreatine were detectable in the NMR spectra compared to controls. Subsequent studies used these approaches to monitor viral gene transfer by ^{31}P MRS using CK (Auricchio et al. 2001) or AK (Walter et al. 2000) constructs as reporter genes. For AK special benefits were suggested since AK is not naturally present in vertebrate cells thus PArg accumulates only in cells where the transgenic gene is located, therefore no background is detected and there is no need for an external probe.

Another potential use of the MRS reporter is based on the in vivo monitoring of the catalytic conversion of a pro-drug into an "active" drug. Stegman et al.

Table 4 Overview of various MRI reporter gene strategies

Reporter Gene	Probe	Contrast	Advantages	Disadvantages
Transferrin receptor	Tranferrin conjugated with monocrystalline iron oxide (Tf-MION)	T2/T2*	High sensitivity	Aspecific uptake of the probe
Ferritin	Endogenous or exogenous iron	T2/T2*	High sensitivity	MR signal depend on iron loading factor. Persistence of signal void after cell death., until ferritin-based nanoparticles are degraded in lysosomes and further metabolized
MagA	Endogenous or exogenous iron	T2/T2*	High sensitivity	Potential immunogenicity
β-Gal	Exogenous probe (such as EgadMe)	T1	Increased signal	Background signal due to aspecific activation of the probe
Tyrosinase	Endogenous or exogenous iron	T1; T2/T2*	Since melanin is a highly stable molecule, MR contrast is preserved for a considerable time	Melanin and its precursor catalyzing and binding iron produce reactive oxygen species that may exhibit significant toxic effects
LRP	None	MRS	Signal switchable and simultaneous imaging of multiple targets (multicolor)	Low sensitivity with current techniques
CK	ATP	^{31}P MRS	No background	Low resolution (spectroscopy)
yCD	5-FC	^{19}F MRS	No background	Low resolution (spectroscopy)

demonstrated the in vivo quantification of yeast cytosine deaminase (yCD) expression in HT29 colon carcinoma xenografts based on the catalyzed conversion of the nontoxic 5-fluorocytosine (5-FC) prodrug into the chemotherapeutic agent 5-Fluorouracil (5-FU), as measured by ^{19}F MRS (Stegman et al. 1999).

A brief overview of the various reporter gene approaches and their basic principles and limitations is given in the Table 4.

6 Future Perspectives

Currently rapid advances are being made in transforming CT and MRI/MRS into molecular imaging modalities. The classic limitations regarding detection sensitivity and monospectral (visualization of one single probe within the same object) capabilities seem to be becoming obsolete. Concurrent development in hardware, software, and innovative imaging probes. However, before these developments become to full fruition several hurdles are still faced. One of the major hurdles faced is in the implementation of the innovative (concepts of) imaging probes. Specific challenges still faced here are in getting to an agent in which optimized characteristics regarding specificity, sensitivity, biocompatibility and biodistribution, and larger scale production. This will require combined efforts from different platforms in academics, industry, and legislative and regulatory bodies.

References

Abdel Razek AA, Gaballa G, Denewer A et al (2010) Diffusion weighted MR imaging of the breast. Acad Radiol 17:382–386

Aime S, Botta M, Gianolio E et al (2000) A p(O(2))-responsive MRI contrast agent based on the redox switch of manganese(II/III)—porphyrin complexes. Angewandte Chemie (International ed) 39:747–750

Aime S, Delli Castelli D, Terreno E (2005) Highly sensitive MRI chemical exchange saturation transfer agents using liposomes. Angew Chem Int Ed Engl 44:5513–5515

Aime S, Delli Castelli D, Lawson D et al (2007) Gd-loaded liposomes as T1, susceptibility, and CEST agents, all in one. J Am Chem Soc 129:2430–2431

Alfke H, Stoppler H, Nocken F et al (2003) In vitro MR imaging of regulated gene expression. Radiology 228:488–492

Allen MJ, Meade TJ (2003) Synthesis and visualization of a membrane-permeable MRI contrast agent. J Biol Inorg Chem 8:746–750

Allen-Auerbach M, Weber WA (2009) Measuring response with FDG-PET: methodological aspects. Oncologist 14:369–377

Ambrose J, Hounsfield G (1973) Computerized transverse axial tomography. Br J Radiol 46:148–149

Amsalem Y, Mardor Y, Feinberg MS et al (2007) Iron-oxide labeling and outcome of transplanted mesenchymal stem cells in the infarcted myocardium. Circulation 116:I38–45

Anderson SA, Glod J, Arbab AS et al (2005) Noninvasive MR imaging of magnetically labeled stem cells to directly identify neovasculature in a glioma model. Blood 105:420–425

Anderson NG, Butler AP, Scott NJ et al (2010) Spectroscopic (multi-energy) CT distinguishes iodine and barium contrast material in MICE. Eur Radiol 20:2126–2134

Artemov D, Solaiyappan M, Bhujwalla ZM (2001) Magnetic resonance pharmacoangiography to detect and predict chemotherapy delivery to solid tumors. Cancer Res 61:3039–3044

Auricchio A, Zhou R, Wilson JM et al (2001) In vivo detection of gene expression in liver by 31P nuclear magnetic resonance spectroscopy employing creatine kinase as a marker gene. Proc Natl Acad Sci U S A 98:5205–5210

Barrett T, Kobayashi H, Brechbiel M et al (2006) Macromolecular MRI contrast agents for imaging tumor angiogenesis. Eur J Radiol 60:353–366

Baudrexel S, Nurnberger L, Rub U et al (2010) Quantitative mapping of T1 and T2* discloses nigral and brainstem pathology in early Parkinson's disease. NeuroImage 51:512–520

Bellin MF (2006) MR contrast agents, the old and the new. Eur J Radiol 60:314–323

Beloueche-Babari M, Chung YL, Al-Saffar NM et al (2010) Metabolic assessment of the action of targeted cancer therapeutics using magnetic resonance spectroscopy. Br J Cancer 102:1–7
Bernsen MR, Moelker AD, Wielopolski PA et al (2010) Labelling of mammalian cells for visualisation by MRI. Eur Radiol 20:255–274
Bertini I, Bianchini F, Calorini L et al (2004) Persistent contrast enhancement by sterically stabilized paramagnetic liposomes in murine melanoma. Magn Reson Med 52:669–672
Blaimer M, Breuer F, Mueller M et al (2004) SMASH, SENSE, PILS, GRAPPA: how to choose the optimal method. Top Magn Reson Imaging 15:223–236
Blankenberg FG, Levashova Z, Sarkar SK et al (2010) Noninvasive assessment of tumor VEGF receptors in response to treatment with pazopanib: a molecular imaging study. Transl oncol 3:56–64
Bloch FHWPEM (1946) Nuclear induction. Phys Rev 69:460–474
Boada FE, Tanase C, Davis D et al (2004) Non-invasive assessment of tumor proliferation using triple quantum filtered 23/Na MRI: technical challenges and solutions. Conf Proc IEEE Eng Med Biol Soc 7:5238–5241
Bogdanov A Jr, Matuszewski L, Bremer C et al (2002) Oligomerization of paramagnetic substrates result in signal amplification and can be used for MR imaging of molecular targets. Mol Imaging 1:16–23
Bohndiek SE, Brindle KM (2010) Imaging and 'omic' methods for the molecular diagnosis of cancer. Expert rev mol diagn 10:417–434
Bolan PJ, Nelson MT, Yee D et al (2005) Imaging in breast cancer: magnetic resonance spectroscopy. Breast Cancer Res 7:149–152
Boll DT, Merkle EM, Paulson EK et al (2008) Calcified vascular plaque specimens: assessment with cardiac dual-energy multidetector CT in anthropomorphically moving heart phantom. Radiology 249:119–126
Bolskar RD, Benedetto AF, Husebo LO et al (2003) First soluble M@C60 derivatives provide enhanced access to metallofullerenes and permit in vivo evaluation of Gd@C60[C(COOH)2]10 as a MRI contrast agent. J Am Chem Soc 125:5471–5478
Boutry S, Burtea C, Laurent S et al (2005) Magnetic resonance imaging of inflammation with a specific selectin-targeted contrast agent. Magn Reson Med 53:800–807
Brix G, Semmler W, Port R et al (1991) Pharmacokinetic parameters in CNS Gd-DTPA enhanced MR imaging. J Comput Assist Tomogr 15:621–628
Caravan P (2009) Protein-targeted gadolinium-based magnetic resonance imaging (MRI) contrast agents: design and mechanism of action. Acc Chem Res 42:851–862
Caride VJ, Sostman HD, Winchell RJ et al (1984) Relaxation enhancement using liposomes carrying paramagnetic species. Magn Reson Imaging 2:107–112
Charnley N, Donaldson S, Price P (2009) Imaging angiogenesis. Methods mol biol (Clifton, N.J) 467:25–51
Chen TJ, Cheng TH, Chen CY et al (2009) Targeted Herceptin-dextran iron oxide nanoparticles for noninvasive imaging of HER2/neu receptors using MRI. J Biol Inorg Chem 14:253–260
Cheon J, Lee JH (2008) Synergistically integrated nanoparticles as multimodal probes for nanobiotechnology. Acc Chem Res 41:1630–1640
Cohen B, Dafni H, Meir G et al (2005) Ferritin as an endogenous MRI reporter for noninvasive imaging of gene expression in C6 glioma tumors. Neoplasia 7:109–117
Cohen B, Ziv K, Plaks V et al (2007) MRI detection of transcriptional regulation of gene expression in transgenic mice. Nat Med 13:498–503
Cyran CC, Fu Y, Raatschen HJ et al (2008) New macromolecular polymeric MRI contrast agents for application in the differentiation of cancer from benign soft tissues. J Magn Reson Imaging 27:581–589
Daldrup H, Shames DM, Wendland M et al (1998) Correlation of dynamic contrast-enhanced MR imaging with histologic tumor grade: comparison of macromolecular and small-molecular contrast media. Am J Roentgenol 171:941–949
Deans AE, Wadghiri YZ, Bernas LM et al (2006) Cellular MRI contrast via coexpression of transferrin receptor and ferritin. Magn Reson Med 56:51–59

DeClerck K, Elble RC (2010) The role of hypoxia and acidosis in promoting metastasis and resistance to chemotherapy. Front Biosci 15:213–225
DeLeo MJ 3rd, Gounis MJ, Hong B et al (2009) Carotid artery brain aneurysm model: in vivo molecular enzyme-specific MR imaging of active inflammation in a pilot study. Radiology 252:696–703
Deng CX, Exner A (2010) Image-guided therapeutics. Mol Pharm 7:1–2
Deoni SC, Peters TM, Rutt BK (2005) High-resolution T1 and T2 mapping of the brain in a clinically acceptable time with DESPOT1 and DESPOT2. Magn Reson Med 53:237–241
Deoni SC, Williams SC, Jezzard P et al (2008) Standardized structural magnetic resonance imaging in multicentre studies using quantitative T1 and T2 imaging at 1.5 T. Neuroimage 40:662–671
Desser TS, Rubin DL, Muller HH et al (1994) Dynamics of tumor imaging with Gd-DTPA-polyethylene glycol polymers: dependence on molecular weight. J Magn Reson Imaging 4:467–472
Devoisselle JM, Vion-Dury J, Galons JP et al (1988) Entrapment of gadolinium-DTPA in liposomes. Characterization of vesicles by P-31 NMR spectroscopy. Invest Radiol 23:719–724
Dhermain F, Saliou G, Parker F et al (2010) Microvascular leakage and contrast enhancement as prognostic factors for recurrence in unfavourable low-grade gliomas. J Neurooncol 97:81–88
Dighe M, Chaturvedi A, Lee JH et al (2008) Staging of gynecologic malignancies. Ultrasound q 24:181–194
Duimstra JA, Femia FJ, Meade TJ (2005) A gadolinium chelate for detection of beta-glucuronidase: a self-immolative approach. J Am Chem Soc 127:12847–12855
Dyke JP, Panicek DM, Healey JH et al (2003) Osteogenic and Ewing sarcomas: estimation of necrotic fraction during induction chemotherapy with dynamic contrast-enhanced MR imaging. Radiology 228:271–278
Eisenhauer EA, Therasse P, Bogaerts J et al (2009) New response evaluation criteria in solid tumours: revised RECIST guideline (version 1.1). Eur J Cancer 45:228–247
Enochs WS, Petherick P, Bogdanova A et al (1997) Paramagnetic metal scavenging by melanin: MR imaging. Radiology 204:417–423
Erlemann R, Sciuk J, Bosse A et al (1990) Response of osteosarcoma and Ewing sarcoma to preoperative chemotherapy: assessment with dynamic and static MR imaging and skeletal scintigraphy. Radiology 175:791–796
Farrell E, Wielopolski P, Pavljasevic P et al (2009) Cell labelling with superparamagnetic iron oxide has no effect on chondrocyte behaviour. Osteoarth Cartil 17:961–967
Fink C, Kiessling F, Bock M et al (2003) High-resolution three-dimensional MR angiography of rodent tumors: morphologic characterization of intratumoral vasculature. J Magn Reson Imaging 18:59–65
Fischer MA, Nanz D, Hany T et al (2011) Diagnostic accuracy of whole-body MRI/DWI image fusion for detection of malignant tumours: a comparison with PET/CT. Eur Radiol 21:246–255
Fleysher L, Oesingmann N, Inglese M (2010) B(0) inhomogeneity-insensitive triple-quantum-filtered sodium imaging using a 12-step phase-cycling scheme. NMR Biomed 23:1191–1198
Flohr TG, McCollough CH, Bruder H et al (2006) First performance evaluation of a dual-source CT (DSCT) system. Eur Radiol 16:256–268
Folkman J (1995) Angiogenesis in cancer, vascular, rheumatoid and other disease. Nat Med 1:27–31
Forstner R (2007) Radiological staging of ovarian cancer: imaging findings and contribution of CT and MRI. Eur Radiol 17:3223–3235
Fossheim SL, Fahlvik AK, Klaveness J et al (1999) Paramagnetic liposomes as MRI contrast agents: influence of liposomal physicochemical properties on the in vitro relaxivity. Magn Reson Imaging 17:83–89
Frich L, Bjornerud A, Fossheim S et al (2004) Experimental application of thermosensitive paramagnetic liposomes for monitoring magnetic resonance imaging guided thermal ablation. Magn Reson Med 52:1302–1309

Fu Y, Raatschen HJ, Nitecki DE et al (2007) Cascade polymeric MRI contrast media derived from poly(ethylene glycol) cores: initial syntheses and characterizations. Biomacromolecules 8:1519–1529

Fuchs VR, Sox HC Jr (2001) Physicians' views of the relative importance of thirty medical innovations. Health Aff (Millwood) 20:30–42

Galban S, Brisset JC, Rehemtulla A et al (2010) Diffusion-weighted MRI for assessment of early cancer treatment response. Curr Pharm Biotechnol 11:701–708

Gao GH, Im GH, Kim MS et al (2010) Magnetite-nanoparticle-encapsulated pH-responsive polymeric micelle as an MRI probe for detecting acidic pathologic areas. Small (Weinheim an der Bergstrasse, Germany) 6:1201–1204

Garcia-Martin ML, Martinez GV, Raghunand N et al (2006) High resolution pH(e) imaging of rat glioma using pH-dependent relaxivity. Magn Reson Med 55:309–315

Gatenby RA, Gillies RJ (2004) Why do cancers have high aerobic glycolysis? Nat Rev Cancer 4:891–899

Genove G, DeMarco U, Xu H et al (2005) A new transgene reporter for in vivo magnetic resonance imaging. Nat Med 11:450–454

Geraldes CF, Laurent S (2009) Classification and basic properties of contrast agents for magnetic resonance imaging. Contrast Media Mol Imaging 4:1–23

Gerber BL, Bluemke DA, Chin BB et al (2002) Single-vessel coronary artery stenosis: myocardial perfusion imaging with Gadomer-17 first-pass MR imaging in a swine model of comparison with gadopentetate dimeglumine. Radiology 225:104–112

Gilad AA, McMahon MT, Walczak P et al (2007a) Artificial reporter gene providing MRI contrast based on proton exchange. Nat Biotechnol 25:217–219

Gilad AA, Winnard PT Jr, van Zijl PC et al (2007b) Developing MR reporter genes: promises and pitfalls. NMR Biomed 20:275–290

Gillies RJ, Morse DL (2005) In vivo magnetic resonance spectroscopy in cancer. Annu Rev Biomed Eng 7:287–326

Gossmann A, Okuhata Y, Shames DM et al (1999) Prostate cancer tumor grade differentiation with dynamic contrast-enhanced MR imaging in the rat: comparison of macromolecular and small-molecular contrast media–preliminary experience. Radiology 213:265–272

Grandin C, Van Beers BE, Demeure R et al (1995) Comparison of gadolinium-DTPA and polylysine-gadolinium-DTPA–enhanced magnetic resonance imaging of hepatocarcinoma in the rat. Invest Radiol 30:572–581

Grange C, Geninatti-Crich S, Esposito G et al (2010) Combined delivery and magnetic resonance imaging of neural cell adhesion molecule-targeted doxorubicin-containing liposomes in experimentally induced Kaposi's sarcoma. Cancer Res 70:2180–2190

Gupta RT, Ho LM, Marin D et al (2010) Dual-energy CT for characterization of adrenal nodules: initial experience. AJR Am J Roentgenol 194:1479–1483

Haberkorn U, Altmann A, Mier W et al (2007) Molecular imaging of tumor metabolism and apoptosis. Ernst Schering Foundation symposium proceedings 125–152

Hanahan D, Weinberg RA (2000) The hallmarks of cancer. Cell 100:57–70

Harisinghani MG, Barentsz J, Hahn PF et al (2003) Noninvasive detection of clinically occult lymph-node metastases in prostate cancer. N Engl J Med 348:2491–2499

Hartman KB, Laus S, Bolskar RD et al (2008) Gadonanotubes as ultrasensitive pH-smart probes for magnetic resonance imaging. Nano Lett 8:415–419

Hayashida Y, Yakushiji T, Awai K et al (2006) Monitoring therapeutic responses of primary bone tumors by diffusion-weighted image: Initial results. Eur Radiol 16:2637–2643

Hayes CE, Hattes N, Roemer PB (1991) Volume imaging with MR phased arrays. Magn Reson Med 18:309–319

Heidemann RM, Ozsarlak O, Parizel PM et al (2003) A brief review of parallel magnetic resonance imaging. Eur Radiol 13:2323–2337

Helfer BM, Balducci A, Nelson AD et al (2010) Functional assessment of human dendritic cells labeled for in vivo (19)F magnetic resonance imaging cell tracking. Cytotherapy 12:238–250

Himmelreich U, Aime S, Hieronymus T et al (2006) A responsive MRI contrast agent to monitor functional cell status. NeuroImage 32:1142–1149
Hogemann-Savellano D, Bos E, Blondet C et al (2003) The transferrin receptor: a potential molecular imaging marker for human cancer. Neoplasia 5:495–506
Hong H, Yang Y, Zhang Y et al (2010) Non-invasive cell tracking in cancer and cancer therapy. Curr Top Med Chem 10:1237–1248
Hounsfield GN (1973) Computerized transverse axial scanning (tomography). 1 Description of system. Br J Radiol 46:1016–1022
Hsiao JK, Chu HH, Wang YH et al (2008) Macrophage physiological function after superparamagnetic iron oxide labeling. NMR Biomed 21:820–829
Hwang do W, Ko HY, Lee JH et al (2010) A nucleolin-targeted multimodal nanoparticle imaging probe for tracking cancer cells using an aptamer. J Nucl Med 51:98–105
Iyer AK, Khaled G, Fang J et al (2006) Exploiting the enhanced permeability and retention effect for tumor targeting. Drug Discov Today 11:812–818
Jastrzebska B, Lebel R, Therriault H et al (2009) New enzyme-activated solubility-switchable contrast agent for magnetic resonance imaging: from synthesis to in vivo imaging. J Med Chem 52:1576–1581
Jiang T, Zhang C, Zheng X et al (2009) Noninvasively characterizing the different alphavbeta3 expression patterns in lung cancers with RGD-USPIO using a clinical 3.0T MR scanner. Int J Nanomedicine 4:241–249
Johnson TR, Krauss B, Sedlmair M et al (2007) Material differentiation by dual energy CT: initial experience. Eur Radiol 17:1510–1517
Juers DH, Jacobson RH, Wigley D et al (2000) High resolution refinement of beta-galactosidase in a new crystal form reveals multiple metal-binding sites and provides a structural basis for alpha-complementation. Protein Sci 9:1685–1699
Kabalka GW, Davis MA, Moss TH et al (1991) Gadolinium-labeled liposomes containing various amphiphilic Gd-DTPA derivatives: targeted MRI contrast enhancement agents for the liver. Magn Reson Med 19:406–415
Kachelriess M, Ulzheimer S, Kalender WA (2000) ECG-correlated image reconstruction from subsecond multi-slice spiral CT scans of the heart. Med Phys 27:1881–1902
Kaiser WA, Zeitler E (1989) MR imaging of the breast: fast imaging sequences with and without Gd-DTPA Preliminary observations. Radiology 170:681–686
Kak ACaS M (1988) Principles of computerized tomographic imaging. IEEE Press
Kalender WA (2005) Computed tomography. Fundamentals, system technology, image quality, applications. Publicis Corporate Publishing, Erlangen
Kalender WA, Perman WH, Vetter JR et al (1986) Evaluation of a prototype dual-energy computed tomographic apparatus I. Phantom studies. Med Phys 13:334–339
Kang JH, Chung JK (2008) Molecular-genetic imaging based on reporter gene expression. J Nucl Med 49(Suppl 2):164S–179S
Karcaaltincaba M, Karaosmanoglu D, Akata D et al (2009) Dual energy virtual CT colonoscopy with dual source computed tomography: initial experience. Rofo 181:859–862
Kharuzhyk SA, Petrovskaya NA, Vosmitel MA (2010) Diffusion-weighted magnetic resonance imaging in non-invasive monitoring of antiangiogenic therapy in experimental tumor model. Exp Oncol 32:104–106
Kobayashi H, Reijnders K, English S et al (2004) Application of a macromolecular contrast agent for detection of alterations of tumor vessel permeability induced by radiation. Clin Cancer Res 10:7712–7720
Kobayashi H, Nishikawa M, Sakamoto C et al (2009) Dual temperature- and pH-responsive fluorescence molecular probe for cellular imaging utilizing a PNIPAAm-fluorescein copolymer. Anal Sci 25:1043–1047
Kodibagkar VD, Cui W, Merritt ME et al (2006) Novel 1H NMR approach to quantitative tissue oximetry using hexamethyldisiloxane. Magn Reson Med 55:743–748

Koenig SH, Brown RD 3rd, Kurland R et al (1988) Relaxivity and binding of Mn2 + ions in solutions of phosphatidylserine vesicles. Magn Reson Med 7:133–142
Koretsky AP, Brosnan MJ, Chen LH et al (1990) NMR detection of creatine kinase expressed in liver of transgenic mice: determination of free ADP levels. Proc Natl Acad Sci U S A 87:3112–3116
Koretsky AP, Lin Y-J, Schorle H, Jaenisch R (1996) Genetic control of MRI contrast by expression of the transferrin receptor. Proc Int Soc Magn Reson Med. 4:69
Krohn KA, Link JM, Mason RP (2008) Molecular imaging of hypoxia. J Nucl Med 49(Suppl 2):129S–148S
Kurhanewicz J, Vigneron DB, Hricak H et al (1996a) Three-dimensional H-1 MR spectroscopic imaging of the in situ human prostate with high (0.24–0.7 cm3) spatial resolution. Radiology 198:795–805
Kurhanewicz J, Vigneron DB, Hricak H et al (1996b) Prostate cancer: metabolic response to cryosurgery as detected with 3D H-1 MR spectroscopic imaging. Radiology 200:489–496
Kurhanewicz J, Vigneron DB, Males RG et al (2000) The prostate: MR imaging and spectroscopy. Present and future. Radiol Clin North Am 38:115–138, viii–ix
Kurhanewicz J, Vigneron D, Carroll P et al (2008) Multiparametric magnetic resonance imaging in prostate cancer: present and future. Curr Opin Urol 18:71–77
Kweon S, Lee HJ, Hyung WJ et al (2010) Liposomes coloaded with iopamidol/lipiodol as a RES-targeted contrast agent for computed tomography imaging. Pharm Res 27:1408–1415
Langereis S, Keupp J, van Velthoven JL et al (2009) A temperature-sensitive liposomal 1H CEST and 19F contrast agent for MR image-guided drug delivery. J Am Chem Soc 131:1380–1381
Lauffer RB, Parmelee DJ, Ouellet HS et al (1996) MS-325: a small-molecule vascular imaging agent for magnetic resonance imaging. Acad Radiol 3(Suppl 2):S356–358
Lee KC, Hamstra DA, Bhojani MS et al (2007) Noninvasive molecular imaging sheds light on the synergy between 5-fluorouracil and TRAIL/Apo2L for cancer therapy. Clin Cancer Res 13:1839–1846
Lee JW, Yoon DY, Choi CS et al (2008) Anaplastic thyroid carcinoma: computed tomographic differentiation from other thyroid masses. Acta Radiol 49:321–327
Lee CM, Jeong HJ, Kim EM et al (2009) Superparamagnetic iron oxide nanoparticles as a dual imaging probe for targeting hepatocytes in vivo. Magn Reson Med 62:1440–1446
Lee CM, Jeong HJ, Cheong SJ et al (2010a) Prostate cancer-targeted imaging using magnetofluorescent polymeric nanoparticles functionalized with bombesin. Pharm Res 27:712–721
Lee S, Xie J, Chen X (2010b) Peptide-based probes for targeted molecular imaging. Biochemistry 49:1364–1376
Lewis JS, Lewis MR, Srinivasan A et al (1999) Comparison of four 64Cu-labeled somatostatin analogues in vitro and in a tumor-bearing rat model: evaluation of new derivatives for positron emission tomography imaging and targeted radiotherapy. J Med Chem 42:1341–1347
Li X, Du X, Huo T et al (2009) Specific targeting of breast tumor by octreotide-conjugated ultrasmall superparamagnetic iron oxide particles using a clinical 3.0-Tesla magnetic resonance scanner. Acta Radiol 50:583–594
Liao C, Sun Q, Liang B et al (2010) Targeting EGFR-overexpressing tumor cells using Cetuximab-immunomicelles loaded with doxorubicin and superparamagnetic iron oxide. Eur J Radiol 80:699–705
Lin C, Luciani A, Itti E et al (2010) Whole-body diffusion-weighted magnetic resonance imaging with apparent diffusion coefficient mapping for staging patients with diffuse large B-cell lymphoma. Eur Radiol 20:2027–2038
Lindfors KK, Boone JM, Nelson TR et al (2008) Dedicated breast CT: initial clinical experience. Radiology 246:725–733
Liu PF, Debatin JF, Caduff RF et al (1998) Improved diagnostic accuracy in dynamic contrast enhanced MRI of the breast by combined quantitative and qualitative analysis. Br J Radiol 71:501–509
Loebinger MR, Kyrtatos PG, Turmaine M et al (2009) Magnetic resonance imaging of mesenchymal stem cells homing to pulmonary metastases using biocompatible magnetic nanoparticles. Cancer Res 69:8862–8867

Lokling KE, Fossheim SL, Skurtveit R et al (2001) pH-sensitive paramagnetic liposomes as MRI contrast agents: in vitro feasibility studies. Magn Reson Imaging 19:731–738
Louie AY, Huber MM, Ahrens ET et al (2000) In vivo visualization of gene expression using magnetic resonance imaging. Nat Biotechnol 18:321–325
Maeda H, Matsumura Y (1989) Tumoritropic and lymphotropic principles of macromolecular drugs. Crit Rev Ther Drug Carrier Syst 6:193–210
Maeng JH, Lee DH, Jung KH et al (2010) Multifunctional doxorubicin loaded super paramagnetic iron oxide nanoparticles for chemotherapy and magnetic resonance imaging in liver cancer. Biomaterials 31:4995–5006
Matuszewski L, Persigehl T, Wall A et al (2005) Cell tagging with clinically approved iron oxides: feasibility and effect of lipofection, particle size, and surface coating on labelling efficiency. Radiology 235:155–161
Meisamy S, Bolan PJ, Baker EH et al (2004) Neoadjuvant chemotherapy of locally advanced breast cancer: predicting response with in vivo (1)H MR spectroscopy–a pilot study at 4 T. Radiology 233:424–431
Melancon MP, Lu W, Huang Q et al (2010) Targeted imaging of tumor-associated M2 macrophages using a macromolecular contrast agent PG-Gd-NIR813. Biomaterials 31:6567–6573
Mikawa M, Kato H, Okumura M et al (2001) Paramagnetic water-soluble metallofullerenes having the highest relaxivity for MRI contrast agents. Bioconjug Chem 12:510–514
Miles KA (2002) Functional computed tomography in oncology. Eur J Cancer 38:2079–2084
Miles KA (2006) Perfusion imaging with computed tomography: brain and beyond. Eur Radiol 16(Suppl 7):M37–43
Misselwitz B, Schmitt-Willich H, Michaelis M et al (2002) Interstitial magnetic resonance lymphography using a polymeric t1 contrast agent: initial experience with Gadomer-17. Invest Radiol 37:146–151
Moats R, Ma LQ, Wajed R et al (2000) Magnetic resonance imaging for the evaluation of a novel metastatic orthotopic model of human neuroblastoma in immunodeficient mice. Clin Exp Metastasis 18:455–461
Montet X, Pastor CM, Vallee JP et al (2007) Improved visualization of vessels and hepatic tumors by micro-computed tomography (CT) using iodinated liposomes. Invest Radiol 42:652–658
Moore A, Josephson L, Bhorade RM et al (2001) Human transferrin receptor gene as a marker gene for MR imaging. Radiology 221:244–250
Morawski AM, Winter PM, Crowder KC et al (2004) Targeted nanoparticles for quantitative imaging of sparse molecular epitopes with MRI. Magn Reson Med 51:480–486
Nilsen L, Fangberget A, Geier O et al (2010) Diffusion-weighted magnetic resonance imaging for pretreatment prediction and monitoring of treatment response of patients with locally advanced breast cancer undergoing neoadjuvant chemotherapy. Acta Oncologica (Stockholm, Sweden) 49:354–360
Ntziachristos V, Bremer C, Tung C et al (2002) Imaging cathepsin B up-regulation in HT-1080 tumor models using fluorescence-mediated molecular tomography (FMT). Acad Radiol 9(Suppl 2):S323–325
O'Connor JP, Jackson A, Parker GJ et al (2007) DCE-MRI biomarkers in the clinical evaluation of antiangiogenic and vascular disrupting agents. Br J Cancer 96:189–195
Oksendal AN, Hals PA (1993) Biodistribution and toxicity of MR imaging contrast media. J Magn Reson Imaging 3:157–165
Olafsen T, Wu AM (2010) Antibody vectors for imaging. Semin Nucl Med 40:167–181
Opsahl LR, Uzgiris EE, Vera DR (1995) Tumor imaging with a macromolecular paramagnetic contrast agent: gadopentetate dimeglumine-polylysine. Acad Radiol 2:762–767
Padhani AR (2002) Dynamic contrast-enhanced MRI in clinical oncology: current status and future directions. J Magn Reson Imaging 16:407–422
Padhani AR (2005) Where are we with imaging oxygenation in human tumours? Cancer Imaging 5:128–130

Padhani AR, Krohn KA, Lewis JS et al (2007) Imaging oxygenation of human tumours. Eur Radiol 17:861–872

Parivar F, Hricak H, Shinohara K et al (1996) Detection of locally recurrent prostate cancer after cryosurgery: evaluation by transrectal ultrasound, magnetic resonance imaging, and three-dimensional proton magnetic resonance spectroscopy. Urology 48:594–599

Pathak AP, Gimi B, Glunde K et al (2004) Molecular and functional imaging of cancer: advances in MRI and MRS. Methods Enzymol 386:3–60

Paulus MJ, Gleason SS, Kennel SJ et al (2000) High resolution X-ray computed tomography: an emerging tool for small animal cancer research. Neoplasia 2:62–70

Plathow C, Weber WA (2008) Tumor cell metabolism imaging. J Nucl Med 49(Suppl 2):43S–63S

Ponce AM, Viglianti BL, Yu D et al (2007) Magnetic resonance imaging of temperature-sensitive liposome release: drug dose painting and antitumor effects. J Natl Cancer Inst 99:53–63

Ponomarev V (2009) Nuclear imaging of cancer cell therapies. J Nucl Med 50:1013–1016

Popovtzer R, Agrawal A, Kotov NA et al (2008) Targeted gold nanoparticles enable molecular CT imaging of cancer. Nano Lett 8:4593–4596

Purcell EMT HC; Pound RV (1946) Resonance absorption by nuclear magnetic moment in a solid. Phys Rev 69:37–38

Qian Y, Stenger VA, Boada FE (2009) Parallel imaging with 3D TPI trajectory: SNR and acceleration benefits. Magn Reson Imaging 27:656–663

Raghunand N, Jagadish B, Trouard TP et al (2006) RedoX-sensitive contrast agents for MRI based on reversible binding of thiols to serum albumin. Magn Reson Med 55:1272–1280

Renan MJ (1993) How many mutations are required for tumorigenesis? Implications from human cancer data. Mol Carcinog 7:139–146

Ritman EL (2002) Molecular imaging in small animals–roles for micro-CT. J Cell Biochem Suppl 39:116–124

Ronald JA, Chen JW, Chen Y et al (2009) Enzyme-sensitive magnetic resonance imaging targeting myeloperoxidase identifies active inflammation in experimental rabbit atherosclerotic plaques. Circulation 120:592–599

Schambach SJ, Bag S, Schilling L et al (2010) Application of micro-CT in small animal imaging. Methods 50:2–13

Schepkin VD, Choy IO, Budinger TF et al (1998) Sodium TQF NMR and intracellular sodium in isolated crystalloid perfused rat heart. Magn Reson Med 39:557–563

Schepkin VD, Chenevert TL, Kuszpit K et al (2006) Sodium and proton diffusion MRI as biomarkers for early therapeutic response in subcutaneous tumors. Magn Reson Imaging 24:273–278

Schottelius M, Laufer B, Kessler H et al (2009) Ligands for mapping alphavbeta3-integrin expression in vivo. Acc Chem Res 42:969–980

Schuhmann-Giampieri G, Schmitt-Willich H, Frenzel T et al (1991) In vivo and in vitro evaluation of Gd-DTPA-polylysine as a macromolecular contrast agent for magnetic resonance imaging. Invest Radiol 26:969–974

Schwendener RA, Wuthrich R, Duewell S et al (1990) A pharmacokinetic and MRI study of unilamellar gadolinium-, manganese-, and iron-DTPA-stearate liposomes as organ-specific contrast agents. Invest Radiol 25:922–932

Schwickert HC, Stiskal M, Roberts TP et al (1996) Contrast-enhanced MR imaging assessment of tumor capillary permeability: effect of irradiation on delivery of chemotherapy. Radiology 198:893–898

Semelka RC, Helmberger TK (2001) Contrast agents for MR imaging of the liver. Radiology 218:27–38

Serganova I, Mayer-Kukuck P, Huang R et al (2008) Molecular imaging: reporter gene imaging. Handb Exp Pharmacol 167–223

Shubayev VI, Pisanic TR 2nd, Jin S (2009) Magnetic nanoparticles for theragnostics. Adv Drug Deliv Rev 61:467–477

Sitharaman B, Wilson LJ (2006) Gadonanotubes as new high-performance MRI contrast agents. Int J Nanomedicine 1:291–295

Sitharaman B, Tran LA, Pham QP et al (2007) Gadofullerenes as nanoscale magnetic labels for cellular MRI. Contrast Media Mol Imaging 2:139–146

Smith TA (2010) Towards detecting the HER-2 receptor and metabolic changes induced by HER-2-targeted therapies using medical imaging. Br J Radiol 83:638–644

So PW, Kalber T, Hunt D et al (2010) Efficient and rapid labeling of transplanted cell populations with superparamagnetic iron oxide nanoparticles using cell surface chemical biotinylation for in vivo monitoring by MRI. Cell Transplant 19:419–429

Spanoghe M, Lanens D, Dommisse R et al (1992) Proton relaxation enhancement by means of serum albumin and poly-L-lysine labeled with DTPA-Gd3+ : relaxivities as a function of molecular weight and conjugation efficiency. Magn Reson Imaging 10:913–917

Stegman LD, Rehemtulla A, Beattie B et al (1999) Noninvasive quantitation of cytosine deaminase transgene expression in human tumor xenografts with in vivo magnetic resonance spectroscopy. Proc Natl Acad Sci U S A 96:9821–9826

Swanson SD, Kukowska-Latallo JF, Patri AK et al (2008) Targeted gadolinium-loaded dendrimer nanoparticles for tumor-specific magnetic resonance contrast enhancement. Int J Nanomedicine 3:201–210

Tang C, Russell PJ, Martiniello-Wilks R et al (2010) Nanoparticles and cellular carriers—allies in cancer imaging and cellular gene therapy? Stem Cells 28:1686–1702

Tei L, Mazooz G, Shellef Y et al (2010) Novel MRI and fluorescent probes responsive to the Factor XIII transglutaminase activity. Contrast Media Mol Imaging 5:213–222

Therasse P, Arbuck SG, Eisenhauer EA et al (2000) New guidelines to evaluate the response to treatment in solid tumors. European Organization for Research and Treatment of Cancer, National Cancer Institute of the United States, National Cancer Institute of Canada. J Natl Cancer Inst 92:205–216

Thorek DL, Tsourkas A (2008) Size, charge and concentration dependent uptake of iron oxide particles by non-phagocytic cells. Biomaterials 29:3583–3590

Thorek DL, Chen AK, Czupryna J et al (2006) Superparamagnetic iron oxide nanoparticle probes for molecular imaging. Ann Biomed Eng 34:23–38

Tofts PS, Brix G, Buckley DL et al (1999) Estimating kinetic parameters from dynamic contrast-enhanced T(1)-weighted MRI of a diffusable tracer: standardized quantities and symbols. J Magn Reson Imaging 10:223–232

Towner RA, Smith N, Asano Y et al (2010a) Molecular magnetic resonance imaging approaches used to aid in the understanding of angiogenesis in vivo: implications for tissue engineering. Tissue Eng 16:357–364

Towner RA, Smith N, Doblas S et al (2010b) In vivo detection of inducible nitric oxide synthase in rodent gliomas. Free Radical Biol Med 48:691–703

Townsend DW (2008) Dual-modality imaging: combining anatomy and function. J Nucl Med 49:938–955

Trubetskoy VS, Cannillo JA, Milshtein A et al (1995) Controlled delivery of Gd-containing liposomes to lymph nodes: surface modification may enhance MRI contrast properties. Magn Reson Imaging 13:31–37

Tsien C, Galban CJ, Chenevert TL et al (2010) Parametric response map as an imaging biomarker to distinguish progression from pseudoprogression in high-grade glioma. J Clin Oncol 28:2293–2299

Tsourkas A, Newton G, Perez JM et al (2005) Detection of peroxidase/H2O2-mediated oxidation with enhanced yellow fluorescent protein. Anal Chem 77:2862–2867

Turetschek K, Floyd E, Helbich T et al (2001a) MRI assessment of microvascular characteristics in experimental breast tumors using a new blood pool contrast agent (MS-325) with correlations to histopathology. J Magn Reson Imaging 14:237–242

Turetschek K, Huber S, Floyd E et al (2001b) MR imaging characterization of microvessels in experimental breast tumors by using a particulate contrast agent with histopathologic correlation. Radiology 218:562–569

Turetschek K, Roberts TP, Floyd E et al (2001c) Tumor microvascular characterization using ultrasmall superparamagnetic iron oxide particles (USPIO) in an experimental breast cancer model. J Magn Reson Imaging 13:882–888

Unger EC, MacDougall P, Cullis P et al (1989a) Liposomal Gd-DTPA: effect of encapsulation on enhancement of hepatoma model by MRI. Magn Reson Imaging 7:417–423

Unger EC, Winokur T, MacDougall P et al (1989b) Hepatic metastases: liposomal Gd-DTPA-enhanced MR imaging. Radiology 171:81–85

van Kasteren SI, Campbell SJ, Serres S et al (2009) Glyconanoparticles allow pre-symptomatic in vivo imaging of brain disease. Proc Nat Acad Sci USA 106:18–23

van Laarhoven HW, Klomp DW, Rijpkema M et al (2007) Prediction of chemotherapeutic response of colorectal liver metastases with dynamic gadolinium-DTPA-enhanced MRI and localized 19F MRS pharmacokinetic studies of 5-fluorouracil. NMR Biomed 20:128–140

van Rijswijk CS, Geirnaerdt MJ, Hogendoorn PC et al (2003) Dynamic contrast-enhanced MR imaging in monitoring response to isolated limb perfusion in high-grade soft tissue sarcoma: initial results. Eur Radiol 13:1849–1858

van Tilborg GA, Strijkers GJ, Pouget EM et al (2008) Kinetics of avidin-induced clearance of biotinylated bimodal liposomes for improved MR molecular imaging. Magn Reson Med 60:1444–1456

van Vliet M, van Dijke CF, Wielopolski PA et al (2005) MR angiography of tumor-related vasculature: from the clinic to the micro-environment. Radiographics 25 Suppl 1:S85–97(discussion S97–88)

Vaupel P (2009a) Prognostic potential of the pre-therapeutic tumor oxygenation status. Adv Exp Med Biol 645:241–246

Vaupel P (2009b) Physiological mechanisms of treatment resistance. In: Molls M, Vaupel P, Nieder C et al (eds) The impact of tumor biology on cancer treatment and multidisciplinary strategies. Springer, Heidelberg

Vaupel P (2009c) Pathophysiology of solid tumors. In: Molls M, Vaupel P, Nieder C et al (eds) The impact of tumor biology on cancer treatment and multidisciplinary strategies. Springer, Heidelberg

Villaraza AJ, Bumb A, Brechbiel MW (2010a) Macromolecules, dendrimers, and nanomaterials in magnetic resonance imaging: the interplay between size, function, and pharmacokinetics. Chem Rev 110:2921–2959

Villaraza AJ, Bumb A, Brechbiel MW (2010b) Macromolecules, dendrimers, and nanomaterials in magnetic resonance imaging: the interplay between size, function, and pharmacokinetics. Chem Rev 110:2921–2959

Wahl RL, Jacene H, Kasamon Y et al (2009) From RECIST to PERCIST: evolving considerations for PET response criteria in solid tumors. J Nucl Med 50(Suppl 1):122S–150S

Walter G, Barton ER, Sweeney HL (2000) Noninvasive measurement of gene expression in skeletal muscle. Proc Natl Acad Sci U S A 97:5151–5155

Wang YX, Hussain SM, Krestin GP (2001) Superparamagnetic iron oxide contrast agents: physicochemical characteristics and applications in MR imaging. Eur Radiol 11:2319–2331

Wang H, Cao F, De A et al (2009) Trafficking mesenchymal stem cell engraftment and differentiation in tumor-bearing mice by bioluminescence imaging. Stem cells (Dayton, Ohio) 27:1548–1558

Warntjes JB, Dahlqvist O, Lundberg P (2007) Novel method for rapid, simultaneous T1, T*2, and proton density quantification. Magn Reson Med 57:528–537

Warntjes JB, Leinhard OD, West J et al (2008) Rapid magnetic resonance quantification on the brain: optimization for clinical usage. Magn Reson Med 60:320–329

Watanabe Y, Uotani K, Nakazawa T et al (2009) Dual-energy direct bone removal CT angiography for evaluation of intracranial aneurysm or stenosis: comparison with conventional digital subtraction angiography. Eur Radiol 19:1019–1024

Watkins GA, Jones EF, Scott Shell M et al (2009) Development of an optimized activatable MMP-14 targeted SPECT imaging probe. Bioorg Med Chem 17:653–659

Weissleder R, Simonova M, Bogdanova A et al (1997) MR imaging and scintigraphy of gene expression through melanin induction. Radiology 204:425–429
Weissleder R, Moore A, Mahmood U et al (2000) In vivo magnetic resonance imaging of transgene expression. Nat Med 6:351–355
Wiener EC, Brechbiel MW, Brothers H et al (1994) Dendrimer-based metal chelates: a new class of magnetic resonance imaging contrast agents. Magn Reson Med 31:1–8
Wikstrom MG, Moseley ME, White DL et al (1989) Contrast-enhanced MRI of tumors. Comparison of Gd-DTPA and a macromolecular agent. Invest Radiol 24:609–615
Willmann JK, van Bruggen N, Dinkelborg LM et al (2008) Molecular imaging in drug development. Nat Rev 7:591–607
Wilson CB, Lammertsma AA, McKenzie CG et al (1992) Measurements of blood flow and exchanging water space in breast tumors using positron emission tomography: a rapid and noninvasive dynamic method. Cancer Res 52:1592–1597
Winter PM, Caruthers SD, Allen JS et al (2010) Molecular imaging of angiogenic therapy in peripheral vascular disease with alphanubeta3-integrin-targeted nanoparticles. Magn Reson Med 64:369–376
World Health Organisation (1979) WHO handbook for reporting results of cancer treatment. WHO
Wu AM, Yazaki PJ (2000) Designer genes: recombinant antibody fragments for biological imaging. Q J Nucl Med 44:268–283
Wu L, Cao Y, Liao C et al (2010) Diagnostic performance of USPIO-enhanced MRI for lymph-node metastases in different body regions: a meta-analysis. Eur J Radiol 80:582–589
Wyss C, Schaefer SC, Juillerat-Jeanneret L et al (2009) Molecular imaging by micro-CT: specific E-selectin imaging. Eur Radiol 19:2487–2494
Yang L, Mao H, Wang YA et al (2009) Single chain epidermal growth factor receptor antibody conjugated nanoparticles for in vivo tumor targeting and imaging. Small (Weinheim an der Bergstrasse, Germany) 5:235–243
Yang X, Gong H, Quan G et al (2010) Combined system of fluorescence diffuse optical tomography and microcomputed tomography for small animal imaging. Rev Sci Instrum 81:054304
Yao W, Qu N, Lu Z et al (2009) The application of T1 and T2 relaxation time and magnetization transfer ratios to the early diagnosis of patellar cartilage osteoarthritis. Skeletal Radiol 38:1055–1062
Yoo B, Pagel MD (2008) An overview of responsive MRI contrast agents for molecular imaging. Front Biosci 13:1733–1752
Yoo B, Raam MS, Rosenblum RM et al (2007) Enzyme-responsive PARACEST MRI contrast agents: a new biomedical imaging approach for studies of the proteasome. Contrast Media Mol Imaging 2:189–198
Yordanov AT, Kobayashi H, English SJ et al (2003) Gadolinium-labeled dendrimers as biometric nanoprobes to detect vascular permeability. J Mater Chem 13:1523–1525
Yu JX, Kodibagkar VD, Cui W et al (2005) 19F: a versatile reporter for non-invasive physiology and pharmacology using magnetic resonance. Curr Med Chem 12:819–848
Yuan F, Dellian M, Fukumura D et al (1995) Vascular permeability in a human tumor xenograft: molecular size dependence and cutoff size. Cancer Res 55:3752–3756
Zahra MA, Hollingsworth KG, Sala E et al (2007) Dynamic contrast-enhanced MRI as a predictor of tumour response to radiotherapy. Lancet Oncol 8:63–74
Zhang X, Lin Y, Gillies RJ (2010) Tumor pH and its measurement. J Nucl Med 51:1167–1170
Zhao D, Ran S, Constantinescu A et al (2003) Tumor oxygen dynamics: correlation of in vivo MRI with histological findings. Neoplasia 5:308–318
Zumsteg A, Strittmatter K, Klewe-Nebenius D et al (2010) A bioluminescent mouse model of pancreatic {beta}-cell carcinogenesis. Carcinogenesis 31:1465–1474
Zurkiya O, Chan AW, Hu X (2008) MagA is sufficient for producing magnetic nanoparticles in mammalian cells, making it an MRI reporter. Magn Reson Med 59:1225–1231

Single Photon Emission Computed Tomography Tracer

Cristina Müller and Roger Schibli

Abstract

Single photon emission computed tomography (SPECT) is the state-of-the-art imaging modality in nuclear medicine despite the fact that only a few new SPECT tracers have become available in the past 20 years. Critical for the future success of SPECT is the design of new and specific tracers for the detection, localization, and staging of a disease and for monitoring therapy. The utility of SPECT imaging to address oncologic questions is dependent on radiotracers that ideally exhibit excellent tissue penetration, high affinity to the tumor-associated target structure, specific uptake and retention in the malignant lesions, and rapid clearance from non-targeted tissues and organs. In general, a target-specific SPECT radiopharmaceutical can be divided into two main parts: a targeting biomolecule (e.g. peptide, antibody fragment) and a γ-radiation emitting radionuclide (e.g. ^{99m}Tc, ^{123}I). If radiometals are used as the radiation source, a bifunctional chelator is needed to link the radioisotope to the targeting entity. In a rational SPECT tracer design these single components have to be critically evaluated in order to achieve a balance among the demands for adequate target binding, and a rapid clearance of the radiotracer. The focus of this chapter is to depict recent developments of tumor-targeted SPECT radiotracers for imaging of cancer diseases. Possibilities for optimization of tracer design and potential causes for design failure are discussed and highlighted with selected examples.

C. Müller (✉) · R. Schibli
Center for Radiopharmaceutical Sciences ETH-PSI-USZ,
Paul Scherrer Institute, 5232 Villigen-PSI, Switzerland
e-mail: cristina.mueller@psi.ch

R. Schibli
Department of Chemistry and Applied Biosciences, ETH Zurich,
8093 Zurich, Switzerland

O. Schober and B. Riemann (eds.), *Molecular Imaging in Oncology*,
Recent Results in Cancer Research 187, DOI: 10.1007/978-3-642-10853-2_2,

Contents

1 Introduction

Single photon emission computed tomography (SPECT) and positron emission tomography (PET) are valuable molecular imaging modalities as both are capable of detecting minute amounts of radioactive tracer (Rowland and Cherry 2008; Spanoudaki and Ziegler 2008). Clinical PET is currently about 2–3 orders of magnitude more sensitive than SPECT, has a better spatial resolution, and offers superior quantification. Nowadays, many nuclear imaging centers possess PET or PET/CT scanners. However, the large infrastructure that is needed for the production of β^+-emitting radioisotopes (e.g. ^{18}F, ^{11}C, ^{64}Cu) make PET an expensive technology. Also, at the moment there are no approved clinical grade generators for PET radioisotopes (e.g. ^{68}Ga, ^{44}Sc). Hence, for routine application SPECT is still the state-of-the-art nuclear imaging modality because it is less expensive and can make use of a broader array of suitable and available radionuclides (Table 1). Importantly, SPECT imaging is a useful technology for monitoring targeted radionuclide therapy employing radioisotopes that emit—concomitantly with the therapeutic radiation—γ-rays of suitable energies for SPECT (e.g. ^{177}Lu, $^{188/186}$Re, ^{67}Cu, ^{131}I, ^{213}Bi) (Alford et al. 2009).

Generally, SPECT radiopharmaceuticals can be classified according to their biodistribution characteristics. There are those whose tissue distribution is determined exclusively by their chemical and physical properties and those whose distribution and accumulation are determined by their specific interaction with a biological target that is expressed at the site of interest (e.g. tumor-associated

Table 1 Selection of radioisotopes for SPECT imaging (and therapy)

SPECT-isotopes	Half-life	γ-Energy	
^{99m}Tc	6.02 h	141 keV (89 %)	
^{111}In	2.80 d	171 keV (91 %), 245 (94 %)	
^{67}Ga	3.26 d	93 (39 %), 185 (21 %), 300 (17 %), 394 (5 %)	
^{123}I	13.22 h	159 (83 %)	
Therapy/SPECT isotopes	Half-life	β^--Energy$_{average}$ [keV]	γ-Energy [keV]
^{177}Lu	6.65 d	134 (100 %)	113 (10 %), 208 (10 %)
^{186}Re	3.72 d	347 (93 %)	137 (9.5 %)
^{188}Re	17.0 h	763 (100 %)	155 (16 %)
^{67}Cu	2.58 d	141 (100 %)	185 (49 %)
^{131}I	8.03 d	182 (100 %)	365 (82 %)

receptor) (Liu 2008; Bartholoma et al. 2010). Herein we focus on the development and (pre) clinical application of target-specific radiotracers. A target-specific SPECT radiopharmaceutical can be divided into two main parts: a targeting biomolecule and a γ-radiation emitting radionuclide (Liu 2008). In the case of using radiometals as the radiation source a bifunctional chelator is needed as an additional component of the radiopharmaceutical. Thus, a metallic radioisotope is coordinated by a suitable chelating agent that is conjugated to the targeting agent via a linker entity (Fig. 1). In a rational design of a SPECT tracer the single components have to be critically evaluated in order to achieve a balance among the demands of an adequate target binding and a rapid excretion.

The majority of diagnostic radiopharmaceuticals currently available in nuclear medicine make use of metallic radioisotopes. For SPECT imaging [^{99m}Tc]-technetium is the most widely applied radioisotope because of its ideal physical decay properties and easy availability by a generator system (Table 1). [^{111}In]-indium is another SPECT radioisotope frequently used in the clinics where it is often employed as a surrogate for [^{90}Y]-yttrium analogs since ^{90}Y that is used for therapeutic purposes is a pure β^--emitter. In contrast, clinical application of [^{67}Ga]-gallium is relatively rare. Non-metallic radionuclides used for SPECT are basically the isotopes of iodine. [^{123}I]-Iodine has dosimetry and imaging characteristics that are superior to [^{131}I]-iodine and [^{125}I]-iodine and is therefore the preferred isotope for imaging purposes (Table 1).

A targeting biomolecule serves as a "carrier" for specific delivery of the radionuclide to the target expressing cells of interest. Such biomolecules could be specific antibodies (or antibody fragments) or small molecular weight molecules (e.g. peptides, vitamins, nucleosides). Each class of targeting agents has its pros and cons for its use in diagnostic nuclear medicine and for a potential translation to therapeutic applications. Peptide-based radiopharmaceuticals represent by far the largest group of tumor-targeted radioimaging agents currently in use.

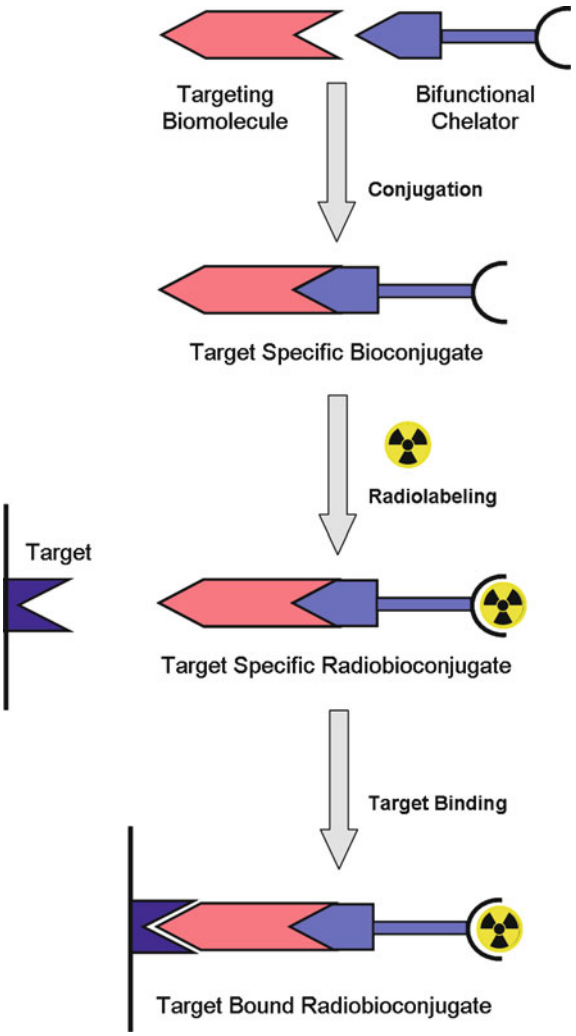

Fig. 1 Schematic representation of a biomolecule that is conjugated to a radiometal. The bifunctional chelator that is conjugated to the target-specific biomolecule is necessary for coordination of the radiometal. The target-specific radiobioconjugate binds to the tumor cell surface associated target (e.g. receptor) and allows visualization of target-expressing malignant lesions via SPECT

During tracer development, the first steps are based on chemistry and molecular biology methods such as peptide syntheses, conventional or combinatorial chemistry, and phage display techniques for preparation, identification, and isolation of high-affinity binders to a particular receptor. Determination of the tumor-targeted radiotracer's stability in vitro and its ability to bind with high affinity to the target structure on cultured cancer cells are first requirements in this early development stage. The in vitro evaluation is followed by investigations in vivo using an adequate animal model, typically tumor-bearing small rodents. It is important to recognize that radiolabeled tumor imaging agents display different biodistribution and pharmacokinetics in animal models compared to humans due to a different metabolism, differences in the volume of distribution and potential

cross-reactivity of the targeting entity with normal tissues expressing the target receptor or antigen in humans (Buchsbaum 1997). Significant variability in the tissue distribution of radiotracers might occur among different animal models (e.g. mice vs. rats) or different animal strains (e.g. nude mice vs. normal mice). However, small rodents have emerged as generally the most useful and cost effective animal models for developing and evaluating radiotracers and to test new experimental approaches to increase their localization in tumors. Post-mortem biodistribution studies allow the detection and quantification of radioactive accumulation in targeted and non-targeted tissues, and thus the determination of the radiotracer's pharmacokinetic profile. Collection of blood and tissue samples for identification of metabolites at different time points after radiotracer application provides information about the radiotracer's circulation time and its in vivo stability. By increasing the availability of small-animal SPECT and SPECT/CT scanners in recent years, the process of radiotracer development has been significantly improved and accelerated while the number of test animals required has been reduced. Thus, a wide variety of targeted SPECT radiotracers are currently being developed and preclinically tested for in vivo imaging of various tumor types expressing one or more of the most relevant receptor types (Schottelius and Wester 2009).

The focus of this chapter is to present general aspects for the design of SPECT tracers followed by specific examples of recent SPECT imaging agents based on antibodies, antibody fragments, peptides, and other small-molecular weight biomolecules such as vitamins or nucleosides. The examples demonstrate possibilities for optimization of the tracer design by tuning single components of these imaging agents. Finally, potential causes for failures in SPECT tracer design are discussed.

2 General Aspects for the Design of SPECT Tracers

The ideal SPECT tracer exhibits excellent tissue penetration, high affinity to the target structure, specific uptake and retention in the target cells, and rapid clearance from non-targeted tissues and organs. In addition, it is highly stable in vivo, easy to prepare, and safe for human application. These aspects are crucial because injected radiotracers that are not stable, not bound to the target, or not rapidly excreted create high background signals resulting in low tumor-to-background contrast and unnecessary radiation dose burden to the patient (Alford et al. 2009).

In the case of metallic radioisotopes, a bifunctional chelator is needed that is covalently linked to a biomolecule (Liu 2008). Since the stability of the radiometal complex is a critical aspect for the success of a radiopharmaceutical, it is important to choose an ideal chelating system that allows the formation of radiometal complexes of high thermodynamic stability and kinetic inertness (Bartholoma et al. 2010). Among the SPECT isotopes currently in use, [^{99m}Tc]-technetium is still the workhorse of diagnostic nuclear medicine. It is used in the majority of diagnostic scans conducted each year in hospitals worldwide. The preferred use of ^{99m}Tc-radiopharmaceuticals reflects the ideal nuclear properties of the isotope and,

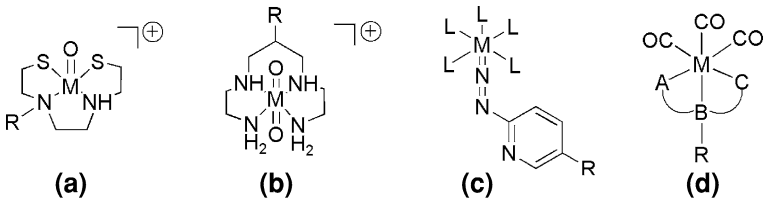

Fig. 2 The most frequently used ^{99m}Tc-complexes for radiobioconjugates. **a** ^{99m}Tc(V)oxo-core, **b** ^{99m}Tc(V)dioxo-core, **c** ^{99m}Tc(V)organohydrazino-core (HYNIC) and **d** ^{99m}Tc(I)-tricarbonyl-core. M = ^{99m}Tc, L = co-ligands

until recently, the convenient availability from commercial ^{99}Mo/^{99m}Tc-generators. Currently, a key challenge is the continuing global shortage of ^{99m}Tc because aging nuclear reactors that provide a large fraction of the world's supply require more frequent repair and/or routine maintenance.

Technetium is a transition metal that presents a major challenge with respect to designing radiopharmaceuticals with favorable in vivo properties. In order to link the radionuclide to a targeting molecule, [^{99m}Tc(VII)]-pertechnetate that is eluted from the ^{99}Mo/^{99m}Tc-generator must be reduced to build a complex with an appropriate bifunctional chelating system, most commonly in the oxidation state +I, +III or +V. The ^{99m}Tc(V)-oxo and ^{99m}Tc(V)-organohydrazino cores are most extensively studied (Fig. 2). The ^{99m}Tc(V)-oxo-core generally adopts a square-pyrimidal geometry with the π-bonding oxo-group in the apical position. The core is stabilized by σ- and π-donating groups where amino, amido, and thiolate ligands as well as tetradentate ligands of the N_xS_{4-x}-class have been investigated (Liu 2008; Bartholoma et al. 2010). A prominent example of a tetradentate chelator is the peptide-based chelator mercapto-acetylglycylglyclgylcine (H_5MAG_3) (Lei et al. 1996).

An alternative approach is the use of the ^{99m}Tc(V)-organohydrazino (HYNIC) core that was first introduced by Abrams et al. 20 years ago (Abrams et al. 1990; Schwartz et al. 1991). The advantages of this system are the facile functionalization of targeting entities via amide linkage. It has therefore been used for ^{99m}Tc-labeling of a variety of high, medium, and small molecular-weight biomolecules (Guo et al. 1999; Steffens et al. 1999; Decristoforo et al. 2000a, b; Tang et al. 2005; Ferro-Flores et al. 2006; von Guggenberg et al. 2007; Liu et al. 2008; Salouti et al. 2008). Since the HYNIC-chelator can only occupy one or two coordination sites on the metal, co-ligands such as tricine are needed to complete the coordination sphere of ^{99m}Tc (Edwards et al. 1997; Liu et al. 1998; Purohit et al. 2003). The possibility for selection of appropriate co-ligands is advantageous for an easy modulation of the hydrophilicity and pharmacokinetics of the ^{99m}Tc-HYNIC-derivatized biomolecules. However, the presence of multiple species in solution due to different bonding modalities of the HYNIC moiety and co-ligands might be problematic for a commercial development, because of the increasing regulatory hurdles and the requirements of fully characterized products. Another, less

frequently employed approach is the use of a ^{99m}Tc(V)-dioxo-core coordinated by nitrogen ligands that form octahedral complexes with the oxygens *trans* to each other (Kastner et al. 1982). The group of Nock and Maina made successful use of a tetramine chelator for ^{99m}Tc-radiolabeling of several peptide-based biomolecules forming monocationic polar complexes with the ^{99m}Tc(V)-dioxo-core (Maina et al. 2002; Nock et al. 2003, 2006). The advantages of this radiolabeling strategy include its easy formation at ambient temperature, its high stability in the biological milieu, and considerable hydrophilicity. A completely different ^{99m}Tc-radiolabeling strategy has been introduced by the development of the tricarbonyl-technique which offered new opportunities for the design of ^{99m}Tc(I)-radiotracers (Egli et al. 1997; Alberto et al. 1998; Alberto et al. 1999a, b; Egli et al. 1999; Schibli et al. 2000; Alberto et al. 2001; Schibli and Schubiger 2002). The water-soluble ^{99m}Tc(I)-tricarbonyl precursor's aqua-ligands are readily exchanged allowing the coordination of preferentially tridentate chelators that can be modified to provide complexes with cationic, neutral, or anionic overall charge (Schibli et al. 2000; Müller et al. 2006b; Garcia Garayoa et al. 2007b; Schweinsberg et al. 2008; Maresca et al. 2009). In addition, the tricarbonyl radiolabeling strategy is also accessible for the preparation of stable radiometal complexes using β-particle emitting rhenium isotopes ($^{186/188}$Re, Table 1). Hence, the production of isostructural compounds with the "matched pair" ^{99m}Tc/$^{188/186}$Re for diagnostic and therapeutic purposes has become feasible thanks to the tricarbonyl strategy, a feature which is often not fulfilled with Re(V)-complexes (Müller et al. 2007).

Radiolanthanides (e.g. ^{177}Lu) and lanthanide-like isotopes as well as indium and gallium are used in an oxidation state +III. They can generally be coordinated by polyamino-polycarboxy chelating systems. Coordination numbers of lanthanides are typically between seven and ten whereas coordination numbers of eight or nine are most common in Ln(III)-complexes with polydentate chelators. The 1,4,7,10-tetraazacyclododecane-1,4,7,10-tetraacetic acid (DOTA)-chelator emerged as particularly useful for lanthanide coordination of therapeutic radiopharmaceuticals because of the formation of metal complexes of extremely high thermodynamic stability and kinetic inertness (Fig. 3). In addition, the hydrophilic acetate chelating arms of DOTA favor a fast clearance of radiotracers from the blood and non-targeted organs and tissues. Despite the similarities of the SPECT radioisotopes [^{67}Ga(III)]-gallium and [^{111}In(III)]-indium they are different in size and charge density. Ga(III) has a small ionic radius (0.65 Å) and the coordination number is six whereas the ionic radius of In(III) is larger (0.92 Å) and it is seven- or eight-coordinated in its complexes. The structural differences among Ga- and In-complexes might have an influence on the overall tissue distribution of one and the same bioconjugate as recently exemplified with a somatostatin-analog (Heppeler et al. 1999). A higher tumor uptake and lower kidney retention has been reported for ^{67}Ga-DOTATOC compared to that of ^{111}In-DOTATOC. Whereas DOTA appears to be an ideal chelator for coordination of lanthanide radioisotopes or ^{111}In(III), its coordination cavity is not ideal for Ga(III) as it is too large. On the other hand there is a perfect fit between the size of Ga(III) and the coordination cavity formed by the N_3O_3 donor atoms of the macrocyclic 1,4,7-triazacyclononane-1,4,7-triacetic acid

(NOTA)-chelator (Liu 2008). Consequently, a higher thermodynamic stability constant has been found for Ga-NOTA complexes compared to those of Ga-DOTA-complexes (Delgado and da Silva 1982). In some cases, open chelating systems are more favorable than macrocycles because they are capable to form radiometal complexes at ambient temperature which is particularly important for temperature-sensitive targeting agents. Examples are variable versions of diethylenetriamine pentaacetic acid (DTPA, CHX-DTPA, etc., Fig. 3). DTPA is one of the most commonly employed acyclic ligands in radiochemistry useful for coordination of ^{111}In, ^{67}Ga, and radiolanthanides. For ^{111}In-complexation DTPA emerged as the ideal chelating agent (Mardirossian et al. 1993).

In addition to the bifunctional chelator's function for stable coordination of the radiometal, the linker-entity is important for conjugation with the biomolecule and might influence the overall pharmacokinetics of the radiopharmaceutical. By affecting the biomolecule's lipophilic or hydrophilic characteristics the linker system can serve for controlling its in vivo behavior. Thus, the nature of a bifunctional chelator in terms of geometry, lipophilicity, and overall charge plays a crucial role in determining the biodistribution of (tumor-) targeted radiopharmaceuticals (Bartholoma et al. 2010).

Functionalization of amino acid side chains (e.g. lysine, cysteine) with chemically reactive probes of bifunctional chelators is a largely uncontrolled random process that results in a heterogeneous mixture of conjugates modified at variable sites. A considerable advantage of small molecular-weight biomolecules (e.g. peptides and vitamins) is the fact that derivatization with a bifunctional chelating agent can be governed by specific chemical reactions that yield a single, clearly defined species. In contrast, loss of binding affinity is of concern during the process of antibody derivatization because modification of the Fab region (antigen binding site) can possibly have deleterious effects on the target binding of the protein. Both loss of binding activity to the target and overlabeling effects are highly undesired processes because they result in unwanted background radiation and unspecific accumulation of the antibody radioconjugates in the liver. For this reason, recent endeavors were undertaken for the development of site-specific derivatization via enzymatic reactions that are selective for a particular amino acid (Josten et al. 2000; Mindt et al. 2008) or sugar residue (Boeggeman et al. 2009) at a specified site of the antibody.

Since small molecular-weight molecules are usually stable at a broad range of temperatures and pH values the radiolabeling procedure is mostly smooth and quantitative. In contrast, proteins are generally sensitive to elevated temperatures. Thus, commonly applied methods for radiometal-labeling of proteins are time-consuming due to the low reaction temperature applicable. To overcome this drawback, pre-labeling strategies have been proposed allowing the preparation of radioimmunoconjugates within a shorter period of time while preventing the risk of affecting the antibody's scaffold under possibly harsh conditions needed for direct radiolabeling strategies (Li et al. 1995; Wängler et al. 2009).

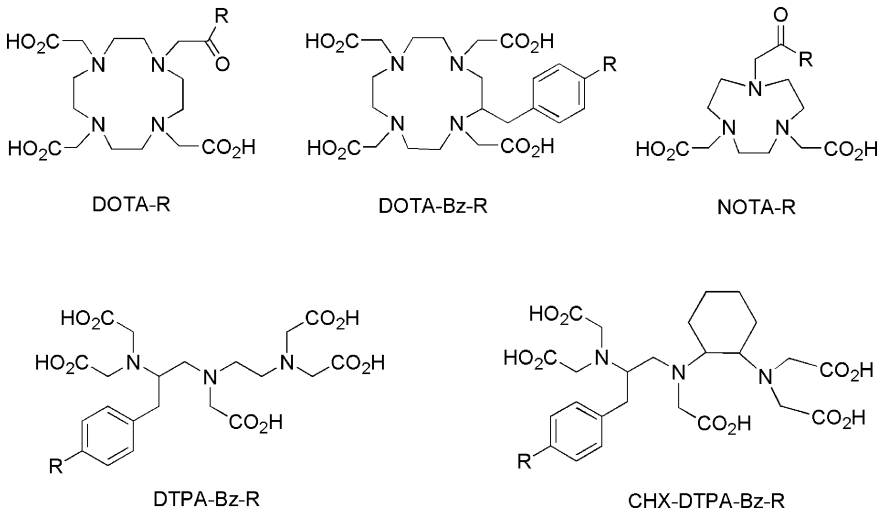

Fig. 3 The most frequently used macrocyclic (DOTA, NOTA) and acyclic (DTPA) chelators for complexation of radioisotopes for SPECT imaging (e.g. ^{111}In, ^{67}Ga) and combined therapy/SPECT imaging (e.g. ^{177}Lu)

3 Peptide-Receptor Radionuclide Imaging

Since receptors for regulatory peptides are overexpressed in a variety of human cancers, it is a prominent strategy to use radiolabeled analogs of these physiologically occurring peptides for tumor-targeted nuclear imaging. Advantages of using peptides are their good tissue penetration, a fast clearance, and minimal immunogenicity (Schottelius and Wester 2009). Small peptides of usually less than 40 amino acid residues are easily accessible through solid phase peptide synthesis. Their tolerance toward bulky modification and resistance toward harsh chemical conditions that are sometimes inevitable during radiolabeling procedures are further advantages of peptides. Importantly, a formulation of a radiolabeled peptide consists of identical molecules with a well-defined structure. Clearly, the most outstanding example of success in the field of peptide-based diagnostic and therapeutic nuclear medicine has been the use of somatostatin analogs for targeting the somatostatin receptor (Kwekkeboom et al. 2000). Somatostatin-derived tracers designed to image somatostatin receptor subtype 2 (sst2)-expressing tumors have enjoyed almost two decades of successful preclinical development and extensive clinical application. This example has paved the path for further exploration of radiolabeled peptides targeting other tumor-associated receptors such as gastrin releasing peptide receptors, neurotensin receptors, or cholecystokinin receptors (Behr et al. 2001).

3.1 Somatostatin Analogs

The prototypes of radiolabeled peptides for SPECT imaging are the somatostatin analogs commonly labeled with ^{111}In or ^{99m}Tc. Somatostatin receptors are overexpressed on neuroendocrine tumors including pituitary adenomas, pheochromocytomas, paragangliomas, neuroblastomas, and medullary thyroid cancers. From the five subtypes of somatostatin receptors belonging to the G-protein coupled receptors, subtype 2 is the most widely overexpressed form in neuroendocrine tumors. In the beginning of their development, somatostatin analogs suffered from rapid degradation in vivo. Such limitations have been overcome by stabilization strategies through the development of synthetic peptides. Peptides of high chemical stability became accessible by introduction of D-amino acids or other unnatural amino acids at known cleavage sites, cyclization, or modification of C- and N-termini via amidation, reduction, alkylation, or acylation (Schottelius and Wester 2009). The clinically approved ^{111}In-labeled DTPA^0-octreotide (OctreoScan) has proven to be a successful and versatile molecular imaging agent (Figs. 4 and 5). The most frequently used DOTA-coupled, somatostatin-based peptides are [DOTA^0,Tyr^3]-octreotide and [DOTA^0,Tyr^3,Thr^8]-octreotate usually referred as DOTATOC and DOTATATE (Fig. 4). These analogs have also been successfully employed for therapeutic purposes when radiolabeled with particle-emitting radioiosopes (e.g. ^{177}Lu, ^{90}Y). Several sst2-binding somatostatin analogs are currently used in the clinic. Further research projects are focusing on the development of new and improved somatostatin analogs with a broader receptor subtype affinity profile. Such compounds would extend the range of targeted cancer candidates and increase the net tumor uptake when several receptor subtypes are expressed on the same tumor cell.

The generally high kidney uptake of radiometallated peptides due to their reabsorption in the renal proximal tubules is a drawback for peptide-based tumor targeting as it may lead to reduced contrast and quality of diagnostic imaging and damage radiosensitive kidneys if applied for therapeutic purposes (Gotthardt et al. 2007). Thus, several strategies to reduce tubular reabsorption of peptidic radiotracers have been investigated. One strategy relies on the chemical modification of the peptide with entities or overall charges that would potentially reduce renal uptake. A successful example of such modification is given by the work of Schwaiger and co-workers who developed ^{125}I-somatostatin analogs modified with carbohydrate-entities (Wester et al. 2002; Schottelius et al. 2002). Glycation modified the physicochemical behavior of the radiotracers in that pharmacokinetics were significantly improved as shown by reduced hepatic uptake and biliary excretion and a rapid clearance from the circulation via the kidneys without increasing renal accumulation of radioactivity. Another approach is based on the administration of additional substances for potential inhibition of peptide reabsorption. In this respect the co-infusion of the cationic amino acids lysine and arginine is the most prominent example since this combination successfully reduced renal accumulation of radiolabeled somatostatin analogs in preclinical studies (de Jong et al. 1996; Bernard et al. 1997; Verwijnen et al. 2005) and in patients (Hammond et al. 1993; Rolleman et al. 2003).

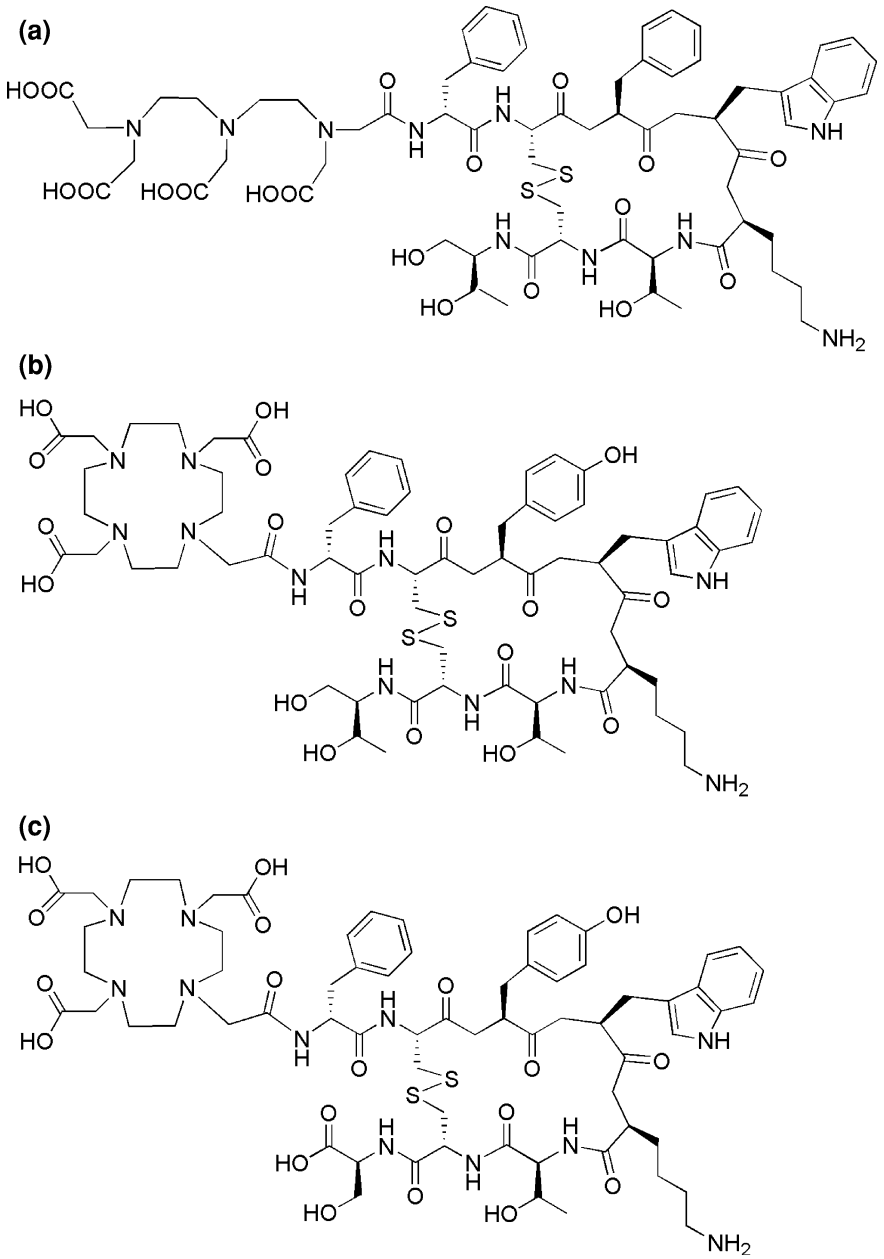

Fig. 4 Chemical structures of DTPA- and DOTA-modified somatostatin analogs for targeted diagnosis and therapy of somatostatin receptor-positive cancer diseases. **a** $DTPA^0$-octreotide, **b** $DOTA^0$-Tyr^3-octreotide (DOTATOC), $DOTA^0$-Tyr^3-Thr^8-octreotate (DOTATATE)

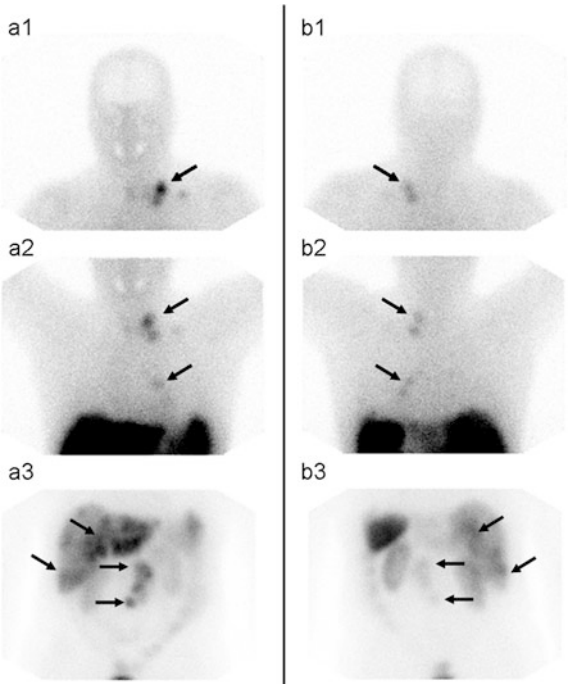

Fig. 5 Scintigraphy [multiple planar spot views, anterior (**a**) and posterior (**b**) of the head/neck (1), thorax (2) and abdomen (3)] performed 24 h after injection of ^{111}In-octreotide (OctreoScan; Covidien, Petten, the Netherlands) in a patient diagnosed with a well-differentiated endocrine carcinoma (carcinoid) with lymphogenic spread in the abdomen and supraclavicular and multiple metastatic lesions in the liver and lungs. The images have been kindly provided by J.J.M. Teunissen (MD, PhD), Erasmus Medical Center, Rotterdam, The Netherlands

Originally, it was proposed that peptide agonists that are efficiently internalized into receptor expressing cancer cells would be the best candidates for tumor imaging (Cescato et al. 2006). However, the two somatostatin analogs ^{111}In-DOTA-sst2-ANT and ^{111}In-DOTA-sst3-ODN-8 showed extremely high tumor accumulation despite being receptor antagonists (Ginj et al. 2006). It could be shown in vitro that a more than 15-fold increased number of binding sites per cell were accessible for antagonists compared to their agonist analogs and in addition slow ligand dissociation from the receptor was determined. These findings attracted the attention of many research groups and led to the development of further sst2-binding somatostatin-based antagonists. The studies confirmed that high-affinity somatostatin receptor antagonists that poorly internalize in tumor cells exhibit improved tumor targeting characteristics than corresponding agonists. The fact that this phenomenon was found not only for sst2-selective compounds but also for sst3-selective compounds suggests that this phenomenon is valid for more than just one particular receptor (Cescato et al. 2008).

3.2 Bombesin Analogs

The bombesin receptor family comprises four receptor subtypes whereof the gastrin releasing peptide (GRP) receptor or bombesin receptor subtype 2 (BB2) has been studied most thoroughly (Smith et al. 2003d, 2005). The impetus for

Table 2 Sequence of various bombesin analogs

Analog	Chelator	Linker			
			1–6	7–13	14
Bombesin			pGlu-Gln-Arg-Leu-Gly-Asn-	-Gln-Trp-Ala-Val-Gly-His-Leu-	-Met-NH_2
Demo-besin-1	N4	-BzDig-	-**DPhe**-	-Gln-Trp-Ala-Val-Gly-His-Leu-**NHEt**	
BBS-1	(N^{π}His)Ac-	-βAla-βAla-		-Gln-Trp-Ala-Val-Gly-His-**Nle**-	
BBS-2	(N^{π}His)Ac-	**Lys**(**sha**)-βAla-βAla-		-Gln-Trp-Ala-Val-Gly-His-**Nle**-	
BBS-3	(N^{π}His)Ac-	-**Lys**(**Amd**)-βAla-βAla-		-Gln-Trp-Ala-Val-Gly-His-**Nle**-	
BBS-4	(N^{π}His)Ac-	-Ala(^{N}**TG**)-βAla-βAla-		-Gln-Trp-Ala-Val-Gly-His-**Nle**-	
MP2653	DTPA		-**aCMpip**-**Tha**-	-Gln-Trp-Ala-Val-**βAla**-His-**Tha**-	-**Nle**-**NH_2**
MP2346	DOTA		-**Pro**-Gln-Arg-**Tyr**-Gly-Asn-	-Gln-Trp-Ala-Val-Gly-His-Leu-	-Met-NH_2
Pesin	DOTA	-dPEG$_4$-		-Gln-Trp-Ala-Val-Gly-His-Leu-	-Met-NH_2
AMBA	DOTA	-CH_2CO-Gly-4-aminobenzyl-		-Gln-Trp-Ala-Val-Gly-His-Leu-	-Met-NH_2
RM 1	DOTA	-CH_2CO-Gly-4-aminobenzyl-	-**Phe**-	-Gln-Trp-Ala-Val-Gly-His-**Sta**-	-**Leu**-NH_2

Lys(sha) = lysine-coupled shikimic acid, Lys(Amd) = Amadori-Product; Ala(^{N}TG) = triazole-coupled glucose, Sta = statyl

targeting the GRP receptor is based on the fact that a variety of human tumors overexpress GRP receptors including prostate, breast, and small cell lung cancers (Moody et al. 1983; Gugger and Reubi 1999; Markwalder and Reubi 1999). The development of ^{99m}Tc-bombesin analogs has been the focus in recent years in many research laboratories (Table 2) (Baidoo et al. 1998; Van de Wiele et al. 2000; Nock et al. 2005). The tricarbonyl technique which was developed in view of the opportunity to use ^{99m}Tc and ^{188}Re as a "matched pair" for diagnosis and therapy (Alberto et al. 2001; Schibli et al. 2002) has been employed most extensively for radiolabeling of bombesin analogs (La Bella et al. 2002; Smith et al. 2003b, c; Garcia Garayoa et al. 2007a, b, 2008; Schweinsberg et al. 2008). A drawback of this strategy is, however, the fact that most ^{99m}Tc/^{188}Re-tricarbonyl-based bombesin derivatives are predominantly cleared via the hepatobiliary excretion pathway because of the tricarbonyl's inherent lipophilicity (Decristoforo and Mather 2002). Increasing the hydrophilicity of radiolabeled GRP-targeting

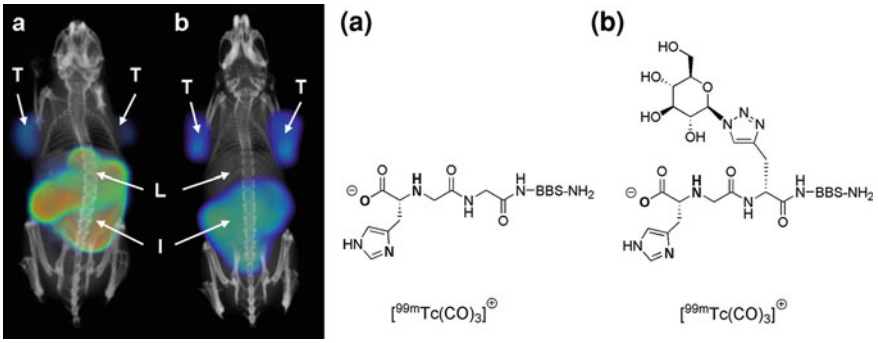

Fig. 6 SPECT/CT images of PC-3 tumor bearing mice 1.5 h after injection of **a** $^{99m}Tc(CO)_3$-(N^{ε}His)Ac-βAla-βAla-[Cha^{13},Nle^{14}]BBS(7–14)-NH_2 (control compound) and **b** $^{99m}Tc(CO)_3$-(N^{ε}His)Ac-Ala(^{N}TG)-βAla-βAla-[Cha^{13},Nle^{14}]BBS(7–14)-NH_2, (^{N}TG = N-linked triazole-linked glucose). T = tumor, L = liver, I = intestines (Schweinsberg et al. 2008)

peptide conjugates is necessary because accumulation of radioactivity in the liver and intestinal tract would compromise their capacity to effectively image solid tumors and metastatic lesions in the abdomen. This has been accomplished for example by introduction of "innocent" peptide sequences such as polylysine, polyglycine, or polyaspartic acid residues (Liu and Edwards 1999). Also, it could be shown that the introduction of a polar serylserylserine spacer into ^{99m}Tc-tricarbonyl pyrazolyl bombesin analogs resulted in a longer retention time of the radiotracer in the tumor tissue compared to analogs with more lipophilic linker entities consisting of β-alanin or glycylglycylglycine (Alves et al. 2006). Based on the promising results experienced with somatostatin analogs conjugated to carbohydrates (Wester et al. 2002; Schottelius et al. 2002), glycation of bombesin tracers was approached with the aim to increase their overall hydrophilicity (Schweinsberg et al. 2008). In this respect Garcia et al. tested three different bombesin analogs in vitro and in vivo. One of the derivatives was modified with a linker bearing a lysine that was coupled to the glycomimetic shikimic acid at the ε-amino group. Another bombesin derivative was glycated via an "Amadori rearrangement" and the third compound was a bombesin analog derivatized with an azido-glucose that was coupled to an alkyne-group of the linker entity via a "click"-chemistry reaction (Table 2). The introduction of polar carbohydrates had no negative effects on the in vitro stability and the internalization or efflux profile of the radiotracers in cultured tumor cells. In contrast, these modifications led to a significant reduction of abdominal radiotracer accumulation, a clearly higher tumor uptake and thus improved tumor-to-background ratios in vivo. The best results were obtained with the bombesin analog modified via a "click"-reaction that contained a triazole coupled glucose entity. The tissue distribution could be clearly ameliorated as demonstrated via SPECT/CT imaging studies where the tumor uptake was shown to be increased (Fig. 6).

On the other hand accumulation in the liver was significantly reduced. Despite the higher kidney uptake found for the carbohydrated bombesin analogs at early time points after injection, this decreased rapidly with time indicating that the radiotracers were not trapped in the renal tissues. By this example the strategy of radiotracer glycation has been demonstrated as a potent method to increase the overall hydrophilicity of a tracer and thus to improve the tissue distribution.

Based on the advantages of using trivalent radiometals for preparation of site-directed diagnostic/therapeutic radiopharmaceuticals (Smith et al. 2003d; Giblin et al. 2005), interest has been sparked into the synthesis and biological evaluation of trivalent radiometalated bombesin derivatives using radioisotopes such as ^{111}In or ^{177}Lu (Table 2) (Breeman et al. 2002; Hoffman et al. 2003; Smith et al. 2003a; Johnson et al. 2006; de Visser et al. 2007). One such example is the bombesin analog referred to as DOTA-AMBA useful for both diagnostic and therapeutic purposes (Lantry et al. 2006; Maddalena et al. 2009). Also, a so-called pan-bombesin analog has been designed with the special characteristic of displaying high affinity to all three bombesin receptor subtypes possibly allowing a broader field of application (Zhang et al. 2004).

The majority of research efforts into the design of bombesin-based radiotracers have been performed by using GRP receptor agonists. Such bombesin analogs undergo receptor-mediated endocytosis enabling residualization of the attached radiometal within the targeted tumor cell. However, ^{99m}Tc-demobesin-1 is a potent antagonist which clearly exhibited high affinity to the GRP receptor even though significant internalization into PC-3 prostate tumor cells was not observed. This radiotracer allowed imaging of PC-3 tumors in mice with better tumor-to-background contrast compared to the best available agonist analog (Nock et al. 2003). Thus, endeavors were directed also toward the development of bombesin antagonists. Recently, superior imaging properties of the ^{111}In-radiolabeled bombesin antagonist RM1 over the agonist ^{111}In-DOTA-AMBA have been demonstrated (Mansi et al. 2009). Whether or not bombesin antagonists are also favorable over agonists for therapeutic purposes remains to be investigated.

3.3 Neurotensin Analogs

Neurotensin (NT) is a linear tridecapeptide that can be found in the central nervous system and in peripheral tissues. Among the three NT receptors (NTR), NTR1 has been found in several neuroendocrine tumor types. Of special interest are exocrine pancreatic carcinomas that overexpress NTR1 with an incidence of 75–88 % (Reubi et al. 1998). Thus, several studies focused on the development of NT analogs for radiolabeling with SPECT radionuclides such as ^{99m}Tc (Garcia-Garayoa et al. 2006; Maina et al. 2007; Garcia-Garayoa et al. 2009) and ^{111}In (de Visser et al. 2003; Alshoukr et al. 2009). Similar to other small neuropeptides, neurotensin is rapidly metabolized in plasma by endogenous peptidases. Thus, neurotensin analogs which are stabilized at one or more of the three potential cleavage sites were developed. In this respect, the research group of Maina and

Table 3 Stability and affinity of different radiolabeled NT analogs (Garcia-Garayoa et al. 2009)

Analog	Amino acid sequence	In vitro stability		In vivo stability	Affinity
		Plasma	HT-29	Blood	Kd (nM)
^{99m}Tc-NT-II	(N^{α}-His)Ac-Arg-Arg-Pro-Tyr-Ile-Leu	5.6 min	n.d.	< 1min	0.3±0.2
^{99m}Tc-NT-XII	(N^{α}-His)Ac-Arg-**(N-CH_3)**-Arg-Pro-Tyr-**Tle**-Leu	21 d	6.5 h	0.75 h	2.0±1.6
^{99m}Tc-NT-XIX	(N^{α}-His)Ac-Arg-**(N-CH_3)**-Arg-Pro-**Dmt-Tle**-Leu	28 d	2.4 d	1.40 h	15.0±9.2

The modifications in the binding sequence are marked in *bold*
(*N^{α} His)Ac* Retro[N^{α} -carboxymethyl-histidine], *Tle* tertiary-leucine, *Dmt* dimethyltyrosine, *n.d.* not determined

Nock developed several ^{99m}Tc(V)-neurotensin analogs, referred to as ^{99m}Tc-demotensin, employing amino acid substitutions and/or reduction of the amide bond Arg^8/Lys^8-Arg^9 to the corresponding amine (Nock et al. 2006; Maina et al. 2007). Garcia and coworkers reported the biological evaluation of neurotensin analogs in which two of the three cleavage sites have been stabilized (Bruehlmeier et al. 2002; Garcia-Garayoa et al. 2006). These interventions allowed preparation of neurotensin analogs of high plasma stability, affinity to the NTR1 in the nanomolar range, and significant tumor uptake in preclinical and clinical studies. A promising candidate is the ^{99m}Tc(CO)$_3$-radiolabeled (N^{α}-His)Ac-Arg-(N-CH_3)-Arg-Pro-Tyr-Tle-Leu (^{99m}Tc-NT-XII), which has been stabilized at the cleavage sites 8–9 and 11–12. Other than in the case of bombesin derivatives (see Sect. 3.2), the introduction of a glycomimetic entity (shikimic acid) coupled to the side chain of an additional lysine residue did not result in an improved tissue distribution of the radiotracer. Although the expected lower kidney and liver uptake could be achieved, both the receptor affinity and the tumor uptake were unfavorably reduced. Recently, the group of Garcia reported the evaluation of a ^{99m}Tc(CO)$_3$-neurotensin analog, ^{99m}Tc-NT-XIX, modified at all three cleavage sites (Garcia-Garayoa et al. 2006, 2006; Garcia-Garayoa et al. 2009). Despite a slight decrease in receptor affinity and a lower rate of internalization, the in vitro and in vivo stability of this novel radiopeptide has been significantly increased (Table 3).

This example of a triple-stabilized neurotensin analog demonstrates the importance of the radiotracer's metabolic stability to increase its accumulation in the tumor tissue which was—in the case of ^{99m}Tc-NT-XIX—even able to compensate a slightly lower receptor binding affinity. The clearly improved tumor-to-background contrast of ^{99m}Tc-NT-XIX over ^{99m}Tc-NT-XII could be visualized by SPECT/CT-imaging (Fig. 7). Thus, the development of neurotensin ^{99m}Tc-radiotracers, where single amino acids have been substituted for peptide stabilization, is an example for optimization of a radiotracer's tissue distribution by increasing its in vivo stability.

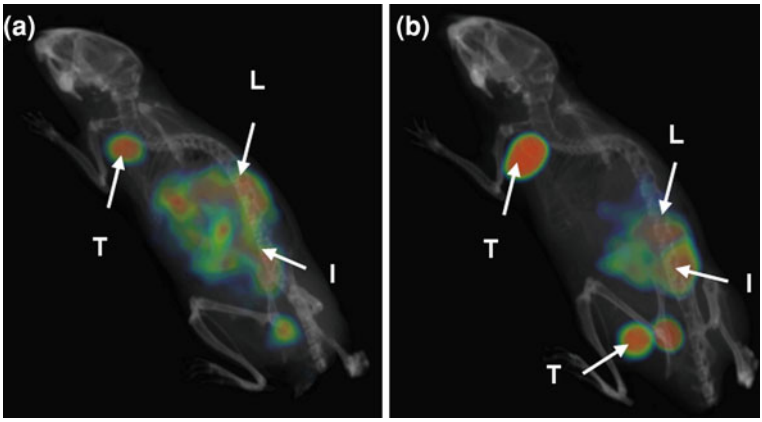

Fig. 7 SPECT/CT images of HT-29 tumor bearing mice 1.5 h after injection of **a** ^{99m}Tc-NT-XII and **b** ^{99m}Tc-NT-XIX. T = tumor, L = liver, I = intestines (Garcia-Garayoa et al. 2009)

3.4 Other Peptides-Based Radiotracers

Beyond somatostatin and GRP receptor targeting with bombesin and neurotensin analogs, many other regulatory peptide receptors are overexpressed on a variety of tumor types. Thus, peptide analogs in various stages of preclinical or clinical development include derivatives of cholecystokinin-2 (CCK-2) (de Jong et al. 1999), glucagon-like peptide-1 (GLP-1) (Körner et al. 2007), neuropeptide Y (NPY) (Zwanziger et al. 2008) and Arg-Gly-Asp (RGD) peptides (Schottelius et al. 2009) among others. CCK-2 receptors are expressed in medullary thyroid cancers. Initial gastrin-ligands for CCK-2 receptor targeting comprising a DTPA-DGlu-chelator showed unfavorable tumor-to-kidney ratios of radioactivity accumulation and were therefore not developed further. New gastrin derivatives lacking the glutamate-moiety showed excellent CCK-2 receptor affinity and lower renal retention in a rat AR42J tumor model (Good et al. 2008). Recently, it was found that GLP-1 receptors are highly overexpressed in virtually all insulinomas and gastrinomas (Körner et al. 2007). Metabolically more stable GLP-1 congeners referred to as exendin-3 and exendin-4 have been derivatized with a DTPA or DOTA chelating system for radiolabeling with ^{111}In or lanthanide radioisotopes. Remarkable tumor targeting was found in a human patient while employing ^{111}In-DOTA-exendin-4 (Christ et al. 2009). NPY analogs are of interest because of the frequent overexpression of NPY receptors in a variety of tumor types including breast cancer. A recent article reports on the synthesis and evaluation of a large number of NPY analogs where a DOTA-derivatized compound radiolabeled with ^{111}In performed as a potent radiotracer (Zwanziger et al. 2008). However, the in vivo studies with this tracer showed only low tumor uptake whereas radioactivity retention in the kidneys was extremely high. RGD-peptides that do not belong to the group of regulatory peptides are of particular interest for targeting integrin receptors such as the $\alpha_v\beta_3$ integrin. This integrin subtype is strongly expressed on

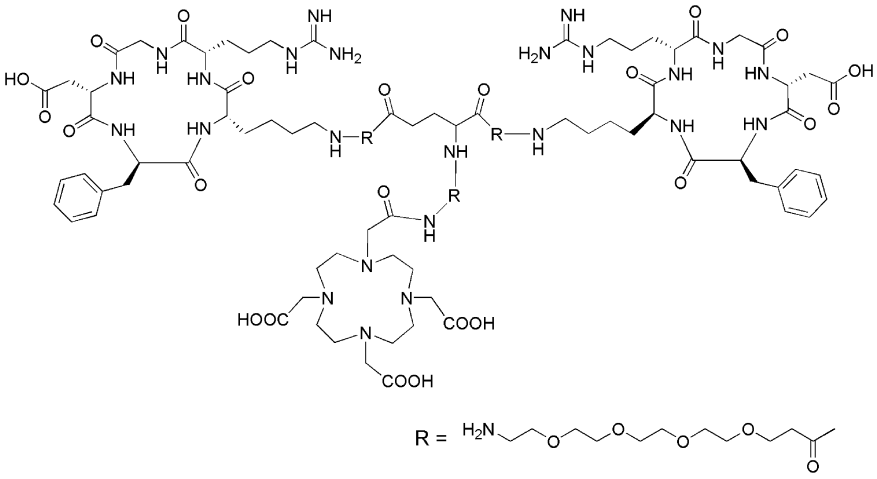

Fig. 8 Chemical structure of DOTA-3PEG$_4$-RGD dimer (Liu 2009; Shi et al. 2009)

activated and proliferating endothelial cells during tumor angiogenesis and metastasis but is not readily detectable in resting endothelial cells and most normal organs. Thus, a variety of RGD-peptide analogs for targeting $\alpha_v\beta_3$ integrins have been developed and the promising potential of RGD-based radiotracers for SPECT radioimaging has been shown (Schottelius et al. 2009). To enhance binding affinity for the $\alpha_v\beta_3$ integrin, various multivalent cyclic RGD-based peptides have been developed. All oligomeric peptide probes bound more strongly to the target cells than the monomeric RGD peptide in an integrin $\alpha_v\beta_3$-positive U87MG xenograft mouse model (Fig. 8) (Shi et al. 2008; Wang et al. 2009).

Through RGD peptides the advantage of multivalent tumor targeting agents over monovalent agents has been demonstrated. Most likely, the employment of the multimer-strategy also improves tumor targeting properties of non RGD-based peptides. Accordingly, investigations of divalent and multivalent peptides are ongoing for targeting of many of the tumor-associated receptors mentioned above, among those imaging agents for targeting the CCK-2 receptor (Sosabowski et al. 2009) and somatostatin receptor (Yim et al. 2009). Also, the strategy of using dual tumor targeting agents that combines targeting ligands for two different receptors (e.g. integrin and GRP receptor) might improve the radiotracer's diagnostic utility and applicability (Liu et al. 2009a, b).

4 Antibodies and Antibody Fragments

Another approach of nuclear imaging is the use of radiolabeled antibodies that target specific cell surface antigens. Radioimmunoimaging has been traditionally developed in parallel with radioimmunotherapy for the evaluation of the

antibodies' targeting properties and for dosimetry. Common tumor associated targets for radioimmunoimaging (and -therapy) are epidermal growth factor receptors (EGFR) (Tolmachev et al. 2009; Xu et al. 2009), the carcinoembryonic antigen (CEA) (Hong et al. 2008), the prostate-specific membrane antigen (PSMA) (Leyton et al. 2008), cluster of differentiation antigens (e.g. CD20), the pancarcinoma antigen (TAG-72), and the HER2 receptor among others. In addition, a number of angiogenesis markers—protein antigens expressed either on blood vessels or in the adjacent matrix of vessels—have been characterized as targets for selective delivery of antibodies to the tumor neovasculature (Brack et al. 2004). Examples are the fibronectin extra-domain B (EDB) (Neri et al. 1997), the integrin $\alpha_v\beta_3$ (Posey et al. 2001), the vascular endothelial growth factor (VEGF) (Brekken et al. 1998), and annexin A1 (Oh et al. 2004).

Potential concerns for radioimmunodiagnosis and strategies for optimization have been summarized in several review articles (Buchsbaum 1995; Buchsbaum 1997; Verhaar-Langereis et al. 2000). The main disadvantage of antibodies, namely their immunogenicity, could be largely overcome by the application of humanized antibodies that evade the immune system and are resistant to degradation. However, the slow vascular clearance (days to weeks) of antibodies as a consequence of their high molecular weight (IgG antibodies: $\sim$150 kDa) and the low tissue penetration are generally disadvantageous for radioimaging because of the resulting low target-to-non-target contrast at early time points after administration. Although it is generally accepted that antibodies are not the preferred biomolecules for nuclear imaging, the application of antibody fragments for SPECT have been successfully exemplified. Similar to peptides, antibody fragments are rapidly cleared from the blood and from non-targeted tissues. The results thereof are higher tumor-to-background ratios compared with intact antibodies and a lower radiation absorbed dose in non-targeted tissues and organs. A reduced percentage of injected doses of radioactivity in the tumor tissue and higher radiation doses in the kidneys are also consequences of the reduced size of antibody fragments (Buchsbaum 1997).

Efforts have been directed toward the development of antibody fragments such as $F(ab')_2$, F(ab') and single chain Fv (scFv) fragments to achieve faster clearance from the blood and in addition a better tumor penetration (Yokota et al. 1992; Yokota et al. 1993). Application of high-affinity scFv resulted in a relatively high tumor uptake combined with a rapid blood clearance and hence favorable targeting ratios (Begent et al. 1996). Multimers of antibody fragments may result in improved tumor localization compared with monomeric species as a result of higher affinity and slower blood clearance (King et al. 1994). Another approach to achieve improved pharmacokinetics is the pre-targeting strategy. Pre-targeting involves an initial targeting agent, which itself can be bound by secondarily injected agents. Secondary agents are either quickly clearing radiotracers that bind the initial agent with high affinity (Goldenberg et al. 2008) or "chase" reagents that clear an unbound radiolabeled antibody in circulation (Kobayashi et al. 1994). The pre-targeting approach is, however, not commonly applied for SPECT. In contrast, this strategy is much more favorable for radioimmunotherapy in order to reduce the

radioactive dose burden to the bone marrow and thus to avoid potential hemotoxicity of long circulating antibodies labeled with particle-emitting radioisotopes.

Radioimmunoimaging is of particular interest to evaluate a potential application of antibodies for targeted radionuclide therapy by interchanging a diagnostic with a therapeutic radioisotope of similar chemical characteristics (e.g. ^{111}In and ^{90}Y) or using a therapeutic radionuclide that emits concomitantly with therapeutic radiation also diagnostic γ-rays of a suitable energy for SPECT (e.g. ^{177}Lu, Table 1). The most prominent example of an antibody employed for radioimmunotherapy is ibritumomab tiuextan (Zevalin), a ^{90}Y-radiolabled monoclonal anti-CD20 antibody for the treatment of non Hodgkins lymphoma. Its ^{111}In-radiolabeled counterpart is usually administrated prior to therapy for detection of receptor-positive malignant tissue via SPECT imaging and for dosimetry.

4.1 Targeting Fibronectin Extra-Domain B: Antiangiogenic Antibody Fragment L19

Angiogenesis is an underlying process in many human diseases, including cancer. An established target in this respect is the extra-domain B of fibronectin (EDB), a domain of 91 amino acids, which is typically inserted in fibronectin molecules at sites of tissue remodeling but not in fibronectin molecules under normal conditions. Thus, the expression of EDB has been shown in malignant tumors but not in healthy tissues (Zardi et al. 1987). The Neri group has isolated a number of human monoclonal antibodies to EDB (Carnemolla et al. 1996; Neri et al. 1997; Pini et al. 1998). The human antibody fragment, scFv(L19) displayed subnanomolar affinity to EDB and has been shown to efficiently localize on tumoral neovasculature in animal models (Demartis et al. 2001). Importantly, the ^{123}I-labeled dimeric L19 antibody fragment L19(scFv)$_2$ has been evaluated for targeting primary tumors and metastatic lesions in cancer patients through immunoscintigraphy (Santimaria et al. 2003). This clinical study was performed with 20 patients whereof the majority had colorectal or lung cancer. It could be demonstrated that the antibody ^{123}I-L19(scFv)$_2$ selectively accumulated in malignancies and allowed distinguishing among actively growing and quiescent lesions. Another Phase I/II clinical immunoscintigraphy study used ^{123}I-L19(scFv)$_2$ in patients with head and neck squamous cell carcinoma (Birchler et al. 2007). It was observed that for head and neck scintigraphy, iodinated antibodies have severe disadvantages. Although the thyroid gland was protected by competitive application of cold iodide, there were substantial artifacts in this area in all cases as a result of the uptake of liberated free iodide that was always present to a certain degree. Since dehalogenases are present in the salivary glands, free iodide also gave a high background in the 4 h post injection scintigraphy in the parotid and submandibular glands as well as in the minor salivary glands of the oral and nasal mucosa. Although the ^{123}I-L19(scFv)$_2$ is probably less suited as a diagnostic imaging modality for head and neck cancer, L19(scFv)$_2$ offers a general potential to be used as a tumor targeting

agent for both diagnostic and therapeutic purposes. Because neovasculature and tissue remodeling are required for the growth of all aggressive solid tumors, imaging approaches that use angiogenesis markers can be used for different types of cancer. An advantage of this strategy might be the fact that noninvasive imaging of angiogenesis via EDB fibronectin targeting allows the discrimination between quiescent and actively growing lesions.

5 Vitamin-Based Radiotracers

The use of small molecular-weight targeting agents is favorable to surmount the drawbacks of long circulation times and thus poor tumor-to-background contrast as well as possible immunogenicity encountered with antibodies. In this respect the application of vitamins as targeting agents provides several advantages: vitamins are small in size, inexpensive, relatively easily amenable for chemical modification, and non-immunogenic. Rapidly dividing cancer cells have an increased demand for certain vitamins such as folates, vitamin B12 (cobalamin), biotin, and riboflavin. These B-group vitamins are required for cell survival and proliferation because they act as co-enzymes of biochemical reactions that are essential for the synthesis of amino acids and for nucleotide bases (Russell-Jones et al. 2004). The most thoroughly investigated vitamin to be used as tumor-targeting agent is folic acid. The utility of folic acid conjugates has been widely exemplified in a variety of (pre)clinical studies for targeting the folate receptor (FR) that is overexpressed on a wide variety of cancer types (Low et al. 2008). Also, it has been demonstrated that vitamin B_{12} has the potential to be used as cancer targeting agent whereas only few studies have focused on the applicability of biotin for direct tumor targeting (Russell-Jones et al. 2004). Since vitamins are indispensable for sustaining life, it is unlikely that a mutational arrest of vitamin uptake would occur with concomitant failure of vitamin-mediated diagnosis or therapy. This is a distinct feature of vitamins and an advantage for their application as tumor targeting agents. Thus, using vitamin-based imaging agents is attractive and the strategy holds promise to also be used for therapeutic purposes.

5.1 Folic Acid Conjugates

Folic acid and folates (reduced forms) are water-soluble vitamins of the B-complex group. Humans cannot synthesize folates and hence must necessarily obtain them from food. Although only small quantities of folates are required, these vitamins are vital for various biochemical reactions including those for the synthesis of RNA and DNA, amino acid metabolism, and gene regulation. Cellular uptake of folates is accomplished by either carrier systems or the high-affinity folate receptor (FR). The FR is a glucosylphosphatidylinositol (GPI)-anchored protein that is frequently overexpressed in a variety of tumor types including cancers of the breast, ovaries, cervix, endometrium, lungs, kidneys, colon, and

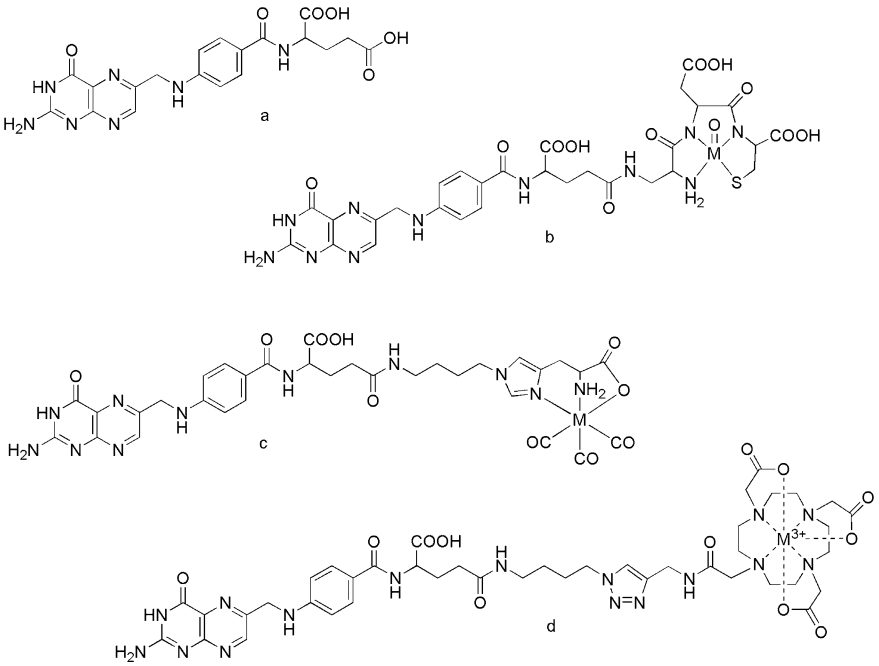

Fig. 9 Chemical Structures of **a** the vitamin folic acid, **b** EC20 (M = ^{99m}Tc), **c** His-folate (M = ^{99m}Tc, ^{188}Re) and **d** DOTA-folate (M = ^{111}In, ^{177}Lu)

brain (Antony 1996; Parker et al. 2005). In normal organs and tissues, FR-expression is highly restricted to only a few sites where it is located on the apical side of polarized epithelia in the lung, the placenta, and the choroid plexus of the brain and in the proximal tubule cells of the kidneys (Weitman et al. 1992; Antony 1996; Parker et al. 2005). Thus, folic acid can be used as a molecular "Trojan horse" for selective delivery of attached probes to FR-positive cancer cells (Low et al. 2008). During the last two decades, a variety of folic acid conjugates of radioisotopes useful for SPECT imaging (^{99m}Tc, ^{111}In, ^{67}Ga) has been developed and evaluated (Fig. 9) (Ke et al. 2003, 2004). Biodistribution studies of radiofolates in mice showed a specific uptake in FR-positive tumor (xeno)grafts, whereas unspecific radioactivity in background tissues was rapidly cleared in particular if the derivatives displayed hydrophilic properties. In the kidneys, however, high radioactivity retention was observed as a consequence of the specific binding of radiofolates to FRs expressed in the proximal tubule cells. This process results in unfavorably low tumor-to-kidney ratios of radiofolates in general. Clinical application of the two most promising candidates, ^{111}In-DTPA-folate (Wang et al. 1997; Mathias et al. 1998; Siegel et al. 2003) and ^{99m}Tc-EC20 (Leamon et al. 2002; Reddy et al. 2004; Fisher et al. 2008) revealed the same phenomenon in humans that was previously found in tumor bearing mice. While imaging of

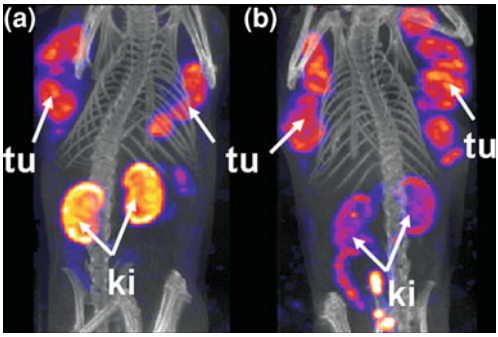

Fig. 10 SPECT/CT of mice injected with **a** ^{111}In-DTPA-folate only and **b** in combination with pre-dosed pemetrexed

malignant tissue could be successfully achieved, high radioactivity uptake was found in the kidneys of patients where the FR is expressed to approximately the same level as in mouse kidneys (Parker et al. 2005).

In an attempt to improve to low tumor-to-kidney ratio of radiofolates it was hypothesized that application of antifolates (e.g. pemetrexed) could increase the "appetite" of the tumor cells for folates and thus lead to an increased accumulation of folic acid conjugates. This hypothesis was confirmed in vitro (Müller et al. 2006a). However, in mice that were treated with antifolates, radiofolate uptake in tumor xenografts was not increased. While approaching this hypothesis, injection of pemetrexed was accomplished at different time points prior to the radiotracer. None of the experiments revealed an increased tumor accumulation of radioactivity, however, surprisingly administration of pemetrexed short before the radiofolate resulted in a significant reduction of kidney uptake (Müller et al. 2006a).

The result was a tremendous increase of the tumor-to-kidney ratio of radioactivity. This effect could be reproduced with a variety of folic acid conjugates radiolabeled with various radionuclides (^{99m}Tc, ^{188}Re, ^{111}In, ^{177}Lu) and in mouse models bearing different tumor (xeno)grafts (KB, IGROV-1, SKOV-3; M109) (Müller et al. 2007, 2008, 2009, 2010). The clearly superior SPECT imaging quality of mice that received pre-dosed pemetrexed could be impressively demonstrated while using ^{111}In-radiolabeled DTPA-folate (Fig. 10). This example demonstrates a pharmacological intervention by a non-radioactive substance that results in an improved tissue distribution of the radiotracer compared to the results obtained after radiotracer administration alone.

5.2 Vitamin B_{12} Conjugates

The earliest studies of radiolabeled vitamin B_{12} (cobalamin) using cobalt radioisotopes (^{57}Co, ^{58}Co, ^{60}Co) showed radioactivity accumulation in peripheral, actively growing tumors with highest accumulation in sarcomas (Flodh 1968; Flodh and Ullberg 1968; Blomquist et al. 1969). Other studies used radioiodinated arylstannylcobalamin conjugates showing enhanced uptake into renal carcinomas in nude mice when compared with other healthy tissues and organs (Wilbur et al.

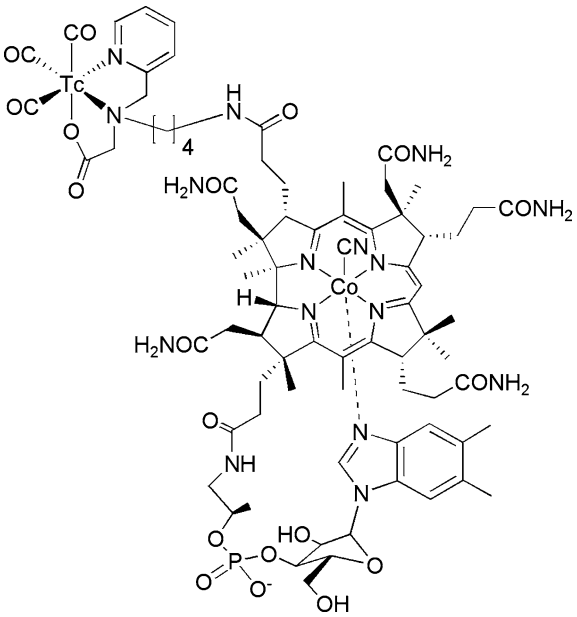

Fig. 11 Chemical Structure of ^{99m}Tc-PAMA-C4-cobalamin, a TCII non-binder vitamin B_{12} derivative

1996). Collins et al. developed ^{111}In-DTPA-analogs of cobalamin (DTPA cobalamin analogs = DACs) and tested them in preliminary biodistribution experiments in mice with CCL8 sarcomas and in swine (Collins and Hogenkamp 1997). The overall biodistribution of DACs showed tumor uptake and high radioactivity accumulation in healthy organs that was almost identical to previous studies performed with copper-radiolabeled vitamin B_{12}. The same group reported the first patient study performed with ^{111}In-DTPA-adenosylcobalamin for cancer imaging (Collins et al. 1999). ^{111}In-DTPA-adenosylcobalamin was found to be effective for detection of high-grade aggressive tumors in humans with the most successful results in patients with breast cancer and high-grade lung, colon, thyroid, and sarcomatous malignancies (Collins et al. 2000). However, the most significant uptake of these cobalamin derivatives was found in the liver, kidneys, and spleen followed by radioactivity accumulation in several glands. Vitamin B_{12} is bound to soluble transport proteins in circulation, namely transcobalamin I (TCI), intrinsic factor (IF), and transcobalamin II (TCII) whereof the latter is the principle vitamin B_{12} binding protein (Seetharam 1999; Seetharam and Li 2000; Seetharam and Yammani 2003). TCII-cobalamin binds to TCII-receptors that are ubiquitously expressed in cells for effective acquisition of this important vitamin. Originally, vitamin B_{12}-mediated tumor targeting was thought to be dependent on undisturbed interaction of cobalamin with these main transport systems and tumor uptake was believed to be mediated via up-regulated TCII receptors (Bauer et al. 2002; Russell-Jones et al. 2004). Later, it was hypothesized that selective TCII non-binders would lead to improved tissue distribution. Various cobalamin derivatives comprising a [pyridine-2-ylmethylamino]-acetic acid (PAMA)-chelator for coordination of the

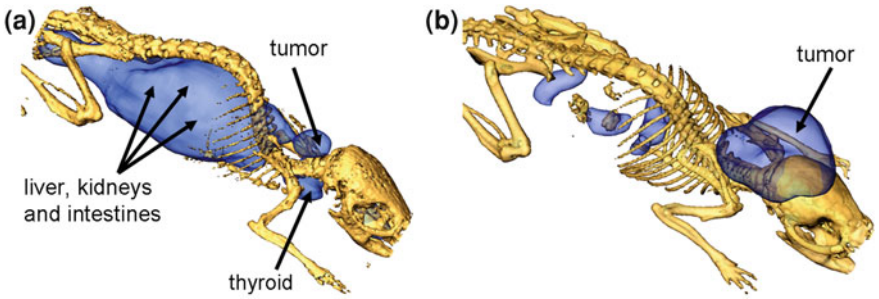

Fig. 12 Whole-body SPECT/CT scans of B16F10 tumor bearing mice, 24 h after injection of **a** $^{99m}Tc(CO)_3$-PAMA-C6-cobalamin (TCII binder) and **b** $^{99m}Tc(CO)_3$-PAMA-C4-cobalamin (TCII non-binder)

^{99m}Tc-tricarbonyl-core were developed with different spacer lengths [C-2 to C-6, i.e. $(-CH_2-)_n$, n = 2–6]. $^{99m}Tc(CO)_3$-PAMA-cobalamin derivatives with a spacer length of C-5 or longer displayed TCII binding affinity whereas those with shorter spacer lengths (C-2 to C-4, Fig. 11) were identified as TCII-non-binders, but displayed retained interaction with IF and TCI (Waibel et al. 2008). The results of biodistribution studies in tumor-bearing mice performed with $^{99m}Tc(CO)_3$-PAMA-C5-cobalamin and $^{99m}Tc(CO)_3$-PAMA-C6-cobalamin were similar to previously evaluated ^{111}In-DTPA-adenosylcobalamin tracers (Waibel et al. 2008). In contrast, data of $^{99m}Tc(CO)_3$-PAMA-cobalamin derivatives with spacer lengths shorter than C-5 showed a significantly improved tumor-to-blood and tumor-to-kidney ratio of radioactivity. Thus, abolished interaction of the radiolabeled cobalamin tracer with TCII resulted in decreased accumulation of the radiotracer in the blood and in organs and tissues that would otherwise be predestined to have high cobalamin uptake such as kidneys and diverse glands (Fig. 12).

$^{99m}Tc(CO)_3$-PAMA-C4-cobalamin (Fig. 11) was selected as the most favorable candidate because it displayed the highest tumor-to-blood and tumor-to-kidney ratios in animal experiments. These findings suggest that the transport of cobalamin derivatives into malignant tissue is not dependent on the transport protein TCII but rather mediated via TCI. By this example it could be demonstrated that variation of the radiotracer's linker length could have a tremendous impact on the overall tissue distribution of a radiotracer and thus, on its successful application. Excellent results achieved in preclinical studies paved the path toward a clinical application of cobalamin-targeted radioimaging in patients using the TCI-selective organometallic ^{99m}Tc-vitamin B_{12} derivative.

5.3 Other Vitamin Targeting Agents

It is likely that carriers and receptors of vitamins other than folates and vitamin B_{12} could be used for tumor targeted radioimaging purposes. Among the vitamins of the B-group it was suggested that cancer cells also overexpress a biotin receptor that

could, however, not yet be identified (Minko et al. 2002; Russell-Jones et al. 2004; Yang et al. 2009). Also, a possible reason for the generally little interest in biotin as a direct tumor targeting agent could be the fact that renal filtration and reabsorption of biotin and its conjugates lead to high renal uptake of radioactivity in the kidneys. Recently, it was shown that vitamin C (ascorbate) conjugated nanoparticles could be delivered into the brain presumably via the sodium-dependent ascorbic acid transporter SVCT2 whose RNA was found in the choroid plexus epithelium (Salmaso et al. 2009). The SVCT2 carrier was found on rat glioma cells (C6 and F98) and on mouse fibroblasts (NIH/3T3). This study introduced the perspective of using the SVCT2 transporter for brain targeting through the choroid plexus where it is selectively expressed. There might also be a potential to use this vitamin C transporter for nuclear imaging purposes of cancer diseases in the future.

6 Intracellular Targets

6.1 ^{99m}Tc-Carbohydrate Complexes

The most frequently used radiotracer for nuclear imaging purposes is currently the glucose analog [^{18}F]-2-fluoro-desoxy glucose ([^{18}F]-FDG). This PET tracer is taken up by tumor cells mainly by facile diffusion through the glucose transport protein 1 (Glut1). In the cell interior [^{18}F]-FDG is phosphorylated by the enzyme hexokinase yielding [^{18}F]-FDG-6-phophate which cannot escape the cell anymore. Thus, this trapping mechanism results in accumulation of radioactivity in metabolically active (cancer) cells. The clinical relevance of [^{18}F]-FDG promoted the development of inexpensive and readily available ^{99m}Tc-labeled glucose analogs. The first derivatives reported in the literature were ^{99m}Tc(V)-glucose complexes (Risch et al. 1977; Torizuka et al. 1995; Ozker et al. 1999). However, these ^{99m}Tc-tracers did not match the criteria and features of [^{18}F]-FDG, such as active transport via Glut1 and phosphorylation via hexokinase. Endeavors have been undertaken by the group of Schibli and others to design organometallic glucose and glucosamine analogs using the matched pair ^{99m}Tc/^{188}Re (Petrig et al. 2001; Dumas et al. 2003; Bayly et al. 2004; Schibli et al. 2005). Biological characterization has been reported from a variety of organometallic ^{99m}Tc(CO)$_3$-glucose complexes, derivatized at the C-1, C-2, C-3 and C-6 positions with various chelating systems. These compounds were tested for their ability to be internalized into Glut1 expressing cancer cells, HT29, and in addition it was investigated on whether or not they would be phosphorylated via the hexokinase reaction. Unfortunately, all of the complexes tested appeared not to be recognized and transported via Glut1. The authors stated the likeliness of ^{99m}Tc(CO)$_3$-glucose complexes being sterically too demanding for recognition at the extracellular binding site and/or transportation via Glut1. Also, other than [^{18}F]-FDG, the organometallic glucose derivatives were not phosphorylated by hexokinase. Orvig and his collaborators reported several new approaches of organometallic

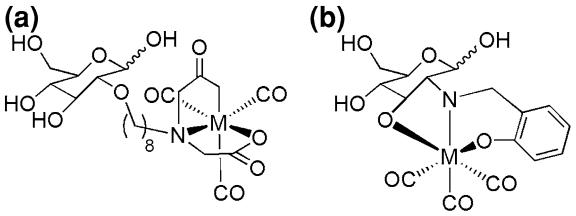

Fig. 13 C-2 functionalized glucose derivatives of an imino diacetic acid chelator (Schibli et al. 2005) and an N-(2′-hydroxybenzyl)-amino-chelating system (Bayly et al. 2004) radiolabeled with ^{99m}Tc-tricarbonyl (M = ^{99m}Tc)

carbohydrate complexes. Among others they synthesized N-hydroxybenzyl-amino-deoxy-glucose derivatives (Fig. 13) and carbohydrate-appended hydroxypyridinone derivatives (Bayly et al. 2004; Storr et al. 2005; Ferreira et al. 2006a, b, Ferreira et al. 2010). However, most of these compounds revealed neither to be hexokinase substrates nor inhibitors. Although basic cell data of these carbohydrate radiometal complexes is lacking, it is likely that they are not taken up via the Glut1 transporter or other specific transport mechanisms and thus would fail to accumulate in cancer cells in vivo.

6.2 Radiolabeled Nucleoside Analogs for Targeting Human Thymidine Kinase

In mammalian cells, salvage pathway phosphorylation of thymidine is catalyzed by two different thymidine kinases (TK): the cell-cycle regulated cytoplasmic TK1 and the constitutively expressed mitochondrial TK2. The human TK1 (hTK1) activity is known to fluctuate with cellular DNA synthesis, the activity being high in proliferating and malignant cells and low or absent in quiescent cells, whereas TK2 activity is low in both dividing and quiescent cells (Munch-Petersen et al. 1995). Since the activity of hTK1 is often dramatically increased in cancer cells, interest has been sparked in targeting this enzyme by radioactive thymidine analogs for selective imaging of proliferating cancer cells. In the cell interior nucleosides are rapidly phosphorylated to nucleotides, which renders them unable to penetrate biological membranes and thus they are “trapped” inside the cells. Thymidine and thymidine analogs labeled with PET radioisotopes such as ^{11}C-methyl-thymidine, ^{76}Br-fluoro-deoxyuridine, and ^{18}F-fluoro-deoxythymidine are either under development or already in use as proliferation marker (Gardelle et al. 2001; Buchmann et al. 2003). However, due to the high costs for the production of PET radioisotopes and the unfavorably short half-lives of PET isotopes, the use of SPECT radioisotopes ^{99m}Tc or ^{111}In would be more advantageous. Schmid et al. focused on the preparation of radiometal labeled thymidine complexes functionalized at position N3 with a DO3A-chelator suitable for radiolabeling with ^{111}In or lanthanide radioisotopes (Schmid et al. 2006). However, cellular uptake of the

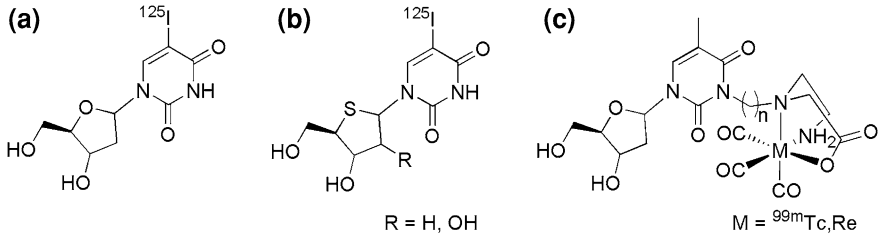

Fig. 14 Chemical structures of nucleoside-based SPECT tracers. **a** 5-[^{125}I]-Iodo-2′-deoxyuridine (IdUrd) (Dupertuis et al. 2001; Semnani et al. 2005), **b** 5-[^{125}I]-iodo-4′-thio-2′-deoxyuridine (ITdU, R = H) and 5-[^{125}I]-iodo-4′-thio-β-arabinofuranosyl)-uracil (ITAU, R = OH) (Toyohara et al. 2002) and **c** ^{99m}Tc(CO)$_3$-thymidine derivatives (n = 2, 3, 5 or 10) (Desbouis et al. 2008)

thymidine metal complexes in DoHH2 and HL60 cells failed. Clearly, there is an interest to develop thymidine derivatives suitable for radiolabeling with ^{99m}Tc. Celen et al. reported the preparation and evaluation of a ^{99m}Tc(V)-MAMA-propyl-thymidine complex as a potential probe for in vivo visualization of tumor cell proliferation via SPECT (Celen et al. 2007). However, this ligand could not be phosphorylated because it was too bulky. The group of Schibli focused on the development of thymidine analogs labeled with the organometallic ^{99m}Tc-tricarbonyl core (Fig. 14) (Desbouis et al. 2008; Struthers et al. 2008, 2009). The design of organometallic ^{99m}Tc-derivatives could be favorable as these complexes were sterically less demanding than previously prepared thymidine radiometal complexes. Those organometallic thymidine derivatives were systematically evaluated regarding the influence of the spacer length between the thymidine and the chelating system, the overall charge of the complex after radiometal coordination and the uptake in human neuroblastoma SKNMC cells. From these studies, it was concluded that neutral and anionic complexes are more readily accepted as substrates than cationic complexes.

Moreover, modeling experiments suggested that the flexibility of a longer spacer between the thymidine molecule and the organometallic core further improves the ability of the complex to be accommodated in the binding site of the enzyme. Cellular uptake was higher for complexes with log P values greater than one but still about 6-fold lower than for the ^{3}H-thymidine control compound. Although some of the organometallic thymidine complexes were identified as enzyme substrates, the low and often almost absent permeability of the thymidine metal complexes through the cellular membrane remains a major hurdle for these compounds.

Another strategy used iodinated thymidine analogs (e.g. 5-iodo-2′-deoxyuridine (IUdR)) as cell proliferation markers for nuclear imaging purposes and potential therapeutic application. However, the imaging quality was found to be impaired by the tracer's rapid in vivo degradation. Pre-application of 5-fluoro-2′-deoxyuridine (FdUrd) was tested with the aim to block thymidine synthesis and thus trigger the tumor uptake of ^{125}I-IdUr (Dupertuis et al. 2001). Indeed, as a result of FDUrd predosing ^{125}I-IdUrd incorporation into gliaoblastoma cells and tumors was increased and thus, the tumor-to-background contrast slightly improved. The same research

group reported a beneficial effect of combining the administration of ^{125}I-IdUrd with unlabeled IdUrd to increase the rate of DNA incorporation of ^{125}I-IdUrd in malignant gliomas (Dupertuis et al. 2002). Apparently, the C–N-glycosidic bond of IUdR is too labile in vivo which leads to metabolites that display reduced tumor affinity. In an attempt to increase the radiotracer's in vivo stability the tracer has been chemically modified by fluorination of the sugar moiety at different positions (3′ or 2′-substitution). However, the preparation of fluorine-stabilized iodinated thymidine analogs with retained cellular uptake, cytosolic phosphorylation, and selectivity for hTK1, appears to be quite challenging (Gati et al. 1984; Mercer et al. 1989). A strategy for stabilizing the C–N-glycosidic bond without interfering with the cytosolic thymidine kinase has been carried out by the replacement of the furanose ring oxygen with sulfur for preparation of 5-^{125}I-iodo-4′-thio-2′-deoxyuridine (ITdU) and 5-^{125}I-iodo-1-(4-thiob-d-arabinofurnosyl)uracil (ITAU) (Fig. 14) (Toyohara et al. 2002). ITdU exhibited a high resistance to the glycosidic bond cleavage reaction provoked by thymidine phosphorylase, while maintaining affinity to nucleoside kinases. Also, the increased in vivo radioiodination stability and rapid DNA incorporation of ITdU resulted in a preferential uptake of radioactivity in the proliferating organs making this tracer a promising tumor-imaging agent. A comparative study of six 5-iodonucleosides revealed that the in vivo proliferation-imaging potential of nucleosides might be estimated by their in vitro affinity for TK1 and their C–N-glycosidic bond stability (Toyohara et al. 2003). However, since these iodo-nucleosides have not been examined with regard to the important step of the nucleoside transport activity, further investigations would be necessary to allow a clear statement which radiotracer would be the most suitable for imaging of tumor cell proliferation.

By the examples of nucleoside derivatives and conjugates of carbohydrates it was demonstrated that the development of radiotracers for intracellular targets might be problematic if bulky metal chelates are employed since cellular uptake of these radiotracers via transmembrane-spanning carriers or passive diffusion could be hindered.

6.3 Radioiodinated Meta-Iodobenzylguanidine

Finally, we would like to highlight a long-serving but still frequently used tumor imaging agent with an intracellular target. Meta-iodobenzylguanidine (MIBG), a catecholamine analog, is suitable for radiolabeling with radioactive iodine (e.g. ^{123}I) for the purpose of SPECT imaging of neuroendocrine and carcinoid tumors, a subtype of neuroendocrine tumors (Khan et al. 2008). Radiolabeled MIBG was first synthesized at the University of Michigan as early as 1980 (Wieland et al. 1980). It localizes through the physiologic nor-epinephrine reuptake mechanisms with uptake into catecholamine storage vesicles of adrenergic nerve ending and the cells of the adrenal medulla. Carcinoid tumor cells share the common characteristic of a sodium-dependent ATP/Mg^{2+} neuronal pump mechanism in their cell membranes that allows the accumulation of norepinephrine and MIBG where MIBG is not

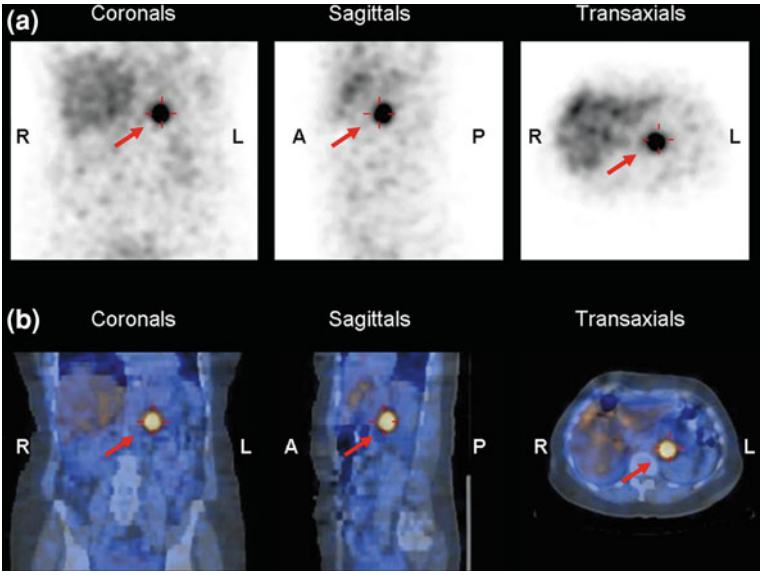

Fig. 15 SPECT images **a** and SPECT/CT overlay **b** of a patient with a neuroendocrine tumor (pheochromocytoma) in the upper thorax. Accumulation of ^{123}I-MIBG in the malignant tissue is indicated with *red arrows*. The images have been kindly provided by N. Schäfer, (MD, Ph.D.), University Hospital, Zurich, Switzerland

significantly metabolized. Initially, ^{131}I-radiolabeled MIBG was used for the detection of neuroendocrine tumors such as pheochromocytomas, but later its application has been extended also to scintigraphic visualization of neuroblastoma and carcinoid tumors. Although both [^{123}I]- and [^{131}I]-MIBG can be used for the purpose of radionuclide imaging, ^{123}I has dosimetry and imaging characteristics superior to ^{131}I and thus, it is the preferred radionuclide for SPECT imaging (Fig. 15). In contrast, ^{131}I is preferred for therapy due to the emission of β-particles and dosimetric considerations (Hoefnagel et al. 1987).

To develop an MIBG analog with improved uptake in tumors, no carrier added [^{131}I]-MIBG has been developed. The methodology for producing high specific activity (no-carrier-added) [^{131}I]-MIBG was originally described in 1993, but only recently it has been developed for clinical application. With this method every molecule of MIBG contains an ^{131}I-radiolabel, whereas prior methods provided a mixture of "cold" and "hot" tracer, wherein only 1 of 2,000 molecules of MIBG contained radioactive iodine. As a result of the high specific activity achieved by the no-carrier-added radiolabeling method, the mass of the MIBG administered can be reduced and thus undesired side-effects caused by the "cold" MIBG, such as hypertension during infusion could be minimized. The only concern of the no-carrier-added [^{131}I]-MIBG has been that normal tissues and organs with relatively low levels of nor-epinephrine uptake might absorb more radioactivity because of the lack of competitive inhibition of radiotracer uptake by the "cold" MIBG.

Table 4 Potential reasons for failure of tumor-targeted nuclear imaging

Possibilities for Failure	Consequences	Examples
Expression of the target structure in normal tissues and organs	Radiotracer accumulation in normal tissues and organs	- Bombesin receptor (pancreas) - Somatostatin receptor (adrenals) - Folate receptor (kidneys)
Long circulation time	High background radiation in the blood—dose burden to healthy tissues (bone marrow)	- Monoclonal antibodies
Short circulation time	Low tumor accumulation	- Small molecular-weight targeting agents (e.g. folic acid)
Rapid enzymatic metabolism	Low tumor accumulation Accumulation of metabolites in kidneys and liver	- Non-stabilized neurotensin-analogs
Binding to physiological transport proteins	High background radiation in the blood	- Vitamin B_{12}/ transcobalamin II
Intracellular targets	Cellular uptake via carrier systems or passive diffusion hindered by bulky radiometal complexes	- ^{99m}Tc-glucose analogs - ^{99m}Tc-thymidine analogs
Lipophilic character	Unspecific accumulation of the radiotracer in the bile, liver and intestinal tract	- $^{99m}Tc(CO)_3$-moiety - Alkyl chain-spacers
Low specific activity	Low tumor uptake Undesired side-effects as a result of substantial amount of injected "cold" tracer	- [^{131}I]-MIBG

7 Optimization of SPECT Tracer Design and Potential Reasons for Failure

The design and development of a nuclear imaging probe comprises an appropriate biomolecule as targeting vector, a site for conjugation that does not interfere with the biomolecule's binding affinity to the tumor-associated target, a suitable linker length and a radioisotope that matches with an appropriate biomolecule. For stable coordination of metallic radioisotopes the choice of a suitable chelator is crucial. There are several possible strategies to optimize SPECT tracers with regard to their specificity to and selectivity for the targeted malignant tissue while minimizing their uptake in normal tissues and organs. Variation of the radionuclide, modification of the bifunctional chelator, introduction of linker-entities of variable spacer length for stabilization or modulation of the overall tracer characteristics, alteration of the radiolabeling technique and manipulation of the radiotracer's

blood, and normal tissue clearance by variation of the biomolecule's overall size (e.g. antibodies versus antibody fragments or peptides). Finally, optimization of the tissue distribution of radiotracers might also be accomplished by a combination with non-radioactive substances whereof the most prominent example is the application of positively charged amino acids (e.g. lysine) that block renal uptake of radiolabeled Fab fragments of antibodies (Behr et al. 1995, 1996) and peptides (de Jong et al. 1996; Rolleman et al. 2003; Verwijnen et al. 2005).

During the course of about two decades of (pre)clinical research with tumor-targeted SPECT tracers several reasons for potential failure of SPECT imaging agents could be identified (Table 4). Based on the data obtained with nuclear imaging agents that initially failed, new strategies to optimize the design and utility of SPECT tracers are currently being developed.

8 Summary and Conclusion

A variety of approaches for the design and improvement of SPECT tracers have been discussed herein. Each class of targeting agents, antibodies, peptides, and non-peptide-based small-molecules such as vitamins has its pros and cons for application in diagnostic nuclear medicine. In principle, it would be ideal to use SPECT tracers that accumulate specifically in malignancies and that are rapidly cleared via kidneys allowing high tumor-to-background contrast of radioactivity already short after administration. Such optimal characteristics are, however, not always easy to achieve.

The recent observation that somatostatin and bombesin analog antagonists provide superior characteristics over agonists with regard to their tumor accumulation is an unexpected finding that is not yet completely understood. Using oligomeric ligands to improve binding and targeting properties of radiolabeled peptides over their monomeric counterparts appears to be a more rational design that could be successfully proven for example with RGD-based analogs. Recently, vitamin-based radioimaging agents have been developed that are selectively accumulated in tumor cells. In the case of vitamin B_{12}, analogs with abolished binding to the ubiquitous protein transcobalalmin II showed a reduced uptake in non-targeted tissues. In the case of FR-targeting it was the combined application with the antifolate pemetrexed that led to an improved tumor selectively of folic acid based radioconjugates while undesired uptake in FR-positive kidneys could be reduced. Targeting of intracellular tumor markers such as the enzymes hexokinase or human thymidine kinase 1 turned out to be a more problematic strategy for SPECT tracers, particularly those that are based on radiometals, compared to the targeting of cell surface-exposed tumor markers. The necessity of the targeting agent to permeate cancer cell membranes via carrier systems or passive diffusion to reach intracellular targets could be a hindrance for a proper function of the targeting system in particular if the radioconjugate is composed of a bulky radiometal complex.

Finally, it has to be critically acknowledged that only a small selection of examples for tracer designs could be included in this chapter. The immense opportunities for the design of radiopharmaceuticals and the enormous potential it

provides for future development of new and improved SPECT tracers holds great promise for early clinical application of novel imaging agents in oncology.

Acknowledgments We thank Dr. D. J. Fitzgerald for reviewing the manuscript.

References

Abrams MJ, Juweid M et al (1990) Technetium-99m-human polyclonal IgG radiolabeled via the hydrazino nicotinamide derivative for imaging focal sites of infection in rats. J Nucl Med 31:2022–2028

Alberto R, Ortner K et al (2001) Synthesis and properties of boranocarbonate: a convenient in situ CO source for the aqueous preparation of $[^{99m}Tc(OH_2)_3(CO)_3]^+$. J Am Chem Soc 123:3135–3136

Alberto R, Schibli R et al (1998) A novel organometallic aqua complex of technetium for the labeling of biomolecules: synthesis of $[^{99m}Tc(OH_2)_3(CO)_3]^+$ from $[^{99m}TcO_4]^-$ in aqueous solution and its reaction with a bifunctional ligand. J Am Chem Soc 120:7987–7988

Alberto R, Schibli R et al (1999a) First application of *fac*-$[^{99m}Tc(OH_2)_3(CO)_3]^+$ in bioorganometallic chemistry: Design, structure, and in vitro affinity of a 5-HT1A receptor ligand labeled with ^{99m}Tc. J Am Chem Soc 121:6076–6077

Alberto R, Schibli R et al (1999b) Basic aqueous chemistry of $[M(OH_2)_3(CO)_3]^+$ (M = Re, Tc) directed towards radiopharmaceutical application. Coord Chem Rev 192:901–919

Alford R, Ogawa M et al (2009) Molecular probes for the in vivo imaging of cancer. Mol BioSyst 5:1279–1291

Alshoukr F, Rosant C et al (2009) Novel neurotensin analogues for radioisotope targeting to neurotensin receptor-positive tumors. Bioconjug Chem 20:1602–1610

Alves S, Correia JD et al (2006) Pyrazolyl conjugates of bombesin: a new tridentate ligand framework for the stabilization of *fac*-$[M(CO)_3]^+$ moiety. Nucl Med Biol 33:625–634

Antony AC (1996) Folate receptors. Ann Rev Nutr 16:501–521

Baidoo KE, Lin KS et al (1998) Design, synthesis, and initial evaluation of high-affinity technetium bombesin analogues. Bioconjug Chem 9:218–225

Bartholoma MD, Louie AS et al (2010) Technetium and gallium derived radiopharmaceuticals: comparing and contrasting the chemistry of two important radiometals for the molecular imaging era. Chem Rev 110:2903–2920

Bauer JA, Morrison BH et al (2002) Effects of interferon beta on transcobalamin II-receptor expression and antitumor activity of nitrosylcobalamin. J Natl Cancer Inst 94:1010–1019

Bayly SR, Fisher CL et al (2004) Carbohydrate conjugates for molecular imaging and radiotherapy: $^{99m}Tc(I)$ and $^{186}Re(I)$ tricarbonyl complexes of N-(2′-hydroxybenzyl)-2-amino-2-deoxy-D-glucose. B. Bioconjug Chem 15:923–926

Begent RH, Verhaar MJ et al (1996) Clinical evidence of efficient tumor targeting based on single-chain Fv antibody selected from a combinatorial library. Nat Med 2:979–984

Behr TM, Becker WS et al (1996) Reduction of renal uptake of monoclonal antibody fragments by amino acid infusion. J Nucl Med 37:829–833

Behr TM, Gotthardt M et al (2001) Imaging tumors with peptide-based radioligands. Q J Nucl Med 45:189–200

Behr TM, Sharkey RM et al (1995) Reduction of the renal uptake of radiolabeled monoclonal antibody fragments by cationic amino acids and their derivatives. Cancer Res 55:3825–3834

Bernard BF, Krenning EP et al (1997) D-lysine reduction of indium-111 octreotide and yttrium-90 octreotide renal uptake. J Nucl Med 38:1929–1933

Birchler MT, Thuerl C et al (2007) Immunoscintigraphy of patients with head and neck carcinomas, with an anti-angiogenetic antibody fragment. Otolaryngol Head Neck Surg 136:543–548

Blomquist L, Flodh H et al (1969) Uptake of labelled vitamin B12 and 4-iodophenylalanine in some tumors of mice. Experientia 25:294–296

Boeggeman E, Ramakrishnan B et al (2009) Site specific conjugation of fluoroprobes to the remodeled Fc N-glycans of monoclonal antibodies using mutant glycosyltransferases: application for cell surface antigen detection. Bioconjug Chem 20:1228–1236

Brack SS, Dinkelborg LM et al (2004) Molecular targeting of angiogenesis for imaging and therapy. Eur J Nucl Med Mol Imaging 31:1327–1341

Breeman WA, de Jong M et al (2002) Preclinical comparison of ^{111}In-labeled DTPA- or DOTA-bombesin analogs for receptor-targeted scintigraphy and radionuclide therapy. J Nucl Med 43:1650–1656

Brekken RA, Huang X et al (1998) Vascular endothelial growth factor as a marker of tumor endothelium. Cancer Res 58:1952–1959

Bruehlmeier M, Garayoa EG et al (2002) Stabilization of neurotensin analogues: effect on peptide catabolism, biodistribution and tumor binding. Nucl Med Biol 29:321–327

Buchmann I, Vogg AT et al (2003) [^{18}F]5-fluoro-2-deoxyuridine-PET for imaging of malignant tumors and for measuring tissue proliferation. Cancer Biother Radiopharm 18:327–337

Buchsbaum DJ (1995) Experimental approaches to increase radiolabeled antibody localization in tumors. Cancer Res 55:5729s–5732s

Buchsbaum DJ (1997) Experimental tumor targeting with radiolabeled ligands. Cancer 80:2371–2377

Carnemolla B, Neri D et al (1996) Phage antibodies with pan-species recognition of the oncofoetal angiogenesis marker fibronectin ED-B domain. Int J Cancer 68:397–405

Celen S, de Groot T et al (2007) Synthesis and evaluation of a ^{99m}Tc-MAMA-propyl-thymidine complex as a potential probe for in vivo visualization of tumor cell proliferation with SPECT. Nucl Med Biol 34:283–291

Cescato R, Erchegyi J et al (2008) Design and in vitro characterization of highly sst2-selective somatostatin antagonists suitable for radiotargeting. J Med Chem 51:4030–4037

Cescato R, Schulz S et al (2006) Internalization of sst2, sst3, and sst5 receptors: effects of somatostatin agonists and antagonists. J Nucl Med 47:502–511

Christ E, Wild D et al (2009) Glucagon-like peptide-1 receptor imaging for localization of insulinomas. J Clin Endocrinol Metab 94:4398–4405

Collins DA, Hogenkamp HP (1997) Transcobalamin II receptor imaging via radiolabeled diethylene-triaminepentaacetate cobalamin analogs. J Nucl Med 38:717–723

Collins DA, Hogenkamp HP et al (1999) Tumor imaging via indium-111-labeled DTPA-adenosylcobalamin. Mayo Clin Proc 74:687–691

Collins DA, Hogenkamp HP et al (2000) Biodistribution of radiolabeled adenosylcobalamin in patients diagnosed with various malignancies. Mayo Clin Proc 75:568–580

de Jong M, Bakker WH et al (1999) Preclinical and initial clinical evaluation of ^{111}In-labeled nonsulfated CCK8 analog: a peptide for CCK-B receptor-targeted scintigraphy and radionuclide therapy. J Nucl Med 40:2081–2087

de Jong M, Rolleman EJ et al (1996) Inhibition of renal uptake of indium-111-DTPA-octreotide in vivo. J Nucl Med 37:1388–1392

de Visser M, Bernard HF et al (2007) Novel ^{111}In-labelled bombesin analogues for molecular imaging of prostate tumours. Eur J Nucl Med Mol Imaging 34:1228–1238

de Visser M, Janssen PJ et al (2003) Stabilised ^{111}In-labelled DTPA- and DOTA-conjugated neurotensin analogues for imaging and therapy of exocrine pancreatic cancer. Eur J Nucl Med Mol Imaging 30:1134–1139

Decristoforo C, Mather SJ (2002) The influence of chelator on the pharmacokinetics of ^{99m}Tc-labelled peptides. Q J Nucl Med 46:195–205

Decristoforo C, Mather SJ et al (2000a) ^{99m}Tc-EDDA/HYNIC-TOC: a new ^{99m}Tc-labelled radiopharmaceutical for imaging somatostatin receptor-positive tumours; first clinical results and intra-patient comparison with ^{111}In-labelled octreotide derivatives. Eur J Nucl Med 27:1318–1325

Decristoforo C, Melendez-Alafort L et al (2000b) ^{99m}Tc-HYNIC-[Tyr^3]-octreotide for imaging somatostatin-receptor-positive tumors: preclinical evaluation and comparison with ^{111}In-octreotide. J Nucl Med 41:1114–1119

Delgado R, da Silva JJ (1982) Metal complexes of cyclic tetra-azatetra-acetic acids. Talanta 29:815–822

Demartis S, Tarli L et al (2001) Selective targeting of tumour neovasculature by a radiohalogenated human antibody fragment specific for the ED-B domain of fibronectin. Eur J Nucl Med 28:534–539

Desbouis D, Struthers H et al (2008) Synthesis, in vitro, and in silico evaluation of organometallic technetium and rhenium thymidine complexes with retained substrate activity toward human thymidine kinase type 1. J Med Chem 51:6689–6698

Dumas C, Schibli R et al (2003) Versatile routes to C-2- and C-6-functionalized glucose derivatives of iminodiacetic acid. J Org Chem 68:512–518

Dupertuis YM, Vazquez M et al (2001) Fluorodeoxyuridine improves imaging of human glioblastoma xenografts with radiolabeled iododeoxyuridine. Cancer Res 61:7971–7977

Dupertuis YM, Xiao WH et al (2002) Unlabelled iododeoxyuridine increases the rate of uptake of [125I]iododeoxyuridine in human xenografted glioblastomas. Eur J Nucl Med Mol Imaging 29:499–505

Edwards DS, Liu S et al (1997) New and versatile ternary ligand system for technetium radiopharmaceuticals: water soluble phosphines and tricine as coligands in labeling a hydrazinonicotinamide-modified cyclic glycoprotein IIb/IIIa receptor antagonist with ^{99m}Tc. Bioconjug Chem 8:146–154

Egli A, Alberto R et al (1999) Organometallic ^{99m}Tc-aquation labels peptide to an unprecedented high specific activity. J Nucl Med 40:1913–1917

Egli A, Hegetschweiler K et al (1997) Hydrolysis of the organometallic aqua ion *fac*-triaquatricarbonylrhenium(I). Mechanism, pK_a, and formation constants of the polynuclear hydrolysis products. Organometallics 16:1833–1840

Ferreira CL, Bayly SR et al (2006a) Carbohydrate-appended 3-hydroxy-4-pyridinone complexes of the $[M(CO)_3]^+$ core (M = Re, ^{99m}Tc, ^{186}Re). Bioconjug Chem 17:1321–1329

Ferreira CL, Ewart CB et al (2006b) Glucosamine conjugates of tricarbonylcyclopentadienyl rhenium(I) and technetium(I) cores. Inorg Chem 45:6979–6987

Ferreira CL, Marques FL et al (2010) Cationic technetium and rhenium complexes with pendant carbohydrates. Appl Radiat Isot 68:1087–1093

Ferro-Flores G, Arteaga de Murphy C et al (2006) Preparation and evaluation of ^{99m}Tc-EDDA/HYNIC-[Lys^3]-bombesin for imaging gastrin-releasing peptide receptor-positive tumours. Nucl Med Commun 27:371–376

Fisher RE, Siegel BA et al (2008) Exploratory study of ^{99m}Tc-EC20 imaging for identifying patients with folate receptor-positive solid tumors. J Nucl Med 49:899–906

Flodh H (1968) Autoradiographic studies on distribution of radiocobalt chloride in pregnant mice. Acta Radiol Ther Phys Biol 7:121–128

Flodh H, Ullberg S (1968) Accumulation of labelled vitamin B_{12} in some transplanted tumours. Int J Cancer 3:694–699

Garcia-Garayoa E, Blauenstein P et al (2009) A stable neurotensin-based radiopharmaceutical for targeted imaging and therapy of neurotensin receptor-positive tumours. Eur J Nucl Med Mol Imaging 36:37–47

Garcia-Garayoa E, Maes V et al (2006) Double-stabilized neurotensin analogues as potential radiopharmaceuticals for NTR-positive tumors. Nucl Med Biol 33:495–503

Garcia Garayoa E, Ruegg D et al (2007a) Chemical and biological characterization of new $Re(CO)_3$/[^{99m}Tc]$(CO)_3$ bombesin analogues. Nucl Med Biol 34:17–28

Garcia Garayoa E, Schweinsberg C et al (2008) Influence of the molecular charge on the biodistribution of bombesin analogues labeled with the [^{99m}Tc$(CO)_3$]-core. Bioconjug Chem 19:2409–2416

Garcia Garayoa E, Schweinsberg C et al (2007b) New [^{99m}Tc]bombesin analogues with improved biodistribution for targeting gastrin releasing-peptide receptor-positive tumors. Q J Nucl Med Mol Imaging 51:42–50

Gardelle O, Roelcke U et al (2001) [^{76}Br]Bromodeoxyuridine PET in tumor-bearing animals. Nucl Med Biol 28:51–57

Gati WP, Misra HK et al (1984) Structural modifications at the 2′- and 3′-positions of some pyrimidine nucleosides as determinants of their interaction with the mouse erythrocyte nucleoside transporter. Biochem Pharmacol 33:3325–3331

Giblin MF, Veerendra B et al (2005) Radiometallation of receptor-specific peptides for diagnosis and treatment of human cancer. In Vivo 19:9–29

Ginj M, Zhang H et al (2006) Radiolabeled somatostatin receptor antagonists are preferable to agonists for in vivo peptide receptor targeting of tumors. Proc Natl Acad Sci U S A 103:16436–16441

Goldenberg DM, Rossi EA et al (2008) Multifunctional antibodies by the Dock-and-Lock method for improved cancer imaging and therapy by pretargeting. J Nucl Med 49:158–163

Good S, Walter MA et al (2008) Macrocyclic chelator-coupled gastrin-based radiopharmaceuticals for targeting of gastrin receptor-expressing tumours. Eur J Nucl Med Mol Imaging 35:1868–1877

Gotthardt M, van Eerd-Vismale J et al (2007) Indication for different mechanisms of kidney uptake of radiolabeled peptides. J Nucl Med 48:596–601

Gugger M, Reubi JC (1999) Gastrin-releasing peptide receptors in non-neoplastic and neoplastic human breast. Am J Pathol 155:2067–2076

Guo W, Hinkle GH et al (1999) ^{99m}Tc-HYNIC-folate: a novel receptor-based targeted radiopharmaceutical for tumor imaging. J Nucl Med 40:1563–1569

Hammond PJ, Wade AF et al (1993) Amino acid infusion blocks renal tubular uptake of an indium-labelled somatostatin analogue. Br J Cancer 67:1437–1439

Heppeler A, Froidevaux S et al (1999) Radiometal-labelled macrocyclic chelator-derivatised somatostatin analogue with superb tumour-targeting properties and potential for receptor-mediated internal radiotherapy. Chem-Eur J 5:1974–1981

Hoefnagel CA, den Hartog Jager FC et al (1987) The role of ^{131}I-MIBG in the diagnosis and therapy of carcinoids. Eur J Nucl Med 13:187–191

Hoffman TJ, Gali H et al (2003) Novel series of ^{111}In-labeled bombesin analogs as potential radiopharmaceuticals for specific targeting of gastrin-releasing peptide receptors expressed on human prostate cancer cells. J Nucl Med 44:823–831

Hong H, Sun J et al (2008) Radionuclide-based cancer imaging targeting the carcinoembryonic antigen. Biomark Insights 3:435–451

Johnson CV, Shelton T et al (2006) Evaluation of combined ^{177}Lu-DOTA-8-AOC-BBN (7-14)NH^2 GRP receptor-targeted radiotherapy and chemotherapy in PC-3 human prostate tumor cell xenografted SCID mice. Cancer Biother Radiopharm 21:155–166

Josten A, Haalck L et al (2000) Use of microbial transglutaminase for the enzymatic biotinylation of antibodies. J Immunol Methods 240:47–54

Kastner ME, Lindsay MJ et al (1982) Synthesis and structure of trans-[O_2(en)2Tc^v]$^+$. Inorg Chem 21:2037–2040

Ke CY, Mathias CJ et al (2003) The folate receptor as a molecular target for tumor-selective radionuclide delivery. Nucl Med Biol 30:811–817

Ke CY, Mathias CJ et al (2004) Folate-receptor-targeted radionuclide imaging agents. Adv Drug Deliv Rev 56:1143–1160

Khan MU, Morse M et al (2008) Radioiodinated metaiodobenzylguanidine in the diagnosis and therapy of carcinoid tumors. Q J Nucl Med Mol Imaging 52:441–454

King DJ, Turner A et al (1994) Improved tumor targeting with chemically cross-linked recombinant antibody fragments. Cancer Res 54:6176–6185

Kobayashi H, Sakahara H et al (1994) Improved clearance of radiolabeled biotinylated monoclonal antibody following the infusion of avidin as a "chase" without decreased accumulation in the target tumor. J Nucl Med 35:1677–1684

Körner M, Stockli M et al (2007) GLP-1 receptor expression in human tumors and human normal tissues: potential for in vivo targeting. J Nucl Med 48:736–743

Kwekkeboom D, Krenning EP et al (2000) Peptide receptor imaging and therapy. J Nucl Med 41:1704–1713

La Bella R, Garcia-Garayoa E et al (2002) A ^{99m}Tc(I)-postlabeled high affinity bombesin analogue as a potential tumor imaging agent. Bioconjug Chem 13:599–604

Lantry LE, Cappelletti E et al (2006) ^{177}Lu-AMBA: Synthesis and characterization of a selective ^{177}Lu-labeled GRP-R agonist for systemic radiotherapy of prostate cancer. J Nucl Med 47:1144–1152

Leamon CP, Parker MA et al (2002) Synthesis and biological evaluation of EC20: a new folate-derived, ^{99m}Tc-based radiopharmaceutical. Bioconjug Chem 13:1200–1210

Lei K, Rusckowski M et al (1996) Technetium-99m antibodies labeled with MAG_3 and SHNH: an in vitro and animal in vivo comparison. Nucl Med Biol 23:917–922

Leyton JV, Olafsen T et al (2008) Humanized radioiodinated minibody for imaging of prostate stem cell antigen-expressing tumors. Clin Cancer Res 14:7488–7496

Li M, Meares CF et al (1995) Prelabeling of chimeric monoclonal antibody L6 with ^{90}yttrium- and ^{111}indium-1,4,7,10-tetraazacyclododecane-N,N',N'',N'''-tetraacetic acid (DOTA) chelates for radioimmunodiagnosis and therapy. Cancer Res 55:5726s–5728s

Liu S (2008) Bifunctional coupling agents for radiolabeling of biomolecules and target-specific delivery of metallic radionuclides. Adv Drug Deliv Rev 60:1347–1370

Liu S (2009) Radiolabeled cyclic RGD peptides as integrin alpha(v)beta(3)-targeted radiotracers: maximizing binding affinity via bivalency. Bioconjug Chem 20:2199–2213

Liu S, Edwards DS (1999) ^{99m}Tc-Labeled small peptides as diagnostic radiopharmaceuticals. Chem Rev 99:2235–2268

Liu S, Edwards DS et al (1998) A novel ternary ligand system for ^{99m}Tc-labeling of hydrazino nicotinamide-modified biologically active molecules using imine-N-containing heterocycles as coligands. Bioconjug Chem 9:583–595

Liu S, Kim YS et al (2008) Coligand effects on the solution stability, biodistribution and metabolism of the ^{99m}Tc-labeled cyclic RGDfK tetramer. Nucl Med Biol 35:111–121

Liu Z, Li ZB et al (2009a) Small-animal PET of tumors with ^{64}Cu-labeled RGD-bombesin heterodimer. J Nucl Med 50:1168–1177

Liu Z, Niu G et al (2009b) ^{68}Ga-labeled NOTA-RGD-BBN peptide for dual integrin and GRPR-targeted tumor imaging. Eur J Nucl Med Mol Imaging 36:1483–1494

Low PS, Henne WA et al (2008) Discovery and development of folic-acid-based receptor targeting for imaging and therapy of cancer and inflammatory diseases. Acc Chem Res 41:120–129

Maddalena ME, Fox J et al (2009) ^{177}Lu-AMBA biodistribution, radiotherapeutic efficacy, imaging, and autoradiography in prostate cancer models with low GRP-R expression. J Nucl Med 50:2017–2024

Maes V, Garcia-Garayoa E et al (2006) Novel ^{99m}Tc-labeled neurotensin analogues with optimized biodistribution properties. J Med Chem 49:1833–1836

Maina T, Nikolopoulou A et al (2007) [^{99m}Tc]Demotensin 5 and 6 in the NTS1-R-targeted imaging of tumours: synthesis and preclinical results. Eur J Nucl Med Mol Imaging 34:1804–1814

Maina T, Nock B et al (2002) [^{99m}Tc]Demotate, a new ^{99m}Tc-based [Tyr^3]octreotate analogue for the detection of somatostatin receptor-positive tumours: synthesis and preclinical results. Eur J Nucl Med Mol Imaging 29:742–753

Mansi R, Wang X et al (2009) Evaluation of a 1,4,7,10-tetraazacyclododecane-1,4,7,10-tetraacetic acid-conjugated bombesin-based radioantagonist for the labeling with single-photon emission computed tomography, positron emission tomography, and therapeutic radionuclides. Clin Cancer Res 15:5240–5249

Mardirossian G, Wu C et al (1993) The stability in liver homogenates of indium-111 and yttrium-90 attached to antibody via two popular chelators. Nucl Med Biol 20:65–74

Maresca KP, Hillier SM et al (2009) Comprehensive radiolabeling, stability, and tissue distribution studies of technetium-99m single amino acid chelates (SAAC). Bioconjug Chem 20:1625–1633

Markwalder R, Reubi JC (1999) Gastrin-releasing peptide receptors in the human prostate: relation to neoplastic transformation. Cancer Res 59:1152–1159

Mathias CJ, Wang S et al (1998) Indium-111-DTPA-folate as a potential folate-receptor-targeted radiopharmaceutical. J Nucl Med 39:1579–1585

Mercer JR, Xu LH et al (1989) Synthesis and tumor uptake of 5-^{82}Br- and 5-^{131}I-labeled 5-halo-1-(2-fluoro-2-deoxy-beta-D-ribofuranosyl)uracils. J Med Chem 32:1289–1294

Mindt TL, Jungi V et al (2008) Modification of different IgG1 antibodies via glutamine and lysine using bacterial and human tissue transglutaminase. Bioconjug Chem 19:271–278

Minko T, Paranjpe PV et al (2002) Enhancing the anticancer efficacy of camptothecin using biotinylated poly (ethylene glycol) conjugates in sensitive and multidrug-resistant human ovarian carcinoma cells. Cancer Chemother Pharmacol 50:143–150

Moody TW, Russell EK et al (1983) Bombesin-like peptides in small cell lung cancer: biochemical characterization and secretion from a cell line. Life Sci 32:487–493

Müller C, Brühlmeier M et al (2006a) Effects of antifolate drugs on the cellular uptake of radiofolates in vitro and in vivo. J Nucl Med 47:2057–2064

Müller C, Mindt TL et al (2009) Evaluation of a novel radiofolate in tumour-bearing mice: promising prospects for folate-based radionuclide therapy. Eur J Nucl Med Mol Imaging 36:938–946

Müller C, Reddy JA et al (2010) Effects of the antifolates pemetrexed and CB3717 on the tissue distribution of ^{99m}Tc-EC20 in xenografted and syngeneic tumor-bearing mice. Mol Pharm 7:597–604

Müller C, Schibli R et al (2008) Pemetrexed improves tumor selectivity of ^{111}In-DTPA-folate in mice with folate receptor-positive ovarian cancer. J Nucl Med 49:623–629

Müller C, Schubiger PA et al (2006b) Synthesis and in vitro/in vivo evaluation of novel ^{99m}Tc(CO)$_3$-folates. Bioconjug Chem 17:797–806

Müller C, Schubiger PA et al (2007) Isostructural folate conjugates radiolabeled with the matched pair ^{99m}Tc/^{188}Re: a potential strategy for diagnosis and therapy of folate receptor-positive tumors. Nucl Med Biol 34:595–601

Munch-Petersen B, Cloos L et al (1995) Human thymidine kinase 1. Regulation in normal and malignant cells. Adv Enzyme Regul 35:69–89

Neri D, Carnemolla B et al (1997) Targeting by affinity-matured recombinant antibody fragments of an angiogenesis associated fibronectin isoform. Nat Biotechnol 15:1271–1275

Nock B, Nikolopoulou A et al (2003) [^{99m}Tc]Demobesin 1, a novel potent bombesin analogue for GRP receptor-targeted tumour imaging. Eur J Nucl Med Mol Imaging 30:247–258

Nock BA, Nikolopoulou A et al (2005) Potent bombesin-like peptides for GRP-receptor targeting of tumors with ^{99m}Tc: a preclinical study. J Med Chem 48:100–110

Nock BA, Nikolopoulou A et al (2006) Toward stable N4-modified neurotensins for NTS1-receptor-targeted tumor imaging with ^{99m}Tc. J Med Chem 49:4767–4776

Oh P, Li Y et al (2004) Subtractive proteomic mapping of the endothelial surface in lung and solid tumours for tissue-specific therapy. Nature 429:629–635

Ozker K, Collier BD et al (1999) Biodistribution of ^{99m}Tc-labelled 5-thio-D-glucose. Nucl Med Commun 20:1055–1058

Parker N, Turk MJ et al (2005) Folate receptor expression in carcinomas and normal tissues determined by a quantitative radioligand binding assay. Anal Biochem 338:284–293

Petrig J, Schibli R et al (2001) Derivatization of glucose and 2-deoxyglucose for transition metal complexation: substitution reactions with organometallic ^{99m}Tc and Re precursors and fundamental NMR investigations. Chemistry 7:1868–1873

Pini A, Viti F et al (1998) Design and use of a phage display library. Human antibodies with subnanomolar affinity against a marker of angiogenesis eluted from a two-dimensional gel. J Biol Chem 273:21769–21776

Posey JA, Khazaeli MB et al (2001) A pilot trial of Vitaxin, a humanized anti-vitronectin receptor (anti alpha v beta 3) antibody in patients with metastatic cancer. Cancer Biother Radiopharm 16:125–132

Purohit A, Liu S et al (2003) Phosphine-containing HYNIC derivatives as potential bifunctional chelators for ^{99m}Tc-labeling of small biomolecules. Bioconjug Chem 14:720–727

Reddy JA, Xu LC et al (2004) Preclinical evaluation of ^{99m}Tc-EC20 for imaging folate receptor-positive tumors. J Nucl Med 45:857–866

Reubi JC, Waser B et al (1998) Neurotensin receptors: a new marker for human ductal pancreatic adenocarcinoma. Gut 42:546–550

Risch VR, Honda T et al (1977) Distribution of ^{99m}Tc-1-thioglucose in rats: effect of administration route on pancreatic specificity. Radiology 124:837–838

Rolleman EJ, Valkema R et al (2003) Safe and effective inhibition of renal uptake of radiolabelled octreotide by a combination of lysine and arginine. Eur J Nucl Med Mol Imaging 30:9–15
Rowland DJ, Cherry SR (2008) Small-animal preclinical nuclear medicine instrumentation and methodology. Semin Nucl Med 38:209–222
Russell-Jones G, McTavish K et al (2004) Vitamin-mediated targeting as a potential mechanism to increase drug uptake by tumours. J Inorg Biochem 98:1625–1633
Salmaso S, Pappalardo JS et al (2009) Targeting glioma cells in vitro with ascorbate-conjugated pharmaceutical nanocarriers. Bioconjug Chem 20:2348–2355
Salouti M, Rajabi H et al (2008) Breast tumor targeting with ^{99m}Tc-HYNIC-PR81 complex as a new biologic radiopharmaceutical. Nucl Med Biol 35:763–768
Santimaria M, Moscatelli G et al (2003) Immunoscintigraphic detection of the ED-B domain of fibronectin, a marker of angiogenesis, in patients with cancer. Clin Cancer Res 9:571–579
Schibli R, Dumas C et al (2005) Synthesis and in vitro characterization of organometallic rhenium and technetium glucose complexes against Glut 1 and hexokinase. Bioconjug Chem 16:105–112
Schibli R, La Bella R et al (2000) Influence of the denticity of ligand systems on the in vitro and in vivo behavior of ^{99m}Tc(I)-tricarbonyl complexes: a hint for the future functionalization of biomolecules. Bioconjug Chem 11:345–351
Schibli R, Schubiger PA (2002) Current use and future potential of organometallic radiopharmaceuticals. Eur J Nucl Med Mol Imaging 29:1529–1542
Schibli R, Schwarzbach R et al (2002) Steps toward high specific activity labeling of biomolecules for therapeutic application: preparation of precursor $[^{188}Re(H_2O)_3(CO)_3]^+$ and synthesis of tailor-made bifunctional ligand systems. Bioconjug Chem 13:750–756
Schmid M, Neumaier B et al (2006) Synthesis and evaluation of a radiometal-labeled macrocyclic chelator-derivatised thymidine analog. Nucl Med Biol 33:359–366
Schottelius M, Laufer B et al (2009) Ligands for mapping alphavbeta3-integrin expression in vivo. Acc Chem Res 42:969–980
Schottelius M, Wester HJ (2009) Molecular imaging targeting peptide receptors. Methods 48:161–177
Schottelius M, Wester HJ et al (2002) Improvement of pharmacokinetics of radioiodinated Tyr^3-octreotide by conjugation with carbohydrates. Bioconjug Chem 13:1021–1030
Schwartz DA, Abrams MJ et al (1991) Preparation of hydrazino-modified proteins and their use for the synthesis of ^{99m}Tc-protein conjugates. Bioconjug Chem 2:333–336
Schweinsberg C, Maes V et al (2008) Novel glycated $[^{99m}Tc(CO)_3]$-labeled bombesin analogues for improved targeting of gastrin-releasing peptide receptor-positive tumors. Bioconjug Chem 19:2432–2439
Seetharam B (1999) Receptor-mediated endocytosis of cobalamin (vitamin B_{12}). Annu Rev Nutr 19:173–195
Seetharam B, Li N (2000) Transcobalamin II and its cell surface receptor. Vitam Horm 59:337–366
Seetharam B, Yammani RR (2003) Cobalamin transport proteins and their cell-surface receptors. Expert Rev Mol Med 5:1–18
Semnani ES, Wang K et al (2005) 5-[^{123}I/^{125}I]iodo-2′-deoxyuridine in metastatic lung cancer: radiopharmaceutical formulation affects targeting. J Nucl Med 46:800–806
Shi J, Kim YS et al (2009) Improving tumor uptake and pharmacokinetics of ^{64}Cu-labeled cyclic RGD peptide dimers with Gly(3) and PEG(4) linkers. Bioconjug Chem 20:750–759
Shi J, Wang L et al (2008) Improving tumor uptake and excretion kinetics of ^{99m}Tc-labeled cyclic arginine-glycine-aspartic (RGD) dimers with triglycine linkers. J Med Chem 51:7980–7990
Siegel BA, Dehdashti F et al (2003) Evaluation of ^{111}In-DTPA-folate as a receptor-targeted diagnostic agent for ovarian cancer: initial clinical results. J Nucl Med 44:700–707
Smith CJ, Gali H et al (2003a) Radiochemical investigations of ^{177}Lu-DOTA-8-Aoc-BBN[7-14]NH_2: an in vitro/in vivo assessment of the targeting ability of this new radiopharmaceutical for PC-3 human prostate cancer cells. Nucl Med Biol 30:101–109
Smith CJ, Sieckman GL et al (2003b) Radiochemical investigations of gastrin-releasing peptide receptor-specific [^{99m}Tc(X)$(CO)_3$-Dpr-Ser-Ser–Ser-Gln-Trp-Ala-Val-Gly-His-Leu-

Met-(NH_2)] in PC-3, tumor-bearing, rodent models: syntheses, radiolabeling, and in vitro/in vivo studies where Dpr = 2,3-diaminopropionic acid and X = H_2O or $P(CH_2OH)_3$. Ca. Cancer Res 63:4082–4088

Smith CJ, Sieckman GL et al (2003c) Radiochemical investigations of [^{188}Re(H_2O)$(CO)_3$-diaminopropionic acid-SSS-bombesin(7-14)NH2]: syntheses, radiolabeling and in vitro/in vivo GRP receptor targeting studies. Anticancer Res 23:63–70

Smith CJ, Volkert WA et al (2003d) Gastrin releasing peptide (GRP) receptor targeted radiopharmaceuticals: a concise update. Nucl Med Biol 30:861–868

Smith CJ, Volkert WA et al (2005) Radiolabeled peptide conjugates for targeting of the bombesin receptor superfamily subtypes. Nucl Med Biol 32:733–740

Sosabowski JK, Matzow T et al (2009) Targeting of CCK-2 receptor-expressing tumors using a radiolabeled divalent gastrin peptide. J Nucl Med 50:2082–2089

Spanoudaki VC, Ziegler SI (2008) PET and SPECT instrumentation. Handb Exp Pharmacol 185:53–74

Steffens MG, Oosterwijk E et al (1999) In vivo and in vitro characterizations of three ^{99m}Tc-labeled monoclonal antibody G250 preparations. J Nucl Med 40:829–836

Storr T, Fisher CL et al (2005) A glucosamine-dipicolylamine conjugate of ^{99m}Tc(I) and ^{186}Re(I) for use in imaging and therapy. Dalton Trans 21(4):654–655

Struthers H, Hagenbach A et al (2009) Organometallic $[Re(CO)_3]^+$ and $[Re(CO)_2(NO)]^{2+}$ labeled substrates for human thymidine kinase 1. I. Inorg Chem 48:5154–5163

Struthers H, Spingler B et al (2008) "Click-to-chelate": design and incorporation of triazole-containing metal-chelating systems into biomolecules of diagnostic and therapeutic interest. Chemistry 14:6173–6183

Tang Y, Scollard D et al (2005) Imaging of HER2/neu expression in BT-474 human breast cancer xenografts in athymic mice using [^{99m}Tc]-HYNIC-trastuzumab (Herceptin) Fab fragments. Nucl Med Commun 26:427–432

Tolmachev V, Friedman M et al (2009) Affibody molecules for epidermal growth factor receptor targeting in vivo: aspects of dimerization and labeling chemistry. J Nucl Med 50:274–283

Torizuka T, Tamaki N et al (1995) In vivo assessment of glucose metabolism in hepatocellular carcinoma with FDG-PET. J Nucl Med 36:1811–1817

Toyohara J, Hayashi A et al (2003) Development of radioiodinated nucleoside analogs for imaging tissue proliferation: comparisons of six 5-iodonucleosides. Nucl Med Biol 30:687–696

Toyohara J, Hayashi A et al (2002) Rationale of 5-^{125}I-iodo-4′-thio-2′-deoxyuridine as a potential iodinated proliferation marker. J Nucl Med 43:1218–1226

Van de Wiele C, Dumont F et al (2000) Technetium-99m RP527, a GRP analogue for visualisation of GRP receptor-expressing malignancies: a feasibility study. Eur J Nucl Med 27:1694–1699

Verhaar-Langereis MJ, Zonnenberg BA et al (2000) Radioimmunodiagnosis and therapy. Cancer Treat Rev 26:3–10

Verwijnen SM, Krenning EP et al (2005) Oral versus intravenous administration of lysine: equal effectiveness in reduction of renal uptake of [^{111}In-DTPA]octreotide. J Nucl Med 46:2057–2060

von Guggenberg E, Dietrich H et al (2007) ^{99m}Tc-labelled HYNIC-minigastrin with reduced kidney uptake for targeting of CCK-2 receptor-positive tumours. Eur J Nucl Med Mol Imaging 34:1209–1218

Waibel R, Treichler H et al (2008) New derivatives of vitamin B_{12} show preferential targeting of tumors. Cancer Res 68:2904–2911

Wang L, Shi J et al (2009) Improving tumor-targeting capability and pharmacokinetics of ^{99m}Tc-labeled cyclic RGD dimers with PEG(4) linkers. Mol Pharm 6:231–245

Wang S, Luo J et al (1997) Design and synthesis of [^{111}In]DTPA-folate for use as a tumor-targeted radiopharmaceutical. Bioconjug Chem 8:673–679

Wängler C, Schirrmacher R et al (2009) Simple and convenient radiolabeling of proteins using a prelabeling-approach with thiol-DOTA. Bioorg Med Chem Lett 19:1926–1929

Weitman SD, Lark RH et al (1992) Distribution of the folate receptor GP38 in normal and malignant cell lines and tissues. Cancer Res 52:3396–3401

Wester HJ, Schottelius M et al (2002) Comparison of radioiodinated TOC, TOCA and Mtr-TOCA: the effect of carbohydration on the pharmacokinetics. Eur J Nucl Med Mol Imaging 29:28–38

Wieland DM, Wu J et al (1980) Radiolabeled adrenergi neuron-blocking agents: adrenomedullary imaging with [^{131}I]iodobenzylguanidine. J Nucl Med 21:349–353

Wilbur DS, Hamlin DK et al (1996) Synthesis and nca-radioiodination of arylstannyl-cobalamin conjugates. Evaluation of aryliodo-cobalamin conjugate binding to transcobalamin II and biodistribution in mice. Bioconjug Chem 7:461–474

Xu N, Cai G et al (2009) Molecular imaging application of radioiodinated anti-EGFR human Fab to EGFR-overexpressing tumor xenografts. Anticancer Res 29:4005–4011

Yang W, Cheng Y et al (2009) Targeting cancer cells with biotin-dendrimer conjugates. Eur J Med Chem 44:862–868

Yim CB, Boerman OC et al (2009) Versatile conjugation of octreotide to dendrimers by cycloaddition ("click") chemistry to yield high-affinity multivalent cyclic peptide dendrimers. Bioconjug Chem 20:1323–1331

Yokota T, Milenic DE et al (1992) Rapid tumor penetration of a single-chain Fv and comparison with other immunoglobulin forms. Cancer Res 52:3402–3408

Yokota T, Milenic DE et al (1993) Microautoradiographic analysis of the normal organ distribution of radioiodinated single-chain Fv and other immunoglobulin forms. Cancer Res 53:3776–3783

Zardi L, Carnemolla B et al (1987) Transformed human cells produce a new fibronectin isoform by preferential alternative splicing of a previously unobserved exon. EMBO J 6:2337–2342

Zhang H, Chen J et al (2004) Synthesis and evaluation of bombesin derivatives on the basis of pan-bombesin peptides labeled with indium-111, lutetium-177, and yttrium-90 for targeting bombesin receptor-expressing tumors. Cancer Res 64:6707–6715

Zwanziger D, Khan IU et al (2008) Novel chemically modified analogues of neuropeptide Y for tumor targeting. Bioconjug Chem 19:1430–1438

Non-peptidyl ^{18}F-Labelled PET Tracers as Radioindicators for the Noninvasive Detection of Cancer

Stefan Wagner and Klaus Kopka

Abstract

Noninvasive molecular imaging of cancer by means of the state-of-the-art scintigraphic imaging modalities PET and PET/CT represents a powerful diagnostic approach in modern nuclear medicine. Radiotracers labelled with the prominent positron emitter ^{18}F can be defined as molecular PET imaging probes targeting discrete biological structures dysregulated in the progression of cancer and, thus, are capable to detect oncological pathologies in vivo at the cellular and subcellular level in a timely manner. The use of such radioindicators, also called radiotracers, allows the detection of their path and fate in the living organism. In the course of tumourigenesis, several molecular processes become dysregulated and radiotracers are available to image these abnormal characteristics. This chapter describes ^{18}F-labelled radiopharmaceuticals that are frequently used in oncological PET and PET/CT. In particular, non-peptidyl radiotracers for the imaging of glucose utilisation, amino acid transport and protein synthesis, membrane lipid synthesis, cell proliferation, hypoxia, oestrogen receptor status and bone mineralisation of tumours are introduced. The compounds are described regarding their radiochemical synthesis approaches and their in vivo metabolism and accumulation mechanisms. Furthermore, concrete clinical perspectives are given, that refer to highly potent and promising oncological radiotracers which are currently in preclinical development.

S. Wagner (✉) · K. Kopka
Department of Nuclear Medicine, University Hospital Münster,
Albert-Schweitzer-Campus 1, 48149 Münster, Germany
e-mail: stwagner@uni-muenster.de

O. Schober and B. Riemann (eds.), *Molecular Imaging in Oncology*,
Recent Results in Cancer Research 187, DOI: 10.1007/978-3-642-10853-2_3,

Contents

1 Introduction

Molecular imaging in vivo is used for the visualisation, characterisation and measurement of biological processes at the molecular and cellular level (Weissleder and Mahmood 2001). The scintigraphic techniques used in nuclear medicine, such as single photon emission computed tomography (SPECT) and positron emission tomography (PET) in combination with appropriate radiolabelled compounds, also called radioindicators or radiotracers, represent a powerful tool for the molecular imaging approach. Recently, SPECT and PET cameras have been extended by incorporating computer tomography (CT) devices resulting in high-end hybrid tomographic imaging devices nowadays available as SPECT/CT or PET/CT scanners. These combine high resolution morphological imaging with highly sensitive molecular imaging and are known to significantly improve diagnostic capabilities in different clinical fields. To answer oncological questions these hybrid systems in combination with the administered radiotracer are helpful diagnostic devices to differentiate malignant from benign disease, to identify the sites of disease in order to plan biopsy or surgery, to detect the primary tumour in patients with metastatic disease with a small or unknown tumour and to grade malignancy based on the quantified amount of tracer uptake in the tumour. Furthermore, the staging of the disease based on the relative tracer uptake in whole-body scans, the identification of residual disease after treatment, the detection of recurrences including the sites of recurrences, the investigation of response to

Table 1 The cyclotron-produced radionuclide ^{18}F for PET application

Radionuclide	$T_{1/2,\ phys.}$	Decay[a]/Energy/keV	Nuclear reaction
^{18}F	109.7 min	β^+/600 γ/511	^{18}O(p,n)^{18}F ^{20}Ne(d,α)^{18}F

[a] Electron capture (EC) contribution: ^{18} F: 3 %

therapy and the planning of radiation therapy based on the identification of the radiosensitivity of tumour tissue are additional parameters that can be determined with these techniques (Schober and Heindel 2008).

In this connection, the availability of specific radiotracers that address these questions is obligatory. Thereby, various radionuclides used to label tailor-made precursor compounds yielding the corresponding radiotracers are well established in the field of radiopharmaceutical chemistry. Among these radionuclides the neutron-deficient positron emitters used in PET diagnostics are generated via cyclotron accelerators. Under no-carrier-added conditions accelerated protons or deuterons react with stable—often rare—isotopes thereby emitting neutrons or α-particles to yield the positron emitter of choice with high specific activity. The produced positron emitter is then introduced in organic compounds like peptides, proteins, drugs or receptor ligands via rapid and reliable syntheses using automated radiochemistry systems that are installed in lead shielded hotcells (Welch and Redvanly 2003). Table 1 summarises the modern nuclear reactions for the production of the positron emitter ^{18}F, which is one of the predominantly used positron emitters in radiopharmaceutical chemistry.

In the following sections, different ^{18}F-labelled radiopharmaceuticals that are used in oncological PET and PET/CT are introduced. They are subdivided in tracer classes that are used for the imaging of discrete tumour characteristics.

2 [^{18}F]FDG for Imaging Glucose Metabolism

In the year 1978, 2-Deoxy-2-[^{18}F]fluoro-D-glucose (**[^{18}F]FDG**), that represents a metabolic radiotracer, was evaluated for the first time (Gallagher et al. 1978). Since then **[^{18}F]FDG** represents the most important radiopharmaceutical and "working horse" in clinical PET. The radiotracer is predominantly used for tumour imaging, particularly for the estimation of enhanced glucose utilisation in malignant lesions where anaerobic and inefficient glycolysis plays the major role (Warburg et al. 1924; Poeppel et al. 2009; Mittra and Quon 2009).

The intracellular uptake mechanism of **[^{18}F]FDG** is similar to that of natural D-glucose. Glucose transport proteins that are classified in the transporters GLUT-1 to GLUT-7 as well as GLUT-10 to GLUT-12 are responsible for the active and stereospecific transport of **[^{18}F]FDG** into the cells. The hexokinase isozymes (hexokinase I to IV) phosphorylate **[^{18}F]FDG** immediately after intracellular

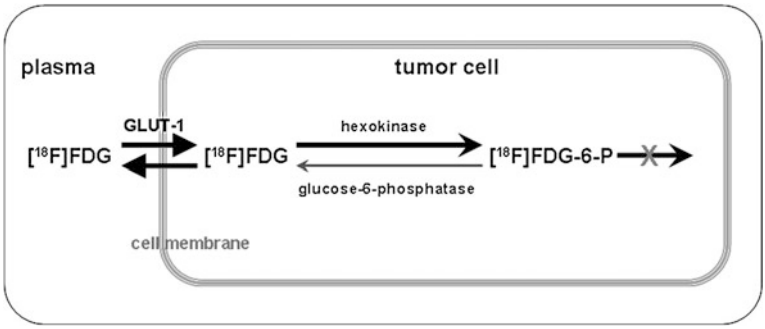

Fig. 1 Amplification mechanism of **[^{18}F]FDG** uptake in tumour cells: *metabolic trapping*

uptake yielding [^{18}F]FDG-6-phosphate ([^{18}F]FDG-6-P) (Smith 2000). The GLUT-1 transporter and hexokinase II are the best-known subtypes with regard to glucose metabolism in tumour cells (Mamede et al. 2005). In contrast to glucose-6-phosphate [^{18}F]FDG-6-P is not a substrate of glycolysis because a subsequent metabolic conversion requires an oxygen atom at the C-2-position, that is not present in [^{18}F]FDG-6-P. Therefore, the next metabolic step realised by conversion of glucose-6-phosphate catalysed by phosphoglucose-isomerase, is not possible with [^{18}F]FDG-6-P. Therefore, this radiolabelled metabolite represents the terminal metabolite which intracellularly "amplifies" over time (Brock et al. 1997). This amplification mechanism is termed metabolic trapping (Fig. 1).

However, ^{19}F-NMR spectroscopic investigations with macroscopic (millimolar) amounts of nonradioactive FDG in vivo manifest that FDG-6-P can be metabolised into 2-deoxy-2-fluoro-D-mannose-6-phosphate in specific organs, such as brain and heart (Brock et al. 1997). On the other hand, glucose-6-phosphatase that is activated in defined organs is able to dephosphorylate [^{18}F]FDG-6-P and as a result decreases the metabolic trapping of **[^{18}F]FDG**. Therefore, **[^{18}F]FDG** uptake is highly upregulated in organs that are characterised by less intracellular amounts of glucose-6-phosphatase (e.g. brain and heart). In contrast, high enterohepatic glucose-6-phosphatase concentrations result in low **[^{18}F]FDG** uptake, e.g. in liver and intestines (Southworth et al. 2002).

The radiosynthesis of **[^{18}F]FDG** can be realised by fully automated remotely controlled PET radiotracer synthesisers. In the first step, the generated [^{18}F]fluoride is separated from the irradiated [^{18}O]water, which is used in the ^{18}O(p,n)^{18}F reaction, with an anion exchange resin and subsequently dried *in vacuo*. The addition of large cations or cryptands (e.g., tetrabutylammonium cation (Bu_4N^+) or potassium-aminopolyether (K^+-Kryptofix^{TM} 2.2.2 = K(K222)$^+$) increases the nucleophilicity of [^{18}F]fluoride for subsequent substitution reaction in organic solvents. Then the precursor 1,3,4,6-tetra-*O*-acetyl-2-*O*-trifluoromethane-sulfonyl-*β*-D-mannopyranose is substituted by [^{18}F]fluoride in a bimolecular nucleophilic substitution (S_N2) reaction and the acetyl (Ac) protection groups are cleaved by an acidic or basic hydrolysis variant to yield **[^{18}F]FDG** (Hamacher et al. 1986;

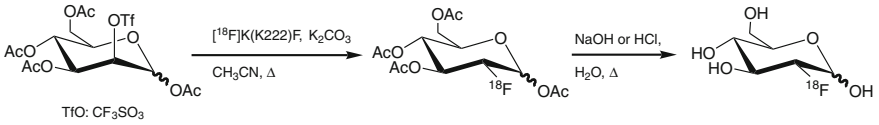

Fig. 2 Radiosynthesis of **[^{18}F]FDG**

Füchtner et al. 1996). Figure 2 shows the synthesis scheme of **[^{18}F]FDG**. After purification via several cartridges **[^{18}F]FDG** is diluted in a physiological buffer ready for injection. The production of **[^{18}F]FDG** is established in many PET centres worldwide and networks that realise the distribution of **[^{18}F]FDG** in a satellite concept are common practice in many countries.

3 ^{18}F-Labelled Amino Acids (AAs) for Imaging AA Transport and Protein Synthesis

3.1 *O*-(2-[^{18}F]Fluoroethyl)-L-tyrosine ([^{18}F]FET)

Although all AAs can diffuse into cells, the main uptake mechanism of AAs into cells is realised via transport systems. To date, more than 20 ubiquitous AA transport systems are known that are responsible for active cellular AA uptake. These transport systems can be divided into two main subgroups. Transporters of the first subgroup are sodium-dependent. This type of transport is achieved by the sodium gradient and the membrane electric potential and is maintained by Na^+ or K^+ adenosine triphosphatase. These AA carriers are responsible for the transport of short side chain AAs, non-ramified side chain AAs and large neutral AAs. The transport system A, ACS and Gly are members of this group. Carrier systems of the second subgroup work sodium-independent and are responsible for the transport of aromatic and ramified side chain AAs. The L, $B^{0,+}$ and y^+ carriers represent members of the sodium-independent AA transporter type. Additionally, non-ubiquitous AA transport systems have been characterised that are located in specific tissues. For example, the transport system T is responsible for the tyrosine, phenylalanine and tryptophan supply of erythrocytes (Oxender and Christensen 1963; Shotwell et al. 1981; Christensen 1990; Souba and Pacitti 1992). Inside the cells AAs can function as precursors of other biomolecules (e.g. hormones, or neurotransmitters) and building blocks for proteins. Additionally, AAs are involved in a plurality of metabolic pathways and transformations (Berg et al. 2006).

Tumour cells possess an increased AA transport and/or protein synthesis rate (Busch et al. 1959; Johnstone and Scholefield 1965; Isselbacher 1972). The increased AA transport can result from specific cell surface changes in malignant cells. For example, the expression of the transport system A is increased in transformed and malignant cells (Saier et al. 1988). Therefore, from a simplified

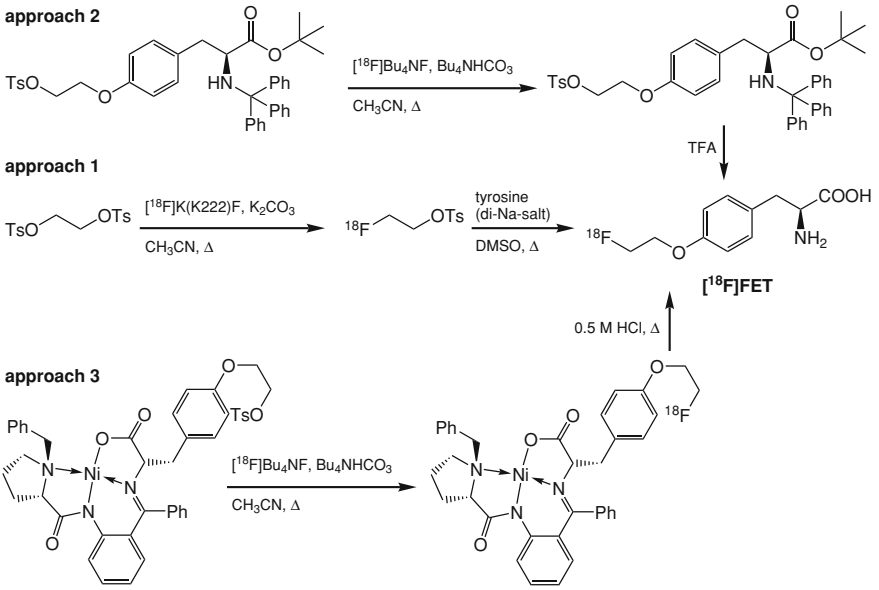

Fig. 3 Different routes for the radiosynthesis of **[^{18}F]FET**

point of view the increased AA transport and/or protein synthesis rate in tumour cells can be interpreted as a consequence of an accelerated and uncontrolled proliferation of tumour cells.

The tyrosine derivative **[^{18}F]FET** represents a tracer of AA transport. The compound was proven to not significantly incorporate into proteins via protein synthesis (Wester et al. 1999; Heiss et al. 1999). In this context **[^{18}F]FET** is, for example, suitable to image glioblastomas (Weckesser et al. 2005; Thiele et al. 2009; Dunet et al. 2012) and squamous cell carcinomas (Pauleit et al. 2005; Haerle et al. 2011) indicating enhanced AA transport into the respective tumour.

Three different approaches for the radiosynthesis of **[^{18}F]FET** have been published. Wester et al. prepared the target compound via the intermediate 1-[^{18}F]fluoro-2-(tosyloxy)ethane (Wester et al. 1999). Therefore, ethylene glycol di-*p*-tosylate was labelled with [^{18}F]fluoride and the resulting labelling synthon was used for the *O*-alkylation of the di-sodium salt of L-tyrosine. After HPLC purification and formulation **[^{18}F]FET** was obtained with a radiochemical yield (ry) of 40 % (decay corrected) and a radiochemical purity (rp) of 97–99 % in approximately 60 min (Fig. 3 approach 1). In a similar approach, the HPLC purification was substituted by a less time-consuming purification procedure using solid phase extraction (SPE) cartridges resulting in a time saving of 10 min (Mueller et al. 2011). In a slightly modified radiosynthesis, 1-bromo-2-[^{18}F]fluoroethane was used instead of 1-[^{18}F]fluoro-2-(tosyloxy)ethane as labelling synthon. Here, the preparation time is shortened (35 min) and the ry slightly increased (45 % not decay corrected). The rp was > 99 % and the specific activity (A_s) was > 80 GBq/

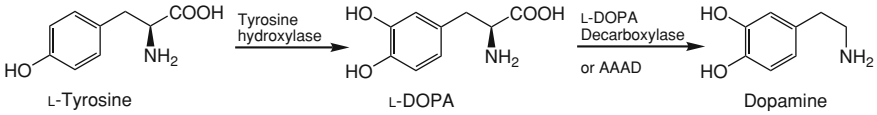

Fig. 4 Biosynthesis of L-DOPA and dopamine

μmol (Zuhayra et al. 2009). In a second approach, *O*-(2-tosyloxyethyl)-*N*-trityl-L-tyrosine tert.-butylester was labelled with [^{18}F]fluoride in the presence of tetrabutylammonium hydrogen carbonate/carbonate. Cleavage of the protecting group, HPLC purification and formulation resulted in an injectable **[^{18}F]FET** solution with a A_s of > 18 GBq/μmol. The synthesis time was 80 min (Fig. 3 approach 2, Hamacher and Coenen 2002). The third approach utilises a novel type of chiral enantiomerically pure labelling precursor for [^{18}F]FET, based on the Ni(II) complex of a Schiff's base of (*S*)-[*N*-2-(*N*'-benzylprolyl)amino]benzophenone (BPB) with alkylated L-tyrosine. Substitution of the complex with [^{18}F]fluoride, complex cleavage, HPLC purification and formulation yielded **[^{18}F]FET** in 40–45 % (decay corrected) in 55 min with a A_s of > 14 GBq/μmol and a rp of > 99 % (Fig. 3 approach 3, Krasikova et al. 2008).

3.2 6-[^{18}F]Fluoro-3,4-dihydroxy-L-phenylalanine ([^{18}F]FDOPA)

The biosynthesis of the neurotransmitter dopamine that is not able to cross the blood–brain barrier starts with L-tyrosine. Hydroxylation of L-tyrosine yields 3,4-dihydroxy-L-phenylalanine (L-DOPA). In a subsequent decarboxylation step of L-DOPA dopamine is synthesised by L-DOPA decarboxylase or aromatic amino acid decarboxylase (AAAD) (Fig. 4, Patrick 2005). The transport of L-DOPA into the brain is realised by a neutral amino acid carrier (L type). In this context, the radiolabelled derivative **6-[^{18}F]FDOPA** was developed to evaluate its transport from blood to brain and to investigate the storage, degradation and turnover of intracerebral dopamine (Garnett et al. 1978, 1983). Several metabolic transformations of **6-[^{18}F]FDOPA** are known. On the one side, *O*-methylation catalysed by the catechol-*O*-methyl transferase (COMT) results in 6-[^{18}F]fluoro-4-hydroxy-3-methoxy-L-phenylalanine ([^{18}F]FHMP). On the other side, decarboxylation by AAAD yields 6-[^{18}F]fluorodopamine ([^{18}F]FDA), that is metabolised to 6-[^{18}F]fluoro-3,4-dihydroxy-phenylacetic acid ([^{18}F]FDPA) by monoamine oxidase. Subsequent transfer of a methyl group by COMT produces the metabolite 6-[^{18}F]fluoro-4-hydroxy-3-methoxy-phenylacetic acid ([^{18}F]FHMPA). To reduce the release of metabolites in blood as well as the decarboxylase activity and to increase the amount of the unmetabolised **6-[^{18}F]FDOPA** parent compound during the PET investigation the decarboxylase inhibitor carbidopa is applied (Fig. 5, Melega et al. 1990; Luxen et al. 1992).

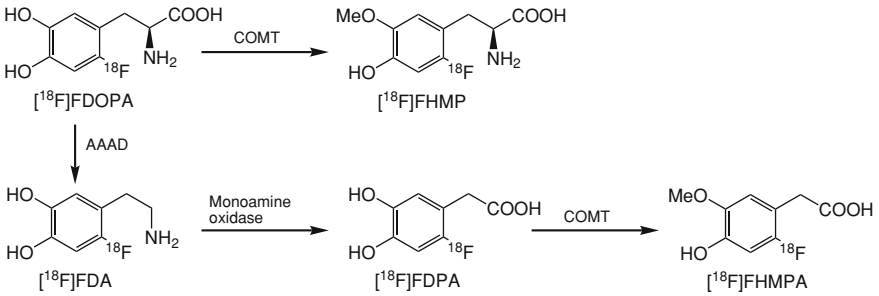

Fig. 5 Metabolism of **[^{18}F]FDOPA**

In tumour diagnostics **6-[^{18}F]FDOPA** represents a useful PET tracer for the in vivo visualisation of pheochromocytomas (Hoegerle et al. 2002; Imani et al. 2009), medullary thyroid carcinomas (Hoegerle et al. 2001; Beheshti et al. 2009; Kauhanen et al. 2011) and neuroendocrine tumours (Jager et al. 2008; Kauhanen et al. 2009; Schiesser et al. 2010.).

The preparation of **6-[^{18}F]FDOPA** can be realised via electrophilic or nucleophilic fluorination methods. The electrophilic approach is based on the aromatic substitution of *N*-formyl-3,4-di-tert.-butoxycarbonyloxy-6-(trimethylstannyl)-L-phenylalanine ethyl ester with [^{18}F]F_2 gas or acetylhypofluoride ([^{18}F]CH_3COOF). Primarily, the electrophilic aromatic substitution of the trimethylstannyl group with [^{18}F]fluorine were performed in freon 11 (CF_3Cl), but current investigations show that this polluting solvent can be replaced by deuterochloroform ($CDCl_3$) (Füchtner et al. 2008). In the next step, an acidic cleavage of the protecting groups (two tert-butyloxycarbonyl groups and one formyl moiety) is performed. Finally, HPLC purification and formulation yielded **6-[^{18}F]FDOPA** in 8–26 % (decay corrected) in 45–60 min with a rp of >99 % (Fig. 6 approach 1, Namavari et al. 1992; Dollé et al. 1998). In this connection, a good manufacturing practice (GMP) synthesis procedure that meets the standards of United States Pharmacopeia (USP) was published (Kao et al. 2011). The nucleophilic radiosynthesis of **6-[^{18}F]FDOPA** starts with an aromatic substitution of 6-trimethylammonium veratraldehyde or 6-nitroveratraldehyde with [^{18}F]fluoride forming 6-[^{18}F]fluoroveratraldehyde. Subsequent reductive iodination with diiodosilane (DIS) yields 2-[^{18}F]fluoro-4,5-dimethoxybenzyliodide. In the third step, a protected glycine derivative is alkylated enantioselectively with the labelled benzyliodide. This reaction uses the chiral phase transfer catalyst (PTC) *O*-allyl-*N*-(9)-anthracenyl-cinchonidinium bromide that induces the enantioselective formation of the L-isomer. Finally, the protecting groups are cleaved under acidic conditions with hydroiodic acid or hydrobromic acid/potassium iodide. After HPLC purification and formulation **6-[^{18}F]FDOPA** were isolated—as shown by Zhang et al. —with a ry of 7–15 % (decay corrected) and a rp of > 99 % in 80–85 min (Fig. 6 approach 2, Zhang et al. 2002). Shen et al. automated the synthesis sequence and achieved a ry of 20 %, an rp of > 95 % and a A_s of 50 GBq/μmol in 120 min (Fig. 6 approach 2, Shen et al. 2009).

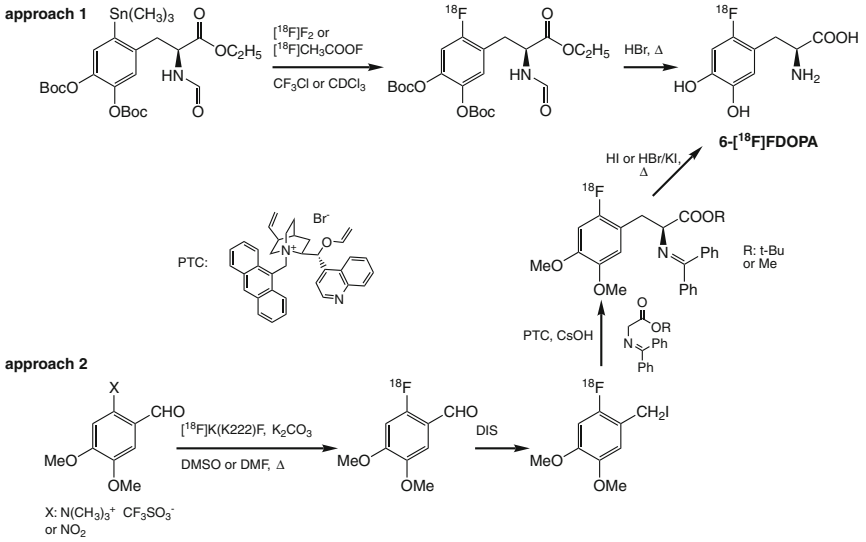

Fig. 6 Different routes for the radiosynthesis of **[^{18}F]FDOPA**

4 ^{18}F-Labelled Choline Derivatives for Imaging Membrane Lipid Synthesis

4.1 [^{18}F]Fluorocholine (Dimethyl-[^{18}F]fluoromethyl-2-hydroxyethylammonium, [^{18}F]FCH)

Choline represents an important component of the cell membrane phospholipids. Malignant tumours are characterised by an increased proliferation rate and an increased metabolism of the cell membrane components, which is associated with an increase of choline accumulation. The cellular metabolism of choline includes the phosphorylation by choline kinase yielding phosphorylcholine and the subsequent incorporation into phospholipids (e.g. phosphatidylcholine) (Podo 1999). Choline is also the metabolic precursor of betaine that is formed by oxidation catalysed by choline and betaine aldehyde dehydrogenase. Furthermore, the neurotransmitter acetylcholine arises from choline by acetylation with choline acetyltransferase (Roivainen et al. 2000). The metabolism of choline is outlined in Fig. 7.

In the year 2000, the choline analogue [^{18}F]fluorocholine (**[^{18}F]FCH**) was developed as tumour imaging agent. Initially, it was evaluated in PC-3 human prostate cancer cells, PC-3 human prostate cancer xenograft studies and human prostate and brain tumour patients (Coleman et al. 2000). The biodistribution of **[^{18}F]FCH** in the murine PC-3 human prostate cancer xenograft model was comparable to that of [^{14}C]choline (DeGrado et al. 2000). Similar to [^{11}C]choline

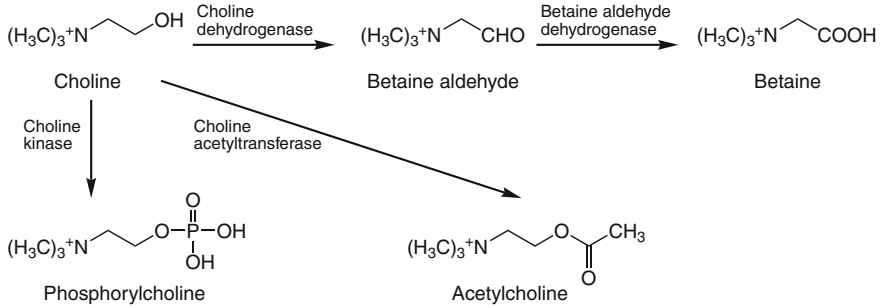

Fig. 7 Metabolism of choline

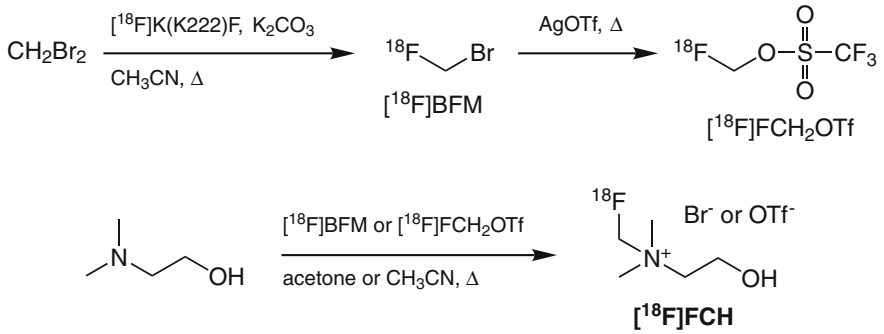

Fig. 8 Radiosynthesis of **[^{18}F]FCH**

[^{18}F]FCH turned out to be a promising agent for prostate cancer imaging with the advantage of a longer radioactive half life compared to the ^{11}C-labelled analogue (Bouchelouche and Oehr 2008; Beheshti et al. 2008; Bauman et al. 2011).

The radiosynthesis of **[^{18}F]FCH** is based on the ^{18}F-fluoroalkylation of *N*,*N*-dimethylaminoethanol with bromo-[^{18}F]fluoromethane ([^{18}F]BFM, DeGrado et al. 2000, 2001) or [^{18}F]fluoromethyl triflate ([^{18}F]FCH$_2$OTf, Iwata et al. 2002). Both synthetic pathways start with the labelling of dibromomethane to yield [^{18}F]BFM, that was used directly for alkylation or was transformed to the labelling synthon [^{18}F]FCH$_2$OTf (Fig. 8). A rcy of up to 40 % (not decay corrected), a rcp of $>$ 98 % and a synthesis time of 30–40 min were reported (Fig. 8). Several fully automated **[^{18}F]FCH** syntheses performed in a commercially available PET tracer radiosynthesiser were published (Kryza et al. 2008; Shao et al. 2011), An effective method developed by Kryza et al. yielded the target compound in 15–25 % (decay corrected), with a rcp of $>$ 99 % and a A_s of $>$ 37 GBq/μmol in $<$ 35 min (Kryza et al. 2008).

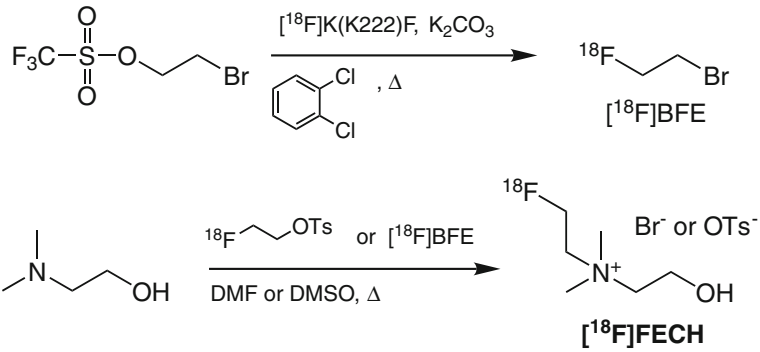

Fig. 9 Radiosynthesis of **[^{18}F]FECH**

4.2 [^{18}F]Fluoroethylcholine (Dimethyl-2-[^{18}F]fluoroethyl-2-hydroxyethylammonium, [^{18}F]FECH)

On the one side, Deves and Krupka studied the binding affinity of the choline transport system for synthetic choline analogues, using red blood cells, and discovered that two methyl groups are essential for choline transport, but the third methyl group is replaceable by a longer alkyl group (Deves and Krupka 1979). On the other side, Clary et al. studied the substrate specificity of choline kinase for synthetic choline analogues, using yeast choline kinase, and found again that the two methyl groups and the hydroxyethyl side chain are essential for successful phosphorylation, but the third methyl group is again replaceable by a longer alkyl group (Clary et al. 1987). Both findings suggest, that the introduction of a longer fluorinated alkyl group is tolerated in the design of a prostate cancer imaging probe based on choline. Therefore, Hara et al. suggested [^{18}F]fluoroethylcholine (**[^{18}F]FECH**) as potential PET tracer and they found that the biodistribution of **[^{18}F]FECH** in normal rabbits and normal humans was similar to that of [^{11}C]choline but **[^{18}F]FECH** was rapidly excreted into urine in contrast to [^{11}C]choline. Anyhow, **[^{18}F]FECH** was successfully used for the imaging of prostate cancer in patients (Hara et al. 2002).

To date, several radiosyntheses of **[^{18}F]FECH** are published. In most cases, 1-[^{18}F]fluoro-2-(tosyloxy)ethane is used to alkylate *N*,*N*-dimethylaminoethanol (Hara et al. 2002; Piel et al. 2007; Pascali et al. 2009; Asti et al. 2010). The synthesis of this intermediate is outlined in the radiosynthesis scheme of **[^{18}F]FET** (Fig. 3). A rcy of up to 48 % (not decay corrected), a rcp of 99 % and a A_s of >55 GBq/μmol in 35–65 min were provided by this approach (Fig. 9). Another investigation used the intermediate 1-bromo-2-[^{18}F]fluoroethane ([^{18}F]BFE) that is generated by ^{18}F-labelling of 2-bromoethyltriflate for alkylation of the aminoethanol derivative. Due to simplified purification procedures of this intermediate the overall rcy of **[^{18}F]FECH** is also satisfying with 47 % (not decay corrected). Moreover, a high rcp (> 99 %) and a short synthesis time (40 min) were achieved (Fig. 9, Zuhayra et al. 2008).

5 ^{18}F-Labelled Nucleoside Derivatives for Imaging Cell Proliferation

5.1 3′-Deoxy-3′-[^{18}F]fluoro-L-thymidine ([^{18}F]FLT)

The DNA synthesis is a measure of proliferation and an increased level of cellular proliferation is a feature of cancer (Hannahan and Weinberg 2000). Particularly, tumour tissue possesses an increased number of cells in the S-phase of the cell cycle which is characterised by DNA synthesis or replication and different from normal tissue. Therefore, the requirement of building blocks for the DNA synthesis, that are represented by the deoxyribonucleosides deoxyadenosine, deoxyguanosine, deoxycytidine and deoxythymidine, is increased in tumours (Cleaver 1967). In this connection, the radiotracer **[^{18}F]FLT** was developed to measure the proliferation rate of tumours (Shields et al. 1998). Similar to the aforementioned deoxyribonucleosides the tracer enters the cells via diffusion and nucleoside transporter proteins, respectively (Belt et al. 1993). In the next step, the deoxyribonucleosides including **[^{18}F]FLT** become phosphorylated by kinases inside the cells. Thymidine kinase 1 (TK1) that is overexpressed and uncoupled from DNA synthesis in tumour cells and to a much lesser extent TK2 are responsible for the phosphorylation of **[^{18}F]FLT** (Sherley and Kelly 1988; Hengstschläger et al. 1994). The resulting [^{18}F]FLT-5'-phosphate is metabolically stable and is trapped intracellularly similar to the metabolic trapping mechanism of the glucose analogue **[^{18}F]FDG** (Been et al. 2004). Recent studies evaluate the benefit of **[^{18}F]FLT** imaging in colorectal cancer (Yamamoto et al. 2009; Muijs et al. 2011), in hepatocellular carcinoma (Eckel et al. 2009) and gastric cancer (Kameyama et al. 2009, 2011). A promising approach for the application of **[^{18}F]FLT** is the monitoring of the tumour response to treatment, as demonstrated in animal studies and human pilot trials (Bading and Shields 2008; Lee et al. 2011).

The most effective radiosynthesis of **[^{18}F]FLT** starts with 5′-*O*-(4,4′-dimethoxytriphenylmethyl)-2′-deoxy-3′-*O*-nosyl-*β*-D-*threo*-pentofuranosyl)-3-*N*-Boc-thymine (FLTPre1). After nucleophilic substitution of the nosyl-group with [^{18}F]fluoride the labelled intermediate is deprotected under acidic conditions to yield **[^{18}F]FLT** that is purified by semi-preparative HPLC (Fig. 10 approach 1, Yun et al. 2003). Oh et al. transferred this approach in a fully automated PET tracer radiosynthesiser and achieved a rcy of 51 % (decay corrected), a rcp of > 98 % and a A_s of 119–285 GBq/μmol in 60 min synthesis time (Oh et al. 2004) whereas Tang et al. developed a purification procedure of **[^{18}F]FLT** that uses SEP cartridges instead of HPLC (Tang et al. 2010). The rcy was further improved by use of the protic solvent tert-butanol (*t*-BuOH) instead of acetonitrile and tetrabutylammonium hydrogen carbonate (Bu_4NHCO_3) instead of K222 in the first step (Lee et al. 2007). An alternative approach uses the precursor 5′-*O*-(4,4′-dimethoxytriphenylmethyl)-2,3′-anhydrothymidine (FLTPre2). After nucleophilic ring opening with [^{18}F]fluoride, hydrolysis of the trityl-group and HPLC purification **[^{18}F]FLT** was obtained with a rcy of 11 % (decay corrected) in 90 min (Fig. 10 approach 2, Machulla et al. 2000; Wodarski et al. 2000).

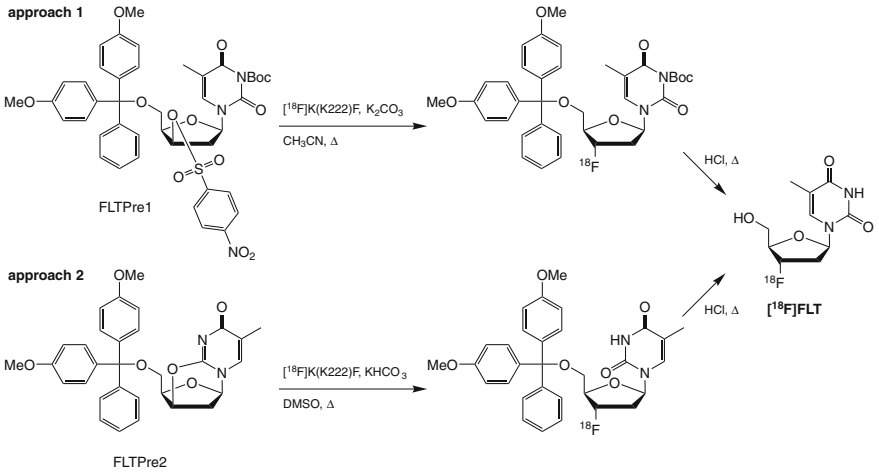

Fig. 10 Different routes for the radiosynthesis of **[^{18}F]FLT**

5.2 1-(2′-Deoxy-2′-[^{18}F]fluoro-β-D-arabinofuranosyl)-5-methyluracil ([^{18}F]FMAU)

[^{18}F]FMAU represents an alternative PET tracer which is useful for the imaging of cell proliferation. Similar to **[^{18}F]FLT** the compound is substituted with a single fluorine within the sugar subunit and is phosphorylated by TKs. **[^{18}F]FMAU** is metabolically stable and most of the intact tracer is renally cleared into the bladder. In contrast to **[^{18}F]FLT**, the uracil derivative is incorporated into DNA (Krohn et al. 2001). In initial patient studies using **[^{18}F]FMAU** tumours in the brain, prostate, thorax and bone were clearly visualised, but in the abdominal region, **[^{18}F]FMAU** imaging is limited due to its physiological uptake into the liver and the kidneys (Sun et al. 2005). A significant bottleneck of the **[^{18}F]FMAU** application is facing the multistep radiosynthesis which is complex to automate. It starts with a protected ribofuranose derivative, that is subjected to nucleophilic substitution with [^{18}F]fluoride. Subsequent bromination, substitution of bromine by a thymine silyl ether derivative and cleavage of the benzoyl (Bz) protecting groups yields crude **[^{18}F]FMAU**, that is purified by semi-preparative HPLC. Independently, Alauddin et al. and Mangner et al. published this synthesis route in the years 2002 and 2003, respectively. In both investigations an overall rcy of 25–45 % (decay corrected), a rcp of >98 % and a A_s of 85–111 GBq/μmol were achieved in 3–4 h synthesis time (Fig. 11, Alauddin et al. 2002, Mangner et al. 2003). The challenging automation of this sophisticated synthesis route was successfully realised by Paolillo et al. (2009). Recently, a simplified approach using a one reactor radiosynthesis module was developed by Li et al. (2011).

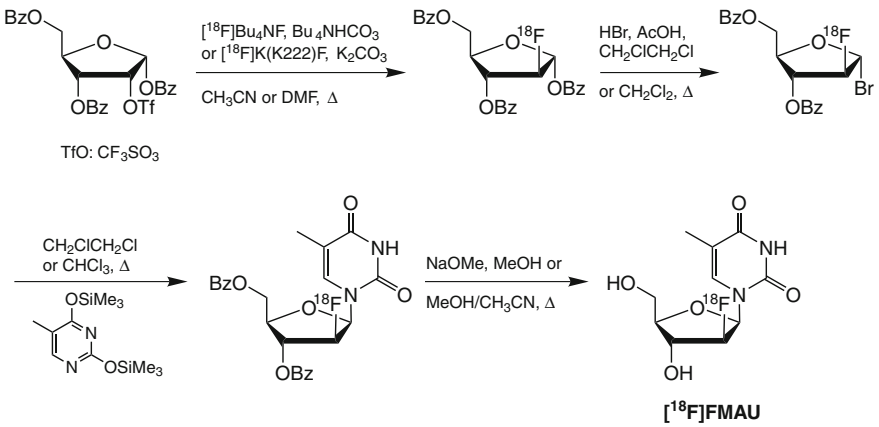

Fig. 11 Radiosynthesis of **[^{18}F]FMAU**

6 ^{18}F-Labelled Nitroimidazole Derivatives for Imaging Tumour Hypoxia

6.1 [^{18}F]Fluoromisonidazole ([^{18}F]FMISO)

The oxygen concentration in tumour cells represents an important prognostic indicator for the tumour response to radiotherapy and chemotherapy (Gray et al. 1953; Moulder and Rockwell 1987). Cells that are well oxygenated (normoxia and hyperoxia) are more sensitive to the radiotoxic effects of ionising radiation than cells that are poorly oxygenated. Therefore, there is a strong clinical demand on estimating the oxygen concentration in tumours in vivo, preferably non-invasively (Foo et al. 2004). In the year 1981, radiolabelled nitroimidazoles were suggested as bioreducible markers of hypoxia and as an important tool to evaluate the tumour response to radiation therapy (Chapman et al. 1981). Nitroimidazol derivatives enter cells via passive diffusion and are reduced by a single electron transfer to form the corresponding nitro radical anions. In the presence of oxygen, the radical anions are immediately reoxidised and oxygen superoxide anions are generated. Under hypoxic conditions the reoxidation step becomes eclipsed and subsequent reduction steps form reactive intermediates such as hydroxylamines that bind to intracellular macromolecules (e.g. proteins, DNA). This mechanism is responsible for the accumulation of nitroimidazoles in hypoxic cells and the basic principle of imaging tumour hypoxia with radiolabelled tracers (Fig. 12, Kizaka-Kondoh and Konse-Nagasawa 2009). Against this background, the nitroimidazole derivative **[^{18}F]FMISO** was proposed by Rasey et al. as useful hypoxia imaging agent for first in vivo applications (Rasey et al. 1987). To date, **[^{18}F]FMISO** represents the standard hypoxia marker for PET and in recent studies the tracer was evaluated in head and neck cancer patients undergoing concurrent chemoradiotherapy

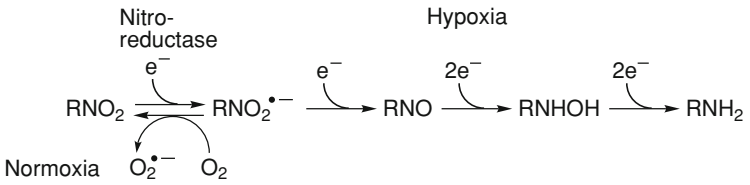

Fig. 12 Oxygen-dependent bioreductive metabolism of nitroimidazoles

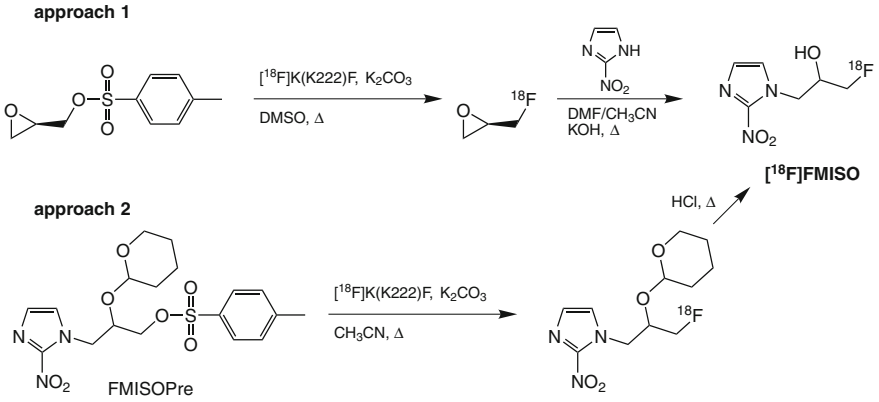

Fig. 13 Different routes for the radiosynthesis of **[^{18}F]FMISO**

(Lee et al. 2009; Kikuchi et al. 2011), in human glioblastomas (Swanson et al. 2009; Kawai et al. 2011) and in a biological image-guided radiotherapy in rectal cancer (Roels et al. 2008).

For the preparation of **[^{18}F]FMISO** two efficient methods are described. The first approach starts with the nucleophilic fluorination of (*2R*)-glycidyl tosylate with [^{18}F]fluoride to yield [^{18}F]epifluorohydrin. The subsequent nucleophilic ring opening with 2-nitroimidazole leads to **[^{18}F]FMISO**. After HPLC purification a rcy of 40 % (decay corrected), a rcp of 99 % and a A_s of 24 GBq/μmol in 140–180 min were reported (Fig. 13 approach 1, Grierson et al. 1989; Kämäräinen et al. 2004). The second approach uses the protected precursor 1-(2′-nitro-1′-imidazolyl)-2-*O*-tetrahydropyranyl-3-*O*-toluenesulphonyl-propanediol (FMISOPre). Nucleophilic fluorination of this compound and subsequent cleavage of the protecting group under acidic conditions yields **[^{18}F]FMISO** which was purified by HPLC and/or SPE. Lim et al. achieved a rcy of 55–80 % (decay corrected), a rcp of > 99 % and a A_s of > 22 GBq/μmol in 50 min (Fig. 13 approach 2, Lim and Berridge 1993, Cherif et al. 1994, Patt et al. 1999, Kämäräinen et al. 2004). In the year 2005, the transfer of this synthesis approach to commercially available PET tracer radiosynthesisers were reported by Oh et al. and Tang et al.. The fully automated radiosyntheses are characterised by high rcy (up to 59 % (decay corrected)) and decreased synthesis times (< 40 min) (Oh et al. 2005; Tang et al. 2005).

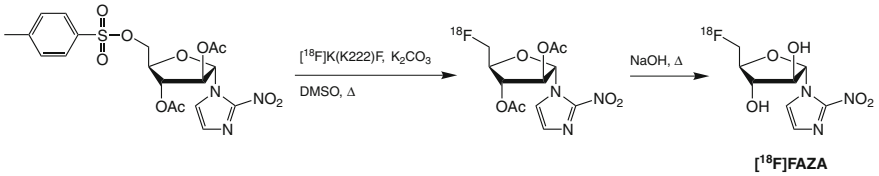

Fig. 14 Radiosynthesis of **[^{18}F]FAZA**

6.2 1-(5-Deoxy-5-[^{18}F]Fluoro-α-D-arabinofuranosyl)-2-nitroimidazole ([^{18}F]FAZA)

[^{18}F]FAZA is a hypoxia marker of the second generation. Compared to **[^{18}F]FMISO** this nitroimidazole derivative is more hydrophilic and shows a more rapid clearance from blood and non-target tissues resulting in an increased tumour-to-background ratio of tracer uptake in different murine tumour models (Piert et al. 2005). Therefore, initial studies demonstrate that FAZA-PET imaging could be used for a hypoxia-directed intensity-modulated radiotherapy approach in head and neck cancer (Grosu et al. 2007). Another study evaluates the safety and general biodistribution patterns of **[^{18}F]FAZA** in patients with squamous cell carcinoma of the head and neck (HNSCC), small-cell lung cancer (SCLC) or non-small-cell lung cancer (NSCLC), malignant lymphoma and high-grade gliomas. This investigation suggests the tracer as useful radiopharmaceutical for the imaging of hypoxia in mentioned tumour types. Especially, the high **[^{18}F]FAZA** uptake by gliomas was encouraging (Postema et al. 2009).

The radiosynthesis of **[^{18}F]FAZA** is based on a nucleophilic substitution step of the tosylate precursor with [^{18}F]fluoride and subsequent hydrolysis of the acetyl protecting groups. After HPLC purification **[^{18}F]FAZA** was obtained with a rcy of 21 % (not decay corrected) in 50 min (Fig. 14, Reischl et al. 2005). The transfer and optimisation of this approach in a automated synthesiser yielded **[^{18}F]FAZA** with a high rcy of 52 % (decay corrected) in 51 min (Hayashi et al. 2011).

7 [^{18}F]FES for Imaging Estrogen Receptor Status

The oestrogen receptor (ER) status represents an important prognostic indicator in breast cancer. Oestrogen receptor positive (ER+) tumours possess a slower rate of growth and are likely to respond to anti-oestrogen therapy (Rose et al. 1985, Fisher et al. 1989). Therefore, a approach for the non-invasive assessment of the ER status of breast tumours in vivo is clinically desirable. For this purpose several radiolabelled ER ligands have been developed, among them 16α-[^{18}F]fluoro-17β-estradiol (**[^{18}F]FES**) represents the most intensively investigated PET tracer (Kiesewetter et al. 1984). Similar to the lead compound estradiol the lipophilic PET tracer **[^{18}F]FES** is transported via the blood stream where **[^{18}F]FES** binds to

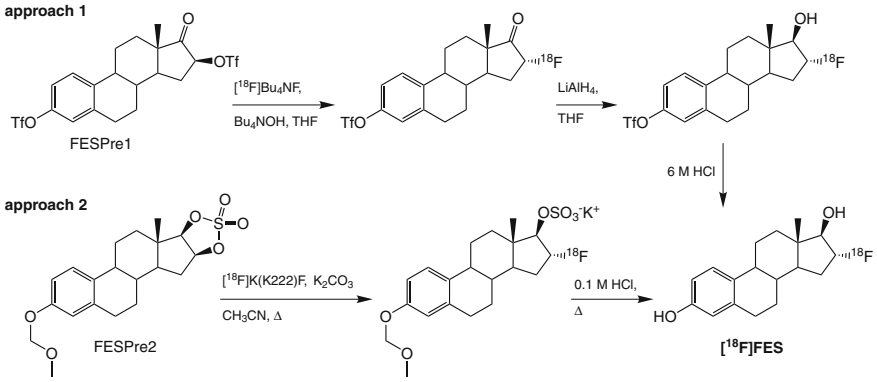

Fig. 15 Different routes for the radiosynthesis of **[^{18}F]FES**

sex hormone binding proteins (SBP) or to albumin (Tewson et al. 1999). The fraction of **[^{18}F]FES** that binds to SBP is protected against liver metabolism facilitating the transport of the unchanged tracer to the target tissue (Van de Wiele et al. 2000). Nevertheless, **[^{18}F]FES** is rapidly metabolised in vivo and the formation of glucuronidated and sulphate conjugated radiometabolites that are not accumulated by ER+ tumours contribute to the high background activity and complicate the quantitative interpretation of **[^{18}F]FES** PET images (Mankoff et al. 1997). In recent clinical studies, **[^{18}F]FES** was evaluated in patients with ovarian cancer (Yoshida et al. 2009) and uterine tumours (Tsujikawa et al. 2008) as well as in patients with breast cancer (Peterson et al. 2008, 2011).

Two different approaches were published for the radiosynthesis of **[^{18}F]FES**. The first approach starts with a triflate precursor (FESPre1) that reacts with [^{18}F]fluoride by nucleophilic substitution. Reduction of the keto moiety and subsequent hydrolysis of the second triflate group yields the target compound. After HPLC purification a rcy of 43 % (decay corrected), a rcp of > 99 % and a A_s of 7–10 GBq/μmol were achieved within a synthesis time of 75–90 min (Fig. 15 approach 1, Kiesewetter et al. 1984). In the second approach, 3-*O*-methoxymethyl-16,17-*O*-sulfuryl-16-epiestradiol (FESPre2) is used as precursor. Nucleophilic ring opening of this cyclic sulphate with [^{18}F]fluoride and simultaneous acidic hydrolysis of the methoxymethyl and sulphate group yielded **[^{18}F]FES** after HPLC purification (Fig.15 approach 2, Lim et al. 1996). Several groups succeeded in automation of this radiosynthesis using commercially available PET tracer radiosynthesisers (Römer et al. 1999; Kumar et al. 2007). Furthermore, Oh et al. transferred the **[^{18}F]FES** synthesis in a conventional [^{18}F]FDG radiosynthesiser with disposable cassette system and reported a rcy of 45 % (decay corrected), a rcp of 99 % and a A_s of 58 GBq/μmol in a synthesis time of 76 min (Oh et al. 2007).

8 [^{18}F]Fluoride for Imaging Bone Metabolism

The ion-pair sodium [^{18}F]fluoride dissociates in blood into sodium cations (Na^+) and [^{18}F]fluoride anions ($^{18}F^-$) that were first described as a potential tracer for bone scintigraphy five decades ago (Blau et al. 1962). Bone uptake of [^{18}F]fluoride is based on its ion exchange with hydroxide ions (OH^-) in the bone mineral hydroxylapatite ($Ca_5(PO_4)_3OH$). This reaction yielding [^{18}F]fluoroapatite ($Ca_5(PO_4)_3[^{18}F]F$) leads to the incorporation of [^{18}F]fluoride into the bone (Hawkins et al. 1992). Increased [^{18}F]fluoride uptake reflects an increase in regional blood flow and bone turnover like that seen in association with malignant bone lesions and osteoblastic activity. Thus, sodium [^{18}F]fluoride PET-CT is a highly sensitive and specific imaging method for the detection of skeletal metastases in patients with prostatic carcinoma (Even-Sapir et al. 2006) and bone metastasis of breast cancer (Kawaguchi et al. 2010).

[^{18}F]Fluoride can be produced directly in the cyclotron target system by irradiation of [^{18}O]water and can be separated subsequently from the irradiated [^{18}O]water by adsorption on anion exchange resins. The desorption of [^{18}F]fluoride from the resin with isotonic NaCl solution yields sodium [^{18}F]fluoride in physiological solution.

9 Perspectives

The ^{18}F-labelled radiotracers described in the preceding sections are clinically established and useful molecular probes for the imaging of dysregulated processes in tumourigenesis and tumour progression. Various novel non-peptidyl ^{18}F-labelled PET radiotracers for answering oncological questions are currently under development which are designed as targeted tracers for the specific visualisation of dysregulated enzymes in tumours and metastases. In this connection, radiolabelled inhibitors of matrix metalloproteinases (MMPs) were synthesised and preclinically evaluated to image increased MMP activity in tumours (e.g. Wagner et al. 2006). Furthermore, radiolabelled inhibitors of the enzyme class of caspases, that are closely related to the programmed cell death, also called apoptosis, may be useful imaging agents for the evaluation of the tumour response to therapy (Faust et al. 2009). ^{18}F-Labelled inhibitors of tyrosine kinases that are overexpressed in numerous malignancies are potentially useful tools for tumour imaging (Veach et al. 2007).

Additionally, targeting dysregulated receptor densities in tumour tissues is also a promising approach. For example, radiolabelled ligands of the endothelin receptors that represent vascular receptors potentially provide information about the angiogenesis status of tumours (Höltke et al. 2009). The folate receptors that are highly expressed on most epithelial cancer cells represent another attractive biological target for tumour imaging and first radiolabelled ligands are in preclinical evaluation (Ross et al. 2008, 2010; Bettio et al. 2006).

In summary, in addition to the clinically well-established non-peptidyl ^{18}F-radiotracers, several novel and promising radiotracer candidates are under development and future in vivo and ex vivo studies will show the potential of these compounds in oncological PET and PET/CT.

References

Alauddin MM, Conti PS, Fissekis JD (2002) Synthesis of [^{18}F]-labeled 2′-deoxy-2′-fluoro-5-methyl-1-β-D-arabinofuranosyluracil ([^{18}F]-FMAU). J Label Compd Radiopharm 45:583–590

Asti M, Farioli D, Iori M, Guidotti C, Versari A, Salvo D (2010) Efficient automated one-step synthesis of 2-[^{18}F]fluoroethylcholine for clinical imaging: optimized reaction conditions and improved quality controls of different synthetic approaches. Nucl Med Biol 37:209–315

Bading JR, Shields AF (2008) Imaging of cell proliferation: status and prospects. J Nucl Med 49:64S–80S

Bauman G, Belhocine T, Kovacs M, Ward A, Beheshti M, Rachinsky I (2012) ^{18}F-fluorocholine for prostate cancer imaging: a systematic review of the literature. Prostate Cancer Prostatic Dis 15:45–55

Beheshti M, Pöcher S, Vali R, Waldenberger P, Broinger G, Nader M, Kohlfürst S, Pirich C, Dralle H, Langsteger W (2009) The value of ^{18}F-DOPA PET-CT in patients with medullary thyroid carcinoma: comparison with ^{18}F-FDG PET-CT. Eur Radiol 19:1425–1434

Been LB, Suurmeijer AJ, Cobben DC, Jager PL, Hoekstra HJ, Elsinga PH (2004) [^{18}F]FLT-PET in oncology: current status and opportunities. Eur J Nucl Med Mol Imaging 31:1659–1672

Beheshti M, Vali R, Waldenberger P, Fitz F, Nader M, Loidl W, Broinger G, Stoiber F, Foglman I, Langsteger W (2008) Detection of bone metastases in patients with prostate cancer by ^{18}F fluorocholine and ^{18}F fluoride PET-CT: a comparative study. Eur J Nucl Med Mol Imaging 35:1766–1774

Belt JA, Marina NM, Phelps DA, Crawford CR (1993) Nucleoside transport in normal and neoplastic cells. Adv Enzyme Regul 33:235–252

Berg JM, Tymoczko JL, Stryer L (2006) Biochemistry, 6th edn. W.H. Freeman & Company, New York

Bettio A, Honer M, Müller C, Brühlmeier M, Müller U, Schibli R, Groehn V, Schubiger AP, Ametamey SM (2006) Synthesis and preclinical evaluation of a folic acid derivative labeled with ^{18}F for PET imaging of folate receptor-positive tumors. J Nucl Med 47:1153–1160

Blau M, Nagler W, Bender MA (1962) Fluorine-18: a new isotope for bone scanning. J Nucl Med 3:332–334

Bouchelouche K, Oehr P (2008) Positron emission tomography and positron emission tomography/computerized tomography of urological malignancies: an update review. J Urol 179:34–45

Brock CS, Meikle SR, Price P (1997) Does fluorine-18 fluorodeoxyglucose metabolic imaging of tumors benefit oncology? Eur J Nucl Med 24:691–705

Busch H, Davis JR, Honig GR, Anderson DC, Nair PV, Nyhan WL (1959) The uptake of a variety of amino acids into nuclear proteins of tumors and other tissues. Cancer Res 19:1030–1039

Chapman JD, Franko AJ, Sharplin J (1981) A marker for hypoxic cells in tumours with potential clinical applicability. Br J Cancer 43:546–550

Cherif A, Yang DJ, Tansey W, Kim EE, Wallace S (1994) Rapid synthesis of 3-[^{18}F]fluoro-1-(2′-nitro-1′-imidazolyl)-2-propanol ([^{18}F]fluoromisonidazole). Pharm Res 11:466–469

Christensen HN (1990) Role of amino acid transport and countertransport in nutrition and metabolism. Phys Rev 70:43–77

Clary GL, Tsai CF, Guynn RW (1987) Substrate specificity of choline kinase. Arch Biochem Biophys 254:214–221

Cleaver JE (1967) Thymidine metabolism and cell kinetics. Front Biol 6:43–100

Coleman R, DeGrado T, Wang S, Baldwin S, Orr M, Reiman R, Price D (2000) Preliminary evaluation of F-18 fluorocholine (FCH) as a PET tumor imaging agent. Clin Positron Imaging 3:147

DeGrado TR, Baldwin SW, Wang S, Orr MD, Liao RP, Friedman HS, Reiman R, Price DT, Coleman RE (2001) Synthesis and evaluation of ^{18}F-labeled choline analogs as oncologic PET tracers. J Nucl Med 42:1805–1814

DeGrado TR, Coleman RE, Wang S, Baldwin SW, Orr MD, Robertson CN, Polascik TJ, Price DT (2000) Synthesis and evaluation of ^{18}F-labeled choline as an oncologic tracer for positron emission tomography: initial findings in prostate cancer. Cancer Res 61:110–117

Deves R, Krupka RM (1979) The binding and translocation steps in transport as related to substrate structure: a study of the choline carrier of erythrocytes. Biochim Biophys Acta 557:469–485

Dollé F, Demphel S, Hinnen F, Fournier D, Vaufrey F, Crouzel C (1998) 6-[^{18}F]Fluoro-L-DOPA by radiofluorodestannylation: a short and simple synthesis of a new labelling precursor. J Label Compd Radiopharm 41:105–114

Dunet V, Rossier C, Buck A, Stupp R, Prior JO (2012) Performance of ^{18}F-Fluoro-Ethyl-Tyrosine (^{18}F-FET) PET for the differential diagnosis of primary brain tumor: a systematic review and metaanalysis. J Nucl Med 53:207–214

Eckel F, Herrmann K, Schmidt S, Hillerer C, Wieder HA, Krause BJ, Schuster T, Langer R, Wester HJ, Schmid RM, Schwaiger M, Buck AK (2009) Imaging of proliferation in hepatocellular carcinoma with the in vivo marker ^{18}F-fluorothymidine. J Nucl Med 50:1441–1447

Even-Sapir E, Metser U, Mishani E, Lievshitz G, Lerman H, Leibovitch I (2006) The detection of bone metastases in patients with high-risk prostate cancer: ^{99m}Tc-MDP planar bone scintigraphy, single- and multi-field-of-view SPECT, ^{18}F-Fluoride PET, and ^{18}F-fluoride PET/CT. J Nucl Med 47:287–297

Faust A, Hermann S, Wagner S, Haufe G, Schober O, Schäfers M, Kopka K (2009) Molecular imaging of apoptosis in vivo with scintigraphic and optical biomarkers—a status report. Anticancer Agents Med Chem 9:968–985

Fisher B, Costantino J, Redmond C, Poisson R, Bowman D, Couture J, Dimitrov NV, Wolmark N, Wickerham DL, Fisher ER, Margolese R, Robidoux A, Shibata H, Terz J, Paterson AHJ, Feldman MI, Farrar W, Evans J, Lickley HL, Ketner M (1989) A randomized clinical trial evaluating tamoxifen in the treatment of patients with node-negative breast cancer who have estrogen-receptor-positive tumors. N Engl J Med 320:479–484

Foo SS, Abbott DF, Lawrentschuk N, Scott AM (2004) Functional imaging of intratumoral hypoxia. Mol Imaging Biol 6:291–305

Füchtner F, Steinbach J, Mäding P, Johannsen B (1996) Basic hydrolysis of 2-[^{18}F]-fluoro-1,3,4,6-tetra-*O*-acetyl-D-glucose in the preparation of 2-[^{18}F]fluoro-2-deoxy-D-glucose. Appl Radiat Isot 47:61–66

Füchtner F, Zessin J, Mäding P, Wüst F (2008) Aspects of 6-[^{18}F]fluoro-L-DOPA preparation. Deuterochloroform as a substitute solvent for Freon 11. Nuklearmedizin 47:62–64

Garnett ES, Firnau G, Chan PK, Sood S, Belbeck LW (1978) [^{18}F]fluoro-dopa, an analogue of dopa, and its use in direct external measurements of storage, degradation, and turnover of intracerebral dopamine. Proc Natl Acad Sci U S A 75:464–467

Garnett ES, Firnau G, Nahmias C (1983) Dopamine visualized in the basal ganglia of living man. Nature 305:137–138

Gallagher BM, Fowler JS, Gutterson NI, McGregor RR, Wan CN, Wolf AP (1978) Metabolic trapping as a principle of radiopharmaceutical design: some factors responsible for the biodistribution of [^{18}F]-2-deoxy-2-fluoro-D-glucose. J Nucl Med 19:1154–1161

Gray LH, Conger AD, Ebert M, Hornsey S, Scott OC (1953) The concentration of oxygen dissolved in tissues at the time of irradiation as a factor in radiotherapy. Br J Radiol 26:638–648

Grierson JR, Link JM, Mathis CA, Rasey JS, Krohn KA (1989) A radiosynthesis of fluorine-18 fluoromisonidazole. J Nucl Med 30:343–350

Grosu AL, Souvatzoglou M, Röper B, Dobritz M, Wiedenmann N, Jacob V, Wester HJ, Reischl G, Machulla HJ, Schwaiger M, Molls M, Piert M (2007) Hypoxia imaging with FAZA-PET and theoretical considerations with regard to dose painting for individualization of radiotherapy in patients with head and neck cancer. Int J Radiat Oncol Biol Phys 69:541–551

Haerle SK, Fischer DR, Schmid DT, Ahmad N, Huber GF, Buck A (2011) ^{18}F-FET PET/CT in advanced head and neck squamous cell carcinoma: an intra-individual comparison with ^{18}F-FDG PET/CT. Mol Imaging Biol 13:1036–1042

Hamacher K, Coenen HH (2002) Efficient routine production of the ^{18}F-labelled amino acid *O*-(2-[^{18}F]fluoroethyl)-L-tyrosine. Appl Radiat Isot 57:853–856

Hamacher K, Coenen HH, Stöcklin G (1986) Efficient stereospecific synthesis of no-carrier-added 2-[^{18}F]-fluoro-2-deoxy-D-glucose using aminopolyether supported nucleophilic substitution. J Nucl Med 27:235–238

Hannanah D, Weinberg RA (2000) The hallmarks of cancer. Cell 100:57–70

Hara T, Kosaka N, Kishi H (2002) Development of ^{18}F-fluoroethylcholine for cancer imaging with PET: synthesis, biochemistry, and prostate cancer imaging. J Nucl Med 43:187–199

Hawkins RA, Choi Y, Huang SC, Hoh CK, Dahlbom M, Schiepers C, Satyamurthy N, Barrio JR, Phelps ME (1992) Evaluation of the skeletal kinetics of fluorine-18-fluoride ion with PET. J Nucl Med 33:633–642

Hayashi K, Furutsuka K, Takei M, Muto M, Nakao R, Aki H, Suzuki K, Fukumura T (2011) High-yield automated synthesis of [^{18}F]fluoroazomycin arabinoside ([^{18}F]FAZA) for hypoxia-specific tumor imaging. Appl Radiat Isot 69:1007–1013

Heiss P, Mayer S, Herz M, Wester HJ, Schwaiger M, Senekowitsch-Schmidtke R (1999) Investigation of transport mechanism and uptake kinetics of *O*-(2-[^{18}F]fluoroethyl)-L-tyrosine in vitro and in vivo. J Nucl Med 40:1367–1373

Hengstschläger M, Knöfler M, Müllner EW, Ogris E, Wintersberger E, Wawra E (1994) Different regulation of thymidine kinase during the cell cycle of normal versus DNA tumor virus-transformed cells. J Biol Chem 269:13836–13842

Hoegerle S, Altehoefer C, Ghanem N, Brink I, Moser E, Nitzsche E (2001) ^{18}F-DOPA positron emission tomography for tumour detection in patients with medullary thyroid carcinoma and elevated calcitonin levels. Eur J Nucl Med 28:64–71

Hoegerle S, Nitzsche E, Altehoefer C, Ghanem N, Manz T, Brink I, Reincke M, Moser E, Neumann HP (2002) Pheochromocytomas: detection with ^{18}F DOPA whole body PET–initial results. Radiology 222:507–512

Höltke C, Faust A, Breyholz HJ, Kopka K, Schober O, Riemann B, Bremer C, Schäfers M, Wagner S (2009) Non-invasive approaches to visualize the endothelin axis in vivo using state-of-the-art molecular imaging modalities. Mini Rev Med Chem 9:1580–1595

Imani F, Agopian VG, Auerbach MS, Walter MA, Imani F, Benz MR, Dumont RA, Lai CK, Czernin JG, Yeh MW (2009) ^{18}F-FDOPA PET and PET/CT accurately localize pheochromocytomas. J Nucl Med 50:513–519

Isselbacher KJ (1972) Sugar and amino acid transport by cells in culture: differences between normal and malignant cells. N Engl J Med 286:929–933

Iwata R, Pascali C, Bogni A, Furumoto S, Terasaki K, Yanai K (2002) [^{18}F]fluoromethyl triflate, a novel and reactive [^{18}F]fluoromethylating agent: preparation and application to the on-column preparation of [^{18}F]fluorocholine. Appl Radiat Isot 57:347–352

Jager PL, Chirakal R, Marriott CJ, Brouwers AH, Koopmans KP, Gulenchyn KY (2008) 6-L-^{18}F-fluorodihydroxyphenylalanine PET in neuroendocrine tumors: basic aspects and emerging clinical applications. J Nucl Med 49:573–586

Johnstone RM, Scholefield PG (1965) Amino acid transport in tumor cells. Adv Cancer Res 9:143–226

Kameyama R, Yamamoto Y, Izuishi K, Sano T, Nishiyama Y (2011) Correlation of ^{18}F-FLT uptake with equilibrative nucleoside transporter-1 and thymidine kinase-1 expressions in gastrointestinal cancer. Nucl Med Commun 32:460–465

Kameyama R, Yamamoto Y, Izuishi K, Takebayashi R, Hagiike M, Murota M, Kaji M, Haba R, Nishiyama Y (2009) Detection of gastric cancer using ^{18}F-FLT PET: comparison with ^{18}F-FDG PET. Eur J Nucl Med Mol Imaging 36:382–388

Kämäräinen EL, Kyllönen T, Nihtilä O, Björk H, Solin O (2004) Preparation of fluorine-18-labelled fluoromisonidazole using two different synthesis methods. J Label Compd Radiopharm 47:37–45

Kao CH, Hsu WL, Xie HL, Lin MC, Lan WC, Chao HY (2011) GMP production of [^{18}F]FDOPA and issues concerning its quality analyses as in USP Fluorodopa F 18 Injection. Ann Nucl Med 25: 309-316

Kauhanen S, Schalin-Jäntti C, Seppänen M, Kajander S, Virtanen S, Schildt J, Lisinen I, Ahonen A, Heiskanen I, Väisänen M, Arola J, Korsoff P, Ebeling T, Sane T, Minn H, Välimäki MJ, Nuutila P (2011) Complementary roles of ^{18}F-DOPA PET/CT and ^{18}F-FDG PET/CT in medullary thyroid cancer. J Nucl Med 52:1855–1863

Kauhanen S, Seppänen M, Ovaska J, Minn H, Bergman J, Korsoff P, Salmela P, Saltevo J, Sane T, Välimäki M, Nuutila P (2009) The clinical value of [^{18}F]fluoro-dihydroxyphenylalanine positron emission tomography in primary diagnosis, staging, and restaging of neuroendocrine tumors. Endocr Relat Cancer 16:255–265

Kawaguchi M, Tateishi U, Shizukuishi K, Suzuki A, Inoue T (2010) ^{18}F-fluoride uptake in bone metastasis: morphologic and metabolic analysis on integrated PET/CT. Ann Nucl Med 24:241–247

Kawai N, Maeda Y, Kudomi N, Miyake K, Okada M, Yamamoto Y, Nishiyama Y, Tamiya T (2011) Correlation of biological aggressiveness assessed by ^{11}C-methionine PET and hypoxic burden assessed by ^{18}F-fluoromisonidazole PET in newly diagnosed glioblastoma. Eur J Nucl Med Mol Imaging 38:441–450

Kiesewetter DO, Kilbourn MR, Landvatter SW, Heiman DF, Katzenellenbogen JA, Welch MJ (1984) Preparation of four fluorine- 18-labeled estrogens and their selective uptakes in target tissues of immature rats. J Nucl Med 25:1212–1221

Kikuchi M, Yamane T, Shinohara S, Fujiwara K, Hori SY, Tona Y, Yamazaki H, Naito Y, Senda M (2011) ^{18}F-fluoromisonidazole positron emission tomography before treatment is a predictor of radiotherapy outcome and survival prognosis in patients with head and neck squamous cell carcinoma. Ann Nucl Med 25:625–633

Kizaka-Kondoh S, Konse-Nagasawa H (2009) Significance of nitroimidazole compounds and hypoxia-inducible factor-1 for imaging tumor hypoxia. Cancer Sci 100:1366–1373

Krasikova RN, Kuznetsova OF, Fedorova OS, Maleev VI, Saveleva TF, Belokon YN (2008) No carrier added synthesis of *O*-(2′-[^{18}F]fluoroethyl)-L-tyrosine via a novel type of chiral enantiomerically pure precursor, NiII complex of a (S)-tyrosine schiff base. Biorg Med Chem 16:4994–5003

Krohn KA, Mankoff DA, Eary JF (2001) Imaging cellular proliferation as a measure of response to therapy. J Clin Pharmacol Suppl:96S–103S

Kryza D, Tadino V, Filannino MA, Villeret G, Lemoucheux L (2008) Fully automated [^{18}F]fluorocholine synthesis in the TracerLab MX FDG Coincidence synthesizer. Nucl Med Biol 35:255–260

Kumar P, Mercer J, Doerkson C, Tonkin K, McEwan AJ (2007) Clinical production, stability studies and PET imaging with 16-α-[^{18}F]fluoroestradiol ([^{18}F]FES) in ER positive breast cancer patients. J Pharm Pharm Sci 10:256s–265s

Lee N, Nehmeh S, Schöder H, Fury M, Chan K, Ling CC, Humm J (2009) Prospective trial incorporating pre-/mid-treatment [^{18}F]-misonidazole positron emission tomography for head-and-neck cancer patients undergoing concurrent chemoradiotherapy. Int J Radiat Oncol Biol Phys 75:101–108

Lee SJ, Oh SJ, Chi DY, Kil HS, Kim EN, Ryu JS, Moon DH (2007) Simple and highly efficient synthesis of 3′-deoxy-3′-[^{18}F]fluorothymidine using nucleophilic fluorination catalyzed by protic solvent. Eur J Nucl Med Mol Imaging 34:1406–1409

Lee WC, Chang CH, Ho CL, Chen LC, Wu YH, Chen JT, Wang YL, Lee TW (2011) Early detection of tumor response by FLT/microPET Imaging in a C26 murine colon carcinoma solid tumor animal model. J Biomed Biotechnol 2011:535902

Li Z, Cai H, Conti PS (2011) Automated synthesis of 2′-deoxy-2′-[^{18}F]fluoro-5-methyl-1-β-D-arabinofuranosyluracil ([^{18}F]-FMAU) using a one reactor radiosynthesis module. Nucl Med Biol 38:201–206

Lim JL, Berridge MS (1993) An efficient radiosynthesis of [^{18}F]fluoromisonidazole. Appl Radiat Isot 44:1085–1091

Lim JL, Zheng L, Berridge MS, Tewson TJ (1996) The use of 3-methoxymethyl-16 β, 17 β-epiestriol-*O*-cyclic sulfone as the precursor in the synthesis of F-18 16 α-fluoroestradiol. Nucl Med Biol 23:911–915

Luxen A, Guillaume M, Melega WP, Pike VW, Solin O, Wagner R (1992) Production of 6-[^{18}F]fluoro-L-dopa and its metabolism in vivo–a critical review. Int J Rad Appl Instrum B 19:149–158

Machulla HJ, Blocher A, Kuntzsch M, Piert M, Wei R, Grierson JR (2000) Simplified Labeling Approach for Synthesizing 3′-Deoxy-3′-[^{18}F]fluorothymidine ([^{18}F]FLT). Radioanal Nucl Chem 243:843–846

Mamede M, Higashi T, Kitaichi M (2005) [^{18}F]FDG uptake and PCNA, Glut-1, and hexokinase-II expressions in cancers and inflammatory lesions of the lung. Neoplasia 7:369–379

Mangner TJ, Klecker RW, Anderson L, Shields AF (2003) Synthesis of 2′-deoxy-2′-[^{18}F]fluoro-β-D-arabinofuranosyl nucleosides, [^{18}F]FAU, [^{18}F]FMAU, [^{18}F]FBAU and [^{18}F]FIAU, as potential PET agents for imaging cellular proliferation. synthesis of [^{18}F]labelled FAU, FMAU, FBAU. FIAU. Nucl Med Biol 30:215–224

Mankoff DA, Tewson TJ, Eary JF (1997) Analysis of blood clearance and labeled metabolites for the estrogen receptor tracer [F-18]-16 α-fluoroestradiol (FES). Nucl Med Biol 24:341–348

Melega WP, Hoffman JM, Luxen A, Nissenson CH, Phelps ME, Barrio JR (1990) The effects of carbidopa on the metabolism of 6-[^{18}F]fluoro-L-dopa in rats, monkeys and humans. Life Sci 47:149–157

Mittra E, Quon A (2009) Positron emission tomography/computed tomography: the current technology and applications. Radiol Clin North Am 47:147–160

Moulder JE, Rockwell S (1987) Tumor hypoxia: its impact on cancer therapy. Cancer Metastasis Rev 5:313–341

Mueller D, Klette I, Kalb F, Baum RP (2011) Synthesis of *O*-(2-[^{18}F]fluoroethyl)-L-tyrosine based on a cartridge purification method. Nucl Med Biol 38:653–658

Muijs CT, Beukema JC, Widder J, van den Bergh AC, Havenga K, Pruim J, Langendijk JA (2011) ^{18}F-FLT-PET for detection of rectal cancer. Radiother Oncol 98:357–359

Namavari M, Bishop A, Satyamurthy N, Bida G, Barrio JR (1992) Regioselective radiofluorodestannylation with [^{18}F]F_2 and [^{18}F]CH_3COOF: a high yield synthesis of 6-[^{18}F]Fluoro-L-dopa. Int J Rad Appl Instrum A 43:989–996

Oh SJ, Chi DY, Mosdzianowski C, Kil HS, Ryu JS, Moon DH (2007) The automatic production of 16α-[^{18}F]fluoroestradiol using a conventional [^{18}F]FDG module with a disposable cassette system. Appl Radiat Isot 65:676–681

Oh SJ, Chi DY, Mosdzianowski C, Kim JY, Gil HS, Kang SH, Ryu JS, Moon DH (2005) Fully automated synthesis of [^{18}F]fluoromisonidazole using a conventional [^{18}F]FDG module. Nucl Med Biol 32:899–905

Oh SJ, Mosdzianowski C, Chi DY, Kim JY, Kang SH, Ryu JS, Yeo JS, Moon DH (2004) Fully automated synthesis system of 3′-deoxy-3′-[^{18}F]fluorothymidine. Nucl Med Biol 31:803–809

Oxender DL, Christensen HN (1963) Distinct mediating systems for the transport of neutral amino acids by the Ehrlich cell. J Biol Chem 238:3686–3699

Paolillo V, Riese S, Gelovani JG, Alauddin MM (2009) A fully automated synthesis of [^{18}F]-FEAU and [^{18}F]-FMAU using a novel dual reactor radiosynthesis module. J Label Compd Radiopharm 52:553–558

Pascali G, D'Antonio L, Bovone P, Gerundini P, August T (2009) Optimization of automated large-scale production of [^{18}F]fluoroethylcholine for PET prostate cancer imaging. Nucl Med Biol 36:569–574

Patrick GL (2005) An introduction in medicinal chemistry, 3rd edn. Oxford University Press, Oxford

Patt M, Kuntzsch M, Machulla HJ (1999) Preparation of [^{18}F]fluoromisonidazole by nucleophilic substitution on THP-protected precursor: Yield dependence on reaction parameters. J Radioanal Nucl Chem 240:925–927

Pauleit D, Stoffels G, Schaden W, Hamacher K, Bauer D, Tellmann L, Herzog H, Bröer S, Coenen HH, Langen KJ (2005) PET with *O*-(2-^{18}F-Fluoroethyl)-L-tyrosine in peripheral tumors: first clinical results. J Nucl Med 46:411–416

Peterson LM, Kurland BF, Link JM, Schubert EK, Stekhova S, Linden HM, Mankoff DA (2011) Factors influencing the uptake of ^{18}F-fluoroestradiol in patients with estrogen receptor positive breast cancer. Nucl Med Biol 38:969–978

Peterson LM, Mankoff DA, Lawton T, Yagle K, Schubert EK, Stekhova S, Gown A, Link JM, Tewson T, Krohn KA (2008) Quantitative imaging of estrogen receptor expression in breast cancer with PET and ^{18}F-fluoroestradiol. J Nucl Med 49:367–374

Piel M, Bauman A, Baum RP, Höhnemann S, Klette I, Wortmann R, Rösch F (2007) Improved automated synthesis of [^{18}F]fluoroethylcholine as a radiotracer for cancer imaging. Bioorg Med Chem 15:3171–3175

Piert M, Machulla HJ, Picchio M, Reischl G, Ziegler S, Kumar P, Wester HJ, Beck R, McEwan AJ, Wiebe LI, Schwaiger M (2005) Hypoxia-specific tumor imaging with ^{18}F-fluoroazomycin arabinoside. J Nucl Med 46:106–113

Podo F (1999) Tumour phospholipid metabolism. NMR Biomed 12:413–439

Poeppel TD, Krause BJ, Heusner TA, Boy C, Bockisch A, Antoch G (2009) PET/CT for the staging and follow-up of patients with malignancies. Eur J Radiol 70:382–392

Postema EJ, McEwan AJ, Riauka TA, Kumar P, Richmond DA, Abrams DN, Wiebe LI (2009) Initial results of hypoxia imaging using 1-α-D-(5-deoxy-5-[^{18}F]-fluoroarabinofuranosyl)-2-nitroimidazole (^{18}F-FAZA). Eur J Nucl Med Mol Imaging 36:1565–1573

Rasey JS, Grunbaum Z, Magee S, Nelson NJ, Olive PL, Durand RE, Krohn KA (1987) Characterization of radiolabeled fluoromisonidazole as a probe for hypoxic cells. Radiat Res 111:292–304

Reischl G, Ehrlichmann W, Bieg C, Solbach C, Kumar P, Wiebe LI, Machulla HJ (2005) Preparation of the hypoxia imaging PET tracer [^{18}F]FAZA: reaction parameters and automation. Appl Radiat Isot 62:897–901

Roels S, Slagmolen P, Nuyts J, Lee JA, Loeckx D, Maes F, Stroobants S, Penninckx F, Haustermans K (2008) Biological image-guided radiotherapy in rectal cancer: is there a role for FMISO or FLT, next to FDG? Acta Oncol 47:1237–1248

Roivainen A, Forsback S, Gronroos T, Lehikoinen P, Kahkonen M, Sutinen E, Minn H (2000) Blood metabolism of [methyl-^{11}C]choline; implications for in vivo imaging with positron emission tomography. Eur J Nucl Med 27:25–32

Rose C, Thorpe SM, Andersen KW, Pedersen BV, Mouridsen HT, Blichert-Toft M, Rasmussen BB (1985) Beneficial effect of adjuvant tamoxifen therapy in primary breast cancer patients with high oestrogen receptor values. Lancet 1:16–19

Ross TL, Honer M, Lam PY, Mindt TL, Groehn V, Schibli R, Schubiger PA, Ametamey SM (2008) Fluorine-18 click radiosynthesis and preclinical evaluation of a new ^{18}F-labeled folic acid derivative. Bioconjug Chem 19:2462–2470

Ross TL, Honer M, Müller C, Groehn V, Schibli R, Ametamey SM (2010) A new ^{18}F-labeled folic acid derivative with improved properties for the PET imaging of folate receptor-positive tumors. J Nucl Med 51:1756–1762

Römer J, Füchtner F, Steinbach J, Johannsen B (1999) Automated production of 16α-[^{18}F]fluoroestradiol for breast cancer imaging. Nucl Med Biol 26:473–479

Saier MH Jr, Daniels GA, Boerner P, Lin J (1988) Neutral amino acid transport systems in animal cells: potential targets of oncogene action and regulators of cellular growth. J Membr Biol 104:1–20

Schiesser M, Veit-Haibach P, Muller MK, Weber M, Bauerfeind P, Hany T, Clavien PA (2010) Value of combined 6-[^{18}F]fluorodihydroxyphenylalanine PET/CT for imaging of neuroendocrine tumours. Br J Surg 97:691–697

Schober O, Heindel W (2008) PET-CT, 1st edn. Georg Thieme Verlag, Stuttgart

Shao X, Hoareau R, Hockley BG, Tluczek LJ, Henderson BD, Padgett HC, Scott PJ (2011) Highlighting the versatility of the tracerlab synthesis modules. Part 1: fully automated production of [^{18}F]labelled radiopharmaceuticals using a tracerlab FX(FN). J Labelled Comp Radiopharm 54:292–307

Shen B, Ehrlichmann W, Uebele M, Machulla HJ, Reischl G (2009) Automated synthesis of n.c.a. [^{18}F]FDOPA via nucleophilic aromatic substitution with [^{18}F]fluoride. Appl Radiat Isot 67:1650–1653

Sherley JL, Kelly TJ (1988) Regulation of human thymidine kinase during the cell cycle. J Biol Chem 263:8350–8358

Shields AF, Grierson JR, Dohmen BM, Machulla HJ, Stayanoff JC, Lawhorn-Crews JM, Obradovich JE, Muzik O, Mangner TJ (1998) Imaging proliferation in vivo with [F-18]FLT and positron emission tomography. Nat Med 4:1334–1336

Shotwell A, Jayme DW, Killberg M, Oxender DL (1981) Neutral amino acid transport systems in Chinese hamster ovary cells. J Biol Chem 256:5422–5427

Smith TA (2000) Mammalian hexokinases and their abnormal expression in cancer. Br J Biomed Sci 57:170–178

Souba WW, Pacitti AJ (1992) How amino acids get into cells: mechanisms, models, menus and mediators. J Parenter Enteral Nutr 16:569–578

Southworth R, Darling JL, Medina RA, Flynn AA, Pedley RB, Garlick PB (2002) Dissociation of glucose tracer uptake and glucose transporter distribution in the regionally ischemic isolated rat heart: application of a new autoradiographic technique. Eur J Nucl Med Mol Imaging 29:1334–1341

Sun H, Sloan A, Mangner TJ, Vaishampayan U, Muzik O, Collins JM, Douglas K, Shields AF (2005) Imaging DNA synthesis with [^{18}F]FMAU and positron emission tomography in patients with cancer. Eur J Nucl Med Mol Imaging 32:15–22

Swanson KR, Chakraborty G, Wang CH, Rockne R, Harpold HL, Muzi M, Adamsen TC, Krohn KA, Spence AM (2009) Complementary but distinct roles for MRI and ^{18}F-fluoromisonidazole PET in the assessment of human glioblastomas. J Nucl Med 50:36–44

Tang G, Tang X, Wen F, Wang M, Li B (2010) A facile and rapid automated synthesis of 3′-deoxy-3′-[^{18}F]fluorothymidine. Appl Radiat Isot 68:1734–1739

Tang G, Wang M, Tang X, Gan M, Luo L (2005) Fully automated one-pot synthesis of [^{18}F]fluoromisonidazole. Nucl Med Biol 32:553–558

Tewson TJ, Mankoff DA, Peterson LM, Woo I, Petra P (1999) Interactions of 16α-[^{18}F]-fluoroestradiol (FES) with sex steroid binding protein (SBP). Nucl Med Biol 26:905–913

Thiele F, Ehmer J, Piroth MD, Eble MJ, Coenen HH, Kaiser HJ, Schaefer WM, Buell U, Boy C (2009) The quantification of dynamic FET PET imaging and correlation with the clinical outcome in patients with glioblastoma. Phys Med Biol 54:5525–5539

Tsujikawa T, Yoshida Y, Mori T, Kurokawa T, Fujibayashi Y, Kotsuji F, Okazawa H (2008) Uterine tumors: pathophysiologic imaging with 16α-[^{18}F]fluoro-17β-estradiol and ^{18}F fluorodeoxyglucose PET–initial experience. Radiology 248:599–605

Van de Wiele C, De Vos F, Slegers G, Van Belle S, Dierckx RA (2000) Radiolabeled estradiol derivatives to predict response to hormonal treatment in breast cancer: a review. Eur J Nucl Med 27:1421–1433

Veach DR, Namavari M, Pillarsetty N, Santos EB, Beresten-Kochetkov T, Lambek C, Punzalan BJ, Antczak C, Smith-Jones PM, Djaballah H, Clarkson B, Larson SM (2007) Synthesis and biological evaluation of a fluorine-18 derivative of dasatinib. J Med Chem 50: 5853–5857

Wagner S, Breyholz HJ, Faust A, Höltke C, Levkau B, Schober O, Schäfers M, Kopka K (2006) Molecular imaging of matrix metalloproteinases in vivo using small molecule inhibitors for SPECT and PET. Curr Med Chem 13:2819–2838

Warburg O, Posener K, Negelein E (1924) VIII. The metabolism of cancer cells. Biochem Zeitschr 152:129–169

Weckesser M, Langen KJ, Rickert CH, Kloska S, Straeter R, Hamacher K, Kurlemann G, Wassmann H, Coenen HH, Schober O (2005) *O*-(2-[^{18}F]fluorethyl)-L-tyrosine PET in the clinical evaluation of primary brain tumours. Eur J Nucl Med Mol Imaging 32:422–429

Weissleder R, Mahmood U (2001) Molecular imaging. Radiology 219:316–333

Welch MJ, Redvanly CS (2003) Handbook of radiopharmaceuticals: radiochemistry and applications. Wiley, London

Wester HJ, Herz M, Weber W, Heiss P, Senekowitsch-Schmidtke R, Schwaiger M, Stöcklin G (1999) Synthesis and radiopharmacology of *O*-(2-[^{18}F]fluoroethyl)-L-tyrosine for tumor imaging. J Nucl Med 40:205–212

Wodarski C, Eisenbarth J, Weber K, Henze M, Haberkorn U, Eisenhut M (2000) Synthesis of 3′-deoxy-3′-[^{18}F]fluoro-thymidine with 2,3′-anhydro-5′-*O*-(4,4′-dimethoxytrityl)-thymidine. J Label Compd Radiopharm 43:1211–1218

Yamamoto Y, Kameyama R, Izuishi K, Takebayashi R, Hagiike M, Asakura M, Haba R, Nishiyama Y (2009) Detection of colorectal cancer using ^{18}F-FLT PET: comparison with ^{18}F-FDG PET. Nucl Med Commun 30:841–845

Yoshida Y, Kurokawa T, Tsujikawa T, Okazawa H, Kotsuji F (2009) Positron emission tomography in ovarian cancer: ^{18}F-deoxy-glucose and 16α-^{18}F-fluoro-17β-estradiol PET. J Ovarian Res 2:7

Yun M, Oh SJ, Ha HJ, Ryu JS, Moon DH (2003) High radiochemical yield synthesis of 3′-deoxy-3′-[^{18}F]fluorothymidine using (5′-*O*-dimethoxytrityl-2′-deoxy-3′-*O*-nosyl-*β*-D-*threo* pentofuranosyl)thymine and its 3-*N*-BOC-protected analogue as a labeling precursor. Nucl Med Biol 30:51–157

Zhang L, Tang G, Yin D, Tang X, Wang Y (2002) Enantioselective synthesis of no-carrier-added (NCA) 6-[^{18}F]fluoro-L-DOPA. Appl Radiat Isot 57:145–151

Zuhayra M, Alfteimi A, Forstner CV, Lützen U, Meller B, Henze E (2009) New approach for the synthesis of [^{18}F]fluoroethyltyrosine for cancer imaging: simple, fast, and high yielding automated synthesis. Bioorg Med Chem 17:7441–7448

Zuhayra M, Alfteimi A, Papp L, Lützen U, Lützen A, Von Forstner C, Meller B, Henze E (2008) Simplified fast and high yielding automated synthesis of [^{18}F]fluoroethylcholine for prostate cancer imaging. Bioorg Med Chem 16:9121–9126

Optical and Opto-Acoustic Imaging

Vasilis Ntziachristos and Daniel Razansky

Abstract

Since the inception of the microscope, optical imaging is serving the biological discovery for more than four centuries. With the recent emergence of methods appropriate for in vivo staining, such as bioluminescence, fluorescent molecular probes, and proteins, as well as nanoparticle-based targeted agents, significant attention has been shifted toward in vivo interrogations of different dynamic biological processes at the molecular level. This progress has been largely supported by the development of advanced optical tomographic imaging technologies suitable for obtaining volumetric visualization of biomarker distributions in small animals at a whole-body or whole-organ scale, an imaging frontier that is not accessible by the existing tissue-sectioning microscopic techniques due to intensive light scattering beyond the depth of a few hundred microns. Biomedical optoacoustics has also emerged in the recent decade as a powerful tool for high-resolution visualization of optical contrast, overcoming a variety of longstanding limitations imposed by light scattering in deep tissues. By detecting tiny sound vibrations, resulting from selective absorption of light at multiple wavelengths, multispectral optoacoustic tomography methods can now "hear color" in three dimensions, i.e., deliver volumetric spectrally enriched (color) images from deep living tissues at high spatial resolution and in real time. These new-found imaging abilities directly relate to preclinical screening applications in animal models and are foreseen to significantly impact clinical decision making as well

V. Ntziachristos (✉) · D. Razansky
Chair for Biological Imaging, Institute for Biological and Medical Imaging Technische Universität München and Helmholtz Zentrum München, Munich, Germany
e-mail: v.ntziachristos@tum.de; vntziachristos@gmail.com

O. Schober and B. Riemann (eds.), *Molecular Imaging in Oncology*,
Recent Results in Cancer Research 187, DOI: 10.1007/978-3-642-10853-2_4,

Contents

1 Introduction

Microscopy has been a major optical imaging tool for more than three centuries. Yet optical imaging is a rapidly emerging imaging science with remarkable new approaches continuously emerging to improve on the capabilities and application potential; ultimately impacting biological discovery and healthcare. A significant role in these developments has played the discovery, development, and propagation of fluorescent proteins and probes, as well as bioluminescence to in vivo imaging applications (Tsien 2005; Giepmans et al. 2006; Contag and Bachmann 2002). Linked to this progress is the ability to visualize cancer features and biomarkers with high versatility, spanning all areas of anatomic, functional, and molecular visualization.

While microscopic viewing of such markers is possible using advanced forms of microscopy such as confocal or two-photon/multi-photon microscopy (Denk et al. 1990; Webb 1999; Helmchen and Denk 2005), the penetration depths of even the most advanced forms of microscopy rarely exceed 500 microns in most tissues in vivo. While in optically cleared (transparent) samples greater depths can be reached, in vivo nontransparent tissues limit the penetration ability of modern microscopy due to strong photon scattering by various cellular organelles and membranes. Therefore imaging of various forms of optical contrast deeper than 500 microns requires the development of different optical imaging approaches that can handle the effects of scattering at greater depths.

Early optical imaging systems were based on photographic principles by simply utilizing a sensitive CCD camera to take pictures of animals at a wavelength range of preference, for example at a range where bioluminescence or fluorescence was emitted. Such systems offered no correction for scattering and for this reason yielded low resolution and generally inaccurate images, since they could not account for the effects of depth or of light attenuation as a function of the possible variation of the tissue's optical properties. In response, optical imaging experienced a slow propagation into the biological practice with mixed experiences reporter depending on the user and the application.

Modern macroscopic optical imaging, however, moves away from these early attempts and utilizes tomographic hybrid approaches to offer highly robust and accurate imaging performance. Technologies such as hybrid Fluorescence Molecular Tomography-X-ray Computer Tomography (FMT-XCT) systems (Schulz et al. 2010) or multi-spectral optoacoustic tomography (MSOT) systems (Razansky et al. 2009; Ntziachristos and Razansky 2010) bring unprecedented levels of performance. This new found performance not only goes well beyond early attempts with photographic imaging but challenges even other established imaging modalities, within the operation range of optical imaging, i.e. 2–5 cm penetration in the near-infrared spectral region. The outcome is a technology that is well-suited for macroscopic imaging of small animals but also clinical endoscopic applications.

In the following we discuss new developments in optical imaging, in particular MSOT and FMT-XCT, which are expected to revolutionize the field of optical imaging in general. Whereas focus is given herein to small animal imaging, since a significant part of recent literature demonstrates these technologies with small animals, we stress again the significant potential for clinical translation of these methodologies.

2 Multi-Spectral Optoacoustic Tomography

Optoacoustic interrogations of biological tissues has been considered since the early 1970s (Rosencwaig 1973; Bowen et al. 1982; Oraevsky and Esenaliev 1994) and offers a powerful methodology for molecular imaging investigations. In vivo imaging of cellular and subcellular markers can be achieved by MSOT, an emerging field in the imaging sciences. MSOT overcomes major limitations of conventional optical imaging while it retains many of the advantages of photonic methods.

The MSOT principle of operation is shown on Fig. 1. Short laser pulses in the nanosecond range illuminate the tissue of interest over an area of interest. Absorption of the fast laser pulses by tissue photoabsorbers, such as oxy- and deoxy-hemoglobin, melanin, or extrinsically administered probes and agents creates a transient temperature increase which in turn leads to a thermoelastic expansion. This process creates acoustic waves in the 1–100 MHz range which can then be detected with multiple ultrasound elements also places around the illuminated area. By combining the ultrasonic measurements in the mathematical data inversion scheme, high resolution images of tissue can be produced. The amplitude of the generated broadband ultrasound waves reflects local optical absorption properties. The spatial resolution of the method is therefore solely determined by the diffraction limit of ultrasound waves or the available bandwidth of the ultrasonic detector.

MSOT further employs spectral identification of known reporter molecules, such as common fluorochrome or other chromophores, dyes and photoabsorbing nanoparticles. Molecules with spectra that are different than the ones of background tissue can be accurately resolved by MSOT with high specificity (Razansky et al. 2007). However, in practice, MSOT images obtained from tissues represent a mixed contribution of photon energy delivered in each volume element

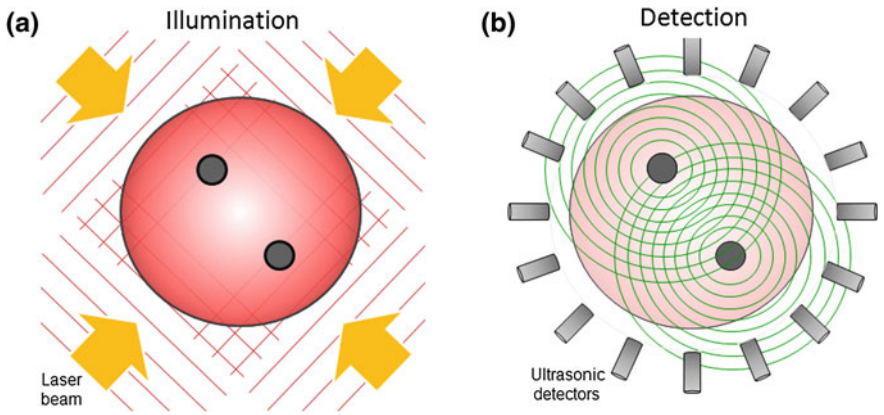

Fig. 1 Principle of MSOT operation. **a** Pulsed light of time-shared multiple wavelengths illuminates the tissue of interest and establishes transient photon fields in tissue. **b** In response to the fast absorption transients by tissue elements, acoustic responses are generated via the thermoacoustic phenomenon, which are then detected with acoustic detectors. By modeling photon and acoustic propagation in tissues and using inversion (tomographic) methods images can then be generated and spectrally unmixed to yield the biodistribution of reporter molecules and tissue biomarkers. Taken from Ref. (Ntziachristos and Razansky 2010)

imaged and the total absorption contribution from the volume element. Consequently significant measures are taken to decompose the resulting image from the effects of inhomogeneous light attenuation in the tissue of interest (Rosenthal et al. 2009; Rosenthal et al. 2010).

The MSOT ability to detect reporter molecules from tissues has been showcased by visualizing common fluorochrome embedded deep in mice (Razansky et al. 2007; Buehler et al. 2010; Li et al. 2008). This was achieved without the need of baseline measurements obtained before the administration of the probe. This approach operates optimally by selecting fluorochromes (or possibly chromophores) with a steep-drop in their absorption spectrum and accordingly selects the imaging wavelengths to capture this absorption change (Fig. 2d). When utilizing fluorescent dyes, the emphasis is on low quantum-yield fluorochrome, which are particularly useful for optoacoustic signal excitation. The absorption spectrum of common organic fluorochromes drops significantly in the spectral window 750–850 nm, compared to the relatively smooth absorption variation of the spectra of common tissue chromophores in the NIR. Therefore intrinsic tissue contrast can be readily suppressed with a multi-spectral approach, yielding highly sensitive imaging of fluorochrome distribution in tissue obtained by spectral matching of photo-acoustic images acquired at several different adjacent wavelengths. Figure 2e shows spectrally-resolved MSOT image (in color), superimposed onto a single-wavelength anatomical image. The imaged is obtained by spectrally processing images at different wavelengths (Fig. 2) a–c for identifying the know spectrum of the AF750 molecule. While the simplest version of spectral matching

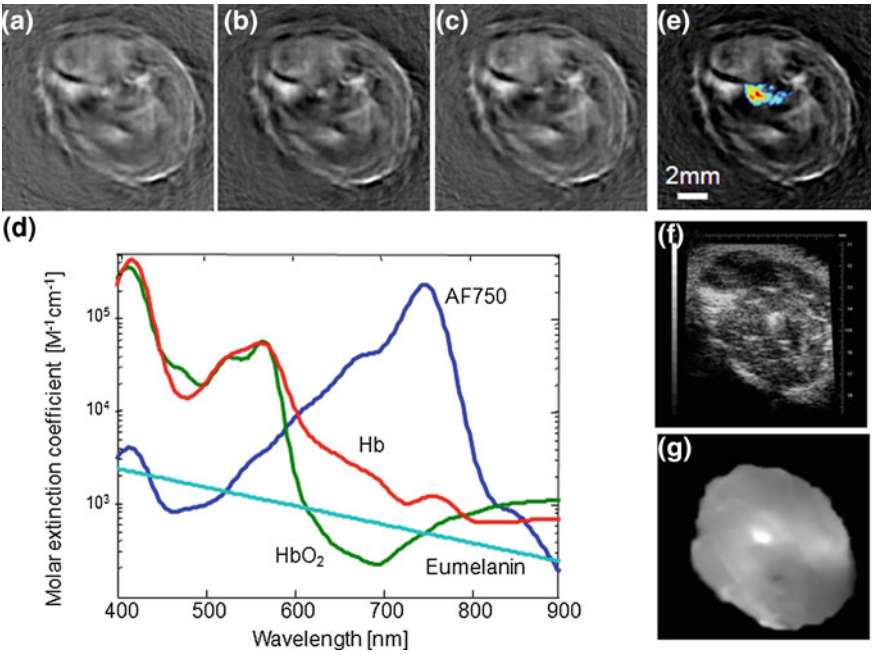

Fig. 2 MSOT visualizes distribution of fluorescent molecular probe (AlexaFluor 750™) in a mouse leg[13]. **a**, **b**, and **c** are cross-sectional optoacoustic tomographic reconstructions acquired at 750, 770, and 790 nm, respectively. **d** Absorption as a function of wavelength for AF750 fluorescent probe as compared to some intrinsic tissue chromophores. Arrows indicate the three wavelengths used to spectrally resolve the probe location. **e** Spectrally-resolved MSOT image that incorporates measurements at all the three indicated wavelengths (in color), superimposed onto a single-wavelength anatomical image. **f** Corresponding ultrasonic image, acquired approximately at the same imaging plane, using 25 MHz high-resolution ultrasound system. **g** Planar epi-fluorescence image of dissected tissue confirms the fluorochrome location. Image and caption taken from Ref. (Ntziachristos and Razansky 2010)

operation can be achieved by image subtraction at two wavelengths, three- and overall multi-spectral imaging further suppress the background signals. Multi-spectral imaging further attains the potential to resolve multiple purely absorbing or absorbing/fluorescing dyes and probes in tissues and the overall method can be improved by more accurately considering the relative background absorption attenuation of tissue at each of the wavelengths used.

Figure 3 shows an additional example of resolving the fluorescent dye ICG perfusing the mouse kidney of a nude female mouse in vivo. In this case MSOT has been implemented in video rate format (Buehler et al. 2010), where a single slice can be obtained out of a single laser pulse without data averaging. In this manner real-time data can be obtained with reduced sensitivity to motion artifacts.

Since fluorescent proteins also have distinct spectra, it is possible to detect them using MSOT as was recently shown in images from the adult zebrafish (Razansky et al. 2009). It was shown that MSOT is possible through several 4–6 mm of

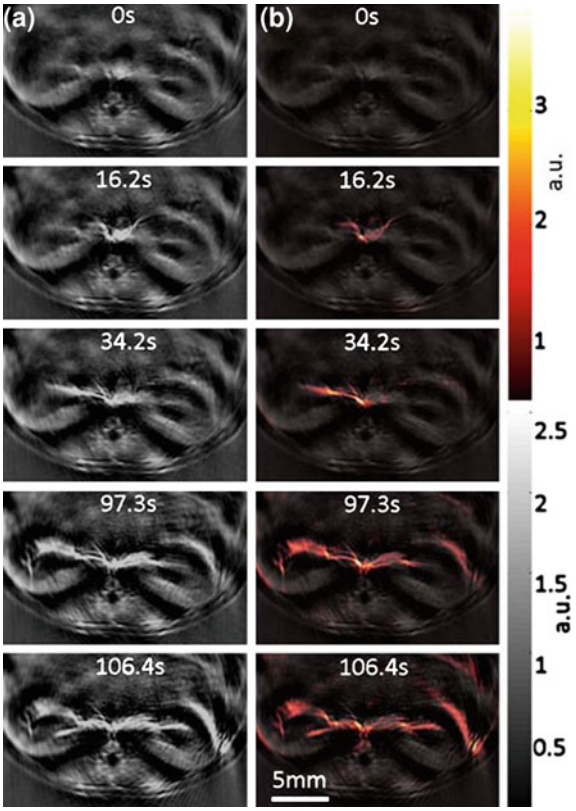

Fig. 3 MSOT of a fluorochrome (*IndoCyanine Green*; ICG) injected intravenously in a mouse leg in vivo. The images are cross-sectional optoacoustic images at different time-points of **a** the kidney anatomy before and as a function of ICG perfusion and **b** ICG distribution (in color) superimposed on the image of the kidneys before injection (*top left* image). The images are obtained from a female CD1 mouse injected with 0.33 μmoles of ICG. Images taken from Ref. (Buehler et al. 2010)

developed non-transparent fish expressing the fluorescent protein mCherry in the brain and notochord. The resolution achieved in this case was 38 microns. Fluorescent proteins were resolved alongside anatomical images of the fish in three dimensions and in vivo. Overall, the development of fluorescent proteins with absorption spectral in the near-infrared opens exciting possibilities for the wide utilization of fluorescent protein MSOT imaging.

A particular strength of the MSOT technology is its ability to simultaneously deliver anatomical, functional, and molecular contrast from tissues, which is usually possible only if several different modalities are used for imaging. Moreover, MSOT scales well with different tissue sizes and, as demonstrated in phantom experiments, several centimeters of penetration with high spatial resolution can be achieved, especially when employing near-infrared light. Indeed, size of many relevant biological samples and model organisms, e.g. worms, developing and adult insects and vertebrates including small mammals and their extremities, lie in this range and could be visualized. Finally, optoacoustics is an inherently fast imaging technology (Buehler et al. 2010) therefore it holds great potential for real-time imaging of fast events and dynamic processes, such as pharmacokinetics, in living organisms.

Other molecules that can be used for MSOT applications include gold and carbon nanoparticles, nanoshells, nanocages, and carbon nanorods (La Zerda et al. 2008; Rayavarapu et al. 2007; Ntziachristos and Razansky 2010), all shown to increase optoacoustic signals in vivo. LacZ gene encoding for the X-gal chromogenic substrate expression and other possible chromogenic assays are also of potential interest (Li et al. 2007). These agents can improve the MSOT sensitivity but may offer other challenges associated with biodistribution and toxicity. Regardless they offer valuable mechanisms for MSOT contrast generation and their use is expected to significantly increase.

Many other dedicated contrast agents could potentially be developed for optoacoustic imaging applications, but additional studies will be required in order to address a variety of efficiency, dosing and safety, and toxicity concerns associated with the in vivo administration of these agents. Moreover, due to their relatively wide absorption spectra, nanoparticle-based contrast approaches typically require a background (before) image in order to attain specificity. On the other hand, MSOT has spectral mechanisms to differentiate molecules of distinct optical signatures, thus, many widely adopted optical contrast agents, such as fluorochromes, or gold nanoparticles can be efficiently used. Many fluorochromes, e. g. Alexa or Cy-based dyes, ICG, fluorescent proteins (GFP, RFP), or gold nanorods exhibit sharp resonances in the vicinity of their peak excitation, making them convenient candidates for highly sensitive multi-wavelength imaging.

2.1 Sensitivity of Biomarker Detection

While the feasibility of different optoacoustic imaging implementations has been showcased, the overall sensitivity of the method for different experimental scenarios needs to be addressed from a theoretical and systematic stand-point (Razansky et al. 2009). This calculation and discussion, modified from Refs. (Razansky et al. 2009; Ntziachristos and Razansky 2010; Razansky and Ntziachristos 2010) considers the theoretically predicted sensitivity of the method over wide range of imaging-related parameters and considers the necessary experimental reference measurements for validating the theoretical findings. Overall, the determination of the MSOT detection sensitivity limits, as it relates to the sensitivity of optoacoustic tomography is not straightforward. This is because optoacoustics is a high resolution modality and an experimental determination of the sensitivity as a function of e.g. marker size or volume remains difficult since this would require reproducible creation of small volumes (e.g. 100 μm or less) containing well-defined concentrations of markers. Nevertheless, a prediction can alternatively be made by imaging larger amounts of the same marker and placing the measured value on the appropriate parameter-dependent signal intensity curve. A performance estimate of particular experimental system and the expected SNR for smaller amounts of markers can then be made (Razansky et al. 2009). To simulate optoacoustic signals emanating from a target biomarker, an absorbing

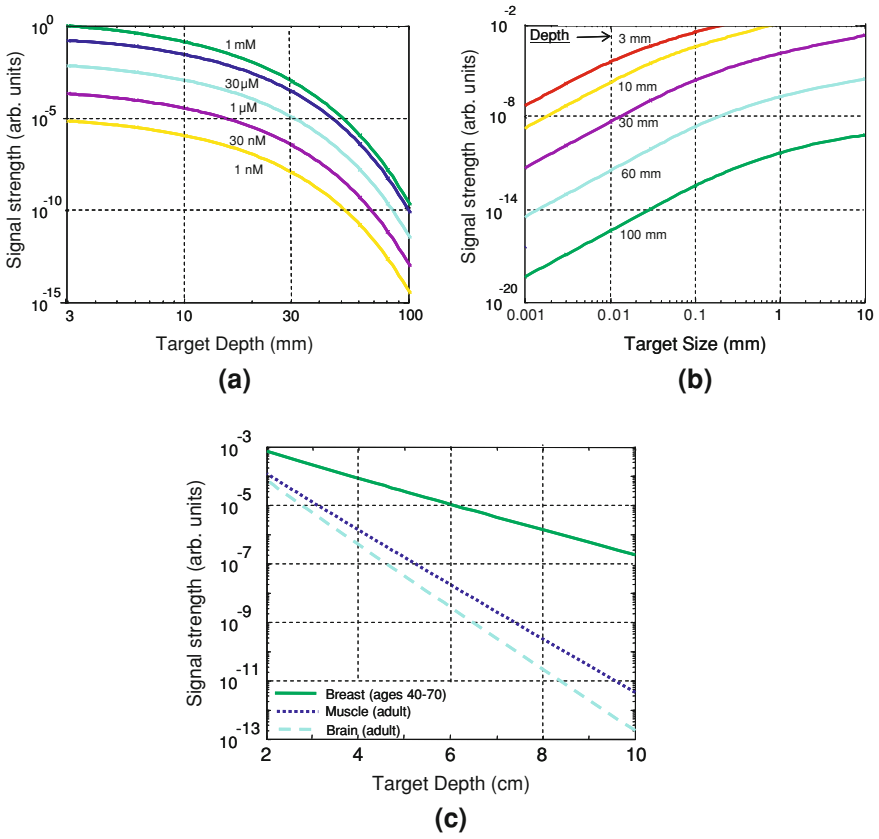

Fig. 4 Simulated optoacoustic signal strengths from an experimental and clinical point of view. **a** Signals detected from a 2 mm diameter target (Cy5.5 fluorescent dye) for increasing target depths at various concentrations. **b** Signals from increasing sized targets containing 5 μM of the dye at various depths. **c** Signals from the 2 mm diameter target containing 1 μM of fluorochrome at increasing depths of media simulating various human tissues. Graphs and the details of the study can be found in Ref. (Razansky et al. 2009)

sphere is considered embedded at different depths in tissue-mimicking scattering and absorbing phantoms. By accounting for diffuse light distribution and ultrasound dispersion as it occurs in tissues, system-dependent characteristics can be removed to yield a better understanding of performance and physical limitations of target detection using optoacoustics. In Fig. 4, a range of clinically relevant biomarker concentrations are examined, covering different target radii, and tissue dimensions.

Using such analysis, the optoacoustic detection limits are found constrained by the interplay of light penetration and ultrasonic frequency-dependent attenuation (dispersion) and exhibit a nonlinear performance in the detection limit, which

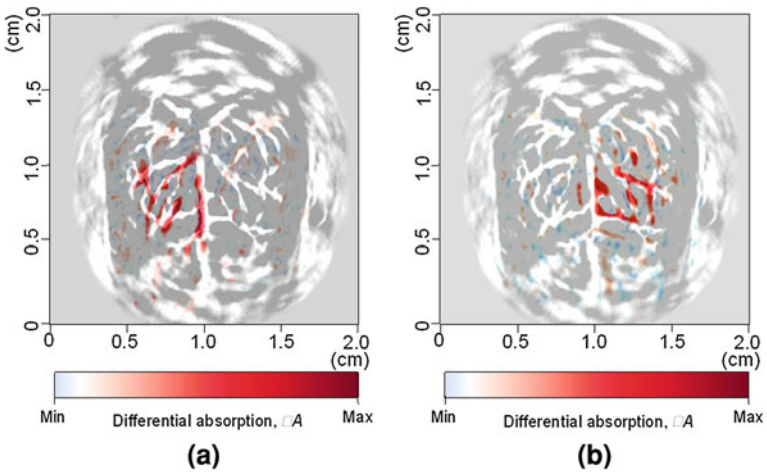

Fig. 5 Visualization of brain structure and function using photoacoustic tomography. Functional maps of brain activities corresponding to the left-side **a** and the right-side **b** whisker stimulations, respectively, acquired with the skin and skull intact. Images taken from review paper (Ntziachristos et al. 2005) originally published in Ref. (Wang et al. 2003)

invalidates simplistic linear predictions of optoacoustic sensitivity (Fig. 5). In particular, while optoacoustic signals depend linearly on probe concentration, they exhibit a nonlinear dependence not only as a function of target depth but also as a function of its volume. Naturally, the dependence of signal intensity on depth for a target of constant volume is determined by the nonlinear light attenuation with depth due to absorption and scattering and the corresponding sound attenuation. In particular, the steep attenuation of light causes a drop in the energy absorbed by targets as a function of depth and the corresponding detected optoacoustic signal intensity. On the other hand, when varying the lesion size instead, additional effects take place. First, as expected, the resulting light energy deposition is decreasing with target volume, simultaneously reducing the detected optoacoustic signal (voltage) as a function of square root of the deposited energy, i.e. as $d^{3/2}$ (d being the characteristic lesion size). It was, however, further noticed that for small targets (in practice, less than 0.2–0.5 mm in size), effects of ultrasonic dispersion start playing increasingly dominant role in the reduction of the detected optoacoustic signal intensity, owing to increased attenuation of high-frequency sound components. This important finding demonstrates that it would be inaccurate to linearly extrapolate the detection limits of optoacoustics from data obtained on larger lesions. All these effects create a complex estimation model on detection limits, which is defined also in the context of lesion size and depth, not only lesion concentration. Recent in vivo and phantom studies predicted detection limits on the order of 300 femtomoles for common fluorochromes in the near-infrared and 300 cells for red-shifted fluorescent proteins (Razansky et al. 2009).

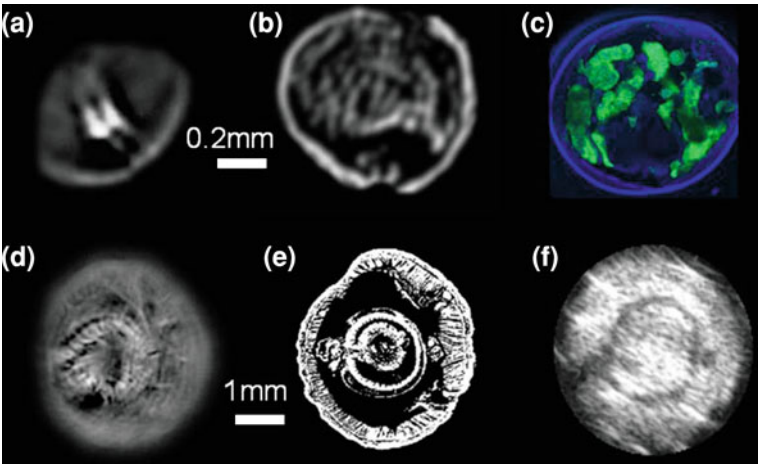

Fig. 6 Images obtained with selective-plane optoacoustic tomography. Cross-sectional optoacoustic images of an intact Drosophila melanogaster pupae from **a** top part containing dark-color (highly absorbing) sensory organ of the pupa; and **b** salivary glands area. **c** Histological section of the pupa at the salivary gland area (*blue*-dapi staining; *green*—GFP fluorescence expressed in the fatty structures). Images from Lumbricus Terrestris (Earthworm) are shown in **d** Selective-plane optoacoustic image; **e** Anatomical diagram; and **f** The corresponding ultrasound image acquired using high-resolution ultrasound imaging system operating at 25 MHz. Images taken from Ref. (Razansky et al. 2009)

2.2 Other Applications of Optoacoustic Imaging

While MSOT offers high potential for molecular imaging investigations, optoacoustic imaging is sensitive to all optical absorbers, the major one in tissues being hemoglobin. Therefore optoacoustic imaging has been extensively used to image vascularization, as shown in Fig. 4. As evident on the figure, it is not only the anatomy but importantly the functional information on oxygen saturation and blood oxygenation that can be measured, with further implications in resolving disease processes in oncology as well, in particularly relating to angiogenesis and hypoxia. In addition, other absorbing structures can be visualized, for example, in imaging anatomical images from other tissues, such as fat, bones, and other structures and organisms having no hemoglobin-based contrast (Fig. 6).

3 FMT-XCT

Fluorescence imaging deep in tissues is also possible using tomographic optical imaging approaches. In contrast to simple photographic imaging where the sample is illuminated with an expanded light beam and using a sensitive camera to collect fluorescence images from the same side as the illumination (epi-illumination) tomography is best implemented in transillumination, i.e. the light sources and the

camera being on opposite sides of the tissue imaged or at some angle to each-other, and approach that allows sampling deeper parts of the tissue (Ntziachristos et al. 2005). Tissue of several centimeters thickness can be imaged when near-infrared light is used, due to the low attenuation of light by tissue in this range. The following discussion showcases progress with FMT, an optical tomography method developed for fluorescence molecular imaging that is combined with an anatomical modality to yield a better optical imaging tomographic system.

The principle of operation of FMT resembles that of XCT in that tissue is illuminated from different angles and at different positions and a mathematical formulation is used to describe photon propagation in tissue. However, a major difference between optical tomography and tomographic methods based on high energy rays is that photons in the optical range are highly scattered by tissue organelles and membranes. Photons do not propagate in straight lines when travelling through tissue, but become diffuse within a few millimeters of propagation. The diffusive nature of the light propagation through tissue limits the quantification ability and maximum resolution that can be achieved. Therefore, FMT attempts to localize and quantify fluorescent signals distributed in tissue. Yet the inversion problem is ill-posed, i.e. it does not have a unique or easy to find solution and for this reason leads to uncertainty that eventually limits the resolution and the overall image fidelity achieved, especially for complex problems such as a distributed fluorescence activity in optically heterogeneous tissue.

One approach to improve on the reconstruction ability is to combine FMT with another anatomical imaging method. The rationale is that by using co-registered anatomical information a hybrid FMT approach can build more accurate problems of photon propagation in tissues and restrain the inverse problems. For this reason there has been an emergence of hybrid imaging systems combining FMT with another modality. MRI can restrict the optical implementation due to the limited bore dimensions of an MRI magnet; eventually restricting the number of optical sources; and detectors that can be placed around an animal or tissue. On the other hand, XCT systems offer gantry implementation with the ability to place freely high quality and spatial sampling optical components, including mounting CCD cameras and scanning laser beams on the tissue surface offering a highly adept data set. This type of hybrid scanner allows therefore 360° projection viewing for both FMT and XCT and high spatial sampling of X-ray and photon fields leading to a high quality data set available for reconstructions. The combination of the FMT and XCT modality into a single system eliminates the need to transfer the imaging subject from one system to the other using elaborate methods for co-registration of images but allows for highly accurate image registration between the two modalities and for the possibility of simultaneous acquisition, although typically the FMT takes 2–10 times longer to acquire due to the laser scanning requirements.

An implementation of a gantry-based FMT-XCT system was proposed (Schulz et al. 2010) and shown in Fig. 7. In this implementation, diode lasers at different wavelengths in the near-infrared range are attached onto the gantry system and used for tissue illumination by employing a scanning mechanism based on motor-

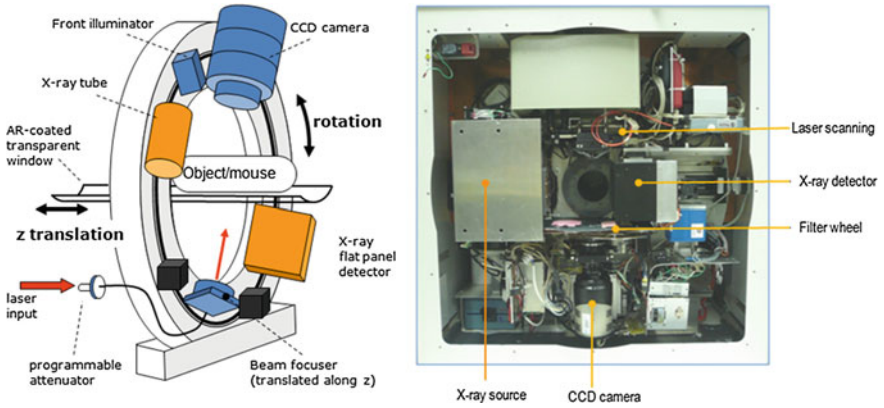

Fig. 7 A hybrid FMT-XCT small animal imaging system implemented within the rotating gantry of a micro-CT scanner from General Electric. System details in Ref. (Schulz et al. 2010)

stages. The tissue illumination is based on a focused laser beam that established a point source on the animals surface. Using the motor stages this point source is scanned in one side of the animal. Data are collected on the other side of the animal using a CCD camera. By rotating the entire gantry around the animal, this process is repeated at different projections and a multi-projection data set is collected as raw data to feed an inversion algorithm for image reconstruction. An imaging example from reconstructing the fluorescence activity of a lung tumor, using the X-ray CT information into the optical inversion code is shown in Fig. 8. The particulars of the algorithm utilized for the reconstruction go beyond the scope of this chapter but can be found in detail in Ref. (Ale et al. 2010).

Typically the illumination utilized in of constant intensity (constant wave or CW) since this approach leads to economical implementations and offers good signal-to-noise characteristics and is generally operationally simple and robust (Ntziachristos et al. 2005). One limitation of using CW light is the difficulty in separating scattering from absorption characteristics when such differentiation is required. This is not necessarily major complication in fluorescent imaging but becomes important when intrinsic tissue contrast is imaged. There are two other possible illumination strategies, one using light of modulated intensity (frequency domain), typically at frequencies of 100 MHz–1 GHz, or the use of ultrafast photon pulses (time-domain) in the 100 fs–100 ps range. In this case, the detection systems employed can measure changes in light attenuation and phase at different frequencies, for intensity modulating sources, or resolve the arrival of photons as a function of time, in time-resolved implementations. Frequency- and time domain methods can separate absorption from scattering and, in principle, also resolve fluorescence lifetime, although it remains difficult to measure the lifetime of fluorochrome deep inside tissues, since the broadening of the fluorescence response due to lifetime is mixed with the broadening of the fluorescence response due to tissue absorption and scattering and as a function of depth, which makes their separation very challenging.

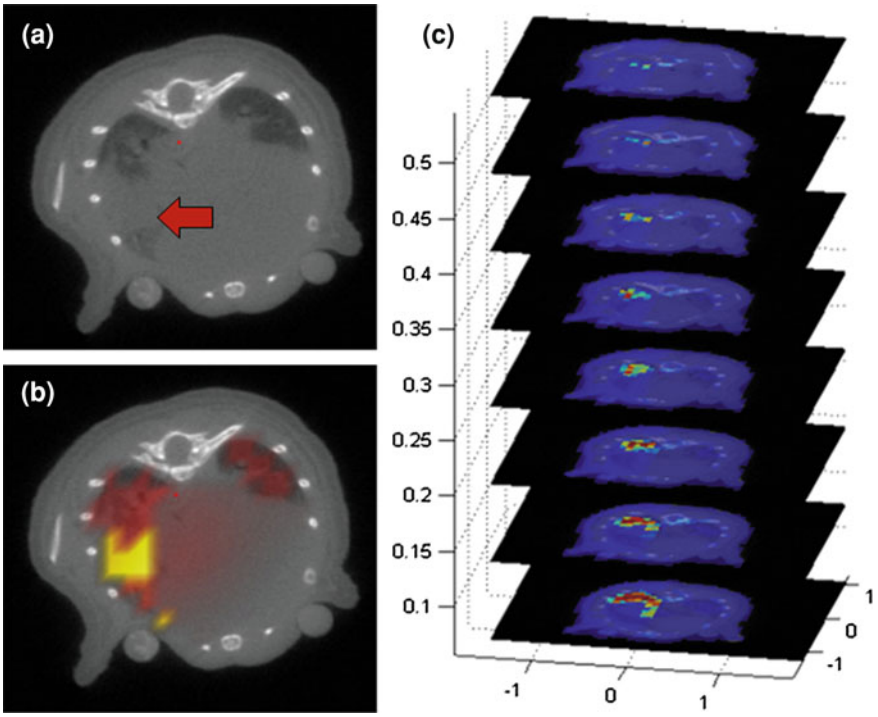

Fig. 8 Imaging of a lung tumor implanted in a nude mouse using the hybrid FMT-XCT system and method. **a** XCT slice obtained from the thorax; the arrow points to the location of the tumor. **b** Fluorescence signal (in color) superimposed to the anatomical image in (a). The fluorochrome utilized here activates in the presence of proteases present in tumors. **c** Three dimensional rendering from the entire upper thorax scanned. Data from the studies included in Ref. (Schulz et al. 2010). The inversion algorithm used is described in Ref. (Ale et al. 2010)

4 Overview of Performance Characteristics

Based on the results of recent studies, hybrid optical methods such as MSOT and FMT-XCT offer revolutionary performance characteristics over other optical imaging approaches. Both methods operate on very versatile molecular contrast, cost-effectiveness, and the use of non-ionizing radiation, as summarized in Fig. 9. MSOT in addition offers high resolution imaging and depending on the optical reporter used can also lead to high sensitivity imaging, in particular, using gold nanoparticles. FMT offers great sensitivity in resolving fluorochrome although with reduced resolution compared to MSOT. For these reasons both methods can find several applications in small animal imaging research, although their sensitivity drops exponentially with depth and it not expected to propagate to whole-body imaging of animals larger than a rat. However, they can still be employed for imaging dedicated organs not only in pre-clinical but also clinical applications, for

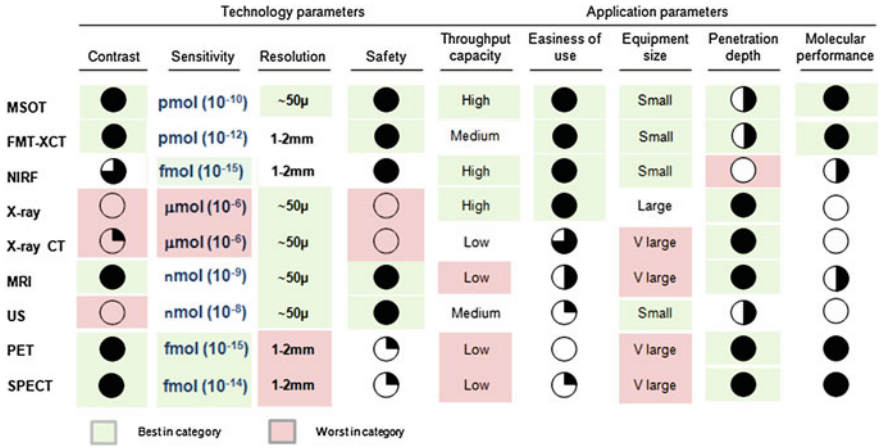

Fig. 9 MSOT and FMT-XCT performance over other imaging modalities as it is considered for small animal imaging. NIRF denotes epi-illumination (photographic) fluorescence imaging

example, in endoscopic imaging. When considering clinical applications, the methods described can find several niche focus points due to the high sensitivity, resolution, and portability, and could shift the paradigm of healthcare offering a safe point-of-care imaging modality for highly disseminated imaging. Both methods are expected to enter focused segments of the therapeutic efficacy and possibly the diagnostic segments, especially in areas not well served by current imaging modalities. Due to the limited penetration these methods do not compete with established modalities such as MRI or PET, but define new operational areas in interventional imaging.

5 Quantification

An important aspect of utilization of the methods discussed herein is their quantification ability. Typically, inaccurate algorithms can still offer images; however, with utility that does not fully capitalize on the potential of the methods considered. One important aspect in optical imaging methods is that of light attenuation with depth and as a function of the spatial variation of the optical properties of tissue. At the absence of accounting for the potentially strong spatial differences changes of photon intensity in tissue, the resulting images can offer significant artifacts, and lead to misleading conclusions.

For MSOT, it has been shown that backprojection-related artifacts can be avoided by use of the so-called model-based inverse methods (Rosenthal et al. 2010; Cox et al. 2006). The following discussion modified from Ref. (Ntziachristos and Razansky 2010) illuminates key aspects of MSOT artifacts and solutions for accurate inversion. In particular, in contrast to back-projection

algorithms, model-based schemes are not based on an approximate analytical solution of the optoacoustic equation. Instead, the forward problem is solved numerically in an iterative optimization algorithm. In each iteration, the reconstructed optoacoustic image is changed to reduce the error between its corresponding acoustic signals and the measured signals. Since the forward problem is linear, the optimization problem has only a single minimum. Ideally, this approach can yield artifact-free quantified reconstructions. However, the computational complexity involved with model-based schemes has so far severely limited their achievable resolution. The two contributing factors to the high complexity were the low efficiency/accuracy of the numerical forward solution and the need of a high number of iterations. Recently, a novel semi-analytical model-based inversion scheme for quantitative optoacoustic image reconstruction was suggested (Rosenthal et al. 2010), where the presented semi-analytical solution is exact for piecewise planar acoustic-source functions, which significantly improves the accuracy and computational speed. The method eliminates image artifacts associated with the approximated back-projection formulations, i.e. no negative absorption values are produced and the reconstructed image corresponds to the true light attenuation and energy deposition within the object.

Clearly, since back-projection falsely emphasizes edges and fast image variations by producing large negative overshoots, it is capable of producing 'good looking' high-contrast images. However, due to its approximate formulation, it fails to reproduce the correct and quantitative image of the actual laser energy deposition in tissue and the underlining optical absorption values. This property is especially important for quantitative imaging applications, i.e. molecular imaging studies, in which obtaining the correct absorption maps is of high importance. Second, the model-based framework admits generalization of the forward solution to a more comprehensive acoustic propagation models without changing the inversion procedure. For instance, the frequency response of the acoustic detector as well as additional linear effects, such as the frequency-dependant acoustic attenuation and the detector's focusing characteristics can also be conveniently and rigorously incorporated into the model. Finally and importantly, the model-based inversion can be seamlessly adapted to any detection geometry.

Of equal importance are adept algorithms utilized in FMT that can correct for light attenuation and offer accurate, artifact free-images. One particular algorithm that has been shown appropriate for in vivo imaging normalizes raw fluorescent data by data obtained under the identical illumination and geometrical conditions by simply switching a filter in front of the camera utilized in order to capture an adjacent spectral window where excitation photons propagate (Ntziachristos and Weissleder 2001). Data obtained in the excitation wavelength contain information on the spatially dependent attenuation of light in tissues and the use of normalization in the data feeding the inversion helps reducing the sensitivity of the imaging method to the variation of optical properties. Regardless, this normalization is not perfect and contains different sensitivity to the variation of absorption vs. the variation of scattering (Soubret et al. 2005). To further improve on the accuracy of the method, it is possible to utilize the XCT information to develop a more accurate reconstruction

problem (Hyde et al. 2009). In that respect the FMT-XCT system not only offers the ability of producing anatomical and molecular imaging data that are accurately registered, but overall leads to a more quantitative optical tomography system.

6 Optical Imaging Applications in Oncology

In addition to microscopy, macroscopic optical imaging has been considered in accelerating biological investigations at different system levels and in unperturbed host environments. While a limiting factor of conventional optical imaging has been the quantitative accuracy and the superficial nature of the images produced, MSOT and FMT-XCT come with performance that can rival many of the other molecular imaging techniques applied to macroscopic optical imaging. Therefore they can play a major role in biological discovery and pharmaceutical research.

Optical imaging significantly benefits from the rich intrinsic and extrinsic optical contrast of tissues in the visible and near-infrared spectra. In addition to specific absorption by natural chromophores (such as oxy- and deoxyhemoglobin or melanin) a large number of commercially available or investigational fluorescent probes and markers have shown ability to enable a highly potent field for biological imaging (Tsien 2005; Giepmans et al. 2006; Ntziachristos et al. 2005; Weissleder and Ntziachristos 2003). So far, optical probes were proven efficient in a number of clinical and small-animal applications, including probing of tissue hemodynamics or gene expression, detecting protease up-regulation associated with cancer growth and inflammation, monitoring apoptosis and the efficacy of anti-cancer treatments, and imaging specific markers involved in cancer growth and metastasis (Ntziachristos 2006).

MSOT in particular can deliver anatomical, functional, and molecular tissue biomarkers opening significant possibilities for a highly versatile interrogation of various tissue biomarkers linked to optical contrast. The method can image and separate different molecules from each other, based on their distinct spectral profiles. In that respect multiple targets and functions can be simultaneously imaged, potentially building a more accurate picture of the underlying biology. Optoacoustic imaging operates seamlessly within scales, within the penetration limits of light, i.e. 2–5 cm in muscle, deeper in lower attenuating tissues such as breast tissue in the near-infrared; the resolution achieved improving at shallower depths. Therefore MSOT offers a complementary method to microscopy—significantly extending the investigational depths available to optical imaging and linking macroscopic observation to microscopy. In addition, the technique is inherently fast, since images can form per single pulse. For this reason real-time imaging of fast dynamic processes is also possible, which allows accurate studies not only of pharmacokinetics but even faster functional events. Due to these features, MSOT can become an important tool in small animal imaging research. Conversely FMT-XCT can capitalize on existing fluorescence imaging probes and resolve them with accuracy and high sensitivity while significantly improving on the capacities of the combined systems, from offering a more accurate FMT method to adding molecular imaging capacity to XCT systems.

References

Ale A, Schulz R, Sarantopoulos A, Ntziachristos V (2010) Imaging performance of a hybrid x-ray computed tomography-fluorescence molecular tomography system using priors. Med Phys 37:1976–1986

Bowen T (1982) Radiation-induced thermoacoustic soft-tissue imaging. IEEE Trans on Son Ultrason 29: 187–187

Buehler A, Herzog E, Razansky D, Ntziachristos V (2010) Video rate optoacoustic tomography of mouse kidney perfusion. Opt Lett 35:2475–2477

Contag CH, Bachmann MH (2002) Advances in in vivo bioluminescence imaging of gene expression. Annu Rev Biomed Eng 4:235–260

Cox BT, Arridge SR, Kostli KP, Beard PC (2006) Two-dimensional quantitative photoacoustic image reconstruction of absorption distributions in scattering media by use of a simple iterative method. Appl Opt 45:1866–1875

De La Zerda A et al (2008) Carbon nano-tubes as photoacoustic molecular imaging agents in living mice. Nat Nanotechnol 3:557–562

Denk W, Strickler JH, Webb WW (1990) Two-photon laser scanning fluorescence microscopy. Science 248:73–76

Giepmans BNG, Adams SR, Ellisman MH, Tsien RY (2006) Review—The fluorescent toolbox for assessing protein location and function. Science 312:217–224

Helmchen F, Denk W (2005) Deep-tissue two-photon microscopy. Nat Methods 2:932–940

Hyde D, Schulz R, Brooks D, Miller E, Ntziachristos V (2009) Performance dependence of hybrid x-ray computed tomography/fluorescence molecular tomography on the optical forward problem. J Opt Soc Am A: 26:919–923

Li L, Zemp R, Lungu G, Stoica G, Wang L (2007) Photoacoustic imaging of lacZ gene expression in vivo. JBO Lett vol. 12

Li ML, Oh JT, Xie XY, Ku G, Wang W, Li C, Lungu G, Stoica G, Wang LV (2008) Simultaneous molecular and hypoxia imaging of brain tumors in vivo using spectroscopic photoacoustic tomography. Proc IEEE 96:481–489

Ntziachristos V (2006) Fluorescence Molecular Imaging. Annu Rev Biomed Eng 8:1–33

Ntziachristos V, Weissleder R (2001) Experimental three-dimensional fluorescence reconstruction of diffuse media using a normalized Born approximation. Opt Lett 26:893–895

Ntziachristos V, Razansky D (2010) Molecular imaging by means of multi-spectral opto-acoustic tomography (MSOT). ACR Chemical Review 110:2783–2794

Ntziachristos V, Ripoll J, Wang LHV, Weissleder R (2005) Looking and listening to light: the evolution of whole-body photonic imaging. Nat Biotechnol 23:313–320

Oraevsky AA, Esenaliev RO, Tittel FK (1994) Laser based optoacoustic imaging in biological tissues. Proc. SPIE 2134A: 122–128

Rayavarapu R, Petersen W, Ungureanu C, Post J, van Leeuwen T, Manohar S (2007) Synthesis and bioconjugation of gold nanoparticles as potential molecular probes for light-based imaging techniques. Int J Biomed Imaging p. 29817

Razansky D, Vinegoni C, Ntziachristos V (2007) Multispectral photoacoustic imaging of fluorochromes in small animals. Opt Lett 32:2891–2893

Razansky D, Ntziachristos V (2010) Multi-spectral optoacoustic tomography. In Knaeblein J (ed) Modern Biopharmaceuticals vol. in press, Wiley

Razansky D, Distel M, Vinegoni C, Ma R, Perrimon N, Koester R, Ntziachristos V (2009a) Going deeper than microscopy with multi-spectral optoacoustic tomography of fluorescent proteins in vivo. Nat Photonics 3:412–417

Razansky D, Baeten J, Ntziachristos V (2009b) Sensitivity of molecular target detection by multispectral optoacoustic tomography (MSOT). Med Phys 36:939–945

Razansky D, Vinegoni C, Ntziachristos V (2009c) Imaging of mesoscopic-scale organisms using selective-plane optoacoustic tomography. Phys Med Biol 54:2769–2777

Rosencwaig A (1973) Photoacoustic spectroscopy of biological materials. Science 181:657–658

Rosenthal A, Razansky D, Ntziachristos V (2009) Quantitative optoacoustic signal extraction using sparse signal representation. IEEE Trans Med Imag. 28:1997–2006

Rosenthal A, Razansky D, Ntziachristos V (2010) Fast semi-analytical model-based acoustic inversion for quantitative optoacoustic tomography. IEEE Trans Med Imaging 29:1275–1285

Schulz R, Ale A, Sarantopoulos A, Freyer M, Soehngen E, Zientkowska M, Ntziachristos V (2010) Hybrid system for simultaneous fluorescence and X-ray computed tomography. IEEE Trans Med Imag. 29:465–473

Soubret A, Ripoll J, Ntziachristos V (2005) Accuracy of fluorescent tomography in presence of heterogeneities: study of the normalized Born ratio. IEEE Med Imag. 24:1369–1376

Tsien RY (2005) Building and breeding molecules to spy on cells and tumors. FEBS Lett 579:927–932

Wang X, Pang Y, Ku G, Xie X, Stoica G, Wang LH (2003) Noninvasive laser-induced photoacoustic tomography for structural and functional in vivo imaging of the brain. Nat Biotechnol 21:803–806

Webb RH (1999) Theoretical basis of confocal microscopy. Methods Enzymol 307:3–20

Weissleder R, Ntziachristos V (2003) Shedding light onto live molecular targets. Nat Med 9: 123–128

Multifunctional Magnetic Resonance Imaging Probes

Ewelina Kluza, Gustav J. Strijkers and Klaas Nicolay

Abstract

Magnetic resonance imaging (MRI) is a key imaging modality in cancer diagnostics and therapy monitoring. MRI-based tumor detection and characterization is commonly achieved by exploiting the compositional, metabolic, cellular, and vascular differences between malignant and healthy tissue. Contrast agents are frequently applied to enhance this contrast. The last decade has witnessed an increasing interest in novel multifunctional MRI probes. These multifunctional constructs, often of nanoparticle design, allow the incorporation of multiple imaging agents for complementary imaging modalities as well as anticancer drugs for therapeutic purposes. The composition, size, and surface properties of such constructs can be tailored as to improve biodistribution and ensure optimal delivery to the tumor microenvironment by passive or targeted mechanisms. Multifunctional MRI probes hold great promise to facilitate more specific tumor diagnosis, patient-specific treatment planning, the monitoring of local drug delivery, and the early evaluation of therapy. This chapter reviews the state-of-the-art and new developments in the application of multifunctional MRI probes in oncology.

E. Kluza · G. J. Strijkers (✉) · K. Nicolay
Biomedical NMR, Department of Biomedical Engineering,
Eindhoven University of Technology, Eindhoven, The Netherlands
e-mail: G.J.Strijkers@tue.nl

E. Kluza
e-mail: E.Kluza@tue.nl

K. Nicolay
e-mail: K.Nicolay@tue.nl

O. Schober and B. Riemann (eds.), *Molecular Imaging in Oncology*,
Recent Results in Cancer Research 187, DOI: 10.1007/978-3-642-10853-2_5,

Contents

1 The Need for Imaging and Contrast Agents in Oncology

Imaging plays a pivotal role in cancer diagnostics and therapy monitoring. Magnetic resonance imaging (MRI) stands out from other imaging modalities as a high spatial resolution technique with unsurpassed soft-tissue contrast, which enables anatomic, functional as well as metabolic characterization of the lesions. The spectrum of MRI diagnostics is rapidly expanding, as a result of intensive research on molecular and cellular MRI contrast agents. Furthermore, recent developments in multimodality imaging, i.e., the combination of several imaging techniques, is showing great promise in providing detailed information on the status of the disease, which is of crucial importance for early detection and proper diagnosis of cancer, as well as for accurate planning and monitoring of anti-cancer therapies.

Tumor detection with MRI can be achieved by exploiting differences in the compositional, metabolic, cellular, and vascular characteristics of malignant and normal tissue, which are of influence on the detected MRI signals. High cellular density and limited water diffusion in the tumor generates a higher signal intensity compared to surrounding tissues in T_2- and diffusion-weighted images, which enables precise assessment of tumor location and size. Moreover, T_2- and diffusion-weighted methods are sensitive to intratumoral heterogeneities such as local hemorrhages and necrosis. Therefore, they are useful to distinguish the viable from the nonviable tumor tissue. Whole body diffusion-weighted imaging shows promise for diagnosing lesions in the entire body as well as for evaluating lymph node metastases, with high spatial resolution, and sensitivity and specificity that rival ^{18}F-FDG (fluorodeoxyglucose) PET imaging (Chen et al. 2010; Heusner et al. 2010). Moreover, the monitoring of changes in water diffusion, which can be measured with diffusion MRI, has been proposed as a method suitable for early assessment of the efficacy of chemotherapy (Ross et al. 2003).

Despite the success and wide application of anatomic imaging in cancer diagnostics, in many cases, e.g., in breast and prostate cancer, it generally fails to distinguish the malignant from benign or normal tissue. Moreover, therapy

evaluation based on monitoring changes in tumor size or morphology, is often not applicable to new treatment strategies which, in contrast to systemic chemotherapy or radiation therapy, aim to attack the tumor cells more specifically, e.g., via molecular targets or via anti-angiogenic and gene therapy approaches. In a response to these new demands for therapy monitoring, alternative methods of cancer imaging are under development. While some of these have already gained an established position in clinical oncology, other imaging strategies are still in the preclinical evaluation phase.

Measurements of vascular function were found to be very useful in cancer detection and therapy monitoring. The idea of this type of imaging is based on the functional and morphologic differences between the tumor and normal vasculature. The tumor blood supply, formed in the process of angiogenesis, is generally characterized by enhanced vessel permeability and density, increased blood volume and irregular flow. Tumor blood vessels often are of variable shape and size, and may be composed of both functional and nonfunctional vessel loops. Among the MRI methods that provide information on the vascular status, arterial spin labeling (ASL) (Detre and Alsop 1999; Detre et al. 2009), and blood oxygenation level dependent (BOLD) imaging (Robinson et al. 1997) do not require injection of a contrast agent. ASL has mainly been used to assess the blood flow in brain tumors (Silva et al. 2000; Wolf et al. 2005; Kimura et al. 2006; Moffat et al. 2006). BOLD imaging has been demonstrated to correlate with blood volume (Lüdemann et al. 2006) and to predict vascular maturation in tumors by measuring the degree of vasoreactivity (Gilead et al. 2004). Nevertheless, the most widespread method for measuring vessel function currently is dynamic contrast-enhanced MRI (DCE-MRI) with low-molecular weight gadolinium (Gd)-based contrast agents.

DCE-MRI allows the assessment of pharmacokinetic parameters, which help to characterize tissue perfusion and vessel permeability. The diagnostic potential of DCE-MRI has been extensively exploited in the detection of breast and prostate cancer (Turnbull 2009). Moreover, due to its sensitivity toward changes in vascular density and permeability, it has become a primary method in monitoring therapy-induced vascular changes. As a result, DCE-MRI is widely applied in clinical trials of angiogenesis inhibitors and vascular disrupting agents (O'Connor et al. 2007). Moreover, the appearance of poorly perfused regions in the tumor, detected with DCE-MRI, has been employed as early marker of the response to chemo- and radiotherapy (Turnbull 2009). The development of new blood pool agents, such as albumin-conjugated Gd chelates and Gd-containing dendrimers, opened a new research line of macromolecular DCE-MRI (Dafni et al. 2003, 2008; Daldrup-Link and Brasch 2003). The macromolecular agents are not able to pass through the normal endothelium, and therefore they are potentially more suitable for selective imaging of tumor vessel permeability and more accurate assessment of tumor blood volume compared to the traditional Gd-based agents. Currently, this imaging strategy is mostly evaluated in preclinical research.

The detection of molecular markers, which are exclusively expressed during a pathological process, is considered the most specific method of characterizing disease. In oncology, the field of molecular imaging has been stimulated by the

development of targeted anti-cancer therapies (Ferrara and Kerbel 2005). The success of these novel treatment strategies is dependent on the presence of the target molecule. Therefore, noninvasive assessment of its expression is considered as the ultimate screening method, enabling selection of patients that are most likely to benefit from a certain type of treatment. Furthermore, molecular imaging can be used for an early evaluation of therapy, since changes on the molecular level precede anatomic and functional alternations, currently used as therapeutic endpoints. By monitoring molecules, which are directly involved in the drug action pathway, the evaluation will be far more specific than that based on secondary (indirect) effects. In addition, the imaging of cancer type-specific markers can be useful in the assessment of the primary origin of tumor metastasis, which has great impact on the choice of the treatment strategy.

Despite its promises and recent successes, imaging of molecular and cellular targets with MRI remains very challenging. The detection of contrast agent by MRI is less sensitive as compared to the nuclear methods and quantification is not as straightforward. Nevertheless, the promise of high-resolution detection and quantification of local marker expression is not easily fulfilled by any other imaging technique. Therefore considerable effort has been put in overcoming these challenges, fueling the design of many new powerful MRI-detectable agents. Potent (nano) particulate Gd- and ironoxide-based constructs have received particular attention in this respect. In addition to generating the desired change in MRI signal, contrast agents for molecular imaging have to specifically and efficiently bind to the biological targets. This can be achieved by functionalizing imaging agents with ligands having high binding affinity to the molecular target of interest.

The MRI visualization of tumor-specific molecular epitopes and processes has been demonstrated in various preclinical studies, showing great promise to this diagnostic strategy (Strijkers et al. 2007, 2010). Next to imaging cancer cell-specific biomarkers, imaging of the vascular endothelium in the tumor received a particular great deal of attention. The interest in this area is related to the clinical application and successes of anti-angiogenic therapies (Ferrara and Kerbel 2005). Moreover, activated endothelium is an attractive imaging target, as it overexpresses multiple receptors, which are absent on the endothelial layer of mature vessels, and it is directly accessible for a systemically administrated agent (Barrett et al. 2007; Neeman et al. 2007). We should realize however that the field of molecular imaging is in an early stage of its development. Hand-in-hand with exciting preclinical results, the research field revealed various difficulties in the practical and clinical application of this concept. Major obstacles are related to the toxicity of new contrast agents, small signal alterations produced in vivo by target-associated media, and the unspecific uptake of contrast agents by other components of the microenvironment. Future improvements in efficacy and specificity of targeted imaging probes will eventually determine their utility in the clinical setting.

Imaging methods, which reliably predict the outcome of the anti-cancer therapy, are highly desired in oncological diagnostics. The information obtained using such early evaluation strategies would enable a rapid patient-specific adjustment of the treatment scheme. Exposure of the tumor tissue to the administered drug is essential

for the therapeutic effects to occur. Therefore, drug delivery monitoring has been proposed as a valuable predictive readout of treatment efficacy. For this purpose, multifunctional probes, combining therapeutic and (multimodal) imaging properties, are desired. Already, successful proof-of-concept applications have been demonstrated in preclinical studies investigating the mechanisms of drug anti-cancer activity, as well as drug pharmacokinetics and biodistribution. Moreover, MR-sensitive systems have been designed to monitor the intratumoral drug release from nanocarriers. The ongoing work in this field will eventually provide insights into the relationship between the local drug accumulation efficacy and the therapeutic effects. This evaluation will determine whether the monitoring of drug delivery to the tumor can be used as a predictive method in cancer treatment.

The above considerations stress the need for novel multifunctional MRI probes that can be applied in tumor diagnostics, patient-specific treatment planning, the monitoring of local drug delivery and the early evaluation of therapy. In this chapter, first the available technology concerning imaging and multifunctional probes will be reviewed in Sects. 2, 3, and 4, which deal with DCE-MRI and novel contrast-enhanced imaging in oncology, respectively. New developments in combined imaging and therapy will be discussed in Sect. 5. Finally, Sect. 6 concludes with some perspectives on translation of the techniques toward clinical use.

2 Imaging Techniques and Contrast Agents

2.1 Magnetic Resonance Imaging of Cancer

The use of MRI has seen a tremendous growth in clinical oncology in the last decade, both in terms of the quantity of examinations as well as in the variety of diagnostic readouts that can be provided by the technique. The success of MRI mainly results from the ability to produce detailed anatomic images of patients with resolutions down to typically 1 mm in routine clinical use. Apart from the anatomic information, which is obviously important in the diagnosis and management of cancer, MRI offers a number of physiologic and metabolic readouts of tissue status, which could reveal important additional information on the tumor tissue status. Contrast agents are frequently applied to enhance the contrast between healthy and tumor tissue or to highlight the vascular bed that supplies the tumor with blood. Extensively discussed in this chapter are the novel MRI contrast agents, designed to report on tumor-specific metabolic processes and cells, providing a molecular fingerprint of the tumor which can be used for diagnosis, to aid in treatment decisions, or to monitor the effects of anti-cancer therapy. Figure 1 schematically shows a collection of MRI techniques that are available for tumor imaging and characterization. Methods range from already clinically applied anatomic imaging techniques to novel experimental techniques, which are currently in a preclinical development stage.

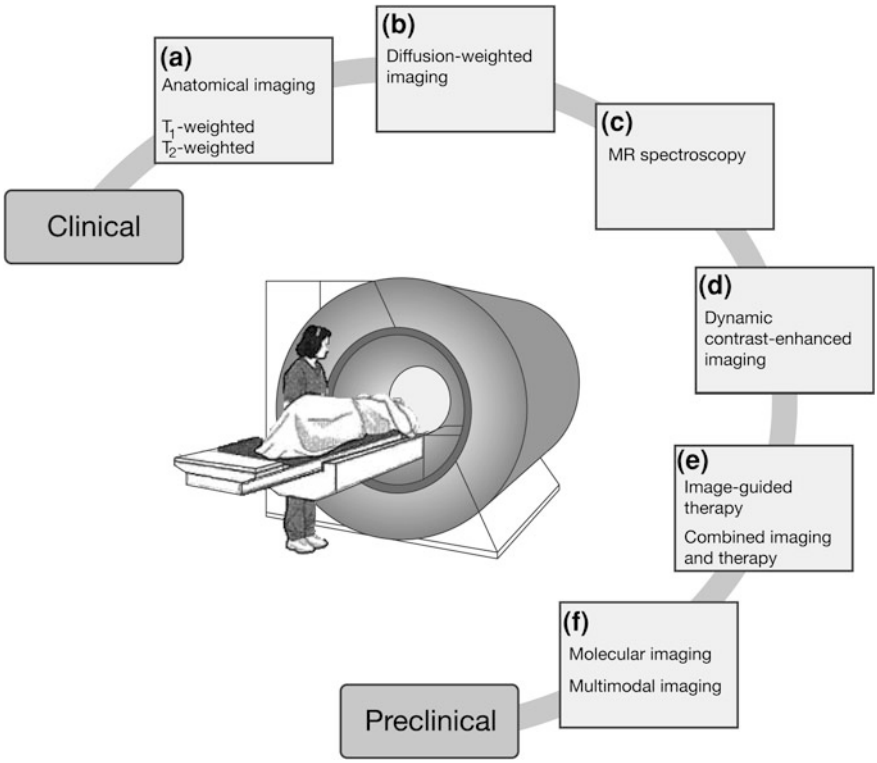

Fig. 1 MRI of cancer—clinical and preclinical techniques. **a** T_1- and T_2-weighted MRI are commonly used to diagnose and localize malignant tissue and in preoperative surgical planning. **b** Diffusion-weighted MRI has the potential to differentiate malignant from benign or healthy tissue and may serve as an imaging biomarker of early response to treatment. **c** MRS provides a metabolic fingerprint of the tumor, which aids in diagnosis and guides detection of early metabolic responses to treatment. **d** Contrast-enhanced imaging using low-molecular weight Gd-based contrast agents provides a clinical tool to characterize the tumor vasculature and its permeability. Novel macromolecular blood pool agents, which report on tumor blood volume and lymphatic drainage, are under preclinical development. **e** Various MRI techniques can be used to monitor the response to treatment. Traditionally, readouts are based on morphometric properties, such as tumor shrinkage. Other readouts include early changes in the tumor vasculature and metabolism. Novel nanoparticles that combine imaging labels with therapeutic drugs in a single agent are under preclinical development. **f** Molecular MRI using targeted contrast agents may someday provide physicians with patient-specific imaging readouts of molecular and cellular processes in the tumor. Multimodal combinations of MRI with other modalities, i.e., nuclear or fluorescence imaging, has the potential to provide complimentary information on the tumor status

MRI exploits the presence of mobile protons present in tissue water and lipids to create images of the interior of the human body (Haacke et al. 1999). For making the MR images, a patient is placed inside the MRI scanner in a strong static magnetic field. The magnetic field induces a minute imbalance in the number of spin-up versus spin-down protons; creating a tiny tissue magnetization, the

magnitude of which is dependent on the local concentration of protons. This magnetization can be disturbed by transient radiation with an external resonant radio-frequency (RF) electromagnetic field—the RF pulse. The RF pulse rotates the tissue magnetization away from the static magnetic field and MRI signals are subsequently recorded as induction voltages. In a typical MRI sequence, series of RF pulses are suitably combined with magnetic field gradients to produce many spatially encoded MRI signals, which are then reconstructed into an MR image. Signal intensities in the MR images reflect the local proton density, but are also influenced by the rate by which the magnetization returns back to equilibrium, a process known as relaxation. Two principal relaxation processes are distinguished: spin–lattice or longitudinal relaxation (T_1) and spin–spin or transversal relaxation (T_2). Transversal relaxation may be accelerated by magnetic field inhomogeneities, in which case it is referred to as T_2^*. T_1 relaxation describes the increase of the magnetization vector toward equilibrium in the direction of the static magnetic field (longitudinal direction), while T_2 and T_2^* reflect the decrease of magnetization in the perpendicular transversal plane. Differences in the intrinsic longitudinal and transversal relaxation times are an important source of contrast between healthy and tumor tissue.

Most solid tumors are characterized by prolonged relaxation times as compared to their host tissue (de Schepper and Bloem 2007). It is essentially impossible to directly relate the higher relaxation times to specific features of the tumor tissue microstructure. The altered relaxation times probably reflect a combination of various factors, including increased tissue water content, changes in intracellular and extracellular volume fractions or water exchange kinetics, and alterations in the way water is interacting with macromolecules. By tuning the MRI sequence to maximize contrast between tumor and host, T_1- and T_2-weighted imaging are powerful tools in the detection and classification of tumors. The elevation of T_1 and T_2 in tumors is usually less than found in inflammatory lesions. However, there is a considerable overlap, which makes distinction between these two kinds of pathologies often not straightforward.

MRI of tumors benefits a lot from the use of contrast agents. Most MRI contrast agents act by shortening the T_1 and T_2 relaxation times of protons in the vicinity of the agent (Caravan et al. 1999; Strijkers et al. 2007). Contrast agents are usually classified according to their preferred use in T_1-weighted or T_2-weighted imaging. Most T_1 contrast agents are based on the paramagnetic metal ion Gd^{3+}. For clinical application the Gd ion is coordinated to a protective chelate to form a stable nontoxic complex. Lowering of the T_1 relaxation time by the contrast agent leads to an increase in the MRI signal intensity in T_1-weighted images and therefore these agents are also referred to as positive contrast agents. T_2 agents are commonly superparamagnetic nanoparticles of iron oxide (SPIO), which locally disturb the magnetic field and therefore lead to a decrease in the signal intensity in T_2-weighted MRI. T_2 agents are therefore also referred to as negative contrast agents. The potency of a contrast agent to shorten the T_1 and T_2 relaxation times is expressed by the relaxivity r_1 and r_2, respectively. Relaxivity r_1 and r_2 are defined by the change in $1/T_1$ and $1/T_2$ as function of contrast agent concentration in

units $mM^{-1}s^{-1}$. Novel multifunctional probes for multimodal imaging are discussed in Sect. 2.2. Traditionally, MRI contrast agents are used to probe the tumor vasculature (Sect. 3). New applications include the use of targeted contrast agent to characterize the tumor on a molecular level and the combination of imaging and therapy. These applications will be discussed in the Sects. 4 and 5 of this chapter.

Although the focus of this chapter is on the use of exogenous MRI probes, two other MR techniques are worth mentioning here: diffusion-weighted MRI and magnetic resonance spectroscopy (MRS). Diffusion, i.e., the thermally driven microscopic motion of water molecules, differs in tumor lesions in comparison to healthy tissue. This has motivated the use of diffusion-weighted MRI techniques for tumor imaging (Chenevert et al. 1997, 2002; Ross et al. 2003; Kwee et al. 2009; Padhani et al. 2009). The MRI signal intensity can be made sensitive to diffusional displacements of water protons by adding a pair of strong magnetic field gradients in the MRI sequence, which leads to an attenuation of the signal that is exponentially dependent on the so-called apparent diffusion coefficient (ADC; units mm^2/s). The diffusion-based contrast is experimentally controlled by the b-value (units s/mm^2), which indicates the degree of diffusion weighting and can be adjusted by changing the strength of the gradients or their timing. The ADC is an attractive imaging parameter as it reflects an endogenous physical tissue property that is essentially independent of the protocol or scanner type. In general, malignant tumors have lower ADC values than benign ones and healthy tissue (Taouli et al. 2003), which is related to a complex mix of microstructural tissue properties, including higher cellular density, structural disorganization, different concentrations of macromolecules, altered water proton exchange kinetics between the intracellular and extracellular compartments, as well as increased extracellular tortuosity. However, differences in ADC values are tumor-type dependent, which limits the sensitivity of the diffusion-weighted MRI technique to provide specific diagnosis and to distinguish benign from malignant tissue (Sinha et al. 2002; Woodhams et al. 2005; Parikh et al. 2008). Nevertheless, changes in cellular density as a result of necrosis or apoptosis, induced by successful anticancer treatment, cause substantial changes in the ADC values. Therefore, diffusion-weighted MRI may be an effective imaging biomarker for treatment outcome. These changes in ADC have been shown to occur well before macroscopic readouts of response, such as tumor volume become apparent (de Vries et al. 2003; Thoeny et al. 2005).

MRS provides chemical information about tissue metabolites. In contrast to conventional MRI, which detects the presence of mainly water and lipids, MRS generally depicts the resonance spectra of chemical compounds other than water to obtain a metabolite fingerprint of the tumor. MRS is not restricted to proton (^1H) detection, but also carbon (^{13}C), phosphorus (^{31}P), and sodium (^{23}Na) are attractive nuclei as they are present in several compounds that play a role in tumor metabolism. Both ^1H- and ^{31}P-MRS have revealed significant disturbances in the levels of amino acids, lipids, and phosphorus-containing metabolites within tumors compared to healthy tissue (Preul et al. 2000; Schwarz et al. 2002; Shukla-Dave et al. 2002; Meisamy et al. 2004; Manton et al. 2006; Wu et al. 2006). The crucial

roles of MRS are in the refinement of differential diagnosis data, which is used to guide surgical procedures, and in the detection and monitoring of the tumor's metabolic response to therapy.

2.2 Multifunctional Imaging Probes

The last decade has witnessed an explosive development of novel multifunctional imaging probes for applications in tumor imaging and treatment. These multifunctional imaging probes show great promise to improve the detection of morphologic and molecular changes responsible for the disease pathogenesis, to aid in disease diagnosis, to monitor therapy, as well as to report on the in vivo delivery of a therapeutic agent. Examples of multifunctional probes are dendrimers, polymeric and lipid-based nanoparticles, magnetic nanocrystals, carbon nanotubes, as well as modified endogenous agents based on proteins, antibodies, lipoproteins, or viruses.

Figure 2 schematically depicts a multifunctional imaging probe of a generic design, which serves here as a model for the nanoparticles used in many cancer-related studies (Guccione et al. 2004a, b; McCarthy et al. 2007; Torchilin 2007; Islam and Harisinghani 2009; Kaneda et al. 2009; Shubayev et al. 2009; Lanza et al. 2010; Strijkers et al. 2010). The nanoparticles for cancer imaging and treatment are commonly submicron-sized particles with a diameter of the order of a few to several hundreds of nanometers. Spherical hollow capsules of well-defined size enclosing an aqueous interior can be made by exploiting the self-organizing capabilities of amphiphilic phospholipids (liposomes) or polymers (polymersomes). Depending on the properties and intended application, a high payload of MRI contrast agent can be physically entrapped in the aqueous interior of the nanoparticle (Caride et al. 1984; Magin et al. 1986; Navon et al. 1986; Devoisselle et al. 1988; Koenig et al. 1988; Unger et al. 1988; Tilcock et al. 1989; Fossheim et al. 1999; 2000), integrated in the corona, or covalently bound to the surface (Kabalka et al. 1991; Mulder et al. 2006; Oliver et al. 2006; Hak et al. 2009). The nanoparticles allow for incorporation of multiple imaging agents for multimodal imaging, e.g., nuclear tracers (Lijowski et al. 2009) and fluorescent dyes (Mulder et al. 2004). Likewise, water-soluble therapeutic compounds can be entrapped in the aqueous interior or covalently bound to the surface, whereas water-insoluble drugs can be incorporated in the corona (Winter et al. 2008). In order to deliver the imaging agent in therapeutic quantities to the tumor, the nanoparticles need to stay in blood circulation for a sufficient amount of time without being excreted. The size of the nanoparticles should be large enough to prevent rapid leakage out of normal capillaries, while small enough to evade fast capture by macrophages. Without suitable surface modifications the particles are generally recognized in the circulation by the reticuloendothelial system (RES) of the liver and the spleen, resulting in rapid blood elimination. A common approach to increase the blood circulation time and improve the pharmacokinetic profile of the nanoparticle is to coat its surface with a hydrophilic polymer, such as

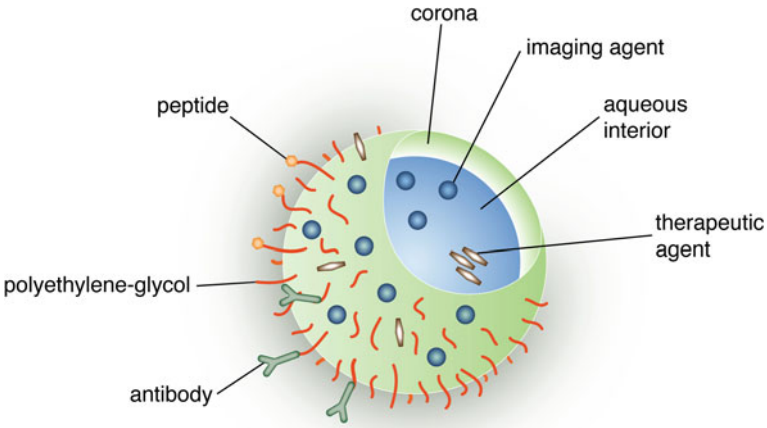

Fig. 2 Generic design of a nanoparticle for combined imaging and therapy. The spherical hollow capsule of well-defined size encloses an aqueous interior. Imaging probes for multimodal imaging can be enclosed in the aqueous interior, be an integral part of the corona, or covalently bound to the surface of the particle. Likewise, water-soluble therapeutics can be entrapped within the aqueous interior or covalently bound to the surface, whereas water-insoluble drugs may be entrapped within the corona. To improve the blood circulation time the surface of the nanoparticle can be coated with a hydrophilic polymer, such as (PEG). The nanoparticles may be further improved for cancer imaging and treatment by functionalizing their surface with ligands, such as antibodies and peptides, for active recognition of tumor-specific biomarkers

polyethylene glycol (PEG), which serves to repel plasma proteins (Klibanov et al. 1990; Drummond et al. 1999).

Tumor vasculature is highly heterogeneous. The tumor blood vessels display an irregular organization with increased tortuosity and enhanced endothelial permeability. Tumors often exhibit areas, which are highly vascularized to sustain sufficient supply of oxygen and nutrients to the metabolically active tumor cells, as well as areas with extensive necrosis. These unique tumor vascular properties enable nanoparticles to extravasate in the tumor by the enhanced permeability and retention (EPR) effect (Greish 2007). Additionally, the lymphatic drainage is compromised, resulting in fluid retention and contributing to the accumulation of the nanoparticles in the interstitial space of the tumor.

The nanoparticles may be further improved for cancer imaging and treatment by functionalizing their surface with ligands for active recognition of tumor -specific biomarkers. Examples of ligands that can be used to target tumor-associated antigens include antibodies, antibody fragments, aptamers, peptides, saccharides, or small molecules. Active targeting of the tumor can be employed to increase the specific accumulation of the nanoparticles in the tumor. Additionally, targeting ligands may be applied to improve the uptake of drug-containing nanoparticles by tumor cells via receptor-mediated endocytosis. Equipping the nanoparticles with active targeting ligands potentially shortens their blood

circulation time, as the ligands may be recognized by macrophages of the RES as well. Type and number of targeting ligands should therefore be carefully balanced with respect to circulation time and targeting properties in order to ensure optimal accumulation of nanoparticles in the tumor.

3 Probing the Tumor Vasculature

Tumor blood vessels are formed in the process of angiogenesis by sprouting from pre-existing host vessels (Folkman 1971). A trigger for angiogenesis is hypoxia, which is induced in the tissue by rapidly multiplying neoplastic cells (Shweiki et al. 1992, 1995). The angiogenic cascade that follows is regulated by pro-angiogenic factors such as vascular endothelial growth factor (VEGF) and basic fibroblast growth factor (bFGF), and involves proliferation, migration and differentiation of endothelial cell to form new capillaries. The newly formed tumor vessels are usually dilated, hyperpermeable, and disorganized. Functional vasculature is essential for tumor growth and metastasis formation (Folkman 2002). Therefore, parameters related to the tumor vascular status serve as important diagnostic and prognostic factors in oncology (Turnbull 2009). Moreover, they are used as surrogate markers of the therapeutic efficacy of anti-cancer agents.

Microvessel density (MVD), which reflects the average vessel count per area of the tumor biopsy section, is currently the most commonly used marker of tumor angiogenesis (Des Guetz et al. 2006). It has been first proposed by Weidner et al. as a predictor of the tumor aggressiveness and metastatic potential (Weidner et al. 1991). MVD assessment, however, is an invasive histologic technique, and this readout is limited to small tissue samples. Crucially, it does not provide information on the functional status (perfusion capacity) of the tumor vessels. In addition to MVD, the tumor tissue expression of the main pro-angiogenic factor VEGF has been shown to be a valuable prognostic biomarker (Des Guetz et al. 2006).

As alternative to the aforementioned histopathologic methods, noninvasive strategies have been developed, among which the vascular imaging with MRI plays a prominent role. MRI readout enables characterization of the vasculature in the entire tumor and stroma volume, and permits the longitudinal follow-up of the patient. Importantly, the functional status of the tumor vessels can be assessed. In addition to functional imaging, intensive research on targeted MRI contrast agents promises to expand the MRI application for the visualization of molecular markers of angiogenesis (Neeman et al. 2007; Strijkers et al. 2010). Molecular imaging of angiogenesis is believed to provide more specific determination of the tumor angiogenic activity compared to the currently used methods. This is particularly important for the selection and monitoring of patients undergoing anti-angiogenic therapies.

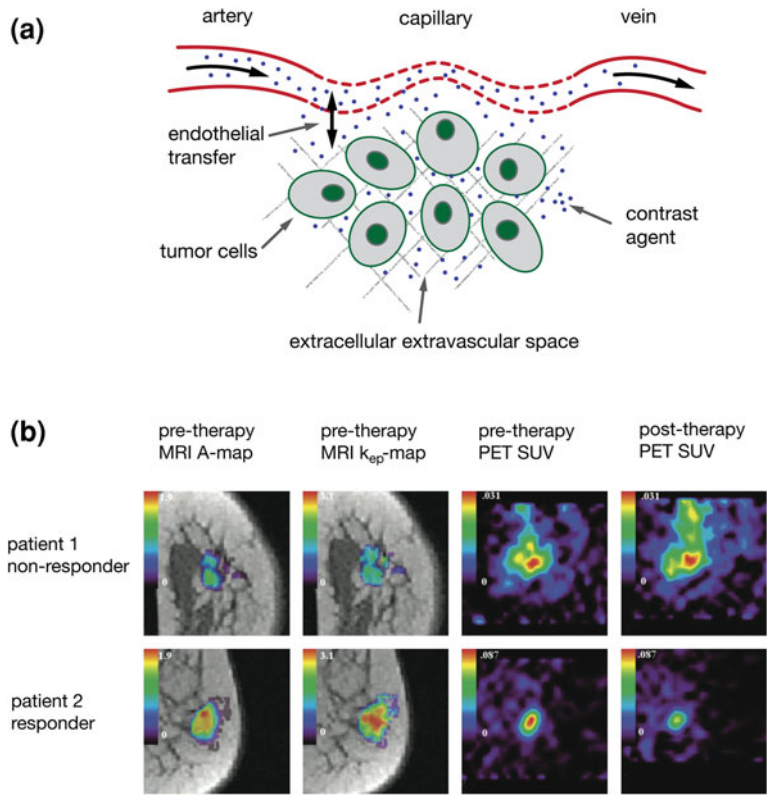

Fig. 3 DCE-MRI. **a** Schematic illustration of the DCE-MRI technique in tumor tissue. Intravenously injected MRI contrast agent arrives from arteries in the capillary bed of the tumor tissue and extravasates into the tumor extracellular space. The kinetics of signal changes observed in the tumor can be fitted qualitatively or quantitatively using pharmacokinetic multi-compartment models to provide characterization of tissue perfusion, capillary permeability, exchange kinetics, and the volume of EES. **b** DCE–MRI results from two patients with advanced ductal carcinomas of the breast. The pre-therapy initial amplitude of DCE–MRI signal enhancement **a** and exchange rate constant (k_{ep}; units min^{-1}) exhibited significant correlation with treatment response as assessed by ^{18}F-FDG PET standardized uptake values (SUV). Patient 1-a non-responder-displayed low pre-therapy A and k_{ep}, with no subsequent changes in post-therapy PET SUV after one cycle of chemotherapy. Patient 2-a responder-revealed higher pre-therapy A and k_{ep}, with a significant reduction in PET SUV after one cycle of chemotherapy. Reproduced with permission (Semple et al. 2006)

3.1 Dynamic Contrast-Enhanced MRI

DCE-MRI with low-molecular weight contrast agents is the most widely applied vascular MRI method, both in the preclinical and clinical settings. In DCE-MRI, the vascular function is assessed indirectly by monitoring the pharmacokinetics of an intravenously administered contrast agent with dynamic T_1-weighted imaging.

Gd-chelates, commonly used for this purpose, are small hydrophilic molecules characterized by short circulation half-life of typically less than half an hour. Examples of these contrast agents are Gd-DTPA (Magnevist), Gd-HP-DO3A (Prohance), and Gd-DOTA (Dotarem). After systemic injection, these agents are rapidly distributed throughout the body, passing through the endothelium of normal vessels, with the exception of those of the central nervous system (CNS). However, in pathological processes such as a brain tumor, which are associated with the disturbance of blood brain barrier, Gd-chelates are able to accumulate in the affected regions of the CNS as well. After reaching the tissue, the agent remains in the extracellular space. A short period with a concentration plateau, regulated by equal influx and efflux rates, is followed by the washout phase.

Although Gd-chelates are able to pass the normal endothelium, generating contrast in normal tissue, specific features of tumor vessels enable their differentiation from the surrounding tissue. Briefly, the degree of signal enhancement depends on the tissue perfusion, the arterial input function (AIF, i.e., the concentration-time course of contrast agent in the artery supplying the tissue), the capillary surface area, the capillary permeability and the volume fraction of the extracellular extravascular space (EES). The hyperpermeability and, usually, large volume of the tumor vascular bed are key factors, which contribute to strong DCE-MRI signal changes in the tumor. Figure 3a schematically illustrates the basic principles of DCE-MRI in tumor tissue. In order to assess kinetic parameters, which reflect the tumor vasculature function, signal changes following the administration of a Gd-chelate must be converted into the contrast agent concentration–time curves. To this aim, baseline T_1 values are measured in the tumor before DCE-MRI acquisition. Alternatively, the reference tissue method is applied (Kovar et al. 1998). The descriptive kinetic parameters such as the initial amplitude of MRI signal enhancement (A), initial area under the contrast agent concentration–time curve (IAUC), initial slope or time to peak (TTP) of the concentration–time curve are derived without using pharmacokinetic modeling. These parameters are straightforward, however, they are highly influenced by the experimental setup (Leach et al. 2005). In contrast, pharmacokinetic parameters, such as the endothelial transfer coefficient (K^{trans}), the exchange rate constant (k_{ep}), the EES fractional volume (v_e), assessed by using mathematical models to fit the data (Tofts et al. 1999), are considered to be more physiologically meaningful and they are less sensitive to the experimental conditions (Leach et al. 2005).

DCE-MRI is increasingly used in cancer diagnostics and screening of patients at high risk of developing breast cancer (Turnbull 2009). The discrimination between malignant and benign or normal tissue is often based on the subjective evaluation of the relative signal–time curves (Kuhl et al. 1999; Turnbull 2009). However, the implementation of the quantitative approach, both empirical and pharmacokinetic, has been shown to improve the accuracy and specificity of lesion differentiation (Turnbull 2009). Because of its sensitivity to vascular alternations, DCE-MRI also plays an important role in monitoring the response to anti-cancer treatment. DCE-MRI has been applied for the assessment of early effects of chemo- and radiotherapy (Martincich et al. 2004; de Lussanet et al. 2005; Semple

et al. 2006). A significantly decreased tumor vascular function was found to be correlated with a positive response to the treatment. Moreover, pharmacokinetic parameters were proposed as potential early predictive markers of long-term therapeutic outcome. Figure 3b shows DCE-MRI results from two patients with advanced ductal carcinomas of the breast (Semple et al. 2006). The pre-therapy DCE-MRI initial amplitude of MRI signal enhancement (A) and exchange rate constant (k_{ep}) exhibited significant correlation with treatment response as assessed by ^{18}F-FDG PET standardized uptake values (SUV). Reduction in ^{18}F-FDG PET metabolism is known to correlate with histologic response to primary chemotherapy. For example, Patient 1-a non-responder-displayed low pre-therapy A and k_{ep}, with no subsequent changes in post-therapy PET SUV after one cycle of chemotherapy. Patient 2-a responder-revealed higher pre-therapy A and k_{ep}, with a significant reduction in PET SUV after one cycle of chemotherapy. A number of patient studies demonstrated a good correlation between the DCE-MRI and histopathologic assessment of the residual disease after neoadjuvant treatment (Akazawa et al. 2006; Belli et al. 2006). Anti-angiogenic and anti-vascular therapies, modulating the tumor vasculature, benefit the most from DCE-MRI-monitoring, since the conventional evaluation criteria, such as tumor shrinkage, are often not applicable for these treatment strategies. The most frequently used quantitative markers of the vascular effects K^{trans} and IAUC (Leach et al. 2005; O'Connor et al. 2007), integrate key features of the tumor vasculature—endothelial permeability and blood flow. Since the treatment may affect only one of these vascular properties, it is desirable to obtain separate estimates of the endothelial permeability and blood flow. This requires, however, high temporal resolution, which can be achieved at the cost of decreasing either the spatial resolution or the coverage of the region of interest (Turnbull 2009). An important feature of the tumor vasculature is its heterogeneity. Therefore, pixel-by-pixel analysis of DCE-MRI data is the preferred method, providing parameter maps (Jackson et al. 2007). The analysis of the distribution has been shown to improve the diagnostic accuracy and prognosis of breast cancer (Issa et al. 1999) and high-grade gliomas (Mills et al. 2006). Moreover, it provided better prediction of the therapeutic response in breast cancer patients (Chang et al. 2004) and tumor recurrence after radiotherapy in patients with cervical carcinoma (Mayr et al. 2000), as compared to mean or median value.

3.2 Macromolecular Dynamic Contrast-Enhanced MRI

Macromolecular DCE-MRI is a novel and increasingly popular preclinical imaging method. It exploits a blood pool agent to assess the tumor vascular characteristics (Daldrup-Link and Brasch 2003). The pharmacokinetic properties of macromolecular contrast media differ considerably from those of the low-molecular weight Gd-chelates. Their macromolecular size, ranging from a few to a few hundred nanometers, does not allow them to cross the endothelial layer of normal vessels.

Moreover, generally they are designed as long-circulating agents with a blood circulation half-life of the order of several hours. In the tumor microenvironment, the enhanced endothelial permeability enables extravasation of macromolecular agents. However, this process is much slower than in the case of low-molecular weight contrast agents. Therefore, the separate assessment of vascular parameters, such as blood volume and vascular permeability, is considered to be more accurate (Daldrup-Link and Brasch 2003). As with conventional DCE-MRI, the arterial input function and baseline T_1 maps are required to convert signal intensity into contrast agent concentration data. Subsequently, using multi-compartment pharmacokinetic models, quantitative values for the tumor blood volume and vascular permeability are obtained (Shames et al. 1993; Brasch et al. 1994).

Albumin functionalized with multiple Gd-DTPA groups (albumin-$(Gd\text{-}DTPA)_x$) is a prototype macromolecular contrast agent (MMCA) (Ogan et al. 1987; Schmiedl et al. 1987). Despite its very high longitudinal relaxivity, albumin-$(Gd\text{-}DTPA)_x$ produces lower contrast enhancement in the tumor compared to Gd-complexes (Daldrup et al. 1998). This is due to its limited distribution volume, which, on the other hand, is beneficial in terms of specificity toward tumor vasculature. Quantitative estimates of the vascular permeability assessed from albumin-$(Gd\text{-}DTPA)_x$-enhanced data are useful in differentiation between benign and malignant tumors (Daldrup et al. 1998), tumor grading (Su et al. 1998; Turetschek et al. 2001) and therapy monitoring (Cohen et al. 1994; Schwickert et al. 1996). Moreover, albumin-$(Gd\text{-}DTPA)_x$ has been applied in imaging of the tumor lymphatic drainage and interstitial convection (Dafni et al. 2003, 2008).

Figure 4 illustrates a preclinical application of a macromolecular contrast agent in a prostate cancer bone metastasis mouse model (Dafni et al. 2008). DCE-MRI using macromolecular biotin-BSA-Gd-DTPA was performed at week 2 and week 4 after intratibial injection of the tumor cells. At the first time-point, the tumor had infiltrated the bone marrow, and at the second time-point the tumor had progressed into neighboring muscle. At week 2 (Fig. 4a), application of the macromolecular contrast agent resulted in high initial contrast enhancement of bone marrow, reflecting a high blood volume fraction and high vascular permeability, whereas contrast enhancement was low in the tumor that infiltrated the bone marrow. At week 4, when the tumor had grown into neighboring muscle, a different picture emerged (Fig. 4b). Injection of macromolecular contrast agent resulted in high contrast enhancement in the tumor. A pixel-wise analysis of the tumor (Fig. 4c) revealed regions of early-enhancing pixels, representing tissue with a high number of permeable tumor blood vessels, as well as slowly enhancing draining pixels into which the macromolecular contrast agent is transported by interstitial convection. In the same study, it was subsequently shown that treatment directed toward the platelet-derived growth factor receptor (PDGFR) resulted in significant reduction of the vascular permeability of the tumor. This study demonstrated that macromolecular MRI provides a powerful tool in the preclinical evaluation of drugs that attack tumor vascular function.

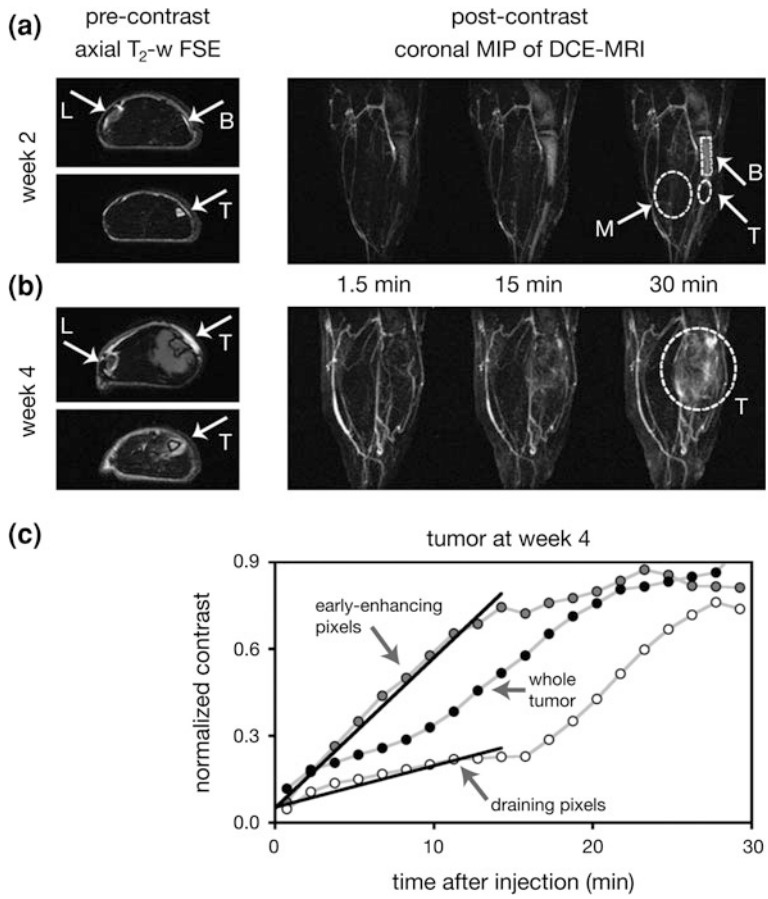

Fig. 4 Macromolecular dynamic contrast-enhanced MRI. (**a**, **b**) Axial and coronal MR images of the hind leg of a mouse 2 and 4 weeks after intratibial injection of prostate cancer cells. Axial pre-contrast T_2-weighted MR images were made with a fast-spin-echo (FSE) sequence. Coronal images were made after intravenous injection of macromolecular biotin-BSA-Gd-DTPA with a three-dimensional spoiled gradient recalled (SPGR) echo sequence and presented as maximum intensity projections (MIP). B = bone; L = lymph node; M = muscle; T = tumor. **a** At week 2, the initial contrast enhancement in bone marrow was high, indicating high blood volume fraction and high vascular permeability, whereas enhancement in the tumor, which was infiltrated in the bone marrow, was low. **b** At week 4, the tumor had spread into surrounding tissue. Contrast enhancement in the tumor was high. **c** Pixel-wise analysis of tumor signal enhancement at week 4 revealed areas of early-enhancing pixels, representing tissue with a high number of permeable tumor blood vessels, as well as slowly enhancing draining pixels into which the macromolecular contrast agent is transported by interstitial convection. Reproduced with permission (Dafni et al. 2008)

Drawbacks for clinical translation of protein-based macromolecular contrast agents are a slow elimination rate and potential immunologic toxicity. Therefore, other types of macromolecular blood pool contrast agents are developed, including non-

protein-based Gd-containing macromolecules, low-molecular weight Gd-chelates that bind to serum albumin and ironoxide particles (Daldrup-Link and Brasch 2003; Barrett et al. 2006).

Among the macromolecular Gd agents, we can distinguish slow- and rapid-clearance media, depending on their molecular weight. The slow-clearance media are larger than 50 kDa, which prevents rapid elimination via glomerular filtration. Example of slow-clearance blood pool agents are biodegradable compounds such as polylysine (Opsahl et al. 1995; Aime et al. 1999) and polysaccharide (Helbich et al. 2000), polyglycol polyethylenimine (Brasch 1992), and dextran (Meyer et al. 1994). Rapid-clearance media are typically 10–50 kDa in size. Examples include the Gd-cascade polymer Gadomer-17 and P792 (Vistarem), which are currently in clinical evaluation. An interesting additional group of MMCAs are Gd-complexes, which bind reversibly to endogenous albumin, such as Gd-BOPTA (MultiHance) or MS-325 (AngioMARK/Vasovist). In the latter case, the albumin-bound molecules exists in equilibrium with the unbound fraction. The unbound component is eliminated via the kidney by glomerular filtration. The coexistence of these two contrast agent populations results in a very complex distribution due to the coexistence of both MMCA and low-molecular weight agent kinetics.

Ultrasmall iron oxide particles (USPIOs), such as Feruglose (Clariscan) or Ferumoxtran-10 (Resovist S), are used as blood pool contrast agents as well. In addition to the above blood volume and vascular permeability assessment, delayed imaging after intravenous injection with USPIOs have been employed to detect metastatic spread in lymph nodes, liver and bone marrow (Hudgins et al. 2002; Michel SCA et al. 2002). Interestingly, the USPIO-based readout also provides estimates of the vessel diameter (Tropres et al. 2001), which can serve as a valuable marker of the anti-angiogenic effects. So far, however, neither of the blood pool MRI contrast agents is routinely used in clinical practice.

4 Molecular Imaging

The tumor microenvironment comprises two interdependent compartments: the parenchyma composed of neoplastic cells and the stroma formed by host cells (de Wever and Mareel 2003). Neoplastic cells are the primary source of malignancy. However, the non-malignant supporting elements, including connective tissue, blood vessels, and often inflammatory cells, are crucial for cancer cell survival and tumor progression. For that reason, both types of tumor tissue components are important therapeutic and imaging targets.

New molecular MRI strategies, intensively under investigation in recent years, hold great promise for the noninvasive assessment of tumor characteristics, based on the presence of specific molecular markers. To provide a reliable readout of the tumor molecular profile, an imaging agent should specifically bind to or be activated by the target molecule, producing a sufficiently strong change in the MRI contrast to enable its robust detection. A potential contrast agent for molecular

imaging should be evaluated with respect to these requirements. Since in vivo MRI does not provide sufficient resolution to directly image at the cellular and subcellular level, in many studies ex vivo optical techniques are used for validation of proof-of-concept MRI data. Therefore, multimodal constructs that can be visualized using supplemental imaging techniques are required for the evaluation of MRI-based molecular and cellular imaging strategies.

The visualization of molecular and cellular targets with MRI requires powerful contrast agents (Strijkers et al. 2007; Mulder et al. 2009). One of the leading concepts is the use of nanoparticulate carriers that contain a high payload of low-molecular weight Gd-based contrast agent. Moreover, ironoxide particles, which generate the strong susceptibility effect that results in T_2^* and T_2* contrast, are very attractive for molecular MRI. Active targeting of an imaging agent can be achieved by conjugating ligands that bind with high affinity to the molecular target of interest. Successful development of targeted contrast agents requires the optimization of their stability, pharmacokinetic properties, targeting efficacy and specificity. Generally, a prolonged circulation time of targeted contrast agents is desired, as this expands the time window for interaction with the molecular target. However, a long circulation half-life might also increase the unwanted background signal. The optimal molecular size of an imaging agent is determined by the accessibility of the molecular target. In order to image the expression of molecular epitopes on cancer cells, the contrast agent must cross the blood vessel wall before it can bind to the target. Thus, the maximum size of the contrast agent is limited by the size of the tumor vessel pores. Oppositely, for imaging endothelial molecular markers, the contrast agent accumulation in the tumor interstitium is undesired. Therefore, the optimal contrast agent size should minimize its extravasation.

The human epidermal growth factor receptor (HER) family of receptor tyrosine kinases control critical pathways involved in epithelial cell differentiation, growth, division, and motility (Cai et al. 2008). Two members of the HER family: the epidermal growth factor receptor (EGFR) and HER-2 are currently the most exploited molecular cancer cell targets, both for therapeutic and imaging purposes. EGFR is overexpressed in many epithelial carcinomas (Arteaga 2003), whereas the upregulation of HER-2 was found mainly in breast cancer (Slamon et al. 1987; Koeppen et al. 2001). Particularly, intensive research has been carried out to design EGFR- and HER-2-specific ligands for PET imaging (Cai et al. 2008). There are also several examples of MRI probes for imaging the expression of these receptors. Suwa et al. introduced ironoxide nanoparticles functionalized with anti-EGFR monoclonal antibody (Suwa et al. 1998). The EGFR-targeted particles were about 13 nm in size and, thus, presumably smaller than capillary pores. In vivo MRI of athymic rats bearing esophageal squamous cell carcinoma revealed a significantly decreased T_2 in the tumor 40 h after administration of EGFR-targeted particles compared to the pre-contrast state. Low signal intensity was sustained until 5 days post injection. The particles were confined in tumor cell lysosomes, as assessed by histologic analysis. Yang et al. used a similar approach for imaging EGFR expression on pancreatic cancer cells with a single-chain EGFR antibody conjugated to iron oxide nanoparticles (Yang et al. 2009). Artemov et al.

investigated molecular MRI of HER-2 expression using a two-step labeling protocol including receptor pre-labeling with biotinylated anti-HER-2 antibody and subsequent follow-up by streptavidin-iron oxide particles (Artemov et al. 2003a). Strong T_2 contrast was generated in HER-2-expressing cells in vitro. The magnitude of the contrast was proportional to the expression level of the receptor as determined by fluorescence activated cell sorting (FACS) analysis. In two other studies from the same research group, a similar approach was applied in vivo using positive contrast agents (Artemov et al. 2003b; Zhu et al. 2008). In the former study, avidin-Gd-DTPA was injected in tumor-bearing mice 12 h after administration of biotin-anti-HER-2 antibody, and monitored with MRI (Artemov et al. 2003b). The enhancement on T_1-weighted images was retained in EGFR-positive tumors at 8–24 h post injection. In contrast, the MRI signal decreased to baseline levels in EGFR-negative tumors after the initial enhancement at early time-points.

Upregulation of the folate receptor (FR) is a characteristic property of many malignant cell types (Low et al. 2008). Compounds combining folic acid, which is a ligand for FR, with mono- and polymeric Gd-chelates (Wiener et al. 1997; Konda et al. 2000, 2002; Corot et al. 2008), ironoxide particles (Choi et al. 2004; Sonvico et al. 2005) and Gd-based nanoemulsions (Oyewumi and Mumper 2002) have been developed. Corot et al. introduced a high-relaxivity dimer of Gd-DOTA conjugated to folic acid (Corot et al. 2008). The uptake of the latter FR-targeted contrast agent and the corresponding nontargeted compound was monitored in vivo in KB tumor-bearing mice using dynamic T_1-weighted MRI. Although both the FR-targeted and nontargeted agent increased the MRI signals in the tumors, a higher enhancement was induced by the FR-targeted agent. Moreover, the kinetic profile of the enhancement indicated longer retention of the FR-targeted agent in the tumor compared to the nonspecific reference compound.

The endothelium of newly formed vessels appears to be an excellent target for molecular imaging because it expresses a variety and high number of specific molecules that are virtually absent in the normal vasculature (Adams et al. 2007; Neeman et al. 2007; Avraamides et al. 2008). Additionally, the endothelium is in contact with blood, making it directly accessible for an intravenously injected contrast agent. Among the receptors upregulated on activated endothelial cells, $\alpha_v\beta_3$ integrin, a molecule involved in the endothelial cell migration and apoptosis, received considerable attention as an imaging target (Brooks et al. 1994). The general idea underlying $\alpha_v\beta_3$ integrin visualization is based on the use of Arg-Gly-Asp (RGD) sequence-containing ligands, which mediate the binding of imaging agents to $\alpha_v\beta_3$ integrin. Sipkins et al. have pioneered this approach for use in MRI (Sipkins et al. 1998). In the latter study, paramagnetic polymerized liposomes functionalized with $\alpha_v\beta_3$ integrin-specific antibody were evaluated in rabbit carcinomas. The MRI signal enhancement produced by targeted liposomes 24 h post injection was significantly (two-fold) higher compared to control particles conjugated with nonspecific immunoglobulin. Furthermore, no signal enhancement was induced by $\alpha_v\beta_3$ integrin-targeted liposomes in the receptor-negative tumor model, confirming the specificity of this approach. Subsequently, several Gd-, ironoxide-, and fluorine-

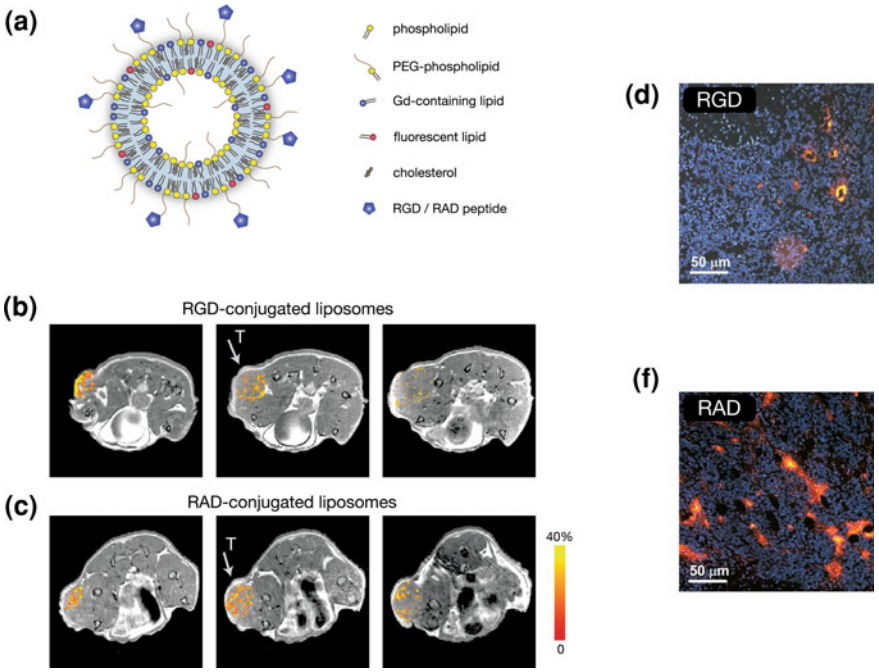

Fig. 5 Multifunctional liposomes for targeting and imaging of activated tumor endothelium. **a** Paramagnetic liposome for multimodal, MR, and fluorescence imaging of activated tumor endothelium. The building blocks of the liposome are shown on the *right*. **b** T_1-weighted MRI of three slices through a subcutaneous xenograft human LS174T colon carcinoma tumor in an athymic mouse after injection with RGD-conjugated liposomes. The tumor is indicated with the letter T. Contrast enhancement, indicated by the pseudo color with scale on the right, was mainly found at the rim of the tumor in the areas with most angiogenic tumor vessels. **c** Injection with nonspecific RAD-conjugated liposomes resulted in contrast enhancement more evenly distributed throughout the tumor. **d** Ex vivo fluorescence microscopy revealed specific association of the RGD-conjugated liposomes with the tumor endothium. **e** Extravasation was observed for RAD-conjugated liposomes. Reproduced with permission (Mulder et al. 2005)

based MRI contrast agents have been developed as $\alpha_v\beta_3$ integrin-specific contrast agents [for recent reviews, see (Strijkers et al. 2007; 2010; Lanza et al. 2010)].

Mulder et al. conjugated cyclic-RGD peptide (RGD) to paramagnetic and fluorescent liposomes to assess angiogenesis in subcutaneous xenograft human LS174T colon adenocarcinomas in athymic mice (Mulder et al. 2005). Figure 5a is a schematic illustration of the design of the liposomes used in this study. The basic building blocks of the approximately 150 nm-diameter liposomes are a naturally occuring phospholid [1,2-Distearoyl-sn-glycero-3-phosphocholine (DSPC)] and a PEG-conugated phospholipid [1,2-Distearoyl-sn-glycero-3-phosphoethanolamine (DSPE) with PEG] to ensure long blood circulation times as explained in Sect. 2.2. Twenty-five mole percent of the liposome consists of a Gd-containing lipid [Gd-DTPA-bis(stearylamide)] to provide MRI contrast and 0.1 mol percent of

fluorescent lipid [rhodamine–phosphatidylethanolamine (PE)] for fluorescence imaging and ex vivo microscopy purposes. RGD peptide was coupled to the distal ends of maleimide-PEG-DSPE. As a negative control, liposomes functionalized with a nonspecific RAD peptide were used. The difference in MRI signal enhancement as brought about by functional and non-functionalized liposomes was mainly manifested in its spatial distribution in the tumor rather than the magnitude. After injection of RGD-conjugated liposomes, the contrast-enhanced pixels were mainly located in the rim of the tumor (Fig. 5b), whereas the enhancement induced by nonspecific RAD-conjugated liposomes was more evenly distributed through the tumor area (Fig. 5c). Ex vivo fluorescence microscopy revealed a different mechanism of accumulation in the tumor; association with the endothelium in the case of RGD-conjugated liposomes (Fig. 5d) and extravasation in the case of RAD-conjugated liposomes (Fig. 5e).

The expression of the VEGF-receptor has been investigated predominantly using PET, SPECT and ultrasound probes (Cai et al. 2006; Backer et al. 2007; Pochon et al. 2010). In a recent study, the capability of MRI for detecting the heterogeneous expression of VEGF-receptor-2 in C6 gliomas by using anti-VEGF-receptor antibody-targeted contrast agent was demonstrated (He et al. 2010). Galectin-1, another important molecular marker of angiogenesis (Thijssen et al. 2006), has been proposed as an endothelial imaging target as well (Brandwijk et al. 2007). Paramagnetic and fluorescence liposomes were functionalized with peptidic galectin-1 antagonist anginex (Anx). In vitro experiments on activated endothelial cells revealed a higher uptake of Anx-conjugated compared to RGD-conjugated liposomes, producing an enhanced MRI signal.

Changes in the extracellular matrix composition are one of the hallmarks of angiogenic activation. These include the degradation of macromolecules, such as collagen, decorin, thrombosponin 1 and 2, and hyaluronian, to yield low-molecular weight fragments exerting pro- or anti-angiogenic activity (Neeman et al. 2007). The expression of extracellular matrix enzymes can therefore serve as an indication of the angiogenic status. Several agents have been developed for the MRI analysis of enzymatic activity (Louie et al. 2000; Bremer and Weissleder 2001; Zhao et al. 2003; Chen et al. 2004; Shiftan et al. 2005; Nahrendorf et al. 2008). Some of these exploit the change in relaxivity that occurs due to the enzymatic reaction. An example of enzyme-sensitive MRI contrast media are hyaluroanan-Gd-DTPA agarose beads (HA-Gd-DTPA beads) (Shiftan et al. 2005). The exposure of the HA-Gd-DTPA beads to hyaluronidase, a key enzyme that alters the angiogenic balance by converting anti-angiogenic hyaluronan into pro-angiogenic low-molecular weight products, significantly decreased the T_1 and T_2 relaxation times in the tumor. The detectable changes in MRI signal, induced by hyaluronidase-excreting ovarian cancer cells, have been observed in vitro as well as in vivo in the surrounding of ovarian tumor xenografts (Shiftan et al. 2005).

In vivo MRI tracking of cells that have been labeled with ironoxide nanoparticles in vitro is a method frequently used in stem cell research (Bulte 2009). This technique has also been applied for monitoring the migration of endothelial progenitor cells to sites of angiogenic activation in the tumor (Anderson et al. 2005; Arbab et al. 2006).

MRI measurements in glioma-bearing mice that received USPIO-labeled precursor cells intravenously revealed the presence of a hypointense ring delineating the tumor (Anderson et al. 2005). Histologic analysis confirmed the accumulation of iron-labeled cells at the tumor periphery. Moreover, the cells were positive for CD31, indicating that transplanted cells differentiated to an endothelial-like phenotype. A similar pattern of the progenitor cell integration within tumors as well as their transformation into endothelial cells was observed in a later MRI study (Arbab et al. 2006).

Tumor fibroblasts and myofibroblasts play an important role in the maintenance of the functional vasculature (de Wever and Mareel 2003; Bissell and Labarge 2005). These cells are recruited to areas of the angiogenic activation to support the endothelium of the newly formed tumor vessels. Even though the stabilizing layer of tumor vessels is generally underdeveloped, it plays an important role in tumor progression. The fibroblast migration to the tumor has been studied in vivo with MRI (Granot et al. 2005, 2007). For this purpose, fibroblasts were ex vivo labeled with either biotin-Gd-DTPA-BSA or ironoxide particles. Both labeled cell populations were tested in mice bearing ovarian carcinoma tumors. As early as 2 days after the intraperitoneal administration of MRI-observable fibroblasts, the cells were detected in the tumor, which was subcutaneously grown on the hind limb, but not in the healthy leg. Microscopical evaluation revealed the localization of the cells at the borders of the tumor, in the proximity of tortuous angiogenic blood vessels.

Despite the use of powerful multifunctional contrast agents that are equipped with target-specific ligands, in vivo molecular MRI remains very challenging. This is due to a number of reasons, such as a low amount of target-associated contrast material, difficulties with the quantitative assessment of the targeting efficacy and the presence of unbound contrast agent in the tumor, producing an unspecific background signal. In order to enhance the delivery of an imaging agent to the target cell and hence improve the MRI detection, a multi-targeting approach has been proposed. This involves the simultaneous targeting of several types of molecular epitopes on the same cellular target. For activated endothelium, which overexpresses a diverse set of molecular markers, this appears to be a very attractive approach (Adams and Alitalo 2007; Avraamides et al. 2008). Recently, the synergistic targeting of galectin-1 and $\alpha_v\beta_3$ integrin to improve the recognition of activated endothelial cells by a liposomal MRI contrast agent was demonstrated in vitro (Kluza et al. 2010). To evaluate this approach, paramagnetic and fluorescent liposomes were used, which were functionalized with two ligands, Anx and RGD, binding with high affinity to galectin-1 and $\alpha_v\beta_3$ integrin, respectively. Optical imaging and MRI revealed that the dual-targeting approach produces synergistic targeting effects with dramatically elevated cellular uptake of nanoparticles as compared to targeting with single ligands. Interestingly, under the in vivo conditions, the same strategy improved significantly the specificity of contrast agent association with the tumor endothelium (Kluza et al. 2011). Dual-targeting has also been applied for MRI of atherosclerosis (McAteer et al. 2008), ultrasound imaging of tumor angiogenesis using micron-sized agents (Willmann et al. 2008), and liposome mediated drug delivery to tumor cells (Saul et al. 2006).

The conversion of in vivo MRI signal changes to local contrast agent concentration is one of the major challenges in the field of molecular MRI. Difficulties among others arise from the internalization of targeted contrast agents into the cell cytoplasm and other subcellular structures. Intracellular compartmentalization of contrast agent may negatively influence the potency of a contrast agent to reduce the T_1 relaxation time (Terreno et al. 2006; Kok et al. 2009; Strijkers et al. 2009). This so-called quenching effect has been attributed to confinement of the contrast agent in a small compartment and relatively slow water exchange across the biological membranes that separate the different compartments. For iron oxide nanoparticles subcellular confinement and clustering may positively influence the potency to lower the T_2 relaxation time. However, also for iron oxides linearity between MRI signal changes and contrast agent concentration is difficult to achieve, which makes quantification a challenging task.

Long-circulating targeted contrast agents provide a long time window for interaction with the molecular target of interest, which can be expected to have a positive effect on the level of target-associated material. However, the prolonged presence of the contrast agent in the blood may lead to high signal from circulating contrast agent and may increase the degree of extravasation, thereby decreasing the target-to-background ratio. Suppression of the signal from flowing blood is an attractive strategy for eliminating the unspecific signal of circulating contrast agent, as was demonstrated for molecular imaging of atherosclerotic plaque (Sirol et al. 2004). However, for tumor imaging this strategy is of limited value, since the structural and functional abnormalities of the tumor vasculature prevent efficient flow suppression in MRI scans. Alternatively, one could wait until all the contrast agent is cleared from the blood circulation. However, this increases the amount of unspecific extravasation. An alternative strategy is an active clearance of the circulating contrast agent by a so-called avidin chase (Dafni et al. 2003; van Tilborg et al. 2008a, b). This can be achieved by equipping the contrast agent, next to the targeting ligands, with biotin. After initial intravenous injection, the contrast agent is allowed to circulate and specifically interact with the target of interest. In a second step avidin is injected, which binds with high affinity to the biotin on the contrast agent. The avidin triggers a fast clearance of the non-target-associated construct from the blood by rapid recognition in liver, spleen and kidneys.

The avidin chase technology was shown to improve the specificity of in vivo molecular MRI of tumor angiogenesis using targeted RGD-conjugated liposomes (van Tilborg et al. 2008a). For this purpose liposomes were equipped with RGD as well as biotin (RGD-biotin-liposomes). Figure 6 summarizes the experiments. Tumor bearing mice were intravenously injected with either RGD-biotin-liposomes or biotin-liposomes. After a circulation time of 100 min, the mice received an intravenous infusion of avidin over a period of approximately 15 min to induce rapid blood clearance of the liposomes. Mice not infused with avidin served as controls. The RGD-biotin-liposome injection resulted in contrast enhancement mainly in the rim of the tumor (Fig. 6a), in agreement with previous findings (Fig. 5). The enhancement pattern changed only slightly between the 90 and 150 min time-points after injection of the liposomes. Conversely, when avidin was infused at 100 min after injection, the percentage of enhanced pixels in the tumor

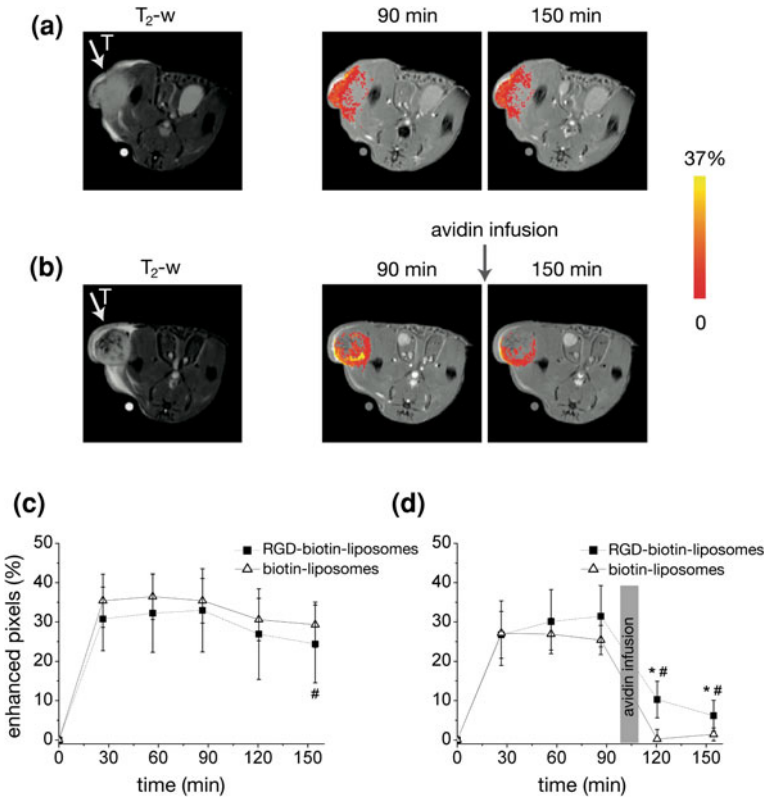

Fig. 6 Improved MRI of tumor angiogenesis by avidin-induced clearance of nonbound liposomes. (**a**, **b**) T_2-weighted (T_2-w, *left*) and T_1-weighted MR images (*right*) of a mouse with a B16F10 melanoma tumor in a subcutaneous position on the right flank (*arrow*). The letter T indicates the position of the tumor. **a** Images of a mouse 90 and 150 min after intravenous injection of liposomes equipped with both RGD peptide as well as biotin (RGD-biotin-liposomes). The significantly enhanced pixels are color coded according to the scale on the *right*. **b** Images of a mouse after intravenous injection of RGD-biotin-liposomes. After 100 min of circulation, circulating liposomes were removed by an intravenous infusion of avidin, which binds with high affinity to the biotin on the liposomes and induces rapid blood clearance. **c** Time dependence of the percentage of enhanced pixels after injection with RGD-biotin-liposomes or liposomes with biotin only (biotin-liposomes). **d** Time dependence of the percentage of enhanced pixels after injection with RGD-biotin-liposomes and biotin-liposomes. After 100 min, the mice received an intravenous infusion of avidin over a period of approximately 15 min (*gray bar*) to induce clearance of nonbound liposomes. Reproduced with permission (van Tilborg et al. 2008a)

decreased and the remaining enhanced pixels were more localized in the rim of the tumor (Fig. 6b). This suggests that part of the enhancement observed at the 90 min time point was caused by circulating liposomes. In Figs. 6c and 6d the time courses of enhancement are plotted for the different experimental groups. Without application of the avidin chase (Fig. 6c), enhancement after injection of RGD-

biotin-liposomes as well as biotin-liposomes decreased only slightly over the 150 min experimental time. After application of the avidin chase (Fig. 6d), the enhancement induced by the nonspecific biotin-liposomes was reduced to almost basal levels, while the enhancement by RGD-biotin-liposomes was still significant, with a much higher target-to-background ratio.

5 Combined Imaging and Therapy

MRI provides the opportunity to trace drugs in vivo, which may enable individualized evaluation of the therapeutic intervention as early as at the time of drug administration. The described concept belongs to a broader field of theragnostics and personalized medicine, and its key attribute is an agent, which accommodates both imaging and therapeutic properties (Ginsburg and McCarthy 2001; Ozdemir et al. 2006). The idea of such a multimodal construct evolved with the advances in the fields of drug discovery, pharmacology, and contrast media technology. However, the most profound impact had the development of targeted therapies (Ferrara and Kerbel 2005) and diagnostics (Neeman et al. 2007). This is due to the fact that these novel strategies are based on improved delivery to the targeted site. The contribution of imaging to the site-specific therapy could provide valuable information on the efficacy of drug delivery, and help to optimize the pharmacokinetics and biodistribution. Therefore, this strategy could serve as a screening method, which enables selection of patients that will benefit the most from a certain therapy.

In the field of oncology, where inter-patient variations are a common and serious issue, the concept of combined imaging and therapy is especially attractive. The application of MRI for this purpose is very desired since both the concentration and the spatial distribution of a therapeutic agent within the tumor are of prime importance. Intensive research in this area resulted in the design of various agent concepts, which accommodate both biological activity and diagnostic properties.

One of the leading strategies for combining imaging and therapy is direct labeling of a therapeutic with an imaging agent via covalent linkage. A great advantage of this method is that the imaging readout is directly related to drug location and concentration. However, this method requires structural changes in a biologically active molecule, which might result in hindrance of the interaction with its biological target, and, thus in impaired pharmacological activity. This is especially relevant for low-molecular weight drugs, as their structure limits this type of manipulation. Moreover, coupling of an imaging agent may result in very different pharmacokinetic properties compared to nonlabeled drug. These restrictions are less relevant for radiolabeling by atom replacement for SPECT and PET imaging, compared to coupling of e.g., a paramagnetic chelate for MRI detection. Although several chemotherapeutics have been labeled with different radionuclides and used in clinical studies, the multistep synthesis, the short life-time of the employed radionuclides and the applicability limited to the monotherapy greatly restricts their

potential (Rottey et al. 2007). Alternatively, more recently introduced anti-cancer therapeutics, which include monoclonal antibodies and peptides, are much more suitable for direct labeling. The favorable features of this type of therapeutics include their relatively large size and chemical structure, which enables introduction of changes without affecting the active site of the molecule. Nevertheless, in the published work on integrated therapy and imaging, antibodies and peptides play mainly a role of targeting moieties rather than therapeutic agents. In this application, they mediate the delivery of other, predominantly cytotoxic, drugs to the tumor.

The tracing of chemotherapeutics in vivo with imaging can provide information on the accumulation efficacy in the tumor, indirectly related the therapeutic efficacy. However, the imaging of therapeutic antibodies and peptides homing to the target cell surface receptors, which is a source of therapeutic effects, can bring far more direct prediction of the therapeutic outcome. As for MRI-based molecular imaging, monitoring of this molecular process requires a powerful contrast agent, which can generate sufficient MRI contrast in vivo. Currently, nanoparticulate agents, such as paramagnetically labeled nanoemulsions, liposomes and micelles, and USPIOs, are the most suitable for this purpose (Winter et al. 2003; Schmieder et al. 2008; Winter et al. 2008; Kaneda et al. 2009; Lijowski et al. 2009; Ma et al. 2009; Soman et al. 2009; Kluza et al. 2010; Lanza et al. 2010). In addition to excellent magnetic properties, required for MRI visualization, they are able to accommodate multiple antibodies or peptides per particle, which in combination with long circulating times may amplify the targeting efficacy via multivalent interactions, and hence increase their therapeutic efficacy. Moreover, the flexibility of these media allows for combining different imaging labels, which enables multimodal evaluation of the investigated therapy (Ma et al. 2009; Kluza et al. 2010).

Kluza et al. proposed a strategy for combined molecular imaging and therapy of angiogenesis, where the same molecule acted as both the targeting moiety and the therapeutic agent (Kluza et al. 2010). In this study, two types of peptidic angiogenesis inhibitors—RGD (Brooks et al. 1994) and Anx (Griffioen et al. 2001; van der Schaft et al. 2002)—were conjugated to multifunctional paramagnetic and fluorescent liposomes (Mulder et al. 2004; Strijkers et al. 2010). The targeting efficacy and the anti-angiogenic activity were studied in vitro using activated endothelial cells. It was demonstrated that, by combining heterogeneous molecules on the same nanoparticle, a synergistic targeting effect could be achieved that led to an enhanced imaging readout. Moreover, cell-cycle analysis revealed significant inhibition of endothelial cell proliferation induced by peptide-functionalized nanoparticles. Interestingly, these inhibitory effects were stronger for liposome-conjugated than free peptides. Considerably enhanced anti-proliferative activity, similar as observed under serum deprivation, was found for Anx and RGD dual-targeted liposomes. Therefore, the conjugation of two populations of angiogenesis inhibitors to the same particle resulted in potent multifunctional nanoparticles for combined imaging and therapy.

Combined imaging and therapy can also be achieved with a delivery vehicle, e.g., a liposome or a polymersome, which contains both the therapeutic as well as the imaging agent. Both therapy and imaging potentially benefit from such a delivery system. The use of nanocarriers has been shown to enhance therapeutic efficacy and

decrease the side effects of anti-cancer drugs (Gabizon 1992, 2001), whereas the incorporation of a high payload of conventional MRI contrast agent in liposomes has been demonstrated to produce very high contrast (Strijkers et al. 2005). Several liposomal formulations containing cytotoxic drugs such as doxorubicin (DOX) and daunorubicin have been approved for clinical application. Moreover, nanocarriers have been demonstrated to form excellent platforms for high-relaxivity contrast agents, e.g., for molecular imaging purposes. Therefore, nanocarriers appear to be an attractive medium to integrate therapy and imaging.

Currently, lipid-based nanocarriers, such as nanoemulsions, liposomes and micelles, are the most frequently used nanoparticles in preclinical studies on targeted drug delivery and monitoring. Also, polymer-based carriers such as polymeric liposomes (Levine et al. 2008) or micelles (Joralemon et al. 2010) are investigated. The choice of the carrier depends on the physical properties of the drug and the imaging agent. Generally, hydrophilic molecules are encapsulated in the aqueous interior of liposomes, whereas hydrophobic agents are incorporated in the lipid bilayer of liposomes or in the core of micelles. In order to broaden the possibilities for MRI labeling, Gd-chelates have been covalently linked to the polar head group of phospholipids or long hydrocarbon chains, which enabled the integration of these amphiphilic molecules with the lipidic components of liposomes or micelles. A high stability of the drug-containing and MRI-detectable construct is essential to assure the site-specific combined delivery and for relating the imaging signal unambiguously to the presence of the drug in the tumor tissue. However, the above stability requirement should not hinder the release of the drug once the target tissue is reached. The balance between these two features is key in obtaining a successful formulation.

Liposomes, which are more stable than micelles, were employed for monitoring of the delivery of chemotherapeutics in several preclinical studies. Paramagnetic polymerized liposomes, developed by Storrs et al., were composed of amphiphilic lipids (Storrs et al. 1995), in which the hydrophobic chains were cross-linked, resulting in structurally stable particles. Nasongkla et al. developed polymeric micelles loaded with doxorubicin and clusters of superparamagnetic ironoxide particles (SPIOs), which were targeted to $\alpha_v\beta_3$ integrin (Nasongkla et al. 2006). The cellular uptake of these micelles, which was confirmed with confocal laser scanning microscopy (CLSM), resulted in a signal loss in T_2^*-weighted images of cell samples. Moreover, the detection of doxorubicin in cell nuclei with CLSM indicated the intracellular release of the drug from the particles. Importantly, a cytotoxic assay confirmed the therapeutic activity of these multifunctional particles.

Targeted nanoparticles containing anti-angiogenic drugs designed to suppress angiogenesis and inhibit tumor growth were demonstrated in a Vx-2 adenocarcinoma rabbit model (Winter et al. 2008). In this study nanoemulsions, consisting of a perfluorocarbon core and a pegylated lipid corona, were equipped with a peptidomimetic $\alpha_v\beta_3$-integrin antagonist. For treatment purposes, fumagillin, a hydrophobic mycotoxin with anti-angiogenic properties, was incorporated in the lipid corona. For MRI readout of angiogenic activity, a paramagnetic Gd-containing $\alpha_v\beta_3$-targeted nanoemulsion was used. In Fig. 7, the study is summarized. Figure 7a

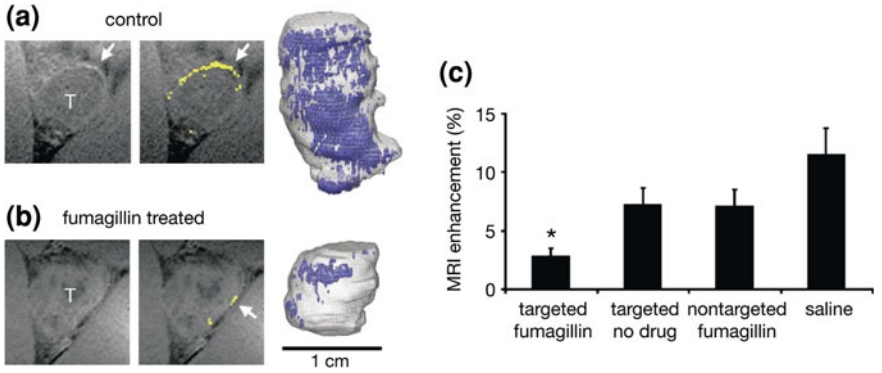

Fig. 7 Targeted nanoparticles for combined imaging and treatment of tumor angiogenesis. In this study, $\alpha_v\beta_3$-targeted fumagillin-containing nanoemulsions were used to suppress angiogenesis and inhibit tumor growth in a Vx–2 adenocarcinoma rabbit model. Paramagnetic Gd-containing $\alpha_v\beta_3$-targeted nanoparticles and MRI were used to quantify the changes in angiogenic activity induced by the treatment. **a** *Left*: T_1-weighted slice through the tumor (indicated with T) of a control animal after injection with paramagnetic Gd-containing $\alpha_v\beta_3$-targeted nanoparticles. This control animal was treated with $\alpha_v\beta_3$-targeted nanoparticles without drugs 16 days prior to imaging. Signal enhancement is visible in the tumor periphery at the locations of pronounced angiogenic activity. *Middle*: Same T_1-weighted slice with significantly enhanced pixels colored in *yellow*. *Right*: Three-dimensional reconstruction of the tumor with angiogenic regions colored in *blue*. **b** *Left*: T_1–weighted slice through the tumor of a treated animal after injection with paramagnetic Gd-containing $\alpha_v\beta_3$-targeted nanoparticles. This animal was treated with $\alpha_v\beta_3$-targeted fumagillin-containing nanoparticles 16 days prior to imaging. Almost no signal enhancement is visible in the tumor periphery indicating suppressed angiogenic activity. *Middle*: Same T_1-weighted slice showing only a few significantly enhanced pixels colored in *yellow*. *Right*: Three-dimensional reconstruction of the tumor with angiogenic regions colored in blue. **c** Quantification of MRI signal enhancement, as percentage area of the tumor periphery, at day 16 after treatment for the various groups. Reproduced with permission (Winter et al. 2008)

shows a T_1-weighted slice through the tumor of a control animal after injection with paramagnetic Gd-containing $\alpha_v\beta_3$-targeted nanoparticles. This control animal was treated with $\alpha_v\beta_3$-targeted nanoparticles without drugs 16 days prior to imaging. Significant signal enhancement is visible in the tumor periphery, revealing a pronounced angiogenic activity at these locations. MRI allowed for the three-dimensional reconstruction of angiogenic activity in the whole tumor. Figure 7b shows a T_1-weighted slice through the tumor of a treated animal after injection with paramagnetic Gd-containing $\alpha_v\beta_3$-targeted nanoparticles. This animal was treated with $\alpha_v\beta_3$-targeted fumagillin-containing nanoparticles 16 days prior to imaging. Almost no signal enhancement is visible in the tumor periphery demonstrating suppressed angiogenic activity. Quantification of the MRI signal enhancement (Fig. 7c showed that treatment with the $\alpha_v\beta_3$-targeted fumagillin-containing nanoparticles induced the largest suppression of angiogenic activity. Also, the nontargeted fumagillin-containing nanoparticles and the $\alpha_v\beta_3$-targeted nanoparticles without fumagillin

displayed some degree of anti-angiogenic activity, but not to the same extent as when both targeting ligand and drugs were used.

Santra et al. designed ironoxide particles coated with poly (acrylic acid) (PAA), co-encapsulating a near infrared dye and a chemotherapeutic agent, Taxol, in the polymer layer (Santra et al. 2009). The surface of these particles was functionalized with folate for targeting cancer cells overexpressing the folic receptor. The dual imaging and therapeutic properties were extensively studied in vitro. The preparation was characterized by very high transverse relaxivity and its uptake by tumor cells resulted in dramatic decrease in T_2 and induced a detectable near infrared fluorescent signal. The therapeutic efficiency and specificity of these particles was demonstrated in cell viability experiment, using lung cancer cells and cardiomyocytes as nonspecific control.

Lipid carriers have been found to be useful vehicles for gene delivery as well. The efficacy of the gene and lipid complexes (lipoplexes) to reach the tumor has been investigated in a number of studies. Leclercq et al. used Gd-containing cationic lipids, synthesized de novo, as the building component of cationic liposomes and micelles for DNA delivery (Leclercq et al. 2003). After intratumor injection, the presence of lipoplexes in the tumor was visualized with MRI, and the changes in signal intensity and its spatial distribution were followed in time. However, the evaluation of those data was purely descriptive. In tumors injected with liposome and DNA complexes, some degree of transfection was revealed. Medarova et al. introduced magnetic and fluorescently labeled nanoparticles for MRI and near-infrared in vivo optical imaging (Medarova et al. 2007, 2009). The nanoparticles were carrying siRNA targeting tumor-specific genes and were conjugated to a membrane translocation peptide for intracellular delivery. In the study by Mikhaylova et al., COX-2-specific siRNA loaded into cationic liposomes was used for imaging of gene delivery to cancer cells (Mikhaylova et al. 2009).

Liposome-encapsulated glucocorticoids (GC) have been shown to be promising anti-cancer agents (Schiffelers et al. 2005). Kluza et al. studied the efficacy of liposomal GC accumulation in the tumor using the multifunctional properties of the paramagnetic Gd-containing and fluorescent liposomes, which allowed for in vivo tracing of the liposome distribution and therapeutic efficacy (Kluza et al. 2009). T_1-weighted MRI and T_1 mapping techniques were used to assess the accumulation efficacy of the GC-containing liposomes. This readout revealed large inter-tumor variations—subject-specific information, which could only be obtained by using the combined imaging and therapy technology. The study revealed little correlation between the amount of drug delivered to the tumor and the therapeutic outcome, suggesting that the origin of the anti-cancer effects might not be limited or exclusively initiated in the tumor microenvironment. Indeed, the GC-containing liposomes induced a systemic response as well, which might be involved in the mechanism of anti-cancer activity.

The drug release is an important feature of a drug delivery system, since only drug in its free form will be able to exert therapeutic activity. For novel therapeutic strategies, which involve the controlled release of a drug at the site of malignancy, the monitoring of this process is of paramount importance. Image guidance using MRI is especially desired for thermosensitive drug delivery systems, since MRI has been

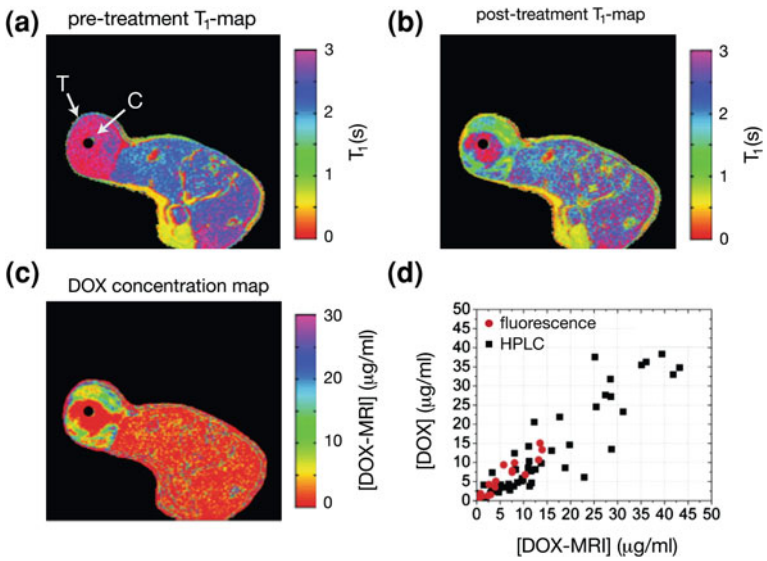

Fig. 8 Imaging the temperature-triggered release of doxorubicin from thermosensitive liposomes. **a** Pretreatment cross-sectional T_1-map of a rat with a fibrosarcoma tumor, indicated with T, on the flank. A catheter, indicated with C, is positioned in the center of the tumor. The catheter was flushed with hot water to induce heating of the tumor and release of doxorubicin and Mn contrast agent from the thermosensitive liposomes. **b** T_1-map of the same slice after intravenous injection of the thermosensitive doxorubicin- and Mn-containing liposomes and heat treatment. The significant decrease in the T_1 relaxation times in the tumor reports on release of the Mn and doxorubicin from the liposomes. **c** Quantitative map of the local doxorubicin concentration [DOX-MRI] calculated from the T_1-map. **d** Validation of the technique showing the correlation between tumor levels of doxorubicin predicted using in vivo MRI and ex vivo fluorescence and high-performance liquid chromatography (HPLC). Reproduced with permission (Viglianti et al. 2006)

shown to be very useful in planning and controlling the heating process (Grenier et al. 2009). Currently, the research on MRI-sensitive detection of drug release is mostly based on the simultaneous release of drug and paramagnetic contrast agent from the aqueous interior of liposomes. The idea is that the effect on the MRI signal is low for encapsulated paramagnetic contrast agent, due to limited water exchange across the liposomal membrane (Terreno et al. 2006; Kok et al. 2009; Strijkers et al. 2009). After release of the drug and the contrast agent, the contrast agent is able to exert its full effect on the MRI signal, hence reporting on release of the drug. For this application, several groups have developed complexes of manganese (Mn) and doxorubicin, encapsulated in thermosensitive liposomes (Abraham et al. 2002; Viglianti et al. 2004, 2006; Chiu et al. 2005; Ponce et al. 2007).

Viglianti et al. have developed a nanoparticle which can be triggered to release a drug in the tumor (Viglianti et al. 2004, 2006). Their approach comprised the use of thermosensitive liposomes for imaging the local triggered release of doxorubicin. The interior of these liposomes contains both doxorubicin for therapy as well as $MnSO_4$ for MRI detection. Release of Mn from the liposomes results in a dramatic

decrease in the T_1 relaxation time, which serves as a surrogate readout for doxorubicin release. Proof-of-principle of the concept is illustrated in Fig. 8. In this preclinical study rats with a fibrosarcoma tumor on the flank were used. A catheter was inserted in the tumor, which was flushed with hot water to induce local hyperthermia in the tumor. The thermosensitive liposomes were designed to release their content at a temperature of about 39–40 °C. Figure 8a shows a pretreatment cross-sectional T_1-map of the tumor. In Fig. 8 the same slice is shown after intravenous injection of the thermosensitive doxorubicin- and Mn-containing liposomes and subsequent heat treatment. Significant decrease in the T_1 relaxation times in the tumor reported on release of the Mn from the liposomes. From the change in T_1 relaxation time quantitative doxorubicin concentration maps were calculated (Fig. 8c). In Fig. 8d shows the excellent correlations between doxorubicin concentrations estimated from in vivo MRI and ex vivo fluorescence and high-performance liquid chromatography (HPLC), which validated that in vivo MRI was capable of providing accurate numbers for the local concentration of doxorubicin in the tumor.

Recently, de Smet et al. demonstrated the co-encapsulation of doxorubicin with Gd-HPDO3A (Prohance), a commercially available contrast agent, as a strategy to monitor the drug release from thermosensitive liposomes (de Smet et al. 2010). The simultaneous release of both the drug and the contrast agent has been found to occur near the melting phase transition temperature of the lipid bilayer. Moreover, the heating-induced decrease in T_1, which signals the release of the contrast agent from the liposomes, was successfully detected with MRI.

Therapy and imaging comprise a complementary team, which has the potential to provide a valuable contribution to therapy monitoring in oncology. The proposed platforms of agents, integrating MRI, and therapeutic properties have been used in preclinical studies predominately as conceptual models. The reported findings demonstrate their potential in noninvasive assessment of drug uptake in the tumor and monitoring of drug release. However, the use of this type of measurements as predictive readout in cancer treatment requires further evaluation. This is due to uncertainties on the relations between the intratumoral drug concentration and the therapeutic outcome. Studies dealing with this issue have reported contradictory results (Rottey et al. 2007). This might be related to the complexity of biological systems such as tumor tissue, which comprises different cellular components. Moreover, the cancer cell population itself is not uniform and thus the cell responsiveness to the treatment varies within the same tumor. Furthermore, the extent of the drug distribution throughout the tissue may greatly contribute to the final therapeutic outcome. Altogether, the added value of the combined therapy and imaging in the clinical setting is still to be established.

6 Translations and Future Outlook

In this chapter, the use of MRI in cancer diagnostics was reviewed, with particular focus on the application of multifunctional contrast agents to obtain specific tumor characterization beyond the basic morphologic features. Most of the novel

multifunctional imaging probes are still in a preclinical development phase. There are a number of reasons for a relatively slow translation of these new contrast agents toward daily clinical practice.

The design and fabrication of the new multifunctional nanoparticles requires a complicated blend of scientific disciplines from basic Chemistry, Physics, and Biology to Biomedical Engineering, Pharmacy, and Medicine. Laboratories, well suited to design and manufacture prototype contrast agents, may not be as well equipped to translate such techniques toward clinical practice. The costly path to human application requires large collaborations between the various disciplines as well as financial commitments from industry and governments, and such collaborations need time to establish. Furthermore, there is still a long way to go before particularly nanoparticles can be safely used in clinical practice. More knowledge is needed on the long-term fate of the bound and cell-internalized nanoparticles and on the organ-clearance kinetics and pathways in view of possible toxicity issues. The field of Gd-based MRI contrast agent is facing a serious setback since the discovery of nephrogenic systemic fibrosis (NSF), a severe disorder that is predominately associated with the use of certain Gd-based low-molecular weight contrast agents in patients with end-stage renal disease (Idee et al. 2009). Also human application of nanoparticles is not without controversy (Holgate 2010). There are still fundamental gaps in the understanding of the toxicity of nanoparticles to humans. Moreover, there is little consensus in the scientific community on the ideal or appropriate design of nanoparticles for human translation. Although the generic scheme of a multifunctional nanoparticle as depicted in Fig. 2 is valid for many of the nanoparticles that successfully were used in preclinical studies, the design allows for endless variations, and each new formulation will have to be tested with respect to safety.

Nevertheless, a recent search revealed 105 currently active clinical trials using the search term nanoparticle and 9 active trials for search term nanoparticle MRI (ClinicalTrials.gov). Liposomes are extensively being tested as drug carrying vehicles (540 hits for search term *liposome*). Many more clinical trials can be found using keywords such as *emulsion*, *micelle*, *polymeric micelle*, and *DCE-MRI cancer*. It is expected that the number of clinical trials involving these multifunctional probes will grow in the future and that knowledge on their potential clinical value will increase rapidly.

MRI applications are becoming more and more dependent on contrast agents. The combination of MRI and contrast agents greatly enhances the possibilities to depict and characterize tumors. With the emerging field of cellular and molecular MRI, contrast agents are no longer an extension of the methodology, but have become an essential element of the application. Multifunctional MRI probes hold great promise to facilitate more specific tumor diagnosis, patient-specific treatment planning, the monitoring of local drug delivery, and the early evaluation of therapy.

Acknowledgments The research on this topic in the authors' laboratory was funded in part by the integrated EU project MEDITRANS (FP6-2004-NMP-NI-4/IP 026668-2), and was performed in the framework of the European Cooperation in the field of Scientific and Technical Research (COST) D38 Action metal-based systems for molecular imaging applications.

References

Abraham SA et al (2002) Formation of transition metal-doxorubicin complexes inside liposomes. Biochim Biophys Acta 1565(1):41–54

Adams RH, Alitalo K (2007) Molecular regulation of angiogenesis and lymphangiogenesis. Nat Rev Mol Cell Biol 8(6):464–478

Aime S et al (1999) Novel paramagnetic macromolecular complexes derived from the linkage of a macrocyclic Gd(III) complex to polyamino acids through a squaric acid moiety. Bioconjug Chem 10(2):192–199

Akazawa K et al (2006) Preoperative evaluation of residual tumor extent by three-dimensional magnetic resonance imaging in breast cancer patients treated with neoadjuvant chemotherapy. Breast J 12(2):130–137

Anderson SA et al (2005) Noninvasive MR imaging of magnetically labeled stem cells to directly identify neovasculature in a glioma model. Blood 105(1):420–425

Arbab AS et al (2006) Magnetic resonance imaging and confocal microscopy studies of magnetically labeled endothelial progenitor cells trafficking to sites of tumor angiogenesis. Stem Cells 24(3):671–678

Arteaga C (2003) Targeting HER1/EGFR: a molecular approach to cancer therapy. Semin Oncol 30(3 suppl 7):3–14

Artemov D et al (2003a) MR molecular imaging of the Her-2/neu receptor in breast cancer cells using targeted iron oxide nanoparticles. Magn Reson Med 49(3):403–408

Artemov D et al (2003b) Magnetic resonance molecular imaging of the HER-2/neu receptor. Cancer Res 63(11):2723–2727

Avraamides CJ et al (2008) Integrins in angiogenesis and lymphangiogenesis. Nat Rev Cancer 8(8):604–617

Backer MV et al (2007) Molecular imaging of VEGF receptors in angiogenic vasculature with single-chain VEGF-based probes. Nat Med 13(4):504–509

Barrett T et al (2006) Macromolecular MRI contrast agents for imaging tumor angiogenesis. Eur J Radiol 60(3):353–366

Barrett T et al (2007) MRI of tumor angiogenesis. J Magn Reson Imaging 26(2):235–249

Belli P et al (2006) MRI accuracy in residual disease evaluation in breast cancer patients treated with neoadjuvant chemotherapy. Clin Radiol 61(11):946–953

Bissell MJ, Labarge MA (2005) Context, tissue plasticity, and cancer: are tumor stem cells also regulated by the microenvironment. Cancer Cell 7(1):17–23

Brandwijk RJ et al (2007) Anginex-conjugated liposomes for targeting of angiogenic endothelial cells. Bioconjug Chem 18(3):785–790

Brasch RC (1992) New directions in the development of MR imaging contrast media. Radiology 183(1):1–11

Brasch RC et al (1994) Quantification of capillary permeability to macromolecular magnetic resonance imaging contrast media in experimental mammary adenocarcinomas. Invest Radiol 29(suppl 2):S8–S11

Bremer C, Weissleder R (2001) In vivo imaging of gene expression. Acad Radiol 8(1):15–23

Brooks PC et al (1994) Requirement of vascular integrin $\alpha_v\beta_3$ for angiogenesis. Science 264(5158):569–571

Bulte JWM (2009) In vivo MRI cell tracking: clinical studies. AJR Am J Roentgenol 193(2):314–325

Cai W et al (2006) PET of vascular endothelial growth factor receptor expression. J Nucl Med 47(12):2048–2056

Cai W et al (2008) Multimodality imaging of the HER-kinase axis in cancer. Eur J Nucl Med Mol Imaging 35(1):186–208

Caravan P et al (1999) Gadolinium(III) chelates as MRI contrast agents: structure, dynamics, and applications. Chem Rev 99(9):2293–2352

Caride VJ et al (1984) Relaxation enhancement using liposomes carrying paramagnetic species. Magn Reson Imaging 2(2):107–112

Chang YC et al (2004) Angiogenic response of locally advanced breast cancer to neoadjuvant chemotherapy evaluated with parametric histogram from dynamic contrast-enhanced MRI. Phys Med Biol 49(16):3593–3602
Chen JW et al (2004) Human myeloperoxidase: a potential target for molecular MR imaging in atherosclerosis. Magn Reson Med 52(5):1021–1028
Chen W et al (2010) Whole-body diffusion-weighted imaging vs. FDG-PET for the detection of non-small-cell lung cancer. How do they measure up. Magn Reson Imaging 28(5):613–620
Chenevert TL et al (1997) Monitoring early response of experimental brain tumors to therapy using diffusion magnetic resonance imaging. Clin Cancer Res 3(9):1457–1466
Chenevert TL et al (2002) Diffusion MRI: a new strategy for assessment of cancer therapeutic efficacy. Mol Imaging 1(4):336–343
Chiu GNC et al (2005) Encapsulation of doxorubicin into thermosensitive liposomes via complexation with the transition metal manganese. J Cont Release 104(2):271–288
Choi H et al (2004) Iron oxide nanoparticles as magnetic resonance contrast agent for tumor imaging via folate receptor-targeted delivery. Acad Radiol 11(9):996–1004
ClinicalTrials.gov. U.S. National Institutes of Health [cited. Available from http://clinicaltrials.gov]
Cohen FM et al (1994) Contrast-enhanced magnetic resonance imaging estimation of altered capillary permeability in experimental mammary carcinomas after X-irradiation. Invest Radiol 29(11):970–977
Corot C et al (2008) Tumor imaging using P866, a high-relaxivity gadolinium chelate designed for folate receptor targeting. Magn Reson Med 60(6):1337–1346
Dafni H et al (2003) Modulation of the pharmacokinetics of macromolecular contrast material by avidin chase: MRI, optical, and inductively coupled plasma mass spectrometry tracking of triply labeled albumin. Magn Reson Med 50(5):904–914
Dafni H et al (2008) Macromolecular dynamic contrast-enhanced (DCE)-MRI detects reduced vascular permeability in a prostate cancer bone metastasis model following anti-platelet-derived growth factor receptor (PDGFR) therapy, indicating a drop in vascular endothelial growth factor receptor (VEGFR) activation. Magn Reson Med 60(4):822–833
Daldrup H et al (1998) Correlation of dynamic contrast-enhanced MR imaging with histologic tumor grade: comparison of macromolecular and small-molecular contrast media. AJR Am J Roentgenol 171(4):941–949
Daldrup-Link HE, Brasch RC (2003) Macromolecular contrast agents for MR mammography: current status. Eur Radiol 13(2):354–365
de Lussanet QG et al (2005) Dynamic contrast-enhanced MR imaging kinetic parameters and molecular weight of dendritic contrast agents in tumor angiogenesis in mice. Radiology 235(1):65–72
de Schepper AM, Bloem JL (2007) Soft tissue tumors: grading, staging, and tissue-specific diagnosis. Top Magn Reson Imaging 18(6):431–444
de Smet M et al (2010) Temperature-sensitive liposomes for doxorubicin delivery under MRI guidance. J Cont Release 143(1):120–127
de Vries AF et al (2003) Tumor microcirculation and diffusion predict therapy outcome for primary rectal carcinoma. Int J Radiat Oncol Biol Phys 56(4):958–965
de Wever O, Mareel M (2003) Role of tissue stroma in cancer cell invasion. J Pathol 200(4): 429–447
Des Guetz G et al (2006) Microvessel density and VEGF expression are prognostic factors in colorectal cancer. Meta-analysis of the literature. Br J Cancer 94(12):1823–1832
Detre JA, Alsop DC (1999) Perfusion magnetic resonance imaging with continuous arterial spin labeling: methods and clinical applications in the central nervous system. Eur J Radiol 30(2):115–124
Detre JA et al (2009) Arterial spin-labeled perfusion MRI in basic and clinical neuroscience. Curr Opin Neurol 22(4):348–355
Devoisselle JM et al (1988) Entrapment of gadolinium-DTPA in liposomes. Characterization of vesicles by P-31 NMR spectroscopy. Invest Radiol 23(10):719–724

Drummond DC et al (1999) Optimizing liposomes for delivery of chemotherapeutic agents to solid tumors. Pharmacol Rev 51(4):691–743
Ferrara N, Kerbel RS (2005) Angiogenesis as a therapeutic target. Nature 438(7070):967–974
Folkman J (1971) Tumor angiogenesis: therapeutic implications. N Engl J Med 285(21): 1182–1186
Folkman J (2002) Role of angiogenesis in tumor growth and metastasis. Semin Oncol 29(6 suppl 16):15–18
Fossheim SL et al (1999) Paramagnetic liposomes as MRI contrast agents: influence of liposomal physicochemical properties on the in vitro relaxivity. Magn Reson Imaging 17(1):83–89
Fossheim SL et al (2000) Thermosensitive paramagnetic liposomes for temperature control during MR imaging-guided hyperthermia: in vitro feasibility studies. Acad Radiol 7(12):1107–1115
Gabizon AA (1992) Selective tumor localization and improved therapeutic index of anthracyclines encapsulated in long-circulating liposomes. Cancer Res 52(4):891–896
Gabizon AA (2001) Stealth liposomes and tumor targeting: one step further in the quest for the magic bullet. Clin Cancer Res 7(2):223–225
Gilead A et al (2004) The role of angiogenesis, vascular maturation, regression and stroma infiltration in dormancy and growth of implanted MLS ovarian carcinoma spheroids. Int J Cancer 108(4):524–531
Ginsburg GS, McCarthy JJ (2001) Personalized medicine: revolutionizing drug discovery and patient care. Trends Biotechnol 19(12):491–496
Granot D et al (2005) Labeling fibroblasts with biotin-BSA-GdDTPA-FAM for tracking of tumor-associated stroma by fluorescence and MR imaging. Magn Reson Med 54(4):789–797
Granot D et al (2007) In vivo imaging of the systemic recruitment of fibroblasts to the angiogenic rim of ovarian carcinoma tumors. Cancer Res 67(19):9180–9189
Greish K (2007) Enhanced permeability and retention of macromolecular drugs in solid tumors: a royal gate for targeted anticancer nanomedicines. J Drug Target 15(7–8):457–464
Grenier N et al (2009) Molecular MR imaging and MR-guided ultrasound therapies in cancer. JBR-BTR 92(1):8–12
Griffioen AW et al (2001) Anginex, a designed peptide that inhibits angiogenesis. Biochem J 354(Pt 2):233–242
Guccione S et al (2004a) Vascular-targeted nanoparticles for molecular imaging and therapy. Methods Enzymol 386:219–236
Guccione S et al (2004b) Molecular imaging and therapy directed at the neovasculature in pathologies. How imaging can be incorporated into vascular-targeted delivery systems to generate active therapeutic agents. IEEE Eng Med Biol Mag 23(5):50–56
Haacke EM et al (1999) Magnetic resonance imaging: physical principles and sequence design. John Wiley & Sons, New York
Hak S et al (2009) A high relaxivity Gd(III)DOTA-DSPE-based liposomal contrast agent for magnetic resonance imaging. Eur J Pharm Biopharm 72(2):397–404
He T et al (2011) Molecular MRI assessment of vascular endothelial growth factor receptor-2 in rat C6 gliomas. J Cell Mol Med 15(4):837–849
Helbich TH et al (2000) A new polysaccharide macromolecular contrast agent for MR imaging: biodistribution and imaging characteristics. J Magn Reson Imaging 11(6):694–701
Heusner TA et al (2010) Diagnostic value of diffusion-weighted magnetic resonance imaging (DWI) compared to FDG PET/CT for whole-body breast cancer staging. Eur J Nucl Med Mol Imaging 37(6):1077–1086
Holgate ST (2010) Exposure, uptake, distribution and toxicity of nanomaterials in humans. J Biomed Nanotechnol 6(1):1–19
Hudgins PA et al (2002) Ferumoxtran-10, a superparamagnetic iron oxide as a magnetic resonance enhancement agent for imaging lymph nodes: a phase 2 dose study. AJNR Am J Neuroradiol 23(4):649–656

Idee JM et al (2009) Involvement of gadolinium chelates in the mechanism of nephrogenic systemic fibrosis: an update. Radiol Clin North Am 47(5):855–869

Islam T, Harisinghani MG (2009) Overview of nanoparticle use in cancer imaging. Cancer Biomark 5(2):61–67

Issa B et al (1999) Heterogeneity analysis of Gd-DTPA uptake: improvement in breast lesion differentiation. J Comput Assist Tomogr 23(4):615–621

Jackson A et al (2007) Imaging tumor vascular heterogeneity and angiogenesis using dynamic contrast-enhanced magnetic resonance imaging. Clin Cancer Res 13(12):3449–3459

Joralemon MJ et al (2010) PEGylated polymers for medicine: from conjugation to self-assembled systems. Chem Commun (Camb) 46(9):1377–1393

Kabalka GW et al (1991) Gadolinium-labeled liposomes containing various amphiphilic Gd-DTPA derivatives: targeted MRI contrast enhancement agents for the liver. Magn Reson Med 19(2):406–415

Kaneda MM et al (2009) Perfluorocarbon nanoemulsions for quantitative molecular imaging and targeted therapeutics. Ann Biomed Eng 37(10):1922–1933

Kimura H et al (2006) Perfusion imaging of meningioma by using continuous arterial spin-labeling: comparison with dynamic susceptibility-weighted contrast-enhanced MR images and histopathologic features. AJNR Am J Neuroradiol 27(1):85–93

Klibanov AL et al (1990) Amphipathic polyethyleneglycols effectively prolong the circulation time of liposomes. FEBS Lett 268(1):235–237

Kluza E et al (2009) Novel anti-tumor therapy with liposomal glucocorticoids: MRI monitoring of drug delivery. Paper read at European society for magnetic resonance in medicine and biology congress, at Antalya

Kluza E et al (2010) Synergistic targeting of $\alpha_v\beta_3$ integrin and galectin-1 with heteromultivalent paramagnetic liposomes for combined MR imaging and treatment of angiogenesis. Nano Lett 10(1):52–58

Kluza E et al (2012) Dual-targeting of $\alpha v\beta 3$ and galectin-1 improves the specificity of paramagnetic/fluorescent liposomes to tumor endothelium in vivo. J Cont Release 158(2): 207–214

Koenig SH et al (1988) Relaxivity and binding of Mn^{2+} ions in solutions of phosphatidylserine vesicles. Magn Reson Med 7(2):133–142

Koeppen HK et al (2001) Overexpression of HER2/neu in solid tumours: an immunohistochemical survey. Histopathology 38(2):96–104

Kok MB et al (2009) Cellular compartmentalization of internalized paramagnetic liposomes strongly influences both T_1 and T_2 relaxivity. Magn Reson Med 61(5):1022–1032

Konda SD et al (2000) Development of a tumor-targeting MR contrast agent using the high-affinity folate receptor: work in progress. Invest Radiol 35(1):50–57

Konda SD et al (2002) Biodistribution of a 153 Gd-folate dendrimer, generation = 4, in mice with folate-receptor positive and negative ovarian tumor xenografts. Invest Radiol 37(4):199–204

Kovar DA et al (1998) A new method for imaging perfusion and contrast extraction fraction: input functions derived from reference tissues. J Magn Reson Imaging 8(5):1126–1134

Kuhl CK et al (1999) Dynamic breast MR imaging: are signal intensity time course data useful for differential diagnosis of enhancing lesions. Radiology 211(1):101–110

Kwee TC et al (2009) Whole-body diffusion-weighted magnetic resonance imaging. Eur J Radiol 70(3):409–417

Lanza GM et al (2010) Theragnostics for tumor and plaque angiogenesis with perfluorocarbon nanoemulsions. Angiogenesis 13(2):189–202

Leach MO et al (2005) The assessment of antiangiogenic and antivascular therapies in early-stage clinical trials using magnetic resonance imaging: issues and recommendations. Br J Cancer 92(9):1599–1610

Leclercq F et al (2003) Design, synthesis, and evaluation of gadolinium cationic lipids as tools for biodistribution studies of gene delivery complexes. Bioconjug Chem 14(1):112–119

Levine DH et al (2008) Polymersomes: a new multi-functional tool for cancer diagnosis and therapy. Methods 46(1):25–32
Lijowski M et al (2009) High sensitivity: high-resolution SPECT-CT/MR molecular imaging of angiogenesis in the Vx2 model. Invest Radiol 44(1):15–22
Louie AY et al (2000) In vivo visualization of gene expression using magnetic resonance imaging. Nat Biotechnol 18(3):321–325
Low PS et al (2008) Discovery and development of folic-acid-based receptor targeting for imaging and therapy of cancer and inflammatory diseases. Acc Chem Res 41(1):120–129
Lüdemann L et al (2006) BOLD signal in the motor cortex shows a correlation with the blood volume of brain tumors. J Magn Reson Imaging 23(4):435–443
Ma LL et al (2009) Small multifunctional nanoclusters (nanoroses) for targeted cellular imaging and therapy. ACS Nano 3(9):2686–2696
Magin RL et al (1986) Liposome delivery of NMR contrast agents for improved tissue imaging. Magn Reson Med 3(3):440–447
Manton DJ et al (2006) Neoadjuvant chemotherapy in breast cancer: early response prediction with quantitative MR imaging and spectroscopy. Br J Cancer 94(3):427–435
Martincich L et al (2004) Monitoring response to primary chemotherapy in breast cancer using dynamic contrast-enhanced magnetic resonance imaging. Breast Cancer Res Treat 83(1):67–76
Mayr NA et al (2000) Pixel analysis of MR perfusion imaging in predicting radiation therapy outcome in cervical cancer. J Magn Reson Imaging 12(6):1027–1033
McAteer MA et al (2008) Magnetic resonance imaging of endothelial adhesion molecules in mouse atherosclerosis using dual-targeted microparticles of iron oxide. Arterioscler Thromb Vasc Biol 28(1):77–83
McCarthy JR et al (2007) Targeted delivery of multifunctional magnetic nanoparticles. Nanomedicine (Lond) 2(2):153–167
Medarova Z et al (2007) In vivo imaging of siRNA delivery and silencing in tumors. Nat Med 13(3):372–377
Medarova Z et al (2009) Development and application of a dual-purpose nanoparticle platform for delivery and imaging of siRNA in tumors. Methods Mol Biol 555:1–13
Meisamy S et al (2004) Neoadjuvant chemotherapy of locally advanced breast cancer: predicting response with in vivo ^{1}H MR spectroscopy−a pilot study at 4 T. Radiology 233(2):424–431
Meyer D et al (1994) Paramagnetic dextrans as magnetic resonance blood pool tracers. Invest Radiol 29(suppl 2):S90–S92
Michel SCA et al (2002) Preoperative breast cancer staging: MR imaging of the axilla with ultrasmall superparamagnetic iron oxide enhancement. Radiology 225(2):527–536
Mikhaylova M et al (2009) Imaging of cationic multifunctional liposome-mediated delivery of COX-2 siRNA. Cancer Gene Ther 16(3):217–226
Mills SJ et al (2006) Do cerebral blood volume and contrast transfer coefficient predict prognosis in human glioma. AJNR Am J Neuroradiol 27(4):853–858
Moffat BA et al (2006) Inhibition of vascular endothelial growth factor (VEGF)-A causes a paradoxical increase in tumor blood flow and up-regulation of VEGF-D. Clin Cancer Res 12(5):1525–1532
Mulder WJ et al (2004) A liposomal system for contrast-enhanced magnetic resonance imaging of molecular targets. Bioconjug Chem 15(4):799–806
Mulder WJ et al (2005) MR molecular imaging and fluorescence microscopy for identification of activated tumor endothelium using a bimodal lipidic nanoparticle. FASEB J 19(14):2008–2010
Mulder WJ et al (2006) Lipid-based nanoparticles for contrast-enhanced MRI and molecular imaging. NMR Biomed 19(1):142–164
Mulder WJ et al (2009) Nanoparticulate assemblies of amphiphiles and diagnostically active materials for multimodality imaging. Acc Chem Res 42(7):904–914
Nahrendorf M et al (2008) Activatable magnetic resonance imaging agent reports myeloperoxidase activity in healing infarcts and noninvasively detects the antiinflammatory effects of atorvastatin on ischemia-reperfusion injury. Circulation 117(9):1153–1160

Nasongkla N et al (2006) Multifunctional polymeric micelles as cancer-targeted, MRI-ultrasensitive drug delivery systems. Nano Lett 6(11):2427–2430

Navon G et al (1986) Liposomes containing paramagnetic macromolecules as MRI contrast agents. Magn Reson Med 3(6):876–880

Neeman M et al (2007) Molecular imaging of angiogenesis. J Magn Reson Imaging 25(1):1–12

O'Connor JPB et al (2007) DCE-MRI biomarkers in the clinical evaluation of antiangiogenic and vascular disrupting agents. Br J Cancer 96(2):189–195

Ogan MD et al (1987) Albumin labeled with Gd-DTPA. An intravascular contrast-enhancing agent for magnetic resonance blood pool imaging: preparation and characterization. Invest Radiol 22(8):665–671

Oliver M et al (2006) MAGfect: a novel liposome formulation for MRI labelling and visualization of cells. Org Biomol Chem 4(18):3489–3497

Opsahl LR et al (1995) Tumor imaging with a macromolecular paramagnetic contrast agent: gadopentetate dimeglumine-polylysine. Acad Radiol 2(9):762–767

Oyewumi MO, Mumper RJ (2002) Engineering tumor-targeted gadolinium hexanedione nanoparticles for potential application in neutron capture therapy. Bioconjug Chem 13(6):1328–1335

Ozdemir V et al (2006) Shifting emphasis from pharmacogenomics to theragnostics. Nat Biotechnol 24(8):942–946

Padhani AR et al (2009) Diffusion-weighted magnetic resonance imaging as a cancer biomarker: consensus and recommendations. Neoplasia 11(2):102–125

Parikh T et al (2008) Focal liver lesion detection and characterization with diffusion-weighted MR imaging: comparison with standard breath-hold T_2-weighted imaging. Radiology 246(3):812–822

Pochon S et al (2010) BR55: a lipopeptide-based VEGFR2-targeted ultrasound contrast agent for molecular imaging of angiogenesis. Invest Radiol 45(2):89–95

Ponce AM et al (2007) Magnetic resonance imaging of temperature-sensitive liposome release: drug dose painting and antitumor effects. J Natl Cancer Inst 99(1):53–63

Preul MC et al (2000) Using proton magnetic resonance spectroscopic imaging to predict in vivo the response of recurrent malignant gliomas to tamoxifen chemotherapy. Neurosurgery 46(2):306–318

Robinson SP et al (1997) The response to carbogen breathing in experimental tumour models monitored by gradient-recalled echo magnetic resonance imaging. Br J Cancer 75(7):1000–1006

Ross BD et al (2003) Evaluation of cancer therapy using diffusion magnetic resonance imaging. Mol Cancer Ther 2(6):581–587

Rottey S et al (2007) Radiolabelled chemotherapeutics. Q J Nucl Med Mol Imaging 51(2):139–151

Santra S et al (2009) Drug/dye-loaded, multifunctional iron oxide nanoparticles for combined targeted cancer therapy and dual optical/magnetic resonance imaging. Small 5(16):1862–1868

Saul JM et al (2006) A dual-ligand approach for enhancing targeting selectivity of therapeutic nanocarriers. J Control Release 114(3):277–287

Schiffelers RM et al (2005) Liposome-encapsulated prednisolone phosphate inhibits growth of established tumors in mice. Neoplasia 7(2):118–127

Schmieder AH et al (2008) Three-dimensional MR mapping of angiogenesis with $\alpha_5\beta_1(\alpha_v\beta_3)$-targeted theranostic nanoparticles in the MDA-MB-435 xenograft mouse model. FASEB J 22(12):4179–4189

Schmiedl U et al (1987) Magnetic resonance imaging of myocardial infarction using albumin-(Gd-DTPA), a macromolecular blood-volume contrast agent in a rat model. Invest Radiol 22(9):713–721

Schwarz AJ et al (2002) Early in vivo detection of metabolic response: a pilot study of ^{1}H MR spectroscopy in extracranial lymphoma and germ cell tumours. Br J Radiol 75(900):959–966

Schwickert HC et al (1996) Contrast-enhanced MR imaging assessment of tumor capillary permeability: effect of irradiation on delivery of chemotherapy. Radiology 198(3):893–898

Semple SI et al (2006) Baseline MRI delivery characteristics predict change in invasive ductal breast carcinoma PET metabolism as a result of primary chemotherapy administration. Ann Oncol 17(9):1393–1398

Shames DM et al (1993) Measurement of capillary permeability to macromolecules by dynamic magnetic resonance imaging: a quantitative noninvasive technique. Magn Reson Med 29(5):616–622

Shiftan L et al (2005) Magnetic resonance imaging visualization of hyaluronidase in ovarian carcinoma. Cancer Res 65(22):10316–10323

Shubayev VI et al (2009) Magnetic nanoparticles for theragnostics. Adv Drug Deliv Rev 61(6):467–477

Shukla-Dave A et al (2002) Prediction of treatment response of head and neck cancers with P-31 MR spectroscopy from pretreatment relative phosphomonoester levels. Acad Radiol 9(6):688–694

Shweiki D et al (1992) Vascular endothelial growth factor induced by hypoxia may mediate hypoxia-initiated angiogenesis. Nature 359(6398):843–845

Shweiki D et al (1995) Induction of vascular endothelial growth factor expression by hypoxia and by glucose deficiency in multicell spheroids: implications for tumor angiogenesis. Proc Natl Acad Sci U S A 92(3):768–772

Silva AC et al (2000) Imaging blood flow in brain tumors using arterial spin labeling. Magn Reson Med 44(2):169–173

Sinha S et al (2002) In vivo diffusion-weighted MRI of the breast: potential for lesion characterization. J Magn Reson Imaging 15(6):693–704

Sipkins DA et al (1998) Detection of tumor angiogenesis in vivo by $\alpha_v\beta_3$-targeted magnetic resonance imaging. Nat Med 4(5):623–626

Sirol M et al (2004) Lipid-rich atherosclerotic plaques detected by gadofluorine-enhanced in vivo magnetic resonance imaging. Circulation 109(23):2890–2896

Slamon DJ et al (1987) Human breast cancer: correlation of relapse and survival with amplification of the HER-2/neu oncogene. Science 235(4785):177–182

Soman NR et al (2009) Molecularly targeted nanocarriers deliver the cytolytic peptide melittin specifically to tumor cells in mice, reducing tumor growth. J Clin Invest 119(9):2830–2842

Sonvico F et al (2005) Folate-conjugated iron oxide nanoparticles for solid tumor targeting as potential specific magnetic hyperthermia mediators: synthesis, physicochemical characterization, and in vitro experiments. Bioconjug Chem 16(5):1181–1188

Storrs RW et al (1995) Paramagnetic polymerized liposomes as new recirculating MR contrast agents. J Magn Reson Imaging 5(6):719–724

Strijkers GJ et al (2005) Relaxivity of liposomal paramagnetic MRI contrast agents. Magn Reson Mater Phy 18(4):186–192

Strijkers GJ et al (2007) MRI contrast agents: current status and future perspectives. Anti-Cancer Agents Med Chem 7:291–305

Strijkers GJ et al (2009) Three-compartment T_1 relaxation model for intracellular paramagnetic contrast agents. Magn Reson Med 61(5):1049–1058

Strijkers GJ et al (2010) Paramagnetic and fluorescent liposomes for target-specific imaging and therapy of tumor angiogenesis. Angiogenesis 13(2):161–173

Su MY et al (1998) Tumor characterization with dynamic contrast-enhanced MRI using MR contrast agents of various molecular weights. Magn Reson Med 39(2):259–269

Suwa T et al (1998) Magnetic resonance imaging of esophageal squamous cell carcinoma using magnetite particles coated with anti-epidermal growth factor receptor antibody. Int J Cancer 75(4):626–634

Taouli B et al (2003) Evaluation of liver diffusion isotropy and characterization of focal hepatic lesions with two single-shot echo-planar MR imaging sequences: prospective study in 66 patients. Radiology 226(1):71–78

Terreno E et al (2006) Effect of the intracellular localization of a Gd-based imaging probe on the relaxation enhancement of water protons. Magn Reson Med 55(3):491–497

Thijssen VL et al (2006) Galectin-1 is essential in tumor angiogenesis and is a target for antiangiogenesis therapy. Proc Natl Acad Sci U S A 103(43):15975–15980

Thoeny HC et al (2005) Diffusion-weighted MR imaging in monitoring the effect of a vascular targeting agent on rhabdomyosarcoma in rats. Radiology 234(3):756–764
Tilcock C et al (1989) Liposomal Gd-DTPA: preparation and characterization of relaxivity. Radiology 171(1):77–80
Tofts PS et al (1999) Estimating kinetic parameters from dynamic contrast-enhanced T_1-weighted MRI of a diffusable tracer: standardized quantities and symbols. J Magn Reson Imaging 10(3):223–232
Torchilin VP (2007) Targeted pharmaceutical nanocarriers for cancer therapy and imaging. AAPS Journal 9(2):E128–E147
Tropres I et al (2001) Vessel size imaging. Magn Reson Med 45(3):397–408
Turetschek K et al (2001) MRI assessment of microvascular characteristics in experimental breast tumors using a new blood pool contrast agent (MS-325) with correlations to histopathology. J Magn Reson Imaging 14(3):237–242
Turnbull LW (2009) Dynamic contrast-enhanced MRI in the diagnosis and management of breast cancer. NMR Biomed 22(1):28–39
Unger E et al (1988) Gadolinium-DTPA liposomes as a potential MRI contrast agent. Work in progress. Invest Radiol 23(12):928–932
van der Schaft DW et al (2002) The designer anti-angiogenic peptide anginex targets tumor endothelial cells and inhibits tumor growth in animal models. FASEB J 16(14):1991–1993
van Tilborg GA et al (2008a) Improved magnetic resonance molecular imaging of tumor angiogenesis by avidin-induced clearance of nonbound bimodal liposomes. Neoplasia 10(12):1459–1469
van Tilborg GA et al (2008b) Kinetics of avidin-induced clearance of biotinylated bimodal liposomes for improved MR molecular imaging. Magn Reson Med 60(6):1444–1456
Viglianti BL et al (2004) In vivo monitoring of tissue pharmacokinetics of liposome/drug using MRI: illustration of targeted delivery. Magn Reson Med 51(6):1153–1162
Viglianti BL et al (2006) Chemodosimetry of in vivo tumor liposomal drug concentration using MRI. Magn Reson Med 56(5):1011–1018
Weidner N et al (1991) Tumor angiogenesis and metastasis–correlation in invasive breast carcinoma. N Engl J Med 324(1):1–8
Wiener EC et al (1997) Targeting dendrimer-chelates to tumors and tumor cells expressing the high-affinity folate receptor. Invest Radiol 32(12):748–754
Willmann JK et al (2008) Dual-targeted contrast agent for US assessment of tumor angiogenesis in vivo. Radiology 248(3):936–944
Winter PM et al (2003) Molecular imaging of angiogenesis in nascent Vx-2 rabbit tumors using a novel $\alpha_v\beta_3$-targeted nanoparticle and 1.5 tesla magnetic resonance imaging. Cancer Res 63(18):5838–5843
Winter PM et al (2008) Minute dosages of $\alpha_v\beta_3$-targeted fumagillin nanoparticles impair Vx-2 tumor angiogenesis and development in rabbits. FASEB J 22(8):2758–2767
Wolf RL et al (2005) Grading of CNS neoplasms using continuous arterial spin labeled perfusion MR imaging at 3 Tesla. J Magn Reson Imaging 22(4):475–482
Woodhams R et al (2005) Diffusion-weighted imaging of malignant breast tumors: the usefulness of apparent diffusion coefficient (ADC) value and ADC map for the detection of malignant breast tumors and evaluation of cancer extension. J Comput Assist Tomogr 29(5):644–649
Wu B et al (2006) In vivo ^{1}H magnetic resonance spectroscopy in evaluation of hepatocellular carcinoma and its early response to transcatheter arterial chemoembolization. Chin Med Sci J 21(4):258–264
Yang L et al (2009) Single chain epidermal growth factor receptor antibody conjugated nanoparticles for in vivo tumor targeting and imaging. Small 5(2):235–243
Zhao M et al (2003) Magnetic sensors for protease assays. Angew Chem Int Ed Engl 42(12):1375–1378
Zhu W et al (2008) PAMAM dendrimer-based contrast agents for MR imaging of Her-2/neu receptors by a three-step pretargeting approach. Magn Reson Med 59(4):679–685

Part II
Preclinical Studies

Preclinical SPECT and SPECT/CT

Youngho Seo, He Jiang and Benjamin L. Franc

Abstract

The molecular processes underlying carcinogenesis and malignant spread are the foundation of future drug development for the treatment of cancer. Understanding these processes requires study of the interaction of complex biologic systems in a way that spatially and temporally recapitulates that seen in humans. Likewise, once an anticancer agent is developed, its intended antitumor action and its unintended side-effects must be studied in a rigorous and reproducible manner prior to its introduction into the clinic, a process that can benefit from methods that elucidate specific molecular processes and that can be performed serially. Recent advances in small-animal models of cancer, radiochemistry of single photon emitting radionuclides, single photon emission tomography systems, and image reconstruction techniques have set the stage for an ever-increasing use of SPECT and SPECT/CT in preclinical oncology-related applications. Several of these advances as well as several specific applications in oncology are highlighted and areas needing further improvement are identified.

Contents

Y. Seo · H. Jiang · B. L. Franc (✉)
Radiological Associate of Sacramento,
University of California, San Francisco, CA, USA
e-mail: francbl@radiological.com

Y. Seo · H. Jiang
925 Tuscan Lane, Sacramento, CA 95864, USA

O. Schober and B. Riemann (eds.), *Molecular Imaging in Oncology*,
Recent Results in Cancer Research 187, DOI: 10.1007/978-3-642-10853-2_6,

1 Introduction

The molecular processes underlying carcinogenesis and malignant spread are the foundation of future drug development for the treatment of cancer. Understanding these processes requires study of the interaction of complex biologic systems in a way that spatially and temporally recapitulates that seen in humans. Likewise, once an anticancer agent is developed, its intended antitumor action and its unintended side-effects must be studied in a rigorous and reproducible manner prior to its introduction into the clinic, a process that can benefit from methods that elucidate specific molecular processes and that can be performed serially. In short, given the recognition that cancer is a dynamic molecular process, traditional methods employing single-tissue culture or tissue sectioning in small animal models no longer appear sufficient to address these complex, highly intertwined processes. Molecular imaging of small animal models enables the study of molecular interactions in a living system. Single photon emission computed tomography (SPECT) imaging of gamma-emitting radionuclides offers a powerful method of observing processes in vivo with many advantages over other

modalities. By incorporating anatomic data from CT, SPECT/CT provides enhanced tissue-specific radiopharmaceutical localization as well as the opportunity to correct the SPECT data for such physical processes as attenuation of the gamma photons by soft tissue, photon scatter, and collimator blurring.

Over the past 5–10 years, small-animal SPECT and SPECT/CT systems have evolved significantly, now enabling submillimeter resolution of targeted biochemical processes in vivo. SPECT-based quantitative imaging has also come a long way in the preclinical realm. Although highly sophisticated commercial SPECT/CT systems are available, the "plug in and play" mentality is flawed and can lead to very disappointing results and sometimes to incorrect scientific conclusions. The choice of SPECT/CT imaging over other modalities, such as PET or MR, also must be well thought out. SPECT/CT can be an extremely powerful tool in the hands of an oncology investigator who understands the underlying physics of image acquisition, reconstruction, and quantification as well as the limitations of the specific animal model utilized and the targeting method(s) of the radiopharmaceutical agent employed in the study. Generally, a successful SPECT/CT program includes a team of individuals with expertise in physiology, physics, and chemistry.

This chapter is meant to provide a place to begin in the implementation of SPECT and SPECT/CT in preclinical oncology work. Certainly, this chapter does not exhaustively address each of the important components of preclinical SPECT. The chapter is presented in four parts: Part I focuses on various considerations when choosing SPECT/CT in preclinical oncology applications; Part II focuses on considerations when implementing SPECT/CT; Part III describes the "state-of-the-art" in small-animal SPECT/CT device and reconstruction technology; and Part IV provides some examples of the types of preclinical questions and molecular processes that SPECT/CT is suited to address.

2 Part I: Considerations when Evaluating the Potential Role of SPECT/CT Imaging in a Preclinical Oncology Research Application

2.1 Choice and Implications of Various Small Animal Models of Cancer

The most widely available and accepted translational and preclinical testing model in oncology is the mouse, but tumor models useful for the in vivo study of cancer and cancer therapy have also been developed in other species (Uchida et al. 2008). The mouse genome is 95 % identical to the human genome, potentially suggesting that many of the biochemical processes in mice could be extrapolated directly to processes governing disease in humans, an assumption that has proved erroneous in several instances. However, if the mouse model of cancer is carefully selected based on the physiology of the cancer being studied and the research question at hand, the mouse model can be a powerful tool in better understanding biochemical processes in vivo. Mouse models include human xenografts grown in

immunodeficient mice, spontaneous tumors in genetically engineered mice, and tumors in syngeneic mice (de Jong and Maina 2010).

Syngeneic mouse models are generated using primary induction of a tumor in a mouse via chemical or surgical means with subsequent orthotopic or subcutaneous implantation of tumor cells from this primary tumor to na animals of the same species, mouse. Orthotopic models attempt to recapitulate the natural environment of a tumor type but require surgical skill and a more sophisticated surgical setup (sometimes even including ultrasound or other imaging method to guide implantation) than simple subcutaneous implantation. While offering a logistically easy and reproducible approach to generating the tumor model in immunocompetent mice, the mapping of biochemical processes from tumors derived from mice to those derived from humans is often not clear and many such models are not representative of the human form of the cancer being modeled. Generally, this risks the development of models of biochemical pathways that are mouse-specific or developing therapeutic agents that treat the mouse form of the disease but not the form seen in humans, although notable exceptions exist (Lanari et al. 2009). From an imaging perspective, these models are quite straightforward to study as they are immunocompetent and therefore do not require the level of sterile conditions as other models. In addition, tumors are in a pre-assigned location, allowing targeted imaging field-of-view of a primary site with SPECT or SPECT/CT. Although theoretically, given these characteristics, the syngeneic mouse models should allow a method of easily performing serial SPECT imaging of a process or tumor response to therapy, logistics of the local small animal resource center (IACUC), or geographic relationship between the institution's animal care center and SPECT imaging facilities may prevent this type of serial imaging, and investigators must take significant care in planning their experiments in light of these potential logistical hurdles. Some institutions' IACUC may allow temporary holding of a small group of animals in the imaging facility itself to enable such long-term studies with limits based upon the total amount of radioactivity emitted from the animals stored at any one time.

Xenografts and allografts utilize human-derived cell lines or explants that are implanted in subcutaneous or orthotopic locations in immunodeficient mice (e.g., athymic (nu/nu) mice or mice with severe combined immunodeficiency—SCID.) Specific human cell lines of a cancer may be chosen because they express a specific molecular marker that can be targeted for imaging or therapy or are derived from malignant cells within a particular phase of a cancers' metastatic progression. For example, more than 30 prostate cancer cell lines developed over the past century show differing levels of expression of androgen receptor and prostate-specific antigen (PSA), two key molecular targets in clinical prostate cancer imaging and therapy (van Weerden et al. 2009). Alternatively, na cell lines can be genetically engineered to express such a specific molecular marker. The mouse environment may or may not accurately reflect the human environment for a specific tumor type, and xenograft models have shown correlation between preclinical and clinical efficacy only in specific cell types and under specific conditions (Voskoglou-Nomikos et al. 2003). Despite this, xenograft models have remained the most widely utilized in vivo tumor models and are particularly

valuable in testing hypotheses about tumor growth and differentiation when those questions are reasonably separable from the tumor environment or in the development and evaluation of therapies that require immune response or that target-specific components of blood vessels or the extracellular matrix (Charafe-Jauffret et al. 2009; Sausville and Burger 2006). SPECT imaging studies with these types of models can be challenging given the higher degree of sterility demanded by immunosuppressed animals and the inherent logistical hurdles of serial studies. Short-term serial studies (over a period of a few days to 2 weeks) may be accomplished using a temporary holding facility in the imaging suite. Alternatively, both institutional-specific and commercial efforts have been made to provide solutions to the transport of small animals between the imaging device and the sterile barrier.

The availability of genetically engineered mouse strains has improved significantly over the past decade due, in part, to multi-institutional collaborative efforts such as the National Cancer Institute's Mouse Models of Human Cancer Consortium in the United States. Genetically engineered spontaneous mouse models of cancer offer the ability to study a malignancy from its initial development through its course of progression to local and eventual distant metastasis in an immunocompetent mouse system (Eyles et al. 2010; Milagre et al. 2010). Broadly, spontaneous mouse models can be separated into 'knock-in' models, where the endogenous sequence of a gene is exchanged for one that mimics carcinogenesis in the human, and 'knock out' models, where the function or expression of an endogenous gene is suppressed. Although these models utilize syngeneic mice, the genetic, molecular, and histologic characteristics of spontaneous tumors in these models often closely reflect those of the human form of the malignancy and have been integral in the elucidation of the molecular mechanisms behind various forms of carcinogenesis (Milagre et al. 2010; Li et al. 2003). The background in which the tumor arises, for instance in BRCA-null murine breast cancer models, may also more closely mimic the clinical patient for whom a drug is being developed (Fasano and Muggia 2009). The ability to study the tumor and its interactions with the molecular environment are invaluable. Drawbacks of these models are the high cost of developing and maintaining such mouse lines and the high degree of expertise maintenance of such strains require, underscoring the advantage of collaborating with a mouse model group.

Within each of these general classifications of mouse tumor models, further refinement of the specific model chosen for study depends on whether primary or metastatic malignancy (e.g. metastatic disease to bone, lung, or brain) is being studied (Palmieri et al. 2006; Zhau et al. 2000). If in vivo characterization of an oncologic process is to be addressed using in vivo imaging, including SPECT, the level of robustness of the animal to withstanding multiple manipulations and the logistics of studying the tumor using in vivo imaging must be considered to ensure the success of the study. The idea of in vivo imaging is to image processes in a live animal. An overview of the advantages and disadvantages of various tumor models is provided in a recently published set of guidelines for the use of animals in cancer research (Workman et al. 2010).

2.2 Framing the Research Question in Imaging Terms

The first step in understanding whether SPECT/CT is an applicable modality to any preclinical oncology research is to define the types of measurements or observations that are required to answer the research question. Is the researcher chiefly interested in monitoring a change in tumor volume or are there other specific processes in the tumor or in its microenvironment that are of interest?

Questions of anatomical growth of a spontaneous tumor are best answered using high resolution anatomical imaging methods, such as MR or CT. Questions related to viable mass of implanted tumor may be most easily addressed with bioluminescence. Perfusion may be studied with MR or fast-acquisition CT or SPECT. Studies of physiologic processes involving major organic molecules or studies requiring absolute quantification may be addressed with PET. SPECT is useful for identifying ligand–receptor relationships, monitoring the locations of administered radiolabeled molecules (over a short time course), and in vivo molecular characterization of tumors. Obviously, it behooves the researcher to thoroughly plan the imaging portion of any research project before even initiating growth of the first tumor in the first animal model as the research questions, required mesasurements, chosen animal model, and available imaging modalities must all be in sync spatially and temporally to ensure valid data.

2.3 Available in vivo Imaging Modalities and Characteristics of Preclinical Oncology Applications Amenable to SPECT

Traditional methods of monitoring molecular processes, tumor growth, and tumor response to therapy in small animals is still often accomplished using tissue sectioning and microscopy or, in the case of radionuclide-based assays, well-counting and autoradiography after euthanasia. These conventional methods provide a relatively inexpensive means of studying large cohorts of animals and the vast majority of molecular markers can only be assayed using histological methods. However, molecular imaging modalities have certainly assumed a critical role in monitoring a single animal over serial timepoints.

In vivo gamma imaging (including SPECT) is most applicable to studying deep tissues and is therefore particularly suited for orthotopic tumor models with/without potential for metastasis (for example, LNCaP orthotopic prostate cancer model) (Wang et al. 2005) or spontaneous tumor models (for e.g,, pancreatic neuroendocrine tumors in transgenic models (Hanahan 1989). Structures at or just below the skin's surface/subcutaneous tissues and tissues able to be assessed via endoscopic means may be more amenable to optical imaging (bioluminescence vs. fluorescence), a group of techniques that are relatively inexpensive, utilize stable imaging agents, and do not subject the animal or tumor to ionizing radiation. MR also provides a means of interrogating deep tissues and does not provide radiation dose to the tumor-bearing animal. MR tends to be quite expensive to implement, usually focuses on a narrow field of view, and provides access to interrogation of a

limited number of processes unless spectroscopic or other advanced time-intensive techniques are employed. There has been continued interest, however, in the development of contrast agents for MR imaging (Ni et al. 2009). PET imaging offers equal or higher sensitivity than SPECT and allows for absolute quantification, an area where significant progress has been made in SPECT in only the past few years. PET radiochemistry is typically far more complex than linking targeting agents to gamma-emitting radionuclides and requires a cyclotron and other sophisticated infrastructure.

Thus, gamma imaging/SPECT is uniquely suited for studying the presence of specific molecular markers or processes in small animal cancer models when a radiolabeled ligand is able to be produced. SPECT is also capable of providing images of multiple probes labeled with different isotopes, enabling simultaneous study of multiple molecular or cellular events. SPECT is capable of resolving very small primary tumors or their metastases (on the order of 1–2 mm), and therefore is a viable method for evaluating all types of mouse models of cancer, including spontaneous models where the primary or metastatic sites may be unknown and can be quite small.

2.4 SPECT Versus SPECT/CT

The integration of SPECT/CT in a single small animal imaging device has been accomplished by mounting both CT and gamma camera components on a single gantry in an "in-line" configuration. The CT portion of these systems are typically comprised of a microfocus X-ray tube source and X-ray detector (e.g., a charge-coupled device or a complementary metal oxide semiconductor with pixels on the order of 50 um), achieving reconstructed resolutions < 100 um. Contrast may also be used to enhance delineation of soft tissues, although this proves to be quite challenging.

When utilizing small animal tumor models in which small tumors are growing in deep tissues, the coregistration of SPECT images with CT can be invaluable as physiologic excretion of the tracer or focal tracer collection in the blood pool can be differentiated from a small soft tissue tumor. In humans, the CT portion of the SPECT/CT often provides near-diagnostic quality images that clearly elucidate the anatomic abnormality associated with the lesion on SPECT and can greatly assist in the diagnosis. In practice, the CT portion of the SPECT/CT for small animals is more limited in its contribution, secondary, in part, to (1) the difficulty in administering the volumes of contrast necessary through the tiny veins of a mouse in any time period in which images could be acquired, (2) the difficulty in timing administration of oral contrasts in feeds with anesthesia and imaging, (3) the compact nature of the organs in lab animals as compared with the typical patient whose slower metabolism allows for the accumulation of a significant amount of fat that separates organs and other anatomic structures, and (4) the relatively low levels of radiation used in small animal CT systems and the limitation on contrast and signal-to-noise ratios imposed by small voxel sizes. Realistically, the

correlation of focal radiopharmaceutical uptake on SPECT within a specific organ location (e.g. the pancreatic head), within a discrete soft tissue structure (e.g. localization within nodule surrounded by fat rather than localization within adjacent muscle), or simply in relation to the skeleton, is considered a successful contribution of CT in small- animal SPECT/CT; it is not common for small tumors within organs to be able to be seen discretely on the CT portion of small-animal SPECT/CT.

A more substantial contribution of CT in SPECT/CT may be its use to assemble an attenuation map and to provide structural data for incorporation into the reconstruction algorithm. By providing correction of the SPECT image for attenuation and blurring, these types of reconstruction algorithms will undoubtedly play a large role in the future of SPECT/CT's use in small animal imaging as there is an ever-increasing demand for quantitatively accurate imaging of radiopharmaceutical distribution. The remainder of this chapter will focus on SPECT/CT as a single–dual modality imaging method for preclinical oncology studies.

3 Part II: Technical Considerations When Implementing SPECT/CT in Preclinical Oncology Research

3.1 Anesthesia and Animal Handling

SPECT/CT imaging typically captures a snapshot of a biochemical/molecular process at a specific time point. Because anesthesia and animal handling can both influence molecular processes systemically, they can potentially have non-negligible effects on the biodistribution of radioactively labeled tracers. Experimental conditions before, during, and after imaging must remain consistent across the population of animals studies and should minimize stress to the animal. The same animal strain and sex should be used throughout a study to avoid altered baseline pharmacokinetics and physiology. The timing of imaging experiments should take the circadian cycle into account to enable reproducibility (Hildebrandt et al. 2008).

It is imperative to keep the animal restrained during SPECT/CT imaging to ensure high spatial resolution and accurate coregistration of the SPECT and CT portions of the exam. More extended anesthesia and special imaging chamber setups may be necessary if the researcher also wants to perform MR or image the distribution of a PET radiopharmaceutical with subsequent coregistration to SPECT/CT images (Chow et al. 2006). Anesthetics commonly employed to restrain small animals during imaging include injected drugs, such as barbiturates and ketamine, and inhaled anesthetics such as isoflurane. Highly lipid-soluble barbiturates, such as pentobarbital, are short- or ultrashort-acting, typically resulting in anesthesia times of < 1 h and total sleep times < 2–3 h. Side effects that could affect image acquisition approach includes respiratory depression and reduced cardiovascular output. Ketamine, another injectable (i.v. or i.p.) drug that is commonly employed along with other anesthetics, lacks a significant effect on respiration or cardiac output. Obviously if a SPECT imaging agent targets

adrenergic receptors or other points along the sympathetic nervous response, ketamine would potentially interfere with the study; however, there is also evidence of other potential changes in tracer biodistribution that depends on the anesthetic agent used, particularly when targeting processes in the brain. In intracranial applications, a mouse conscious restrain system may be preferred over anesthesia. Ketamine is commonly administered with a muscle relaxant/sedative (e.g. xylazine) and, as such, can provide anesthesia for < 30 min and total sleep times < 1–2 h. Importantly, potential side effects of the ketamine/xylazine combination include respiratory depression, hypotension, bradycardia, hypothermia, and hypoglycemia (Hildebrandt et al. 2008). The experimental setup must take into account these potential side effects. For example, an i.v. catheter may need to be maintained during the imaging study in case hydrating fluids or glucose needs to be administered. Likewise, all setups should include a heat lamp to avoid hypothermia. Even throughout the imaging period, anesthetized animals require constant attention. Although rodents have very rapid heart and respiratory rates, equipment is available for monitoring the physiology of small animals. In vivo studies can go very badly, very quickly, and ex vivo imaging is usually not the primary goal in SPECT/CT. Inhalation anesthetics offer significantly improved control of anesthesia than injectable anesthetics and possess less potential for impaired cardiac function as well as more rapid recovery times. Special preparations may be required to implement inhaled anesthesia in the SPECT/CT imaging suite, depending on the configuration of the SPECT/CT imaging system and the space available. Dead space in the anesthesia circuit should be minimized (Colby and Morenko 2004).

In general, the stress of anesthesia, and in particular, multiple sequential episodes of anesthesia must be considered and minimized when designing experiments. Complications of anesthesia include hypothermia, pulmonary telectasis, hypercapnia, acidosis, hypoxia, hepatic toxicity, and tracheal irritation from repeated intubations (Colby and Morenko 2004). Not only can these cause significant alterations in the biodistribution of the radiopharmaceutical, but they can be life-threatening to the animal research subject. Simple strategies, such as employing multiple animal cohorts with imaging timepoints that partially overlap, can be useful in reducing the risk of losing critical amounts of data secondary to imaging-related complications.

3.2 Availability of Radiopharmaceuticals and Evaluation of Their Biodistribution Characteristics

Several commercially available single photon-emitting radiopharmaceuticals are available for clinical use and can also have applications in small animal imaging. These include In-111-labeled pentetreotide, a somatostatin analog that can image neuroendocrine tumors; (Bombardieri et al. 2010) Tc-99m—sestamibi and Tc-99m tetrofosmin, two cardiac perfusion agents that have also been utilized in a number

of oncologic applications such as in brain cancer, lung cancer, and lymphoma; (Schillaci et al. 2005) and In-111-labeled capromab pendetide (Prostascint) for tumors expressing prostate-specific antigen. In addition, other indirect tumor imaging agents, such as Tc-99m-methylene diphosphonate (MDP) that targets osteoblastic activity surrounding osseous metastatic disease, have proven useful in proving the validity of various mouse bone metastatic models using small-animal SPECT (Yang et al. 2009).

In addition, relatively straightforward chemistry has also been developed to label molecules for specific applications in small-animal SPECT. For example, radiolabeled antibodies (such as Tc-99m epidermal growth factor receptor (EGFR) (Meenakshi et al. 2003) and labeled peptides can be prepared using direct labeling of a moiety or via a linkage/chelator mechanism (Gooden et al. 1995). Some molecules that have been extensively studied, such as annexin V, have been labeled with a variety of gamma-emitting radionuclides, each with their own set of advantages and disadvantages (Boersma et al. 2005). In single chain antibody fragment synthesis and peptide synthesis, there is greater flexibility in techniques as amino acids enabling direct labeling can be incorporated outside of the active targeting site (Verhaar et al. 1996; Bolton and Hunter 1973). Manual or automated peptide synthesis can be used to produce targeting probes containing synthetic amino acids with sites for post-synthesis radiometal chelation (Stephenson et al. 2004). Alternatively, disulfide bonds, strategies utilizing high affinity streptavidin–biotin interactions, or other techniques can be used to link the targeting portion of the molecule to the radionuclide-containing residues (Virzi et al. 1991). Other small molecule classes, such as nucleic acids, have also been radiolabeled with radionuclides capable of being imaged with SPECT (Mamede et al. 2004; Mardirossian et al. 1997).

Of paramount importance is optimizing the radiopharmaceutical for SPECT/CT imaging by optimizing its ratio of uptake in the tumor to that in background (T:B) through chemistry-mediated methods and timing, as well as optimization of its biodistribution. Selection of chemistry techniques and strategies can have significant ramifications on the biodistribution of the resulting radiopharmaceutical. For example, non-specific binding of Tc-99m to the amino group when labeling antibodies has been shown to occur in a significant fraction of the labeled molecules and can lead to increased hepatic uptake and resulting diminished uptake in the tumor itself (John et al. 1994). One strategy to enhance target-to-background activity has been to image farther out from the time of radiopharmaceutical administration as the non-specific uptake in organs often dissipates over time. By maintaining targeted molecular imaging agents in circulation, modification with polyethylene glycol chains allows greater bioavailability for tumor uptake (Kim et al. 2004). Coupling of antibody fragments with larger molecules, such as albumin, have also demonstrated increased tumor targeting, deposition and retention, as well as high tumor to blood ratios (Dennis et al. 2007).

Such techniques are especially useful in designing effective molecular radiopharmaceuticals for small-animal SPECT applications because of the high metabolic rates of rodents and the resulting rapid extraction of agents from the blood by the liver and kidneys. When using conjugate linkers, stability of the chelate is a

key factor in acquiring high-quality images and parameters of stability should be provided by the radiochemistry laboratory. Methods to improve stability, such as modifying peptide sequences to enable better coordination with chelator, can be useful (King et al. 2009).

3.3 Injection of the Radiopharmaceutical

As a rule of thumb, the maximum volume of an intravenous injection should not exceed 4–5 % of the animal's blood volume. Thus, coordination between the animal imaging researcher and the radiochemistry laboratory is imperative. Increasing the time between radiochemistry preparation and purification results in decreasing the dose/volume injected and can result in decreased sensitivity for the detection of a specific molecular target. Potential for breakdown of the radiopharmaceutical must also be considered when planning for the time before dose administration as well as the pH, buffer capacity, and other characteristics of the solvent in which the radiopharmaceutical is administered. Some purified agents may be highly acidic or basic, and care must be taken to provide these to the animal in a form that does not damage the vein or adversely affect the animals' health. The specific activity (radioactivity per mass) will also decrease over time for any given radiopharmaceutical. As this occurs, for any administered dose, a larger number of molecules are injected. The relatively lower initial specific activity of many SPECT imaging probes in general and the requirements of high specific activity for increased spatial resolution equate into an elevated risk that a higher binding occupancy of receptors will be achieved, enabling a pharmacologic effect rather than simply providing labeling of a small number of receptors for imaging (Hildebrandt et al. 2008).

Of course, if more than a single imaging time point is planned prior to animal sacrifice, the injection must be made only following sterile preparation of the injection site. More complicated injection scenarios (such as under a biologics hood) may be required in the case of immunodeficient mice (e.g. SCID mice).

3.4 Injection of CT Contrast Agent

In small animals, constant infusion of CT contrast agents is typically required, with exact volume rates depending on the concentration of iodine in the contrast agent. Thus, volumes of administered fluid may exceed those that can be handled by the circulatory system. Complications of CT contrast agents in mice include renal toxicity and hypersensitivity.

3.5 Radiation Exposure

One drawback to SPECT/CT is the added dose of ionizing radiation in forming the CT image over that of SPECT alone. Radiation doses to the small animal subject

during SPECT during a single study are probably non-significant, with whole body exposure estimates ranging from 6 to 90 cGy in mice and 1–27 cGy for rats (Funk et al. 2004). Tissue activity concentrations in small animal studies is higher than in humans but the small size of rodents results in a higher fraction of gamma radiation escaping prior to interaction with the animals' soft tissues. Cumulative effects of radiation provided by multiple administrations of radiopharmaceuticals is not negligible. For instance, the kidneys retain circulating peptides for significant periods and long-term nephrotoxic effects have been observed in mice administered In-111-labeled peptides (octreotide, exendin, octreotate, neurotensin, and minigastrin analogs) for imaging at 3–6 week intervals over a course of 16–20 weeks. Murine gene expression can be altered at doses of 20 cGy (Melis et al. 2010; Amundson et al. 2001).

Radiation provided to the small animal during a single CT exam is probably also insignificant in most cases. Using thermoluminescent dosimeters (TLDs), Figueroa et al. (2008) showed that the average mouse organ received a radiation absorbed dose of 76.0 ± 5.0 mGy (Figueroa et al. 2008). Others have reported radiation doses ranging from 35 to 300 mGy (Boone et al. 2004). A more recent investigation of the biologic effects of CT obtained as an anatomic reference image in a small animal SPECT/CT imaging system found that DNA damage was evident in the liver and small bowel for up to 3 days following CT. Although the investigators concluded that reference CT images could be produced without observable DNA damage or compromised image quality if low voltage, flux, and exposure time were implemented, the standard settings provided by the manufacturer tended to underestimate the actual absorbed dose. Care must be given to truly understand the parameters of the imaging system and not treat the system as ready to use "out of the box" (Kersemans et al. 2011).

Radiation-induced tumorigenesis is not generally a concern given the relatively short timeframes of any serial mouse imaging studies and the long time frame of radiation-induced malignancy. However, multiple exposures to radiation from CT may have a positive or a negative effect on tumor growth. Using histomorphometry, a study evaluating the effect of weekly small-animal CT studies over a course of 5 weeks on a mouse model of breast cancer metastatic to bone found a significant increase in tumor areas in the leg bones of mice that received weekly CT exposure when compared to mice without such exposure (Cowey et al. 2007). On the other hand, there is a theoretical possibility of some therapeutic effect of the radiation provided to tumors by CT over multiple serial imaging timepoints. Even over multiple studies, however, there is an ability to minimize CT radiation dose to a level that would be unlikely to have any such therapeutic effect by adjusting various acquisition parameters or utilizing a multidetector system that is capable of ultrafast CT (Carlson et al. 2007). These parameters will be discussed later in this chapter. In extreme cases, such as monitoring expression of a tumor receptor with SPECT/CT imaging on a near daily basis over a prolonged period (e.g. over the course of several weeks), SPECT—alone could be considered, but, for the foreseeable future, SPECT/CT will be the standard modality for in vivo gamma imaging in small animals.

4 Part III: State-of-the-Art Preclinical SPECT/CT Systems

4.1 SPECT/CT System Design

While it is unlikely that the small animal imaging researcher in oncology will have the opportunity to choose the exact model of SPECT/CT imaging system used and will likely have to accept whatever is available at the given research institution, it is important to understand the general parameters governing the acquisition of quality SPECT images and any particular characteristics inherent to the system being utilized. Over the past decade, there have been significant innovations in small-animal SPECT and SPECT/CT that address camera sensitivity, spatial resolution, and image reconstruction, and quantification. The earliest systems were composed of a single scintillation camera with a single pinhole collimator. Systems have now evolved to include multiple detectors, each with multipinhole collimators, allowing a combination of high (millimeter or submillimeter) spatial resolution and rapid acquisition speed (Fig. 1). The multipinhole design can increase the system sensitivity by approximately a factor equal to the number of pinholes allowing better spatial resolution from the use of smaller pinholes without sacrificing counting statistics. When using a multipinhole collimator, an important distinction to make is whether the collimator design is non-overlapping or overlapping (multiplexing). Multiplexing can diminish the signal-to-noise ratio and may facilitate artifacts. Of course, the choice of collimators also depends on the application: small field-of-view acquisitions (e.g. of an intracranial malignancy) can benefit from pinhole collimation while parallel-hole collimation is required on traditional systems to achieve large FOV acquisitions (e.g. when imaging the whole animal to evaluate extent of metastatic disease).

A critical step in the image-making process is acquisition of projection information about the radiopharmaceutical distribution by the detector. In order to enable eventual reconstruction of high-quality images, detectors must have a high intrinsic efficiency, good energy resolution, and good intrinsic spatial resolution (Madsen 2007). Detector technology has itself advanced, moving from traditional scintillators to small compact detectors specifically designed for application in small-animal SPECT. For example, position-sensitive photomultiplier tubes and segmented scintillation crystals allow more efficient use of detector area and enable greater magnification. When utilizing cameras with position-sensitive photomultiplier tubes, it is important to pay close attention to calibration to achieve good spatial uniformity and to correct for pincushion distortion. In general, a rigorous quality assurance process should be implemented with regular evaluations of camera spatial resolution, spatial uniformity, energy resolution, and counting-rate response. SPECT/CT imaging systems are often shared by numerous laboratories, each of which may require different system configurations (in terms of collimators, etc.). The more users and changes made to the configuration, generally the more often recalibration will be necessary. What may seem a mild misalignment or minimal change in calibration can have devastating effects on the quality of imaging data in longitudinal studies.

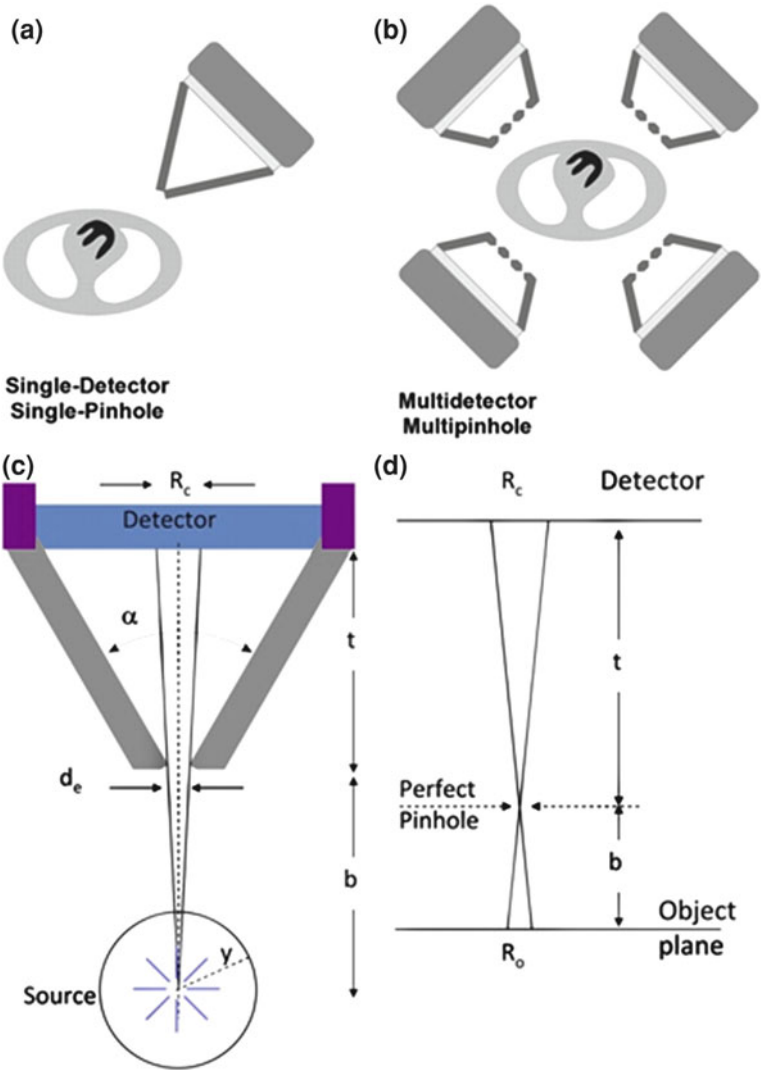

Fig. 1 Schematic diagrams of single- (**a**), multi-pinhole-multi-detector (**b**) small-animal SPECT systems. The image magnification is achieved by the source-to-pinhole-to-detector geometry (**c** and **d**). R_c = geometric resolution measured on detector plane; R_0 = detector point-spread function projected to object plane; d_e = pinhole aperture; α = angle between collimator walls, t = pinhole aperture-to-detector distance; b = pinhole-aperture-to-object distance. Reprinted with permission from Ref. Franc et al. (2008)

Solid-state materials, such as cadmium zinc telluride (CZT), have been implemented in some detectors to directly convert the gamma photon into an electrical signal and have proven to provide images with very high spatial resolution as well as both high- and low- energy resolution (Kastis et al. 2004). Older

CZT detector systems can be prone to minute impurities associated with low-energy spectral tailing, pixel dropout, hot spots, and nonuniform response (Takahashi and Watanabe 2001).

4.2 A Sampling of Available Small-Animal SPECT- and SPECT/CT Systems

Some of the first and most advanced systems are "one-of-a-kind" and are housed in specific research institutions. The preclinical SPECT/CT scanner built at UCSF has an in-plane SPECT/CT configuration with single pinhole collimation. Both the SPECT and CT components are made of semiconductor materials (CdZnTe and gadolinium oxysulfide, respectively) and both have helical scan capability. A compact SPECT/CT system designed and built at the University of Arizona's Center for Gamma-Ray Imaging has an in-plane SPECT/CT configuration and utilizes the CdZnTe detector materials as the SPECT camera (Kastis et al. 2004). However, it utilizes a rotating stage (vertical animal holder), similar to that reported earlier from the University of Amsterdam (Habraken et al. 2001) rather than the traditional rotating detector model. Collimation is high resolution parallel-hole with a matching pitch on detector pixels. A SPECT unit with a high degree of flexibility in the pinhole collimation configuration and magnification has also been developed by the same group (Hesterman et al. 2007). There are two generations of the preclinical SPECT/CT development from the group from Jefferson Lab and University of Virginia in collaboration with Johns Hopkins University (Stolin et al. 2005; Weisenberger et al. 2006). These are notable for their use of position-sensitive photomultiplier tubes in the SPECT detector (NaI(Tl)-PSPMT). Either parallel-hole or pinhole collimation is possible. A current configuration of this imaging system allows imaging unanesthetized mice using infrared tracking for animal motion (Weisenberger et al. 2005).

The first commercially available preclinical integrated SPECT/CT scanner was the Gamma Medica-Ideas X-SPECT^{TM} that combined a NaI(Tl)- or CdZnTe—based gamma camera with a microfocus conebeam X-ray CT scanner with solid-state detector (GOS/CMOS) in an in-plane configuration. Various collimator configurations are available, including parallel-hole, single pinhole, and multi-pinhole with different fields of view (FOVs) depending on whether mice or rats are imaged. A single platform incorporating this SPECT/CT system with PET has also been introduced by the company and is currently marketed by GE as the Triumph (Carcieri et al. 2006).

Another commercially available preclinical system capable of configuration as a triple-modality system (SPECT and CT in plane and PET module adjacent) is Siemens' Inveon. The Inveon SPECT detector features NaI(Tl)-PSPMT and the CT detector is composed of GOS/CCD. Collimation can be parallel-holes-, single pinhole-, or multipinhole- type.

Not all commercially available SPECT/CT systems are in-plane. Bioscan's NanoSPECT and MILabs' U-SPECT II, both multipinhole SPECT systems that

provide stationary acquisition modes and very high spatial resolution, are offered as a docked or serial configuration combining two separate SPECT and CT modules. This configuration requires a animal bed that translates between the two imaging modalities, a fact that needs to be taken into consideration when setting up the animal's anesthesia apparatus. One advantage of such a configuration, however, is the ability to acquire SPECT and CT images independently. This could be beneficial in the setting of serial imaging studies where the potential effect of CT dose on the tumor or animal may be non-negligible. The U-SPECT I is also notable for its high sensitivity, with a reported discrimination between molecular concentrations of radiopharmaceutical in adjacent volumes as small as 0.1 μL in a small FOV, achieved by a multi-pinhole collimation configuration that uses 75 micropinhole apertures in a cylindrical imaging cavity (Beekman et al. 2005). High resolution whole-body imaging has also been performed using the same system (Vastenhouw and Beekman 2007). The U-SPECT II system improved upon U-SPECT I by enabling sophisticated focusing capabilities to regions of interest chosen "on-line" by the user and allowing the high sensitivity required for dynamic imaging (van der Have et al. 2009).

An alternative to a dedicated small-animal SPECT or SPECT/CT camera is the use of a clinical SPECT system in combination with a multipinhole collimator (Difilippo 2008). This may be the most efficient use of space for an imaging laboratory that performs studies in animals of a range of sizes (e.g. mice, rats, sheeps, pigs, dogs, and/or horses).

The discussion of systems above is certainly not exhaustive and does not include all of the systems developed or being developed. However, many of the key features of all current systems have been included in the sampling of systems described above.

4.3 Image Reconstruction Techniques and the Quest for Quantitative SPECT

A SPECT study essentially is composed of multiple planar images acquired at a number of angles, creating a set of projection data. An image dataset is then reconstructed from this projection data. The most basic of tomographic image reconstruction algorithms, filtered backprojection (FBP) takes the counts in the projections from thin "slices" of the imaged subject and redistributes them in a spatial distribution by "backprojecting" the data (with or without prior filtering) by smearing the projected data back along the same line as from where the photon was emitted. Obviously, this is an imperfect solution to the reconstruction problem that produces adequate images in many instances but is not amenable to quantitative applications.

Iterative reconstruction techniques, including ordered subsets expectation maximization (OSEM) and maximum likelihood expectation maximization (MLEM) essentially predict what the final image should look like, create a

projected dataset from that predicted image, compare the acquired projected dataset to the projection data of the predicted image and makes some adjustments, repeating the process iteratively for a set number of iterations or until some stop condition is met. Although these techniques may be more susceptible to motion artifacts and artifacts induced from spurious noise, they enable further corrections to be incorporated during or after (post-) reconstruction and are therefore the basis of quantitative SPECT imaging reconstruction techniques.

The concept of quantitative SPECT is only recently being realized. The ability to achieve accurate and quantitative image data is complicated by limitations in instrumentation and the imaging process. The imaging system possesses an intrinsic resolution, blurring the distribution of radioactivity, and contributing to partial-volume effect. When traveling through tissue, gamma photons may be scattered or absorbed. Photon attenuation and scatter play a much smaller role in small animal imaging than in human imaging. Attenuation of photons by soft tissue is estimated to be up to 50 % when imaging I-125 and up to 25 % when imaging Tc-99m in rodent-sized objects. In general, an estimated 20–25 % of the total counts in the projected image dataset may be accounted for by scattered photons, although the number falls to 10 % in the case of Tc-99m and the overall contribution to scatter effect to quantitative error turns out to be relatively small for numerous reasons (Hwang et al. 2008; Hwang and Hasegawa 2005).

Photon attenuation can be accounted for in reconstruction or post-reconstruction processing. The reconstructed image can be used to extract an animal boundary used in post-processing calculations. More accurately, an external radiation source (e.g. CT) can be used to map the attenuation distribution of the animal, making the advantage of dual-modality SPECT/CT obvious (Kastis et al. 2004; Weisenberger et al. 2003). Early work in the area of improving the quantitative abilities of small-animal SPECT by utilizing data from the CT to provide specific attenuation maps was focused on cardiac applications (Hwang 2006). More recently, using CT to provide attenuation maps for incorporation into iterative reconstruction of scatter- and attenuation-corrected pinhole SPECT images, researchers have achieved quantitative measurements of activity concentrations in a mouse with an average error of -8 ± 10 % when compared to measurements from a dose calibrator (Vanhove et al. 2011). Using body outline contours obtained with optical cameras, another group has implemented the post-reconstruction correction algorithm developed by Chang, (Chang 1978) a first order attenuation correction algorithm, to correct data acquired with focusing pinhole SPECT for attenuation (Beekman et al. 2005; Beekman and Vastenhouw 2004). In combination with scatter correction, the method derived from the Chang algorithm produced images with average quantitative measurement error of 1.7 % in phantoms and 2.1 % in animal studies (Wu et al. 2010). Other promising approaches to improving the quantitative accuracy of SPECT data have been designed for human clinical systems, and hopefully some of these same techniques will prove useful in small animal imaging (Dewaraja et al. 2010).

5 Part IV: Recent Examples of SPECT/CT as Applied in the Preclinical Oncology Setting

5.1 Characterizing Tumor Perfusion or Other Inherent Characteristics

One of the most promising areas in the application of molecular imaging in oncology is the characterization of molecular processes underlying tumorigenesis and malignant spread in a spatial and temporal manner. SPECT agents approved for use in humans, such as the perfusion agents Tc-99m-sestamibi (Tc-99m-MIBI) and Tc-99m-Tetrofosmin uptake (Tc-99m-TF) have found new applications in evaluation of tumors for expression of P-glycoprotein (Pgp) and multidrug resistance-related protein-1 (MRP), potential factors in failure of tumors to respond to chemotherapy (Fuster et al. 2003). The high resolution of small-animal SPECT imaging systems enables inherent heterogeneities in tumor perfusion or in the distribution of other radiopharmaceuticals to be visualized (Umeda et al. 2012).

Many novel molecules have been developed and radiolabeled with the specific purpose of providing in vivo characterization of processes of tumor genesis or progression. For example, integrins, specifically the alpha(v)beta(3) heterodimers, have been linked to tumor-induced angiogenesis and invasiveness and radiolabeled ligand analogs to these receptors have been imaged with SPECT with the goal of mapping the distribution of receptors in tumors as well as the biodistribution of these molecular reporters (Edwards et al. 2009; Dijkgraaf et al. 2009). SPECT imaging of IGF-1R expression has been demonstrated using the radiolabeled antibody R1507 in a triple-negative breast cancer model (Heskamp et al. 2010). The temporal changes in apoptosis of numerous cancer types during therapy have been monitored qualitatively and quantitatively with SPECT using Tc-99m-hydrazinonicotinamide (HYNIC)-annexin V (Vangestel et al. 2011). Other molecules developed specifically for tumor characterization, such as hypoxic agents, have been adapted for potential imaging with SPECT (Chapman et al. 1996).

5.2 Imaging the Targeting Abilities of Molecules in the Development of Potential Therapeutics and Molecular Imaging Agents

Antibody-based therapies have evolved to become important tools in cancer therapy and several have shown efficacy in slowing progression of a malignancy and improving progression-free survival. The targeted nature of these therapies allows increased localization at the site of disease, affording less side effects from non-specific delivery of therapy to normal tissues and potentially increased efficacy. Evaluation and honing of this targeting capacity in small animals is an

important tool in the development of immune- and radioimmuno-therapies. The biodistribution of antibody therapy, and whether a sufficient amount of antibody will ultimately reach its target, can often best be assessed with in vivo studies, and imaging a single animal serially can help to fully understand the pharmacokinetics and elucidate and evaluate potential strategies to improve the targeting rate of the antibody.

In the case of xenografts implanted in the subcutaneous tissues of the small animal model, such as in a study evaluating the biodistribution and pharmacokinetics of a fully humanized anti-EGFR mAb using an In-111—labeled version of the Ab in multiple tumor cell lines, planar scintigraphy may provide sufficient imaging data if the targeted disease is easily separated from areas of physiologic tracer distribution. For instance, if the tumor is located in the flank or near the hindlimb, it can be easily separated from the non-specific uptake in the kidneys and liver. The fine anatomic localization provided by CT in SPECT/CT would not have added much value in this set of experiments. Interestingly, the significant findings in this study were the differing pharmacokinetics of the antibody depending on the presence or absence of tumor in the animal (Ray et al. 2009). In another xenograft-based study of Ab therapeutic efficacy, a Tc-99m—labeled mouse mAb that binds to the DR5 death receptor for tumor necrosis factor-related apoptosis-inducing ligand (TRAIL/Apo2L), TRA-8, was imaged with SPECT. The SPECT imaging data provided a significant piece of information by demonstrating comparable 99 mTc-TRA-8 delivery to all of the animals studied. This information helped to support the hypothesis that increased efficacy observed when TRA-8 was given in combination with CPT-11 was due to the combination of drugs rather than spurious improved delivery of TRA-8 in one particular animal (Oliver et al. 2008).

Baranowska-Kortylewicz et al. 2005 used SPECT imaging of I-125-labeled tumor-specific antibody to provide evidence of increased antibody uptake in colon adenocarcinomas grown subcutaneously in SCID mice following administration of the tumor stroma–reactive STI571, a platelet-derived growth factor receptor-B (PDGFr-B) antagonist (Baranowska-Kortylewicz et al. 2005). Similarly, imaging radiolabeled antibodies with SPECT has provided important information in targeting and dose optimization of several potential antibody-based therapies (Ray et al. 2009; Hoeben and 2010).

Significantly increased interest in peptides and other small molecules as cancer therapeutics has recently encouraged the design and use of radiolabeled forms of these molecules to better understand their pharmacokinetics and biodistributions in small animal models. Sosabowski et al. (2009) evaluated the biodistribution of a divalent peptide targeting gastrin/cholecystokinin subtype 2 receptors (CCK-2Rs) with SPECT/CT as one of a battery of tests to evaluate its use as a potential targeting agent for peptide receptor radionuclide therapy (PRRT) of cancer. Important information obtained from these studies included the fact that the rate of washout of the divalent peptide from the tumor was lower than its monomeric form (Sosabowski et al. 2009).

He et al. (2010) used SPECT/CT to evaluate the tumor targeting capability and potential of an internalizing human antibody fragment (UA20) labeled with

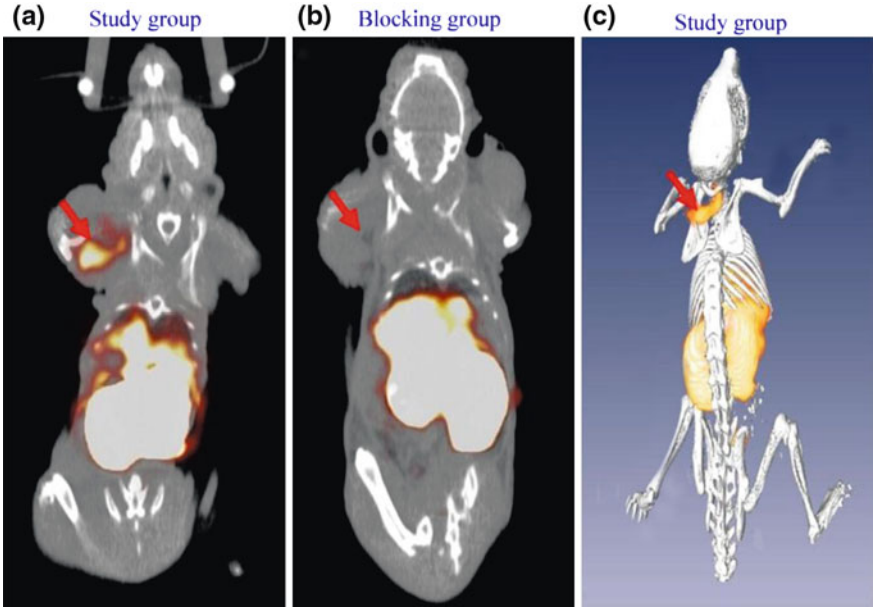

Fig. 2 Small-animal SPECT/CT of nude mice bearing DU145 xenograft at front flank. **a** Image taken at 3 h after injection of Tc-99m-UA20 scFv. **b** Image taken at 3 h after injection of Tc-99m-labeled UA20 scFv. In this experiment, 10-fold excess of unlabeled UA20 scFv was injected 1 h before injection of Tc-99m-UA20 scFv. **c** Representative image of 3-dimensional rendering of tumor targeting by Tc-99m-labeled UA20 scFv. Ref. He et al. (2010)

Tc-99m (Tc-99m-UA20) as a molecular imaging agent in a mouse model of human prostate carcinoma. SPECT/CT imaging of Tc-99m-UA20 demonstrated rapid distribution and tumor visualization as early as 1 h after injection (Fig. 2; He et al. 2010).

To evaluate the in vivo targeting of a novel internalizing human single chain antibody fragment (scFv) to all subtypes of mesothelioma, Iyer et al. (2011) radiolabeled the scFv directly and imaged its biodistribution a xenograft mouse model with SPECT/CT. Iyer et al. (2011) further used SPECT imaging of In-111-labeled immunoliposome anchored by internalizing single chain antibody fragment that targets all types of mesothelioma (Iyer et al.). Marked uptake of this radioimmunoliposome was seen in M28 (epithelioid type) and VAMT-1 (sarcomatoid type) tumor xenografts in mice in vivo (Fig. 3). This imaging result presented a promising strategy for development of enhanced targeting of liposomal drugs and targeted radionuclide therapy for malignant mesothelioma. Other nanoparticles can also serve as the base for biologic targeting radiolabeled imaging agents (Loudos et al. 2011).

Other examples of SPECT/CT imaging of small molecules in their evaluation for potential use for therapy include imaging of radioiodinated androgen receptor ligands in ovarian adenocarcinoma (Kortylewicz et al. 2009).

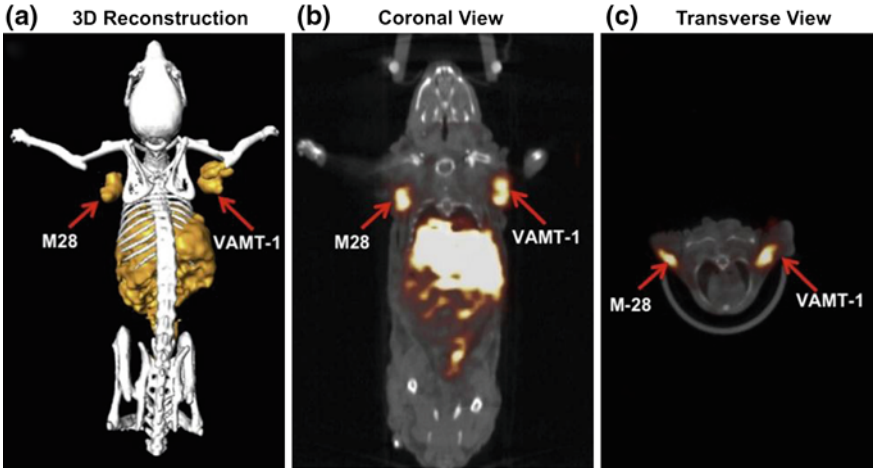

Fig. 3 SPECT/CT images of a mouse model with epithelioid (M28) and sarcomatoid (VAMT-1) mesothelioma tumors. 3D-rendered images of SPECT/CT (**a**), and two cross-section views to show the tumor uptake of In-111-labeled immunoliposome anchored by a single chain antibody fragment, M1. Reprinted with permission from Ref. Iyer et al. (2011)

5.3 Imaging Cell Trafficking

Cell trafficking studies can help establish the stability of disease models and assess cellular migration. For example, In the development of orthotopic tumor models in mice, SPECT/CT imaging utilized to trace the location of injected lung tumor cells in the lung parenchyma via intratracheal instillation (Buckle and van Leeuwen 2010). Human embryonic stem cell (hESC) engraftment and proliferation has been monitored with I-125-FIAU SPECT/CT in mice after transplantation of HSV1-TK-infected cells (Pomper et al. 2009).

Another potential area where cell trafficking studies are important is in understanding the effects of disease processes or drugs on normal or pathologic cells, particularly those interacting with the immune system (Naqvi et al. 2010; Beck et al. 2010).

5.4 Imaging Gene Transfer and Expression

As gene therapies for cancer move into the clinic, there has been a significant interest in developing methods to monitor the activity of gene expression in a systemic manner without repeated tissue biopsy. Small imaging SPECT/CT provides the means to evaluate strategies to track gene expression. Several methods have shown promise. For example, using I-125-labeled radiolabeled 2′-fluoro-2′-deoxy-h–D-5-iodouracil-arabinofuranoside (FIAU) and SPECT/CT, Fu et al. (2007) demonstrated the ability to image chemotherapy (bortezomib) -induced

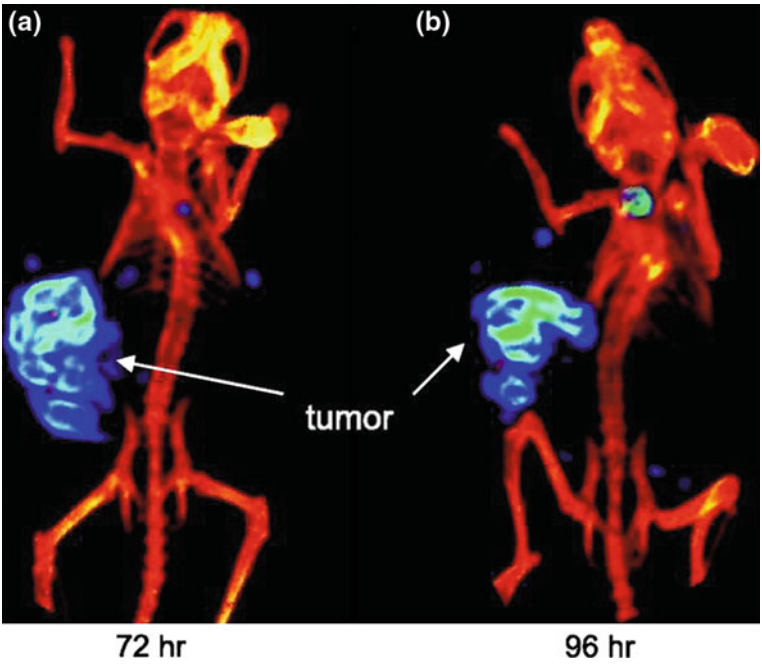

Fig. 4 SPECT/CT images of 1-125-FIAU by a EBV(+) Burkitt's xenograft (Akata) at 72 and 96 h time points. Reprinted with permission from Ref. Fu et al. (2007)

thymidine kinase (TK) expression indicating viral lytic induction in EBV(+) Burkitt's lymphoma xenografts in severe combined immunodeficient mice (Fig. 4; Fu et al. 2007).

Investigators have monitored replication of an adenovirus encoding the Na/I symporter (hNIS) using SPECT/CT following Tc-99m-O_4^- administration. Like iodine, Tc-99m-O_4^-, is taken up by cells expressing hNIS, thereby acting as a surrogate indicator of potential to concentrate iodine. hNIS can be used as a reporter gene with either Tc-99m-O_4^- or I-125 or I-123 radioiodine administration for imaging viral biodistribution with SPECT/CT, enabling the ability to follow the selectivity and timecourse of a replicating adenovirus. Additionally, hNIS can be used in a therapeutic strategy in combination with I-131 administration (Peerlinck et al. 2009; Merron et al. 2010). SPECT/CT imaging of the hNIS reporter gene has also been utilized to monitor the biodistribution of gene transfer of polypropylenimine dendrimer PPIG3/DNA nanoparticles and prove the specific delivery and transgene expression of these agents in tumors grown subcutaneously in mice (Chisholm et al. 2009).

Similarly, the expression of an oncolytic engineered measles virus (MV) for pancreatic cancer therapy has been monitored in preclinical studies using a form of the virus expressing the sodium-iodide symporter gene (MV-NIS) in combination with I-123 SPECT/CT (Carlson et al. 2009).

Chen et al. (2010) have incorporated two reporters into a single construct, allowing both optical and SPECT imaging of gene expression. SCC-9 human squamous cell carcinomas in mice were infected with adenovirus containing the investigators' somatostatin receptor-enhanced green fluorescent protein fusion construct (AdSSTR2-EGFP) and imaged in vivo with SPECT/CT after the administration of In-111-DTPA-Tyr3-octreotate. The same tumors were also imaged with fluorescence (Chen et al. 2010). In mouse studies, the ability to perform multimodality imaging is very advantageous as cells can be evaluated in vivo and ex vivo using one or both modalities. In addition, if frequent monitoring of a subcutaneous tumor is required, some time points could potentially be evaluated with only optical imaging, minimizing the amount of radiation to the animal and tumor but also allowing occasional evaluations with a high spatial-resolution-combined functional/anatomic imaging modality such as SPECT/CT.

By demonstrating a method of monitoring biodistribution and transgene expression in mice using SPECT/CT, these types of studies pave the way for direct translation of monitoring techniques when these therapies are introduced into humans.

5.5 Imaging Biodistributions and Evaluating Dosimetry—Chemotherapeutics and Combined Therapeutic/Imaging Agents

Nanoparticles and nanomolecules can serve as carriers of radiotracers or combined imaging/therapeutic agents. Incorporation into nanocarriers accomplishes two goals: 1) enabling increased tumor targeting and resulting increased therapeutic efficacy with reduced toxicity, and 2) allowing increased sensitivity of detection with SPECT/CT, enabling tracking of therapeutics in vivo. For example, in order to evaluate the tumor targeting capability and biodistribution of Re-188-N, N-bis (2-mercaptoethyl)-N', N'-diethylethylenediamine (BMEDA)-labeled pegylated liposomal doxorubicin (DXR) (Re-188-DXR-liposome) in a C26 murine colon carcinoma solid tumor model, Chang et al. (2010) used small-animal SPECT/CT imaging in tandem with pharmacokinetic studies. Once targeting had been proven with imaging, separate therapeutic efficacy studies were performed, showing a synergistic therapeutic effect of the combination radiochemotherapeutics (Chang et al. 2010).

The biodistribution of Lu-177-labeled bombesin (BN)-like peptide having high affinity with gastrin-releasing peptide receptors with potential to be a systemic radiotherapy for hormone refractory prostate cancer was studied using SPECT/CT in PC-3 M prostate tumor-bearing mice, showing retention of the molecular radiotherapy in the tumor for a 24-h period (Liu et al. 2010).

Other radioactive therapeutic agents that have undergone preclinical study with SPECT- or SPECT/CT include I-131-labeled benzamide for targeted radiotherapy of metastatic melanoma, (Joyal et al. 2010) I-131-labeled arginine-arginine-z peptide in nude mice bearing human prostate carcinoma, (Yu et al. 2010) Re-188-(I)-tricarbonyl-labeled trastuzumab (Herceptin) in BT-474 human breast cancer

xenografts (Chen et al. 2009). An area where much future work will have to be performed is evaluating the dosimetry of many of these agents, an application where SPECT/CT may provide a significant advantage (Andersson et al. 2009).

5.6 Imaging Other Pathologic Processes Associated with Cancer or Cancer Therapies

Finally, smal-animal SPECT and SPECT/CT has found utility in the development of methods to detect complications associated with cancer or cancer therapies. For example, peptide receptor radionuclide therapy (PRRT) is known to be associated with renal failure several months following therapy. The effects of methods to mitigate this complication, such as coadministration of the peptide lysine, can be studied via means of histology, but ongoing evaluation of renal function during and following therapy would be much more desirable in animal studies and required in translation to human use. Melis et al. (2010) have monitored renal function in vivo in rats using SPECT/CT following Lu-177-DOTA-Tyr3-octreotate therapy, demonstrating the increased accuracy of this method over the use of serum chemistry alone using a radiolabeled molecule (Tc-99m-MAG3) commonly employed in the clinical setting in the evaluation of kidney function (Melis et al. 2010; Amundson et al. 2001).

6 Conclusion

In many ways, the nature of single photon emitters make them specifically suitable for applications in the evaluation of molecular targeting agents. Their chemistry, decay characteristics, and relative cost-efficiency allow wide use of these radionuclides. Recent advances in small-animal SPECT and SPECT/CT imaging systems, imaging reconstruction algorithms, and radiochemistry have facilitated significant growth in the field of preclinical SPECT and have thus provided greater accessibility to these tools. The oncology researcher interested in preclinical SPECT/SPECT/CT needs to carefully plan experiments, keeping in mind the nuances that specific small animal models, imaging timepoints, or challenging radiochemistry may have in the overall research plan.

References

Amundson SA, Bittner M, Meltzer P, Trent J, Fornace AJ Jr (2001a) Biological indicators for the identification of ionizing radiation exposure in humans. Expert Rev Mol Diagn 1:211–219

Amundson SA, Bittner M, Meltzer P, Trent J, Fornace AJ Jr (2001b) Induction of gene expression as a monitor of exposure to ionizing radiation. Radiat Res 156:657–661

Andersson H et al (2009) Intraperitoneal alpha-particle radioimmunotherapy of ovarian cancer patients: pharmacokinetics and dosimetry of (211)At-MX35 F(ab')2—a phase I study. J Nucl Med 50:1153–1160

Baranowska-Kortylewicz J et al (2005) Effect of platelet-derived growth factor receptor-beta inhibition with STI571 on radioimmunotherapy. Cancer Res 65:7824–7831
Beck BH et al (2010) Adoptively transferred ex vivo expanded gammadelta-T cells mediate in vivo antitumor activity in preclinical mouse models of breast cancer. Breast Cancer Res Treat 122:135–144
Beekman FJ, Vastenhouw B (2004) Design and simulation of a high-resolution stationary SPECT system for small animals. Phys Med Biol 49:4579–4592
Beekman FJ et al (2005) U-SPECT-I: a novel system for submillimeter-resolution tomography with radiolabeled molecules in mice. J Nucl Med 46:1194–1200
Boersma HH et al (2005) Past, present, and future of annexin A5: from protein discovery to clinical applications. J Nucl Med 46:2035–2050
Bolton AE, Hunter WM (1973) The labelling of proteins to high specific radioactivities by conjugation to a ^{125}I-containing acylating agent. Biochem J 133:529–539
Bombardieri E et al (2010) Imaging of neuroendocrine tumours with gamma-emitting radiopharmaceuticals. Q J Nucl Med Mol Imaging 54:3–15
Boone JM, Velazquez O, Cherry SR (2004) Small-animal X-ray dose from micro-CT. Mol Imaging 3:149–158
Buckle T, van Leeuwen FW (2010) Validation of intratracheal instillation of lung tumour cells in mice using single photon emission computed tomography/computed tomography imaging. Lab Anim 44:40–45
Sausville EA, Burger AM (2006) Contributions of human tumor xenografts to anticancer drug development. Cancer Res 66:3351–3354 (discussion 3354)
Carcieri S et al (2006) Integrated imaging now: PET, SPECT, and CT imaging in small animals J Nucl Med 47 (S1): 399
Carlson SK, Classic KL, Bender CE, Russell SJ (2007) Small animal absorbed radiation dose from serial micro-computed tomography imaging. Mol Imaging Biol 9:78–82
Carlson SK et al (2009) Quantitative molecular imaging of viral therapy for pancreatic cancer using an engineered measles virus expressing the sodium-iodide symporter reporter gene. AJR Am J Roentgenol 192:279–287
Chang LT (1978) A method for attenuation correction in radionuclide computed tomography. IEEE Trans Nucl Sci 25:638–643
Chang YJ et al (2010) Therapeutic efficacy and microSPECT/CT imaging of 188Re-DXR-liposome in a C26 murine colon carcinoma solid tumor model. Nucl Med Biol 37:95–104
Chapman JD et al (1996) Prediction of tumour hypoxia and radioresistance with nuclear medicine markers. Br J Cancer Suppl 27:S204–S208
Charafe-Jauffret E, Ginestier C, Birnbaum D (2009) Breast cancer stem cells: tools and models to rely on. BMC Cancer 9:202
Chen KT, Lee TW, Lo JM (2009) In vivo examination of ^{188}Re(I)-tricarbonyl-labeled trastuzumab to target HER2-overexpressing breast cancer. Nucl Med Biol 36:355–361
Chen R et al (2010) Multimodality imaging of gene transfer with a receptor-based reporter gene. J Nucl Med 51:1456–1463
Chisholm EJ et al (2009) Cancer-specific transgene expression mediated by systemic injection of nanoparticles. Cancer Res 69:2655–2662
Chow PL, Stout DB, Komisopoulou E, Chatziioannou AF (2006) A method of image registration for small animal, multi-modality imaging. Phys Med Biol 51:379–390
Colby LA, Morenko BJ (2004) Clinical considerations in rodent bioimaging. Comp Med 54:623–630
Cowey S et al (2007) Breast cancer metastasis to bone: evaluation of bioluminescent imaging and microSPECT/CT for detecting bone metastasis in immunodeficient mice. Clin Exp Metastasis 24:389–401
de Jong M, Maina T (2010) Of mice and humans: are they the same?—Implications in cancer translational research. J Nucl Med 51:501–504
Dennis MS et al (2007) Imaging tumors with an albumin-binding Fab, a novel tumor-targeting agent. Cancer Res 67:254–261

Dewaraja YK, Koral KF, Fessler JA (2010) Regularized reconstruction in quantitative SPECT using CT side information from hybrid imaging. Phys Med Biol 55:2523–2539
Difilippo FP (2008) Design and performance of a multi-pinhole collimation device for small animal imaging with clinical SPECT and SPECT-CT scanners. Phys Med Biol 53:4185–4201
Dijkgraaf I, Beer AJ, Wester HJ (2009) Application of RGD-containing peptides as imaging probes for alphavbeta3 expression. Front Biosci 14:887–899
Edwards WB et al (2009) Multimodal imaging of integrin receptor-positive tumors by bioluminescence, fluorescence, gamma scintigraphy, and single-photon emission computed tomography using a cyclic RGD peptide labeled with a near-infrared fluorescent dye and a radionuclide. Mol Imaging 8:101–110
Eyles J et al (2010) Tumor cells disseminate early, but immunosurveillance limits metastatic outgrowth, in a mouse model of melanoma. J Clin Invest 120:2030–2039
Fasano J, Muggia F (2009) Breast cancer arising in a BRCA-mutated background: therapeutic implications from an animal model and drug development. Ann Oncol 20:609–614
Figueroa SD, Winkelmann CT, Miller HW, Volkert WA, Hoffman TJ (2008) TLD assessment of mouse dosimetry during microCT imaging. Med Phys 35:3866–3874
Franc BL, Acton PD, Mari C, Hasegawa BH (2008) Small-animal SPECT and SPECT/CT: important tools for preclinical investigation. J Nucl Med 49:1651–1663
Fu DX et al (2007) Virus-associated tumor imaging by induction of viral gene expression. Clin Cancer Res 13:1453–1458
Funk T, Sun M, Hasegawa BH (2004) Radiation dose estimate in small animal SPECT and PET. Med Phys 31:2680–2686
Fuster D et al (2003) Tetrofosmin as predictors of tumour response. Q J Nucl Med 47:58–62
Gooden CS et al (1995) Direct technetium-99m labeling of three anticancer monoclonal antibodies: stability, pharmacokinetics and imaging. J Nucl Med 36:842–849
Habraken JB et al (2001) Evaluation of high-resolution pinhole SPECT using a small rotating animal. J Nucl Med 42:1863–1869
Hanahan D (1989) Transgenic mice as probes into complex systems. Science 246:1265–1275
He J et al (2010) Targeting prostate cancer cells in vivo using a rapidly internalizing novel human single-chain antibody fragment. J Nucl Med 51:427–432
Heskamp S et al (2010) ImmunoSPECT and immunoPET of IGF-1R expression with the radiolabeled antibody R1507 in a triple-negative breast cancer model. J Nucl Med 51:1565–1572
Hesterman JY, Kupinski MA, Furenlid LR, Wilson DW, Barrett HH (2007) The multi-module, multi-resolution system (M3R): a novel small-animal SPECT system. Med Phys 34:987–993
Hildebrandt IJ, Su H, Weber WA (2008) Anesthesia and other considerations for in vivo imaging of small animals. ILAR J 49:17–26
Hoeben BA et al (2011) Radiolabeled cetuximab: Dose optimization for epidermal growth factor receptor imaging in a head-and-neck squamous cell carcinoma model. Int J Cancer 129:870–878
Hwang AB Taylor CC VanBrocklin HF Dae MW & Hasegawa BH (2006) Attenuation correction of small animal SPECT images acquired with ^{125}I-iodorotenone. IEEE Trans Nucl Sci 53(3):1213–1219
Hwang AB, Hasegawa BH (2005) Attenuation correction for small animal SPECT imaging using x-ray CT data. Med Phys 32:2799–2804
Hwang AB, Franc BL, Gullberg GT, Hasegawa BH (2008) Assessment of the sources of error affecting the quantitative accuracy of SPECT imaging in small animals. Phys Med Biol 53:2233–2252
Iyer AK et al (2011) The effect of internalizing human single chain antibody fragment on liposome targeting to epithelioid and sarcomatoid mesothelioma. Biomaterials 32:2605–2613
John E, Thakur ML, Wilder S, Alauddin MM, Epstein AL (1994) Technetium-99m-labeled monoclonal antibodies: influence of technetium-99m binding sites. J Nucl Med 35:876–881
Joyal JL et al (2010) Preclinical evaluation of an ^{131}I-labeled benzamide for targeted radiotherapy of metastatic melanoma. Cancer Res 70:4045–4053
Kastis GA et al (2004) Compact CT/SPECT small-animal imaging system. IEEE Trans Nucl Sci 51:63–67

Kersemans V et al (2011) Micro-CT for anatomic referencing in PET and SPECT: radiation dose, biologic damage, and image quality. J Nucl Med 52:1827–1833

Kim EM et al (2004) Monitoring the effect of PEGylation on polyethylenimine in vivo using nuclear imaging technique. Nucl Med Biol 31:781–784

King R et al (2009) 99mTc-HYNIC-Gastrin peptides: assisted coordination of ^{99m}Tc by amino acid side chains results in improved performance both in vitro and in vivo. J Nucl Med 50:591–598

Kortylewicz ZP, Nearman J, Baranowska-Kortylewicz J (2009) Radiolabeled 5-iodo-3′-O-(17beta-succinyl-5alpha-androstan-3-one)-2′-deoxyuridine and its 5′-monophosphate for imaging and therapy of androgen receptor-positive cancers: synthesis and biological evaluation. J Med Chem 52:5124–5143

Lanari C et al (2009) The MPA mouse breast cancer model: evidence for a role of progesterone receptors in breast cancer. Endocr Relat Cancer 16:333–350

Li Y et al (2003) Evidence that transgenes encoding components of the Wnt signaling pathway preferentially induce mammary cancers from progenitor cells. Proc Natl Acad Sci U S A 100:15853–15858

Liu IH et al (2010) Multimodality imaging and preclinical evaluation of ^{177}Lu-AMBA for human prostate tumours in a murine model. Anticancer Res 30:4039–4048

Loudos G, Kagadis GC, Psimadas D (2011) Current status and future perspectives of in vivo small animal imaging using radiolabeled nanoparticles. Eur J Radiol 78:287–295

Madsen MT (2007) Recent advances in SPECT imaging. J Nucl Med 48:661–673

Mamede M et al (2004) Hepatocyte targeting of ^{111}In-labeled oligo-DNA with avidin or avidin-dendrimer complex. J Control Release 95:133–141

Mardirossian G et al (1997) In vivo hybridization of technetium-99m-labeled peptide nucleic acid (PNA). J Nucl Med 38:907–913

Meenakshi A, Ganesh V, Suresh Kumar R, Siva Kumar N (2003) Radioimmuno targetting ^{99m}technetium labeled anti-epidermal growth factor receptor monoclonal antibodies in experimental tumor models. Q J Nucl Med 47:139–144

Melis M et al (2010a) Dynamic and static small-animal SPECT in rats for monitoring renal function after ^{177}Lu-labeled Tyr3-octreotate radionuclide therapy. J Nucl Med 51:1962–1968

Melis M et al (2010b) Nephrotoxicity in mice after repeated imaging using ^{111}In-labeled peptides. J Nucl Med 51:973–977

Merron A et al (2010) Assessment of the Na/I symporter as a reporter gene to visualize oncolytic adenovirus propagation in peritoneal tumours. Eur J Nucl Med Mol Imaging 37:1377–1385

Milagre C et al (2010) A mouse model of melanoma driven by oncogenic KRAS. Cancer Res 70:5549–5557

Naqvi SA et al (2010) Insertion of a lysosomal enzyme cleavage site into the sequence of a radiolabeled neuropeptide influences cell trafficking in vitro and in vivo. Cancer Biother Radiopharm 25:89–95

Ni Y et al (2009) Tumor models and specific contrast agents for small animal imaging in oncology. Methods 48:125–138

Oliver PG et al (2008) Treatment of human colon cancer xenografts with TRA-8 anti-death receptor 5 antibody alone or in combination with CPT-11. Clin Cancer Res 14:2180–2189

Palmieri D et al (2006) Brain metastases of breast cancer. Breast Dis 26:139–147

Peerlinck I et al (2009) Targeted radionuclide therapy using a Wnt-targeted replicating adenovirus encoding the Na/I symporter. Clin Cancer Res 15:6595–6601

Pomper MG et al (2009) Serial imaging of human embryonic stem-cell engraftment and teratoma formation in live mouse models. Cell Res 19:370–379

Ray GL et al (2009) Preclinical evaluation of a monoclonal antibody targeting the epidermal growth factor receptor as a radioimmunodiagnostic and radioimmunotherapeutic agent. Br J Pharmacol 157:1541–1548

Schillaci O, Spanu A, Madeddu G (2005) [^{99m}Tc]sestamibi and [^{99m}Tc]tetrofosmin in oncology: SPET and fusion imaging in lung cancer, malignant lymphomas and brain tumors. Q J Nucl Med Mol Imaging 49:133–144

Sosabowski JK et al (2009) Targeting of CCK-2 receptor-expressing tumors using a radiolabeled divalent gastrin peptide. J Nucl Med 50:2082–2089

Stephenson KA et al (2004) A new strategy for the preparation of peptide-targeted radiopharmaceuticals based on an fmoc-lysine-derived single amino acid chelate (SAAC). automated solid-phase synthesis, NMR characterization, and in vitro screening of fMLF(SAAC)G and fMLF[(SAAC-Re(CO)3)+]G. Bioconjug Chem 15:128–136

Stolin A et al (2005) In: Yu B (ed) IEEE Nuclear Science Symposium Conference Record. Fajardo, Puerto Rico, pp 2183–2186

Takahashi T, Watanabe S (2001) Recent Progress in CdTe and CdZnTe detectors. IEEE Trans Nucl Sci 48:950–959

Uchida E et al (2008) Experimental pancreatic cancer model using PGHAM-1 cells: characteristics and experimental therapeutic trials. J Nippon Med Sch 75:325–331

Umeda IO et al (2012) High resolution SPECT imaging for visualization of intratumoral heterogeneity using a SPECT/CT scanner dedicated for small animal imaging. Ann Nucl Med 26:67–76

van der Have F et al (2009) U-SPECT-II: an ultra-high-resolution device for molecular small-animal imaging. J Nucl Med 50:599–605

van Weerden WM, Bangma C, de Wit R (2009) Human xenograft models as useful tools to assess the potential of novel therapeutics in prostate cancer. Br J Cancer 100:13–18

Vangestel C et al (2011) In vivo imaging of apoptosis in oncoloty: an update. Mol Imaging 10:340–358

Vanhove C, Defrise M, Bossuyt A, Lahoutte T (2011) Improved quantification in multiple-pinhole SPECT by anatomy-based reconstruction using microCT information. Eur J Nucl Med Mol Imaging 38:153–165

Vastenhouw B, Beekman F (2007) Submillimeter total-body murine imaging with U-SPECT-I. J Nucl Med 48:487–493

Verhaar MJ et al (1996) Technetium-99m radiolabeling using a phage-derived single-chain Fv with a C-terminal cysteine. J Nucl Med 37:868–872

Virzi F et al (1991) New indium-111 labeled biotin derivatives for improved immunotargeting. Int J Rad Appl Instrum B 18:719–726

Voskoglou-Nomikos T, Pater JL, Seymour L (2003) Clinical predictive value of the in vitro cell line, human xenograft, and mouse allograft preclinical cancer models. Clin Cancer Res 9:4227–4239

Wang Y et al (2005) An orthotopic metastatic prostate cancer model in SCID mice via grafting of a transplantable human prostate tumor line. Lab Invest 85:1392–1404

Weisenberger AG et al (2006) in IEEE Nuclear Science Symposium Conference Record pp 3000–3003

Weisenberger AG et al (2005) In: Kupinski MA, Barrett HH (eds) Small-animal SPECT imaging. Springer, New York, pp 239–242

Weisenberger AG et al (2003) SPECT-CT system for small animal imaging. IEEE Trans Nucl Sci 50:74–79

Workman P et al (2010) Guidelines for the welfare and use of animals in cancer research. Br J Cancer 102:1555–1577

Wu C et al (2010) Absolute quantitative total-body small-animal SPECT with focusing pinholes. Eur J Nucl Med Mol Imaging 37:2127–2135

Yang S et al (2009) Establishment of an experimental human lung adenocarcinoma cell line SPC-A-1BM with high bone metastases potency by ^{99m}Tc-MDP bone scintigraphy. Nucl Med Biol 36:313–321

Yu M et al (2010) Study on biodistribution and imaging of radioiodinated arginine-arginine-leucine peptide in nude mice bearing human prostate carcinoma. Ann Nucl Med 24:13–19

Zhau HE, Li CL, Chung LW (2000) Establishment of human prostate carcinoma skeletal metastasis models. Cancer 88:2995–3001

Optical Imaging

Jochen Müller, Andreas Wunder and Kai Licha

Abstract

Non-invasive optical imaging techniques, such as fluorescence imaging (FI) or bioluminescence imaging (BLI) have emerged as important tools in biomedical research. As demonstrated in different animal disease models, they enable visualization of physiological and pathophysiological processes at the cellular and molecular level in vivo with high specificity. Optical techniques are easy to use, fast, and affordable. Furthermore, they are characterized by their high sensitivity. In FI, very low amounts of the imaging agent (nano- to femtomol or even less) can be detected. Due to the absorption and scattering of light in tissue, optical techniques exhibit a comparably low spatial resolution in the millimeter range and a depth limit of a few centimeters. However, non-invasive imaging of biological processes in small animals and in outer or inner surfaces as well as during surgery even in humans is feasible. Currently two agents for fluorescence imaging are clinically approved, namely indocyanine green (ICG) and 5-aminolevulinic acid (5-ALA). In the past years, a number of new optical imaging agents for FI and reporter systems for BLI have been developed and successfully tested in animal models. Some of the FI agents might promise the application in clinical oncology. In this chapter, we describe the basic principles of non-invasive optical imaging techniques, give examples for the visualization of biological processes in animal models of cancer, and discuss potential clinical applications in oncology.

J. Müller (✉) · A. Wunder
Center for Stroke Research Berlin (CSB), Department of Experimental Neurology, Charité University Medicine, Charitéplatz 1, 10098 Berlin, Germany
e-mail: jochen.mueller@charite.de

K. Licha
mivenion, GmbH, Robert-Koch-Platz 4, 10115 Berlin, Germany

O. Schober and B. Riemann (eds.), *Molecular Imaging in Oncology*, Recent Results in Cancer Research 187, DOI: 10.1007/978-3-642-10853-2_7,

Contents

1 Non-Invasive Optical Imaging Techniques

Fluorescence imaging (FI) techniques utilize the property of fluorescence dyes to emit light with a longer wavelength when excited with light of a lower wavelength. The fluorescent light can be detected with highly sensitive CCD cameras using appropriate filters, which allow only the emitted light (fluorescence) to pass, but not the excitation light. For FI, the near-infrared (NIR) range from 700 to 900 nm is the most applicable because hemoglobin and water have a relatively low absorption at these wavelengths and therefore the penetration depth of light is relatively high. Moreover, the tissue autofluorescence in the NIR range is low compared to the VIS spectral range. There are several FI techniques available. Most commonly used are so-called planar techniques such as fluorescence reflectance imaging (FRI) or transillumination fluorescence imaging (TFI), but there are also tomographic techniques available (fluorescence mediated tomography, FMT). In FRI, the light source and the detector are at the same side of the investigated object. In TFI, the light source and detector are positioned on opposite sides and the specimen is in the middle. FRI- as well as TFI-systems deliver two-dimensional, surface-weighted images. Due to scattering and absorption of the excitation and the emitted light in the tissue, fluorescent sources in deep tissue layers appear less intense than superficial located with the same amount of dye. Therefore, both systems do not deliver absolute quantitative data. In contrast to the planar systems, FMT-systems produce three-dimensional images about the fluorescence distribution in the investigated object. This is possible due to illumination with multiple light sources or by means of a mobile light source, illuminating the object from different angles. The fluorescence light is detected with multiple detectors or with a mobile detector. This produces data, which allow for a three-dimensional and quantitative reconstruction of the fluorescence distribution with a resolution in the millimeter range

by means of algorithms that take into consideration the dispersion of photons in the tissue and across tissue layers (Wunder and Klohs 2008).

Bioluminescence imaging (BLI) does not need any excitation light source, since bioluminescence derives from the ability of several proteins to produce light in an enzymatic reaction. Bioluminescence is an oxygen and ATP-consuming biological process, catalyzed by the enzyme luciferase that oxidizes its substrate luciferin, thereby emitting light. Detection is accomplished with cooled sensitive CCD cameras, as for fluorescence imaging, but with the advantage of a lower background, due to the lack of an external light source for excitation. Therefore, BLI is useful to detect very low target levels.

The system can be used for imaging purposes by inserting the luciferase gene into the genome of cells or organisms of interest. This can be done under a constitutively active promotor or under a gene of interest, thereby producing targeted luciferin expression in a subset of cells or tissue. With BLI gene expression can be visualized, but also cell tracking and other mechanisms, as described later in this chapter.

2 Imaging Agents for Fluorescence Imaging

The agents for FI can be classified into three different categories. These are so-called unspecific or passively distributing agents, targeted conjugates, and activatable or smart probes (Klohs et al. 2008).

Unspecific contrast agents do not have specificity for certain cells of molecules, but enable non-invasive visualization of permeability or perfusion differences in tissues. FITC-labeled Albumin is an example for such an unspecific probe, but also Indocyanine green (ICG), being the first clinically approved FI agent and successfully used in the clinic since years (Flower et al. 1976).

In contrast to unspecific fluorescent optical contrast agents, targeted and activatable probes can, through specific binding to specific cellular or molecular targets, visualize biological processes at the cellular and molecular level. Unlike activatable contrast agents targeted contrast agents are detectable regardless of their binding situation being either target bound or freely circulating. This means that imaging agents not bound to the target can produce background signals. Although these background signals are relatively high directly after application, they diminish due to the elimination (wash out) of the unbound contingent, so that contrast is strongly depending not only on binding affinity but also on the elimination kinetics. Activatable contrast agents are detectable only after interaction with a target structure, meaning they are undetectable before target interaction. The background signals are, therefore, compared to targeted contrast agents, significantly lower (Massoud and Gambhir 2003; Grimm and Wunder 2005; Klohs et al. 2008).

During the past years, an impressive development of optical contrast agents has occurred. However, most of these imaging agents have not found their way into the clinic although there are some interesting approaches. In the following, a selection of preclinical as well as clinical imaging approaches are described, ordered by biological processes.

3 Reporter Systems for Bioluminescence Imaging

Luciferase is a naturally occurring enzyme found in insects, mainly firefly (*Photinus pyralis*, de Wet et al. 1987), but also sea pansy (*Renilla reniformis*, Bhaumik and Gambhir 2002), green or red click beetle (*Pyrophorus plagiophthalamus*, Miloud et al. 2007) and copepod (*Gaussia princeps*, Tannous 2009).

In order to exploit this system for BLI, the luciferase gene has to be expressed in cells transgenically and its substrate luciferin has to be injected. Since this process requires genetic alterations of the target tissue, it finds application in animal models but is not likely to be transferred into clinical settings (for review see Dothager et al. 2009; Michelini 2009).

So far, light emission of luciferin has mainly been confined to green light, which provides very limited tissue penetration and attenuates substantially while traversing tissue. In case of Renilla and Gaussia luciferases, both emitting blue light, this is even more substantial. However, novel luciferases with red-shifted emitting substrates with better light penetration through tissue may improve BLI for larger animals (Li et al. 2009; Wang et al. 2009a).

4 Biological Processes

4.1 Activity of Matrix Degrading Enzymes

Matrix degrading enzymes are important for the normal function of cells and tissues. On the other hand, they also play a key role in cancer. Invasion of malignant cells and metastasis is possible due to the degradation of the extracellular matrix, which prevents migration of cells under normal conditions. Several matrix degrading enzymes are upregulated in cancer tissue, thereby enabling cancer cells to invade surrounding healthy tissue. There are at least two different proteolytic systems for matrix degradation: Urokinase/plasminogen activator network, cysteine proteinases and matrix metalloproteinases (McIntyre and Matrisian 2003). Since matrix degrading enzymes in cancerous tissue are present at high levels and are elevated at an early stage, they represent an attractive target for imaging and therapeutic strategies. The fact that matrix degrading enzymes are secreted, present and active in the extracellular space is an advantage for imaging purposes, because the transfer of the probe to intracellular compartments is not necessary, and, even more important, their catalytic activity exhibits a way for signal amplification that is not possible with direct binding of a fluorescent ligand to a target.

The possibility to image the activity of matrix degrading enzymes in vivo was first demonstrated by Weissleder et al. (1999) in a xenograft tumor mouse model. The authors used fluorophores attached to a polymer comprising a Cathepsin B specific cleavage site. The attachment of a high number of fluorophores in close proximity to each other on the substrate quenched the fluorescent signal. After enzymatic cleavage of sites in the polymeric backbone or of specifically cleavable

linker peptides, the NIR fluorescent signal was substantially restored, being detectable in the tumor area.

In the last years there have been several reports about activatable or smart probes, following this or similar approaches (for review see Scherer et al. 2008). A probe specific for cleavage by MMP-2 was presented in 2001 (Bremer et al. 2001), one for MMP-7 in 2004 (McIntyre et al. 2004) and one for urokinase-type plasminogen activator in 2004 (Law et al. 2004; Hsiao et al. 2006) all of them tested in xenograft models in mice, to mention just a few.

Interestingly, von Burstin et al. (2008) reported about a combination of two optical in vivo MMP imaging modalities to detect pancreatic cancer in nude mice. The authors used whole body NIRF imaging for macroscopic detection and confocal flexible laser microscopy for molecular histopathology in vivo, enabling them to detect tumors of one millimeter in diameter.

The development of new probes targeting proteolytic enzymes is ongoing. It should be mentioned, however, that not all of them focus on activatable probes. A recent example of a different approach is a publication from Wang et al. (2009b) (Fig. 1). They constructed a cyclic peptide linked to Cy5.5 inhibiting gelatinases and being selectively taken up by MMP-2 expressing human glioma U87 cells.

It is clear that research on matrix degrading enzymes as a target for optical imaging is still in its infancy. However, activatable probes have proven to be powerful tools, because they can detect early molecular alterations ahead of anatomical manifestation of the disease, promising a substantial increase in detection rates of early onset of cancer and the progression of metastases.

4.2 Glucose Metabolism

By far the most commonly used tracer in clinical nuclear imaging is fluorodeoxyglucose labeled with fluorine-18 (^{18}F-FDG). ^{18}F-FDG PET deploys the increased glucose metabolism of tumor tissue, due to an up-regulation of glucose transport proteins such as GLUT1 in tumor cells. Once ^{18}F-FDG is internalized, it is phosphorylated to FDG-6-phosphate, but FDG-6-phosphate does not enter glycolysis, because of the fluorine substitution at the 2-position. The tracer becomes metabolically trapped and accumulates in metabolically active cells, hence causing specific radioemission in PET imaging. However, highly metabolic tissues such as muscle and normal brain exhibit a high background, which is, in addition to nonspecific accumulation by inflammatory processes, a key drawback of ^{18}F-FDG (Peterson and Manning 2009).

Given the considerable role of ^{18}F-FDG in nuclear medicine and the extensive improvement in fluorescence imaging, the development of NIRF deoxyglucose analogs may lead to novel possibilities to evaluate the glucose metabolic rate of animal models. A set of newly developed probes could be of importance for both the non-invasive therapy monitoring, as well as the accurate detection of pathologies in living small animals.

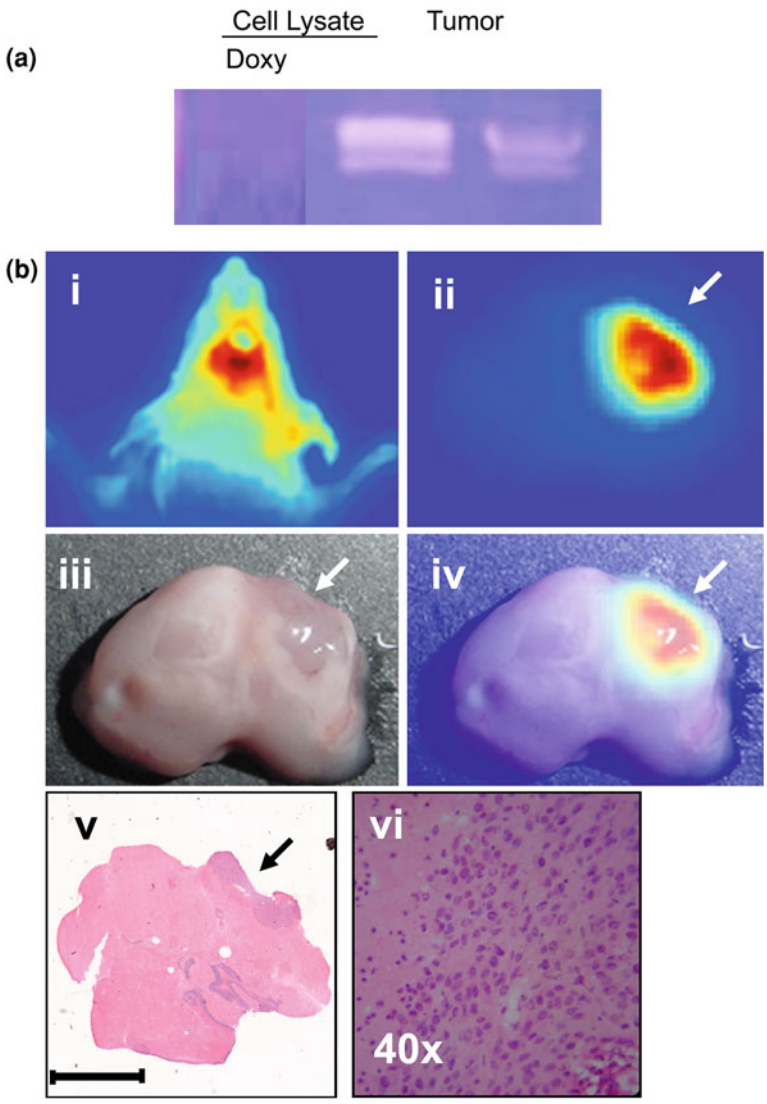

Fig. 1 **a** Zymograph of cell lysate and tumor tissue extract from U87 cells. The cell lysate was either treated or not treated with 100 μg/ml doxycycline (Doxy) before being applied to the gel. Equal amounts of proteins were applied. **b** Representative images of a mouse with an intracranially implanted U87 brain tumor. (*i*) in vivo NIRF image acquired 24 h after intravenous injection of Cy5.5-C6 at a dose of 15 nmol/mouse. Fluorescence (*ii*), bright light (*iii*), and the corresponding merged images of the excised brain (*iv*) are also shown. The fluorescence signal in NIRF images corresponded to the presence of tumor (*v* and *vi*) in the brain. *Arrows* indicate tumor. Scale bar: 0.5 cm. Taken with permission from Wang et al. (2009b)

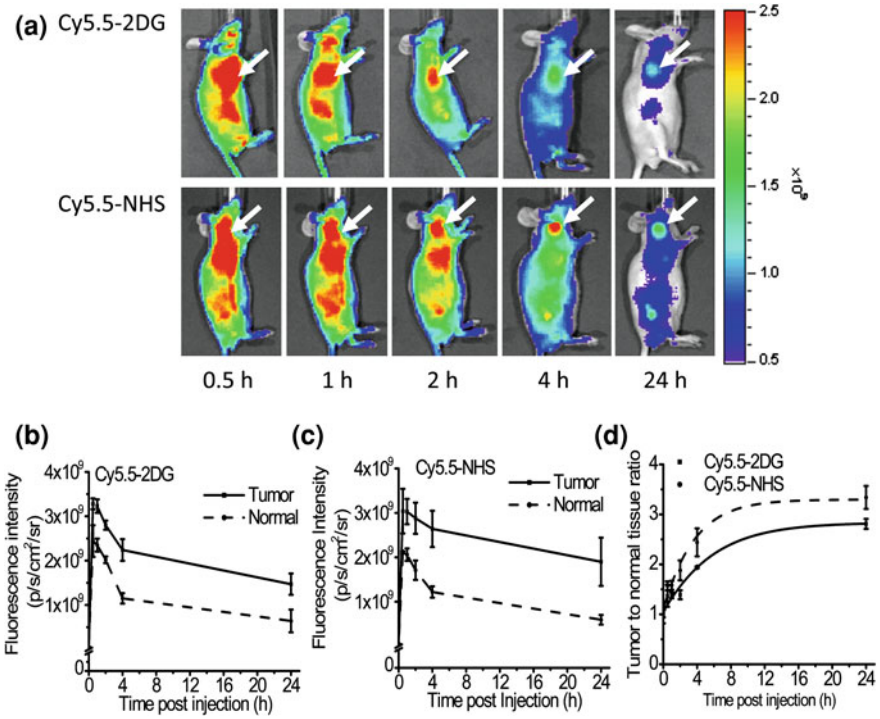

Fig. 2 **a** In vivo fluorescence imaging of subcutaneous U87MG glioblastoma tumor-bearing nude mice after intravenous injection of 0.5 nmol of Cy5.5-2DG (top) or Cy5.5-NHS (*bottom*). The position of the tumor is indicated by an arrow. The fluorescence signal from probes was pseudo-colored red. Quantification and kinetics of in vivo targeting characterististics of Cy5.5-2DG (**b**); and Cy5.5-NHS. **c** The fluorescence intensity was recorded as photons per second per centimeter squared per steradian (p s-1 cm-2 sr-1). Tumor fluorescence was higher than that in the normal tissue. **d** Tumor contrast (tumor/normal tissue ratio) as a function of time postadministration of Cy5.5-2DG (n, -) and Cy5.5-NHS (u,- - -). The tumor/normal tissue ratio of Cy5.5-NHS at 4 and 24 h pi is significantly higher than that of Cy5.5-2DG ($p < 0.05$). Taken with permission from Cheng et al. (2006)

A fluorescent derivative of 2-deoxyglucose, 2-[N-(7-nitrobenz-2-oxa-1,3-diazol-4-yl)amino]-2-deoxy-glucose (2-NBDG, excitation, 475 nm; emission, 550 nm) was reported to be delivered and trapped in cells via the GLUT/hexokinase pathway (Yoshioka et al. 1996a, b; Lloyd et al. 1999; Yamada et al. 2000; Oh and Matsuoka 2002). However, due to its low excitation and emission wavelength, the utility of 2-NBDG for non-invasive FI is questionable. Cheng et al. (2006) conjugated the NIRF dye Cy5.5 (excitation, 675 nm; emission, 694 nm) with D-glucosamine (Cy5.5-2DG) and tested it successfully in a preclinical xenograft tumor mouse model (Fig. 2), thereby overcoming the disadvantages of 2-NBDG. They concluded from their results, however, that in vitro uptake of the Cy5.5 conjugates did not occur via the GLUT pathway demonstrating that in vivo

contrast has to be carefully evaluated with respect to whether passive or targeted accumulation is the most relevant underlying mechanism. A tumor-targeted NIRF imaging probe as well as photodynamic therapy (PDT) agent for the treatment of tumors is Pyro-2DG, a pyropheophorbide derivative of 2-deoxyglucose (excitation 667 nm, emission 679 and 720 nm) (Zhang et al. 2003; Zhang et al. 2004). The authors evaluated the in vivo uptake of Pyro-2DG and report that it selectively accumulates in two tumor models, 9L rat glioma and c-MYC-induced mouse mammary tumor with a considerable ratio of about 10:1. To present Pyro-2DG as a PDT agent the authors demonstrated that this agent caused selective mitochondrial damage to the illuminated tumor area only after administration of this agent. However, it should be mentioned that Zhang and coworkers did not detect Pyro-2DG fluorescence non-invasively but with deep frozen tissue blocks.

Ye et al. (2004, 2005) connected cypate, a NIR chromophore core, to multiple D-(+)-glucosamines to generate multivalent carbocyanine molecular beacons. Biodistribution studies in tumor-bearing mice showed that all of the NIR fluorescent glucosamine derivatives localized in the tumor. It remains, generally, unclear in these type of approaches employing extremely bulky fluorophores whether uptake and trapping in the tumor is achieved through the GLUT/hexokinase pathway.

4.3 Hypoxia

Hypoxia is the condition in which tissue oxygen levels are insufficient to support metabolism. It can occur when the vascular supply of tissue is decreased, as in stroke or infarction, or when a tumor outgrows its vasculature. In an acute loss of oxygen supply to, otherwise, healthy tissue, the tissue normally dies due to necrotic or apoptotic processes. In contrast to this, cells undergoing gradually hypoxic conditions react with activation of the hypoxia inducible factor one (HIF-1) and subsequent up-regulation of a number of proteins to promote their survival. This is the case for tumor cells, which gradually outgrow their vascular supply (Serganova et al. 2004; Viola et al. 2008). Serganova et al. (2004) inserted HIF-1 inducible GFP via retroviral vector. With this technique the authors were able to show that with increasing tumor diameter (> 3 mm), a marked increase in HIF-1 transcriptional activity was observed in the core regions of tumors. To directly measure the activity of HIF-1 transgenes coding for luciferase of green fluorescent protein (GFP) were inserted under the promotor control of hypoxic response elements. Hypoxia induced a 100-fold increase in luciferase expression, enabling this method for in vivo BLI. The method was used to evaluate hypoxia-directed therapy in animals (Harada et al. 2005; Viola et al. 2008), since even under low PO_2 enough O_2 remains to oxidize luciferin to oxyluciferin (Fig. 3).

These imaging methods are helpful tools on the experimental level to investigate the operating mode of and treatment against hypoxia, but are not applicable for human imaging for obvious reasons.

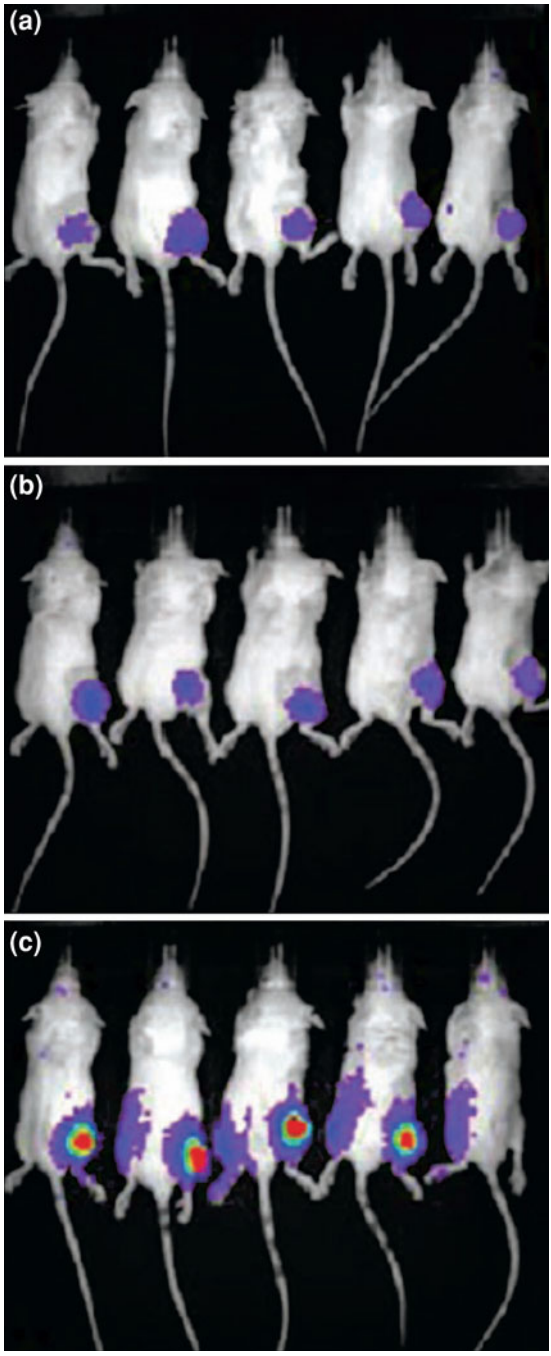

Fig. 3 Representative reporter levels in right rear flank tumors of mice on day 10, peak of HIF-1α activity for cyclophosphamide group. **a–c**, Hypoxia-inducible factor 1 (HIF-1) bioluminescence images of control **a** paclitaxeltreated **b** and cyclophosphamide-treated **c** mice show high levels of HIF-1α in red and low and baseline levels in blue. In **c**, mouse on far right has no palpable tumor and does not have appreciable luciferase signal. Low-level bioluminescence in left flanks of four mice in **c** is false-positive signal (light reflection of true-positive signal from right flank tumors); mouse on far left does not have this false-positive signal. Taken with permission from Viola et al. (2008)

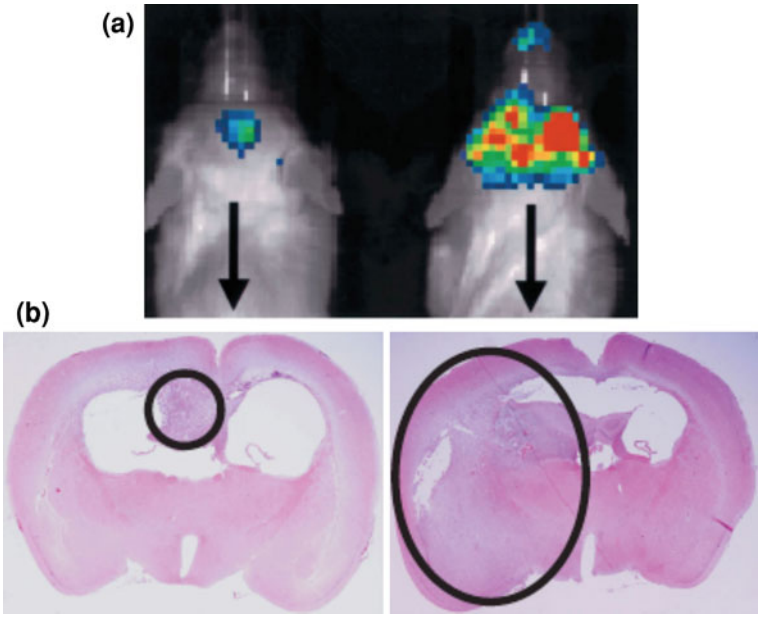

Fig. 4 Approximate correlation between BLI output and tumor size. **a** Ef-luc BLI of PDGF-induced oligodendrogliomas. Luciferase activity in tumor-bearing Ef-luc N-tv-a transgenic mice. **b** Whole mount histologica analysis of the brains from the same mice as imaged in (**a**). Tumor size roughy correlates with the amount of emitted light. Taken with permission from Uhrbom et al. (2004)

4.4 Proliferation

Uncontrolled proliferation of cells is a hallmark of cancer. Therefore, it is an important objective for biomedical imaging to be able to monitor cell proliferation in tumor models.

Inactivation of tumor suppressors, such as the retinoblastoma protein (RB) and the p53 transcription factor, will lead to activation of E2F-regulated transcription, which is normally active only during late G1 to S phase. Constitutive activity of E2F-regulated transcription will lead to higher proliferative activity (Uhrbom et al. 2004). E2F1 is a protein that is selectively expressed in proliferating cells. Uhrbom et al. (2004) developed a BLI model to assess cellular proliferation, developing a transgenic mouse that forms glioma and expresses luciferase under control of the E2F1 promotor (Fig. 4). Measuring luciferase activity in living mice was used to monitor proliferation of glioma. The system was also used to monitor response to therapy. Drugs inhibiting platelet-derived growth factor receptor (PDGFR) or mammalian target of rapamycin (mTOR) were shown to decrease cell proliferation by a proportional decrease in luminescence signal intensity.

4.5 Angiogenesis

Angiogenesis, the formation of new blood vessels, is crucial for further tumor development after growing to a few millimeters in diameter. There are a variety of proteins that regulate tumor angiogenesis, including growth factors (like vascular endothelial growth factor, VEGF), growth factor receptors (like VEGF receptor, VEGFR), G-protein-coupled receptors (for angiogenesis-modulating proteins), several endogenous angiogenesis-modulating proteins, and integrins. (For review see Cai et al. 2008).

Integrins, a family of cell adhesion molecules (Hynes 2002), are promising targets used for angiogenic cancer therapy, since they play an important role in tumor angiogenesis and metastasis (Hood and Cheresh 2002). When expressed on endothelial cells, integrins modulate cell survival and migration during tumor angiogenesis. Being expressed on carcinoma cells integrins facilitates invasion and movement across blood vessels, thereby potentiating metastasis. Among all of the integrins discovered to date, integrin $\alpha_v\beta_3$ is the most extensively studied member of the integrin family. It binds to components of the extracellular matrix containing arginine-glycine-aspartic acid (RGD), and is significantly upregulated on tumor vasculature but not on quiescent endothelium (Hood and Cheresh 2002; Xiong et al. 2002). Many compounds have been used for antiangiogenic cancer therapy, among them monoclonal antibodies, cyclic RGD peptide antagonists, and peptidomimetic agents against integrin $\alpha_v\beta_3$ (Cai and Chen 2006).

Adressing integrins as molecular targets for angiogenesis imaging and therapy, the group of Xiayou Chen followed two approaches to image vasculature in tumor models in mice. U87MG glioma cells were transfected with firefly luciferase gene under the integrin $\alpha_v\beta_3$ promotor (Hsu et al. 2006, see Fig. 5). Glioma cells were injected into nude mice in the right frontal lobe and tumor growth was imaged for 46 days. BLI was used in parallel with Gd-enhanced MRI to verify tumor growth in vivo (see Fig. 5). On day 46, post tumor injection mice were injected with cyclic RGD peptide linked to Cy5.5 (Fig. 5). Specific binding of the agent to both U87MG tumor vessels and cells but not to normal tissue was reported. In the same year, the group reported NIRF imaging of integrin $\alpha_v\beta_3$ (Cai et al. 2006) on tumor vasculature with RGD peptide-conjugated Quantum Dots (QD705, emission max 705 nm, Fig. 5). The authors describe high affinity and specific binding and used spectral imaging techniques to separate the fluorescent signals from background signal.

Due to the large size of the Qd705-RGD conjugates extravasation and penetration into tumor tissue is limited. This led conjugates mainly targeting integrin $\alpha_v\beta_3$ intraluminal on the tumor vasculature instead of tumor cells. Nonetheless, since integrin $\alpha_v\beta_3$ is overexpressed by sprouting neovasculature in many tumor types, this probe seems promising for tumor angiogenesis imaging.

Human VEGF was fluorescently labeled with Cy5.5 (emission 696 nm) and tested for in vivo imaging (Backer et al. 2005, 2006). Although contrast was observed after administration of the probe, no information about the whole-body

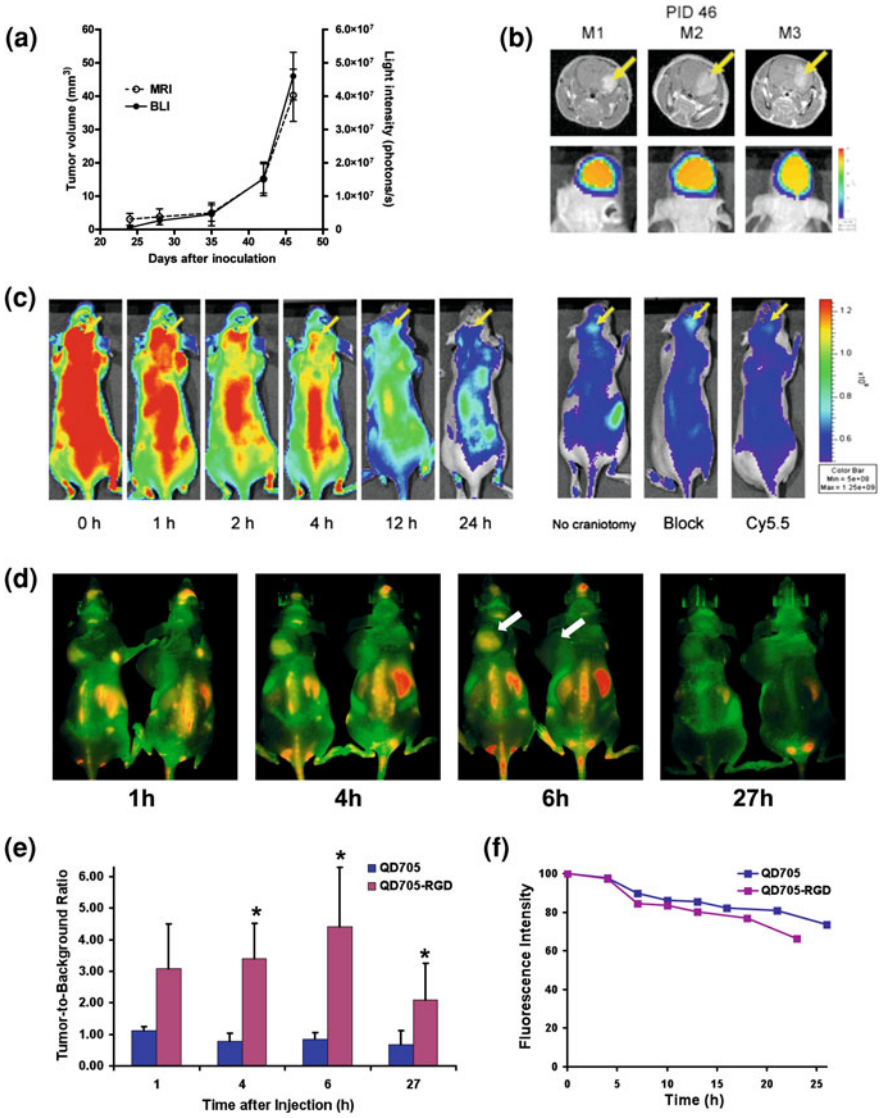

distribution of Cy5.5–VEGF was reported in these studies. Interestingly, the bioluminescence signal of luciferase-transfected tumor cells did not co-localize well with the fluorescence signal of Cy5.5–VEGF in some cases (Backer et al. 2007).

VEGF expression is challenging to image, due to the soluble and dynamic nature of VEGF proteins. Imaging of VEGFR expression is, therefore, easier.

◀ **Fig. 5** **a** MRI assessed tumor volume (mm^3) using gadolinium contrast and BLI measured volume (photons/second) using peak signal intensity from post injection day (PID) 24-46 ($n = 3$). **b** T1-weighted contrast-enhanced MRI and corresponding IVIS 200 BLI images (scale: 5.00 x 10^6–6.00 x 10^7) for experimental mice on PID 46, *yellow arrows* indicate tumor location. **c** NIRF images of Cy5.5-RGD time course taken with IVIS 200 from 0 to 24 h postinjection, block using c(RGDyK) 2 h postinjection, and Cy5.5 dye alone 2 h postinjection, yellow arrows indicate intracranial tumor signal (scale: 5.00 x 10^8–1.25 x 10^9). MRI acquired tumor size before in vivo NIRF imaging was 40.3 ± 7.8 mm^3. **d** In vivo NIR fluorescence imaging of U87MG tumor-bearing mice (left shoulder, pointed by *white arrows*) injected with 200 pmol of QD705-RGD (*left*) and QD705 (*right*), respectively. All images were acquired under the same instrumental conditions. The mice autofluorescence is color-coded green while the unmixed QD signal is color-coded red. Prominent uptake in the liver, bone marrow, and lymph nodes was also visible. **e** Tumor-to-background ratios of mice injected with QD705 or QD705-RGD. The data were represented as mean [standard deviation (SD)]. Using one-tailed paired Student's t test (n) 3), "*" *denotes where* $P < 0.05$ *as compared to the mice* injected with QD705. **f** Serum stability of QD705 and QD705-RGD in complete mouse serum over the course of 24 h. Taken with permission from Hsu et al. (2006) and Cai et al. (2006)

However, both expression of VEGF and VEGFR are important imaging targets to study cancer diagnosis and monitor therapeutic efficacy. Examination of tumors with targeted tracers against both targets can provide important insight into the expression and kinetics of VEGF and VEGFR during development and therapy of cancers.

In another approach, activatable probes, cleaved by enzymes that are associated with invasiveness, such as MMPs, have been used for non-invasive optical imaging of angiogenesis (Bremer et al. 2001). Also nonspecific contrast agents have been successfully employed such as FITC conjugated Dextrans or ICG. This NIRF agent has been used to visualize angiogenic vasculature in breast tumors (Ntziachristos et al. 2000) and adenocarcinomas (Cuccia et al. 2003).

4.6 Cell Death

Specific visualization of cell death has numerous biomedical applications. In oncology, specific cell death imaging can be used to monitor the response to therapy and in the development of new treatment strategies (for review see Corsten et al. 2006).

In order to image cell death non-invasively annexin V can be used as a reporter agent (Ntziachristos et al. 2004). Annexin V is a protein, which shows binding in high affinity to anionic phospholipids such as phosphatidyl serine (PS). PS is, usually, restricted to the inner leaflet of the cell membrane. However, in the process of cell death, PS is translocated to the outer surface of the cell membrane being accessible for Annexin V. Since exposition of PS is observed in necrotic as well as apoptotic tissues, the distinction between apoptosis and necrosis with

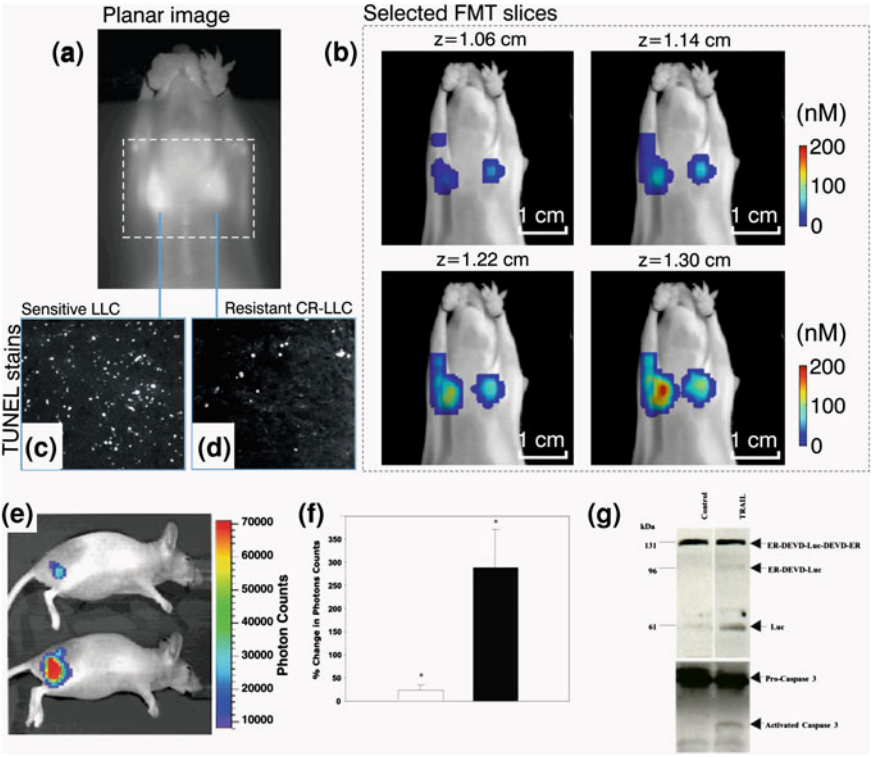

Fig. 6 Imaging apoptotic response in vivo with an annexin V-Cy5.5 conjugate (**a**–**d**) and in vivo imaging of caspase-3 activation (**e**–**g**). **a** Planar fluorescence image. **b** Four consecutive FMT slices (in color) superimposed on the planar image of the mouse obtained at the excitation wavelength. The bottom right slice is the one closer to the surface of the animal as seen in a, and successive slices are reconstructed from deeper in the animal. **c** and **d** TUNELstained histological slices from the sensitive LLC and resistant CR-LLC tumors. **e** In vivo bioluminescence image of a mouse with a s.c. D54-LucER glioma obtained before (*top*) and 60–75 min after (*bottom*) TRAIL treatment. Note the significant increase in photons collected from the same animal after TRAIL treatment. **f** Average percentage change in photon output in PBS-treated (open bar, 21 ± 28 %) and TRAIL treated (filled bar, 287 ± 186 %, P = 0.04) D54-LucER glioma tumors ($n = 5$ animals per group) that revealed a 3-fold mean increase in bioluminescence on apoptosis induction. Error bars represent SD. **g** Western blot analysis of PBS- and tumor necrosis factor α-related apoptosis-inducing Ligand (TRAIL)-treated excised tumors using antibodies specific for Luc or caspase-3 revealed activation of caspase-3 in TRAIL-treated tumors but not in control (PBS-treated) tumors. A concomitant cleavage (activation) of the 131-kDa reporter was observed in TRAIL-treated tumors. Taken with permission from Ntziachristos et al. (2004) and Laxman et al. (2002)

Annexin V is difficult. Still, annexin V has been used to image cell death occurring in cancer (Ntziachristos et al. 2004; Choi et al. 2005, Fig. 6).

However, there is a feature of the apoptotic cascade that enables a more specific imaging. Apoptosis involves three different pathways (Schmitt and Lowe 1999),

differing in their initiation way, like death receptor signaling (Fas or TNF), withdrawal of growth factors and cytochrome C release from mitochondria or DNA damage, triggering p53 pathway. All of these pathways have in common that they lead to activation of caspase-3. The proteolysis mediated by caspase-3 involves irreversible cellular changes, among them cell shrinkage, membrane blebbing, chromatin condensation, and nuclear fragmentation. The difficulty in imaging caspases lies within the fact that probes have to penetrate the cell membrane to reach their targets.

To circumvent this problem and to image caspase activity Laxmann et al. (2002) constructed a reporter gene that produced a recombinant luciferase fusion protein. The activity of the luciferase reporter was silenced by fusion to another protein via a linker cleavable by Activation of caspase-3 was visualized by BLI in a subcutaneous xenograft model. This produced real-time imaging of apoptosis in vivo (see Fig. 6).

Lee et al. (2009) have recently developed a combined activatable NIRF and radio-labeled multimodality probe, specific for cleavage by caspase-3 enabling localization, and quantification of the distribution of the probe. However, this agent awaits testing in an oncologic animal model.

4.7 Blood Flow

A number of studies were able to show that non-specific dyes like ICG can be used to visualize blood flow and perfusion in animals as well as humans. Blood flow and extravasation of blood constituents can also be studied with fluorescent-labeled albumin (Becker et al. 2000). Albumin labeled with a NIR fluorophore was used to study drainage in a lung cancer model in rats and pigs (Parungo et al. 2004).

Albumin coated nanoparticles were used as an angiographic contrast agent for vessels surrounding and penetrating a murine squamous cell carcinoma in a C3H mouse (Morgan et al. 2005). The albumin coating was used to minimize non-specific interactions without significantly affecting the optical properties of the semiconductor core. More importantly, as long as the core is well-encapsulated, the specific photochemical reactions that cause organic dyes to photo bleach are not a problem for inorganic nanoparticles. However, because of concerns over potential toxicity, organic alternatives to QDs will be required for initial clinical studies.

Preclinically ICG was used for imaging of cerebrospinal fluid space (Shibata 2007), estimation of blood content in tumors (Valentini et al. 2008) as well as for quantitative measurement of peripheral tissue perfusion (Kang et al. 2009). A recently established non-oncological application of ICG is the clinical imaging of disturbed microvasculature in the hands of patients suspicious for arthritic diseases (Bremer et al. 2009).

A variety of research approaches deal with the improvement of ICG with respect to its weak fluorescence properties and chemical instability in aqueous solution. The rationale has been to apply ICG in different formats of pharmaceutical formulations, thereby modulating the chemical and pharmacokinetic properties

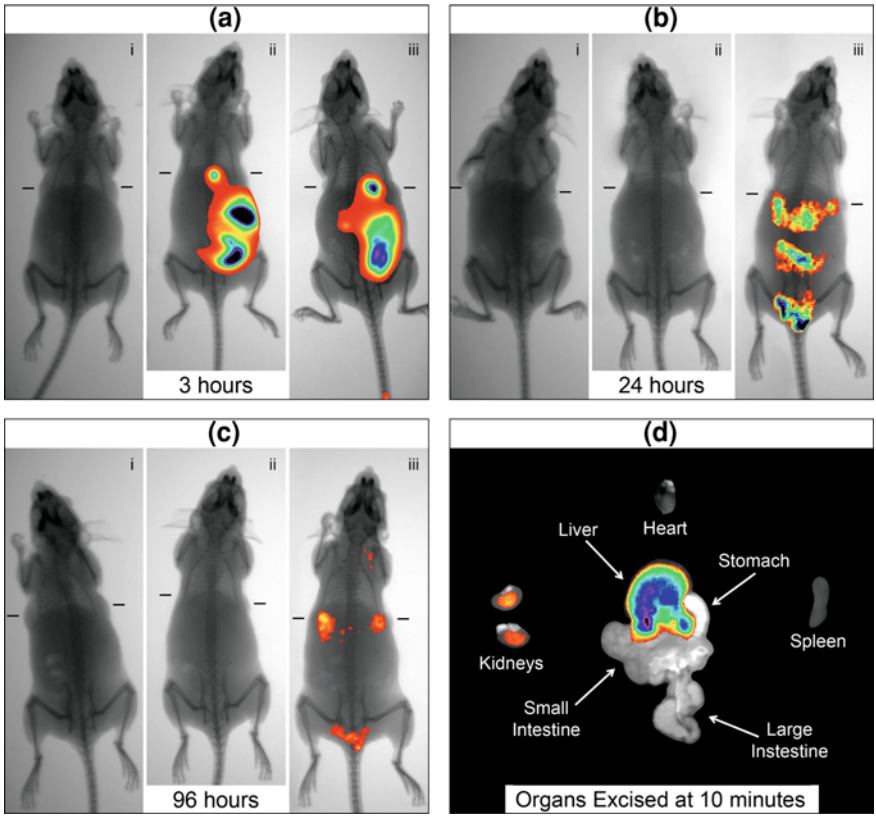

Fig. 7 **a** NIR transillumination images (Ex. 755 nm, Em. 830 nm) taken at various times track fluorescence signals and pharmacokinetic distributions for the ICG-calcium phosphate nanoparticles (CPNPs) and controls delivered systemically via tail vein injections in nude mice implanted with subcutaneous human breast adenocarcinoma tumors. Hash marks next to each mouse indicate the position of the 5 mm tumors. Two control samples, (i) carboxylate-terminated CPNPs without ICG encapsulant and (ii) free ICG, match the particle concentration and fluorophore content (10^{-13} particles/mL and 10^{-5} M, respectively) of a (iii) PEGylated ICG-CPNP sample. **b** (ii) No fluorescence signal is detected from the free ICG at 24 h postinjection, while the PEG-ICG-CPNP sample (**c** iii) retains significant signal even after 96 h. (**b** iii) Fluorescence signal is unmistakably localized in tumors 24 h after administration with PEGylated ICG-CPNPs. The excised organs in panel (**d**) illustrate the biliary clearance route 10 min postinjection of PEG-ICG-CPNPs. Fluorescence signal is not seen from the stomach or spleen with minimal renal involvement. Taken with permission from Altinoğlu et al. (2008)

without employing a newly synthesized fluorophore. Yaseen et al. (2009) encapsulated ICG in electrostatically assembled mesocapsules (MCs) to explore the potential for targeted optical imaging and therapy. Altinoğlu et al. (2008) developed calcium phosphate nanoparticles doped with ICG with a 2-fold increase in emission intensity, when compared with pure ICG, to image human breast adenocarcinoma tumors subcutaneously implanted in nude mice (Fig. 7). Interestingly, Makino

et al. (2009) labeled lactosomes with ICG, which were stable in blood circulation and gradually accumulated specifically at a model liver tumor site.

Although several promising approaches have been followed in the past few years, ICG is still the gold standard and only available clinical contrast agent for imaging of blood flow and extravasation due to damages in blood tissue barriers. However, optical imaging techniques offer the possibility to image characteristics of vasculature without applying contrast agents, since the absorption of hemoglobin and deoxyhemoglobin can be used to calculate the regional concentration of hemoglobin and oxygen saturation (Cuccia et al. 2003; Miller et al. 2005).

5 Clinical Perspective

As shown in this chapter, optical imaging techniques have numerous applications in oncologic research. For clinical applications, however, optical imaging has inherent limitations due to the underlying physical nature of this imaging modality. Scattering and absorption of photons in the tissue leads to a depth limit of a few centimeters at best, which makes optical imaging in clinical applications suitable only for superficial targets and instrumentally accessible body regions of limited size. Nevertheless, there are many different examples to be mentioned showing the successful improvement of contrast agents as well as detection technology (Pichler et al. 2008).

Beyond the many different research approaches, the clinical application of optical imaging involves the detection of superficial malignant skin lesions. An intensively studied clinical field has been the diagnostic imaging of breast cancer, using both the intrinsic optical properties of tissues, as well as exogenous contrast agents. With the latter technique, called transillumination (Cutler 1931), it was possible to detect tumor lesions. However, it was not possible to reliably differentiate between malignant and benign lesions.

The invention of tomographic techniques, not only with respect to breast imaging, was an important step towards clinical applications of in vivo optical imaging (Ntziachristos and Chance 2001). One example for this is an advanced optical breast scanner currently developed from a dutch technological company. This optical mammography system makes use of laser light illuminating the breast from all sides. The detected fluorescence signal is computed to deliver a 3-D tomographic image of the breast pathology. As indicated above, also the pharmaceutical industry has made attempts to develop new optical contrast agents. The optical mammographic tomograph provided an example for a joint development, since the development of the detection technology has to be closely linked to the development of a specific fluorescence probe for breast imaging. A german pharmaceutical company unfortunately stopped the developments recently due to uncertain results.

Since, the development of new and more sensitive fluorescence detection technologies has led to the possibility to apply optical imaging also in clinical oncology, the development of new suitable optical imaging agents is the key step towards its broad practical application in the clinic.

Fluorescein angiography (FA) was discovered by Novotny and Alvis in the 1960s and became a standard technique for macular diagnostics (Novotny and Alvis 1961). The best-known example for a clinically approved optical contrast agent is ICG. ICG was used as a contrast agent in retinal perfusion (Flower et al. 1976; Herbort et al. 1998), myocardial perfusion (Schad et al. 1977; Taggart et al. 2003), as well as cerebral perfusion (Liebert et al. 2006; Steinbrink et al. 2008).

Haglund et al. (1996) described Indocyanine green as contrast agent suitable to image human gliomas and tumor margins back in 1996.

ICG enhanced optical imaging of human gliomas was shown to have the potential to localize tumors, identify tumor remaining at the resection margins, and determine the grade of the tumor. ICG was used for breast cancer imaging (Ntziachristos et al. 2000 and as shown in this book by Grosenick et al.). In ophthalmology ICG has been used in glaucoma surgery (Harris et al. 2008, see also reviews by 2009; Farah et al. 2009; Hassenstein et al. 2009), but it has also been used for functional lymphatic imaging (Sharma et al. 2008).

Ito et al. (2006) developed an infrared fluorescence endoscope (IRFE) and ICG derivatives as infrared fluorescence labeling materials to evaluate gastrointestinal neoplastic lesions. Finally, the diagnosis of arthritic diseases in the joints of hands based on the imaging of disturbed microvasculature is a recently established clinical imaging method employing ICG (Bremer et al. 2009)

An example for another optical contrast agent with clinical application is 5-aminolevulinic acid (ALA), which is an injectable biosynthetic precursor of intracellularly synthesized fluorescent protoporphyrin IX (see review by Da Costa et al. 2007). ALA has shown the ability to differentiate normal from neoplastic tissue. It is available in three different forms, as "pure" ALA, ALA-hexylester, or ALA-methyl ester. ALA is taken up by cells and metabolized to protoporphyrin IX (PpIX) via the heme biosynthesis pathway (Krammer and Uberriegler 1996; Kennedy et al. 1996).

PpIX emits fluorescence between 625 and 725 nm, which is on the one hand advantageously within the NIRF window of low tissue autofluorescence and on the other hand is tissue specific, since it is endogeneously generated preferentially in dysplastic tissue, although the reasons for this are not well understood and some of the results being reported in in vitro studies about differential synthesis of ALA-induced PpIX in dysplastic and normal tissue is contradictory (Peng et al. 1997). There have been several reasons discussed for the increased production of PpIX in tumor cells, among them concentration differences of endogeneous iron or porphobilinogen deaminase. Also the enzyme involved in conversion of PpIX to heme, ferrochelatase could be responsible (Battle 1993).

Nevertheless, PpIX can be used in the mucosal layer of internal hollow organs, such as lung (Baumgartner et al. 1996), bladder (Leveckis et al. 1994; Kriegmair et al. 1994; Karl et al. 2008, see Fig. 8), gastrointestinal tract (Loh and Vernon 1993) and oral cavity (Leunig et al. 1996) with only little side effects, and a rather

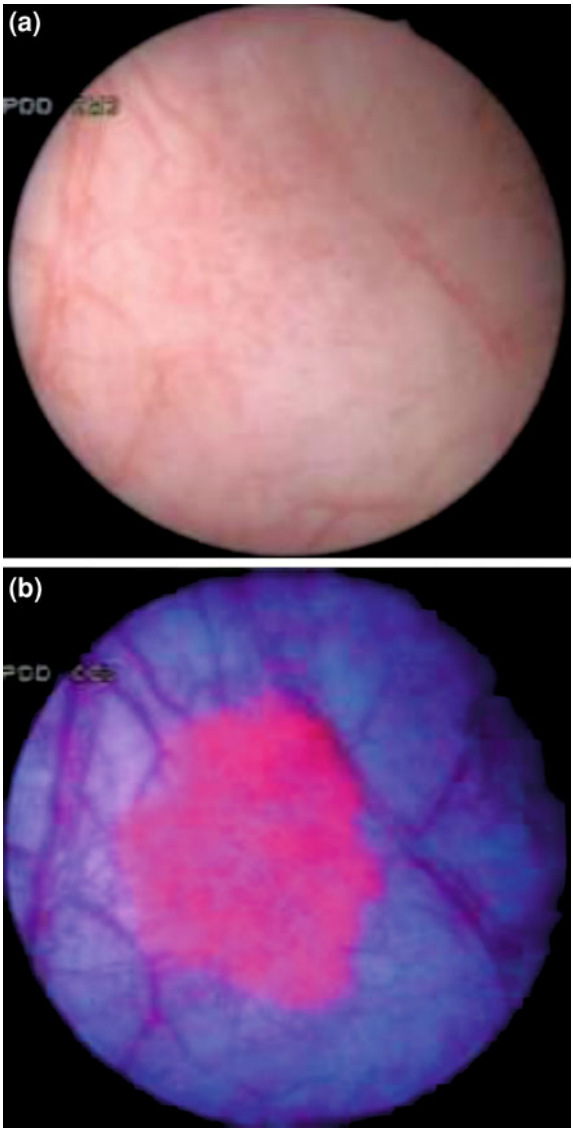

Fig. 8 **a** Carcinoma in situ in white light endoscopy, **b** Carcinoma in situ in fluorescence endoscopy. Taken with permission from Karl et al. (2008)

short phase of skin photosensitivity (Webber et al. 1997). ALA-PpIX fluorescence has also been studied in brain (Stummer et al. 1998) and ALA is clinically approved for intraoperative brain tumor surgery and dermatology. The hexylester form (trademark HexVix) is clinically approved for endoscopic bladder tumor diagnostics (Fig. 8) and the methyl ester form (trademark MetVix) for dermatology. There have been several articles recently reviewing the use of porphyrins or porphyrin precursors for PDT (Silva et al. 2008; Klein et al. 2008; Fritsch et al. 2006; Brown et al. 2004).

Taken together, the investigation of the approved exogenous fluorescent agents and the accompanying development of detection systems adapted to these agents will continue to expand into further clinical indications, influenced by regulatory approval, drug-related side effects, and costs.

6 Outlook/A Critical View

Non-invasive optical imaging techniques are powerful tools to study the physiology and pathophysiology in animal models of diseases and for the development of specific ligands for molecular imaging. They have the potential to improve the accuracy of disease detection and predict treatment response.

Since optical imaging techniques use nonionizing radiation with high sensitivity for label detection, require relatively simple and affordable instrumentation and are easy to use, they provide high-throughput capabilities, making them suitable for target screening, and preclinical drug development. In addition to this, they can be combined with histological microscopy for immunohistochemical identification of cells investigated, thereby offering unique benefits. All things considered they are very well suited for preclinical investigations in oncology research and other fields. In the clinic, the main difficulty is the applicability which is narrowed to particular techniques and body regions not allowing to provide a broadly applicable imaging system, such as given with MRI and PET/CT. However, there are already promising approaches and distinct instrumental solutions in the respective clinical disciplines, making it possible that optical imaging techniques will find increasing clinical application in the future.

When administering a fluorescent contrast agent, optical imaging exerts drawbacks attributed to the physical nature of this imaging technique. As usual for contrast agents, similar to nuclear medicine, one has to deal with background signals due to unspecific localization of the injected probe, which can make signal detection difficult particularly when the signal is of low intensity and located beyond tissue volumes of high blood content. In principle, diagnosis and imaging is advantageous when the detected area is accessible in direct view, such as in surgery. However, in the area that needs to be visually investigated, the practitioner has to be very careful, since even little injuries will produce a strong background due to inflammatory responses or bleedings. Besides this, tissue always exhibits a certain level of autofluorescence, which is strong in the VIS spectral range but rather negligible in the NIR. Therefore, a careful selection of fluorophores with emission spectra in the NIR window is necessary. Still optical imaging has an ultimate depth limit of a few centimeters at best, due to scattering and absorption, making it an inappropriate technique for whole-body clinical application. Even in laboratory animals, like mice, scattering and absorption remains an issue, since fur is a highly absorbing, and scattering material. Therefore, mice need to be depilated when signal quantification is required.

The confinement to the NIR window implicates another difficulty, since it is demanding to spectrally separate the channels from each other in this narrow window, especially when the emission peaks of the fluorophores partially overlap. There are some possibilities, like spectral unmixing routines, to separate signals from each other a posteriori. However, these routines will always have influence on the output signal.

Since planar optical imaging techniques are always surface weighted, a true quantification of fluorophore concentrations is impossible, permitting only a semiquantitative signal evaluation for a given experimental or technical approach. With the development of FMT systems, quantification based on sophisticated reconstruction algorithms became theoretically possible, but remain challenging especially for tissue volumes relevant in clinical practice.

Taken together, the systems for optical imaging constantly require adaption according to the tissue area that is intended to be evaluated by imaging, like deep tissue (e.g. brain), or surface (e.g. skin) imaging. Furthermore, the paradigm to be addressed needs to be evaluated, such as if a molecule is chosen to be targeted or if imaging remains on the anatomical level.

After having taken the different concepts into consideration; however, optical imaging techniques offer unique benefits for oncologic and numerous other applications covering many different clinical disciplines.

References

Altinoğlu EI, Russin TJ, Kaiser JM, Barth BM, Eklund PC, Kester M, Adair JH (2008) Near-infrared emitting fluorophore-doped calcium phosphate nanoparticles for in vivo imaging of human breast cancer. ACS Nano 2(10):2075–2084

Backer MV, Gaynutdinov TI, Patel V, Bandyopadhyaya AK, Thirumamagal BT, Tjarks W, Barth RF, Claffey K, Backer JM (2005) Vascular endothelial growth factor selectively targets boronated dendrimers to tumor vasculature. Mol Cancer Ther 4(9):1423–1429

Backer MV, Patel V, Jehning BT, Backer JM (2006) Self-assembled "dock and lock" system for linking payloads to targeting proteins. Bioconjug Chem 17(4):912–919

Backer MV, Levashova Z, Patel V, Jehning BT, Claffey K, Blankenberg FG, Backer JM (2007) Molecular imaging of VEGF receptors in angiogenic vasculature with single-chain VEGF-based probes. Nat Med 13(4):504–509

Battle A (1993) Porphyrins, porphyrias, cancer and photodynamic therapy: a model of carcinogenesis. J Photochem Photobiol, B 20:5–22

Baumgartner R, Huber RM, Schulz H, Stepp H, Rick K, Gamarra F, Leberig A, Roth C (1996) Inhalation of 5-aminolevulinic acid: a new technique for fluorescence detection of early stage lung cancer. J Photochem Photobiol, B 36(2):169–174

Becker A, Riefke B, Ebert B, Sukowski U, Rinneberg H, Semmler W, Licha K (2000) Macromolecular contrast agents for optical imaging of tumors: comparison of indotricarbocyanine-labeled human serum albumin and transferrin. Photochem Photobiol 72(2):234–241

Bhaumik S, Gambhir SS (2002) Optical imaging of Renilla luciferase reporter gene expression in living mice. Proc Natl Acad Sci U S A 99(1):377–382

Bremer C, Bredow S, Mahmood U, Weissleder R, Tung CH (2001) Optical imaging of matrix metalloproteinase-2 activity in tumors: feasibility study in a mouse model. Radiology 221(2):523–529

Bremer C, Werner S, Langer HE (2009) Assessing activity of rheumatic arthritis with fluorescence optical imaging. Eur Muscoloskeletal Rev 4(2):96–100

Brown SB, Brown EA, Walker I (2004) The present and future role of photodynamic therapy in cancer treatment. Lancet Oncol 5(8):497–508

Cai W, Chen X (2006) Anti-angiogenic cancer therapy based on integrin alphavbeta3 antagonism. Anticancer Agents Med Chem 6(5):407–428

Cai W, Shin DW, Chen K, Gheysens O, Cao Q, Wang SX, Gambhir SS, Chen X (2006) Peptide-labeled near-infrared quantum dots for imaging tumor vasculature in living subjects. Nano Lett 6(4):669–676

Cai W, Chen X (2008) Multimodality molecular imaging of tumor angiogenesis. J Nucl Med 49(Suppl 2):113S–128S

Cheng Z, Levi J, Xiong Z, Gheysens O, Keren S, Chen X, Gambhir SS (2006) Near-infrared fluorescent deoxyglucose analogue for tumor optical imaging in cell culture and living mice. Bioconjugate Chem 17(3):662–669

Choi HK, Yessayan D, Choi HJ, Schellenberger E, Bogdanov A, Josephson L, Weissleder R, Ntziachristos V (2005) Quantitative analysis of chemotherapeutic effects in tumors using in vivo staining and correlative histology. Cell Oncol 27(3):183–190

Corsten MF, Hofstra L, Narula J, Reutelingsperger CP (2006) Counting heads in the war against cancer: defining the role of annexin A5 imaging in cancer treatment and surveillance. Cancer Res 66(3):1255–1260

Cuccia DJ, Bevilacqua F, Durkin AJ, Merritt S, Tromberg BJ, Gulsen G, Yu H, Wang J, Nalcioglu O (2003) In vivo quantification of optical contrast agent dynamics in rat tumors by use of diffuse optical spectroscopy with magnetic resonance imaging coregistration. Appl Opt 42(16):2940–2950

Cutler M (1931) Transillumination of the breast. Ann Surg 93(1):223–234

DaCosta RS, Wilson BC, Marcon NE (2007) Fluorescence and spectral imaging. Scientific World J 7:2046–2071

de Wet JR, Wood KV, DeLuca M, Helinski DR, Subramani S (1987) Firefly luciferase gene: structure and expression in mammalian cells. Mol Cell Biol 7(2):725–737

Dothager RS, Flentie K, Moss B, Pan MH, Kesarwala A, Piwnica-Worms D (2009) Advances in bioluminescence imaging of live animal models. Curr Opin Biotechnol 20(1):45–53

Farah ME, Maia M, Rodrigues EB (2009) Dyes in ocular surgery: principles for use in chromovitrectomy. Am J Ophthalmol 148(3):332–340

Flower RW, Hochheimer BF (1976) Indocyanine green dye fluorescence and infrared absorption choroidal angiography performed simultaneously with fluorescein angiography. Johns Hopkins Med J 138(2):33–42

Fritsch C, Ruzicka T (2006) Fluorescence diagnosis and photodynamic therapy in dermatology from experimental state to clinic standard methods. J Environ Pathol Toxicol Oncol 25(1–2):425–439

Grimm J, Wunder A (2005) Current state of molecular imaging research. Fortschr Röntgenstr 177(3):326–337

Haglund MM, Berger MS, Hochman DW (1996) Enhanced optical imaging of human gliomas and tumor margins. Neurosurgery 38(2):308–317

Harada H, Kizaka-Kondoh S, Hiraoka M (2005) Optical imaging of tumor hypoxia and evaluation of efficacy of a hypoxia-targeting drug in living animals. Mol Imaging 4(3):182–193

Harris A, Kagemann L, Ehrlich R, Rospigliosi C, Moore D, Siesky B (2008) Measuring and interpreting ocular blood flow and metabolism in glaucoma. Can J Ophthalmol 43(3):328–336

Hassenstein A, Meyer CH (2009) Clinical use and research applications of Heidelberg retinal angiography and spectral-domain optical coherence tomography—a review. Clin Experiment Ophthalmol 37(1):130–143

Herbort CP, LeHoang P, Guex-Crosier Y (1998) Schematic interpretation of indocyanine green angiography in posterior uveitis using a standard angiographic protocol. Ophthalmology 105(3):432–440

Hood JD, Cheresh DA (2002) Role of integrins in cell invasion and migration. Nat Rev Cancer 2(2):91–100

Hsiao JK, Law B, Weissleder R, Tung CH (2006) In vivo imaging of tumor associated urokinase-type plasminogen activator activity. J Biomed Opt 11(3):34013

Hsu AR, Hou LC, Veeravagu A, Greve JM, Vogel H, Tse V, Chen X (2006) In vivo near-infrared fluorescence imaging of integrin alphavbeta3 in an orthotopic glioblastoma model. Mol Imaging Biol 8(6):315–323

Hynes RO (2002) Integrins: bidirectional, allosteric signaling machines. Cell 110(6):673–687

Ito S, Muguruma N, Kimura T, Yano H, Imoto Y, Okamoto K, Kaji M, Sano S, Nagao Y (2006) Principle and clinical usefulness of the infrared fluorescence endoscopy. J Med Invest 53(1–2):1–8

Kang Y, Choi M, Lee J, Koh GY, Kwon K, Choi C (2009) Quantitative analysis of peripheral tissue perfusion using spatiotemporal molecular dynamics. PLoS ONE 4(1):e4275

Karl A, Zaak D, Tilki D, Hungerhuber E, Staehler M, Denzinger S, Stanislaus P, Tritschler S, Strittmatter F, Stief C, Burger M (2008) Diagnosis of urothelial carcinoma. Urologe 47(3):357–367

Kennedy JC, Marcus SL, Pottier RH (1996) Photodynamic therapy (PDT) and photodiagnosis (PD) using endogenous photosensitization induced by 5-aminolevulinic acid (ALA): mechanisms and clinical results. J Clin Laser Med Surg 14(5):289–304

Klein A, Babilas P, Karrer S, Landthaler M (2008) Photodynamic therapy in dermatology–an update. J Dtsch Dermatol Ges 6(10):839–846

Klohs J, Wunder A, Licha K (2008) Near-Infrared fluorescent probes for imaging vascular pathophysiology. Basic Res Cardiol 103(2):144–151

Krammer B, Uberriegler K (1996) In vitro investigation of ALA-induced protoporphyrin IX. J Photochem Photobiol, B 36(2):121–126

Kriegmair M, Baumgartner R, Knuechel R, Steinbach P, Ehsan A, Lumper W, Hofstädter F, Hofstetter A (1994) Fluorescence photodetection of neoplastic urothelial lesions following intravesical instillation of 5-aminolevulinic acid. Urology 44(6):836–841

Law B, Curino A, Bugge TH, Weissleder R, Tung CH (2004) Design, synthesis, and characterization of urokinase plasminogen-activator-sensitive near-infrared reporter. Chem Biol 11(1):99–106

Laxman B, Hall DE, Bhojani MS, Hamstra DA, Chenevert TL, Ross BD, Rehemtulla A (2002) Noninvasive real-time imaging of apoptosis. Proc Natl Acad Sci U S A 99(26):16551–16555

Lee H, Akers WJ, Cheney PP, Edwards WB, Liang K, Culver JP, Achilefu S (2009) Complementary optical and nuclear imaging of caspase-3 activity using combined activatable and radio-labeled multimodality molecular probe. J Biomed Opt 14(4):040507

Leunig A, Rick K, Stepp H, Gutmann R, Alwin G, Baumgartner R, Feyh J (1996) Fluorescence imaging and spectroscopy of 5-aminolevulinic acid induced protoporphyrin IX for the detection of neoplastic lesions in the oral cavity. Am J Surg 172(6):674–677

Leveckis J, Burn JL, Brown NJ, Reed MW (1994) Kinetics of endogenous protoporphyrin IX induction by aminolevulinic acid: preliminary studies in the bladder. J Urol 152(2 Pt 1):550–553

Li X, Nakajima Y, Niwa K, Viviani VR, Ohmiya Y (2009) Enhanced red-emitting railroad worm luciferase for bioassays and bioimaging. Protein Sci Oct 28

Liebert A, Wabnitz H, Obrig H, Erdmann R, Möller M, Macdonald R, Rinneberg H, Villringer A, Steinbrink J (2006) Non-invasive detection of fluorescence from exogenous chromophores in the adult human brain. Neuroimage 31(2):600–608

Lloyd PG, Hardin CD, Sturek M (1999) Examining glucose transport in single vascular smooth muscle cells with a fluorescent glucose analog. Physiol Res 48(6):401–410

Loh CS, Vernon D, MacRobert AJ, Bedwell J, Bown SG, Brown SB (1993) Endogenous porphyrin distribution induced by 5-aminolaevulinic acid in the tissue layers of the gastrointestinal tract. J Photochem Photobiol, B 20(1):47–54

Makino A, Kizaka-Kondoh S, Yamahara R, Hara I, Kanzaki T, Ozeki E, Hiraoka M, Kimura S (2009) Near-infrared fluorescence tumor imaging using nanocarrier composed of poly(L-lactic acid)-block-poly(sarcosine) amphiphilic polydepsipeptide. Biomaterials 30(28):5156–5160

Massoud TF, Gambhir SS (2003) Molecular Imaging in living subjects: seeing fundamental biological processes in a new light. Genes Dev 17(5):545–580

McIntyre JO, Matrisian LM (2003) Molecular imaging of proteolytic activity in cancer. J Cell Biochem 90(6):1087–1097

McIntyre JO, Fingleton B, Wells KS, Piston DW, Lynch CC, Gautam S, Matrisian LM (2004) Development of a novel fluorogenic proteolytic beacon for in vivo detection and imaging of tumour-associated matrix metalloproteinase-7 activity. Biochem J 377(Pt 3):617–628

Michelini E, Cevenini L, Mezzanotte L, Roda A (2009) Luminescent probes and visualization of bioluminescence. Methods Mol Biol 574:1–13

Miller JC, Pien HH, Sahani D, Sorensen AG, Thrall JH (2005) Imaging angiogenesis: applications and potential for drug development. J Natl Cancer Inst 97(3):172–187

Miloud T, Henrich C, Hämmerling GJ (2007) Quantitative comparison of click beetle and firefly luciferases for in vivo bioluminescence imaging. J Biomed Opt 12(5):054018

Morgan NY, English S, Chen W, Chernomordik V, Russo A, Smith PD, Gandjbakhche A (2005) Real time in vivo non-invasive optical imaging using near-infrared fluorescent quantum dots. Acad Radiol 12(3):313–323

Novotny HR, Alvis DL (1961) A method of photographing fluorescence in circulation blood in the human retina. Circulation XXIV, 82-86

Ntziachristos V, Yodh AG, Schnall M, Chance B (2000) Concurrent MRI and diffuse optical tomography of breast after indocyanine green enhancement. Proc Natl Acad Sci U S A 97(6):2767–2772

Ntziachristos V, Chance B (2001) Probing physiology and molecular function using optical imaging: applications to breast cancer. Breast Cancer Res 3(1):41–46

Ntziachristos V, Schellenberger EA, Ripoll J, Yessayan D, Graves E, Bogdanov A Jr, Josephson L, Weissleder R (2004) Visualization of antitumor treatment by means of fluorescence molecular tomography with an annexin V-Cy5.5 conjugate. Proc Natl Acad Sci U S A 101(33):12294-12299

Oh KB, Matsuoka H (2002) Rapid viability assessment of yeast cells using vital staining with 2-NBDG, a fluorescent derivative of glucose. Int J Food Microbiol 76(1–2):47–53

Parungo CP, Ohnishi S, De Grand AM, Laurence RG, Soltesz EG, Colson YL, Kang PM, Mihaljevic T, Cohn LH, Frangioni JV (2004) In vivo optical imaging of pleural space drainage to lymph nodes of prognostic significance. Ann Surg Oncol 11(12):1085–1092

Peterson TE, Manning HC (2009) Molecular imaging: ^{18}F-FDG PET and a whole lot more. J Nucl Med Technol 37(3):151–161

Peng Q, Berg K, Moan J, Kongshaug M, Nesland JM (1997) 5-Aminolevulinic acid-based photodynamic therapy: principles and experimental research. Photochem Photobiol 65(2):235–251

Pichler BJ, Wehrl HF, Judenhofer MS (2008) Latest advances in molecular imaging instrumentation. J Nucl Med 49(Suppl 2):5S–23S

Rodrigues EB, Costa EF, Penha FM, Melo GB, Bottós J, Dib E, Furlani B, Lima VC, Maia M, Meyer CH, Höfling-Lima AL, Farah ME (2009) The use of vital dyes in ocular surgery. Surv Ophthalmol 54(5):576–617

Schad H, Brechtelsbauer H, Kramer K (1977) Studies on the suitability of a cyanine dye (Viher-Test) for indicator dilution technique and its application to the measurement of pulmonary artery and aortic flow. Pflugers Arch 370(2):139–144

Scherer RL, McIntyre JO, Matrisian LM (2008) Imaging matrix metalloproteinases in cancer. Cancer Metastasis Rev 27(4):679–690

Schmitt CA, Lowe SW (1999) Apoptosis and therapy. J Pathol 187(1):127–137

Shibata Y, Kruskal JB, Palmer MR (2007) Imaging of cerebrospinal fluid space and movement of hydrocephalus mice using near infrared fluorescence. Neurol Sci 28(2):87–92

Serganova I, Doubrovin M, Vider J, Ponomarev V, Soghomonyan S, Beresten T, Ageyeva L, Serganov A, Cai S, Balatoni J, Blasberg R, Gelovani J (2004) Molecular Imaging of temporal dynamics and spatial heterogeneity of hypoxia-inducible factor-1 signal transduction activity in tumors in living mice. Cancer Res 64(17):6101–6108

Sharma R, Wendt JA, Rasmussen JC, Adams KE, Marshall MV, Sevick-Muraca EM (2008) New horizons for imaging lymphatic function. Ann N Y Acad Sci 1131:13–36

Silva JN, Filipe P, Morlière P, Mazière JC, Freitas JP, Gomes MM, Santus R (2008) Photodynamic therapy: dermatology and ophthalmology as main fields of current applications in clinic. Biomed Mater Eng 18(4–5):319–327

Steinbrink J, Liebert A, Wabnitz H, Macdonald R, Obrig H, Wunder A, Bourayou R, Betz T, Klohs J, Lindauer U, Dirnagl U, Villringer A (2008) Towards noninvasive molecular fluorescence imaging of the human brain. Neurodegener Dis 5(5):296–303

Stummer W, Stocker S, Novotny A, Heimann A, Sauer O, Kempski O, Plesnila N, Wietzorrek J, Reulen HJ (1998) In vitro and in vivo porphyrin accumulation by C6 glioma cells after exposure to 5-aminolevulinic acid. J Photochem Photobiol, B 45(2–3):160–169

Taggart DP, Choudhary B, Anastasiadis K, Abu-Omar Y, Balacumaraswami L, Pigott DW (2003) Preliminary experience with a novel intraoperative imaging technique to evaluate the patency of bypass grafts in total arterial revascularization. Ann Thorac Surg 75(3):870–873

Tannous BA (2009) Gaussia luciferase reporter assay for monitoring biological processes in culture and in vivo. Nat Protoc 4(4):582–591

Uhrbom L, Nerio E, Holland EC (2004) Dissecting tumor maintenance requirements using bioluminescence imaging of cell proliferation in a mouse glioma model. Nat Med 10(11):1257–1260

Valentini G, D'Andrea C, Ferrari R, Pifferi A, Cubeddu R, Martinelli M, Natoli C, Ubezio P, Giavazzi R (2008) In vivo measurement of vascular modulation in experimental tumors using a fluorescent contrast agent. Photochem Photobiol 84(5):1249–1256

Viola RJ, Provenzale JM, Li F, Li CY, Yuan H, Tashjian J, Dewhirst MW (2008) In vivo bioluminescence imaging monitoring of hypoxia-inducible factor 1alpha, a promoter that protects cells, in response to chemotherapy. AJR Am J Roentgenol 191(6):1779–1784

von Burstin J, Eser S, Seidler B, Meining A, Bajbouj M, Mages J, Lang R, Kind AJ, Schnieke AE, Schmid RM, Schneider G, Saur D (2008) Highly sensitive detection of early-stage pancreatic cancer by multimodal near-infrared molecular imaging in living mice. Int J Cancer 123(9):2138–2147

Wang H, Cao F, De A, Cao Y, Contag C, Gambhir SS, Wu JC, Chen X (2009a) Trafficking mesenchymal stem cell engraftment and differentiation in tumor-bearing mice by bioluminescence imaging. Stem Cells 27(7):1548–1558

Wang W, Shao R, Wu Q, Ke S, McMurray J, Lang FF Jr, Charnsangavej C, Gelovani JG, Li C (2009b) Targeting gelatinases with a near-infrared fluorescent cyclic His-Try-Gly-Phe peptide. Mol Imaging Biol 11(6):424–433

Webber J, Kessel D, Fromm D (1997) Side effects and photosensitization of human tissues after aminolevulinic acid. J Surg Res 68(1):31–37

Weissleder R, Tung CH, Mahmood U, Bogdanov A Jr (1999) In vivo imaging of tumors with protease-activated near-infrared fluorescent probes. Nat Biotechnol 17(4):375–378

Wunder A, Klohs J (2008) Optical Imaging of Vascular Pathophysiology. Basic Res Cardiol 103(2):182–190

Xiong JP, Stehle T, Zhang R, Joachimiak A, Frech M, Goodman SL, Arnaout MA (2002) Crystal structure of the extracellular segment of integrin alpha Vbeta3 in complex with an Arg-Gly-Asp ligand. Science 296(5565):151–155

Yamada K, Nakata M, Horimoto N, Saito M, Matsuoka H, Inagaki N (2000) Measurement of glucose uptake and intracellular calcium concentration in single, living pancreatic beta-cells. J Biol Chem 275(29):22278–22283

Yaseen MA, Yu J, Jung B, Wong MS, Anvari B (2009) Biodistribution of encapsulated indocyanine green in healthy mice. Mol Pharm 6(5):1321–1332

Ye Y, Bloch S, Achilefu S (2004) Polyvalent carbocyanine molecular beacons for molecular recognitions. J Am Chem Soc 126:7740–7741

Ye Y, Bloch S, Kao J, Achilefu S (2005) Multivalent carbocyanine molecular probes: synthesis and applications. Bioconjugate Chem 16(1):51–61

Yoshioka K, Takahashi H, Homma T, Saito M, Oh KB, Nemoto Y, Matsuoka H (1996a) A novel fluorescent derivative of glucose applicable to the assessment of glucose uptake activity of *Escherichia coli*. Biochim Biophys Acta 1289(1):5–9

Yoshioka K, Saito M, Oh KB, Nemoto Y, Matsuoka H, Natsume M, Abe H (1996b) Intracellular fate of 2-NBDG, a fluorescent probe for glucose uptake activity, in Escherichia coli cells. Biosci Biotechnol Biochem 60(11):1899–1901

Zhang M, Zhang Z, Blessington D, Li H, Busch TM, Madrak V, Miles J, Chance B, Glickson JD, Zheng G (2003) Pyropheophorbide 2-deoxyglucosamide: a new photosensitizer targeting glucose transporters. Bioconjugate Chem 14(4):709–714

Zhang Z, Li H, Liu Q, Zhou L, Zhang M, Luo Q, Glickson J, Chance B, Zheng G (2004) Metabolic imaging of tumors using intrinsic and extrinsic fluorescent markers. Biosens Bioelectron 20(3):643–650

Applications of Small Animal PET

Cristina Nanni and Stefano Fanti

Abstract

The small animal PET is an innovative preclinical imaging technique that is meant to visualise biological processes of tissues in a living organism. The most important characteristic is the very high spatial resolution that makes those tomographs suitable for imaging small animals like mice. The employment of different radiolabelled compounds allows to highlight the overexpression or nonexpression of many metabolic pathways, helping to profile in vivo the cancer from a biological point of view, to predict or measure the response to experimental therapies, to observe the metabolic modification of the cancer over time, and to test new labelled compound to be eventually used for clinical PET. Main drawback is the very high cost of the scanners and the need of a radiopharmacy, partly cyclotron based, to synthesise as many PET tracers as possible.

Contents

C. Nanni · S. Fanti (✉)
UO Medicina Nucleare, Azienda Ospedaliero-Universitaria di Bologna
Policlinico S.Orsola-Malpighi, Via Massarenti 9, 40138 Bologna, Italy
e-mail: stefano.fanti@aosp.bo.it

C. Nanni
e-mail: cristina.nanni@aosp.bo.it

O. Schober and B. Riemann (eds.), *Molecular Imaging in Oncology*,
Recent Results in Cancer Research 187, DOI: 10.1007/978-3-642-10853-2_8,

1 Introduction

Currently, the most advanced techniques to evaluate molecular events in vivo come from nuclear medicine. Above all, PET (positron emission tomography) allows the quantification of different metabolic functions in organs and tissues and it is clinically widely used both for diagnostics and assessing therapy response in oncology, cardiology, and neurology.

Recently, the PET technology was introduced in the preclinical field since new small animal PET tomographs were implemented. This was possible thanks to new technologies (Wang et al. 2006) that are meant to enhance as much as possible the spatial resolution, therefore becoming appropriate for the evaluation of small-sized animals as rodents (Cherry 2006; Lewisa et al. 2002).

As for the clinical PET, in the preclinical field the PET imaging is addressed to the macroscopic visualisation of cellular processes by means of positron emitter radiolabelled compounds. This can be done with unspecific compounds that highlight general metabolic processes within the cells (e.g. ^{18}F-FDG, ^{11}C-Methionine etc.), with specific compounds (among which the receptor-tracers are the most commonly employed), or with the reporter-gene reporter-probe technique for cell tracking (Yaghoubi et al. 2006; Sossi and Ruth 2005).

The main advantage of microPET over the standard way of performing preclinical experiments (mainly based on the sacrifice of the animal) is the possibility to longitudinally follow the development of the disease (or the response to a specific new therapy) over time and in the same subject, significantly reducing the number of animals employed and increasing the reliability of the results. The high penetration power of the gamma rays created from the annihilation associated to the limited thickness of the rodents body allow a precise quantitation of the uptake even in deep anatomical structures (e.g., abdominal organs) and makes the microPET technology the most accurate tool to observe deeply located events. Furthermore, the microPET technology allows the detection of very low concentrations of tracers (picomolar order of magnitude), leading to an unequalled sensitivity in the visualisation and quantitative measurement of molecular processes (Sossi and Ruth 2005).

Another very interesting characteristic of the preclinical PET imaging is summarised in the word "translational". By employing the same technology in an experimental setting and in the clinical practice (in this case the PET imaging), in fact, the step between preclinical science and clinical applications in human patients becomes shorter and faster, reducing the overall time to effectively verify the clinical utility of the new approach. The most significant example in this field is the in vivo testing of new radiolabelled compounds meant to increase the specificity of the PET imaging for a specific disease. The creation of animal models of human diseases to test new compounds in vivo allows to avoid the translation into the clinical situation of those molecular imaging probes which do not bind selectively and with high affinity to the pathophysiological target molecules.

The translational applicability of this technique, the possibility to accurately quantify (in terms of time-activity curves, target to background ratio or standardised uptake ratio) (Myers and Hume 2002), the improved spatial resolution (that reaches 1 mm), the high sensitivity, the possibility to use targeted probes increasing the specificity of the metabolic information obtained from the scan, and the repeatability of the procedure on the same animal (a relatively limited dose is delivered to the animal for each scan) are features that make the microPET one of the most appreciated oncoming imaging technologies in the preclinical scenario, despite its relatively high costs related to the need of a cyclotron-based radiopharmacy.

2 Small Animal PET

2.1 General Aspects

Positron emission tomography (PET) is a nuclear medicine imaging technique which produces a three-dimensional image or picture of molecular processes in the body. The system detects pairs of gamma rays emitted indirectly by a positron-emitting radionuclide (tracer), which is introduced into the body on a biologically active molecule. Images of tracer concentration in three-dimensional space within the body are then reconstructed by computer analysis. In modern scanners, this reconstruction is often accomplished with the aid of a CT X-ray scan performed during the same session, in the same machine.

If the biologically active molecule chosen for PET is ^{18}F-FDG, an analogue of glucose, the concentrations of the tracer imaged yield quantitative data on tissue metabolic activity, in terms of regional glucose uptake. Although use of this tracer results in the most common type of PET scan, other tracer molecules are used in PET to image the tissue concentration of many other types of molecules of interest.

To conduct the scan, a short-lived radioactive tracer isotope is injected into the living subject (usually into blood circulation) (Fig. 1) (Fueger et al. 2006). The tracer is chemically incorporated into a biologically active molecule. There is a waiting period while the active molecule becomes concentrated in tissues of interest; then the research subject is placed in the imaging scanner. The molecule most commonly used for this purpose is fluor-18-fluorodeoxyglucose (^{18}F-FDG), a sugar, for which the waiting period is typically one hour. During the scan a record of tissue concentration is made as the tracer decays.

As the radioisotope undergoes positron emission decay (also known as positive beta decay), it emits a positron, an antiparticle of the electron with opposite charge. After travelling up to a few millimetres the positron encounters an electron. The encounter annihilates them both, producing a pair of annihilation (gamma) photons moving in opposite directions. These are detected when they reach a scintillator in the scanning device, creating a burst of light which is detected by photomultiplier tubes or silicon avalanche photodiodes. The technique

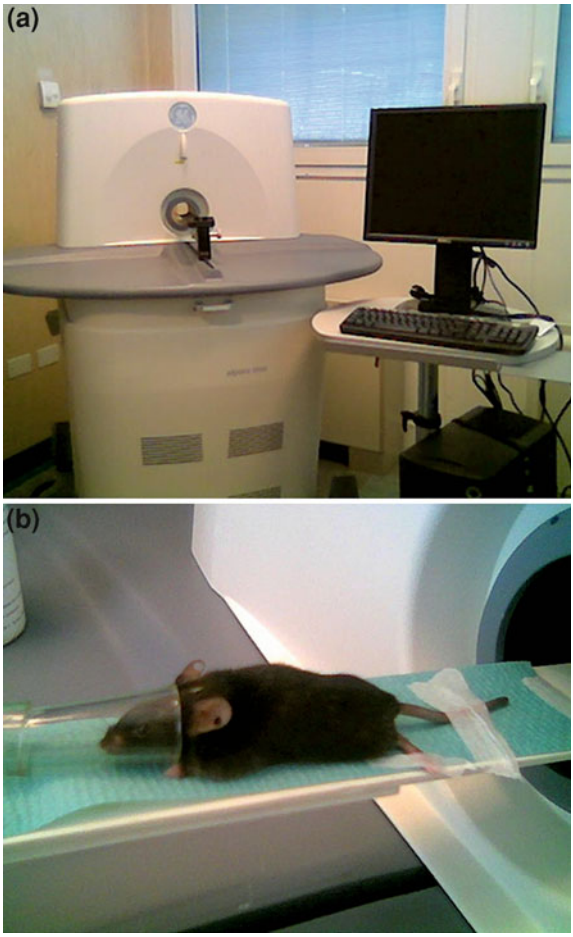

Fig. 1 **a** Small animal PET tomograph. **b** An animal model of cancer during gas anaesthesia on the scanner bed

depends on simultaneous or coincident detection of the pair of photons moving in approximately opposite direction (it would be exactly opposite in their centre of mass frame, but the scanner has no way to know this, and so has a built-in slight direction-error tolerance). Photons that do not arrive in temporal "pairs" (i.e., within a timing window of few nanoseconds) are ignored.

Radionuclides used in PET scanning are typically isotopes with short half-lives such as carbon-11 ($\sim$20 min), nitrogen-13 ($\sim$10 min), oxygen-15 ($\sim$2 min), and fluorine-18 ($\sim$110 min). These radionuclides are incorporated either into compounds normally used by the body such as glucose (or glucose analogues), water or ammonia, or into molecules that bind to receptors or other sites of drug action. Such labelled compounds are known as radiotracers. It is important to recognise that PET technology can be used to trace the biologic pathway of any compound in living organisms, provided it can be radiolabelled with a PET isotope. Thus, the specific processes that can be probed with PET are virtually limitless, and radiotracers for

new target molecules and processes are being synthesised all the time. Due to the short half-lives of most radioisotopes, the radiotracers must be produced using a cyclotron and a radiochemistry laboratory that are in close proximity to the PET imaging facility. The half-life of fluorine-18 is long enough such that fluorine-18-labelled radiotracers can be manufactured commercially at an offsite location.

2.2 Small Animal PET

In the literature, the vast majority of studies employing a small animal PET scanner are not based on the comparison between PET results and other preclinical imaging procedures but take into consideration histochemical analysis or autoradiography to verify imaging results. This is mainly due to the high costs of the scanners that make it very difficult to access a multiple modality technology. In the future this approach will change, and more and more complementary imaging techniques will be employed for evaluating the same animal model.

Small animal PET allows the non-invasive measurement of a range of tumour-relevant parameters at both the cellular and the molecular level that can be observed longitudinally over time. Studies to evaluate tumour response to a therapeutic intervention can achieve statistical significance using smaller groups of animals, as tumour cell physiology and tumour burden can be accurately determined pre- and post-therapy without assumptions.

Usually, the small animal PET imaging can be used for predicting tumoural cell engraftment (Fueger et al. 2006; Apisarnthanarax et al. 2006; Su et al. 2006; Hsueh et al. 2006; Hoekstra et al. 2000) in xenograft animal models, for assessing new therapies response in vivo, for the biological profiling of tumours by combining different tracers, for observing in vivo the metabolic behaviour of a tumour model over time, and for testing the accuracy of new PET compounds that eventually will be introduced into clinical practice.

The most widely employed PET imaging probe is ^{18}F-labelled glucose, which achieves tumour-specific accumulation on the basis that tumour cells have a higher rate of glucose uptake and metabolism (glycolysis) than normal tissues. ^{18}F-FDG is basically used in oncology to predict cancer cell engraftment (Nanni et al. 2007) and to measure the response to therapy. ^{18}F-FLT and its analogues (like ^{18}F-FMAU) are another family of compounds that are widely used in preclinical PET because they demonstrate the proliferative index of tumour masses with high accuracy, which is far higher in animal models than in patients (Sossi and Ruth 2005) (Fig. 2). ^{11}C-choline is a compound demonstrating the cell membrane proliferative activity, while ^{11}C-methionine highlights the rate of protein synthesis within the cells since it is an amino acid analogue.

Another small animal PET diagnostic method is the reporter-gene reporter-probe mechanism (HSV1—^{18}F-FHBG is the most validated) that allows the detection of genetically labelled viable cells injected into a living animal over a long time in vivo. This is particularly useful for tracking stem cells used for experimental and innovative regenerative therapies (Yaghoubi et al. 2006).

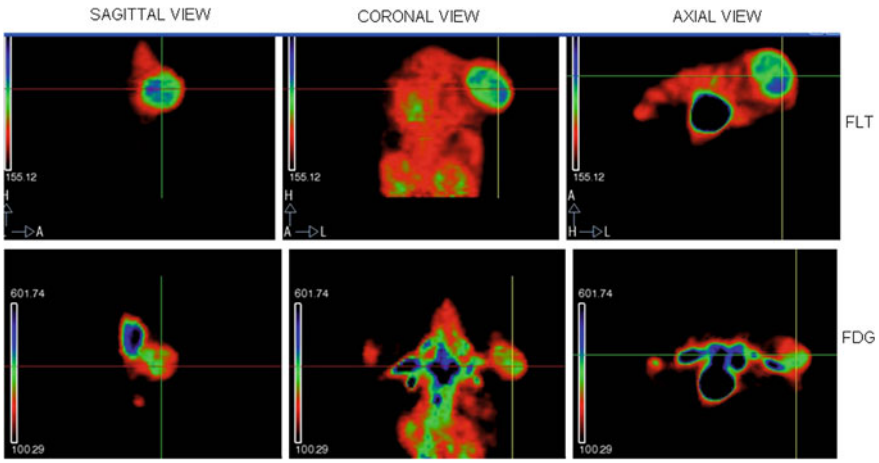

Fig. 2 Subcutaneous xenograft animal model of gastrointestinal stromal tumour evaluated with FLT and FDG PET. FLT images show the quote of proliferating cells while FDG images show the amount of glucose metabolism within the mass (reflecting the degree of malignancy)

Many other PET probes have been developed and are under development to obtain tumour specificity via a variety of tumour-specific mechanisms. The development of targeted radiolabelled ligands has further enabled PET to image many aspects of tumour biology in vivo. Radiolabelled annexin V, RDG peptide, VEGF, and $\alpha_v\beta_3$ integrin, for example, have been successfully tested in tumour models as well as in models of cardiac infarction, respectively, demonstrating apoptosis and perfusion (Cai et al. 2006; Liu 2006; Cauchon et al. 2007; Dobrucki and Sinusas 2005; Bauwens et al. 2011; Sherif et al. 2012; Cheng et al. 2011). The pharmacokinetics and pharmacodynamics of radiolabelled anticancer therapeutics can, in principle, also be monitored by these methods, thereby leading to rapid improvements in drug scheduling or design.

Finally, the effects of receptor therapies (e.g., inhibitors of androgen or oestrogen receptors or of epithelial growth factor receptor) can theoretically be predicted, thanks to the in vivo demonstration of the receptor after injection of the radiolabelled ligand (Myers and Hume 2002).

The literature includes a wide number of PET radiolabelled compounds for preclinical evaluation of specific molecular events, and it would be very difficult to provide a complete list of all the proposed compounds for oncological studies in the past decade.

2.3 Small Animal CT and Small Animal PET

The small animal CT can be used as a supporting method for small animal PET basically for three reasons. First of all it allows, as in the clinical setting, the correct anatomical localisation of PET findings. This is of particular interest in the

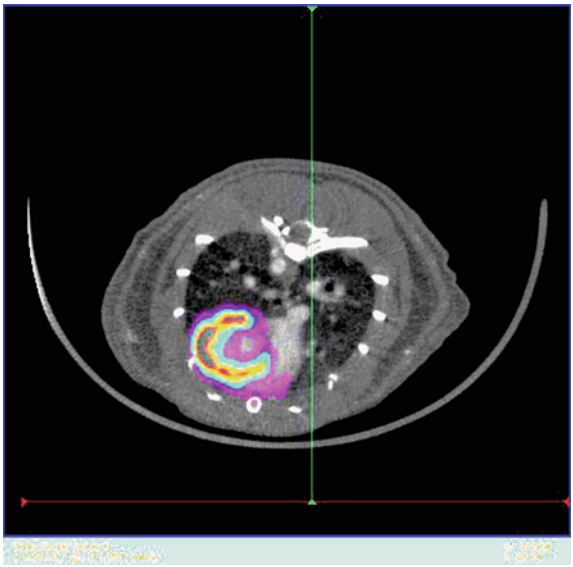

Fig. 3 Axial view of the fusion between FDG small animal PET and vascular contrast CT, showing the left ventricle of the heart

field of small animal imaging, because the use of experimental and very specific tracers prevents the PET from delineation of the animal shape. So, the PET image sometimes represents just a hot spot, whose anatomical localisation is impossible in absence of an anatomical reference (Fig. 3).

Second, the CT image can be used as an attenuation correction map, exactly as for clinical patients. Actually this is not of much interest, since the animal body is very small and therefore highly energetic photons are subjected to a negligible attenuation, but it can be important when studying bigger animals like primates to achieve a correct quantification of PET tracer uptake.

Last, but not the least, CT images can be very useful for integrating the metabolic results obtained by the PET. The CT can be used, for example, to exactly measure the organ sizes or the tumour diameters, and these parameters can be noninvasively monitored over time. The CT provides a density map and can be very useful to diagnose, for example, the onset of necrosis, of small liver nodules, of ascites, and so on. However, the bigger contribution of small animal CT is in the field of bone structure evaluation (osteoporosis, osteomyelitis, and fractures) and lung evaluation.

Recently, the technological development led to the possibility to acquire CT images with cardiac gating and respiratory gating. While the respiratory gating is aimed just to the improvement of spatial resolution at the base of the animal lungs, the cardiac gating has much more scientific importance. In fact, it can be used as an alternative method to measure the ejection fraction for cardiac studies, also because it is possible to intravenously inject vascular contrast agents helping in the visual differentiation between the ventricular wall and the ventricular cavity. These data can be combined with all the PET metabolic results that have been already explained in the previous paragraphs.

Most of the published studies regarding the small animal PET-CT imaging are performed by using two separate scanners. This is possibly due to the introduction of multimodality beds on the market that can be shifted from one scanner to the other with the same subject on. In this way the position of the experimental animal does not change (or at least is subjected only to minimal variations) and the two image sets (usually in DICOM format) can be subsequently co-registered with specific software.

It is important to point out that, to co-register a PET and a CT image, it is necessary to have at least three reference points, aimed at guaranteeing a slice by slice correct alignment. These reference points must be external to the animal, radioactive for PET imaging, radio-opaque for CT imaging, and must be positioned for example on the multimodality bed before starting the imaging session.

Despite, as explained, the acquisition image technique may be quite complicated in practice when two separate scanners are used, after a short training very high quality images can be obtained, especially if a sufficiently long anaesthesia is provided to the animal.

3 Conclusion

The preclinical functional imaging (in particular small animal PET) is a niche but an important field of preclinical basic research. It allows to observe the development of a specific disease on animal models in vivo, to highlight their molecular profile, to evaluate their response to new experimental therapies in vivo, and to test new radiolabelled compounds for the clinical PET imaging. In this way the step from bench to bedside may become shorter, accelerating the introduction of new therapies or imaging methods in the clinical practice.

References

Apisarnthanarax S, Alauddin MM, Mourtada F, Ariga H, Raju U, Mawlawi O, Han D, Bornmann WG, Ajani JA, Milas L, Gelovani JG, Chao KS (2006) Early detection of chemoradioresponse in esophageal carcinoma by 3-deoxy-3-3H-fluorothymidine using preclinical tumor models. Clin Cancer Res 12:4590–4597

Bauwens M, De Saint-Hubert M, Devos E, Deckers N, Reutelingsperger C, Mortelmans L, Himmelreich U, Mottaghy FM, Verbruggen A (2011) Site-specific ^{68}Ga-labeled annexin A5 as a PET imaging agent for apoptosis. Nucl Med Biol 38:381–392

Cai W, Chen K, Mohamedali KA, Cao Q, Gambhir SS, Rosenblu MG, Chen X (2006) PET of vascular endothelial growth factor receptor expression. J Nucl Med 47:2048–2056

Cauchon N, Langlois R, Rousseau JA, Tessier G, Cadorette J, Lecomte R, Hunting DJ, Pavan RA, Zeisler SK, van Lier JE (2007) PET imaging of apoptosis with ^{64}Cu-labeled streptavidin following pretargeting of phosphatidylserine with biotinylated annexin-V. Eur J Nucl Med Mol Imaging 34:247–258

Cheng C, Pan L, Dimitrakopoulou-Strauss A, Schafer M, Wangler C, Wangler B, Haberkorn U, Strauss LG (2011) Comparison between ^{68}Ga-bombesin (^{68}Ga-BZH3) and the cRGD tetramer ^{68}Ga-RGD$_4$ studies in an experimental nude rat model with a neuroendocrine pancreatic tumor cell line. EJNMMI Res 1:34

Cherry SR (2006) The 2006 Henry N. Wagner lecture: of mice and men (and Positrons)—advances in PET imaging technology. J Nucl Med 47:1735–1745

Dobrucki LW, Sinusas AJ (2005) Molecular imaging: a new approach to nuclear cardiology. Q J Nucl Med Mol Imaging 49:106–115

Fueger BJ, Czernin J, Hildebrandt I, Tran C, Halpern BS, Stout D, Phelps ME, Weber WA (2006) Impact of animal handling on the results of ^{18}F-FDG PET studies in mice. J Nucl Med 47:999–1006

Hoekstra CJ, Paglianiti I, Hoekstra OS, Smit EF, Postmus PE, Teule GJJ, Lammertsma AA (2000) Monitoring response to therapy in cancer using [^{18}F]-2-fluoro-2-deoxy-D-glucose and positron emission tomography: an overview of different analytical methods. Eur J Nucl Med 27:731–743

Hsueh WA, Kesner AL, Gangloff A, Pegram MD, Beryt M, Czernin J, Phelps ME, Silverman DHS (2006) Predicting chemotherapy response to paclitaxel with ^{18}F-fluoropaclitaxel and PET. J Nucl Med 47:1995–1999

Lewisa JS, Achilefub S, Garbowc JR, Laforesta R, Welch MJ (2002) Small animal imaging: current technology and perspectives for oncological imaging. Eur J Cancer 38:2173–2188

Liu S (2006) Radiolabeled multimeric cyclic RGD peptides as integrin $\alpha_v\beta_3$ targeted radiotracers for tumor imaging. Mol Pharm 3:472–487

Myers R, Hume S (2002) Small animal PET. Eur Neuropsychopharmacol 12:545–555

Nanni C, Di Leo K, Tonelli R, Pettinato C, Rubello D, Spinelli A, Trespidi S, Ambrosini V, Castellucci P, Farsad M, Franchi R, Pession A, Fanti S (2007) FDG small animal PET permits early detection of malignant cells in a xenograft murine model. Eur J Nucl Med Mol Imaging 34:755–762

Sherif HM, Saraste A, Nekolla SG, Weidl E, Reder S, Tapfer A, Rudelius M, Higuchi T, Botnar RM, Wester HJ, Schwaiger M (2012) Molecular imaging of early $\alpha_v\beta_3$ integrin expression predicts long-term left-ventricle remodeling after myocardial infarction in rats. J Nucl Med 53:318–323

Sossi V, Ruth TJ (2005) Micropet imaging: in vivo biochemistry in small animals. J Neural Transm 112:319–330

Su H, Bodenstein C, Dumont RA, Seimbille Y, Dubinett S, Phelps ME, Herschman H, Czernin J, Weber W (2006) Monitoring tumor glucose utilization by positron emission tomography for the prediction of treatment response to epidermal growth factor receptor kinase inhibitors. Clin Cancer Res 12:5659–5667

Yaghoubi SS, Couto MA, Chen CC, Polavaram L, Cui G, Sen L, Gambhir SS (2006) Preclinical safety evaluation of ^{18}F-FHBG: a PET reporter probe for imaging herpes simplex virus type 1 thymidine kinase (HSV1-tk) or mutant HSV1-sr39tk's expression. J Nucl Med 47:706–715

Wang Y, Seidel J, Tsui BM, Vaquero JJ, Pomper MG (2006) Performance evaluation of the GE healthcare eXplore VISTA dual-ring small-animal PET scanner. J Nucl Med 47:1891–1900

Preclinical Molecular Imaging Using PET and MRI

Gunter Wolf and Nasreddin Abolmaali

Abstract

Molecular imaging fundamentally changes the way we look at cancer. Imaging paradigms are now shifting away from classical morphological measures towards the assessment of functional, metabolic, cellular, and molecular information in vivo. Interdisciplinary driven developments of imaging methodology and probe molecules utilizing animal models of human cancers have enhanced our ability to non-invasively characterize neoplastic tissue and follow anti-cancer treatments. Preclinical molecular imaging offers a whole palette of excellent methodology to choose from. We will focus on positron emission tomography (PET) and magnetic resonance imaging (MRI) techniques, since they provide excellent and complementary molecular imaging capabilities and bear high potential for clinical translation. Prerequisites and consequences of using animal models as surrogates of human cancers in preclinical molecular

G. Wolf
Clinical Chemistry, University Hospital Carl Gustav Carus
at the Technische Universität Dresden, Fetscherstr. 74,
01307 Dresden, Germany
e-mail: Gunter.Wolf@uniklinikum-dresden.de

G. Wolf · N. Abolmaali (✉)
OncoRay National Center of Radiation Research in Oncology,
Biological and Molecular Imaging, Medical Faculty Carl Gustav Carus
at the Technische Universität Dresden, Fetscherstr. 74,
01307 Dresden, Germany
e-mail: Nasreddin.Abolmaali@uniklinikum-dresden.de

N. Abolmaali
Radiology, University Hospital Carl Gustav Carus at the Technische Universität Dresden,
Fetscherstr. 74, 01307 Dresden, Germany

O. Schober and B. Riemann (eds.), *Molecular Imaging in Oncology*,
Recent Results in Cancer Research 187, DOI: 10.1007/978-3-642-10853-2_9,

imaging are outlined. We present physical principles, values and limitations of PET and MRI as molecular imaging modalities and comment on their high potential to non-invasively assess information on hypoxia, angiogenesis, apoptosis, gene expression, metabolism, and cell trafficking in preclinical cancer research.

Contents

1 Introduction

Non-invasive imaging techniques are already for some time being utilized as biomarker of disease in oncology, mainly involved in (i) pretreatment tissue characterization and monitoring progression, (ii) therapy planning and (iii) therapy response evaluation and follow-up. Traditionally, imaging has been generally based on morphological criteria of tumor size and location, which are likely not to be influenced in the early, i.e., interesting and potentially main relevant, phases of modern cancer therapies. However, current advances in molecular cancer biology and imaging technology shift imaging paradigms away from solely morphological imaging towards molecular imaging (MI)—the direct or indirect assessment of spatial and/or temporal distribution of physiologic, metabolic and cellular or molecular processes within tissues in vivo (Thakur and Lentle 2005). Besides detection, (differential) diagnosis and staging of neoplastic tissue during disease progression, tissue characterization with MI techniques also enables assessment of

therapeutically relevant biological properties such as metabolism, proliferation, hypoxia, angiogenesis, apoptosis, and gene and receptor expression of tumors. Such features are related to important hallmarks of cancer (Hanahan and Weinberg 2000) and themselves targets for modern treatment strategies. Thus, thorough evaluation of biological tumor characteristics may impact on currently morphology-based treatment planning and help to improve future therapeutical strategies (Kauczor et al. 2006). In this way, it is of great importance to assess changes of cancer biology in response to therapy early during the course of treatment (before apparent changes in morphological imaging become visible) to be able to timely adjust potentially ineffective treatment concepts that may be expensive and largely impacting on patients quality of life. Consequently, MI will likely contribute to the realization of concepts of modern individualized medicine.

Animal models of cancer have ever played an important role in oncological research. Current and future MI developments have been and will be almost exclusively tested and optimized in preclinical studies. However, from its artificial nature, experimental tumor models do often only sparsely resemble patient requirements and are currently in discussion. Nevertheless, with a careful selection of appropriate experimental tumor models according to research purposes, it will be possible to evaluate ongoing methodological developments and to validate underlying imaging principles using animal models.

Investigation of physiologic, metabolic and cellular or molecular processes in vivo in experimental tumor models can be performed non-invasively with a variety of small animal imaging modalities, which all have their inherent strengths and weaknesses. We will focus on the two major imaging modalities positron emission tomography (PET) and magnetic resonance imaging (MRI) and spectroscopy (MRS) that are widely accessible and clinically well established, thus, allowing fast translation of experimental imaging findings into clinics.

In this chapter, we will comment on the use of experimental animal models of cancer and associated challenges for imaging. We introduce basic principles, values and limitations of PET, and MRI/MRS as MI modalities. Finally, we present applications in preclinical cancer research, indicating the high potential of MI to non-invasively assess information on hypoxia, angiogenesis, apoptosis, gene expression, metabolism, and cell migration in tumors.

2 Experimental Models of Cancer

Oncological studies in human patients confront strict ethical regulations and are time and resource intensive with often shortages of sound scientific evidence and in vitro cell culture and biochemical assays usually may not adequately reflect in vivo conditions. The use of clinically relevant animal tumor models as workable surrogates for human patients represent an important step in translational research bridging the gap between cell laboratory and clinical application. In the European Union, approximately 99 % of laboratory animals used in 2008 in the field of cancer

research were mice (94 %) and rats (5 %) (European Commission 2010). Consequently, a variety of animal tumor models in mice and rats exist in experimental oncology (Croft 2002; Herzig and Christofori 2002; Kelland 2004; Ostrand-Rosenberg 2004; Sharpless and Depinho 2006; Talmadge et al. 2007; Ni et al. 2009). They possess rather widely differing features such as growth pattern (diffuse over body vs. single solid lesion), dignity (less differentiated malignant tumor with infiltrating growth and raised metastatic potential vs. well-differentiated benign tumor with expanding growth and encapsulation), vascularity (highly vascularized vs. avascular), and incidence of spontaneous necrosis. Primary tumors (malignant or benign) can be spontaneously formed or artificially induced by chemicals, ionizing radiation and genetic engineering, whereas secondary tumors (only malignant) can be created as allografts (from the same species) or xenografts (across different species; most often from human to animal) by cell suspension inoculation or tissue piece implantation. Xenograft tumor models may successfully be established only in immune-suppressed animals. Tumors may grow ectopically (in an unusual place), such as most subcutaneous tumor models, or orthotopically (in the usual position), like lymphoma in spleen.

However, available animal models are discussed rather controversial for their capabilities in efficient cancer therapy development (Schuh 2004; Suggitt and Bibby 2005; Schein and Scheffler 2006). Although ectopic human tumor xenograft models of non-small cell lung and ovarian cancers may predict phase II clinical trial performance of cancer drugs, they have not yet proven to be general predictors of clinical outcome (Voskoglou-Nomikos et al. 2003). This might be due to various variables impacting on outcome of therapeutic experimental models: site of implantation, growth properties of xenograft and size at treatment initiation, agent formulation, scheduling, route of administration and dose, and the selected endpoint for assessing activity. In studies of anti-angiogenic or anti-vascular and immunotherapeutical strategies the targeted structures of interest in xenografts are predominantly of host origin. They are also less useful for assessment of anti-metastatic strategies since subcutaneously implanted tumors generally do not metastasize. Animal models using orthotopically implanted tumors may be more appropriate (Kubota 1994; Suggitt and Bibby 2005; Talmadge et al. 2007). Due to these shortcomings, there has been much interest in genetically engineered models, in which genes of interest can be selectively overexpressed, additionally inserted or deleted in all cells or only in a specific tissue compartment and/or developmental stage (Sharpless and Depinho 2006; Raman et al. 2007; Talmadge et al. 2007). Such sophisticated models are able to produce orthotopic primary tumors that closely mimic human cancer. However, the use of artificial promoters which drive transgene expression can influence affected cell type, vary expression based on genetic background and decrease cellular heterogeneity, which, in turn, can affect tumor progression and metastasis (Talmadge et al. 2007).

Although the ideal experimental cancer model that can reliably predict the extent of clinical efficacy has not yet been identified, selection of models suiting the desired research purpose may finally be achieved by thoroughly taking into account the specialties and features of present tumor models. If particular abnormalities of

human cancer are sufficiently represented, experimental tumor models can still be valuable for in vivo proof-of-principle of new therapeutical (target identification, optimization of pharmaceutically tractable molecules, selection of lead candidates for clinical evaluation, optimization of scheduling and combination with other drugs to guide clinical development, study of acquired drug resistance, and its circumvention), and imaging concepts (tracer and contrast agent development, visualization and quantification of biological tumor properties, validation of non-invasive cancer biomarkers). For many applications, it will be critical to incorporate pharmacological and toxicological considerations as well as mechanistic concepts of tumor induction, progression, and metastasis. Some models may be even more suited for diagnostic rather than therapeutic assessments. Molecular imaging can promote development of improved animal models and anticancer agents by providing a time- and labor-efficient way of non-invasively evaluating effectiveness of novel treatment strategies to identify most promising candidates for clinical application. In contrast to markers circulating in blood or tissue sampling, non-invasive imaging biomarkers may more efficiently sample tumor heterogeneity, and thus impact on proposed treatment scheme. Conversely, new insights in cancer biology may also stimulate the development of innovative imaging approaches.

3 Small Animal Molecular Imaging

Imaging experimental models of cancer in small animals requires special consideration of their altered morphology and physiology with respect to humans. Selected morphological and physiological characteristics of mice, rats, and humans are summarized in Table 1 (Wolf and Abolmaali 2009). In order to obtain comparable resolution—related to body size—as in human imaging, voxel dimension need to be scaled down in small animal imaging by a factor of approximately 10 (in every spatial direction), which will result in 1,000-fold less signal. This has led to the development of dedicated scanners, which are particularly designed to meet small animal imaging needs. With current advances in clinical scanner and detector technology small animal imaging can successfully be performed using clinical scanners too (Brockmann et al. 2007; Wolf and Abolmaali 2009). Dedicated small animal scanners typically present better imaging performance, but their clinical counterparts can compete in many applications and generally warrant a more direct and fast translatability of experimental imaging methods into clinics. Nevertheless, applications with ultra-high resolution requirements may be restricted to dedicated scanners exclusively.

Most widely used modalities in molecular imaging include PET and MRI/MRS, which are clinically well established, and optical imaging (Graves et al. 2004; Shah and Weissleder 2005), which is very powerful in experimental molecular imaging, but clinically less relevant. Other modalities like ultrasound (Liang and Blomley 2003; Kiessling et al. 2009) and computed tomography (Popovtzer et al. 2008; Wyss et al. 2009) are progressively developing MI capabilities. A summary

Table 1 Selected characteristic morphological and physiological values for mouse, rat and human [reprinted with permission of Informa Healthcare from (Wolf and Abolmaali 2009)]

	Mouse	Rat	Human
Body mass (g)	20–40	250–400	70,000
Blood volume (ml)	1.5–3.2	15–28	6,000–7,000
Brain size (mm)	6	10	105
Heart mass (g)	0.1	1	300
Heart rate (min^{-1})	630	330–480	60–80
Breathing rate (min^{-1})	163	66–114	12–18

of these imaging modalities and their key physical performance is given in Table 2 (Cassidy and Radda 2005; Shah and Weissleder 2005; Koo et al. 2006; Culver et al. 2008; Gore et al. 2009; Wolf and Abolmaali 2009). In this overview we will focus primarily on PET and MRI/MRS, since these techniques show good MI capability combined with excellent clinical translatability.

4 Positron Emission Tomography

PET relies on administration of exogenous probe molecules labeled with radioisotopes (tracers) that emit positrons (β^+ radiation) over time. Each positron undergoes an annihilation reaction with a nearby electron in tissue, which results in two high energy photons (511 keV γ-rays) with opposite propagation direction. These γ-rays are detected in coincidence and converted into visible light upon hitting the detector, which is subsequently registered and processed to form a tomographic representation of the subject. Typical positron-emitting isotopes used to modify biologically active molecules for PET possess half-lives of minutes to days, e.g., oxygen (^{15}O): 2 min, carbon (^{11}C): 20.4 min, gallium (^{68}Ga): 68.3 min, fluorine (^{18}F): 110 min, copper (^{64}Cu): 12.7 h, iodine (^{124}I): 4.2 d. The contrast of PET images largely depends on different tracer uptake and wash-out kinetics of tissue.

Small animal PET imaging allows quantitative measurement of numerous biological processes in vivo (Aboagye 2005; Ambrosini et al. 2009). It is one of the most sensitive imaging techniques and can detect tracer amounts in nano- to picomolar concentrations, irrespective of tissue depth. Depending on cancer type and tracer accumulation in surrounding tissues, typically several million cells in relatively close proximity must accumulate tracer for a PET scanner to visualize them against background (Ruf et al. 2004; Fischer et al. 2006). Due to extremely low tracer amount, biological processes can be imaged without disturbance on the underlying physiological principles and kinetics. Radiopharmaceuticals can be designed to specifically interact with molecular targets within defined in vivo biochemical pathways and processes (Aboagye 2005; Ambrosini et al. 2009),

Table 2 Modalities for preclinical in vivo (molecular) imaging and key physical performance parameters of experimental and clinical scanners

Imaging technique	Physical basis	Spatial resolution[a]	Time resolution	Depth	Sensitivity[b]	MI capability[c]	Clinical translatability[c]
Positron emission tomography (PET)	High-energy γ-rays		s–min	Unlimited	nM–pM	+++	+++
Experimental		1–2 mm					
Clinical		5–8 mm					
Magnetic resonance imaging (MRI)	Radio-frequency waves		s–min	Unlimited	μM–mM[e]	++	+++
Experimental		> 50 μm[d]					
Clinical		> 100–200 μm					
Magnetic resonance spectroscopy (MRS)			min	Unlimited	μM–mM[e]	++	++
Experimental		1 mm					
Clinical		10 mm					
Computed tomography	X-rays		s	Unlimited	cM–mM	+	++
Experimental		> 50 μm[f]					
Clinical		> 400–600 μm					
Ultrasound with micro bubbles	High-frequency sound	50–500 μm	ms	mm–cm	1 bubble	+	+
Optical imaging[g]	Visible and near-infrared light	μm–mm	s–min	μm–cm	mM–fM	+++	+

[a] typical isotropic voxel sizes that can be achieved

[b] detectable concentration range of molecular probe: *fM* femtomolar (10^{-15} mol/l); *pM* picomolar (10^{-12} mol/l); *nM* nanomolar (10^{-9} mol/l); μ*M* micromolar (10^{-6} mol/l); *mM* millimolar (10^{-3} mol/l); *cM* centimolar (10^{-2} mol/l)

[c] score: +++ excellent, ++ good, + moderate

[d] may be much less with magnetic resonance microscopy (> 2 μm)

[e] may range down to nM-pM ranges with appropriate signal amplification strategies

[f] much lower resolution can be achieved with higher X-ray doses, which is usually not suitable for in vivo imaging

[g] Due to variety of optical methods (e.g., optical tomography, near-infrared fluorescence imaging, bioluminescence imaging) spatial resolution, penetration depth, and sensitivity present large ranges

including glucose, amino acid, nucleic acid and lipid metabolism, hypoxia, angiogenesis, apoptosis, gene expression, and even cell tracking. PET is clinically used in tumor diagnosis and staging, therapy response and prognostic evaluation, treatment planning, and anti-cancer drug development (Saleem et al. 2006).

PET is a relatively expensive and technically demanding imaging approach. Typically, a local cyclotron and radiochemical synthesis unit to generate positron-emitting isotopes and subsequently produce biological tracers is required, especially for short-lived isotopes. However, generators for certain isotopes such as gallium (^{68}Ga) (Fani et al. 2008) and limited number of commercial radiolabeling kits are available. Another limitation of PET is its inherently low spatial resolution, and thus little anatomical information. This is due to several factors including (i) positron range, i.e., distance traveled by positron before annihilation with electron, (ii) non-colinearity of annihilation photons, i.e., deviation from exactly opposite (180°) photon emission, (iii) detector geometry and scatter, and (iv) statistical data quality. In small animal PET scanners, these factors will probably restrict maximum resolution for low-energy positron emitters like ^{11}C and ^{18}F to 0.4–1 mm (Cherry and Gambhir 2001; Chatziioannou 2002; Cherry 2006), whereas in clinical whole-body PET systems highest theoretically attainable resolution will most likely be on the order of 2 mm (Cherry 2006). Typical real resolution of current clinical whole-body PET scanners ranges from 5 to 8 mm. PET is, therefore, often combined with an imaging modality of superior anatomical depiction (e.g., computed tomography or more recently MRI). Furthermore, PET is unable to distinguish between the chemical species attached to the radionuclide, which means that, for example, administered radiotracer and metabolites cannot easily be differentiated without further investigations in blood. Another limitation of PET is ionizing radiation to the subject, which especially for repeated measurements of small animals in therapeutical follow-up studies might not be negligible. Depending on the organ and its function in tracer biodistribution, absorbed dose estimates calculated from Monte Carlo simulations of an anatomically defined mouse phantom may range between 19 and 4,000 mGy after injection of 7.4 MBq of activity (Taschereau and Chatziioannou 2007). Although the absorbed radiation doses calculated are lower than the lethal doses of about 7 Gy reported for mice and rats (Hall and Giaccia 2006), they are more than 10 times higher than for human PET studies, possibly limiting repeated examinations.

5 Magnetic Resonance Imaging and Spectroscopy

Magnetic resonance (MR) techniques rely on the behavior of nuclei in strong magnetic fields under the influence of radiofrequency (RF) waves. To be actively exploited with MR, isotopes must possess a nuclear spin (e.g., hydrogen (^{1}H), carbon (^{13}C), fluorine (^{19}F), sodium (^{23}Na), phosphorus (^{31}P)). In living subjects, the protons (^{1}H) of water and lipids are the primary signal source, whereas other isotopes are less abundant, and thus more difficult to assess. In a magnetic field, protons act as little bar magnets. According to Boltzmann distribution they tend to orient themselves parallel (spin up) and anti-parallel (spin down) with respect to

the direction of the externally applied magnetic field, respectively, thereby building up a net equilibrium magnetization. Typically, the number of excess spins in energetically more favorable parallel alignment is in the order of 10 in one million at clinically relevant field strengths. Additionally, spins precess at a frequency proportional to magnetic field strength, which is known as Larmor frequency. Excitation of spins with a sequence of RF pulses at the Larmor frequency disturbs the thermal equilibrium spin distribution and temporarily promotes spins to the high-energy anti-parallel alignment. This tilts overall magnetization away from the static magnetic field direction; thus, decreasing longitudinal and increasing transverse magnetization components. Relaxation of excited spins to their thermal equilibrium state is governed by realignment with main magnetic field (B_0) and recovery of longitudinal magnetization (T_1 relaxation) as well as dephasing due to local and global field inhomogeneities and decay of transverse magnetization (T_2^* relaxation). RF waves sent out during relaxation are detected with specialized coils and amplified to form the MR signal.

In MRI, spatial information of each voxel within the imaging volume is encoded in the signal by application of magnetic field gradients during and in between RF pulses and signal reception. From raw data an image is reconstructed using Fourier transformation. Since relaxation times differ among tissues, MRI can be predominantly weighted by proton density, T_1 or T_2^* relaxation time, depending on timing of RF pulse excitation, and signal detection. Additionally, sophisticated MR techniques enable the generation of contrast based on diffusion or perfusion of nuclei.

MRS utilizes the fact that spins resonate at slightly different frequencies (chemical shift) depending on different nuclear shielding by electrons due to molecular chemical environment. This is expressed in a spectrum of resonance lines stemming from endogenous as well as exogenous substances, thus enabling the investigation of molecular composition of tissues and metabolism of pharmaceuticals. The most commonly used nucleus in MRS is ^{1}H. It offers the best sensitivity and spatial resolution, but also necessitates the suppression of highly abundant water and lipid signals in order to detect metabolites. Other nuclei used in MRS comprise ^{19}F, ^{23}Na, ^{31}P, and ^{13}C. Especially, ^{19}F is nearly as sensitive as ^{1}H and has no endogenous physiological background, thus, offering straightforward molecular identification. The features of spatial resolution of MRI and spectral resolution of MRS can be combined in magnetic resonance spectroscopic imaging (MRSI), which is able to generate spatially resolved maps of tumor metabolic markers for cancer diagnosis, metabolic phenotyping, and characterization of tumor microenvironment (He et al. 2004). In rat tumors, MRSI could non-invasively follow the metabolism of hyperpolarized ^{13}C-labeled pyruvate into lactate and alanine (Golman et al. 2006).

MR techniques offer the advantages of not exposing subjects to ionizing radiation, thus enabling repeated measurements, high spatial and temporal resolution, and high imaging flexibility with various contrast mechanisms (e.g., T_1, T_2^*, proton density, diffusion, perfusion) for excellent tissue characterization. MR techniques, including imaging, functional MRI and spectroscopy, are able to assess

morphological, physiological, functional, and metabolic information in one session. However, MR is expensive and demands a rather high level of expertise. Due to safety considerations MR is not amenable for some subjects. Most inauspicious for molecular imaging with MRI is the inherently low sensitivity in the micro- to millimolar range as compared to PET. Therefore, it is essential to employ efficient signal amplification strategies.

5.1 Contrast Agents

Contrast agents (CAs) are continuously being developed and employed as signal amplifiers to overcome the inherently low sensitivity of MRI (Strijkers et al. 2007; Yan et al. 2007). CAs may be either (i) targeted to directly image molecular and cellular processes (MI in its strictest sense) (Artemov 2003; Morawski et al. 2005; Caruthers et al. 2006), (ii) activated to generate contrast only in response to changes in their physical environment to indirectly image underlying biological processes (De Leon-Rodriguez et al. 2009; Major and Meade 2009), or (iii) non-targeted to image surrogate biomarkers of function and physiology (MI in its broadest sense) (Knopp et al. 2001; Hylton 2006; O'Connor et al. 2007). Strategies to modify contrast in proton MRI are based on alteration of T_1 and T_2 relaxation times, proton density, and nuclear polarization, respectively. Alternatively, CAs based on non-proton nuclei like ^{19}F can be used to produce MR signal without physiological background.

T_1 contrast agents most commonly incorporate paramagnetic ions, e.g., gadolinium (Gd), manganese (Mn), and lead to positive signal enhancement in T_1-weighted imaging by locally increasing the longitudinal relaxation rate ($R_1 = 1/T_1$) of water protons. Sensitivity of commercially available Gd-based small molecules, e.g., Gd-DTPA (Magnevist®), Gd-DTPA-BMA (Omniscan®), Gd-DOTA (Dotarem®), is typically in the millimolar range (Strijkers et al. 2007), which precludes direct imaging of molecular receptors with typically nanomolar abundance. Nevertheless, they are extensively being used to assess functional and physiological biomarkers of cancer using dynamic contrast-enhanced MRI (Knopp et al. 2001; Hylton 2006; O'Connor et al. 2007). Unfortunately, commonly applied small molecule CAs are known to diffuse quickly from blood into extracellular space for both normal and pathologic tissues. This can be overcome with the use of macromolecular CAs (Preda et al. 2006), which cannot easily leak out of normal vasculature. The apparent threshold in effective molecular weight with no measurable leakage into normal tissue is between 194 and 323 kDa (Cyran et al. 2008). High sensitivity can be attained by exploiting macromolecules or nanocarriers (e.g., micelles, microemulsions, liposomes) containing hundreds to thousands of Gd entities (Morawski et al. 2004; Mulder et al. 2006; Aime et al. 2009; Gore et al. 2009). For the detection of vascular endothelial growth factor (VEGF) receptor with a small lysine-based dendron consisting of eight Gd-DOTA units conjugated to a

specific dimeric peptoid the in vitro detection limit was in the submicromolar range (790 nM) (De Leon-Rodriguez et al. 2009).

T_2^* contrast agents are usually iron oxide particles which typically result in signal loss in T_2^*-weighted images by dramatically increasing transverse relaxation rate ($R_2^* = 1/T_2^*$) due to induction of strong local susceptibility differences. Iron oxide particles are available with different magnetic properties and in various sizes, e.g., superparamagnetic iron oxide (SPIO) nanoparticles (50–150 nm), ultrasmall superparamagnetic iron oxide (USPIO) nanoparticles (20–30 nm), very small superparamagnetic iron oxide particles (VSOP; 7–10 nm), microparticles of iron oxide (MPIO; 0.35–1.6 μm), cross-linked iron oxide (CLIO) nanoparticles (30–50 nm), monocrystalline iron oxide nanoparticles (MION), magnetism-engineered iron oxide (MEIO) nanoparticles, and are usually coated with polymers or monomers that prevent aggregation and allow functionalization (Taupitz et al. 2003; Lee et al. 2009; Muja and Bulte 2009). They have been used as organ-specific contrast agent, for vascular characterization, tumor targeting, and cell labeling (Taupitz et al. 2003; Wu et al. 2004; Yan et al. 2007; Himmelreich and Dresselaers 2009; Muja and Bulte 2009). The detection threshold of iron oxide agents is suggested in the submicromolar range (Mahmood and Josephson 2005; Gore et al. 2009), but for SPIO-labeled cells even PET-comparable sensitivity in the pico- to femtomolar range was reported (Heyn et al. 2005).

Reduction of total water signal (proton density) can be achieved with chemical exchange saturation transfer (CEST) agents. This interesting and comparatively new CA class relies on diamagnetic (Ward et al. 2000) or paramagnetic (Zhang et al. 2003a; Woods et al. 2006) compounds with slowly exchanging protons, which possess a largely different resonance frequency than protons of the bulk water pool. Irradiation at the resonance frequency of exchangeable protons leads to a reduction of bulk water signal via saturation transfer due to chemical exchange of protons from CEST agent and water pool. Interestingly, CEST contrast can be turned on or off at will, since saturation transfer can only occur, if exchangeable protons are irradiated at the proper resonance frequency. The sensitivity of CEST agents is in the millimolar range for low molecular weight small molecules and can be enhanced to micromolar concentrations with macromolecular compounds (Aime et al. 2009; Gore et al. 2009). Liposome-trapped CEST (LIPOCEST) agents increase sensitivity even up to subnanomolar (90 pM) concentrations (Aime et al. 2005a). They can be designed to be sensitive to glucose concentration (Zhang et al. 2003b; Ren et al. 2008), lactate concentration (Aime et al. 2002c), enzymatic activity (Yoo et al. 2007; Chauvin et al. 2008), pH (Aime et al. 2002b), or temperature (Zhang et al. 2005; Li et al. 2008a). Additionally, the concept of CEST contrast can be extended to simultaneously detect two CEST agents (Ali et al. 2009b) or diamagnetic multi-label polypeptide CEST (DIACEST) agents (McMahon et al. 2008) at different resonance frequency in the same region. This has been demonstrated to work in phantoms (Aime et al. 2005b; McMahon et al. 2008), in vitro in labeled rat tumor hepatoma cells (Aime et al. 2005b), and in vivo in a mouse model of mammary carcinoma (Ali et al. 2009a). Thus, CEST agents bear a high potential for MI applications.

Thermal equilibrium of spin distribution (nuclear polarization) can be artificially changed in favor of energetically lower state by hyperpolarization techniques which results in huge signal enhancement (> 100000), thus enabling imaging with non-proton nuclei like ^{13}C (Golman et al. 2003) and ^{19}F (Kuhn et al. 2006). The half-life of hyperpolarization is limited by T_1 relaxation time. Hyperpolarized ^{13}C-labeled pyruvate and its metabolites lactate and alanine could be successfully imaged in vivo in rat tumors using MRSI (Golman et al. 2006).

An alternative to generate contrast in MRI is the utilization of nuclei other than ^{1}H. ^{19}F appears to be especially suited since it is nearly as sensitive as ^{1}H and lacks endogenous physiological background signal. Several fluorine-containing agents ranging from small molecules to nanoparticulate assemblies are used in ^{19}F MRI and MRS to derive information on various subjects including pH, tissue oxygenation and hypoxia, metabolism, and cellular imaging (Yu et al. 2005; Partlow et al. 2007). To obtain detectable signals sufficient amounts of fluorinated probe must be administered, but care must be given to avoid physiological perturbations or toxic side effects.

5.2 Dynamic Contrast-Enhanced MRI

Dynamic contrast-enhanced (DCE-) MRI serially monitors signal intensity after intravenous administration of CA using either T_2^*- or T_1-weighted sequences (Hylton 2006; O'Connor et al. 2007). On the one hand, T_2^*- or dynamic susceptibility-contrast (DSC-) MRI can be used within first few seconds after contrast bolus injection to observe the transient first-pass effects of contrast agent, i.e., initial rapid drop and fast subsequent recovery of signal intensity. On the other hand, T_1-weighted DCE-MRI is used to observe the extravasation of CA from vascular to interstitial space over several minutes. Pharmacokinetic modeling of dynamic signal change can provide useful hemodynamic parameters of tumor vasculature including tumor perfusion, vascular permeability, and blood volume.

Measurements of tumor microvasculature with DCE-MRI have been correlated with prognostic factors (e.g., tumor grade, metastatic potential) and with recurrence and survival outcomes. DCE-MRI parameters were found to be associated with common angiogenesis markers (e.g., microvascular density (MVD), VEGF expression), thus indicating the enormous potential of DCE-MRI as non-invasive biomarker for tumor detection and characterization, monitoring tumor response to anti-cancer therapies that affect angiogenesis or perfusion, and outcome prediction (Hylton 2006). In human lung tumor xenografts, the effects of anti-angiogenic treatment on tumor vasculature were evaluated in vivo using DCE-MRI. Treated tumors showed decreased contrast uptake and transfer constant on day 7 of treatment, which was associated with significant growth retardation and lower MVD compared with controls (Muruganandham et al. 2006). DCE-MRI with intravascular macromolecular CA in breast and prostate cancer xenograft models of different metastatic potential revealed higher blood volume and permeability in metastatic tumors, which also matched VEGF expression (Winnard et al. 2008). The assessment of vascular endothelial leakiness using new PEG-core, (Gd-DOTA)-

conjugated macromolecular contrast agents proved applicable for the differentiation of human breast cancer from normal soft tissue (Cyran et al. 2008).

5.3 Steady-State Susceptibility-Contrast MRI

Steady-state susceptibility-contrast (ssSC) MRI after application of CA allows the assessment of vessel morphology and blood volume (Dennie et al. 1998; Tropres et al. 2001). Intravascular CAs induce long range field perturbations that extend into tissues and increase transverse relaxation rates R_2 and R_2^*. These effects are differently expressed in spin-echo- and gradient-echo-type MRI in dependence on vessel size. Thus, from measured changes in relaxation times (ΔR_2 and ΔR_2^*) induced by CA injection maps of vessel size index and additionally fractional blood volume can be estimated. CAs with high T_2^* relaxivity (e.g., SPIO) increase induced changes in transverse relaxation rates, which allows assessing smaller vessel size differences. In comparison to DSC-MRI, steady-state methods offer the potential of a higher signal-to-noise ratio, and thus a higher spatial resolution.

This imaging approach can be used to assess differences in morphology of neoplastic and normal vessels and response to therapies directed to tumor vasculature. In a rat glioma model, vessel size imaging revealed larger mean vessel size in tumors than in surrounding normal brain, which was correlated significantly with histological data (Tropres et al. 2004). In GH3 prolactinoma and RIF-1 fibrosarcoma grown in mice, ssSC MRI with a blood pool CA could correctly identify the larger blood volume (four-fold) and capillary size (two-fold) in GH3 tumors in agreement with histological analysis of MVD, perfused MVD, and perfused vessel fraction (Robinson et al. 2003). In two rat glioma (C6 and RG2) models, repeated SPIO-enhanced MRI of blood volume fraction and vessel size index indicated significantly different microvascular evolution during tumor progression between the two models, in good agreement with histology-derived vascular parameters (MVD, vascular fraction), expression of angiogenic factors (VEGF, angiopoietin-2), and activities of matrix metalloproteinases (Valable et al. 2008). Repeated injection of SPIO particles as CA did not affect the physiological status of animals and the accuracy of MR estimates of microvascular parameters. In melanoma tumors overexpressing platelet-derived growth factor, thus leading to enhanced blood vessel pericyte coverage, ssSC MRI with USPIO particles revealed a significant reduction in vessel size index compared to control melanoma, which was validated histologically by the presence of significantly smaller, and more punctate blood vessels (Robinson et al. 2008). In colon carcinoma mouse models, steady-state MRI with intravascular paramagnetic or superparamagnetic CA demonstrated highly sensitive and early reduction of tumor blood volume in response to anti-angiogenic treatment with a VEGF receptor tyrosine kinase inhibitor, concomitant to increased apoptosis of tumor and endothelial cells, and decreased vascular density (Kim et al. 2005; Reichardt et al. 2005). In a squamous cell carcinoma tumor model, a strong decrease of blood volume 4 days after anti-angiogenic treatment initiation was observed, which was in line with MVD assessment (Hyodo et al. 2009).

5.4 Diffusion-Weighted MRI

Diffusion-weighted imaging (DWI) assesses the random translational (Brownian) motion (diffusion) of water molecules in tissues. Generally, MRI sequences are made sensitive to diffusion through application of a pair of strong magnetic field gradients, which induce a controlled position-dependent spread of resonance frequency. The first gradient is used to encode initial spin position, while the second gradient encodes final position. Diffusion leads to an imbalance of dephasing effects due to first and second gradient. This, finally, results in signal attenuation due to incomplete spin rephasing. The amount of diffusion-weighting in final MRI signal depends on gradient parameters (strength, duration, separation) which are collectively summarized in the b value. From a series of differently diffusion-weighted images, diffusion can be quantified by means of apparent diffusion coefficient (ADC). Reduced diffusion leads to less dephasing and appears bright on DWI and dark on ADC maps.

DWI is sensitive to tissue microstructure on a cellular level including cellularity, presence and integrity of membranes, extracellular matrix composition, interaction with intracellular elements, and water distribution between intra- and extracellular space (Chenevert et al. 2006; Patterson et al. 2008; Padhani et al. 2009). Additionally, perfusion in capillaries, ducts and interstitial space may also impact on DWI leading to deviations from monoexponential signal decay. As an example, Fig. 1a shows the signal intensity decay of kidney and tumor in a human tumor xenograft model. In the logarithmic plot of signal intensity versus b value (middle panel) the biexponential decay behavior in kidney and less pronounced also in tumor becomes obvious at low b values as a deviation from a single straight line. However, this can be used to extract perfusion-related ADC_{perf} (left panel) from low b values (blue area) and pure diffusion-related ADC_{diff} (right panel) from high b values (green area). Indeed, it was shown with correlative in vivo and ex vivo DWI of hepatic tumors that ADC determined at low b and high b relates to perfusion and diffusion, respectively (Sun et al. 2009). We exploited this approach in tumor xenograft models with different vascularization (b), which were induced by tumor cell inoculation without and with additional endothelial cell coinoculation (Mirus et al. 2010). Tumors with endothelial cell coinoculation exhibited higher vascularity as proven with histology. As expected, kidneys (left panel) showed no apparent differences in ADC_{perf} (blue) and ADC_{diff} (green) between both model systems. However, in tumors (right panel) with endothelial cell coinoculation and associated higher vascularization significantly higher ADC_{perf} ($p = 0.02$) was observed, whereas ADC_{diff} was largely unchanged (Wolf et al. 2010).

Pathological processes or therapeutic interventions that alter tissue microstructure and microcirculation affect water mobility, and thus are accessible by DWI. The basic principle of cancer detection and therapy response monitoring with DWI is schematically illustrated in Fig. 2. Normal appearing non-diseased tissue shows up with low cell density and exhibit comparatively free water diffusion (high ADC) (a). During tumor progression enhanced cell and matrix

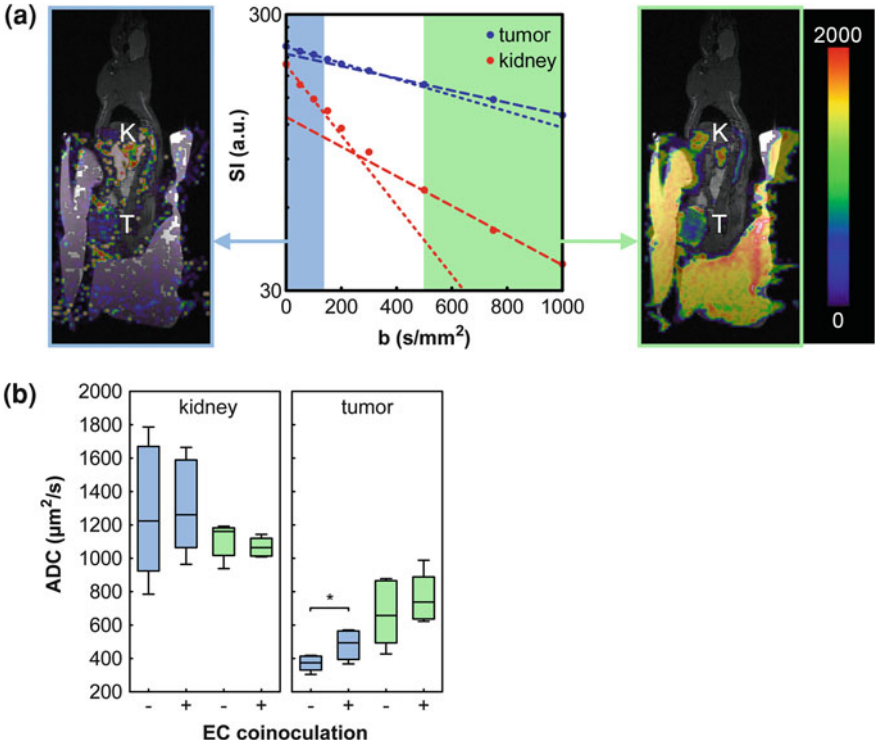

Fig. 1 **a** Decay of signal intensity (SI) with increasing b value (*middle panel*) in kidney (K) and tumor (T) deviate from monoexponential behavior due to influences of microcirculation. This can be exploited to extract perfusion-related ADC_{perf} maps (*left panel*) from low b values (*blue area*) and pure diffusion-related ADC_{diff} maps (*right panel*) from high b values (*green area*). Images show color-coded ADC maps (*blue*—low value, *red*—high value) superimposed on morphological images. Tumors are covered with anti-susceptibility device to reduce image distortions related to DWI. **b** Human tumor xenograft models with different degree of vascularization were induced by tumor cell inoculation without (–) and with (+) additional endothelial cell (EC) coinoculation. As expected, kidneys (*left panel*) show no apparent differences in ADC_{perf} (*blue*) and ADC_{diff} (*green*). In tumors (*right panel*) with EC coinoculation (+) and histologically proven higher vascularization significantly higher ADC_{perf} (* $p = 0.02$) was observed, whereas ADC_{diff} was largely unchanged. Box plots indicate median (*horizontal bar*), interquartile range (box) and minimum-to-maximum range (whiskers) from $n = 6$ tumors (Wolf et al. 2010)

proliferation lead to increased tissue cellularity (b) which becomes obvious in reduced diffusion (lower ADC) of water molecules through these pathologically changed areas. Correspondingly, changes in tissue microstructure in response to successful therapy (c) usually result in increased diffusion (higher ADC). This can be detected with DWI and quantified by ADC before any detectable change in size (Pickles et al. 2006). DWI has indicated its potential as imaging biomarker in oncology in tissue characterization and differentiation, therapy response monitoring, and outcome prediction.

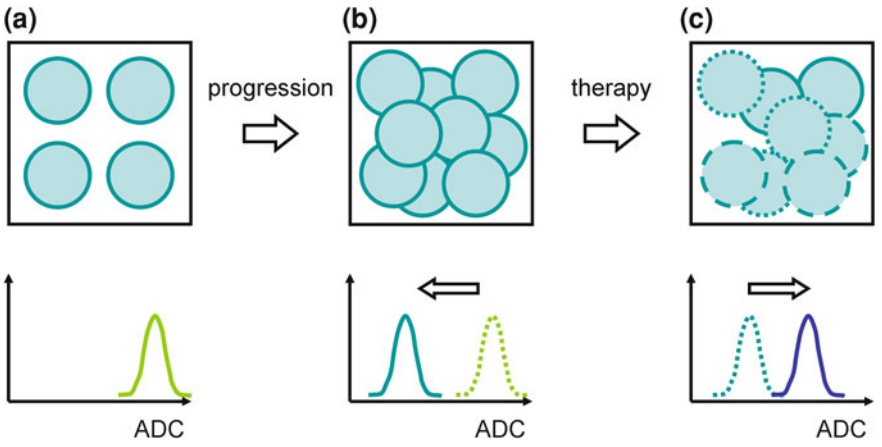

Fig. 2 Illustration of principles of cancer detection and therapy monitoring with DWI: Progression from loosely packed (normal) tissue associated with high ADC due to comparatively unrestricted diffusion (**a**) towards pathologically changed (cancer) tissue of high cellular density leads to decreased ADC due to diffusion restriction (**b**). Successful cancer therapy leads to early disintegration of cells, and thus less restricted diffusion (**c**). This is reflected by an increasing ADC, already before changes in morphological size criteria become obvious

DWI has been used in tissue characterization for improved detection of small (< 1 mm) prostate tumors in a transgenic mouse model (Song et al. 2002) and nodal staging with less false-positive results than PET/CT (Nomori et al. 2008). It may potentially differentiate among benign and malignant primary and metastatic lesions with fewer false-positives for active inflammatory lesions than PET (Mori et al. 2008; Xue et al. 2008), identify viable and necrotic tumor regions (Herneth et al. 2003; Deng et al. 2006; Youn et al. 2008; Sun et al. 2009) and discriminate tumor recurrence, and post-therapeutic tissue change (Asao et al. 2005; Vandecaveye et al. 2006). An example for identification of potentially pathological tissue change using DWI is presented in Fig. 3. In a human tumor xenograft model, we observed high signal intensity in DWI for pathologically changed lymph nodes that were characterized by dense cell packing in histology, whereas normal lymph nodes with a rather loose cell packing presented without detectable DWI signal (Wolf et al. 2007). Furthermore, we systematically investigated this dependence in vitro in phantoms with varying cellular density and found an inverse correlation of ADC and cell density.

A very important potential application of DWI is to monitor early tumor response to treatment (Moffat et al. 2004; Hamstra et al. 2007; Padhani et al. 2009). Successful applications have shown early effects on ADC in various tumor entities in response to chemotherapy (Reichardt et al. 2009), chemoradiotherapy (Kim et al. 2009), anti-angiogenic treatment (Kim et al. 2005), anti-vascular therapy (Thoeny et al. 2005; Vogel-Claussen et al. 2007; Wang et al. 2009a), and apoptosis-inducing antibody treatment (Kim et al. 2008a).

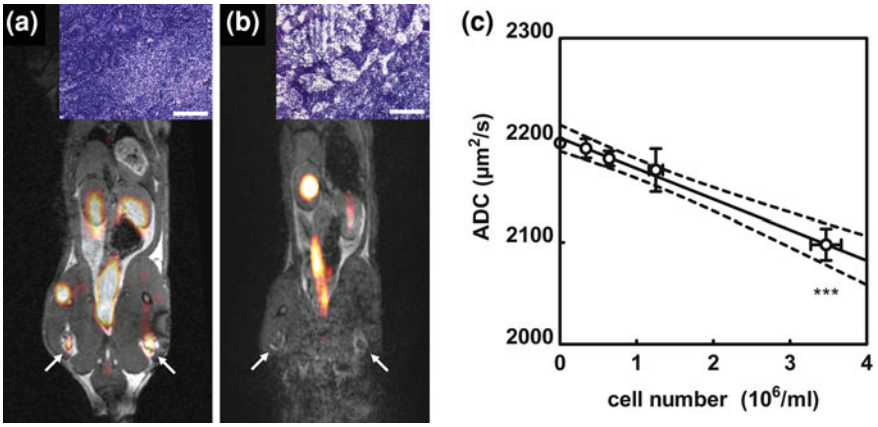

Fig. 3 **a**, **b** Fusion of morphological MRI and DWI (b = 500 s/mm^2; colored overlay) of tumor-bearing rats presenting different signal intensity of lymph nodes (*arrows*): **a** high DWI signal was associated with histopathologically changed lymph nodes of high cellular density, whereas **b** undetectable DWI signal was related to normal lymph nodes with loose cell packing. Insets show corresponding histopathological H&E staining (scale bar: 200 μm). **c** In in vitro 3-D cell phantoms ADC significantly decreases (*** $p < 0.001$) with increasing cell density. [a and b reprinted with permission of Informa Healthcare from (Wolf and Abolmaali 2009)]

Furthermore, DWI has been evaluated as prognostic biomarker of outcome. Pretreatment ADC was indicative of survival in postoperative radiation therapy of malignant supratentorial astrocytoma in patients (Murakami et al. 2007) and in a colon carcinoma mouse model treated with chemotherapy (Roth et al. 2004). Early ADC changes were reported to be predictive of survival in gene-dependent enzyme prodrug therapies in an orthotopic animal model of high-grade glioma (Hamstra et al. 2004), combined anti-death receptor 5 antibody, and gemcitabine treatment in orthotopic pancreatic tumor xenografts (Kim et al. 2008b) and radiotherapy in rabbit VX2 tumor model (Li et al. 2008b).

The widespread implementation of DWI to assess cancer is currently challenged by a lack of methodological standardization across instruments, data acquisition protocols and analysis methods between and among manufacturers, accepted quality assurance standards and realistic phantoms as well as proper evaluation of reproducibility, thus rendering multicenter studies practically unfeasible. In order to assess reproducibility of DWI we have designed a tissue-equivalent phantom, which resembles T_1, T_2, and ADC of various tissues (Wolf et al. 2012a). Using this phantom in different scanners at different centers revealed a high inter-scanner ADC variability of 15 % (range: 10–37 %), while intra-scanner variability (assessed in the same scanner over several weeks) ranged between 3 and 6 % depending on instrument (Wolf et al. 2012b). Additionally, the underlying biological principles of DWI at the microscopic level are still only poorly understood. However, recommendations on how to perform DWI in clinical cancer imaging (Padhani et al. 2009) as well as special advice on practical aspects

of technical adaption and optimization of protocols for DWI of small rodents with tumors in clinical scanners have been published (Chen et al. 2007).

5.5 Arterial Spin Labeling

An alternative to contrast-enhanced MRI for assessment of perfusion is arterial spin labeling (ASL). Instead of exogenous CA, ASL utilizes endogenous contrast which can be generated by magnetically inverting inflowing arterial blood prior to entering the imaging plane. The small ASL signal change, obtained as difference of tag and control experiment with labeled and unlabeled blood, respectively, is directly related to absolute blood perfusion. ASL has been shown to correlate with blood flow measures from ^{15}O-water PET (Ye et al. 2000) and DSC-MRI (Warmuth et al. 2003; Weber et al. 2003) in normal brain tissue. However, ASL is one of the more demanding MRI techniques associated with potential issues including low sensitivity, inaccurate bolus preparation, and complex flow quantification (Golay et al. 2004; Petersen et al. 2006), which has been partly addressed in recent methodological developments (Meng and Lei 2009).

ASL perfusion imaging shows promising results for potential application in tumor detection and monitoring of interventions. In experimental brain tumor models, blood flow exhibited pronounced heterogeneity, corresponding to MVD, with much higher blood flow in normal brain than in tumor periphery, and tumor core (Silva et al. 2000; Sun et al. 2004). Changes in blood flow could be detected in experimental glioma models in response to vasodilatation by carbogen breathing (Moffat et al. 2005) and inhibition of vascular endothelial growth factor (Moffat et al. 2006).

5.6 Blood Oxygen Level Dependent MRI

Blood oxygen level dependent (BOLD) MRI utilizes the different magnetic properties of oxygenated (diamagnetic) and deoxygenated (paramagnetic) hemoglobin in blood, thus requiring no administration of exogenous CA. Changes in blood concentrations of paramagnetic deoxyhemoglobin induce local magnetic field inhomogeneities within blood vessels, which extend into adjacent tissue, and modulate the signal in T_2^*-weighted images, which can be obtained with high spatial and temporal resolution and repeated as necessary. Blood itself is acting as an endogenous CA and tissues with reduced oxygenation are seen brightly on resulting BOLD images. However, only vessels that are perfused by red blood cells can be assessed, which is not generally the case in tumors (Padhani et al. 2007).

BOLD MRI may assess tissue oxygenation and vascular maturation and function in response to vasomodulation by hypercapnia and hyperoxia. In a rat rhabdomyosarcoma model, changes in tumor oxygenation in response to carbogen inhalation were readily detected with BOLD MRI, which might serve in the selection of responsive tumors (Landuyt et al. 2001). In a mouse melanoma model, BOLD MRI revealed pericyte-dependent changes in function of perfused tumor vasculature under normal, hypercapnic, and hyperoxic conditions (Robinson et al. 2008).

The response of melanoma xenografts in mice to photodynamic therapy was reflected as severe signal decrease solely within illuminated tumor areas in BOLD MRI (Gross et al. 2003).

6 Multimodality Imaging

Each imaging modality has its own advantages and limitations, but together they form a set of highly complementary tools for MI. Multimodality imaging has become an increasingly common means to utilize and combine the strengths of different approaches in one study. It provides flexibility in selection of imaging modalities for specific purposes, enables cross-correlation between imaging modalities and allows processes to be studied at anatomic, organ, cellular, and subcellular levels. Multimodality imaging employs either simultaneous or nearly simultaneous image acquisition using integrated systems or fusion of separately acquired images from different instruments with probably different subject positioning and necessity of sophisticated image registration software tools, e.g., Rover (ABX, Radeberg, Germany).

In an attempt to combine high spatial resolution of CT and high sensitivity of PET an integrated PET/CT imaging platform has been developed for preclinical imaging (Goertzen et al. 2002). In contrary to current clinical PET/CT scanners, this system enabled accurately aligned anatomical and functional information to be obtained truely simultaneously. More recently, the highly versatile imaging capabilities of MR techniques (e.g., MRI with its various contrast mechanisms, functional MRI and MRS) have been merged with PET into integrated small animal PET/MRI systems (Judenhofer et al. 2008; Wehrl et al. 2009; Yamamoto et al. 2010; Maramraju et al. 2011). Besides many other prerequisites, due to truly simultaneous acquisition of PET and MRI images, motion correction of PET data is possible. Recent research deals with methods (e.g., ultrashort echo time imaging) to generate attenuation correction maps for PET from MRI data. This is even relevant for small animal imaging. Both PET/CT and PET/MRI are highly competitive and subject to controversial discussion (Zaidi et al. 2007). In an experimental tumor model, simultaneous ^{18}F-FDG PET/MRI demonstrated low FDG uptake coincident with a region of hyperintensity on MRI close to the tumor center, most likely representing necrosis (Catana et al. 2008). In a colon carcinoma mouse model, tumor areas with high ^{18}F-FLT uptake matched areas of fast CA enhancement in MRI and were associated with increased proliferation in histology, while slowly enhancing tumor regions in MRI were related to low ^{18}F-FLT uptake in PET and necrosis in histology (Judenhofer et al. 2008). Alternatively, images from virtually all single modalities can be coregistered after acquisition. To improve coregistration, immobilization devices which keep animal positioning during instrument change and provide multimodal markers to guide image registration have been applied (Allard et al. 2007; Christian et al. 2008; Rommel et al. 2008; Zhang et al. 2008), yielding positioning errors due to animal transport of approximately 0.2–0.4 mm. The combination of optical imaging with MRI (Allard et al. 2007) and PET (Culver et al. 2008) seems potentially useful for probe development and validation, since optical methods provide rapid and cost-

effective real-time readout, while PET and MRI provide tomographic, as well as quantitative measures.

Multimodality imaging will substantially benefit from multifunctional probes that may be designed as nanoparticulate assemblies (Mulder et al. 2009b) or reporter gene systems (Doubrovin et al. 2004; Kang and Chung 2008). In two separate tumor models the accumulation of SPIO nanoparticles functionalized with a near-infrared dye, a membrane translocation peptide for intracellular delivery and siRNA specific for model or therapeutic targets could be demonstrated in vivo by MRI and near-infrared fluorescence imaging (NIRF) (Medarova et al. 2007). In a glioblastoma model, integrin-binding ^{64}Cu-DOTA-labeled quantum dots selectively targeted tumor vasculature as revealed by histology, which could be noninvasively quantified in vivo by PET and ex vivo by NIRF (Cai et al. 2007b). Similarly, integrin-targeted ^{64}Cu-DOTA-labeled iron oxide nanoparticles showed specific accumulation in a glioblastoma model with PET and MRI (Lee et al. 2008). Recently, integrin-targeted paramagnetically labeled micelle-coated quantum dots allowed detection of angiogenic vasculature in melanoma xenografts utilizing positive contrast MRI and FI (Mulder et al. 2009a). Despite the attractiveness and capabilities of multifunctional probes, it must be kept in mind that combined multifunctional probes are always designed as compromise and might be limited compared to optimally used corresponding single components (Boerman and Oyen 2008). For example, MRI requires multiple amounts of probe to be administered compared to PET, thus not fully exploiting the sensitivity of PET and potentially promoting non-specific tumor uptake. Generally, multimodality imaging with multifunctional probes poses the challenge of generating optimal imaging performance while still maintaining beneficial complementary information associated with each modality. In future, the combination of multimodal diagnostic imaging probes with therapeutic agents might envisage theragnostic imaging capabilities.

7 Applications

7.1 Metabolism

Tumors, generally, present severely altered metabolic properties compared to normal tissue. Increased metabolism of glucose, amino acids, nucleosides and lipids and their changes may be exploited to image neoplastic disease, and monitor cancer treatment.

7.1.1 PET

The, generally, high rates of aerobic glycolysis in tumors (Gatenby and Gillies 2004) can be exploited with PET using ^{18}F-fluoro-2-deoxy-D-glucose (^{18}F-FDG). In preclinical studies, ^{18}F-FDG has been mostly applied to detect early engraftment of tumor cells, to assess disease extension, to monitor variations of tumor metabolism over time and to assess treatment response (Ambrosini et al. 2009). ^{18}F-FDG accumulates in regions with increased glucose transporter expression and

metabolic activity in comparison to normal tissue (Griffin and Shockcor 2004). Additionally, hypoxia, proliferation, perfusion, and physiology may eventually influence ^{18}F-FDG uptake (Pugachev et al. 2005). Clinical utility of ^{18}F-FDG PET is limited in slowly growing or highly differentiated, less metabolically active tumors (e.g., prostate cancer, thyroid cancer, hepatocellular carcinoma). Additionally, action of ^{18}F-FDG is not entirely specific to tumor tissue, particularly also highlighting inflammation, infection, and therapy related changes. Physiologically highly active normal tissues like brain, and variably the heart, will show ^{18}F-FDG uptake alike excretion into the urinary tract and eventually into the gastrointestinal tract, thus complicating diagnostic evaluation of tumors in these locations (McConathy and Goodman 2008). Targeted therapies may not impact on glucose metabolism, requiring additional imaging probes complementary to ^{18}F-FDG to monitor targeted cancer treatment.

Proliferating cells in most cancer types also display enhanced protein synthesis and amino acid transport, which can be exploited in PET with radiolabeled natural and non-natural amino acids (McConathy and Goodman 2008; van Waarde and Elsinga 2008) including ^{11}C-methionine (^{11}C-Met), ^{18}F-fluoromethyl tyrosine (^{18}F-FMT), ^{18}F-fluoroethyl tyrosine (^{18}F-FET), or ^{18}F-1-amino-3-fluorocyclobutane-1-carboxylic acid (^{18}F-FACBC). The main cause of contrast for these probes seems to be increased amino acid transport. Metabolism of natural amino acids in vivo may generate multiple radioactive metabolites which renders tracer kinetic modeling difficult, but artificial amino acids are designed to be metabolically inert and show greater tumor specificity (van Waarde and Elsinga 2008). In general, radiolabeled amino acids present higher specificity for cancer and are less influenced by inflammation than ^{18}F-FDG, as could be demonstrated, for example, in an orthotopic prostate cancer model using ^{18}F-FACBC (Oka et al. 2007) and in epidermoid lung carcinoma in mice using FET (Chang et al. 2006). Correspondingly, the potential of methionine to differentiate malignant from granulomatous or inflammatory tissue was demonstrated in experimental rat models (Zhao et al. 2008). However, relative tumor uptake and tumor-to-normal tissue contrast are typically lower than with ^{18}F-FDG, thus decreasing sensitivity. Nevertheless, treatment response monitoring and possibly outcome prediction may be achievable with ^{18}F-FMT PET. In a squamous cell carcinoma model, ^{18}F-FMT showed early and persisting decrease of tumor uptake in response to single-dose radiotherapy, which correlated with tumor volume at later time points (Murayama et al. 2009).

Enhanced cancer cell proliferation can be assessed using radiolabeled nucleoside analogs like ^{11}C-thymidine, ^{18}F-3′-deoxy-3′-fluorothymidine (^{18}F-FLT), or ^{18}F-5-fluoro-2′-deoxyuridine (^{18}F-FUdR), which are taken up and metabolically trapped in proliferating cells and partly incorporated into DNA (van Waarde and Elsinga 2008). Especially thymidine, which accurately probes DNA replication, is taken up almost exclusively by viable tumor cells and, in contrast to ^{18}F-FDG, less in inflammation, and infection. This holds equivalently true also for ^{18}F-FLT, but sensitivity is somewhat lower than with ^{18}F-FDG. However, ^{18}F-FDG showed variable uptake in various experimental models being highest in syngeneic models and low in xenograft models, which were better visualized with ^{18}F-FLT (Ebenhan

et al. 2009). Although ^{18}F-FLT is only very sparsely incorporated into DNA, it was suggested as a good surrogate marker of tumor proliferation and have shown rapid decline in response to cytostatic or cytotoxic therapies in various animal models of cancer (Buck et al. 2009). However, it was also shown that under certain treatment conditions FLT uptake was initially uncoupled from proliferation (van Waarde and Elsinga 2008). ^{18}F-FUdR PET reliably detected proliferating tumor tissue in a sarcoma model and was suitable to assess tumor response to ganciclovir prodrug activated HSV1-tk gene therapy (Wang et al. 2006).

Additionally, proliferation is associated with an increased cell membrane phospholipid synthesis in tumors. This can be utilized in PET by probing transport and metabolism of radiolabeled lipid precursors like ^{11}C-choline, ^{18}F-fluorocholine, ^{18}F-fluoroethylcholine, or ^{11}C-acetate. Choline-based proliferation tracers were found to rapidly accumulate in tumors with low muscle background activity, but under certain circumstances also in non-tumor inflammatory or infectious lesions, indicating that overall tumor specificity of cholines and ^{18}F-FDG is for the most part not significantly different (van Waarde and Elsinga 2008). Nevertheless, ^{11}C-choline and ^{11}C-acetate are clinically used to evaluate prostate cancer.

7.1.2 MRI/MRS

MRS can be used to repeatedly and non-invasively study metabolism of tumors in vivo (Beloueche-Babari et al. 2010). It can detect several metabolites in one measurement without prior specification, particularly phospholipid metabolites (e.g., phosphomonoesters, phosphodiesters, choline/phosphocholine, glycerophosphocholine), bioenergetic metabolites (e.g., creatine/phosphocreatine, nucleotide triphosphates, inorganic phosphate), and glycolytic metabolites (e.g., glucose, glutamine/glutamate, lactate). Tumors, typically, show characteristic metabolic features in ^{1}H and ^{31}P MRS (e.g., high levels of phosphomonoesters, phosphodiesters, total choline), which are often reversed on successful treatment with chemo- or radiotherapy and currently considered as biomarkers for tumor diagnosis, staging, and clinical response monitoring (Beloueche-Babari et al. 2010). High glucose consumption and lactate production in tumors can be monitored in preclinical models of cancer with ^{1}H and ^{13}C MRS. Preclinical studies have demonstrated the potential of spectroscopic measurements to non-invasively detect the action of new therapeutic agents (Beloueche-Babari et al. 2010). A limitation associated mostly with ^{31}P and ^{13}C MRS is their low sensitivity, which leads to long data acquisition times and poor spectral resolution. In this respect, MRS may benefit from high magnetic field strength offered by dedicated small animal scanners. Alternatively, hyperpolarization of exogenous probe molecules may greatly enhance sensitivity and enable in vivo metabolic imaging of tumors (Golman et al. 2006). Additionally, MRI with a PARACEST agent may provide metabolic maps of glucose over a range of physiologic interest (Zhang et al. 2003b). MRSI may be used to assess tumor metabolic markers for cancer diagnosis, metabolic phenotyping, and characterization of tumor microenvironment (He et al. 2004).

7.2 Hypoxia

Hypoxia is a characteristic pathophysiological property of many cancers, commonly arising as regions of low oxygen concentration as a result of increased oxygen consumption in neoplastic tissue and inadequate oxygen supply (Vaupel and Mayer 2007). It is associated with an aggressive tumor phenotype, risk of invasion and metastasis, treatment resistance, and poor prognosis (Gatenby and Gillies 2004; Weinmann et al. 2004; Tatum et al. 2006). Knowledge of oxygenation status of tumors may help to improve tumor therapy and select patients that may benefit from novel therapy options or eventually exclude patients with limited chance of cure from more invasive therapeutic strategies (Brown and Wilson 2004; Williams et al. 2004). Both, PET and MRI may serve in noninvasive characterization of tumor hypoxia (Tatum et al. 2006; Padhani et al. 2007; Krohn et al. 2008).

7.2.1 PET

PET directly contributes to hypoxia imaging due to several potential tracers sensitive to tumor oxygenation including the large group of ^{18}F-labeled nitroimidazoles and Cu-ATSM; even ^{18}F-FDG uptake has demonstrated dependence on hypoxia (Tatum et al. 2006; Krohn et al. 2008; Mees et al. 2009).

^{18}F-labeled nitroimidazoles are reduced in hypoxic cells to form reactive intermediary species and subsequently bound to intracellular proteins, thereby accumulating in viable hypoxic cells. ^{18}F-fluoromisonidazole (^{18}F-FMISO) is probably the most prominent hypoxia imaging agent of this class of substances, while several variants including ^{18}F-fluoroazomycin-arabinoside (^{18}F-FAZA), ^{18}F-fluoroetanidazole (^{18}F-FETA), ^{18}F-fluoroerythronitroimidazole (^{18}F-FETNIM), ^{18}F-EF5, ^{18}F-EF3 and ^{18}F-EF1 exist, which were designed to improve hypoxia imaging over ^{18}F-FMISO performance.

^{18}F-FMISO accumulates in areas with $pO_2 < 10$ mm Hg (Padhani et al. 2007). Initial ^{18}F-FMISO distribution depends on blood flow, but later local oxygen tension determines ^{18}F-FMISO uptake. An example of ^{18}F-FMISO uptake in a mouse xenograft model of colorectal cancer at early and late time points is presented in Fig. 4. During a dynamic study, at 5 min after injection (a) the tumor rim shows elevated ^{18}F-FMISO uptake due to blood perfusion, while at 220 min (b) ^{18}F-FMISO accumulates predominantly to the hypoxic tumor core. ^{18}F-FMISO is thought to be more sensitive to demonstrate chronic than acute, e.g., thrombosis related, hypoxia. Unbound ^{18}F-FMISO is eliminated with a half-life of about 1 h. Thus, contrast is typically low in raw ^{18}F-FMISO images, but can be corrected for high background signal in relation to blood or muscle uptake to extract hypoxia-specific tissue uptake. Consequently, appropriate timing is a prerequisite for meaningful ^{18}F-FMISO hypoxia imaging. Mostly, ^{18}F-FMISO PET at 2 h after injection reflects local oxygen concentration in a clinically significant range. In our own clinical experience, imaging after 4 h of uptake proved to provide higher contrast as compared to 2 h uptake imaging, hence improving diagnostic quality (Abolmaali et al. 2011). Since ^{18}F-FMISO PET is characterized by comparatively low contrast and limited signal,

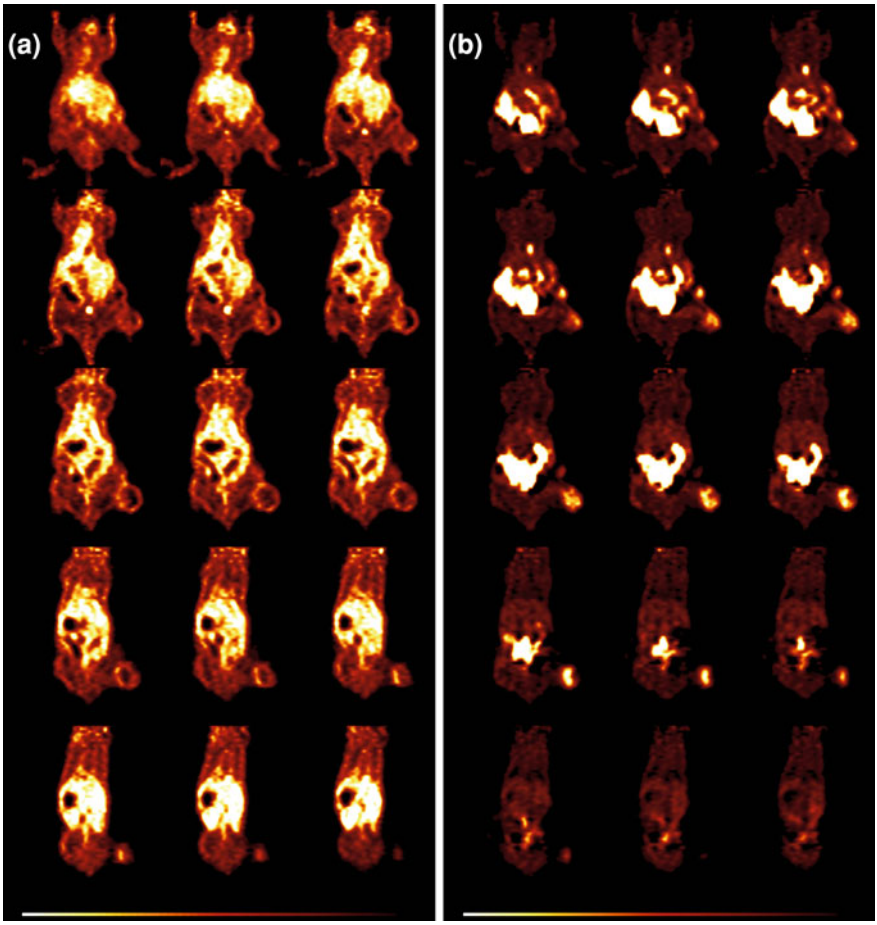

Fig. 4 FMISO PET slice series of **a** early uptake at 5 min and **b** late uptake at 220 min after injection in a mouse xenograft model of colorectal cancer. At early phases ^{18}F-FMISO PET is dominated by blood perfusion, while late time points represent tissue hypoxia (Images are by courtesy of Dr. Ralf Bergmann, Forschungszentrum Dresden-Rossendorf and Dr. Christina Schütze, Clinic for Radiotherapy and Radiation Oncology, Medizinische Fakultät Carl Gustav Carus, Technische Universität Dresden)

visual analysis of static data or complex mathematical analysis of dynamic data are applied. Automated segmentation of low contrast ^{18}F-FMISO PET data was done with source-to-background algorithms and gradient-based approaches only with limited success. More sophisticated tools are currently under investigation (Haase et al. 2011). ^{18}F-FMISO PET has demonstrated controversial results regarding correlation with polarographic needle electrode oxygen measurements in xenograft models (Bentzen et al. 2002; Gagel et al. 2004), most probably since ^{18}F-FMISO (in contrast to electrode measurements) is sensitive only to hypoxia in viable cells.

^{18}F-FMISO PET was correlated with immunohistochemical staining of exogenous hypoxia marker pimonidazole and endogenous hypoxia marker carbonic anhydrase IX (Dubois et al. 2004). FMISO presented heterogeneous uptake (independent of tumor size and injected tracer mass) and correlated with ^{18}F-FDG in various tumor xenografts (Wyss et al. 2006). ^{18}F-FMISO may be predictive of treatment response and prognosis, but has demonstrated limited reproducibility in tumors, probably due to its high sensitivity to pathophysiologic changes (Nehmeh et al. 2008). In this publication the measure of reproducibility is debatetable. Other measures more appropriate for such comparisions resulted in much better reproducibility (personal calculations).

Several alternative nitroimidazole derivatives have been designed with possibly faster clearance properties, less non-specific retention or fewer metabolites. ^{18}F-FAZA was suggested as an excellent hypoxia marker. It showed a hypoxia-specific uptake in the same range as ^{18}F-FMISO but with superior biokinetics in murine tumor models (Piert et al. 2005). ^{18}F-FAZA uptake was consistent with invasive electrode pO_2 measurements and immunohistochemical pimonidazole staining. In a squamous cell carcinoma mouse model, a clear spatial link between ^{18}F-FAZA and pimonidazole and an excellent correlation between ^{18}F-FAZA uptake and hypoxic cell density was observed, suggesting that ^{18}F-FAZA PET is able to generate quantitative tumor maps that accurately reflect the underlying microscopic reality (Busk et al. 2009). However, due to its low resolution, PET might miss hypoxic cells, particularly if intermixed with necrotic cells (Busk et al. 2008). High ^{18}F-FAZA uptake was predictive of the success of chemoradiotherapy. ^{18}F-FETA shows comparable oxygen dependence as ^{18}F-FMISO in vitro, but advantageous biodistribution in vivo because of less non-hypoxic degradation. Tumor retention of ^{18}F-FETA was related to radiobiological hypoxia and invasive pO_2 status. ^{18}F-FETNIM indicated comparable uptake in mouse tumors as ^{18}F-FMISO, which correlated with tumor oxygenation status, but with less background signal in normal tissue (Grönroos et al. 2004). Early tissue accumulation was highly variable and mainly dependent on perfusion. High ^{18}F-FETNIM uptake was associated with potentially poorer overall survival after radiation therapy. ^{18}F-EF5 exhibits high stability and rapid and uniform distribution in vivo and could detect hypoxia differences in diverse tumor types, even small tumors with modest hypoxia. ^{18}F-EF1 proved as an excellent radiotracer for non-invasive imaging of tumor hypoxia in rat tumors. Finally, ^{18}F-EF3 uptake was inversely correlated with oxygen concentration and showed similar pharmacokinetics, biodistribution, metabolism, and tumor hypoxia detection as ^{18}F-FMISO, thus indicating that it is not superior to ^{18}F-FMISO.

Non-imidazole-based hypoxia tracers include copper(II)-diacetyl-bis(N4-methylthiosemicarbazone) (^{64}Cu-ATSM) and potentially ^{18}F-FDG. ^{18}F-FDG uptake relies largely on expression of proteins that are also controlled by hypoxia and might, therefore, indirectly reflect tumor hypoxia. In vitro studies suggested that ^{18}F-FDG should accumulate in hypoxic cells because of their changed metabolism. However, in vivo experiments showed conflicting results for correlation of ^{18}F-FDG uptake and tumor hypoxia (Dierckx and Van de Wiele 2008).

In contrast, Cu-ATSM, which is typically prepared for animal studies with the long-lived positron-emitting isotope ^{64}Cu (12.7 h) and for patient investigation with the short-lived isotope ^{60}Cu (0.4 h), seems to be a more promising hypoxia indicator. Cu-ATSM is highly membrane permeable and becomes selectively trapped in hypoxic cells after reduction in vitro and in vivo at a higher level than ^{18}F-FMISO, while quickly washing out from normal, non-hypoxic tissue, thus yielding higher signal-to-noise ratio. However, hypoxia-independent retention may also occur. Cu-ATSM uptake is particularly dependent on time and tumor type. Uptake and retention in vitro was found to be cell line dependent and in vivo results also suggested that ^{64}Cu-ATSM is a suitable hypoxia marker in many tumor types, but not in all. In an anaplastic rat prostate tumor model ^{64}Cu-ATSM uptake at 4 h after injection did not correlate with ^{18}F-FMISO uptake, invasive pO_2 measurements and pimonidazole immunostaining, while it showed a good correlation with tumor hypoxia and ^{18}F-FMISO uptake at 16–20 h after injection. In FaDu tumors early and late ^{64}Cu-ATSM uptake was in concordance with ^{18}F-FMISO (O'Donoghue et al. 2005). ^{64}Cu-ATSM showed poor correlation of regional distribution with ^{18}F-FDG in experimental tumor models. ^{60}Cu-ATSM uptake seems to be predictive of response to therapy in patients with various cancers and inversely related to progression free and overall survival.

7.2.2 MRI/MRS

MRI and MRS may contribute to hypoxia imaging by several approaches including BOLD MRI, ^{19}F MRI/MRS of fluorinated substances and indirectly lactate imaging, respectively (Tatum et al. 2006; Padhani et al. 2007; Krohn et al. 2008).

Since BOLD MRI is sensitive to the oxygenation status of hemoglobin in perfused blood vessels, which might not, generally, be the case in tumor vasculature, it reflects more the effects of acute hypoxia (Baudelet et al. 2004; Padhani et al. 2007). Therefore, only qualitative but no direct correlation between R_2^* and tissue pO_2 was found (Baudelet and Gallez 2002; Fan et al. 2002), and knowledge of blood volume distribution is necessary to correctly infer tissue oxygenation status from R_2^*. However, changes in R_2^* can be used to measure changes in tissue pO_2 upon vasomodulation. This technique has been demonstrated to predict radiotherapeutical response in rodent tumors (Rodrigues et al. 2004). BOLD contrast may be confounded by blood flow effects, which may be uncoupled from static R_2^* effects (Howe et al. 2001).

^{19}F MRI can be used to assess tissue oxygenation using perfluorocarbons and fluorinated nitroimidazoles (Zhao et al. 2003; Robinson and Griffiths 2004; Yu et al. 2005). Perfluorocarbon reporter molecules may determine absolute oxygen levels with estimated precision of 1–3 mm Hg in the crucial low oxygen tension range (< 5 mm Hg) (Zhao et al. 2003). Perfluorocarbons display temperature-dependent transverse relaxation rates (R_1) that linearly relate to pO_2 (Yu et al. 2005). Importantly, R_1 of perfluorocarbons is essentially independent on pH, carbon dioxide, paramagnetic ions, common proteins, mixing with blood or emulsification,

and dilution (Yu et al. 2005). They may be introduced by direct intratumoral injection or systemic application of biocompatible emulsions, thus providing oxygen levels consistent with electrode and fiber optic measurements, while being less invasive, covering multiple locations simultaneously and allowing sequential assessments (Zhao et al. 2003; Yu et al. 2005). Measurements after systemic application of perfluorocarbon emulsions may be subject to flow effects, represent only the most well-perfused areas in tumor periphery and require large injection volumes since most material is sequestered in the reticuloendothelial system, which may lead to adverse side effects (Krohn et al. 2008). Instead, most successful approaches used intratumoral injections of perfluorocarbons that exhibit only a single resonance line (e.g., hexafluorobenzene), thus maximizing signal-to-noise ratio, and pO_2-sensitive R_1 across the entire range of oxygenation, including anoxia, hypoxia, normoxia, hyperoxia, and even hyperbaric (Tatum et al. 2006). In analogy to PET, ^{19}F-labeled nitroimidazoles have been evaluated to assess hypoxia by ^{19}F MRS. ^{19}F-TFMISO was suggested as a potential MR hypoxia marker (Procissi et al. 2007). On the other hand, ^{19}F-EF5 could not be evaluated as a valid MR indicator of hypoxia (Salmon and Siemann 2004; Hoff et al. 2008). Additionally, these approaches generally require large amounts of reporter molecule to be present in the region of interest, which may be associated with adverse side effects. Upon chemical trapping in hypoxic cells multiple ^{19}F-labeled species (including macromolecular) with individual chemical shifts may be generated contributing to poor signal-to-noise ratio, which necessitates long acquisition times. Moreover, retention of ^{19}F-labeled nitroimidazoles did not demonstrate clear correlation with tissue pO_2 (Yu et al. 2005), in analogy to their analogs for PET and histology.

Due to limited clinical availability of ^{19}F imaging capabilities, proton imaging of silanes for tissue oxygen levels (PISTOL) has been proposed as an alternative (Kodibagkar et al. 2008). The reporter molecule hexamethyldisiloxane (HMDSO) exhibits strong hydrophobicity, high oxygen solubility, low toxicity, ready availability, inertness, and most importantly oxygen-sensitive T_1 relaxation. Its single resonance line is far away from water and fat signal, and thus can be readily detected after water and fat suppression to interrogate tissue oxygen level after direct intratumoral injection.

Lactate accumulates in tumors as a consequence of hypoxia. Lactate levels have been indicative of metastasis and survival and may provide metabolic classification of tumors that might lead to improved prognosis in clinical oncology (Walenta and Mueller-Klieser 2004; Walenta et al. 2004). Lactate can be quantified non-invasively by ^{1}H MRS (Matsumura et al. 2005) and lactate-sensitive CEST agents (Aime et al. 2002c), which may, therefore, represent (although not directly) tissue pO_2.

7.3 Reporter Gene

Advances in gene therapy increase the importance of MI to non-invasively determine tissues which potentially benefit from gene therapy, to guide gene delivery, to assess local gene expression, and to monitor response to gene therapy (Serganova and

Blasberg 2005; Waerzeggers et al. 2009). Therefore, several reporter genes have been proposed for PET and MRI (Herschman 2004; Gilad et al. 2008; Waerzeggers et al. 2009). On the one hand, use of constitutive promoters renders transgenes always active, which can, then, be targeted to identify the site, extent and duration of vector delivery and to monitor efficiency of tissue and cell transduction, as well as for long-term cell trafficking. On the other hand, reporter gene constructs can be made sensitive to activation and regulation of inducible promoters by specific endogenous pathways, exogenous drugs, or tissue specific overexpression of transcription factors (Waerzeggers et al. 2009). Reporter gene imaging can, thus, be made cell or tissue specific, providing a valuable insight into specific molecular/genetic mechanisms of tumors. The interaction of reporter gene products (e.g., enzymes, membrane transporter, membrane receptor, artificial cell surface antigen, protein) with suitable reporter molecules produces measurable signal and enables indirect imaging of gene expression. The combination of imaging reporter and therapeutic genes allows non-invasive determination of gene expression, and thus gene therapeutic efficiency.

7.3.1 PET

In rodent glioma models that expressed herpes simplex virus type 1 thymidine kinase (HSV1-tk) reporter gene, PET could non-invasively assess gene expression level using the tracer 9-[4-^{18}F-fluoro-3-(hydroxymethyl)butyl]guanine (^{18}F-FHBG), which correlated with therapeutic efficiency as measured by ^{18}F-FLT (Jacobs et al. 2007). Additionally, multitracer PET using ^{18}F-FDG, ^{11}C-Met or ^{18}F-FLT could identify viable target tissue amenable for application of HSV1-tk gene therapy. Prostate cancer cells showed a linear relationship between HSV1-tk expression and ^{18}F-FHBG uptake with a detection limit of approximately 10,000 cells (Johnson et al. 2009). Equivalently, ^{18}F-FHBG PET in B16 melanoma-bearing mice demonstrated a detection limit of approximately 10,000 self-antigen-specific T cells expressing HSV1-tk reporter gene in lymph nodes and 70,000 T cells in spleen, while T cell quantification in tumors was hampered by HSV1-tk-independent tracer uptake (Shu et al. 2009). The therapeutic efficacy of bone marrow-derived tumor-infiltrating cells expressing HSV1-tk was non-invasively demonstrated by ^{18}F-FHBG PET (Miletic et al. 2007). In an experimental sarcoma model, the ganciclovir prodrug-activated HSV1-tk gene therapy could be monitored with PET and resulted in significantly decreased tumor uptake of ^{18}F-fluorodeoxyuridine compared to pretreament levels (Wang et al. 2006).

7.3.2 MRI/MRS

In subcutaneous breast tumor xenografts simultaneously expressing endostatin therapeutic gene and transferrin receptor reporter gene, the therapeutic effect of endostatin (as obvious from growth delay, reduced MVD and VEGF levels) was well visualized by T_2 decrease after intravenous injection of transferrin-conjugated USPIO as reporter probe (Wang et al. 2009b). Using the gene magA from naturally occurring magnetotactic bacteria in a human cell line resulted in in vivo production of magnetic iron oxide nanoparticles from endogenous iron and led to signal loss in T_2^*-weighted images after transplantation into mouse brain, thus allowing long-

term non-invasive visualization of magA-positive cells (Zurkiya et al. 2008). In our opinion, this approach may be promising for longitudinal cellular imaging in experimental systems. The activation of cytosine deaminase, uracil phosphoribosyltransferase and HSV1-tk genes by exogenous prodrugs ganciclovir and 5-fluorocytosine could be monitored using ^{1}H MRS, ^{19}F MRS and DWI in experimental colon carcinoma and glioma tumor models, respectively (Hamstra et al. 2004; Valonen et al. 2004; Dubois et al. 2007; Liimatainen et al. 2009).

7.4 Angiogenesis

Angiogenesis is a critical requirement during cancer progression. Tumors reaching a few millimeters in size need an increased supply of oxygen and nutrients, which activates the development of new vasculature characterized by aberrant vascular structure, altered endothelial cell-pericyte interactions, abnormal blood flow, increased permeability, enlargement of vessel diameter, basement membrane degradation, thin endothelial cell lining, increased number of endothelial cells, decreased number of pericytes, and delayed maturation (Bergers and Benjamin 2003). The process of angiogenesis generally encompasses several mechanisms like sprouting angiogenesis, intussusceptive angiogenesis, recruitment of endothelial progenitor cells, vessel cooption, vasculogenic mimicry, and lymphangiogenesis (Hillen and Griffioen 2007). It is regulated by a variety of pro- and anti-angiogenic factors, of which $\alpha_v\beta_3$ integrins and VEGF, and its receptors are considered key regulators (Bergers and Benjamin 2003; Ferrara and Kerbel 2005; Milkiewicz et al. 2006). Angiogenesis has become an important therapeutic target, mainly directed against either existing tumor blood vessels (vascular disrupting agents), or tumor blood vessel development (antiangiogenic agents) (Alessi et al. 2004; Ferrara and Kerbel 2005; Jain 2005). MI may explore new molecular measures of biological response based on targeting molecules selectively expressed by angiogenic vessels. In addition, morphological and functional imaging biomarkers of tumor vasculature (e.g., blood flow, blood volume, vessel permeability, vessel size, vessel density) may also be promising for therapy evaluation (Barrett et al. 2007; Kiessling et al. 2007; Neeman et al. 2007).

7.4.1 PET

Integrins are cell-adhesion molecules that play a key role in endothelial cell migration, survival and maturation during angiogenesis, but also facilitate invasion, metastasis, and therapy resistance of cancer cells (Hehlgans et al. 2007). $\alpha_v\beta_3$ integrin is significantly upregulated during angiogenesis on activated tumor vasculature but not quiescent endothelial cells. Small peptides containing the arginine-glycine-aspartic acid (RGD) sequence are ligands of $\alpha_v\beta_3$ integrin. Several RGD-linked radiolabeled tracers have been developed for integrin imaging with PET, which mostly show high affinity and selectivity for $\alpha_v\beta_3$ integrin in vitro and receptor-specific accumulation in various tumor types in vivo (Haubner 2006).

For example, the tumor uptake of ^{18}F-labeled dimeric RGD peptide ^{18}F-FRGD2 revealed a good linear relation with tumor integrin levels in various xenograft models (Zhang et al. 2006). Integrin-targeted ^{64}Cu-DOTA-labeled quantum dots (Cai et al. 2007b) and iron oxide nanoparticles (Lee et al. 2008), which selectively targeted tumor vasculature in experimental glioblastoma as revealed by histology, enabled multimodal imaging of integrin combining PET with NIRF and MRI, respectively. A ^{18}F-labeled PEGylated heterodimeric RGD-bombesin peptide (^{18}F-Glu-RGD-BBN) have shown high tumor-to-background contrast in PC-3 tumor model and comparable high binding affinities for dual-receptor targeting of $\alpha_v\beta_3$ integrin and gastrin-releasing peptide receptors (Liu et al. 2009).

VEGF release is upregulated in tumors, controlled by hypoxia, activated oncogenes, inactivated tumor suppressors and a variety of growth factors, and induces endothelial cell proliferation, migration and survival as well as vascular permeabilization, thereby promoting tumor angiogenesis (Neufeld et al. 1999; Ferrara et al. 2003). Thus, VEGF signaling may be non-invasively imaged to provide valuable information on tumor angiogenesis and antiangiogenic treatments. Radiolabeled VEGF has been one approach to imaging angiogenesis with PET. ^{64}Cu-DOTA-conjugated $VEGF_{121}$ presented high binding affinity to VEGF receptor 2 in mouse glioblastoma models and PET uptake at 4 h was linearly correlated with levels of receptor expression (Chen et al. 2009). However, VEGF receptor expression was found to vary with tumor size, presenting only a narrow range with high levels, which may limit translation to clinical situations. The mutant version ^{64}Cu-DOTA-$VEGF_{DEE}$ showed comparable targeting efficacy and tumor accumulation in breast tumor models, but presented lower affinity for VEGF receptor 1 and therefore less renal toxicity in rodents (Wang et al. 2007). Considering current advances in antibody-based cancer treatment, the possibility to directly label antibodies against VEGF seems particularly interesting for imaging. In an angiosarcoma mouse model, anti-VEGF receptor 2 antibodies conjugated with ^{18}F-labeled lipid perfluorocarbon microbubbles showed significantly higher accumulation in tumor than in adjacent muscle tissue, accompanied by fast blood clearance but also high uptake in liver and spleen, as demonstrated with in vivo dynamic PET and ex vivo gamma counting, and immunohistochemistry (Willmann et al. 2008). In experimental teratomas, the angiogenesis-associated expression of fibronectin could be non-invasively assessed with PET using a ^{76}Br-labeled human antibody derivative (^{76}Br-L19-SIP) that specifically targets the extra domain B of fibronectin (Rossin et al. 2007).

7.4.2 MRI/MRS

Current MR approaches in angiogenesis imaging rely mainly on indirect imaging of biomarkers of vascular morphology and function and targeted imaging of $\alpha_v\beta_3$ integrin, respectively.

Non-targeted imaging with advanced MRI techniques like ASL, BOLD MRI, DCE-MRI and ssSC MRI can be used to indirectly characterize angiogenic tumor vasculature and treatment-related changes of vascular function (Barrett et al. 2007;

Kiessling et al. 2007; Neeman et al. 2007). High resolution MR angiography allowed non-invasive characterization of intratumoral vasculature (Fink et al. 2003). Vessels diameters down to 100–200 μm can be visualized accordingly in clinical scanners using optimized instrumentation and long scan times. ssSC MRI can quantify vessel size and blood volume and changes due to angiogenesis or therapy. A new approach has recently combined microscopic MR angiography and ssSC MRI blood volume mapping to simultaneously provide high-resolution 3-D information on morphology, in vivo microvascular architecture and hemodynamic response, which can be used to monitor changes in microvasculature (Lin et al. 2009). DCE-MRI, preferably with macromolecular CAs, can be used to assess vascular permeability, which develops as an immediate consequence of VEGF stimulation. In DCE-MRI in an experimental tumor treatment model, fractional plasma volume and transendothelial permeability decreased significantly in response to treatment with anti-VEGF monoclonal antibody using macromolecular CA, but did not change significantly using low-molecular-weight CAs (Turetschek et al. 2004). Additionally, DCE-MRI and ASL can monitor blood perfusion and blood flow during angiogenesis or in response to antiangiogenic treatment. In human lung tumor xenografts, DCE-MRI could evaluate the effects of anti-angiogenic treatment on tumor vasculature, which was associated with growth retardation and lower MVD compared with controls (Muruganandham et al. 2006). In rat glioma models, ASL and ssSC MRI showed significant change in tumor blood flow and blood volume in dependence on VEGF expression levels (Moffat et al. 2006). Perfusion changes in response to vasomodulation can be used to probe vascular maturation with BOLD MRI, which revealed pericyte-dependent changes in function of perfused tumor vasculature under normal, hypercapnic, and hyperoxic conditions in a mouse melanoma model (Robinson et al. 2008).

Targeted MRI of angiogenesis for the most part explored binding of RGD-linked nanoparticles to $\alpha_v\beta_3$ integrins (Cai and Chen 2008). In human melanoma tumor xenografts, angiogenic vasculature could be successfully detected and characterized in vivo with positive MRI contrast using $\alpha_v\beta_3$ integrin-targeted paramagnetic nanoparticles (Schmieder et al. 2005) and paramagnetically labeled micelle-coated quantum dots (Mulder et al. 2009a), which additionally allowed FI. Alternatively, RGD-conjugated USPIO nanoparticles showed efficient targeting of $\alpha_v\beta_3$-integrin and were able to non-invasively distinguish between tumors with different integrin expression (Zhang et al. 2007). A bimodal ^{64}Cu-DOTA-labeled RGD-conjugated iron oxide probe showed efficient integrin binding in vitro and delivery to glioblastoma in vivo with both MRI and PET (Lee et al. 2008). This probe combines high sensitivity of PET and high spatial resolution of MRI, which will become increasingly important with ongoing development of combined PET/MRI technology. In squamous cell carcinomas with up-regulated microvasculature, ^{19}F diffusion-weighted MRS has been used to detect specific binding of integrin-targeted perfluorocarbon nanoparticles, while selectively suppressing background ^{19}F signal from unbound, freely circulating nanoparticles (Waters et al. 2008). We believe that ^{19}F MRI/MRS will develop into a viable alternative to current standard MR measures, if ^{19}F imaging capabilities will become more broadly available (which is

currently only rarely the case, especially with clinical equipment). Targeted MRI of VEGF receptors is hardly performed. However, a recent study reported for the first time on detection of increased VEGF receptor 2 expression in vivo in a rat glioma model using CLIO-conjugated anti-VEGF receptor 2 antibodies, which were specifically retained in tumor tissue as evident from signal loss in T_2-weighted MRI and histological evaluations (Towner et al. 2010).

Additionally, magnetically labeled stem/progenitor cells, which are known to migrate to areas of active angiogenesis (Milkiewicz et al. 2006), have been used to assess neovascularization in tumors with MRI. For example, MRI has demonstrated the incorporation of SPIO-labeled endothelial progenitor cells in tumors at sites of active angiogenesis a few days after systemic administration (Arbab et al. 2006; Schindler et al. 2010).

7.5 Apoptosis

Apoptosis is a form of genetically controlled (programmed) cell death and besides proliferation an important physiologic cell function. Loss of normal apoptosis may lead to enhanced cellular proliferation and subsequently tumor growth and resistance to classical anti-neoplastic therapy. During apoptotic process cells experience typical morphological and biochemical changes including phosphatidylserine (PS) externalization, cell shrinkage, nuclear condensation and DNA degradation, membrane blebbing and finally cell disintegration and phagocytosis, mostly initiated by death receptor and mitochondria pathways, and mediated by activation of caspases (Hengartner 2000; Debatin and Krammer 2004; Mishra and Kumar 2005). These changes provide a wealth of markers and targets for non-invasively visualizing apoptosis in vivo by modern magnetic resonance and nuclear imaging technology (Hakumaki and Liimatainen 2005; Blankenberg 2008).

Caspase activation occurs early in the process of apoptosis. Targeting the intracellular caspase signaling pathway could offer a valuable and highly specific tool for early detection of apoptosis. However, due to the intracellular target localization, reporter probes must successfully reach site of apoptosis and penetrate cell membrane. A number of radiolabeled caspase inhibitors have been designed for nuclear imaging (Lahorte et al. 2004). Recently, ^{18}F- and ^{11}C-labeled isatin derivates have been developed as PET probes for targeted caspase imaging in apoptosis (Podichetty et al. 2009; Zhou et al. 2009). In a mouse model of liver apoptosis clearly more activity was retained compared to control animals. In apoptotic macrophages, a decrease of ADC was observed in vitro with diffusion-weighted MRS in response to caspase activation but preceding PS membrane turnover and nucleosomal DNA cleavage (Hortelano et al. 2001).

Externalization of PS is an important step in the apoptotic process following caspase activation. Externalized PS is readily accessible on cell surface and can be targeted by annexin V. For nuclear imaging, a variety of radiolabeled annexin V are available to assess anti-cancer therapy efficacy (Lahorte et al. 2004; Yuji et al. 2009). Using an indirect three-step targeting strategy with pretargeting of PS by biotinylated annexin V

followed by an avidin chase and administration of ^{64}Cu-labeled streptavidin, apoptosis could be imaged with PET in tumor-bearing mice after photodynamic therapy (Cauchon et al. 2007). In an in vitro MRI experiment, apoptotic cells incubated with annexin V conjugated to CLIO nanoparticles showed significant signal decrease relative to control cells (Schellenberger et al. 2002). Externalized PS can be further targeted by the C2 domain of synaptotagmin I. This was demonstrated with MRI using synaptotagmin-conjugated SPIO nanoparticles in murine lymphoma models (Zhao et al. 2001). A new tool for molecular MRI of apoptosis uses magnetophages, i.e., SPIO-conjugated phages that specifically bind to PS, to discriminate between normal and apoptotic cells in vitro and in vivo (Segers et al. 2007). However, due to loss of cell membrane integrity by necrosis and diffusion of probe inside cells, PS-targeting may also detect a certain amount of necrotic cells.

Changes in lipid, amino acid and energy metabolism can be followed by ^{1}H, ^{13}C and ^{31}P MRS (Brauer 2003; Hakumaki and Liimatainen 2005; Blankenberg 2008). Apoptosis leads to increased levels of mobile lipids during gene therapy of rat glioma model detectable by ^{1}H MRS in vivo (Liimatainen et al. 2009). In contrast, necrosis is generally characterized by a completely different ^{1}H MRS profile. In vitro ^{13}C MRS demonstrated protein synthesis through incorporation of ^{13}C-labeled amino acids during apoptosis in human leukemia cells (Scott and Adebodun 1999). However, ^{13}C MRS is severely limited by low sensitivity, which might be overcome with hyperpolarization techniques (Golman et al. 2006). In a mouse mammary carcinoma model, the metabolic changes associated with inhibition of nicotinamide adenine dinucleotide (NAD^+) synthesis were examined with ^{31}P MRS. Treatment-induced tumor growth delay and enhanced radiation sensitivity associated with significant increases in the ^{31}P MR signal of phosphomonoesters and a decrease in NAD^+ levels, pH, and bioenergetic status (Muruganandham et al. 2005).

Cell shrinkage and tissue destruction occur as rather late events in apoptosis and might be addressed with DWI (Chenevert et al. 2006; Patterson et al. 2008; Padhani et al. 2009). However, treatment-induced necrosis may, in the end, lead to equivalent DWI appearance. In apoptotic rat brain BT4C gliomas, ADC increase during ganciclovir-thymidine kinase gene therapy directly correlates with cell loss (Valonen et al. 2004). Water diffusion and mobile lipid content assessed by MRS in glioma showed clearly increasing and interconnected trends during treatment (Liimatainen et al. 2009). Similarly, ADC was linearly proportional to apoptotic cell and cleaved caspase density in orthotopic pancreatic tumor xenografts (Kim et al. 2008b) and breast tumor xenografts (Kim et al. 2008a) after treatment with anti-death receptor 5 antibody (TRA-8).

7.6 Cellular Imaging

With advances in cell-based therapies (e.g., use of (stem) cells to replace defective cell populations or to deliver therapeutic agents) (Bajada et al. 2008; Corsten and Shah 2008; Kosztowski et al. 2009), non-invasive detection and tracking of

transplanted or transfused cells in vivo becomes increasingly important (Bulte and Kraitchman 2004). Cellular imaging may contribute to the understanding of the current role of certain cell populations in disease and repair processes and help to guide further developments. For example, endothelial progenitor cells are known to migrate to areas of active angiogenesis and contribute to neovascularization (Milkiewicz et al. 2006). Cancer stem cells have attracted much of recent scientific interest in cancer therapy (Koch et al. 2010). Given the current progress in molecular and cellular imaging, non-invasive in vivo detection of cancer stem cells as potential therapeutic targets may ultimately come into reach (Hart and El-Deiry 2008).

7.6.1 PET

PET has been used to directly track transplanted ^{18}F-labeled bone marrow-derived dendritic cells in vivo (Olasz et al. 2002). However, the utility of PET for monitoring directly radiolabeled cells is generally limited with comparatively short-lived isotopes like ^{18}F, but longer-lived isotopes (^{64}Cu) have been tested. ^{64}Cu-PTSM and ^{64}Cu-polyethylenimine have been used for ex vivo labeling of C6 and U87MG glioma cells without compromising cell viability and proliferation, which were found to traffic to lungs, and liver in vivo in mice (Adonai et al. 2002; Li et al. 2009). For CD34+ hematopoietic and mesenchymal stem cells, that have been labeled in vitro with ^{64}Cu-PTSM without adverse cellular effects, a minimum of 25,000 and 6,300 labeled cells could be detected, respectively (Huang et al. 2008). Alternatively, reporter gene technology may allow for extended indirect monitoring of cell engraftments with PET (Herschman 2004).

7.6.2 MRI/MRS

Although MRI is limited by inherently low sensitivity compared to PET, it is the most widely applied modality for in vivo cellular imaging (Modo et al. 2005; Kim et al. 2007; Himmelreich and Dresselaers 2009; Muja and Bulte 2009), since it offers high resolution anatomical imaging with excellent contrast. In order to visualize cells against the background of host cells and to increase sensitivity, MRI-based cellular imaging generally requires labeling of cells with CAs. Incorporation of CA into cells can be achieved with several strategies (e.g., transfection, electroporation) without adverse effects on cell proliferation, differentiation and migration or cell toxicity (Bulte 2006; Himmelreich and Dresselaers 2009). CAs used for cell labeling comprise mainly SPIO nanoparticles, but also paramagnetic Gd-chelates, CEST agents, or fluorine-containing compounds have been used. However, cellular labeling with exogenous substances may lead to label dilution upon cell division and disables differentiation between dead and live cells, thus limiting their potential for long-term non-invasive monitoring of cell therapy. A viable alternative may be reporter genes that encode for proteins specifically influencing MR contrast (Gilad et al. 2008; Himmelreich and Dresselaers 2009).

Cell labeling with SPIO leads to signal loss in T_2^*-weighted MRI. Sensitivity comparable to PET was reported (Heyn et al. 2005). Detection limits of SPIO-labeled cells are currently in the range of 100–500 cells down to single cells in

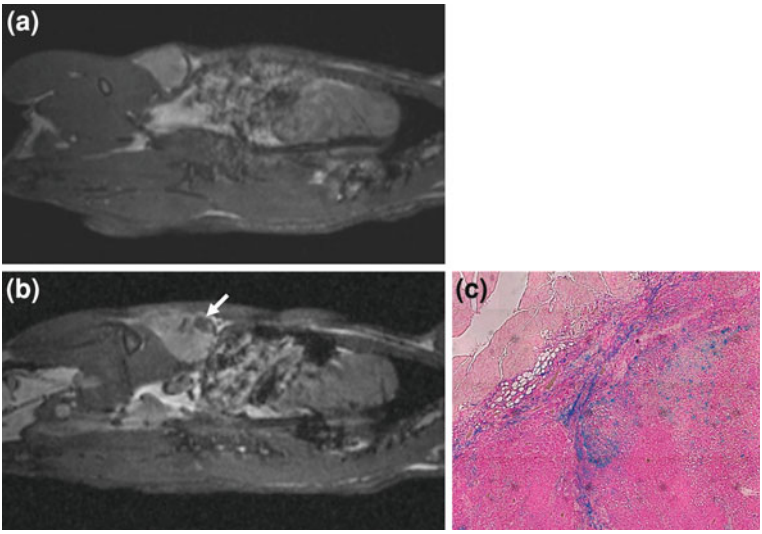

Fig. 5 Morphological MRI of tumor-bearing rat before (**a**) and 5 days after (**b**) intraperitoneal administration of superparamagnetically labeled mesenchymal stem cells using clinical scanner. Arrow indicates signal void in tumor due to incorporation of labeled stem cells, which was histologically proven with Prussian blue staining (**c**). [a and b reprinted with permission of Informa Healthcare from (Wolf and Abolmaali 2009)]

non-clinical dedicated animal scanners at high field (Muja and Bulte 2009). For example, in lymph nodes of mice as few as 100 SPIO-labeled metastatic melanoma cells could be detected after direct injection and their development into intranodal tumors could be monitored over time in a 1.5T clinical MRI system (Foster et al. 2008). Single cell detection capability at clinical field strength was demonstrated both in vitro (Foster-Gareau et al. 2003) and in vivo with direct fluorescence microscopic validation (Heyn et al. 2006). An example of in vivo detection of SPIO-labeled cells in a clinical scanner at 1.5T is given in Fig. 5. In a human tumor xenograft model of lung cancer, the incorporation of SPIO-labeled bone marrow-derived mesenchymal stem cells (MSCs) in subcutaneous tumors could be detected at 5 days after intraperitoneal administration (Schindler et al. 2010). Intratumoral incorporation of MSCs as assessed by R_2^* quantification was well correlated with histological evaluations in explanted tumors and corresponded to areas of neovascularization as exemplified in Fig. 6. Equivalently, SPIO-labeled AC133+ progenitor cells could be detected at 3 days after intravenous injection to traffic to sites of tumor angiogenesis in glioma xenografts (Arbab et al. 2006). SPIO-labeled and genetically transformed AC133+ progenitor cells were found to accumulate in subcutaneous breast cancer xenografts after intravenous administration and selectively express human sodium iodide symporter gene at tumor site, indicating that such multifunctional cells can be used both as cellular probes and gene carrier systems for cancer treatment (Rad et al. 2009).

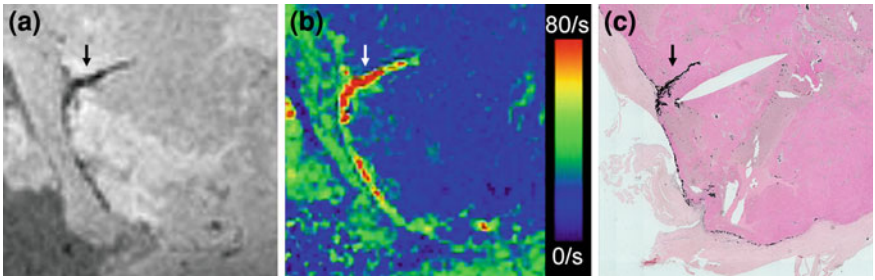

Fig. 6 Detection of incorporation and quantification of mesenchymal stem cells labeled with superparamagnetic iron-oxide nanoparticles in excised tumors 5 days after intraperitoneal administration in human tumor xenograft model using clinical MRI scanner: **a** areas of signal loss on morphological MRI and **b** increased iron content on color-coded R_2^* quantification (*red*—high R_2^* = high iron content) correspond to **c** iron-positive areas on histological Prussian blue staining (converted to *black* for better visualization) as indicated by *arrows*

Although paramagnetic Gd-chelates lead to positive contrast, due to the relatively lower sensitivity, large amounts of intracellular Gd-CA are needed. It was suggested that with clinically approved CAs of low relaxivity about 10^9 Gd-complexes per cell (Aime et al. 2002a) or cellular Gd concentrations exceeding 50 μM (Ahrens et al. 1998) are required to provide sufficient contrast for MRI visualization. In a phantom, the detection limit of cells labeled with a Gd-chelate was estimated to approximately 2,000–3,000 cells (Crich et al. 2004).

The concept of CEST can be used for cellular imaging by either labeling cells with CEST agents or engineering cells that express CEST agents themselves. Rat hepatoma cells labeled with either of two or both PARACEST agents could be selectively detected in phantom experiments based on the agent-specific resonance line that was saturated (Aime et al. 2005b). 9L glioma cells that were genetically altered to express lysine-rich protein as CEST agent produced a significant CEST signal in vivo following cell delivery into striatum of mice (Gilad et al. 2007). To us, the opportunity to label cells with multiple CEST agents or potentially design multi-label CEST MRI reporters (McMahon et al. 2008) seems to be very attractive for future MI applications. In this way, multi-CEST agents, which may be responsive to several saturation frequencies and display their own unique "color", may enable simultaneous non-invasive imaging of multiple cell types and/or expression patterns of multiple genes.

^{19}F MRI can directly detect appropriately labeled cells in the absence of biological background signal in vivo (Ahrens et al. 2005; Bulte 2005; Partlow et al. 2007). Additionally, ^{19}F MRS may allow cell number estimation. Anatomical localization can be achieved by fusion with simultaneously acquired conventional ^{1}H images. Cellular imaging with ^{19}F MRI requires intracellular incorporation of fluorine-containing agents like perfluorocarbon nanoparticles. In phantoms approximately 6,000 labeled cells could be detected by ^{19}F MRI at 11.7 T (Partlow et al. 2007).

8 Animal Welfare and its Impact on Imaging

Besides all improvements in imaging technology and imaging probes that have enabled MI in experimental oncology, the welfare of animals is an extremely important aspect to consider during imaging. Maintaining an animal within a stable and narrow physiologic range is a prerequisite for measuring meaningful physiologic responses related to the experimental action and not to animal manipulation. Anesthetic regimes as well as animal handling may impact on MI studies by affecting, for example blood flow, tissue oxygenation as well as distribution and metabolism of substances (LaManna and Harik 1986; Toyama et al. 2004; Lee et al. 2005; Fueger et al. 2006). Therefore, it may be advisable to thoroughly consider, test and practice procedures for animal handling, anesthesia, monitoring, and application of substances beforehand (Diehl et al. 2001; Colby and Morenko 2004; Hildebrandt et al. 2008).

For in vivo imaging studies, animals generally have to be immobilized by anesthesia. Anesthesia should be easy to administer, safe, reliable and of sufficient depth, and duration for the intended purpose. Therefore a variety of different regimes exist. For a detailed description of available anesthetic regimes the interested reader is directed to the literature (Flecknell 1993; Lukasik and Gillies 2003; Hanusch et al. 2007). Usually, anesthesia of small animals can be effectively induced and continuously maintained via inhalant, intraperitoneal, and intravenous routes, respectively. Due to its easy controllability and rapid induction and recovery, inhalation anesthesia may be preferable for long procedures (> 30–45 min).

Anesthetic regimes may be accompanied by metabolic and physical stress, such as hypothermia, hypercapnia, acidosis, hypoxia and hepatic toxicity (Topal et al. 2003; Szczesny et al. 2004), and influence on cardiovascular, respiratory and central nervous systems functions, which potentially introduces unwanted biases (LaManna and Harik 1986). For example, in the frequently used injectable mixture ketamine/xylazine, ketamine is known to cause mild respiratory depression, increased heart rate and cardiac output, hypertension (due to a release of catecholamines), hypersalivation and direct vasodilatation of vascular smooth muscle, while xylazine leads to reduced heart rate, cardiac output (up to 30 %), and blood pressure (after an initial period of hypertension) and no or moderate breathing depression. The common inhalant isoflurane may lead to increased heart rate, decreased cardiac output, hypotension, minimal respiration depression, and vasodilatation. In Fig. 7 , we demonstrate the influence of the injectable anesthetic mixture ketamine/xylazine after intraperitoneal administration and isoflurane inhalation anesthesia on breathing and heart rate of rats. Both anesthetic protocols lead to respiration depression, while the heart rate was reduced only for ketamine/xylazine.

Studies with MRI and PET strongly illustrate the importance of understanding the likely physiological effects of anesthesia, animal preparation, and maintenance as well as standardizing methods. BOLD MRI demonstrated the effect of different anesthetics (injection: pentobarbital, ketamine/xylazine, fentanyl/droperidol; inhalation: isoflurane) in experimental mouse tumors and revealed dramatic

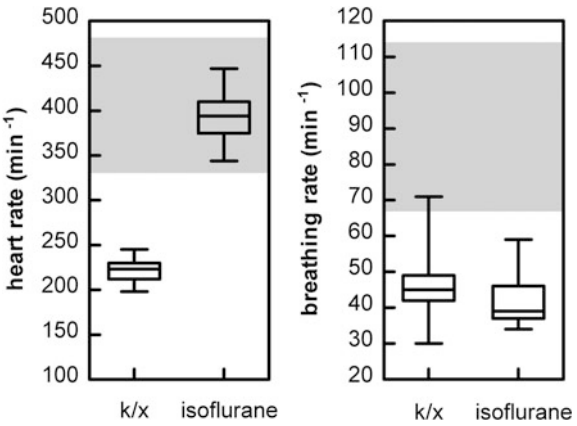

Fig. 7 Effect of ketamine/xylazine (k/x) and isoflurane anesthesia on heart and breathing rate of healthy rats. Box plots indicate median (horizontal bar), interquartile range (box) and minimum-to-maximum range (whiskers) of 3 rats for k/x, and 5 rats for isoflurane (sampling of 50 data points over 10 min for each animal). *Gray* areas represent normal physiological range as given in Table 1. Heart rate was significantly reduced only by k/x, while normal values were maintained by isoflurane. Both anesthetic protocols lead to breathing depression

decrease of BOLD signal intensity, which was well correlated with corresponding pO_2 and blood perfusion measurements, after administration of injectable anesthetic agents, whereas the inhalant isoflurane presented constant pO_2 and perfusion in muscle, although transient fluctuations were reported in some tumors (Baudelet and Gallez 2004). In PET, anesthetics are known to reduce delivery and elimination of radiotracers to tumors (Aboagye 2005). It has been shown, that anesthesia impedes ^{18}F-FDG uptake in mouse brain and affects ^{18}F-FDG uptake in heart (Toyama et al. 2004). However, the effects in brain and heart differed depending on type of anesthesia used. Anesthesia and also fasting may influence the biodistribution of ^{18}F-FDG in mouse tumor imaging (Lee et al. 2005). Markedly elevated ^{18}F-FDG activity in blood and reduced tumor uptake in mice kept fasting 4 h were observed with ketamine/xylazine. Depending on dose a transient insulin release inhibition may cause hyperglycemia. Pentobarbital induced a similar but less severe response through insulin resistance. After 20 h of fasting these metabolic effects were substantially attenuated. In contrast, isoflurane anesthesia only mildly increased blood glucose levels and had no significant effect on tumor ^{18}F-FDG uptake. In Figs. 8 and 9 we demonstrate the effects of route of tracer administration, anesthesia, and fasting on ^{18}F-FDG uptake in healthy rats. It appears that tracer uptake in brain was significantly lower in anesthetized rats and that biodistribution was influenced by fasting and route of tracer administration (Tokalov et al. 2010). In addition, due to the large surface area-to-body mass ratio and rapid body metabolism of small animals as well as the suppression of thermoregulatory mechanisms by anesthetic agents, hypothermia may develop already after relatively brief imaging sessions (10–15 min) (Flecknell 1993; Balaban and

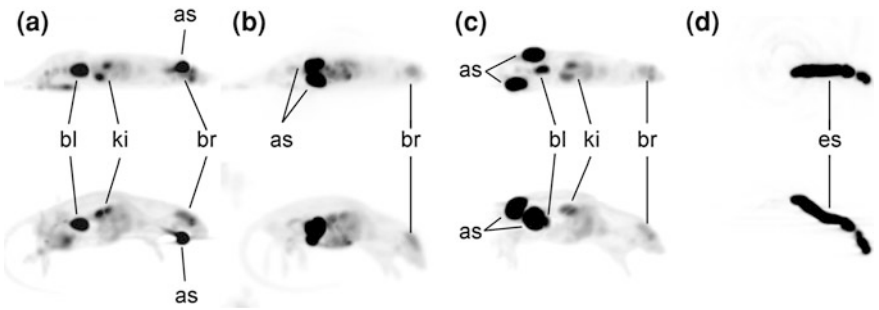

Fig. 8 Effect of administrative route on PET imaging at 30 min after **a** intravenous, **b** intraperitoneal, **c** subcutaneous and **d** oral administration of ^{18}F-FDG (20 MBq) in healthy rats: maximum intensity projections in anterior-posterior (*top*) and *right–left* (*bottom*) directions at 20 min after initiation of anesthesia with ketamine/xylazine. Identical window settings were applied in all cases. Annotations denote: *as* application site, *bl* bladder, *br* brain, *es* esophagus, *ki* kidneys

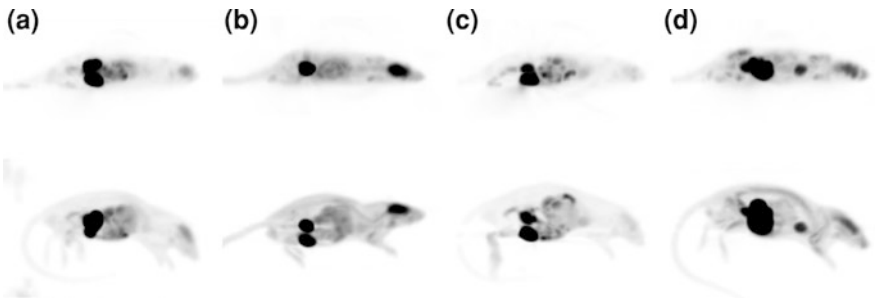

Fig. 9 Effect of fasting and anesthesia on PET imaging at 30 min after intraperitoneal administration of ^{18}F-FDG (20 MBq) in healthy rats: maximum intensity projections in anterior-posterior (*top*) and *right–left* (*bottom*) directions in fasting (**a**, **b**) and non-fasting (**c**, **d**) animals at 20 min prior to (**a**, **c**) or after (**b**, **d**) anesthesia initiation with ketamine/xylazine. Identical window settings were applied in all cases

Hampshire 2001). In turn, this may besides the animal's health status also affect metabolism and heart rate (Qiu et al. 1997). Body temperature was reported to have an influence on BOLD signal changes in response to vasomodulation by carbogen and corresponding invasive pO_2 electrode measurements in experimental squamous cell carcinoma (Reijnders et al. 2004). In this study, tumor pO_2 was lower and BOLD signal enhancement higher in animals maintained at 30 °C than at 37 °C, suggesting significant changes in oxygenation and/or blood flow in tumors with temperature. ^{18}F-FDG PET was found to be influenced also by temperature conditions (Fueger et al. 2006). Warming and fasting markedly improved visualization of tumor xenografts and reduced the intense ^{18}F-FDG uptake of brown adipose tissue. It may, therefore, be essential to monitor body temperature and provide external heating and insulation, especially for long time

experiments. Additionally, it must be kept in mind, that if an animal is very active after ^{18}F-FDG administration, high levels of ^{18}F-FDG can be detected in muscle tissues and proportionally decreased levels may be detected in the tumor.

The tolerable injection volume of exogenous substances is generally limited by the small circulating blood volume of small animals and largely depends on the administrative route (Diehl et al. 2001; Morton et al. 2001). For small animal PET imaging it must be, especially, kept in mind that due to radioactive decay the required tracer volume increases over time, which may lead to pharmacologic and/or physiologic effects. If PET is to be combined with contrast-enhanced computed tomography, one has to additionally note, that the low concentration and quick clearance from blood circulation of most iodinated CAs increase injection volume, thus potentially resulting in complications such as renal toxicity (Gale et al. 1984) and hypersensitivity reactions (Gueant-Rodriguez et al. 2006). However, animal-specific blood-pool CAs for computed tomography based on gold nanoparticles may reduce injected volumes, while providing low toxicity, viscosity and osmolality, longer blood retention and up to 10-fold or more contrast enhancement in comparison to conventional iodinated contrast agents (Hainfeld et al. 2006); thus, enabling the assessment of tumor vasculature (Cai et al. 2007a) and molecular imaging of cancer with computed tomography (Popovtzer et al. 2008).

9 Summary and Outlook

MI aims at understanding biological processes of cancer in vivo at the levels of compartments, organs, tissues, cells, or molecules. It has been proven in preclinical experiments as a powerful tool in cancer characterization and treatment monitoring, mainly facilitated by tremendous developments in imaging technology, and imaging probes. MRI and PET have in many aspects highlighted their potential as MI modalities. MRI is still challenged by its inherently low sensitivity, but efficient signal amplification strategies are pushing limits forward towards PET sensitivity. PET is limited by its low resolution although technological developments are slowly approaching maximum theoretically attainable resolution. Due to their very different nature and inherent strengths and weaknesses, MRI and PET should be used as complementary rather than competing modalities. Especially, the use of integrated PET/MRI scanner technology in combination with multifunctional imaging probes seems to be very promising for future applications to obtain highly sensitive molecular information at high spatial resolution. However, to fully exploit the potential of such multimodal MI approaches, multifunctional probes need to be optimized to promote both imaging modalities at the same time. In addition, probe development may concentrate on multi-purpose agents that combine diagnostic and therapeutic functionality, thus enabling theragnostic imaging.

MI has changed the way we are looking at tumors and shifts imaging paradigms away from classical morphological measures towards functional assessments, thus finally leading to personalized treatment of patients. Preclinical experiments in animal models have provided numerous diagnostic agents and imaging

approaches. These possibilities need to be selected and translated to clinical practice to diagnose disease and to monitor treatment. The selection of suitable experimental imaging methodology needs to be based on sound scientific rationale, substantial and immediate impacts on patient care, and easy accessibility to patients and referring clinicians. Considering these factors, PET and MRI will continue to be the dominant molecular imaging modalities for clinical imaging in near future. Furthermore, the successful translation into clinical applications will require thorough clinical validation of methods and careful correlation with established prognostic markers, standardization and active interdisciplinary collaboration among basic researchers, imaging experts and referring clinicians. Thus, higher investments in the quality of clinical studies are necessary. To better realize the potential of new developments for clinical translation already in an early preclinical stage, improved in vitro models and animal models of disease that closely represent patient requirements are highly needed. Currently available genomic information of species can be used to develop animal models that better recapitulate human disease at both the phenotypic and the genomic levels. Despite all challenges, MI is already approaching clinical reality (Josephs et al. 2009; Wong and Kim 2009).

Acknowledgments The authors thank Arne Koch for his exhaustive commitment, his assistance and responsibility. The authors are supported by the Federal Ministry of Education and Research, Germany (BMBF contract 03ZIK042).

References

Aboagye EO (2005) Positron emission tomography imaging of small animals in anticancer drug development. Mol Imaging Biol 7:53–58

Abolmaali N, Haase R, Koch A et al (2011) Two or four hour [^{18}F]FMISO-PET in HNSCC. When is the contrast best. Nuklearmedizin 50:22–27

Adonai N, Nguyen KN, Walsh J et al (2002) Ex vivo cell labeling with ^{64}Cu-pyruvaldehyde-bis(N4-methylthiosemicarbazone) for imaging cell trafficking in mice with positron-emission tomography. Proc Natl Acad Sci U S A 99:3030–3035

Ahrens ET, Rothbacher U, Jacobs RE et al (1998) A model for MRI contrast enhancement using T1 agents. Proc Natl Acad Sci U S A 95:8443–8448

Ahrens ET, Flores R, Xu H et al (2005) In vivo imaging platform for tracking immunotherapeutic cells. Nat Biotechnol 23:983–987

Aime S, Cabella C, Colombatto S et al (2002a) Insights into the use of paramagnetic Gd(III) complexes in MR-molecular imaging investigations. J Magn Reson Imaging 16:394–406

Aime S, Barge A, Castelli DD et al (2002b) Paramagnetic Lanthanide(III) complexes as pH-sensitive chemical exchange saturation transfer (CEST) contrast agents for MRI applications. Magn Reson Med 47:639–648

Aime S, Delli Castelli D, Fedeli F et al (2002c) A paramagnetic MRI-CEST agent responsive to lactate concentration. J Am Chem Soc 124:9364–9365

Aime S, Castelli DD, Terreno E (2005a) Highly sensitive MRI chemical exchange saturation transfer agents using liposomes. Angew Chem Int Ed Engl 44:5513–5515

Aime S, Carrera C, Castelli DD et al (2005b) Tunable imaging of cells labeled with MRI-PARACEST agents. Angew Chem Int Ed Engl 44:1813–1815

Aime S, Castelli DD, Crich SG et al (2009) Pushing the sensitivity envelope of lanthanide-based magnetic resonance imaging (MRI) contrast agents for molecular imaging applications. Acc Chem Res 42:822–831

Alessi P, Ebbinghaus C, Neri D (2004) Molecular targeting of angiogenesis. Biochim Biophys Acta Rev Cancer 1654:39–49

Ali MM, Yoo B, Pagel MD (2009a) Tracking the relative in vivo pharmacokinetics of nanoparticles with PARACEST MRI. Mol Pharm 6:1409–1416

Ali MM, Liu G, Shah T et al (2009b) Using two chemical exchange saturation transfer magnetic resonance imaging contrast agents for molecular imaging studies. Acc Chem Res 42:915–924

Allard M, Cote D, Davidson L et al (2007) Combined magnetic resonance and bioluminescence imaging of live mice. J Biomed Opt 12:034018

Ambrosini V, Quarta C, Nanni C et al (2009) Small animal PET in oncology: the road from bench to bedside. Cancer Biother Radiopharm 24:277–285

Arbab AS, Pandit SD, Anderson SA et al (2006) Magnetic resonance imaging and confocal microscopy studies of magnetically labeled endothelial progenitor cells trafficking to sites of tumor angiogenesis. Stem Cells 24:671–678

Artemov D (2003) Molecular magnetic resonance imaging with targeted contrast agents. J Cell Biochem 90:518–524

Asao C, Korogi Y, Kitajima M et al (2005) Diffusion-weighted imaging of radiation-induced brain injury for differentiation from tumor recurrence. Am J Neuroradiol 26:1455–1460

Bajada S, Mazakova I, Richardson JB et al (2008) Updates on stem cells and their applications in regenerative medicine. J Tissue Eng Regen Med 2:169–183

Balaban RS, Hampshire VA (2001) Challenges in small animal noninvasive imaging. ILAR J 42:248–262

Barrett T, Brechbiel M, Bernardo M et al (2007) MRI of tumor angiogenesis. J Magn Reson Imaging 26:235–249

Baudelet C, Gallez B (2002) How does blood oxygen level-dependent (BOLD) contrast correlate with oxygen partial pressure (pO_2) inside tumors? Magn Reson Med 48:980–986

Baudelet C, Gallez B (2004) Effect of anesthesia on the signal intensity in tumors using BOLD-MRI: comparison with flow measurements by Laser Doppler flowmetry and oxygen measurements by luminescence-based probes. Magn Reson Imaging 22:905–912

Baudelet C, Ansiaux R, Jordan BF et al (2004) Physiological noise in murine solid tumours using T_2*-weighted gradient-echo imaging: a marker of tumour acute hypoxia. Phys Med Biol 49:3389–3411

Beloueche-Babari M, Chung YL, Al-Saffar NM et al (2010) Metabolic assessment of the action of targeted cancer therapeutics using magnetic resonance spectroscopy. Br J Cancer 102:1–7

Bentzen L, Keiding S, Horsman MR et al (2002) Assessment of hypoxia in experimental mice tumours by [18F]fluoromisonidazole PET and pO_2 electrode measurements. Influence of tumour volume and carbogen breathing. Acta Oncol 41:304–312

Bergers G, Benjamin LE (2003) Tumorigenesis and the angiogenic switch. Nat Rev Cancer 3:401–410

Blankenberg FG (2008) In vivo detection of apoptosis. J Nucl Med 49(Suppl 2):81S–95S

Boerman OC, Oyen WJ (2008) Multimodality probes: amphibian cars for molecular imaging. J Nucl Med 49:1213–1214

Brauer M (2003) In vivo monitoring of apoptosis. Prog Neuropsychopharmacol Biol Psychiatry 27:323–331

Brockmann MA, Kemmling A, Groden C (2007) Current issues and perspectives in small rodent magnetic resonance imaging using clinical MRI scanners. Methods 43:79–87

Brown JM, Wilson WR (2004) Exploiting tumour hypoxia in cancer treatment. Nat Rev Cancer 4:437–447

Buck AK, Herrmann K, Shen C et al (2009) Molecular imaging of proliferation in vivo: positron emission tomography with [^{18}F]fluorothymidine. Methods 48:205–215

Bulte JW, Kraitchman DL (2004) Monitoring cell therapy using iron oxide MR contrast agents. Curr Pharm Biotechnol 5:567–584
Bulte JW (2005) Hot spot MRI emerges from the background. Nat Biotechnol 23:945–946
Bulte JW (2006) Intracellular endosomal magnetic labeling of cells. Methods Mol Med 124:419–439
Busk M, Horsman MR, Overgaard J (2008) Resolution in PET hypoxia imaging: voxel size matters. Acta Oncol 47:1201–1210
Busk M, Horsman MR, Jakobsen S et al (2009) Can hypoxia-PET map hypoxic cell density heterogeneity accurately in an animal tumor model at a clinically obtainable image contrast. Radiother Oncol 92:429–436
Cai QY, Kim SH, Choi KS et al (2007a) Colloidal gold nanoparticles as a blood-pool contrast agent for X-ray computed tomography in mice. Invest Radiol 42:797–806
Cai W, Chen K, Li ZB et al (2007b) Dual-function probe for PET and near-infrared fluorescence imaging of tumor vasculature. J Nucl Med 48:1862–1870
Cai W, Chen X (2008) Multimodality molecular imaging of tumor angiogenesis. J Nucl Med 49(Suppl 2):113S–128S
Caruthers SD, Winter PM, Wickline SA et al (2006) Targeted magnetic resonance imaging contrast agents. Methods Mol Med 124:387–400
Cassidy PJ, Radda GK (2005) Molecular imaging perspectives. J R Soc Interface 2:133–144
Catana C, Procissi D, Wu Y et al (2008) Simultaneous in vivo positron emission tomography and magnetic resonance imaging. Proc Natl Acad Sci U S A 105:3705–3710
Cauchon N, Langlois R, Rousseau JA et al (2007) PET imaging of apoptosis with ^{64}Cu-labeled streptavidin following pretargeting of phosphatidylserine with biotinylated annexin-V. Eur J Nucl Med Mol Imaging 34:247–258
Chang CH, Wang HE, Wu SY et al (2006) Comparative evaluation of FET and FDG for differentiating lung carcinoma from inflammation in mice. Anticancer Res 26:917–925
Chatziioannou AF (2002) Molecular imaging of small animals with dedicated PET tomographs. Eur J Nucl Med Mol Imaging 29:98–114
Chauvin T, Durand P, Bernier M et al (2008) Detection of enzymatic activity by PARACEST MRI: a general approach to target a large variety of enzymes. Angew Chem Int Ed Engl 47:4370–4372
Chen F, De Keyzer F, Wang H et al (2007) Diffusion weighted imaging in small rodents using clinical MRI scanners. Methods 43:12–20
Chen K, Cai W, Li ZB et al (2009) Quantitative PET imaging of VEGF receptor expression. Mol Imaging Biol 11:15–22
Chenevert TL, Sundgren PC, Ross BD (2006) Diffusion imaging: insight to cell status and cytoarchitecture. Neuroimaging Clin N Am 16:61–632, viii-ix
Cherry SR, Gambhir SS (2001) Use of positron emission tomography in animal research. ILAR J 42:219–232
Cherry SR (2006) The 2006 Henry N. Wagner lecture: of mice and men (and positrons)–advances in PET imaging technology. J Nucl Med 47:1735–1745
Christian N, Lee JA, Bol A et al (2008) Immobilization device for in vivo and in vitro multimodality image registration of rodent tumors. Radiother Oncol 87:147–151
Colby LA, Morenko BJ (2004) Clinical considerations in rodent bioimaging. Comp Med 54:623–630
Corsten MF, Shah K (2008) Therapeutic stem-cells for cancer treatment: hopes and hurdles in tactical warfare. Lancet Oncol 9:376–384
Crich SG, Biancone L, Cantaluppi V et al (2004) Improved route for the visualization of stem cells labeled with a Gd-/Eu-chelate as dual (MRI and fluorescence) agent. Magn Reson Med 51:938–944
Croft BY (2002) Animal models for imaging. Dis Markers 18:365–374
Culver J, Akers W, Achilefu S (2008) Multimodality molecular imaging with combined optical and SPECT/PET modalities. J Nucl Med 49:169–172
Cyran CC, Fu Y, Raatschen HJ et al (2008) New macromolecular polymeric MRI contrast agents for application in the differentiation of cancer from benign soft tissues. J Magn Reson Imaging 27:581–589

De Leon-Rodriguez LM, Lubag AJ, Malloy CR et al (2009) Responsive MRI agents for sensing metabolism in vivo. Acc Chem Res 42:948–957

Debatin KM, Krammer PH (2004) Death receptors in chemotherapy and cancer. Oncogene 23:2950–2966

Deng J, Rhee TK, Sato KT et al (2006) In vivo diffusion-weighted imaging of liver tumor necrosis in the VX2 rabbit model at 1.5 Tesla. Invest Radiol 41:410–414

Dennie J, Mandeville JB, Boxerman JL et al (1998) NMR imaging of changes in vascular morphology due to tumor angiogenesis. Magn Reson Med 40:793–799

Diehl KH, Hull R, Morton D et al (2001) A good practice guide to the administration of substances and removal of blood, including routes and volumes. J Appl Toxicol 21:15–23

Dierckx RA, Van de Wiele C (2008) FDG uptake, a surrogate of tumour hypoxia. Eur J Nucl Med Mol Imaging 35:1544–1549

Doubrovin M, Serganova I, Mayer-Kuckuk P et al (2004) Multimodality in vivo molecular-genetic imaging. Bioconjug Chem 15:1376–1388

Dubois L, Landuyt W, Haustermans K et al (2004) Evaluation of hypoxia in an experimental rat tumour model by [^{18}F]fluoromisonidazole PET and immunohistochemistry. Br J Cancer 91:1947–1954

Dubois L, Dresselaers T, Landuyt W et al (2007) Efficacy of gene therapy-delivered cytosine deaminase is determined by enzymatic activity but not expression. Br J Cancer 96:758–761

Ebenhan T, Honer M, Ametamey SM et al (2009) Comparison of [^{18}F]-tracers in various experimental tumor models by PET imaging and identification of an early response biomarker for the novel microtubule stabilizer patupilone. Mol Imaging Biol 11:308–321

European Commission (2010) Commission staff working paper: sixth report on the statistics on the number of animals used for experimental and other scientific purposes in the member states of the European Union. Report nr SEC(2010) 1107 final/2, COM(2010) 511 final/2. Released 08.12.2010, Brussels

Fan X, River JN, Zamora M et al (2002) Effect of carbogen on tumor oxygenation: combined fluorine-19 and proton MRI measurements. Int J Radiat Oncol Biol Phys 54:1202–1209

Fani M, Andre JP, Maecke HR (2008) 68 Ga-PET: a powerful generator-based alternative to cyclotron-based PET radiopharmaceuticals. Contrast Media Mol Imaging 3:67–77

Ferrara N, Gerber HP, LeCouter J (2003) The biology of VEGF and its receptors. Nat Med 9:669–676

Ferrara N, Kerbel RS (2005) Angiogenesis as a therapeutic target. Nature 438:967–974

Fink C, Kiessling F, Bock M et al (2003) High-resolution three-dimensional MR angiography of rodent tumors: morphologic characterization of intratumoral vasculature. J Magn Reson Imaging 18:59–65

Fischer BM, Olsen MW, Ley CD et al (2006) How few cancer cells can be detected by positron emission tomography? A frequent question addressed by an in vitro study. Eur J Nucl Med Mol Imaging 33:697–702

Flecknell PA (1993) Anaesthesia of animals for biomedical research. Br J Anaesth 71:885–894

Foster-Gareau P, Heyn C, Alejski A et al (2003) Imaging single mammalian cells with a 1.5 T clinical MRI scanner. Magn Reson Med 49:968–971

Foster PJ, Dunn EA, Karl KE et al (2008) Cellular magnetic resonance imaging: in vivo imaging of melanoma cells in lymph nodes of mice. Neoplasia 10:207–216

Fueger BJ, Czernin J, Hildebrandt I et al (2006) Impact of animal handling on the results of ^{18}F-FDG PET studies in mice. J Nucl Med 47:999–1006

Gagel B, Reinartz P, DiMartino E et al (2004) pO_2 polarography versus positron emission tomography ([^{18}F]Fluoromisonidazole, [^{18}F]-2-Fluoro-2′-Deoxyglucose). Strahlenther Onkol 180:616–622

Gale ME, Robbins AH, Hamburger RJ et al (1984) Renal toxicity of contrast agents: iopamidol, iothalamate, and diatrizoate. AJR Am J Roentgenol 142:333–335

Gatenby RA, Gillies RJ (2004) Why do cancers have high aerobic glycolysis. Nat Rev Cancer 4:891–899

Gilad AA, McMahon MT, Walczak P et al (2007) Artificial reporter gene providing MRI contrast based on proton exchange. Nat Biotechnol 25:217–219
Gilad AA, Ziv K, McMahon MT et al (2008) MRI reporter genes. J Nucl Med 49:1905–1908
Goertzen AL, Meadors AK, Silverman RW et al (2002) Simultaneous molecular and anatomical imaging of the mouse in vivo. Phys Med Biol 47:4315–4328
Golay X, Hendrikse J, Lim TC (2004) Perfusion imaging using arterial spin labeling. Top Magn Reson Imaging 15:10–27
Golman K, Olsson LE, Axelsson O et al (2003) Molecular imaging using hyperpolarized ^{13}C. Br J Radiol 76:S118–S127
Golman K, Zandt RI, Lerche M et al (2006) Metabolic imaging by hyperpolarized ^{13}C magnetic resonance imaging for in vivo tumor diagnosis. Cancer Res 66:10855–10860
Gore JC, Yankeelov TE, Peterson TE et al (2009) Molecular imaging without radiopharmaceuticals. J Nucl Med 50:999–1007
Graves EE, Weissleder R, Ntziachristos V (2004) Fluorescence molecular imaging of small animal tumor models. Curr Mol Med 4:419–430
Griffin JL, Shockcor JP (2004) Metabolic profiles of cancer cells. Nat Rev Cancer 4:551–561
Grönroos T, Bentzen L, Marjamäki P et al (2004) Comparison of the biodistribution of two hypoxia markers [^{18}F]FETNIM and [^{18}F]FMISO in an experimental mammary carcinoma. Eur J Nucl Med Mol Imaging 31:513–520
Gross S, Gilead A, Scherz A et al (2003) Monitoring photodynamic therapy of solid tumors online by BOLD-contrast MRI. Nat Med 9:1327–1331
Gueant-Rodriguez RM, Romano A, Barbaud A et al (2006) Hypersensitivity reactions to iodinated contrast media. Curr Pharm Des 12:3359–3372
Haase R, Böhme H-J, Zips D et al (2011) Swarm intelligence for medical volume segmentation: the contribution of self-reproduction. KI 2011: advances in artificial intelligence. Berlin 7006:111–121
Hainfeld JF, Slatkin DN, Focella TM et al (2006) Gold nanoparticles: a new X-ray contrast agent. Br J Radiol 79:248–253
Hakumaki JM, Liimatainen T (2005) Molecular imaging of apoptosis in cancer. Eur J Radiol 56:143–153
Hall EJ, Giaccia AJ (2006) Radiobiology for the radiologist. Lippincott Williams & Wilkins, Philadelphia
Hamstra DA, Lee KC, Tychewicz JM et al (2004) The use of ^{19}F spectroscopy and diffusion-weighted MRI to evaluate differences in gene-dependent enzyme prodrug therapies. Mol Ther 10:916–928
Hamstra DA, Rehemtulla A, Ross BD (2007) Diffusion magnetic resonance imaging: a biomarker for treatment response in oncology. J Clin Oncol 25:4104–4109
Hanahan D, Weinberg RA (2000) The hallmarks of cancer. Cell 100:57–70
Hanusch C, Hoeger S, Beck GC (2007) Anaesthesia of small rodents during magnetic resonance imaging. Methods 43:68–78
Hart LS, El-Deiry WS (2008) Invincible, but not invisible: imaging approaches toward in vivo detection of cancer stem cells. J Clin Oncol 26:2901–2910
Haubner R (2006) alpha(v)beta (3)-integrin imaging: a new approach to characterise angiogenesis? E. Eur J Nucl Med Mol Imaging 33(Suppl 13):54–63
He Q, Xu RZ, Shkarin P et al (2004) Magnetic resonance spectroscopic imaging of tumor metabolic markers for cancer diagnosis, metabolic phenotyping, and characterization of tumor microenvironment. Dis Markers 19:69–94
Hehlgans S, Haase M, Cordes N (2007) Signalling via integrins: implications for cell survival and anticancer strategies. Biochim Biophys Acta 1775:163–180
Hengartner MO (2000) The biochemistry of apoptosis. Nature 407:770–776
Herneth AM, Guccione S, Bednarski M (2003) Apparent diffusion coefficient: a quantitative parameter for in vivo tumor characterization. Eur J Radiol 45:208–213

Herschman HR (2004) PET reporter genes for noninvasive imaging of gene therapy, cell tracking and transgenic analysis. Crit Rev Oncol Hematol 51:191–204
Herzig M, Christofori G (2002) Recent advances in cancer research: mouse models of tumorigenesis. Biochim Biophys Acta 1602:97–113
Heyn C, Bowen CV, Rutt BK et al (2005) Detection threshold of single SPIO-labeled cells with FIESTA. Magn Reson Med 53:312–320
Heyn C, Ronald JA, Mackenzie LT et al (2006) In vivo magnetic resonance imaging of single cells in mouse brain with optical validation. Magn Reson Med 55:23–29
Hildebrandt IJ, Su H, Weber WA (2008) Anesthesia and other considerations for in vivo imaging of small animals. ILAR J 49:17–26
Hillen F, Griffioen AW (2007) Tumour vascularization: sprouting angiogenesis and beyond. Cancer Metastasis Rev 26:489–502
Himmelreich U, Dresselaers T (2009) Cell labeling and tracking for experimental models using magnetic resonance imaging. Methods 48:112–124
Hoff MN, Yapp DT, Yung AC et al (2008) In vivo measurement of the hypoxia marker EF5 in Shionogi tumours using ^{19}F magnetic resonance spectroscopy. Int J Radiat Biol 84:237–242
Hortelano S, Garcia-Martin ML, Cerdan S et al (2001) Intracellular water motion decreases in apoptotic macrophages after caspase activation. Cell Death Differ 8:1022–1028
Howe FA, Robinson SP, McIntyre DJO et al (2001) Issues in flow and oxygenation dependent contrast (FLOOD) imaging of tumours. NMR Biomed 14:497–506
Huang J, Lee CC, Sutcliffe JL et al (2008) Radiolabeling rhesus monkey CD34+ hematopoietic and mesenchymal stem cells with ^{64}Cu-pyruvaldehyde-bis(N4-methylthiosemicarbazone) for microPET imaging. Mol Imaging 7:1–11
Hylton N (2006) Dynamic contrast-enhanced magnetic resonance imaging as an imaging biomarker. J Clin Oncol 24:3293–3298
Hyodo F, Chandramouli GV, Matsumoto S et al (2009) Estimation of tumor microvessel density by MRI using a blood pool contrast agent. Int J Oncol 35:797–804
Jacobs AH, Rueger MA, Winkeler A et al (2007) Imaging-guided gene therapy of experimental gliomas. Cancer Res 67:1706–1715
Jain RK (2005) Normalization of tumor vasculature: an emerging concept in antiangiogenic therapy. Science 307:58–62
Johnson M, Karanikolas BD, Priceman SJ et al (2009) Titration of variant HSV1-tk gene expression to determine the sensitivity of ^{18}F-FHBG PET imaging in a prostate tumor. J Nucl Med 50:757–764
Josephs D, Spicer J, O'Doherty M (2009) Molecular imaging in clinical trials. Target Oncol 4:151–168
Judenhofer MS, Wehrl HF, Newport DF et al (2008) Simultaneous PET-MRI: a new approach for functional and morphological imaging. Nat Med 14:459–465
Kang JH, Chung JK (2008) Molecular-genetic imaging based on reporter gene expression. J Nucl Med 49(Suppl 2):164S–179S
Kauczor HU, Zechmann C, Stieltjes B et al (2006) Functional magnetic resonance imaging for defining the biological target volume. Cancer Imaging 6:51–55
Kelland LR (2004) Of mice and men: values and liabilities of the athymic nude mouse model in anticancer drug development. Eur J Cancer 40:827–836
Kiessling F, Jugold M, Woenne EC et al (2007) Non-invasive assessment of vessel morphology and function in tumors by magnetic resonance imaging. Eur Radiol 17:2136–2148
Kiessling F, Huppert J, Palmowski M (2009) Functional and molecular ultrasound imaging: concepts and contrast agents. Curr Med Chem 16:627–642
Kim D, Hong KS, Song J (2007) The present status of cell tracking methods in animal models using magnetic resonance imaging technology. Mol Cells 23:132–137
Kim H, Morgan DE, Zeng H et al (2008a) Breast tumor xenografts: diffusion-weighted MR imaging to assess early therapy with novel apoptosis-inducing anti-DR5 antibody. Radiology 248:844–851

Kim H, Morgan DE, Buchsbaum DJ et al (2008b) Early therapy evaluation of combined anti-death receptor 5 antibody and gemcitabine in orthotopic pancreatic tumor xenografts by diffusion-weighted magnetic resonance imaging. Cancer Res 68:8369–8376

Kim S, Loevner L, Quon H et al (2009) Diffusion-weighted magnetic resonance imaging for predicting and detecting early response to chemoradiation therapy of squamous cell carcinomas of the head and neck. Clin Cancer Res 15:986–994

Kim YR, Yudina A, Figueiredo J et al (2005) Detection of early antiangiogenic effects in human colon adenocarcinoma xenografts: in vivo changes of tumor blood volume in response to experimental VEGFR tyrosine kinase inhibitor. Cancer Res 65:9253–9260

Knopp MV, Giesel FL, Marcos H et al (2001) Dynamic contrast-enhanced magnetic resonance imaging in oncology. Top Magn Reson Imaging 12:301–308

Koch U, Krause M, Baumann M (2010) Cancer stem cells at the crossroads of current cancer therapy failures-radiation oncology perspective. Semin Cancer Biol 20:116–124

Kodibagkar VD, Wang X, Pacheco-Torres J et al (2008) Proton imaging of siloxanes to map tissue oxygenation levels (PISTOL): a tool for quantitative tissue oximetry. NMR Biomed 21:899–907

Koo V, Hamilton PW, Williamson K (2006) Non-invasive in vivo imaging in small animal research. Cell Oncol 28:127–139

Kosztowski T, Zaidi HA, Quinones-Hinojosa A (2009) Applications of neural and mesenchymal stem cells in the treatment of gliomas. Expert Rev Anticancer Ther 9:597–612

Krohn KA, Link JM, Mason RP (2008) Molecular imaging of hypoxia. J Nucl Med 49(Suppl 2):129S–148S

Kubota T (1994) Metastatic models of human cancer xenografted in the nude mouse: the importance of orthotopic transplantation. J Cell Biochem 56:4–8

Kuhn LT, Bommerich U, Bargon J (2006) Transfer of parahydrogen-induced hyperpolarization to 19F. J Phys Chem A 110:3521–3526

Lahorte CM, Vanderheyden JL, Steinmetz N et al (2004) Apoptosis-detecting radioligands: current state of the art and future perspectives. Eur J Nucl Med Mol Imaging 31:887–919

LaManna JC, Harik SI (1986) Regional studies of blood-brain barrier transport of glucose and leucine in awake and anesthetized rats. J Cereb Blood Flow Metab 6:717–723

Landuyt W, Hermans R, Bosmans H et al (2001) BOLD contrast fMRI of whole rodent tumour during air or carbogen breathing using echo-planar imaging at 1.5 T. Eur Radiol 11:2332–2340

Lee HY, Li Z, Chen K et al (2008) PET/MRI dual-modality tumor imaging using arginine-glycine-aspartic (RGD)-conjugated radiolabeled iron oxide nanoparticles. J Nucl Med 49:1371–1379

Lee JH, Lee K, Moon SH et al (2009) All-in-one target-cell-specific magnetic nanoparticles for simultaneous molecular imaging and siRNA delivery. Angew Chem Int Ed Engl 48:4174–4179

Lee KH, Ko BH, Paik JY et al (2005) Effects of anesthetic agents and fasting duration on 18F-FDG biodistribution and insulin levels in tumor-bearing mice. J Nucl Med 46:1531–1536

Li AX, Wojciechowski F, Suchy M et al (2008a) A sensitive PARACEST contrast agent for temperature MRI: Eu3+-DOTAM-glycine (Gly)-phenylalanine (Phe). Magn Reson Med 59:374–381

Li S, Xue HD, Wang XH et al (2008b) MR diffusion weighted imaging for evaluation of radiotherapeutic effects on rabbit VX2 tumor model. Chin Med Sci J 23:172–177

Li ZB, Chen K, Wu Z et al (2009) ^{64}Cu-labeled PEGylated polyethylenimine for cell trafficking and tumor imaging. Mol Imaging Biol 11:415–423

Liang HD, Blomley MJ (2003) The role of ultrasound in molecular imaging. Br J Radiol 76 Spec No 2:S140–150

Liimatainen T, Hakumaki JM, Kauppinen RA et al (2009) Monitoring of gliomas in vivo by diffusion MRI and (1)H MRS during gene therapy-induced apoptosis: interrelationships between water diffusion and mobile lipids. NMR Biomed 22:272–279

Lin CY, Lin MH, Cheung WM et al (2009) In vivo cerebromicrovasculatural visualization using 3D DeltaR2-based microscopy of magnetic resonance angiography (3DDeltaR2-mMRA). Neuroimage 45:824–831

Liu Z, Yan Y, Chin FT et al (2009) Dual integrin and gastrin-releasing peptide receptor targeted tumor imaging using ^{18}F-labeled PEGylated RGD-bombesin heterodimer ^{18}F-FB-PEG3-Glu-RGD-BBN. J Med Chem 52:425–432

Lukasik VM, Gillies RJ (2003) Animal anaesthesia for in vivo magnetic resonance. NMR Biomed 16:459–467

Mahmood U, Josephson L (2005) Molecular MR Imaging Probes. Proc IEEE Inst Electr Electron Eng 93:800–808

Major JL, Meade TJ (2009) Bioresponsive, cell-penetrating, and multimeric MR contrast agents. Acc Chem Res 42:893–903

Maramraju SH, Smith SD, Junnarkar SS et al (2011) Small animal simultaneous PET/MRI: initial experiences in a 9.4 T microMRI. Phys Med Biol 56:2459–2480

Matsumura A, Isobe T, Takano S et al (2005) Non-invasive quantification of lactate by proton MR spectroscopy and its clinical applications. Clin Neurol Neurosurg 107:379–384

McConathy J, Goodman MM (2008) Non-natural amino acids for tumor imaging using positron emission tomography and single photon emission computed tomography. Cancer Metastasis Rev 27:555–573

McMahon MT, Gilad AA, DeLiso MA et al (2008) New "multicolor" polypeptide diamagnetic chemical exchange saturation transfer (DIACEST) contrast agents for MRI. Magn Reson Med 60:803–812

Medarova Z, Pham W, Farrar C et al (2007) In vivo imaging of siRNA delivery and silencing in tumors. Nat Med 13:372–377

Mees G, Dierckx R, Vangestel C et al (2009) Molecular imaging of hypoxia with radiolabelled agents. Eur J Nucl Med Mol Imaging 36:1674–1686

Meng Y, Lei H (2009) A novel continuous arterial spin labeling approach for CBF measurement in rats with reduced labeling time and optimized signal-to-noise ratio efficiency. MAGMA 22:135–142

Miletic H, Fischer Y, Litwak S et al (2007) Bystander killing of malignant glioma by bone marrow-derived tumor-infiltrating progenitor cells expressing a suicide gene. Mol Ther 15:1373–1381

Milkiewicz M, Ispanovic E, Doyle JL et al (2006) Regulators of angiogenesis and strategies for their therapeutic manipulation. Int J Biochem Cell Biol 38:333–357

Mirus M, Tokalov SV, Koch A et al (2010) Effects of co-transplantation of endothelial cells on the vascularization of human tumor xenografts. Eur J Cell Biol 89(S1):22

Mishra NC, Kumar S (2005) Apoptosis: a mitochondrial perspective on cell death. Indian J Exp Biol 43:25–34

Modo M, Hoehn M, Bulte JW (2005) Cellular MR imaging. Mol Imaging 4:143–164

Moffat BA, Hall DE, Stojanovska J et al (2004) Diffusion imaging for evaluation of tumor therapies in preclinical animal models. Magma 17:249–259

Moffat BA, Chenevert TL, Hall DE et al (2005) Continuous arterial spin labeling using a train of adiabatic inversion pulses. J Magn Reson Imaging 21:290–296

Moffat BA, Chen M, Kariaapper MS et al (2006) Inhibition of vascular endothelial growth factor (VEGF)-A causes a paradoxical increase in tumor blood flow and up-regulation of VEGF-D. Clin Cancer Res 12:1525–1532

Morawski AM, Winter PM, Crowder KC et al (2004) Targeted nanoparticles for quantitative imaging of sparse molecular epitopes with MRI. Magn Reson Med 51:480–486

Morawski AM, Lanza GA, Wickline SA (2005) Targeted contrast agents for magnetic resonance imaging and ultrasound. Curr Opin Biotechnol 16:89–92

Mori T, Nomori H, Ikeda K et al (2008) Diffusion-weighted magnetic resonance imaging for diagnosing malignant pulmonary nodules/masses: comparison with positron emission tomography. J Thorac Oncol 3:358–364

Morton DB, Jennings M, Buckwell A et al (2001) Refining procedures for the administration of substances. report of the BVAAWF/FRAME/RSPCA/UFAW joint working group on refinement. British veterinary association animal welfare foundation/fund for the replacement of animals in medical experiments/royal society for the prevention of cruelty to animals/ universities federation for animal welfare. Lab Anim 35:1–41

Muja N, Bulte JWM (2009) Magnetic resonance imaging of cells in experimental disease models. Progr NMR Spectrosc 55:61–77

Mulder WJ, Castermans K, van Beijnum JR et al (2009a) Molecular imaging of tumor angiogenesis using alphavbeta3-integrin targeted multimodal quantum dots. Angiogenesis 12:17–24

Mulder WJ, Strijkers GJ, van Tilborg GA et al (2009b) Nanoparticulate assemblies of amphiphiles and diagnostically active materials for multimodality imaging. Acc Chem Res 42:904–914

Mulder WJM, Strijkers GJ, Tilborg GAFv et al (2006) Lipid-based nanoparticles for contrast-enhanced MRI and molecular imaging. NMR Biomed 19:142–164

Murakami R, Sugahara T, Nakamura H et al (2007) Malignant supratentorial astrocytoma treated with postoperative radiation therapy: prognostic value of pretreatment quantitative diffusion-weighted MR imaging. Radiology 243:493–499

Murayama C, Harada N, Kakiuchi T et al (2009) Evaluation of D-^{18}F-FMT, ^{18}F-FDG, L-^{11}C-MET, and ^{18}F-FLT for monitoring the response of tumors to radiotherapy in mice. J Nucl Med 50:290–295

Muruganandham M, Alfieri AA, Matei C et al (2005) Metabolic signatures associated with a NAD synthesis inhibitor-induced tumor apoptosis identified by ^{1}H-decoupled-^{31}P magnetic resonance spectroscopy. Clin Cancer Res 11:3503–3513

Muruganandham M, Lupu M, Dyke JP et al (2006) Preclinical evaluation of tumor microvascular response to a novel antiangiogenic/antitumor agent RO0281501 by dynamic contrast-enhanced MRI at 1.5 T. Mol Cancer Ther 5:1950–1957

Neeman M, Gilad AA, Dafni H et al (2007) Molecular imaging of angiogenesis. J Magn Reson Imaging 25:1–12

Nehmeh SA, Lee NY, Schroder H et al (2008) Reproducibility of intratumor distribution of (18)F-fluoromisonidazole in head and neck cancer. Int J Radiat Oncol Biol Phys 70:235–242

Neufeld G, Cohen T, Gengrinovitch S et al (1999) Vascular endothelial growth factor (VEGF) and its receptors. FASEB J 13:9–22

Ni Y, Wang H, Chen F et al (2009) Tumor models and specific contrast agents for small animal imaging in oncology. Methods 48:125–138

Nomori H, Mori T, Ikeda K et al (2008) Diffusion-weighted magnetic resonance imaging can be used in place of positron emission tomography for N staging of non-small cell lung cancer with fewer false-positive results. J Thorac Cardiovasc Surg 135:816–822

O'Connor JPB, Watson Y, Jackson A (2007) Dynamic contrast-enhanced MR imaging in cancer. Radiography 13:e45–e53

O'Donoghue JA, Zanzonico P, Pugachev A et al (2005) Assessment of regional tumor hypoxia using ^{18}F-fluoromisonidazole and ^{64}Cu(II)-diacetyl-bis(N4-methylthiosemicarbazone) positron emission tomography: comparative study featuring microPET imaging, Po2 probe measurement, autoradiography, and fluorescent microscopy in the R3327-AT and FaDu rat tumor models. Int J Radiat Oncol Biol Phys 61:1493–1502

Oka S, Hattori R, Kurosaki F et al (2007) A preliminary study of anti-1-amino-3-^{18}F-fluorocyclobutyl-1-carboxylic acid for the detection of prostate cancer. J Nucl Med 48:46–55

Olasz EB, Lang L, Seidel J et al (2002) Fluorine-18 labeled mouse bone marrow-derived dendritic cells can be detected in vivo by high resolution projection imaging. J Immunol Methods 260:137–148

Ostrand-Rosenberg S (2004) Animal models of tumor immunity, immunotherapy and cancer vaccines. Curr Opin Immunol 16:143–150

Padhani AR, Krohn KA, Lewis JS et al (2007) Imaging oxygenation of human tumours. Eur Radiol 17:861–872

Padhani AR, Liu G, Mu-Koh D et al (2009) Diffusion-weighted magnetic resonance imaging as a cancer biomarker: consensus and recommendations. Neoplasia 11:102–125

Partlow KC, Chen J, Brant JA et al (2007) ^{19}F magnetic resonance imaging for stem/progenitor cell tracking with multiple unique perfluorocarbon nanobeacons. FASEB J 21:1647–1654

Patterson DM, Padhani AR, Collins DJ (2008) Technology insight: water diffusion MRI–a potential new biomarker of response to cancer therapy. Nat Rev Clin Oncol 5:220–233

Petersen ET, Zimine I, Ho YC et al (2006) Non-invasive measurement of perfusion: a critical review of arterial spin labelling techniques. Br J Radiol 79:688–701

Pickles MD, Gibbs P, Lowry M et al (2006) Diffusion changes precede size reduction in neoadjuvant treatment of breast cancer. Magn Reson Imaging 24:843–847

Piert M, Machulla H-J, Picchio M et al (2005) Hypoxia-specific tumor imaging with 18f-fluoroazomycin arabinoside. J Nucl Med 46:106–113

Podichetty AK, Wagner S, Schroer S et al (2009) Fluorinated isatin derivatives. Part 2. New N-substituted 5-pyrrolidinylsulfonyl isatins as potential tools for molecular imaging of caspases in apoptosis. J Med Chem 52:3484–3495

Popovtzer R, Agrawal A, Kotov NA et al (2008) Targeted gold nanoparticles enable molecular ct imaging of cancer. Nano Lett 8:4593–4596

Preda A, van Vliet M, Krestin GP et al (2006) Magnetic resonance macromolecular agents for monitoring tumor microvessels and angiogenesis inhibition. Invest Radiol 41:325–331

Procissi D, Claus F, Burgman P et al (2007) In vivo ^{19}F magnetic resonance spectroscopy and chemical shift imaging of tri-fluoro-nitroimidazole as a potential hypoxia reporter in solid tumors. Clin Cancer Res 13:3738–3747

Pugachev A, Ruan S, Carlin S et al (2005) Dependence of FDG uptake on tumor microenvironment. Int J Radiat Oncol Biol Phys 62:545–553

Qiu HH, Cofer GP, Hedlund LW et al (1997) Automated feedback control of body temperature for small animal studies with MR microscopy. IEEE Trans Biomed Eng 44:1107–1113

Rad AM, Iskander AS, Janic B et al (2009) AC133+ progenitor cells as gene delivery vehicle and cellular probe in subcutaneous tumor models: a preliminary study. BMC Biotechnol 9:28

Raman V, Pathak AP, Glunde K et al (2007) Magnetic resonance imaging and spectroscopy of transgenic models of cancer. NMR Biomed 20:186–199

Reichardt W, Hu-Lowe D, Torres D et al (2005) Imaging of VEGF receptor kinase inhibitor-induced antiangiogenic effects in drug-resistant human adenocarcinoma model. Neoplasia 7:847–853

Reichardt W, Juettner E, Uhl M et al (2009) Diffusion-weighted imaging as predictor of therapy response in an animal model of ewing sarcoma. Invest Radiol 44:298–303

Reijnders K, English SJ, Krishna MC et al (2004) Influence of body temperature on the BOLD effect in murine SCC tumors. Magn Reson Med 51:389–393

Ren J, Trokowski R, Zhang S et al (2008) Imaging the tissue distribution of glucose in livers using a PARACEST sensor. Magn Reson Med 60:1047–1055

Robinson SP, Rijken PF, Howe FA et al (2003) Tumor vascular architecture and function evaluated by non-invasive susceptibility MRI methods and immunohistochemistry. J Magn Reson Imaging 17:445–454

Robinson SP, Griffiths JR (2004) Current issues in the utility of ^{19}F nuclear magnetic resonance methodologies for the assessment of tumour hypoxia. Philos Trans R Soc Lond B Biol Sci 359:987–996

Robinson SP, Ludwig C, Paulsson J et al (2008) The effects of tumor-derived platelet-derived growth factor on vascular morphology and function in vivo revealed by susceptibility MRI. Int J Cancer 122:1548–1556

Rodrigues LM, Howe FA, Griffiths JR et al (2004) Tumor R_2* is a prognostic indicator of acute radiotherapeutic response in rodent tumors. J Magn Reson Imaging 19:482–488

Rommel D, Abarca-Quinones J, Christian N et al (2008) Alginate moulding: an empirical method for magnetic resonance imaging/positron emission tomography co-registration in a tumor rat model. Nucl Med Biol 35:571–577

Rossin R, Berndorff D, Friebe M et al (2007) Small-animal PET of tumor angiogenesis using a (76)Br-labeled human recombinant antibody fragment to the ED-B domain of fibronectin. J Nucl Med 48:1172–1179

Roth Y, Tichler T, Kostenich G et al (2004) High-b-value diffusion-weighted MR imaging for pretreatment prediction and early monitoring of tumor response to therapy in mice. Radiology 232:685–692

Ruf J, Amthauer H, Oettle H et al (2004) Role of F^{18}-FDG PET for monitoring of radiochemotherapy: estimation of detectable number of tumour cells. Onkologie 27:287–290

Saleem A, Charnley N, Price P (2006) Clinical molecular imaging with positron emission tomography. Eur J Cancer 42:1720–1727

Salmon HW, Siemann DW (2004) Utility of ^{19}F MRS detection of the hypoxic cell marker EF5 to assess cellular hypoxia in solid tumors. Radiother Oncol 73:359–366

Schein PS, Scheffler B (2006) Barriers to efficient development of cancer therapeutics. Clin Cancer Res 12:3243–3248

Schellenberger EA, Bogdanov A Jr, Hogemann D et al (2002) Annexin V-CLIO: a nanoparticle for detecting apoptosis by MRI. Mol Imaging 1:102–107

Schindler S, Tokalov S, Wolf G et al (2010) Mesenchymal progenitor cells visualized in a clinical 1.5 Tesla MRI. Cell Oncol 32:237

Schmieder AH, Winter PM, Caruthers SD et al (2005) Molecular MR imaging of melanoma angiogenesis with alphanubeta3-targeted paramagnetic nanoparticles. Magn Reson Med 53:621–627

Schuh JC (2004) Trials, tribulations, and trends in tumor modeling in mice. Toxicol Pathol 32(Suppl 1):53–66

Scott CE, Adebodun F (1999) ^{13}C-NMR investigation of protein synthesis during apoptosis in human leukemic cell lines. J Cell Physiol 181:147–152

Segers J, Laumonier C, Burtea C et al (2007) From phage display to magnetophage, a new tool for magnetic resonance molecular imaging. Bioconjug Chem 18:1251–1258

Serganova I, Blasberg R (2005) Reporter gene imaging: potential impact on therapy. Nucl Med Biol 32:763–780

Shah K, Weissleder R (2005) Molecular optical imaging: applications leading to the development of present day therapeutics. NeuroRx 2:215–225

Sharpless NE, Depinho RA (2006) The mighty mouse: genetically engineered mouse models in cancer drug development. Nat Rev Drug Discov 5:741–754

Shu CJ, Radu CG, Shelly SM et al (2009) Quantitative PET reporter gene imaging of CD8+ T cells specific for a melanoma-expressed self-antigen. Int Immunol 21:155–165

Silva AC, Kim SG, Garwood M (2000) Imaging blood flow in brain tumors using arterial spin labeling. Magn Reson Med 44:169–173

Song SK, Qu Z, Garabedian EM et al (2002) Improved magnetic resonance imaging detection of prostate cancer in a transgenic mouse model. Cancer Res 62:1555–1558

Strijkers GJ, Mulder WJ, van Tilborg GA et al (2007) MRI contrast agents: current status and future perspectives. Anticancer Agents Med Chem 7:291–305

Suggitt M, Bibby MC (2005) 50 years of preclinical anticancer drug screening: empirical to target-driven approaches. Clin Cancer Res 11:971–981

Sun X, Wang H, Chen F et al (2009) Diffusion-weighted MRI of hepatic tumor in rats: comparison between in vivo and postmortem imaging acquisitions. J Magn Reson Imaging 29:621–628

Sun Y, Schmidt NO, Schmidt K et al (2004) Perfusion MRI of U87 brain tumors in a mouse model. Magn Reson Med 51:893–899

Szczesny G, Veihelmann A, Massberg S et al (2004) Long-term anaesthesia using inhalatory isoflurane in different strains of mice-the haemodynamic effects. Lab Anim 38:64–69

Talmadge JE, Singh RK, Fidler IJ et al (2007) Murine models to evaluate novel and conventional therapeutic strategies for cancer. Am J Pathol 170:793–804

Taschereau R, Chatziioannou AF (2007) Monte Carlo simulations of absorbed dose in a mouse phantom from 18-fluorine compounds. Med Phys 34:1026–1036

Tatum JL, Kelloff GJ, Gillies RJ et al (2006) Hypoxia: importance in tumor biology, noninvasive measurement by imaging, and value of its measurement in the management of cancer therapy. Int J Radiat Biol 82:699–757

Taupitz M, Schmitz S, Hamm B (2003) Superparamagnetic iron oxide particles: current state and future development. Rofo 175:752–765

Thakur M, Lentle BC (2005) Report of a summit on molecular imaging. Radiology 236:753–755

Thoeny HC, De Keyzer F, Vandecaveye V et al (2005) Effect of vascular targeting agent in rat tumor model: dynamic contrast-enhanced versus diffusion-weighted MR imaging. Radiology 237:492–499

Tokalov SV, Heinold J, Koch A et al (2010) Analysis of the cellular glucose metabolism in small animals by positron emission tomography using a clinical scanner. Eur J Cell Biol 89(S1):33

Topal A, Gul N, Ilcol Y et al (2003) Hepatic effects of halothane, isoflurane or sevoflurane anaesthesia in dogs. J Vet Med A Physiol Pathol Clin Med 50:530–533

Towner R, Smith N, Asano Y et al (2010) Molecular MRI approaches used to aid in the understanding of angiogenesis in vivo: implications for tissue engineering. Tissue Eng Part A 16:357–364

Toyama H, Ichise M, Liow JS et al (2004) Evaluation of anesthesia effects on [^{18}F]FDG uptake in mouse brain and heart using small animal PET. Nucl Med Biol 31:251–256

Tropres I, Grimault S, Vaeth A et al (2001) Vessel size imaging. Magn Reson Med 45:397–408

Tropres I, Lamalle L, Peoc'h M et al (2004) In vivo assessment of tumoral angiogenesis. Magn Reson Med 51:533–541

Turetschek K, Preda A, Novikov V et al (2004) Tumor microvascular changes in antiangiogenic treatment: assessment by magnetic resonance contrast media of different molecular weights. J Magn Reson Imaging 20:138–144

Valable S, Lemasson B, Farion R et al (2008) Assessment of blood volume, vessel size, and the expression of angiogenic factors in two rat glioma models: a longitudinal in vivo and ex vivo study. NMR Biomed 21:1043–1056

Valonen PK, Lehtimaki KK, Vaisanen TH et al (2004) Water diffusion in a rat glioma during ganciclovir-thymidine kinase gene therapy-induced programmed cell death in vivo: correlation with cell density. J Magn Reson Imaging 19:389–396

van Waarde A, Elsinga PH (2008) Proliferation markers for the differential diagnosis of tumor and inflammation. Curr Pharm Des 14:3326–3339

Vandecaveye V, de Keyzer F, Vander Poorten V et al (2006) Evaluation of the larynx for tumour recurrence by diffusion-weighted MRI after radiotherapy: initial experience in four cases. Br J Radiol 79:681–687

Vaupel P, Mayer A (2007) Hypoxia in cancer: significance and impact on clinical outcome. Cancer Metastasis Rev 26:225–239

Vogel-Claussen J, Gimi B, Artemov D et al (2007) Diffusion-weighted and macromolecular contrast enhanced MRI of tumor response to antivascular therapy with ZD6126. Cancer Biol Ther 6:1469–1475

Voskoglou-Nomikos T, Pater JL, Seymour L (2003) Clinical predictive value of the in vitro cell line, human xenograft, and mouse allograft preclinical cancer models. Clin Cancer Res 9:4227–4239

Waerzeggers Y, Monfared P, Viel T et al (2009) Methods to monitor gene therapy with molecular imaging. Methods 48:146–160

Walenta S, Schroeder T, Mueller-Klieser W (2004) Lactate in solid malignant tumors: potential basis of a metabolic classification in clinical oncology. Curr Med Chem 11:2195–2204

Walenta S, Mueller-Klieser WF (2004) Lactate: mirror and motor of tumor malignancy. Semin Radiat Oncol 14:267–274

Wang H, Cai W, Chen K et al (2007) A new PET tracer specific for vascular endothelial growth factor receptor. Eur J Nucl Med Mol Imaging 34:2001–2010

Wang H, Sun X, Chen F et al (2009) Treatment of rodent liver tumor with combretastatin a4 phosphate: noninvasive therapeutic evaluation using multiparametric magnetic resonance imaging in correlation with microangiography and histology. Invest Radiol 44:44–53

Wang HE, Yu HM, Liu RS et al (2006) Molecular imaging with ^{123}I-FIAU, ^{18}F-FUdR, ^{18}F-FET, and ^{18}F-FDG for monitoring herpes simplex virus type 1 thymidine kinase and ganciclovir prodrug activation gene therapy of cancer. J Nucl Med 47:1161–1171

Wang K, Wang K, Shen B et al (2010) MR reporter gene imaging of endostatin expression and therapy. Mol Imaging Biol 12:520–529

Ward KM, Aletras AH, Balaban RS (2000) A new class of contrast agents for MRI based on proton chemical exchange dependent saturation transfer (CEST). J Magn Reson 143:79–87

Warmuth C, Gunther M, Zimmer C (2003) Quantification of blood flow in brain tumors: comparison of arterial spin labeling and dynamic susceptibility-weighted contrast-enhanced MR imaging. Radiology 228:523–532

Waters EA, Chen J, Yang X et al (2008) Detection of targeted perfluorocarbon nanoparticle binding using ^{19}F diffusion weighted MR spectroscopy. Magn Reson Med 60:1232–1236

Weber MA, Gunther M, Lichy MP et al (2003) Comparison of arterial spin-labeling techniques and dynamic susceptibility-weighted contrast-enhanced MRI in perfusion imaging of normal brain tissue. Invest Radiol 38:712–718

Wehrl HF, Judenhofer MS, Wiehr S et al (2009) Pre-clinical PET/MR: technological advances and new perspectives in biomedical research. Eur J Nucl Med Mol Imaging 36(Suppl 1): S56–S68

Weinmann M, Belka C, Plasswilm L (2004) Tumour hypoxia: impact on biology, prognosis and treatment of solid malignant tumours. Onkologie 27:83–90

Williams KJ, Cowen RL, Brown LM et al (2004) Hypoxia in tumors: molecular targets for anti-cancer therapeutics. Adv Enzyme Regul 44:93–108

Willmann JK, Cheng Z, Davis C et al (2008) Targeted microbubbles for imaging tumor angiogenesis: assessment of whole-body biodistribution with dynamic micro-PET in mice. Radiology 249:212–219

Winnard PT Jr, Pathak AP, Dhara S et al (2008) Molecular imaging of metastatic potential. J Nucl Med 49(Suppl 2):96S–112S

Wolf G, Grüner S, Schindler S et al (2007) Diffusionsgewichtete und morphologische Ganzkörper-MRT der Ratte bei 1.5 T. RoFo 179:S272

Wolf G, Abolmaali N (2009) Imaging tumour-bearing animals using clinical scanners. Int J Radiat Biol 85:752–762

Wolf G, Tokalov S, Mirus M et al (2010) Quantifying vascularity in human tumor xenograft models using clinical scanners. Eur Radiol 20(Suppl 1):S287

Wolf G, Laniado M, Abolmaali N et al (2012a) Development of a tissue-equivalent phantom for standardisation of diffusion-weighted MRI. Insights Imaging 3(Suppl 1):S167

Wolf G, De Keyzer F, Paulus T et al (2012b) Towards standardisation of diffusion-weighted MRI: status survey across instruments using a tissue-equivalent phantom. Insights Imaging 3(Suppl 1):S168

Wong FC, Kim EE (2009) A review of molecular imaging studies reaching the clinical stage. Eur J Radiol 70:205–211

Woods M, Woessner DE, Sherry AD (2006) Paramagnetic lanthanide complexes as PARACEST agents for medical imaging. Chem Soc Rev 35:500–511

Wu EX, Tang H, Jensen JH (2004) Applications of ultrasmall superparamagnetic iron oxide contrast agents in the MR study of animal models. NMR Biomed 17:478–483

Wyss C, Schaefer SC, Juillerat-Jeanneret L et al (2009) Molecular imaging by micro-CT: specific E-selectin imaging. Eur Radiol 19:2487–2494

Wyss M, Honer M, Schubiger P et al (2006) NanoPET imaging of [^{18}F]fluoromisonidazole uptake in experimental mouse tumours. Eur J Nucl Med Mol Imaging (in press)

Xue HD, Li S, Sun HY et al (2008) Experimental study of inflammatory and metastatic lymph nodes with diffusion weighted imaging on animal model: comparison with conventional methods. Chin Med Sci J 23:166–171

Yamamoto S, Imaizumi M, Kanai Y et al (2010) Design and performance from an integrated PET/MRI system for small animals. Ann Nucl Med 24:89–98

Yan G-P, Robinson L, Hogg P (2007) Magnetic resonance imaging contrast agents: overview and perspectives. Radiography 13:e5–e19

Ye FQ, Berman KF, Ellmore T et al (2000) $H_2{}^{15}O$ PET validation of steady-state arterial spin tagging cerebral blood flow measurements in humans. Magn Reson Med 44:450–456

Yoo B, Raam MS, Rosenblum RM et al (2007) Enzyme-responsive PARACEST MRI contrast agents: a new biomedical imaging approach for studies of the proteasome. Contrast Media Mol Imaging 2:189–198

Youn BJ, Chung JW, Son KR et al (2008) Diffusion-weighted MR: therapeutic evaluation after chemoembolization of VX-2 carcinoma implanted in rabbit liver. Acad Radiol 15:593–600

Yu JX, Kodibagkar VD, Cui W et al (2005) ^{19}F: a versatile reporter for non-invasive physiology and pharmacology using magnetic resonance. Curr Med Chem 12:819–848

Yuji K, Songji Z, Toshiki T et al (2009) Molecular imaging of apoptosis with radio-labeled annexin A5 focused on the evaluation of tumor response to chemotherapy. Anticancer Agents Med Chem11:233–241

Zaidi H, Mawlawi O, Orton CG (2007) Point/counterpoint. simultaneous PET/MR will replace PET/CT as the molecular multimodality imaging platform of choice. Med Phys 34:1525–1528

Zhang C, Jugold M, Woenne EC et al (2007) Specific targeting of tumor angiogenesis by RGD-conjugated ultrasmall superparamagnetic iron oxide particles using a clinical 1.5-T magnetic resonance scanner. Cancer Res 67:1555–1562

Zhang M, Huang M, Le C et al (2008) Accuracy and reproducibility of tumor positioning during prolonged and multi-modality animal imaging studies. Phys Med Biol 53:5867–5882

Zhang S, Merritt M, Woessner DE et al (2003a) PARACEST agents: modulating MRI contrast via water proton exchange. Acc Chem Res 36:783–790

Zhang S, Trokowski R, Sherry AD (2003b) A paramagnetic CEST agent for imaging glucose by MRI. J Am Chem Soc 125:15288–15289

Zhang S, Malloy CR, Sherry AD (2005) MRI thermometry based on PARACEST agents. J Am Chem Soc 127:17572–17573

Zhang X, Xiong Z, Wu Y et al (2006) Quantitative PET imaging of tumor integrin {alpha}v{beta}3 expression with ^{18}F-FRGD2. J Nucl Med 47:113–121

Zhao D, Ran S, Constantinescu A et al (2003) Tumor oxygen dynamics correlation of in vivo MRI with histological findings. Neoplasia 5:308–318

Zhao M, Beauregard DA, Loizou L et al (2001) Non-invasive detection of apoptosis using magnetic resonance imaging and a targeted contrast agent. Nat Med 7:1241–1244

Zhao S, Kuge Y, Kohanawa M et al (2008) Usefulness of ^{11}C-methionine for differentiating tumors from granulomas in experimental rat models: a comparison with ^{18}F-FDG and ^{18}F-FLT. J Nucl Med 49:135–141

Zhou D, Chu W, Chen DL et al (2009) [^{18}F]- and [^{11}C]-labeled N-benzyl-isatin sulfonamide analogues as PET tracers for apoptosis: synthesis, radiolabeling mechanism, and in vivo imaging study of apoptosis in Fas-treated mice using [^{11}C]WC-98. Org Biomol Chem 7:1337–1348

Zurkiya O, Chan AW, Hu X (2008) MagA is sufficient for producing magnetic nanoparticles in mammalian cells, making it an MRI reporter. Magn Reson Med 59:1225–1231

Part III
Clinical Applications

Quantitative SPECT/CT

Philipp Ritt and Torsten Kuwert

Abstract

Conventional nuclear medical imaging uses radiopharmaceuticals labeled by single-photon emitters such as Tc-99m, I-123, or I-131 in vivo. Classical clinical examples are the study of bone metabolism by bone scintigraphy with the Tc-99m-labeled polyphosphonates or of iodine transport into the thyroid gland using Tc-99m-pertechnetate. With single-photon emission-computed tomography (SPECT), the distribution of these radiopharmaceuticals within the human body is three-dimensionally visualized. Contrary to positron emission tomography (PET), current SPECT technology does not allow the quantification of regional values of radioactivity tissue concentration as SPECT images are grossly compromised by artifacts caused by photon scatter and attenuation. With the advent of hybrid imaging systems combining a SPECT camera with an X-ray computerized (CT) scanner in one gantry, reliable corrections for these artifacts seem possible, allowing truly quantitative SPECT.

Contents

P. Ritt (✉) · T. Kuwert
Nuklearmedizinische Klinik, Universität Erlangen-Nürnberg,
Ulmenweg 18, 91054 Erlangen, Germany
e-mail: philipp.ritt@uk-erlangen.de

O. Schober and B. Riemann (eds.), *Molecular Imaging in Oncology*,
Recent Results in Cancer Research 187, DOI: 10.1007/978-3-642-10853-2_10,

1 Introduction

Single-Photon Emission-Computed Tomography (SPECT) is widely used in the field of nuclear medicine for various purposes. The most important applications nowadays are skeletal imaging using Tc-99m-labeled polyphosphonates or thyroid imaging using Tc-99m-pertechnetate. Additionally, SPECT is frequently applied for the confirmation of desired tracer distribution under I-131 therapy or the diagnosis of diseases of the neuronal system like Tc-99m-ECD for epilepsy or I-123-FP-CIT for dopamine transporter function. An emerging field of application is the individualized dosimetry for e.g., I-131, Y-90, or Lu-177 labeled antibody therapies. For the purpose of dosimetry an exact representation of the radioactive substance is especially desirable, which subsequently leads to the need of absolute quantification with SPECT. This process is compromised by photon scatter (Jaszczak et al. 1984; Koral et al. 1988; Frey and Tsui 1994), photon attenuation (LaCroix et al. 1994; Blankespoor et al. 1996; Römer et al. 2006; El Fakhri et al. 1999), and partial volume artifacts (Kessler et al. 1984; Geworski et al. 2000). Thus, the following chapters are focused on SPECT/CT instrumentation, correction techniques of the aforementioned effects, and additional steps that are necessary for quantitative accurate absolute quantification in clinical application.

2 Technical Aspects

2.1 SPECT/CT Instrumentation

Modern SPECT devices are based on the gamma camera principle by Hal Anger (Anger 1958; 1964). Its main components are a collimator, a scintillation crystal (mainly NaI), which is read out by photomultipliers, and subsequent electronics. The unit of these components is commonly referred to as detector. The detector itself is mounted onto a gantry, which allows movements of the detector head. For SPECT, nowadays the application of dual detector head cameras can be considered as the standard, single, or triple detector head cameras are more uncommon. The SPECT camera setup is completed by the patient bed and computers for the data processing.

Image spatial resolution is in the following defined as the full-width half maximum (FWHM) of a point source. In SPECT, it is mainly limited by collimator performance. SPECT utilizes absorptive collimation to identify the direction of the photon line-of-response (LOR). Positron emission tomography (PET), for example, uses electronic (coincidence) collimation to identify the LORs. Only a little fraction

of the gamma quanta that reach the collimator surface pass through it. As a consequence the detection efficiency of SPECT when compared to PET (see, e.g., Cherry et al. 2003, p 340) is diminished to a large extent. It is important to notice that there is always a tradeoff between spatial resolution and detection efficiency in SPECT. The collimators are typically designed with the maximum allowable resolution in order to partially compensate for the limited detection efficiency.

The achievable spatial resolution is also influenced by the detectors' intrinsic resolution defined as the spatial resolution of the detector without a collimator. The detectors of most clinical SPECT systems are made of a single crystal plate of NaI, which acts as scintillator and illuminates an array of photomultipliers. The intrinsic resolution of the detector depends on the photo-peak energy of the radionuclide used and the crystal thickness of the NaI. Higher gamma quantum energy allows a better intrinsic resolution due to the higher light output of the scintillation. Larger crystal thickness increases intrinsic resolution. This is a consequence of the broader spread of the scintillation light before it exits the crystal and is detected with the photomultipliers.

Typical SPECT detectors have an intrinsic spatial resolution in the range of 3–5 mm for Tc-99m. However, the image resolution for the whole SPECT system depends mainly on the collimator design and the source-to-collimator distance. For parallel-hole collimation of Tc-99m and typical source-to-collimator distances, it ranges from 7 to 15 mm FWHM. This is considerably higher than that seen in PET (2–5 mm FWHM). By using other collimator geometries, e.g., (multi-) pinhole, even lower spatial resolution than in PET can be achieved (Schramm et al. 2003). Branderhorst et al. (2011), for example, obtained submillimeter (FWHM) resolution for their small animal SPECT camera for Tc-99m. However, these collimator geometries nowadays seem to be used more frequently for small animal studies than in clinical practice. An in-detail description on collimator geometries can be found in Cherry et al. (2003). An improved spatial resolution of the imaging system helps to avoid partial volume effects.

The SPECT/CT is a combination of a SPECT camera and an X-ray computed tomograph (CT). SPECT and CT are in these systems installed in sequential order, attached to a common gantry with just one patient bed.

This setup helps to solve two major problems, registration and attenuation correction, of multimodality imaging at the same time, as will be discussed in the following chapters.

2.2 Registration of Multimodal Images

In typical systems, SPECT and CT data acquisition is performed sequentially: Usually, SPECT is carried out first, followed by CT. The patients are transferred by a table movement from one modality to the other. A huge advantage of this procedure is that the patient is scanned by both modalities in roughly the same position. SPECT and CT thus are acquired in good approximation at the same

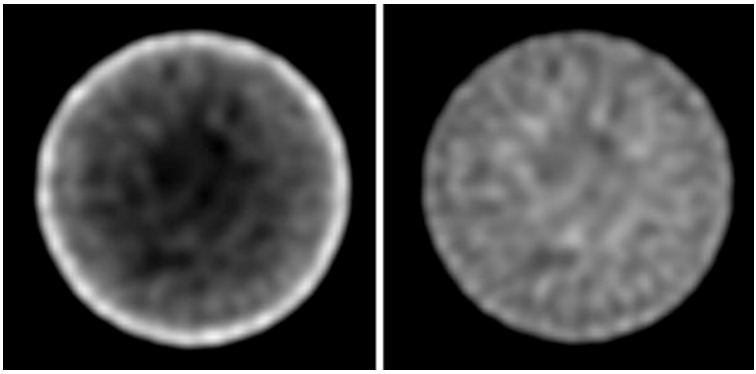

Fig. 1 A reconstructed SPECT image of a homogenously filled phantom (Tc-99m). The uncorrected image (*left* side) shows a relative overestimation of the activity at the rim of the phantom and an underestimation at the center. The attenuation-corrected image (*right* side) restores the homogenous distribution

patient position. Together with the information of the parameters of the table movement between both acquisitions, this can be used to facilitate a precise assignment between functional (SPECT) and anatomic (CT) image. This so-called "hardware fusion" is, in general, superior to retrospective fusion with regard to image alignment. The registration accuracy of the hardware fusion reaches 1–2 mm for organs which are not affected by respiratory movement (Nömayr et al. 2006). However, the registration accuracy for organs that are affected by respiratory movements is reported to be significantly higher (5–7 mm) (Han et al. 2008). Partially, this is caused by differences in acquisition time between the modalities. While a SPECT scan usually takes 10–30 min and spans over a lot of respiratory cycles, a CT scan often is acquired in one phase of the respiratory cycle only. Nevertheless, in order to minimize misalignment, the CT should be acquired in a resting expiratory position (Gilman et al. 2006).

2.3 Attenuation Correction of SPECT

SPECT images are heavily affected by the effect of photon attenuation (Fig. 1).

The probability P_{Det} for gamma quanta emitted at d for reaching a detector at position D (under the assumption that it is emitted in the proper direction) is calculated according to Eq. 1 (Fig. 2 for a simplified illustration):

$$P_{\mathrm{Det}} = \exp\{\int_{\vec{d}}^{\vec{D}} -\mu(\vec{r})d\vec{r}\} \tag{1}$$

Fig. 2 A simplified illustration of the detection of a decay event: The signal from the decay at position d is lowered by photon attenuation. The amount of attenuation depends on the spatially non-constant linear attenuation coefficients $\mu(x,y,z)$ and on the distance between the detector and the decay, $|D\text{-}d|$

The line integral covers the path of the radiation from its origin through the object, to the location of its detection.

For SPECT imaging, the probability depends on the (unknown) location of the decay d and on the linear attenuation coefficients $\mu(r)$ of the object.

For the correction of the attenuation effect, the spatial distribution of the attenuation coefficients of the examined object for the photon energy of the used radionuclide needs to be known. The distribution of attenuation coefficients (called attenuation map) can be generated through a simple transformation of a transmission scan. First, the transmission images need to be converted to the attenuation factors valid at the effective energy of the emission scan (140 keV for Tc-99m); then, they need to be corrected for the spatial registration between the emission and transmission images. The resulting attenuation map can, for example, be integrated into the reconstruction step in order to correct for photon attenuation.

Before the introduction of hybrid SPECT/CT devices, radionuclide (source-based) transmission measurements (e.g., using Gd-153, Tc-99m, or Ba-133) were used for obtaining the attenuation map. These methods have the advantage that the same detectors can be used for both the emission and the transmission scans. This made the method very cost-efficient. However, using the same detectors for the emission and the transmission scans often leads to poor image quality for the transmission image due to a poor signal-to-noise ratio and due to the limited spatial resolution of the gamma camera detectors. Additionally, radiation safety considerations play a role: Only relatively weak transmission sources can be used, which resulted in lengthy transmission scans, lasting 10 min and more, and which further limited count statistics and image quality. Finally, the relatively high photon energies of the transmission source (100–400 keV) when compared to effective X-ray energies (40–90 keV) lead to a poor soft-tissue contrast in the transmission images, which lowers the clinical benefit of using those images for image fusion.

With the availability of SPECT/CT hybrid devices, and with their ability to perform highly correlated high quality X-ray CT transmission scans, it is nowadays the clinical standard to use these scans not only for fused viewing, but also for attenuation correction. The CT scans are obtained in Hounsfield units. These units have to be converted to the linear attenuation coefficients valid at the respective photon energy of the radionuclide, which is for, e.g., Tc-99m 140 keV. It is important to remember that this transformation of the CT transmission image to attenuation factors can be a source for errors (Zaidi and Hasegawa 2003): First of all, the transformation has to be adapted to different acceleration voltages and beam filters of the CT. Second, the polychromaticity (multitude of energies) of the X-ray beam introduces artifacts, mainly due to beam hardening.

In rare cases, patient motion could occur between the emission and transmission acquisitions in a hybrid system. This can lead to artifacts in reconstructed attenuation-corrected images, which in turn could lead to false readings of the corrected SPECT images. A manual post-registration could help to prevent such artifacts (Chen et al. 2006).

Still, the methods that rely on the segmentation of contours in SPECT can be sufficient for SPECT quantification in "easy" anatomies like the brain. Nevertheless, the attenuation correction by SPECT/CT has become the clinical standard and is, in general, highly recommended. Attenuation and other corrections are obligatory for accurate quantification with SPECT/CT, which will be discussed in the following chapter.

2.4 Quantitatively Accurate SPECT/CT

SPECT allows the visualization of the distribution of radioactivity within the human body. The modality is widely used for clinical purposes [for more details, see the recent articles by, e.g., Bockisch et al. (2009) or Schulthess et al. (2006)]. SPECT also holds the promise to exactly quantify the concentration of radioactivity within a given volume in absolute units, e.g., as kBq/cm^3. This process is heavily compromised by photon scatter (Jaszczak et al. 1984; Koral et al. 1988; Frey and Tsui 1994), photon attenuation (LaCroix et al. 1994; Blankespoor et al. 1996; Römer et al. 2006; El Fakhri et al. 1999), and partial volume artifacts (Kessler et al. 1984; Geworski et al. 2000). In SPECT, technical progress in that regard has been considerably slower than in PET. Various reports point to its lack of quantitative abilities (Germain et al. 2000; Lewis et al. 2006; Sidoti and Agrillo 2006). In this chapter, we outline the recent progress in that field for SPECT/CT. A simplified diagram of the image formation chain for quantitative SPECT is given in Fig. 3 for the purpose of orientation. We will begin with the reconstruction methods that nowadays incorporate many corrections mentioned in the latter paragraphs. We will then focus on scatter and partial volume artifacts; in each of these paragraphs, a short explanation of the underlying physical effect, and an overview of the appropriate correction techniques are given. In addition, we will briefly introduce an easy calibration technique.

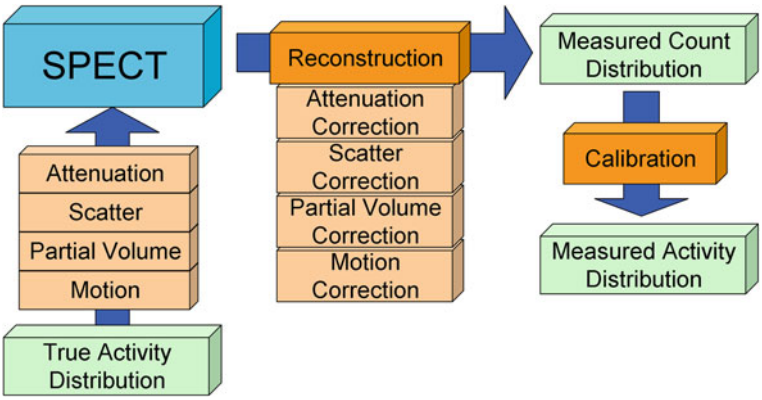

Fig. 3 Illustration of a simplified image formation chain. The image of the true activity distribution is influenced by several effects, namely attenuation, scatter, partial volume, and motion. The SPECT reconstruction, along with possible corrections for those effects, results in a measured, 3D count distribution. By calibration, the count distribution can be translated into a measured activity distribution

Please note: In the following, it has to be assumed that the kinetics of the radioactive tracer of interest are slow with respect to the imaging time. If this is not true, significant quantification errors are very likely to occur and other approaches (e.g., dynamic SPECT) should be considered (Gullberg et al. 2010).

2.4.1 Quantitative Reconstruction

There exist two main families of reconstruction techniques which are commonly used in clinical SPECT: Non-iterative (e.g., filtered back-projection, FBP) and iterative (e.g., maximum-likelihood expectation maximization, MLEM or ordered-subset expectation maximization, OSEM) methods. Although more demanding on computational power, the family of iterative reconstructions seems to be superior in terms of quantification, when compared to non-iterative methods. This is mainly due to the possibility to implement corrections and system modeling into iterative reconstruction in an easier and more intuitive way than into non-iterative methods. Thus a variety of publications reports higher quantitative accuracy of iterative algorithms when compared to non-iterative methods (Gilland et al. 1991; Rosenthal et al. 1995; Tsui et al. 1994).

In the following paragraphs, the main parts of system modeling will be outlined (Fig. 4).

For example, in the FBP algorithm, it is assumed that the sensitive volume of one collimator hole has a cylindrical shape. In reality, however, the sensitive volume can be more accurately described as cone-shaped. As a consequence, the system resolution, FWHM, depends in very good approximation linearly on the distance between source and detector for SPECT that employs absorptive parallel-hole collimation. This effect is known as geometric response function.

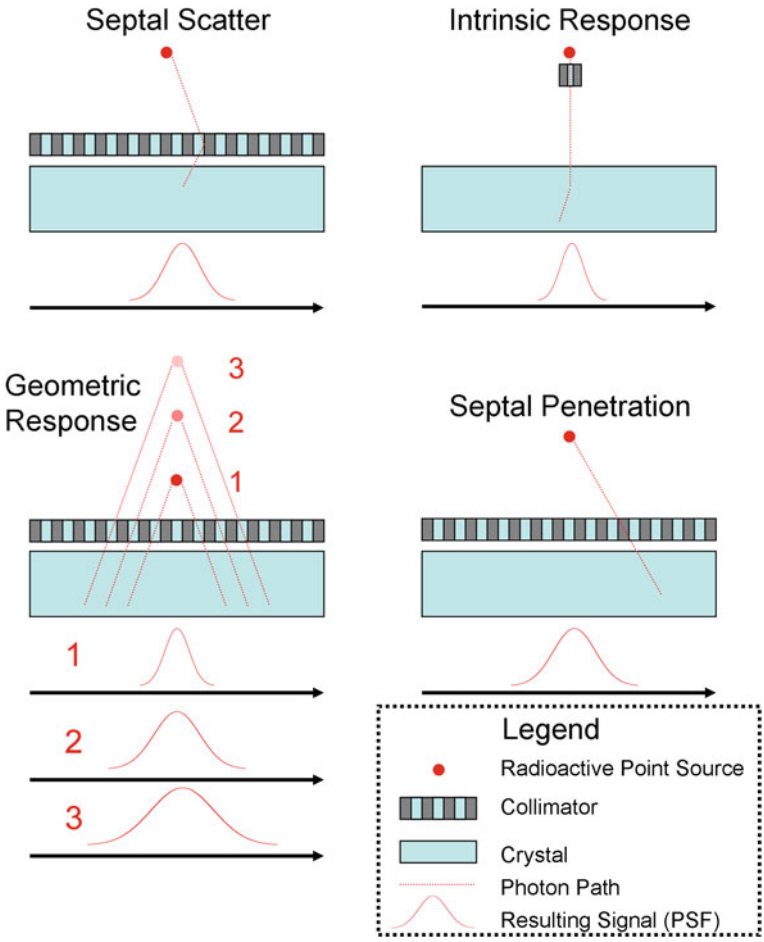

Fig. 4 Illustration of the different components that form the collimator-detector response function. *Lower left:* The geometric response function models source-to-collimator distance effects: The measured response in the crystal varies with source-to-collimator distance. *Upper right:* The intrinsic response function describes the effects of interactions in the detector crystal (please note: the point source is collimated to form a pencil beam). *Upper left & lower right:* The septal scatter and septal penetration functions model the interactions between the photons and the collimator

It can be incorporated as a mathematical model into the iterative reconstruction in a straightforward and simple way, which is in contrast to FBP.

Photon interactions that happen inside the detector can be characterized by an intrinsic response function. This function mainly models the effect of scatter in the crystal itself and the uncertainty in the position estimation of the detected photons.

Another part of the system modeling in SPECT is the septal penetration function: A compromise between collimator efficiency and image quality has to be made for

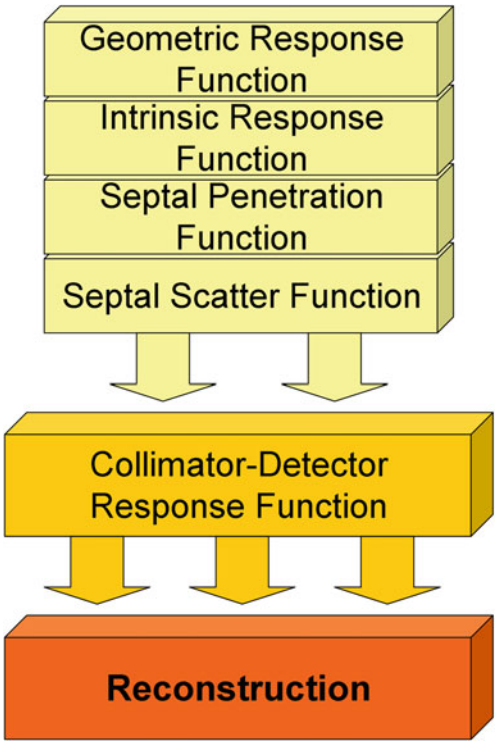

Fig. 5 The combination of intrinsic response, geometric response, and septal scatter and penetration functions form the collimator-detector response function. It is integrated in the (iterative) reconstruction step

absorptive collimation (like in SPECT): Thicker collimator septa reduce the amount of septal penetration when compared to thinner septa of the same material. Nevertheless, this reduces the efficiency of the collimator by covering sensitive area of the detector as well. A result of the compromise made is that a certain amount of septal penetration will be allowed (e.g., 5 %). Thus, the septal penetration function models the probability that photons penetrate the septa of the collimator.

Photons and collimator septa can as well interact by forming scattered radiation. Again, the probability that photons are scattered by the septa can be mathematically described by a septal scatter function. The scatter effect is, in general, more distinct for medium- and high-energy nuclides.

The previously described four parts of the response function (Fig. 5) can be combined and are then known as the collimator-detector response function. This is often used to correct for the different effects in the reconstruction step and subsequently leads to improved system resolution and quantitative accuracy.

Several reports show that superior resolution can be achieved when corrections are implemented using iterative reconstruction techniques (Kohli et al. 1998) and

quantitative measures (Kohli et al. 1998; Pretorius et al. 1998) when compared to implementations for non-iterative reconstruction methods. Römer et al. (2006) report the use of a 3D depth-dependent blur modeling (OS-EM 3D reconstruction) for clinical applications. An in-depth review on the modeling of the collimator-detector response function is beyond the scope of this chapter and can be found in (Zaidi and Koral 2006).

In clinical SPECT, iterative reconstruction can be considered state-of-the-art and is, in general, highly recommended. The gained improvement in spatial resolution will significantly decrease the extent of the partial volume effect and thus result in higher quantitative accuracy, especially for small structures.

2.4.2 Scatter Correction

In simple reconstructions used in SPECT (e.g., backprojection), it is assumed that cross-talk between individual lines of response of a collimator does not exist. This assumption fails when it comes to photon scatter as is necessarily the case in clinical SPECT. Therefore, scatter correction is an important requirement for (quantitative) imaging. Scattered radiation is produced when gamma quanta after the emission from decaying nuclei interact with surrounding atoms like, e.g., atoms of a patient's body. The most dominant scatter process in the energy range of clinically utilized radiotracers is Compton scattering, which is explained in the following paragraph.

The energy E_S of the scattered photon depends only on the scattering angle φ. It is given by Eq. 2, where E_0 is the energy of the photon before the scattering process and $m_e c^2$ the invariant mass of the electron. It is notable that the energy transfer does not depend on the density or the atomic number of the interacting matter. By contrast, the total probability that a photon is scattered by this effect depends to a high degree on the properties (most importantly electron density) of the absorbing material.

It can be seen in Eq. 2 that the loss of energy of the gamma quanta depends on the change of their momentum and direction in the scatter process. Due to the limited energy resolution of the SPECT system's detectors, the system can not discriminate between unscattered quanta and scattered quanta that have only lost a small amount of energy in the process. Consequently, a certain degree of scattered radiation is allowed to get into the image formation chain, which reduces image quality.

$$E_S = E_0 / \left[1 + \left(E_0 / m_e c^2\right) \cdot (1 - \cos(\varphi))\right] \tag{2}$$

In case of parallel-hole collimation, for simple filtered back-projection reconstruction, it is assumed that the decay took place exactly perpendicular to the detection plane at the location of detection. If the photons undergo scatter, their direction is changed: If one of the photons now is detected and used for the image formation, not only the distance of the decay to the detector along the LOR will be unknown, but also the correct position of the LOR itself. However, not all information about the photon's originating nucleus is lost, depending on the extent

of scatter. Scattered radiation, therefore, can be understood as anisotropic noise that reduces image quality.

The methods for scatter correction are multifold: Some rely on "passive" methods. For example, the photopeak energy window can be narrowed or the lower discriminator cutoff of the energy window can be increased. This can help avoiding acceptance of scattered photons. Koral et al. (1986) report an improved quantitative accuracy with this technique. However, by changing the acceptance energy window, one will also reject unscattered photons, which are detected at lower energies only due to the limited energy resolution of the gamma camera. Even when applying a relatively small energy window of $\pm$ 5 keV for Tc-99m (140 keV), on basis of Eq. 2, photons with scatter angles of up to 30° will be accepted.

A very common approach in clinical routine is based on utilizing dual- (Jaszczak et al. 1984), triple-(Ogawa et al. 1991) or even multi-energy (Koral et al. 1988) windows. The additional scatter energy windows are placed below and/or above the photopeak energy window. Additional projections are acquired at those windows simultaneously to the image at the photopeak window. Subsequently, for each pixel of the projections at the photopeak window, the amount of scattered radiation can be estimated from the scatter window images. This amount is subtracted from the projections or incorporated in the iterative reconstruction.

Besides this rather simple multi-energy window approach, a multitude of other approaches exists for estimating and correcting for scattered radiation [for an overview see (Zaidi and Koral 2006)]. For quantitative SPECT, scatter correction is essential. This is proven in the work of various groups: Shcherbinin et al. (2008) and Vandervoort et al. (2007) apply a method founded on the work of Wells et al. (Wells et al. 1998). They integrate corrections based on the Klein–Nishina formula in their iterative reconstruction forward projection step and report an improved quantitative accuracy in phantoms measurements.

Another approach, the application of Monte Carlo based methods, is heavily limited in clinical routine due to high computational costs and patient specificity, even if they seem to promise even more accurate results (Floyd et al. 1984; Ljungberg and Strand 1990; Frey and Tsui 1990).

A review shows that a huge variety of scatter correction techniques is available. Unfortunately, in a clinical environment, only very few of them are applicable. In spite of their simplicity, dual- or multi-energy window approaches are recommended in clinical applications due to their sufficient ability for the correction for scattered radiation and their easy implementation. More sophisticated techniques such as Monte Carlo methods still have to prove their superiority and applicability in the daily clinical routine.

2.4.3 Partial Volume Correction

Partial volume effects are caused by the limited spatial resolution of the SPECT device. Radioactivity concentration in regions of interest (ROI) in structures smaller than approximately 2–3 times of the FWHM is misquantified: The activity

in ROIs of that size is either under- or overestimated, depending on the combination of "spill-in" and "spill-out" effects. Spill-in means that activity from outside the ROI or structure due to the limited spatial resolution is integrated (added) to the activity inside the ROI: The activity inside the ROI is erroneously increased. Spill-out implies that the activity of the ROI or structure is distributed over its borders (again due to limited spatial resolution), and therefore "lost": The activity measured inside the ROI is then underestimated.

Most importantly, the degree of the partial volume effect depends on the system resolution of the imaging system relative to the size of structures in which activity is to be quantified. Patient motion can be another cause for increased partial volume effects, especially in clinical settings.

The approaches for a correction of the partial volume effect are divided into two groups: Approaches that are based on additional information from images (e.g. CT, MR) of the structures in question and methods that work solely on the emission images.

A very common and simple post-reconstruction approach in the latter group is founded on measurements with physical phantoms, simulation studies, or theoretical derivations: As outlined by Hoffman et al. (1979) and Kessler et al. (1984) recovery coefficients (the ratio of apparent activity concentration to true activity concentration) for simple geometries (e.g., spheres, discs, cylinders) can be measured or estimated and consequently be used to calculate corrected values for the amount of radioactivity in those structures. Several groups report that this successfully improves quantification accuracy (Blankespoor et al. 1996; Geworski et al. 2000; Chen et al. 1998). However, a limitation of this approach is its applicability to only simple geometries; in general, the radioactive distribution in a patient will not follow this assumption. Another method is the deconvolution-based partial volume correction: Seo et al. (Seo et al. 2009) report with their implementation an accuracy of 10 % for In-111 in lesions with a volume of down to 8 ml.

Every technique that results in an improved spatial resolution of the imaging system helps to avoid or lower the influence of the partial volume effect. For example, some methods that are described in the *Quantitative Reconstruction* paragraph, which incorporate information about the collimator-detector response function will improve the systems spatial resolution to some extent, and therefore can be interpreted as partial volume correction technique. For example, Hutton et al. (Hutton and Lau 1998) report improved accuracy for the simulated Mathematical Cardiac Torso (MCAT) phantom for their implementation of the detector-response modeling into the ML-EM and OS-EM reconstruction.

The other group of methods utilizes structural and anatomic information in the form of segmented images from another imaging modality (CT, MR, US) for partial volume correction. The segmentation itself can be done in a fully automatic fashion or by manually outlining ROIs. The simple methods rely on multiple two-class segmentation (regions with activity and regions without activity). Pretorius et al. (Pretorius and King 2009), Da Silva et al. (2001), and Tang et al. (1996) apply this approach to co-registered myocardial CT images on the MCAT phantom

and are able to obtain improved visual characteristics as well as a higher quantitative accuracy of the corrected SPECT data.

A more complex method is based on the geometric transfer matrix (GTM), which was first applied by Rousset et al. (1993, 1998) on brain PET studies: It basically can handle any desired number n of regions, in which the activity distribution is assumed to be homogenous. The observed activity t_i of a tissue class i is modeled as a linear combination of the true activities T_j of all other tissues classes $j = 1 \ldots n$. The spatial definition of those regions is done by segmenting (automatically or manually) CT or MRI images. The matrix components ω_{ij} describe the regional transfer coefficients: The diagonal terms represent the spill-out of the regions; the off-diagonal terms define the spill-in from other regions. The ω_{ij} can be modeled on basis of the definition of the regions and the point spread function of the SPECT system. As soon as all the components ω_{ij} are known (full-rank transfer matrix) the true activities T_j can be computed by solving the linear equation defined in Eq. 3.

$$\begin{bmatrix} t_1 \\ t_2 \\ \vdots \\ t_n \end{bmatrix} = \begin{bmatrix} \omega_{11} & \omega_{21} & \cdots & \omega_{n1} \\ \omega_{12} & \ddots & & \omega_{n2} \\ \vdots & & \ddots & \vdots \\ \omega_{1n} & \omega_{2n} & \cdots & \omega_{nn} \end{bmatrix} \times \begin{bmatrix} T_1 \\ T_2 \\ \vdots \\ T_n \end{bmatrix} \tag{3}$$

Du et al. (2005) compare variants of the GTM approach to uncorrected images in a physical brain phantom for Tc-99m; they find a substantial reduction of the bias caused by the partial volume effect. Soret et al. (2003) studied the effect of the GTM correction on I-123 using a physical brain phantom and segmentations of CT images. They found an underestimation of up to 50 % when compared to the true activity concentration for uncorrected images and small structures (e.g., putamen). The application of the partial volume correction leads to an overestimation of about 10 %, which is a significant improvement.

2.4.4 Calibration

An important requirement for quantitative accurate SPECT is the determination of the system volume sensitivity S_{Vol} (Eq. 4). This is needed for the calibration of the scanner to absolute values and typically obtained by a correlation of measured results to a calibrated well counter. This process is standardized and its description can be found in detail, for example, in the NEMA protocols (National Electrical Manufacturers Association 2007). Its principle is briefly outlined in the following: In order to avoid partial volume effects, a large cylindrical phantom with known activity concentration c_{Vol} is scanned with the SPECT system. Subsequently, corrections for attenuated and scattered photons are applied and a large VOI with volume V_{VOI} is defined in the reconstructed image. T_0 is the start time, T_{acq} the duration of the acquisition, $T_{1/2}$ is the half time of the used radionuclide, T_{cal} the time of the activity calibration, and R represents the counting rate measured in the

VOI. Finally, based on Eq. 4, a calibration factor, which allows conversion from detected counts per second to Becquerel is calculated.

$$S_{Vol} = \frac{R}{V_{VOI} \cdot c_{vol}} \times \exp\left(\frac{T_0 - T_{cal}}{T_{1/2}} \cdot \ln 2\right) \times \left(\frac{T_{acq}}{T_{1/2}} \cdot \ln 2\right) \times \left(1 - \exp\left(-\frac{T_{acq}}{T_{1/2}} \cdot \ln 2\right)\right)^{-1} \quad (4)$$

This calibration factor is specific for every radionuclide as well as for different intrinsic detector sensitivities and collimators. It is possible and in some cases beneficial to have count rate dependent calibration factors. Reasons for this are thought to be nonlinearities of the detector at the different count rates and dead time effects at high activities. Those effects will be stronger for higher energy radionuclides (e.g., I-131). Dewaraja et al. (2008) report about dead time and pulse pileup effects for the SPECT quantification of therapeutic activities of 2–6 GBq I-131.

3 Clinical Aspects

One of the applications that benefits from absolute quantification is the individualized dosimetry for planning and monitoring therapies with internally applied radionuclides, see e.g., Geworski et al. (2010). Dewaraja et al. (2010) underline the outstanding role of SPECT-dosimetry for the therapy with I-131-tositumomab. Sandström et al. (Sandström et al. 2010) performed a SPECT-dosimetry on 24 patients for Lu-177-DOTA-D-Phe^{1}-Tyr^{3}-octreotate and compared the data thus obtained to values from dosimetry based on planar imaging. They conclude that the SPECT-based method is more accurate. Further literature to this effect is found in the review article of Flux et al. (2006).

Unfortunately, so far, only very few studies validated the in vivo quantification accuracy of SPECT. Zeintl et al. (2010) evaluated the activity of Tc-99m-DPD in the bladder of 16 patients. The reference activity was determined by measuring the activity concentration in the urine immediately after the SPECT imaging. With the application of their correction methods, they reached a deviation of 7 % between the well counter measured and SPECT determined activity concentrations.

Da Silva et al. (2001) evaluated the quantification accuracy of Tc-99m-Sestamibi in the myocardium of eight pigs. They found a deviation of 10 % when comparing between SPECT and activity measurements of the excised myocardia with their version of partial volume and attenuation correction.

Almeida et al. (1999) evaluated the uptake in the striatum of I-123 labeled epidepride in Papio Anubis baboons. They reached quantification accuracy with errors less than 10 % with corrections for attenuation, scatter, and partial volume effects.

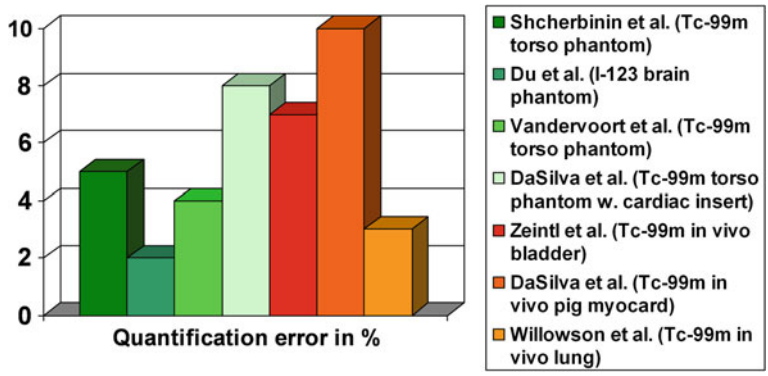

Fig. 6 Overview of the quantification accuracy in a literature survey. *Green* bars indicate results of phantom experiments, *red* bars results of in vivo studies

4 Summary and Outlook

A review of the current literature (Fig. 6) as well as our own work (e.g., Zeintl et al. 2010) shows that clinical SPECT can yield quantitative errors below 10 %. However, that requires a careful setup and calibration, as well as state-of-the-art SPECT/CT systems and iterative reconstruction software which is able to incorporate system modeling parameters into the reconstruction process.

Most of the work was carried out using Tc-99m tracers. It is still not known how the absolute quantification in SPECT in a variety of clinical setups (e.g., Tc-99m-DPD uptake in the human bone or I-131 uptake in the thyroid gland) should be evaluated and validated. It is also to be expected that the accuracy of quantifying tissue radioactivity concentration is worse for high-energy radionuclides such as I-131 than for low-energy radionuclides such as Tc-99m.

Ongoing research and further improved technical details of SPECT/CT will lead to an increased application of absolute quantification in clinical setups.

References

Almeida P, Ribeiro MJ, Bottlaender M, Loc'h C, Langer O, Strul D, Hugonnard P, Grangeat P, Mazière B, Bendriem B (1999) Absolute quantitation of iodine-123 epidepride kinetics using single-photon emission tomography: comparison with carbon-11 epidepride and positron emission tomography. Eur J Nucl Med Mol Imag 26(12):1580–1588

Anger HO (1958) Scintillation Camera. Rev Sci Instrum 29(1):27–33

Anger HO (1964) Scintillation camera with multichannel collimators. J Nucl Med 5(7):515–531

Blankespoor SC, Xu X, Kaiki K, Brown JK, Tang HR, Cann CE, Hasegawa BH (1996) Attenuation correction of SPECT using X-ray CT on an emission-transmission CT system: myocardial perfusion assessment. IEEE T Nucl Sci 43(4):2263–2274

Bockisch A, Freudenberg LS, Schmidt D, Kuwert T (2009) Hybrid imaging by SPECT/CT and PET/CT: proven outcomes in cancer imaging. Semin Nucl Med 39(4):276–289

Branderhorst W, Vastenhouw B, van der Have F, Blezer E, Bleeker W, Beekman F (2011) Targeted multi-pinhole SPECT. Eur J Nucl Med Mol Imaging 38(3):552–556

Chen CH, Muzic RF Jr, Nelson AD, Adler LP (1998) A nonlinear spatially variant object-dependent system model for prediction of partial volume effects and scatter in PET. IEEE Trans Med Imag 17(2):214–227

Chen J, Caputlu-Wilson S, Shi H, Galt J, Faber T, Garcia E (2006) Automated quality control of emission-transmission misalignment for attenuation correction in myocardial perfusion imaging with SPECT-CT systems. J Nucl Cardiol 13(1):43–49

Cherry SR, Sorenson JA, Phelps ME (2003) Physics in Nuclear Medicine. Elsevier, Philadelphia

Da Silva AJ, Tang HR, Wong KH, Wu MC, Dae MW, Hasegawa BH (2001) Absolute quantification of regional myocardial uptake of ^{99m}Tc-sestamibi with SPECT: experimental validation in a porcine model. J Nucl Med 42(5):772–779

Dewaraja Y, Ljungberg M, Koral K (2008) Effects of dead time and pile up on quantitative SPECT for I-131 dosimetric studies. J Nucl Med 49:47

Dewaraja YK, Schipper MJ, Roberson PL, Wilderman SJ, Amro H, Regan DD, Koral KF, Kaminski MS, Avram AM (2010) ^{131}I-tositumomab radioimmunotherapy: initial tumor dose–response results using 3-dimensional dosimetry including radiobiologic modeling. J Nucl Med 51(7):1155–1162

Du Y, Tsui BMW, Frey EC (2005) Partial volume effect compensation for quantitative brain SPECT imaging. IEEE Trans Med Imag 24(8):969–976

El Fakhri GN, Buvat I, Pélégrini M, Benali H, Almeida P, Bendriem B, Todd-Pokropek A, Di Paola R (1999) Respective roles of scatter, attenuation, depth-dependent collimator response and finite spatial resolution in cardiac single-photon emission tomography quantitation: a monte carlo study. Eur J Nucl Med Mol Imaging 26(5):437–446

Floyd CE et al (1984) Energy and spatial distribution of multiple order compton scatter in SPECT: a monte carlo investigation. Phys Med Biol 29(10):1217–1230

Flux G, Bardies M, Monsieurs M, Savolainen S, Strands SE, Lassmann M (2006) The impact of PET and SPECT on dosimetry for targeted radionuclide therapy. Z Med Phys 16(1):47–59

Frey EC, Tsui BMW (1990) Parameterization of the scatter response function in SPECT imaging using monte carlo simulation. IEEE Trans Nucl Sci 37(3):1308–1315

Frey EC, Tsui BMW (1994) Modeling the scatter response function in inhomogenous scattering media for SPECT. IEEE T Nucl Sci 41(4):1585–1593

Germain P, Baruthio J, Roul G, Dumitresco B (2000) First-pass MRI compartmental analysis at the chronic stage of infarction: myocardial flow reserve parametric map. In: Computers in Cardiology 2000, pp675–678

Geworski L, Knoop BO, de Cabrejas ML, Knapp WH, Munz DL (2000) Recovery correction for quantitation in emission tomography: a feasibility study. Eur J Nucl Med 27(2):161–169

Geworski L, Schaefer A, Knoop BO, Pinkert J, Plotkin M, Kirsch CM (2010) Physikalische Aspekte szintigraphisch basierter Dosimetrie bei nuklearmedizinischen Therapien. Nuklearmedizin 49(3):79–123

Gilland DR, Jaszczak RJ, Liang Z, Greer KL, Coleman RE (1991) Quantitative SPECT brain imaging: effects of attenuation and detector responses. In: Nuclear Science Symposium and Medical Imaging Conference, 1991, Conference Record of the 1991 IEEE, vol. 1723, pp.1723–1727

Gilman MD, Fischman AJ, Krishnasetty V, Halpern EF, Aquino SL (2006) Optimal CT breathing protocol for combined thoracic PET/CT. Am J Roentgenol 187(5):1357–1360

Gullberg GT et al (2010) Dynamic single photon emission computed tomography-basic principles and cardiac applications. Phys Med Biol 55(20):R111–R191

Han J, Köstler H, Bennewitz C, Kuwert T, Hornegger J (2008) Computer-aided evaluation of anatomical accuracy of image fusion between X-ray CT and SPECT. Comput Med Imaging Graph 32(5):388–395

Hoffman EJ, Huang S-C, Phelps ME (1979) Quantitation in positron emission computed tomography: 1. effect of object size. J Comput Assist Tomogr 3(3):299–308

Hutton BF, Lau YH (1998) Application of distance-dependent resolution compensation and post-reconstruction filtering for myocardial SPECT. Phys Med Biol 43(6):1679–1693

Jaszczak RJ, Greer KL, Floyd CE Jr, Harris CC, Coleman RE (1984) Improved SPECT quantification using compensation for scattered photons. J Nucl Med 25(8):893–900

Kessler RM, Ellis JRJ, Eden M (1984) Analysis of emission tomographic scan data: limitations imposed by resolution and background. J Comput Assist Tomogr 8(3):514–522

Kohli V et al (1998a) Comparison of frequency-distance relationship and gaussian-diffusion-based methods of compensation for distance-dependent spatial resolution in SPECT imaging. Phys Med Biol 43(4):1025

Kohli V, King MA, Tin-Su P, Glick SJ (1998b) Compensation for distance-dependent resolution in cardiac-perfusion SPECT: impact on uniformity of wall counts and wall thickness. IEEE T Nucl Sci 45(3):1104–1110

Koral KF, Clinthorne NH, Leslie Rogers W (1986) Improving emission-computed-tomography quantification by compton-scatter rejection through offset windows. Nucl Instrum Methods Phys Res Sect A: Accelerators, Spectrometers, Detectors and Associated Equipment 242(3):610–614

Koral KF, Wang X, Rogers WL, Clinthorne NH, Wang X (1988) SPECT compton-scattering correction by analysis of energy spectra. J Nucl Med 29(2):195–202

LaCroix KJ, Tsui BMW, Hasegawa BH, Brown JK (1994) Investigation of the use of X-ray CT images for attenuation compensation in SPECT. IEEE T Nucl Sci 41(6):2793–2799

Lewis DH, Bluestone JP, Savina M, Zoller WH, Meshberg EB, Minoshima S (2006) Imaging cerebral activity in recovery from chronic traumatic brain injury: a preliminary report. J Neuroimaging 16(3):272–277

Ljungberg M, Strand S-E (1990) Scatter and attenuation correction in SPECT using density maps and monte carlo simulated scatter functions. J Nucl Med 31(9):1560–1567

National Electrical Manufacturers Association (2007) Performance measurements of gamma cameras. In: NEMA NU 1-2007ed. National Electrical Manufacturers Association

Nömayr A, Römer W, Strobel D, Bautz W, Kuwert T (2006) Anatomical accuracy of hybrid SPECT/spiral CT in the lower spine. Nucl Med Commun 27(6):521–528

Ogawa K, Harata Y, Ichihara T, Kubo A, Hashimoto S (1991) A practical method for position-dependent Compton-scatter correction in single photon emission CT. IEEE Trans Med Imag 10(3):408–412

Pretorius PH, King MA (2009) Diminishing the impact of the partial volume effect in cardiac SPECT perfusion imaging. Med Phys 36(1):105–115

Pretorius PH et al (1998) Reducing the influence of the partial volume effect on SPECT activity quantitation with 3D modelling of spatial resolution in iterative reconstruction. Phys Med Biol 43(2):407–420

Römer W, Reichel N, Vija HA, Nickel I, Hornegger J, Bautz W, Kuwert T (2006) Isotropic reconstruction of SPECT data using OSEM3D: Correlation with CT. Acad Radiol 13(4): 496–502

Rosenthal MS, Cullom J, Hawkins W, Moore SC, Tsui BMW, Yester M (1995) Quantitative SPECT imaging: a review and recommendations by the focus committee of the society of nuclear medicine computer and instrumentation council. J Nucl Med 36(8):1489–1513

Rousset O, Ma Y, Kamber M, Evans AC (1993) 3D simulations of radiotracer uptake in deep nuclei of human brain. Comput Med Imaging Graph 17(4–5):373–379

Rousset OG, Ma Y, Evans AC (1998) Correction for partial volume effects in PET: principle and validation. J Nucl Med 39(5):904–911

Sandström M, Garske U, Granberg D, Sundin A, Lundqvist H (2010) Individualized dosimetry in patients undergoing therapy with ^{177}Lu-DOTA-D-Phe^{1}-Tyr^{3}-octrcotate. Eur J Nucl Med Mol Imag 37(2):212–225

Schramm NU, Ebel G, Engeland U, Schurrat T, Behe M, Behr TM (2003) High-resolution SPECT using multipinhole collimation. IEEE T Nucl Sci 50(3):315–320

Seo Y, Aparici CM, Cooperberg MR, Konety BR, Hawkins RA (2009) In vivo tumor grading of prostate cancer using quantitative ^{111}In-capromab pendetide SPECT/CT. J Nucl Med 51(1):31–36

Shcherbinin S et al (2008) Accuracy of quantitative reconstructions in SPECT/CT imaging. Phys Med Biol 53(17):4595–4604

Sidoti C, Agrillo U (2006) Chronic cortical stimulation for amyotropic lateral sclerosis: a report of four consecutive operated cases after a 2-year follow-up: technical case report. Neurosurgery 58(2):E384

Soret M, Koulibaly PM, Darcourt J, Hapdey S, Buvat I (2003) Quantitative accuracy of dopaminergic neurotransmission imaging with ^{123}I SPECT. J Nucl Med 44(7):1184–1193

Tang HR, Brown JK, Hasegawa BH (1996) Use of X-ray CT-defined regions of interest for the determination of SPECT recovery coefficients. In: Nuclear Science Symposium, 1996 Conference Record, IEEE, vol.1843, pp1840–1844

Tsui BM, Frey EC, Zhao X, Lalush DS, Johnston RE, McCartney WH (1994) The importance and implementation of accurate 3D compensation methods for quantitative SPECT. Phys Med Biol 39(3):509–530

Vandervoort E et al (2007) Implementation of an iterative scatter correction, the influence of attenuation map quality and their effect on absolute quantitation in SPECT. Phys Med Biol 52(5):1527

von Schulthess GK, Steinert HC, Hany TF (2006) Integrated PET/CT: current applications and future directions1. Radiology 238(2):405–422

Wells RG, Celler A, Harrop R (1998) Analytical calculation of photon distributions in SPECT projections. IEEE Trans Nucl Sci 45(6):3202–3214

Zaidi H, Hasegawa B (2003) Determination of the attenuation map in emission tomography. J Nucl Med 44(2):291–315

Zaidi H, Koral K (2006) Scatter correction strategies in emission tomography. In: Quantitative Analysis in Nuclear Medicine Imaginged. Springer US, pp 205–235

Zaidi H, Frey EC, Tsui BMW (2006) Collimator-detector response compensation in SPECT. In: Quantitative Analysis in Nuclear Medicine Imaginged. Springer US, pp 141–166

Zeintl J, Vija AH, Yahil A, Hornegger J, Kuwert T (2010) Quantitative accuracy of clinical ^{99m}Tc SPECT/CT using ordered-subset expectation maximization with 3-dimensional resolution recovery, attenuation, and scatter correction. J Nucl Med 51(6):921–928

Optical Imaging of Breast Tumors and of Gastrointestinal Cancer by Laser-Induced Fluorescence

Bernd Ebert and Dirk Grosenick

Abstract

Optical imaging offers a high potential for noninvasive detection of cancer in humans. Recent advances in instrumentation for diffuse optical imaging have led to new capabilities for the detection of cancer in highly scattering tissue such as the female breast. We review recent developments in the detection of breast cancer in humans by fluorescent contrast agents. So far, the unspecific contrast agents indocyanine green (ICG) and omocyanine have been applied, whereas molecular probes for direct targeted imaging of this disease are still in preclinical research. We discuss recent improvements in the differentiation of malignant and benign lesions with ICG based on its enhanced extravasation in breast cancer. Whereas fluorescence imaging in thick tissue layers is hampered by strong light scattering, tissue surfaces can be investigated with high spatial resolution. As an example for superficial tumors, lesions of the gastrointestinal tract (GI) are discussed. In these investigations, protoporphyrin IX is used as a tumor-specific (due to its strong enhancement in tumor cells) target for spectroscopic identification and imaging. We present a time-gated method for fluorescence imaging and spectroscopy with strong suppression of tissue autofluorescence and show results on patients with Barrett's esophagus and with colitis ulcerosa.

B. Ebert (✉) · D. Grosenick
Physikalisch-Technische Bundesanstalt (PTB), Abbestr. 2-12,
10587 Berlin, Germany
e-mail: bernd.ebert@ptb.de

D. Grosenick
e-mail: dirk.grosenick@ptb.de

O. Schober and B. Riemann (eds.), *Molecular Imaging in Oncology*,
Recent Results in Cancer Research 187, DOI: 10.1007/978-3-642-10853-2_11,

Contents

1 Introduction

Optical imaging of head, breast, and skin, as well as of inner cavities of the human body, e.g., bladder or colon, is a powerful diagnostic tool to detect beginning malignant alterations or tumors. Apart from measurements of intrinsic tissue optical parameters like absorption and scattering, fluorescence imaging in medical diagnostics and therapy has attracted increasing interest over the past decade (Richards-Kortum and Sevick-Muraca 1996; Wagnieres et al. 1998). Fluorescence detection plays an important role for the increasing array of molecular probes developed to image specific molecular processes (Becker et al. 2001; Mahmood 2004).

When performing fluorescence imaging on superficial lesions, scattering of light in the tissue is of less importance, and wavelengths across the whole spectrum of light can be applied to excite fluorescence of appropriate exogenous contrast agents or endogenous markers. The situation is quite different when deeper tissue layers have to be investigated. Since biological tissue is a highly scattering medium, the excitation light as well as the emitted fluorescence light are scattered many times and accordingly, the corresponding optical path lengths are significantly increased. To obtain a sufficient penetration depth of the excitation light and a measurable fluorescence signal, excitation, and emission wavelengths have to fall into the so-called diagnostic window between about 650 nm and 1000 nm. Recent developments in experimental methods have allowed to extend the application of fluorescence imaging to diseases of highly scattering tissue such as breast cancer (Corlu et al. 2007; Hagen et al. 2009; van de Ven et al. 2010); stroke (Liebert et al. 2006), or rheumatoid arthritis (Fischer et al. 2010). These techniques offer ways to translate probes for molecular imaging from preclinical research to clinical applications on highly scattering tissue.

In the following, we discuss two approaches for clinical fluorescence diagnosis of tumors and their precursors. First, as an example for imaging in highly scattering tissue we briefly review results on the detection of carcinomas in the female

breast using either indocyanine green (ICG) or omocyanine as contrast agent. We report on a recently explored method to characterize differences in the extravasation of ICG between malignant and benign breast lesions and compare this approach to the application of ICG as a marker for tissue vascularization which was the preferred method in previous investigations. Second, as an example for superficial lesions we discuss detection of tumors in the gastrointestinal tract (GI) based on fluorescence of protoporphyrin IX (PpIX) which acts as a specific target for malignancy.

2 Fluorescence Imaging of Breast Cancer

Due to the high relevance of breast cancer many efforts are undertaken to develop targeted contrast agents for early detection of this disease. Hereby, optical imaging plays an important role in understanding the properties of the agent and its action on the cellular level, since the presence of the agent can easily be detected by exciting fluorescence light. Basic investigations are often performed on small animal models (Ebert et al. 2001; Bremer et al. 2005). Due to the small dimensions of such animal models, tumors are easily accessible by optical methods despite of light scattering. In contrast, when applying the molecular contrast agent to investigate the human breast, fluorescence imaging is much more hampered by light scattering due to the drastically enlarged tissue dimensions. Recent studies have shown that fluorescence imaging of the human breast is possible by appropriate techniques (Corlu et al. 2007; Hagen et al. 2009; Van de Ven et al. 2010). However, one probably needs a higher concentration of the molecular contrast agent in the human tumor to be detectable, compared to small animals.

At present, there is no targeted contrast agent available for optical imaging of breast cancer in humans. So far, optical investigations have been performed with either ICG or omocyanine. Both these agents are nontargeted contrast agents. ICG shows high binding to plasma proteins. After intravenous injection, it distributes in the vascular compartment, thus allowing for imaging the vessel density in the breast. Hence, tumors can be detected provided that neoangiogenesis has resulted in a locally increased capillary density. In recent studies this mechanism was used for imaging of either the increased absorption (Ntziachristos et al. 2000; Rinneberg et al. 2008) or the fluorescence (Corlu et al. 2007; Hagen et al. 2009) due to the contrast agent in the tumor. Hereby, fluorescence imaging resulted in an improved contrast because of the reduced influence of the overall background absorption (Corlu et al. 2007). Generally, results of these measurements with ICG correspond to imaging of hemoglobin absorption in the breast without any exogenous contrast agent. The latter investigations use the neoangiogenesis for tumor detection, too. Several clinical studies have shown that hemoglobin based contrast does not allow to safely distinguish between malignant and benign tumors in the breast (Grosenick et al. 2005; Taroni et al. 2005). Accordingly, neoangiogenesis based optical imaging with ICG cannot really improve this situation (Rinneberg et al. 2008). Using

absorption measurements, Intes and coworkers observed for carcinomas a delay of both the inflow and the wash-out of ICG from the blood, compared to healthy tissue (Intes et al. 2003). These differences were explained by an increased resistance of the chaotic vasculature in carcinomas to blood flow and by extravasation of ICG. In contrast to these results, measurements of the ICG wash-out reported by Rinneberg et al. did not show significant delays between carcinomas and healthy tissue (Rinneberg et al. 2008). Poellinger et al. 2011 mentioned a delayed inflow of ICG into the central cancer region for a necrotic tumor.

Compared to ICG, omocyanine (also known as TSC) has a weaker binding to plasma proteins and a higher fluorescence quantum yield (Perlitz et al. 2005). Whereas ICG is washed-out from the blood by the liver within typically 10 min, omocyanine remains in the blood vessels for more than 24 h. Recently, this dye was used in a feasibility study on patients (van de Ven et al. 2010). The best lesion-to-background contrast was observed about 8 h after dye injection. At this time, the enhanced omocyanine fluorescence signal from a tumor reflects essentially the neoangiogenesis at this location. Generally, due to its small molecular weight omocyanine is expected to extravasate from the blood vessels to the extracellular space for both healthy as well as tumor tissue.

In contrast, extravasation of ICG is suppressed in healthy vessels as well as in benign lesions since ICG is bound to high molecular weight plasma molecules, and the resulting volume of this compound is too large to pass the vessel walls. Hence, ICG effectively acts as a macromolecule. According to the enhanced permeability and retention effect (Maeda et al. 2000) this macromolecule is expected to extravasate in a malignant tumor, and to stay in the extracellular space for a longer time. As recently shown by a feasibility study on patients (Hagen et al. 2009; Poellinger et al. 2011), imaging of the extravasated part of ICG allows to consider the vessel permeability towards macromolecules as a new criterion for the detection of tumors and for the differentiation of malignant from benign lesions. This concept is similar to the development of new macromolecular contrast agents for the detection of breast tumors by magnetic resonance imaging (MRI), e.g., Gd-DTPA covalently bound to albumin (Daldrup-Link and Brasch 2003).

In the following, we report on the methods developed at the Physikalisch-Technische Bundesanstalt Berlin (PTB) to record fluorescence mammograms and to get access to extravasated ICG (Hagen et al. 2009). We present some examples of measurements on patients with malignant and benign lesions, and we compare these results with previous approaches based on neoangiogenesis.

2.1 The PTB Fluorescence Mammograph

Our optical mammograph is designed to detect the fluorescence of the contrast agent ICG in the breast as well as absorption and scattering properties of the tissue at selected wavelength in the near infrared spectral range (Hagen et al. 2009). The device is based on the parallel plate geometry. As shown in Fig. 1, the breast to be

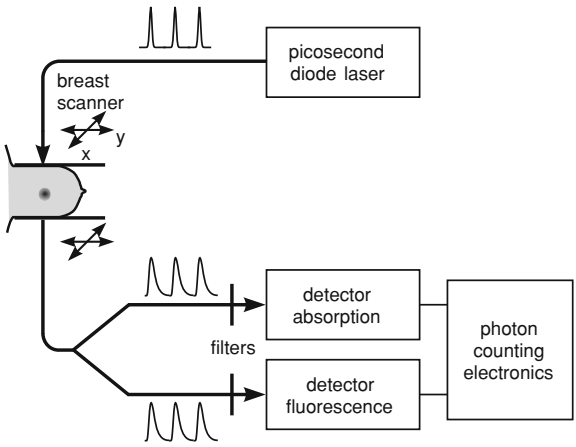

Fig. 1 Block diagram of the PTB fluorescence mammograph (from Hagen et al. 2009)

investigated is gently compressed between two parallel glass plates. In this way, a constant breast thickness is obtained, apart from the edges of the breast. To excite the fluorescence of the contrast agent distributed in the breast tissue, a picosecond diode laser module with a wavelength of 780 nm is employed (pulse duration about 380 ps, repetition rate 64 MHz). Typically, an average power of 15 mW is used at the surface of the breast. The laser pulses are guided by an optical fiber to the upper glass plate of the mammograph, where the light is collimated prior to entering the breast tissue. The 6 mm diameter fiber bundle below the second glass plate collects laser photons transmitted through the breast as well as fluorescence photons originating from excited ICG molecules. The bundle is split into two equal parts. Half of the collected light is directed to a photomultiplier tube equipped with a long pass filter to allow detection of fluorescence photons. The other half is directed to a second photomultiplier equipped with a short pass filter to detect the transmitted laser signal. Measurements are performed time resolved by employing time-correlated single photon counting. In this way, distributions of times of flight of photons are recorded yielding the broadening of the laser pulse after transmission through the breast and the temporal shape of the fluorescence signal. The breast is scanned by continuously moving source and detector fibers in tandem in a meander-like fashion. The total time to record an image of the breast takes between 3 and 10 min, depending on breast size.

The optical mammograph is equipped with six more detection fiber bundles and photomultipliers (not shown in Fig. 1) to record data for additional detector positions in transmission and reflection. These data are taken to derive 3-D information about the breast tissue (Grosenick et al. 2011). For spectroscopic measurements, the mammograph contains four additional picosecond diode lasers with emission wavelengths of 660 nm, 797 nm, 934 nm and 1066 nm. Corresponding distributions of times of flight of photons are measured by automatically placing appropriate spectral filters in front of the photomultipliers. The two shorter

wavelengths are sensitive to absorption by oxy- and deoxyhemoglobin, whereas the two longer wavelengths give access to absorption by lipids and water. Generally, optical mammograms can be recorded in craniocaudal, mediolateral, or oblique projection. To this end, the compression unit can be rotated accordingly.

The distribution of the contrast agent in the breast is visualized by fluorescence ratio mammograms corrected for edge effects (Hagen et al. 2009). These mammograms display fluorescent regions in the breast as bright areas over a homogeneous background, since the intrinsic heterogeneity of the tissue absorption caused primarily by the hemoglobin in the breast is well compensated. Furthermore, absorption mammograms are generated for the laser wavelengths employed by plotting photon counts in a suited late time window versus scan position.

2.2 Examination Protocol

The fluorescence mammograph was used to perform a feasibility study on a small number of patients with highly suspicious lesions in the breast (Hagen et al. 2009; Poellinger et al. 2011). The contrast agent ICG was administered intravenously in aqueous solution. Optical measurements were performed on the suspicious breast; the contralateral breast was not investigated. The mammograms were recorded at three different times: (i) prior to application of ICG (native phase) (ii) when the dye was distributed in the blood vessels (vascular phase), and (iii) after the dye had been washed-out from the blood by the liver. This last time period is called the extravascular phase, since it gives access to the small amount of ICG that had been extravasated from the vessels to the extracellular space during the vascular phase.

In case of an ICG bolus, the optical measurement during the vascular phase is strongly effected by the fast washout of the dye by the liver due to the long scan times (Ntziachristos et al. 2000; Corlu et al. 2007; Rinneberg et al. 2008). Therefore, to allow an optical measurement during the vascular phase at constant plasma level of ICG the dye was applied in the form of an infusion (rate of 2 mg ICG per min, duration about 20 min). To quickly obtain steady-state conditions, a starting bolus with 0.25 mg ICG per kg body weight was employed additionally. During the examination, the plasma level of ICG was monitored by conventional transcutaneous pulse densitometry using a finger clip. After recording of the mammograms for the vascular phase was finished, the breast was released from the compression plates. When the monitor signal of ICG plasma concentration had returned to the baseline level, the breast was again positioned between the compression plates to record fluorescence and excitation laser mammograms for the extravascular phase. Figure 2 summarizes the examination protocol.

For each patient conventional X-ray mammograms were available for comparison with optical mammograms. Furthermore, in selected cases MR breast imaging was performed. Classification of the lesion type was obtained from histology after biopsy.

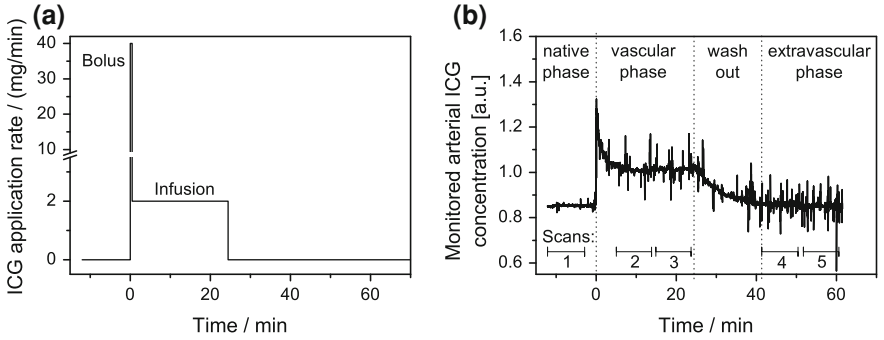

Fig. 2 Examination protocol; **a** temporal profile of ICG application (data refer to the case in Fig. 3) **b** corresponding monitored arterial ICG concentration with labeling of the various phases of the examination and of the time intervals of the five breast scans performed

2.3 Results on Malignant and Benign Tumors

Investigations were performed on patients with malignant as well as benign breast lesions. To demonstrate typical results of the approach, we consider two cases with invasive ductal carcinomas, an older and a younger woman, and a third example with a fibroadenoma as a benign tumor. The first case is a 72-years-old patient with a histologically proven medium differentiated invasive ductal carcinoma with a maximum extension of 1.6 cm in the right breast. Since the breast of this older woman consisted mainly of adipose tissue, it was radiologically transparent, and the carcinoma was clearly visible in the X-ray mammogram. According to results of a previous clinical study on intrinsic contrast breast imaging (Grosenick et al. 2005) we expect for such a case, that the tumor becomes also clearly visible in the intrinsic absorption mammogram (without any contrast agent). Figure 3a and 3b show the corresponding mammograms obtained in the native phase at 660nm and 797 nm, respectively. Data refer to normalized photon counts in the late time window of the measured distributions of times of flight. Generally, due to the low amount of glandular tissue, the breast is highly transparent for optical radiation, too. The expected position of the carcinoma in the optical mammograms was obtained by comparison with the X-ray mammogram. At 660 nm, the carcinoma is clearly visible at high contrast. The elongated structures in the optical mammogram reflect the absorption of superficial blood vessels. The vessels appear with similar contrast at the longer wavelength, whereas the contrast of the carcinoma at 797 nm is reduced. However, the locally increased absorption at 797 nm, which is close to the isosbestic point of oxy- and deoxyhemoglobin absorption, indicates an increased concentration of total hemoglobin in the carcinoma, caused by neoangiogenesis. The stronger tumor absorption at 660 nm compared to the superficial blood vessels reflects a high concentration of deoxyhemoglobin, i.e., the carcinoma is characterized by a decrease in blood oxygen saturation compared to the surrounding tissue which is a sign of high metabolic activity. Figure 3c shows the breast absorption at the excitation

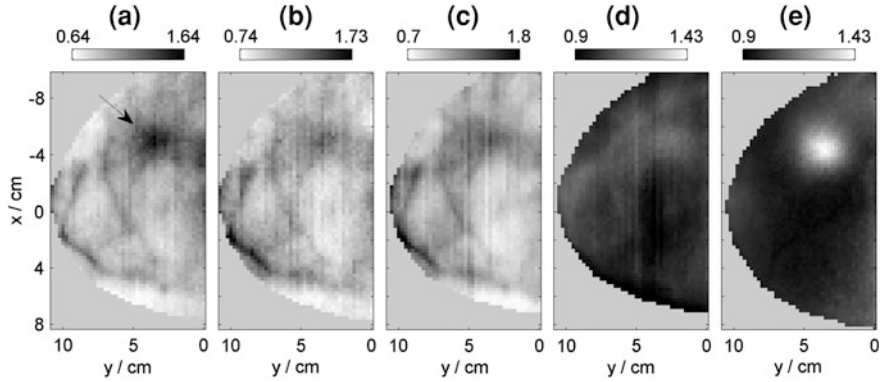

Fig. 3 Optical mammograms (case 1, craniocaudal view) of a 72-years-old patient with an invasive ductal carcinoma in the right breast, indicated by the *arrow*; **a** intrinsic absorption at 660 nm (native phase) **b** intrinsic absorption at 797 nm **c** contrast-enhanced absorption during vascular phase **d** fluorescence ratio mammogram for the vascular phase, and **e** fluorescence ratio mammogram for the extravascular phase. Absorption mammograms display normalized reciprocal photon counts in a late time window

wavelength (780 nm) for the first scan during the vascular phase. Now, absorption is enhanced by ICG which is distributed in the vessels at this measurement time. According to the general discussion on ICG in Sect. 11.2.1, the mammogram gives the same information as the intrinsic absorption image at the nearby wavelength of 797 nm (cf. Fig. 3b) due to the strong binding of ICG to plasma proteins.

Figure 3d shows the corresponding fluorescence ratio mammogram for the vascular phase, and Fig. 3e displays the fluorescence ratio mammogram for the second scan of the extravascular phase. For comparison, these two images are given with the same grayscale. Bright structures in the mammograms indicate a locally enhanced concentration of ICG. Generally, the absolute number of measured fluorescence photons in the extravascular phase is smaller than in the vascular phase. However, this information is not visible from the mammograms. Instead, the fluorescence ratio images display relative changes in fluorescence intensity with respect to the averaged signal level of the mammogram represented by a grayscale value of 1. In Fig. 3d we see fluorescence from the superficial blood vessels, as well as from the site of the carcinoma, which is highly vascularized. The information on the image is slightly different to the contrast-enhanced absorption image in Fig. 3c, since the fluorescence ratio is essentially free of the strong intrinsic tissue absorption by hemoglobin. However, the visibility of the carcinoma is worse than in the short wavelength mammogram of the native phase (Fig. 3a). In opposite, the fluorescence ratio mammogram for the extravascular phase displays the carcinoma with the highest contrast. The carcinoma is the only visible object. All other structures that appear in the native phase absorption mammograms and during the vascular phase are suppressed now. The fluorescence at the site of the carcinoma indicates that ICG has been extravasated here during

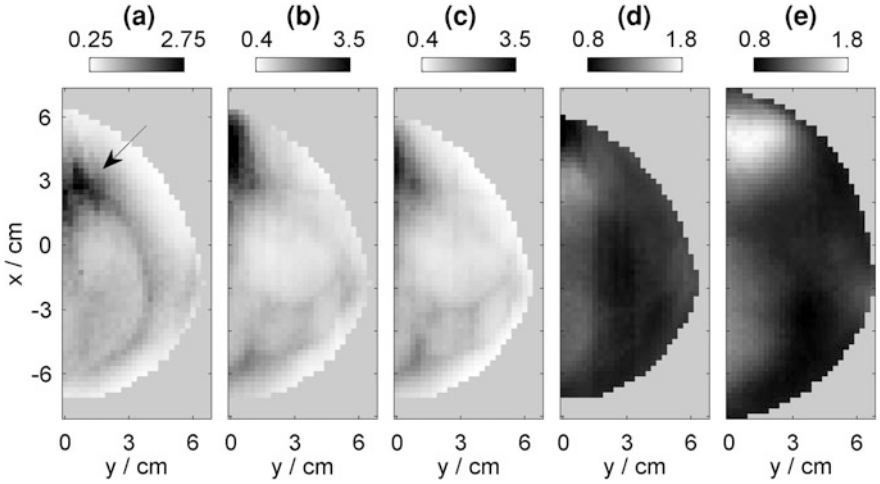

Fig. 4 Optical mammograms (case 2, craniocaudal view) of a 51-years-old patient with an invasive ductal carcinoma in the left breast, indicated by the *arrow*; **a** intrinsic absorption at 660 nm (native phase) **b** intrinsic absorption at 797 nm, **c** contrast-enhanced absorption during vascular phase, **d** fluorescence ratio mammogram for the vascular phase, and **e** fluorescence ratio mammogram for the extravascular phase. Absorption mammograms display normalized reciprocal photon counts in a late time window

the vascular phase with an enhanced rate. It should be noted, however, that a fluorescence signal was obtained at all scan positions, which indicates a low extravasation in all parts of the breast.

The second patient is a 51-years-old woman with a well differentiated invasive ductal carcinoma. The size given by histology was $1.1 \times 1.0 \times 0.8$ cm^3. The suspicious lesion was found by ultrasound. The X-ray mammogram revealed dense glandular tissue and showed only a badly visible architectural distortion. The expected position of the lesion in the optical mammograms was derived from dynamic contrast-enhanced MRI measurements which showed the lesion at the lateral side of the breast close to the chest wall. MRI offered a second lesion nearby, which was histologically classified as low-grade ductal carcinoma in situ.

Figure 4a and b display the absorption at 660 nm and 797 nm without contrast agent (native phase), based on normalized photon counts in the late time window. We expect to see the carcinoma in the upper left part of the mammograms. Both images show here a lesion of strongly increased absorption. However, the location differs between both wavelengths making a decision about lesion visibility for the native phase difficult. As for the first case, the contrast-enhanced absorption mammogram for the vascular phase (Fig. 4c) is very similar to the intrinsic absorption mammogram at 797 nm. Figure 4d and 4e display the fluorescence ratio mammograms for this patient. Similar to case 1, the image for the vascular phase is of flat contrast only compared to the extravascular phase. The latter mammogram clearly displays the strong enrichment of the contrast agent at the expected tumor position. Besides the carcinoma, we observe

a moderate fluorescence signal from the tissue close to the chest wall in the lower left part of the mammograms in Fig. 4d,e, and some contrast behind the nipple position. Compared to the carcinoma, these regions did not essentially change contrast from the vascular to the extravascular phase. During the vascular phase, blood vessels are visible in the bottom part of the image, similar to the vessel structures in the 797 nm absorption mammogram. At this phase, the ICG fluorescence at the supposed site of the carcinoma coincides with the lesion location in the 660 nm absorption mammogram. The deviation of the shape of the breast in Fig. 4e from the other mammograms is caused by a slightly different positioning of the breast during recompression for the extravascular phase measurements. Therefore, the location of the lesion in Fig. 4e cannot be directly transferred to the other mammograms.

The third case is an example of a benign lesion. The 52-years-old patient had a fibroadenoma in her left breast, which was finally validated by histology. From ultrasound examination the size of the lesion was estimated as 1.8 cm × 1.0 cm. The X-ray image did not show any abnormality. For this patient, data at 660 nm and 797 nm were not recorded. Instead, the excitation laser for fluorescence measurements was used in the native phase, too. Figure 5a displays the corresponding absorption mammogram at 780 nm. Since only the ultrasound information is available, it is difficult to decide about the position of the tumor in the optical mammogram. It is known that the fibroadenoma lies in the left part of the breast. Having in mind that fibroadenomas often exhibit increased absorption due to an increased hemoglobin concentration (Rinneberg et al. 2005; Floery et al. 2005; Enfield et al. 2007), we presume that its position corresponds to the absorbing region in the left part of the breast, indicated by the arrow in Fig. 5a. However, there remains some uncertainty in this decision. Similar to the other two cases, the contrast-enhanced absorption mammogram for the vascular phase in Fig. 5b shows the same structures as the intrinsic absorption mammogram in Fig. 5a which were both recorded at the same wavelength here.

In Fig. 5c and d the fluorescence ratio mammograms for the vascular and the extravascular phase are displayed. Apart from the blood vessels, which are only visible in Fig. 5c, both images are very similar. We do not see any noticeable change in the contrast pattern from the vascular to the extravascular phase. In other words, the fibroadenoma does not show any particular enrichment of ICG due to extravasation. This result corresponds to our expectation that the capillary walls in benign lesions are not sufficiently leaky to allow enhanced extravasation of macromolecules.

2.4 Advances of Permeability Sensitive Fluorescence Imaging with ICG

Our measurements on patients with breast tumors have confirmed the expected differences in ICG-based fluorescence contrast during the vascular phase and the extravascular phase of our examination protocol. Fluorescence ratio images, recorded during the infusion period, essentially display the vascular structures in

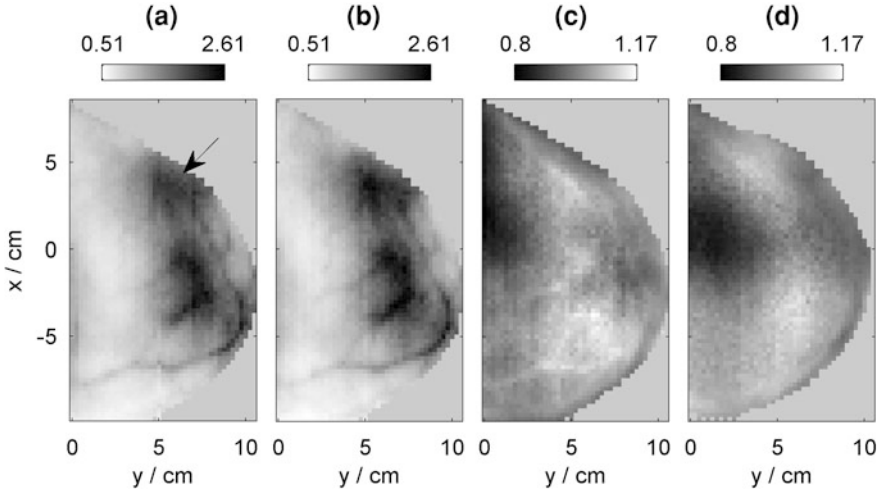

Fig. 5 Optical mammograms (case 3, craniocaudal view) of a 52-years-old patient with a fibroadenoma in the left breast. The presumed position of the lesion is indicated by the *arrow*; **a** intrinsic absorption at 780 nm (native phase), **b** contrast–enhanced absorption during vascular phase, **c** fluorescence ratio mammogram for the vascular phase, and **d** fluorescence ratio mammogram for the extravascular phase. Absorption mammograms display normalized reciprocal photon counts in a late time window

the breast tissue, similar to mammograms based on the intrinsic hemoglobin absorption. Generally, some part of ICG extravasates during circulation through the blood vessels. However, due to the known strong binding of ICG to plasma proteins, the extravasation rate is very small. Therefore, as long as ICG is distributed in the blood vessels, the contribution of extravasated ICG to the fluorescence signal is negligible. At this time, ICG fluorescence reflects the vessel density, i.e., tumors can be recognized due to increased hemoglobin concentration caused by angiogenesis.

Compared to the vascular phase, the fluorescence signal measured during the extravascular phase is small. However, it is far above the autofluorescence background, i.e., it is caused by ICG. Hence, the extravasated part of ICG can be detected after the contrast agent had been washed-out from the vessels by the liver. Generally, ICG fluorescence was found from the whole breast tissue in the extravascular phase, i.e., extravasation occurred everywhere in the tissue. However, the fluorescence of the healthy tissue was small compared to those of the invasive carcinomas, resulting in high tumor contrast. In opposite, the fibroadenoma did not show local enrichment of ICG. These observations can be explained by a higher permeability of the capillaries in the malignant lesions compared to the healthy tissue and to the benign case. Due to the macromolecular appearance of ICG when bound to plasma proteins, only capillaries in malignant lesions are sufficiently leaky to be passed by the bound dye (Ebert et al. 2011). Our results are

in consistence with the enhanced permeability and retention (EPR) effect which implies enhanced extravasation of macromolecules in solid tumors due to the leakiness of their capillaries, and a large dwell time due to impaired lymphatic drainage. The latter effect could also be confirmed by a measurement 1 day after ICG application, in which ICG fluorescence was still detectable (Hagen et al. 2009).

Previous investigations on breast tumors with ICG were performed during the washout period after a bolus (Ntziachristos et al. 2000; Corlu et al. 2007; Rinneberg et al. 2008). This time window is similar to the washout phase after our infusion (cf. Fig. 2), which is the transition period from the vascular to the extravascular phase. Although the contribution from extravasated ICG in the bolus measurement is increasing with preceding time, the main signal originates from vascular ICG. Hence, tumor contrast in these investigations is predominantly based on angiogenesis. For absorption measurements, tumor contrast with ICG should correspond to measurements without contrast agent performed at a wavelength around 785 nm, which is sensitive to total hemoglobin absorption. Rinneberg et al. reported this result (Rinneberg et al. 2008), whereas Ntziachristos et al. did not compare their contrast-enhanced absorption mammograms with the intrinsic tissue absorption (Ntziachristos et al. 2000). As mentioned above, Corlu and coworkers described for their fluorescence measurements an improved contrast compared to differences in hemoglobin concentration (Corlu et al. 2007). This result corresponds mainly to the differences that we have observed between absorption and fluorescence ratio mammograms in the vascular phase. However, as shown in the preceding section, tumor contrast at the shortest wavelength of the native phase can be considerably larger than fluorescence contrast in the vascular phase. In opposition to these previous approaches, the present investigation gives, besides information on angiogenesis, access to the permeability of capillaries. This additional information could be helpful to overcome the insufficient specificity of optical imaging based on variations in the hemoglobin concentration alone. To fully explore the potential of the approach, a sufficiently large number of patients have to be investigated in future. Furthermore, a quantitative analysis of the extravasation process should provide deeper insight in the action mechanism of the contrast agent in various types of lesions.

The presented optical method for breast imaging has some similarities with dynamic contrast-enhanced MRI of the breast, where a bolus of a Gd chelate, e.g. Gd-DTPA, is applied. However, Gd-DTPA acts as a small molecule that nonselectively extravasates in tumors as well as in healthy tissue (Daldrup-Link and Brasch 2003). To obtain a more specific enhancement, several macromolecular contrast agents for MRI are under development. Up to now no such agent became available for clinical applications. A main problem is safety concerns related to the slow excretion and high tissue accumulation of toxic Gd ions (Feng et al. 2008). In contrast, ICG in connection with sensitive fluorescence imaging techniques offers the chance to improve diagnosis of breast cancer now.

3 Cancer and Early Malignancies of the GI

The spectral region used for the detection of deeper lying lesions, e.g., for optical investigation of breast tissue as presented before, is not a prerequisite for the monitoring of superficial lesions. Superficial tumors such as skin tumors and tumors of the GI are easily accessible using the visible spectral range in reflection geometry. Whereas skin tumors are recognized by experienced physicians to a sufficient extend (about 85 %) (Braun-Falco and Landthaler 1990), about 30 % of flat intraepithelial neoplasias are not visible by conventional white light endoscopy (Rubin et al. 2007). Besides chromoendoscopy (Rutter et al. 2004) and endomicroscopy (Hurlstone et al. 2008) the administration of the precursor substance of heme pathway, δ-aminolevulinic acid, which preferentially in tumor tissue is transformed to protoporphyrin IX, is actually the most promising way to cause selective enhancement of a fluorescent dye in tumor tissue.

3.1 Protoporphyrin IX as Tumor Marker

PpIX accumulates in tumor cells to such an amount that it can be visualized and quantized if underlying autofluorescence is suppressed (Moesta et al. 1997). Human tumors of the GI and their metastases show PpIX fluorescence when excited with blue or green light. This effect is evident even without any systemic administration of precursor substances like δ-aminolevulinic acid. There is a wide field for application of δ-aminolevulinic acid supported PpIX fluorescence for the diagnosis of bladder cancer (Betz et al. 2002; Cauberg et al. 2009), lung cancer (Baumgartner et al. 1996; Hautmann et al. 2007), and skin cancer (Cubeddu et al. 1999). In the following we discuss in more detail our investigations on tumors of the GI.

3.2 Time-Gated Fluorescence Imaging

Generally, two different technical approaches are commonly used continuous wave (cw) and time-gated fluorescence imaging or spectroscopy. The cw fluorescence measurements relay on different spectral characteristics like excitation and absorption bands which might overlap and hence a differentiation between chromophores of interest is difficult (Panjehpour et al. 1996). Other problems, i.e., motional artifacts arise from the fact that fluorescence and white light images based on cw measurements must be performed subsequently. Time-gated approaches allow additionally to the spectral separation the use of fluorescence decay times for differentiation and the suppression of ambient white light. Based on time-gated techniques, e.g., fluorescence lifetime imaging has been developed and tested for the detection of skin tumors in humans (Cubeddu et al. 1999). In our own studies to monitor PpIX fluorescence in the GI tract and in primary tumors as well as in lymph nodes (Moesta et al. 2000, 2001) we used an optical parametric oscillator (OPO, GWU-Lasertechnik) with ß-BaB_2O_4 as nonlinear medium, pumped by the third harmonic ($\lambda = 355$ nm, $E_{pulse} \geq 100$ mJ) of a

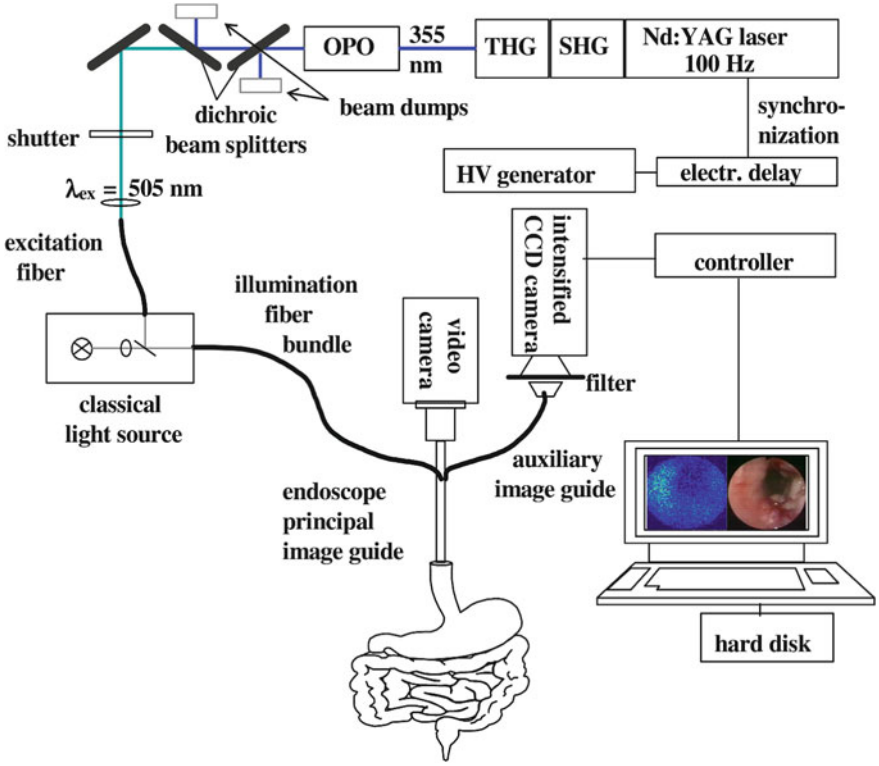

Fig. 6 Typical scheme of a setup for endoscopic investigation of time delayed fluorescence of the gastrointestinal tract after topical application of δ-aminolevulinic acid

Q-switched Nd:YAG laser (Infinity, Coherent, USA). This excitation source provided pulsed ($\tau \sim 3$ ns) laser radiation tunable between 410 nm and 2.2 μm. The output energy of the tunable laser beam was reduced to 300 μJ and coupled into a 600 mm hard clad silica fiber. The laser-induced fluorescence of human tissue was collected by the same fiber and guided to the entrance slit of an optical multichannel analyzer, consisting of an imaging polychromator (Axon) and a cooled, intensified CCD camera (Princeton Instruments). A dichroic beam splitter served to decouple excitation and observation optical paths, and to separate laser-induced fluorescence from backscattered laser light. In addition a long wave pass filters ($\lambda_{50\ \%} = 550$ nm) were used to suppress the remaining backscattered excitation light. In order to avoid interference with the conventional white light, the intensifier of the diode array detector was gated by an electrical pulse (−180 V) of about 20 ns duration. For this purpose, the pulse generator was triggered by an appropriately delayed pulse provided by the power supply of the Nd:YAG laser. A typical scheme of a setup for time delayed imaging and time delayed spectroscopy (if combined with a monochromator) is shown in Fig. 6. For quantification of tumor-specific fluorescence we used the ratio R = I(633 nm, 20 sns)/I(595 nm, 0 ns) derived from differently delayed spectra (Fig. 7).

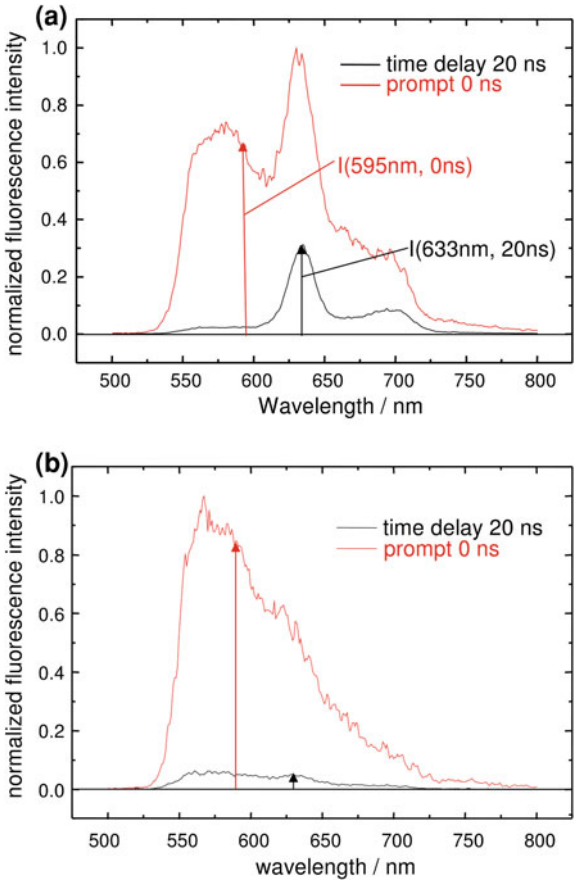

Fig. 7 Normalized fluorescence intensity of PpIX and autofluorescence background in dependence on wavelength. **a** Immediate and time delayed fluorescence spectrum of a carcinoma in vivo and **b** Immediate and time delayed fluorescence spectrum of normal mucosa in vivo

The tissue autofluorescence is superimposed on the fluorescence of PpIX ($\tau_{decay} \sim 16$ ns); therefore, we used the gating technique to suppress unspecific faster decaying spectral components ($\tau_{decay} \sim 3$ ns) of autofluorescence of gastrointestinal cancer and their metastases by simultaneous detection of prompt and time delayed fluorescence spectra (Moesta et al. 2001) as shown in Fig. 7a and 7b. Presented are immediate and delayed ($\tau_d = 20$ ns) fluorescence spectra of a particular primary colorectal carcinoma (Fig. 7a) and normal mucosa (Fig. 7b). For comparison, immediate and delayed fluorescence spectra have been normalized to the maximum intensity of the nondelayed fluorescence spectrum. Fluorescence spectra of primary tumors and their surrounding tissue are considerably different. A well defined fluorescence band with a maximum at $\lambda \approx 633$ nm and a second minor band at $\lambda \approx 700$ nm appear in the delayed fluorescence spectrum of the carcinoma (see Fig. 7a).

The developed technique is very sensitive which allows the detection of naturally in tumor cells occurring concentrations of PpIX without application of δ-aminolevulinic acid. Similar spectra can be obtained in lymph nodes and liver metastases. Fluorescence spectra of metastatic lymph nodes and liver metastases at a delay of 20 ns clearly show emission peaks similar to those measured for gastrointestinal primary tumors (Moesta et al. 2001).

3.3 Clinical Studies

The time-gated laser-induced fluorescence endoscopy has been applied in two clinical trials simultaneously with white light endoscopy of the esophagus (Ortner et al. 2003) and the colon (Ortner et al. 2010; Fusco et al. 2012). In these studies, besides the suppression of autofluorescence the pulsed measurement of fluorescence is used to suppress the white light needed for conventional endoscopy. To increase the sensitivity, the heme precursor δ-aminolevulinic acid, which promotes the preferential accumulation of the endogenous PpIX in proliferative tissue, is used as an exogenous marker to target malignant tissue in Barrett′s esophagus or in patients with colitis ulcerosa. To this end δ-aminolevulinic acid is topically administered to the patient 2 h before the measurement. For investigation of the esophagus besides the spectroscopy a two working channels endoscope (GIF 2T20, Olympus, Japan) was equipped with an auxiliary image guide (Medisecur AG, Germany), which was imaged onto the photocathode of an intensified CCD camera (Roper Scientific, USA). This auxiliary image guide was fixed in one of the working channels of the endoscope in such a way to cover nearly the same field of view for fluorescence imaging and white light imaging. A video camera and an intensified CCD camera were used to record conventional white light images and delayed (20 ns) fluorescence images, respectively (Fig. 8). The slight discrepancy between the white light image and the time delayed fluorescence image in Fig. 8 is caused by the slow refreshment rate of the fluorescence image (2 images/s). The malignant lesion is easily recognized by the red color i.e., stronger PpIX fluorescence. The images are processed in real time in order to identify malignant spots in the white light image for biopsy. Using this technique the number of biopsies could be decreased. Recently, a new synchronous fluorescence imaging system and data analysis methods have been developed by Liu et al. 2007.

The mechanism leading to accumulation of PpIX in tumor cells at the end of the heme biosynthetic pathway has been elucidated. Already in a study by Tan et al. 1997 was suggested that iron plays an important role. They found on gastric cancer cells that the inhibition of ferrochelatase by desferrioxomine in the presence of δ-aminolevulinic acid led to an increase of PpIX. High doses of desferrioxomine (more than 40 molar), however, showed a protective effect. In a recent study, Kemmner et al. 2008 were able to demonstrate that in malignant tissue a transcriptional down-regulation of ferrochelatase occurs, which causes accumulation of PpIX. Moreover, the enhancement of intracellular PpIX due to ferrochelatase

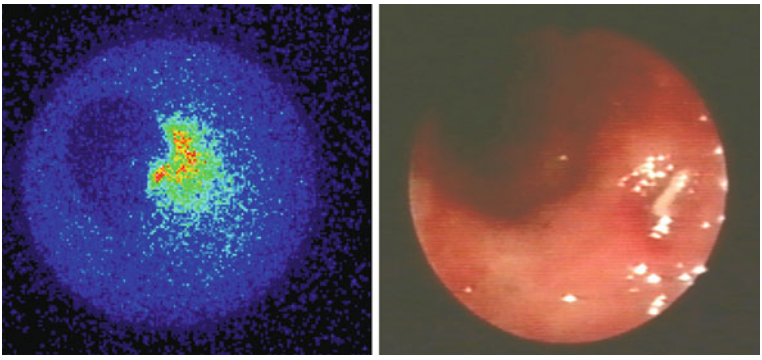

Fig. 8 Simultaneously taken fluorescence image **a** and white light image **b** of an esophagial carcinoma

siRNA silencing is a new step towards molecular imaging of tumors and a prerequisite for targeted use of photodynamic therapy using PpIX as photosensitizer.

To visualize tumor cells exogenous markers must be administered systemically or locally in order to create a sufficient contrast between malignant and normal tissue based on absorption or fluorescence. The nonfluorescing δ-aminolevulinic acid e.g., is metabolized in the heme synthesis pathway to protoporhyrin IX in high turnover tissues, which show typical porphyrin-like fluorescence characteristics. The sensitivity of the fluorescence detection system is determined by its ability to differentiate the fluorescence of the exogenous fluorophore from the underlying, unspecific tissue autofluorescence.

PpIX fluorescence as an intrinsic parameter of malignant biological tissues is suitable for molecular diagnostic application due to its relatively slow decay time compared to unspecific fluorescence background. The detection limit is clearly improved after suppression of short-lived autofluorescence components by time-gated detection. The discussed results demonstrate that time-gated fluorescence guided endoscopy is superior to conventional white light endoscopy for detection of early malignancies in Barrett′s esophagus and colitis ulcerosa.

4 Outlook

The discussed examples of fluorescence imaging on humans are based on application of the nontargeted contrast agent ICG and the endogenous fluorophor PpIX. So far, these molecules represent the most frequently used contrast agents in clinical environment for optical imaging. The translation of tumor targeting markers for optical imaging from research to the clinics will offer new perspectives in early detection of diseases. In terms of image contrast, the new markers are expected to considerably improve the tumor-to-background signal ratio. On the other hand, to detect small concentrations of tumor markers, in particular through

several centimeters of diffusely scattering tissue, a high fluorescence quantum yield and high detection sensitivity will be required. The discussed experimental methods and investigations on patients offer the possibility to estimate the detection limits in fluorescence imaging, and they provide results for future developments of instrumentation and data analysis. The improvement of tumor detection comprises the development of methods for a quantitative analysis of the enrichment of the contrast agent which is, in particular, difficult in highly scattering tissue. Quantification in fluorescence imaging could be an important step towards characterization of tumor grades as well as of therapy monitoring.

References

Baumgartner R, Huber RM, Schulz H et al (1996) Inhalation of 5-aminolevulinic acid: a new technique for fluorescence detection of early stage lung cancer. J Photochem Photobiol, B 36:169–174

Becker A, Hessenius C, Licha K et al (2001) Receptor-targeted optical imaging of tumors with near-infrared fluorescent ligands. Nature Biotechnol 19:327–331

Betz CS, Stepp H, Janda P et al (2002) A comparative study of normal inspection, autofluorescence and 5-ALA-induced PPIX fluorescence for oral cancer diagnosis. Int J Cancer 97:245–252

Braun-Falco O, Landthaler M (1990) Das maligne Melanom der Haut. Dt Ärztebl 87:933–936

Bremer C, Ntziachristos V, Weitkamp B et al (2005) Optical imaging of spontaneous breast tumors using protease sensing 'smart' optical probes. Invest Radiol 40:321–327

Cauberg EC, de Bruin DM, Faber DJ et al (2009) A new generation of optical diagnostics for bladder cancer: technology, diagnostic accuracy, and future applications. Eur Urol 56:287–296

Corlu A, Choe R, Durduran T et al (2007) Three-dimensional in vivo fluorescence diffuse optical tomography of breast cancer in humans. Opt Expr 15:6696–6716

Cubeddu R, Pifferi A, Taroni P et al (1999) Fluorescence lifetime imaging: an application to the detection of skin tumors. IEEE J Sel Top Quant Electron 5:923–929

Daldrup-Link HE, Brasch RC (2003) Macromolecular contrast agents for MR mammography: current status. Eur Radiol 13:354–365

Ebert B, Sukowski U, Grosenick D et al (2001) Near-infrared fluorescent dyes for enhanced contrast in optical mammography: phantom experiments. J Biomed Opt 6:134–140

Ebert B, Riefke B, Sukowski U et al. (2011) Cyanine dyes as contrast agents for near-infrared imaging in vivo: acute tolerance, pharmacokinetics, and fluorescence imaging. J Biomed Opt 16:066003-1-9

Enfield LC, Gibson AP, Everdell NL et al (2007) Three-dimensional time-resolved optical mammography of the uncompressed breast. Appl Opt 46:3628–3638

Feng Y, Jeong EK, Mohs AM et al (2008) Characterization of tumor angiogenesis with dynamic contrast enhanced magnetic resonance imaging and biodegradable macromolecular contrast agents in mice. Magn Reson Med 60:1347–1352

Fischer T, Ebert B, Voigt J et al (2010) Detection of rheumatoid arthritis using non-specific contrast enhanced fluorescence imaging. Acad Radiol 17:375–381

Floery D, Helbich TH, Riedl CC et al (2005) Characterization of benign and malignant breast lesions with computed tomography laser mammography (CTLM): initial experience. Invest Radiol 40:328–335

Fusco V, Ebert B, Weber-Eibel J et al (2012) Cancer prevention in ulcerative colitis: long-term outcome following fluorescence-guided colonoscopy. Inflamm Bowel Dis 18:489–495

Grosenick D, Moesta KT, Möller M et al (2005) Time-domain scanning optical mammography: I. recording and assessment of mammograms of 154 patients. Phys Med Biol 50:2429–2449

Grosenick D, Hagen A, Steinkellner O et al (2011) A multichannel time-domain scanning fluorescence mammograph: Performance assessment and first in vivo results. Rev Sci Instrum 82:024302

Hagen A, Grosenick D, Macdonald R et al (2009) Late-fluorescence mammography assesses tumor capillary permeability and differentiates malignant from benign lesions. Opt Expr 17:17016–17033

Hautmann H, Pichler JP, Stepp H et al (2007) In vivo kinetics of inhaled 5-aminolevulinic acid-induced protoporphyrin IX fluorescence in bronchial tissue. Respir Res 8:1–7

Hurlstone DP, Kiesslich R, Thomson M et al (2008) Confocal chromoscopic endomicroscopy is superior to chromoscopy alone for the detection and characterisation of intraepithelial neoplasia in chronic ulcerative colitis. Gut 57:196–204

Intes X, Ripoll J, Chen Y et al (2003) In vivo continuous-wave optical breast imaging enhanced with Indocyanine Green. Med Phys 30:1039–1047

Liebert A, Wabnitz H, Obrig H et al (2006) Non-invasive detection of fluorescence from exogenous chromophores in the adult human brain. Neuroimage 31:600–608

Liu Q, Chen K, Martin M et al (2007) Development of a synchronous fluorescence imaging system and data analysis methods. Opt Express 15:12583–12594

Kemmner W, Wan K, Rüttinger S et al (2008) Silencing of human ferrochelatase causes abundant protoporphyrin-IX accumulation in colon cancer. FASEB J 22:500–509

Maeda H, Wu J, Sawa T et al (2000) Tumor vascular permeability and the EPR effect in macromolecular therapeutics: a review. J Controlled Release 65:271–284

Mahmood U (2004) Near infrared optical applications in molecular imaging. Earlier, more accurate assessment of disease presence, disease course, and efficacy of disease treatment. IEEE Eng Med Biol Mag 23:58–66

Moesta KT, Ebert B, Rinneberg H et al (1997) Techniken zur Erkennung minimal residueller Erkrankungen—Fluoreszenzdiagnostik. Der Onkologe 3:422–428

Moesta KT, Ebert B, Handke T et al (2000) Fluorescence as a concept in colorectal lymph node diagnosis. Recent Results Cancer Res 157:293–304

Moesta KT, Ebert B, Handke T et al (2001) Protoporphyrin IX occurs naturally in colorectal cancers and their metastases. Cancer Res 61:991–999

Ntziachristos V, Yodh AG, Schnall M et al (2000) Concurrent MRI and diffuse optical tomography of breast after indocyanine green enhancement. Proc Natl Acad Sci USA 97:2767–2772

Ortner M-AEJ, Ebert B, Hein E et al (2003) Time gated fluorescence spectroscopy in Barrett′s esophagus. Gut 52:28–33

Ortner M-AEJ, Fusco V, Ebert B et al (2010) Time-gated fluorescence spectroscopy improves endoscopic detection of low-grade dysplasia in ulcerative colitis. Gastrointest Endosc 71:312–318

Panjehpour M, Overholt BF, Vo-Dinh T et al (1996) Endoscopic fluorescence detection of high-grade dysplasia in Barrett's esophagus. Gastroenterology 111:93–101

Perlitz C, Licha K, Scholle FD et al (2005) Comparison of two tricarbocyanine-based dyes for fluorescence optical imaging. J Fluoresc 15:443–454

Poellinger A, Burock S, Grosenick D et al (2011) Breast cancer: early- and late-fluorescence near-infrared imaging with indocyanine green—a preliminary study. Radiology 258:409–416

Richards-Kortum R, Sevick-Muraca E (1996) Quantitative optical spectroscopy for tissue diagnosis. Annu Rev Phys Chem 47:555–606

Rinneberg H, Grosenick D, Moesta KT et al (2005) Scanning time-domain optical mammography: detection and characterization of breast tumors in vivo. Technol Cancer Res Treat 4:483–496

Rinneberg H, Grosenick D, Moesta KT et al (2008) Detection and characterization of breast tumors by time-domain scanning optical mammography. Opto-Electron Rev 16:147–162

Rubin DT, Rothe JA, Hetzel JT et al (2007) Are dysplasia and colorectal cancer endoscopically visible in patients with ulcerative colitis? Gastrointest Endosc 65:998–1004

Rutter M, Saunders B, Wilkinson K et al (2004) Severity of inflammation is a risk factor for colorectal neoplasia in ulcerative colitis. Gastroenterology 126:451–459

Taroni P, Torricelli A, Spinelli L et al (2005) Time-resolved optical mammography between 637 and 985 nm: clinical study on the detection and identification of breast lesions. Phys Med Biol 50:2469–2488

Van de Ven S, Wiethoff A, Nielsen T et al (2010) A novel fluorescent imaging agent for diffuse optical tomography of the breast: first clinical experience in patients. Mol Imaging Biol 12:343–348

Wagnieres G, Hadjur C, Grosjean P et al (1998) Clinical evaluation of the cutaneous phototoxicity of 5,10,15,20-tetra(m-hydroxyphenyl)chlorin. Photochem Photobiol 68:382–387

FDG PET and PET/CT

Berud J. Krause, Sarah Schwarzenböck
and Michael Souvatzoglou

Abstract

Molecular imaging with positron emission tomography (PET) using tumour-seeking radiopharmaceuticals has gained wide acceptance in oncology with many clinical applications. The hybrid imaging modality PET/CT allows assessing molecular as well as morphologic information at the same time. Therefore, PET/CT represents an efficient tool for whole body staging and re-staging within one imaging modality. In oncology the glucose analogue ^{18}F-fluorodeoxyglucose (FDG) is the most widely used PET and PET/CT radiopharmaceutical in clinical routine. FDG PET and PET/CT have been used for staging and re-staging tumour patients in numerous studies. This chapter will discuss the use and the main indications of FDG PET and PET/CT in oncology with special emphasis on lung cancer, oesophageal cancer, colorectal cancer, head and neck cancer, lymphoma and breast cancer (among other tumour entities). A review of the current literature will be given with respect to primary diagnosis, staging and diagnosis of recurrent disease (local, lymph node and distant metastases). Besides its integral role in diagnosis, staging and re-staging of disease in oncology, there is increasing evidence that FDG PET and PET/CT can significantly contribute to therapy response assessment possibly influencing therapeutic management and treatment planning, to therapy tumour control and prediction of prognosis in oncologic patients, which will also be discussed in this chapter.

B. J. Krause (✉) · S. Schwarzenböck
Department of Nuclear Medicine, Universitätsklinikum Rostock,
Gertrudenplatz 1, 18057, Rostock, Germany
e-mail: bernd.krause@med.uni-rostock.de

M. Souvatzoglou
Department of Nuclear Medicine, Klinikum rechts der Isar,
Technische Universität, Munich, Germany

O. Schober and B. Riemann (eds.), *Molecular Imaging in Oncology*,
Recent Results in Cancer Research 187, DOI: 10.1007/978-3-642-10853-2_12,

Contents

1 Introduction

Molecular imaging with positron emission tomography (PET) using tumor-seeking radiopharmaceuticals has gained wide acceptance in oncology with many clinical applications. In oncology the glucose analogue ^{18}F-fluorodeoxyglucose (FDG) is the most widely used radiopharmaceutical. FDG follows a metabolic pathway similar to glucose in vivo, except that it is not metabolised to CO_2 and water, but is trapped within cells. Increased consumption of glucose is a characteristic of most tumor cells and is partially related to overexpression of the GLUT-1 glucose transporters and increased hexokinase activity. FDG enables to visualize regional glucose metabolism with high sensitivity and somewhat lower specificity. Despite the high sensitivity of FDG PET false positive findings occur due to physiologic processes, such as brown fat, colonic and gynecologic activity, infectious and inflammatory processes, and rebound thymic hyperplasia. FDG accumulation can be assessed visually, semi-quantitatively, and quantitatively. The most commonly used technique is the standardized uptake value (SUV): a semi-quantitative index of tumor uptake normalized to the injected dose and a measure of the total volume of distribution, such as the patient's body weight.

The hybrid imaging modality PET/CT has been introduced in the late 1990s. PET/CT imaging allows assessing molecular as well morphologic information at the same time. PET/CT represents an efficient tool for whole-body staging and re-staging within one imaging modality. PET/CT over PET or CT alone improves lesion localization as well as lesion characterization in oncologic imaging.

FDG PET and PET/CT have been used for staging and re-staging tumor patients in numerous studies (Fletcher et al. 2008). This chapter provides an overview of the main clinical applications of FDG PET and PET/CT in oncology.

2 Clinical Applications of FDG PET and PET/CT in Oncology

2.1 Non-Small Cell Lung Cancer

In Europe and the United States, non-small cell lung cancer (NSCLC) is the leading cause of cancer-related deaths in both men and women. Accurate diagnostic work-up and staging of NSCLC is mandatory with respect to mediastinal lymph node involvement and distant metastases, therapy management, and prognosis. A considerable number of studies have provided evidence that FDG PET/CT improves diagnostic accuracy.

In a systematic review by Gould et al. (2001). PET showed a sensitivity of 83–100 % (mean 96 %) with an highly variable specificity of 0–100 % (mean 73 %) for the detection of pulmonary lesions of any size ($n = 1.474$). Analysis of pulmonary nodules only ($n = 450$) revealed a mean sensitivity and specificity of 98 and 83 %, respectively (Gould et al. 2001). Another systematic review including four prospective studies assessing the effectiveness of PET in differentiating malignant from benign lesions demonstrated a sensitivity of 86–100 % and a specificity of 40–90 % (Fletcher et al. 2008). As the positive predictive value of PET will be higher in high-risk patients and the negative predictive value will be higher in low-risk patients, PET will be most useful in patients at an intermediate risk of lung cancer. In their review analyzing 800 patients Fischer et al. (2001) reported a sensitivity of 96 % and a specificity of 78 % for FDG PET/CT in the diagnosis and staging of lung cancer (Fischer et al. 2001). Schreyögg et al. evaluated the diagnostic- and cost-effectiveness of integrated PET/CT for staging of NSCLC. The authors reported a diagnostic effectiveness in terms of correct TNM staging of 40 % for CT alone and 60 % for PET/CT. For the assessment of resectability 84 % of patients were staged correctly by PET/CT vs. 70 % by CT alone. The cost-effectiveness analyses showed that costs for PET/CT were within the commonly accepted range for diagnostic tests or therapies (Schreyogg et al. 2010).

With respect to the detection of mediastinal lymph node metastases comparing PET and CT a systematic review by Birim et al. showed an overall sensitivity and specificity of 83 and 92 %, respectively, for CT 59 and 78 %, respectively (Birim et al. 2005). Lv et al. performed a meta-analysis determining the pooled sensitivity and specificity of FDG PET/CT for mediastinal lymph node staging in NSCLC. The authors reported a pooled sensitivity and specificity of 73 and 92 %, respectively. The authors concluded that integrated FDG PET/CT demonstrated an accurate imaging technique with excellent specificity for mediastinal lymph node staging in patients suffering from NSCLC (Lv et al. 2011) (Fig. 1).

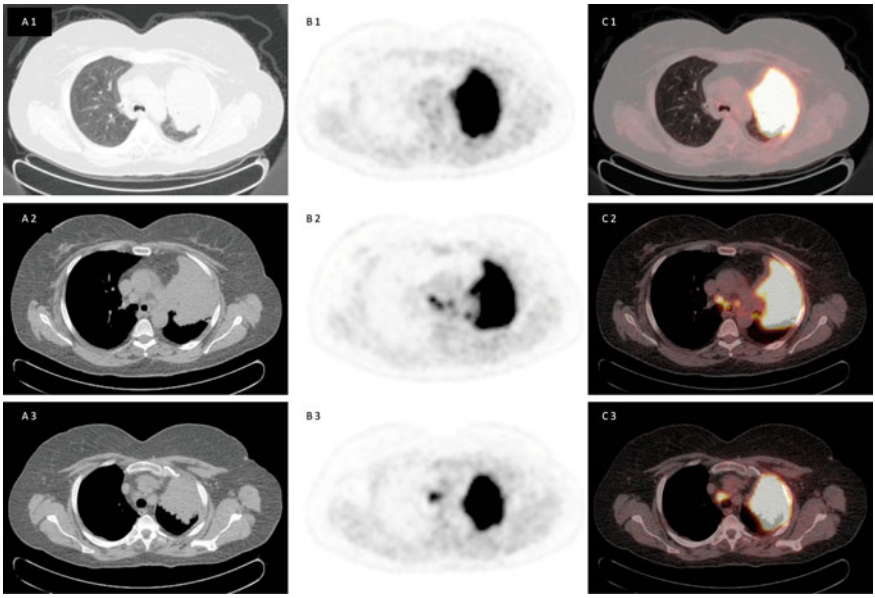

Fig.1 62 year old patient under suspicion of bronchial cancer of the left upper lobe referred for FDG PET/CT for primary staging. FDG PET/CT revealed FDG-positive primary tumour and contralateral lymph node metastases (N3); (A 1-3) CT scan, (B 1-3) PET scan, (C 1-3) PET/CT fused images

A systematic review revealed that FDG PET detected 10–20 % more distant metastases in comparison to other imaging modalities and led to a therapy management change in 9–64 % [for more information see (Fletcher et al. 2008)]. The PLUS trial studied the effect of PET in the reduction of futile thoracotomies in patients with suspected NSCLC referred for surgery after conventional work-up. The trial reported a significant higher number of patients with futile surgery in the conventional work-up arm compared to the conventional work-up plus PET arm [relative risk reduction, 51 %, 95 % CI 32–80 % ($p = 0.003$) in favor of PET] (van Tinteren et al. 2002). Viney et al. addressed the impact of FDG PET on the clinical management and surgical outcome of patients with NSCLC stage I-II examining 92 patients using conventional work-up and 91 patients using conventional work-up plus PET. The sensitivity and specificity of FDG PET for the detection of mediastinal disease was 73 and 90 %, respectively. FDG PET could potentially have an impact on management in 26 % of patients. With a minimum 1-year survival, 77 % of patients were alive in the non-PET arm and 80 % in the PET arm (Viney et al. 2004). FDG PET/CT may also be helpful with respect to radiation treatment planning of NSCLC causing a change in radiation volume in up to 25–60 % [for further information see (Fletcher et al. 2008)].

2.2 Oesophageal Cancer

Preoperative assessment of prognostic factors is important in clinical management of patients suffering from oesophageal cancer. Relevant pre-therapeutic prognostic factors are local tumor invasion, locoregional lymph node stage, and distant metastases. Sensitivity and specificity of FDG PET and PET/CT for staging oesophageal cancer have been investigated in many studies. Endoscopic ultrasound and CT represent the most widely used imaging modalities for the assessment of local tumor invasion (T category) and locoregional lymph node involvement. Precise pre-therapeutic staging is important in choosing the best available therapy for the patient. Van Westreenen et al. published a systematic review and showed that FDG PET had a sensitivity of 51 % and a specificity of 84 % for the detection of lymph node staging (van Westreenen et al. 2004). In a more recent meta-analysis van Vliet et al. concluded that endoscopic ultrasound CT and PET contribute to detect metastases in oesophageal cancer. EUS turned out to be more sensitive for locoregional lymph node staging. In turn CT and FDG PET proved to be more specific (van Vliet et al. 2008).

FDG PET and PET/CT can add clinically relevant information with respect to M staging. It is crucial to be able to differentiate patients with locoregional disease from patients with systemic disease. Distant metastases have to be ruled out before the initiation of therapy. FDG PET has a sensitivity and specificity of 67 and 97 %, respectively, in M staging of oesophageal cancer (Fletcher et al. 2008). In systemic disease, there is no curative option and the patients will receive palliative treatment. After exclusion of distant metastases, the selection of the therapeutic regimen depends on the T stage. Localized tumors (T1/T2) have a high likelihood of R0 resection, and primary oesophagectomy represents the most frequent therapeutic procedure. In cases of locally advanced tumors (T3/T4, N1), surgery remains the mainstay of therapy, preceded by a neoadjuvant chemotherapy or radiochemotherapy.

In conclusion, the use of FDG PET and PET/CT is useful for staging oesophageal cancer for the detection of distant metastases.

2.3 Gastric Cancer

FDG PET and PET/CT for staging gastric cancer is limited by a limited sensitivity. Only 60 % of gastric cancers are FDG avid. Especially tumors with non-intestinal-type histology according to Lauren's classification (signet ring cell carcinoma, diffuse type) are often not FDG avid and can therefore not be imaged with FDG PET and PET/CT. Sensitivities for FDG PET range from 47 to 96 % (mean sensitivity, 77 %; mean specificity, 99 %) for the detection of gastric cancer (Herrmann et al. 2007). Wu et al. carried out a systematic review and meta-analysis. Across nine studies the overall sensitivity of FDG PET for the detection of recurrent gastric cancer was 78 % and the overall specificity was 82 % (Wu et al. 2011).

Fig. 2 89 year old patient with suspicion of recurrent rectal cancer after rectum amputation 09/10 (CEA 21 ng/ml) referred for FDG PET/CT for restaging. FDG PET/CT revealed local recurrence; (**a**) CT scan, (**b**) PET scan, (**c**) PET/CT fused images

2.4 Colorectal Cancer

A number of FDG PET studies on staging, detection of recurrence, and changes of therapy management in patients with colorectal cancer have been published [for reviews see (Brush et al. 2011; Fletcher et al. 2008)]. A systematic review and meta-analysis of studies evaluating the diagnostic test accuracy of FDG PET reported a sensitivity of 94 % and a specificity of 98 % in patients with locally recurrent rectal cancer (Fig. 2). Additional information provided by FDG PET is important for the clinical therapy management of patients with recurrent colorectal carcinoma. Visualization of CT negative lesions by FDG PET potentially allows an earlier change of the therapy regimen. Detection of distant metastases and better preoperative assessment of tumor spread can avoid unnecessary surgery, leading to a reduction of morbidity, and mortality associated with aggressive and futile therapies. When data related to changes in the management of these patients were pooled, 29 % of management decisions were changed. The majority were related to the avoidance of surgery as a result of the upstaging of the patients' disease classification (Huebner et al. 2000).

An expert panel concluded that the use of FDG PET is not beneficial in the primary diagnosis but recommended the use of FDG PET for the detection of extrahepatic recurrence and local relapse (Fletcher et al. 2008). In a more recent systematic review Brush et al. investigated the value of FDG PET and PET/CT in staging and re-staging of colorectal cancer (Brush et al. 2011). The systematic review found insufficient evidence to support the routine use of FDG PET/CT in primary colorectal cancer and only a small amount of evidence supporting its use in the pre-operative staging of recurrent and metastatic CRC. Although FDG PET/CT was shown to change patient management, the data were divergent and the quality of studies was limited.

2.5 Gastrointestinal Stromal Tumors

Because sarcomas, including gastrointestinal stromal tumors (GISTs) often show a high FDG avidity, FDG PET and PET/CT can be used to evaluate these tumors and the response to therapy [for a review see (Van den Abbeele 2008)]. This is of

special importance as morphological changes occur late in the course of therapy. Metabolic response as assessed by FDG PET is closely related to clinical response and changes of FDG uptake occur early in the course of imatinib therapy. New CT criteria for therapy response have been proposed for GISTs combining morphological as well as density criteria. Therefore, tumor response to therapy in GISTs is best monitored by the hybrid imaging modality PET/CT.

2.6 Head and Neck Cancer

FDG PET and PET/CT studies in patients with head and neck cancer on diagnosis and staging have been published [for reviews see (Duet et al. 2010; Fletcher et al. 2008)]. There are not sufficient data to support the use of FDG PET and PET/CT in primary diagnosis of head and neck cancer. In patients with advanced disease FDG PET and PET/CT is useful if metastases or a secondary cancer is suspected. In initial M staging a meta-analysis by Xie et al. showed pooled sensitivity estimates for FDG PET/CT of 88 % and specificity estimates of 95 % (Xie et al. 2011). Kubicek et al. demonstrated in a large cohort of patients that the positive predictive value of N staging for patients was 94 % going along with a negative predictive value of 89 %. FDG PET also revealed prognostic information with respect to overall survival (Kubicek et al. 2010).

A systematic review and meta-analysis of studies evaluating post-treatment FDG PET or PET/CT imaging in head and neck cancer was published by Gupta et al. (2011). The aim of the analysis was to assess the diagnostic performance of FDG PET or PET/CT in post-treatment response assessment and/or surveillance imaging of head and neck squamous cell carcinoma. The pooled sensitivity and specificity of post-treatment PET or PET/CT for the primary site were 80 and 88 %, respectively; for the neck the corresponding values were 72 and 88 %. The authors concluded that overall diagnostic performance of post-treatment FDG PET or PET/CT for response assessment and surveillance imaging of head and neck cancer was good, but the positive predictive value was somewhat limited. However, the negative predictive value was shown to be high and therefore an FDG negative post-treatment scan most probably indicates the absence of viable tumor tissue.

2.7 Melanoma

FDG PET has been extensively studied as imaging modality for the detection of metastatic cutaneous melanoma [for reviews see (Fletcher et al. 2008; Patnana et al. 2011)]. In general, sensitivity and specificity for detecting metastases are higher for FDG PET or PET/CT than for conventional imaging modalities. However, for the detection of regional lymph node metastases, sensitivities were lower compared to sentinel node biopsy and FDG PET also showed a lower

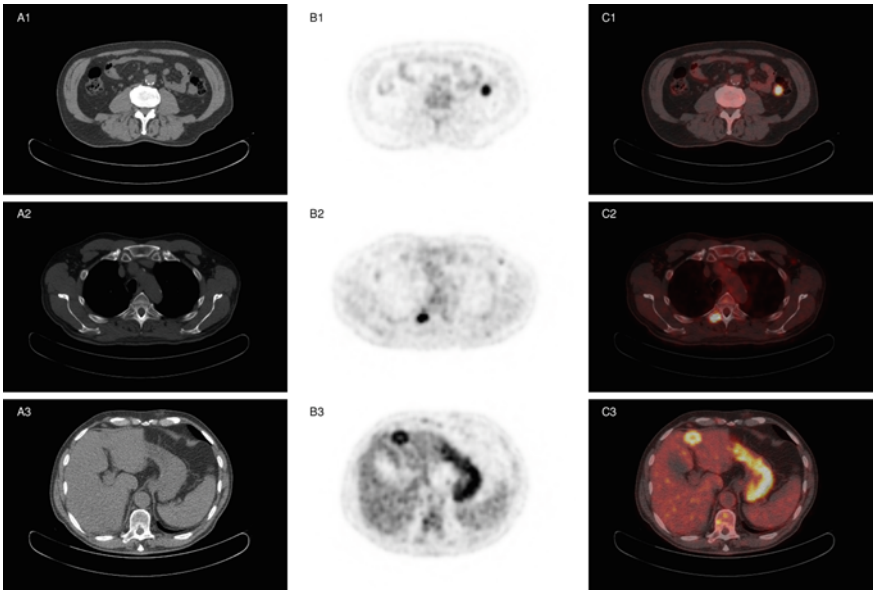

Fig. 3 64 year old patient suffering from pulmonal metastasized malignant melanoma (initial diagnosis thoracal left 07/04) referred for FDG PET/CT for re-staging after resection of a pulmonal metastasis of the right lower lobe 02/11. FDG PET/CT revealed FDG-positive soft tissue lesions (**A1**) CT scan, (**B1**) PET scan, (**C1**) PET/CT fused images, bone metastasis (**A2**) CT scan, (**B2**) PET scan, (**C2**) PET/CT fused images and hepatic metastasis (**A3**) CT scan, (**B3**) PET scan, (**C3**) PET/CT fused images

sensitivity for the detection of lung metastases. Additionally MRI should be performed to exclude brain metastases.

It has also been proposed that FDG PET or PET/CT could be useful in patients who are at high risk for systemic relapse and as additional imaging tool for the detection of recurrent disease. Essler et al. published a study analyzing the predictive values, sensitivity, and specificity of FDG PET/CT compared with the tumor markers S100B and MIA in the follow-up of high-risk melanoma patients. All three biomarkers detected metastases of malignant melanoma with clinically valuable sensitivity and specificity. Among these, FDG PET/CT was the most effective modality. Sensitivity and specificity of PET/CT were 97 %, respectively (Essler et al. 2011) (Fig. 3).

2.8 Lymphoma

Accurate staging is of critical importance in both, Hodgkin's disease (HD) and non-Hodgkin's lymphoma (NHL), as treatment is varying according to the stage of the disease (Fletcher et al. 2008). Sensitivity and specificity of FDG PET is different in the various histological lymphoma subtypes. However, it exhibits a

high sensitivity in the major classes of lymphoma in clinical practice: HD, diffuse large B cell lymphoma and follicular lymphoma, usually exhibit high FDG uptake. FDG PET has emerged in the last 15 years as a powerful imaging modality in assessing patients with such lymphoma types, and provides substantial information regarding identification of the most suitable site for biopsy, initial staging, response to therapy, assessment of post-treatment residual masses, identification of recurrent disease and potentially, radiotherapy planning. FDG PET has lower sensitivity in some less common NHL subtypes, such as marginal zone lymphoma, especially concerning extranodal manifestations of this subtype, peripheral T cell lymphoma, small lymphocytic NHL, and the mucosa-associated lymphoid tissue (MALT) subtype (Elstrom et al. 2003). In those subtypes FDG avidity has to be assessed by a pretreatment FDG PET almost mandatory, to be able to apply FDG PET in the further clinical workflow.

FDG PET/CT is superior to CT alone in staging and re-staging nodal disease as well as in detecting extranodal involvement including hepatic, splenic, bone marrow, and gastric involvement (Moog et al. 1998). A criterion for splenic involvement in FDG PET is when the uptake in the spleen is higher than in the liver. Concerning bone marrow involvement because of the high proportion of false-negative results, conventional masked biopsies are still needed (Fletcher et al. 2008).

FDG PET imaging predicts therapeutic response in lymphoma at various time points after initiation or completion of treatment [for a review see (Czernin et al. 2010; Hutchings and Barrington 2009)]. This has been published by the Consensus of the Imaging Subcommittee of the International Harmonization Project in Lymphoma that has re-defined the roles of PET and CT imaging in assessing therapeutic responses in lymphoma. For more detailed information concerning this issue the reader is directed to the manuscripts by Juweid et al. (2007) and Cheson et al. (2007). In summary FDG PET response is assessed visually by comparing FDG lesion uptake with mediastinal blood pool activity. Lesions with FDG uptake at or below blood pool activity following treatment would strongly suggest a complete response. It has to be kept in mind that lesions with increased FDG uptake do not necessarily represent residual disease because infectious or inflammatory lesions can accumulate the radiotracer. Further, thymic hyperplasia is common after chemotherapy and is a common cause of false positive results. In FDG PET it is often presented as a V-shaped uptake in the anterior mediastinum. Additionally, diffuse bone marrow uptake or splenic uptake post granulocyte colony-stimulating factor therapy can mimic lymphomatous bone marrow or splenic involvement.

2.9 Breast Cancer

Mammography remains the principal imaging tool to screen for breast cancer. There is a high risk of false negative results, when FDG PET is applied to characterize breast lesions. Small lesions cannot be characterized due to the partial volume effects.

Histopathological entities including invasive lobular carcinoma, tubular carcinoma, and carcinoma in situ are often not FDG avid enough to be detected by PET.

Local and distant staging has important implications on management and prognosis in patients with breast cancer. Regarding axillary lymph node staging the sensitivity and specificity of FDG PET/CT is higher than that of CT alone; however, the overall accuracy of 79 % was not sufficiently high to suggest that PET/CT imaging could replace the sentinel node biopsy approach (Heusner et al. 2009). Several studies have shown that FDG PET/CT is not sufficiently accurate to permit reliable axillary lymph node staging (Czernin et al. 2010). FDG PET and PET/CT can add substantial diagnostic information in patients clinically suspected to have distant metastases. It is most valuable mainly in patients with locally advanced breast cancer and when neoadjuvant therapy is planned without axillary dissection or sentinel node sampling. For the latter it can be used to evaluate response to treatment.

Concerning tumor recurrence, FDG PET has a high accuracy in detecting locoregional and distant tumor manifestations. It has gained a valuable role in the evaluation of patients with clinical suspicion for recurrence and negative tumor markers as well as in asymptomatic patients with increased tumor markers. Sensitivity and specificity have been reported with a median of 92 % (range, 57–97 %) and 89 % (range, 79–96 %), respectively (Fletcher et al. 2008). However, it has to be noticed that false negative results can be obtained in case of a non FDG avid primary such as the invasive lobular carcinoma.

Regarding the detection of bone metastases, concerning staging and restaging, FDG PET, and bone scintigraphy provide complemental information. Osteolytic metastases are better detected with PET, while osteoblastic metastases often do not exhibit increased glucose utilization and are better detected with bone scintigraphy. Further, FDG PET and PET/CT is helpful to characterize treatment effects in osseous lesions.

2.10 Ovarian Cancer

Ovarian cancer is the leading cause of death from gynecologic cancer in the Western World. Ovarian cancer spreads early by implantation on both the parietal and the visceral peritoneum before spreading through the lymphatics and involving the inguinal, pelvic, paraaortic, and mediastinal lymph nodes. The serum tumor marker CA-125 is widely used to assess the effectiveness of therapy and to detect tumor recurrence.

Unclear ovarian masses are evaluated with ultrasound and/or MRI. FDG PET has been shown to be limited in the diagnosis of cancer of the ovaries. Physiologic FDG uptake observed in the ovaries of women of reproductive age even after hysterectomy is reasonably common and may be mistaken for pathologic uptake. However, focal uptake in the region of the ovaries in postmenopausal women is suspicious of malignancy and should be further evaluated. Surgical exploration remains the standard of reference for the initial staging of ovarian cancer. CT and MRI have been accepted as useful imaging modalities for preoperative staging of ovarian cancer.

FDG PET may be useful as an adjunct to diagnostic CT for staging ovarian cancer (Schwarz et al. 2009). FDG PET is more sensitive than CT in detecting small peritoneal deposits and distant metastases. Therefore, it is recommended in the guidelines of the European Society of Urogenital Radiology (ESUR) in suspected stage IV disease (advanced ovarian cancer) and in the presence of indeterminate lymph node appearance (Forstner et al. 2010). FDG PET and PET/CT can be used to monitor response to treatment in advanced ovarian cancer as it is more accurate in characterizing residual disease after chemotherapy than CT alone. However, it cannot replace second-look laparotomy (Schwarz et al. 2009).

Several studies have shown that FDG PET and PET/CT is most useful in the evaluation of tumor recurrence (Schwarz et al. 2009). It has a higher accuracy than conventional imaging in detecting recurrence of ovarian cancer in both rising CA-125 level, and clinical suspicion of recurrence with not elevated CA-125 level (Havrilesky et al. 2005).

2.11 Sarcomas

Sarcomas are a rare heterogeneous group of tumors composing about 1 % of all malignancies, presenting with varied radiologic appearances. With respect to the biologic potential, the World Health Organization (WHO) has classified soft tissue tumors in four categories: benign, intermediate (locally aggressive), intermediate (rarely metastasize), and malignant (Fletcher et al. 2002). A detailed presentation of the different types is beyond the scope of this chapter. A recent meta-analysis of FDG PET studies in patients with sarcoma concluded, that FDG PET can discriminate between benign tumors and low grade tumors and intermediate and high grade tumors. However, using FDG PET it is difficult to distinguish low grade tumors from benign tumors (Bastiaannet et al. 2004). Czernin's group investigated the baseline glucose metabolic phenotype of sarcoma in more than 100 patients with soft tissue sarcoma. The SUV differed considerably and significantly among the many histological subtypes. Liposarcomas, especially the myxoid variants exhibited low FDG uptake. Sarcomas not otherwise specified (NOS), the most de-differentiated variants, had the highest FDG uptake. Overall, SUVmax was significantly higher in high grade than in low grade sarcomas (11.7 ± 9.1 g/ml vs. 3.7 ± 1.8 g/ml; $p < 0.001$) (Czernin et al. 2010). FDG PET can be useful in the evaluation of soft tissue tumors, by guiding biopsy, helping to sample in the area with highest glucose utilization. CT or MRI is essential for planning of surgical interventions or radiation treatment. However, in FDG avid sarcomas FDG PET can play a role in staging and restaging (Fig. 4). A limitation of FDG PET that has been alleviated by PET/CT is the detection of pulmonary metastases, presenting as small parenchymal nodules. They are sometimes missed by FDG PET imaging and the CT information is essential to detect them. Furthermore, FDG PET may have a role in assessing response to neoadjuvant chemotherapy, and potentially modify treatment.

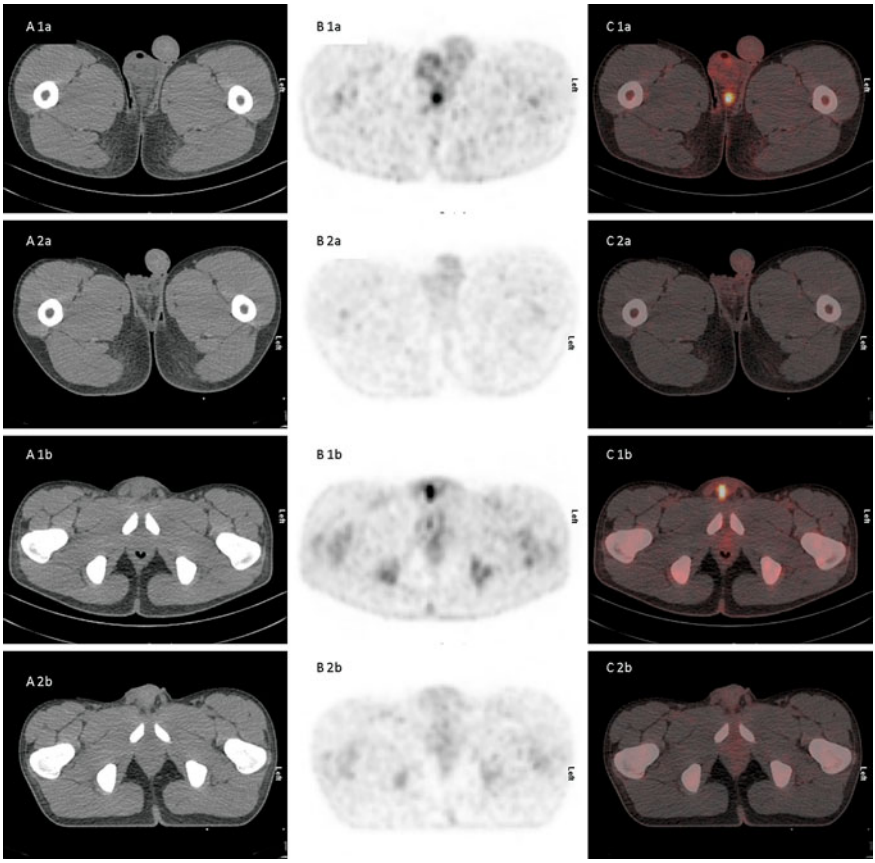

Fig. 4 14 year old patient with a penile rhabdomyosarcoma referred for FDG PET/CT two times. 1. For restaging after R2 resection 03/11: (A 1a and A 1b) CT scan, (B 1a and B 1b) PET scan, (C 1a and C 1b) PET/CT fused images. 2. For restaging after chemotherapy 05/11: (A 2a and A 2b) CT scan, (B 2a and B 2b) PET scan, (C 2a und C 2b) PET/CT fused images. FDG PET/CT 03/11 revealed two tumor lesions after R2-resection, FDG PET/CT 05/11 showed a good therapy response after chemotherapy

2.12 Pancreatic Cancer

Pancreatic cancer is the fifth most common cancer in both men and women in the US and is associated with a poor overall survival (< 4 %) as curative therapy is restricted to patients suffering from limited disease referred for surgery.

Commonly used imaging tools for the diagnosis of exocrine pancreatic cancer are ultrasound, endosonography, CT, MRI, magnetic resonance, and endoscopic retrograde cholangio-pancreatography (MRCP and ERCP). As 80–90 % of exocrine pancreatic cancers show a high FDG-uptake FDG PET was introduced to potentially improve detection of pancreatic adenocarcinomas. Fletcher et al.

reported that FDG PET should additionally be used in selected patients demonstrating inconclusive conventional imaging findings (Fletcher et al. 2008).

In a meta-analysis performed by Orlando et al. comparing PET/CT and CT for the differentiation between benign and malignant pancreatic lesions sensitivity and specificity of FDG PET was 71–100 % and 53–100 %, respectively (for CT 53–100 % and 0–100 %, respectively) (Orlando et al. 2004). In another review comparing the use of PET and conventional work-up (CT, MRI, ultrasonography, and Tl-201-SPECT) in the diagnosis of pancreatic cancer PET showed a pooled sensitivity and specificity of 91 and 86 % and was superior to the other imaging modalities. With respect to a change in patient management caused by PET findings no conclusion could be made due to considerably differing results of these studies (for further information see (Fletcher et al. 2008)). Schick et al. assessed the diagnostic impact of FDG PET evaluating solid pancreatic lesions vs. endosonography, ERCP with intraductal ultrasonography and abdominal ultrasound. The authors reported that the evaluation of dignity of pancreatic lesions was almost equal between FDG PET and the other modalities (Schick et al. 2008).

Fletcher et al. concluded that PET improved differentiation between benign and malignant pancreatic tissue in the diagnostic work-up of patients with suspected pancreatic lesions and might reduce the need for biopsy and surgery influencing morbidity (Fletcher et al. 2008). The value of FDG PET in imaging pancreatic cancer is limited concerning lymph node staging, detection of peritoneal disease, and liver metastasis (especially < 1 cm). In extratumoral staging FDG PET may play a role in the detection of occult lesions (such as e. g. non-hepatic distant metastases and synchronous tumours) (Reske 2009). With respect to re-staging of pancreatic cancer after pancreatic resection Ruf et al. reported that FDG PET and -PET/CT might be superior compared to CT and MRI (sensitivity of 96 and 39 % for PET and CT/MRI, respectively) (Ruf et al. 2005).

2.13 Thyroid Cancer

Differentiated thyroid cancer (papillary or follicular) is highly treatable and curable. However, 10–30 % of patients will develop recurrence or metastases, which cannot be detected by I-131 whole-body scintigraphy. FDG PET is used in patients treated for well-differentiated thyroid cancer showing a rising thyreoglobulin serum marker (Tg) $>$ 10 ng/ml with negative findings of I-131 whole-body scintigraphy. The diagnostic accuracy of FDG PET is generally high in patients with negative radioiodine scans and high Tg levels (Bertagna et al. 2010). In a systematic review Hoof et al. reported a sensitivity and specificity of 70–95 % and 77–100 %, respectively, for the detection of thyroid cancer recurrence using FDG PET. In 82 % of patients with raised tumor markers and negative findings on I-131 whole-body scintigraphy PET localized FDG-positive foci suggestive for recurrence (Hooft et al. 2001) (Fig. 5). In another review evaluating the detection of thyroid cancer recurrence in previously treated patients with elevated serum markers and negative I-131 scan

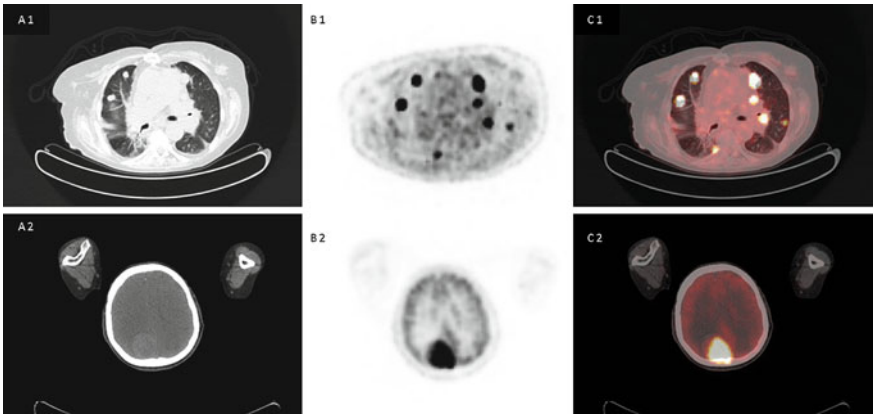

Fig. 5 70 year old patient with follicular thyroid cancer (pT3acN0cM1/UICC 1987), increasing thyreoglobulin serum marker and negative findings of I-131 whole body scintigraphy referred for FDG PET/CT for restaging. FDG PET/CT revealed multiple FDG-positive pulmonal metastases and cerebral metastasis; (A 1 and 2) CT scan, (B 1 and 2) PET scan, (C 1 and 3) PET/CT fused images

PET showed a sensitivity and specificity of 84 and 56 %, respectively [for further information see (Fletcher et al. 2008)]. With respect to Tg level "cut off", studies have shown controversial results. However a "cut off" of 10 ng/ml seems to be a reasonable value maintaining high accuracy in terms of a good compromise between sensitivity and specificity. The impact of thyroid-stimulating hormone (TSH) on FDG PET imaging is still an open issue, no complete consensus has been reached about the usefulness of high TSH levels. Levothyroxine withdrawal or alternatively the use of rTSH might be preferable, especially in cases of relatively low Tg levels (< 10 ng/ml) trying to improve sensitivity of FDG PET (Bertagna et al. 2010).

2.14 Cancer of Unknown Primary

About 2–7 % of all malignancies are cancers of unknown primary (CUP) mostly associated with a poor prognosis. As CUPs can often not be identified on conventional imaging, PET might improve the detection rate of CUPs and potentially improve patient outcome by optimizing treatment planning. In a systematic review Delgado-Bolton et al. reported a sensitivity and specificity of 87 and 71 %, respectively, for detecting the primary tumor by PET imaging; overall PET detected 45 % (range, 35–49 %) of the tumors (Delgado-Bolton et al. 2003). Another review evaluated the use of FDG PET for detecting primary tumors in patients with cervical lymph node metastases after conventional imaging (panendoscopy, CT, MRI, or chest radiography). The sensitivity, specificity, and accuracy of PET was 88, 75, and 79 %,

respectively. PET was responsible for a therapeutic change in 25 % of patients (Rusthoven et al. 2004). A recent meta-analysis by Kwee et al. reported a primary detection rate of 37 %. Lung, oropharyngeal and pancreatic cancer were reported to represent the most frequently detected primary tumors (Kwee and Kwee 2009).

Further studies are needed to assess the impact that cancer-specific treatments based on PET findings might have on the survival of patients suffering from CUPs.

2.15 Testicular Cancer

Most testicular neoplasms (95 %) are germ cell tumors. The other 5 % include lymphoma and metastases. Testicular germ cell tumors, the commonest tumor in young males (aged 15–35), are divided into seminoma and nonseminomatous germ cell tumors (NSGCT). The NSGCT group includes teratomas of varying degrees of differentiation, tumors containing mixed cell lines of teratomas, and mixed tumors with both teratoma and seminoma components. Pure seminomas may have an elevation of human chorionic gonatotropin-β (β-HCG) but α-fetoprotein (AFP) should be normal. AFP is a tumor marker for NSGCT. An elevation of both β-HCG and AFP reflects different cell lines that accordingly will not necessarily respond the same way to chemotherapy.

CT is usually applied for staging. Pelvic and retroperitoneal lymph node dissection can deliver diagnostic information concerning nodal metastatic disease. FDG PET may be valuable in stage II testicular germ cell tumor (any pT $pN_{1\text{-}3}$) if it is of importance to accurately define the metastatic extent prior to chemotherapy, but it may not be of additional value in patients with stage I tumors (Albers et al. 1999).

FDG PET and PET/CT is most helpful in the setting of tumor recurrence. However, it is important to have information regarding the composition of the primary lesions. Mature teratoma do not show increased FDG uptake. As mature teratoma is present in more than 40 % of resected masses in NSGCT, this is a major source of false negative results. In seminomas the fraction of mature teratoma in residual lesions is much lower (< 5 %). Thus, FDG PET has a greater role in evaluating tumor recurrence in seminoma than in NSGCT (De Santis et al. 2004). The main indications of FDG PET and PET/CT in recurrence of testicular cancer are: (1) differentiation of residual tumor from fibrosis, in particular in lesions > 3 cm; (2) elevation of tumor markers whether or not a residual mass is seen on CT (De Santis et al. 2004; Hain et al. 2000). In the assessment of residual tumor tissue after chemotherapy FDG PET should be performed 4–12 weeks after the end of the treatment, as earlier imaging may result in false-positive results from inflammation following therapy (De Santis et al. 2004).

2.16 Prostate Cancer

FDG PET/CT has shown only limited sensitivity for the detection of differentiated prostate cancer and imaging of recurrent prostate cancer in various studies. Increased FDG uptake and accumulation is regularly only found in dedifferentiated, aggressive, and metastasized prostate cancer (Jadvar 2011; Schoder et al. 2005).

3 Therapy Response Assessment with FDG PET and PET/CT

FDG PET and PET/CT play an integral role in diagnosis, staging, and re-staging of disease in oncology. In addition to that there is increasing evidence that FDG PET and PET/CT can also significantly contribute to evaluation of therapy response, tumor control, and prediction of prognosis in oncologic patients [for a review see (Herrmann et al. 2012)]. Conventional imaging modalities are of limited use to assess response to therapy. FDG has been proposed as imaging surrogate parameter of therapy response. FDG provides several highly reproducible quantitative parameters of tumor glucose metabolism. Changes of glucose consumption can therefore be used to define a metabolic response to therapy. Recently, PET Response Criteria in Solid Tumors (PERCIST 1.0) have been published (Wahl et al. 2009). The authors argued that anatomic imaging alone using standard WHO, and Response Criteria in Solid Tumors (RECIST) criteria have limitations, particularly in assessing the activity of newer cancer therapies that stabilize disease, whereas FDG PET appears particularly valuable in such cases.

FDG PET and PET/CT can be used to assess response to therapy early and late in the course of therapy. From the perspective of a clinician, it is very important to differentiate non-responders to chemotherapy or radiochemotherapy early in the course of treatment to possibly change the therapeutic management. Tumor response can also be assessed early in the course of therapy (i.e., chemotherapy or radio-chemotherapy) with FDG PET and PET/CT. The first scan will take place before therapy, and a second scan is performed 2–4 weeks after initiation of the first therapy cycle (often within the first cycle). Changes in FDG uptake between the pre-therapeutic scan and the early follow-up scan are used to predict histopathological response, and patient survival. The standardized uptake value is the most widely used FDG PET parameter, and in most studies, relative changes (%) are calculated to quantify metabolic response. In summary, numerous studies have investigated post-therapeutic PET scanning in order to define the predictive and prognostic value. Most studies show a clear correlation of metabolic response as assessed by FDG PET on the one hand and response and survival on the other hand (Herrmann et al. 2012).

Early assessment with FDG PET of the response to therapy in oncologic patients has shown promising results in single-center studies and should now be evaluated in randomized, prospective multicenter trials. Such trials are an

important step toward possible implementation in clinical practice. Standardization of patient preparation, data acquisition and processing, and data interpretation is an important issue, especially for prospective randomized multicenter studies.

References

Albers P, Bender H, Yilmaz H et al (1999) Positron emission tomography in the clinical staging of patients with Stage I and II testicular germ cell tumors. Urology 53(4):808–811

Bastiaannet E, Groen H, Jager PL et al (2004) The value of FDG-PET in the detection, grading and response to therapy of soft tissue and bone sarcomas; a systematic review and meta-analysis. Cancer Treat Rev 30(1):83–101

Bertagna F, Biasiotto G, Orlando E et al (2010) Role of ^{18}F-fluorodeoxyglucose positron emission tomography/computed tomography in patients affected by differentiated thyroid carcinoma, high thyroglobulin level, and negative ^{131}I scan: review of the literature. Jpn J Radiol 28(9):629–636

Birim O, Kappetein AP, Stijnen T et al (2005) Meta-analysis of positron emission tomographic and computed tomographic imaging in detecting mediastinal lymph node metastases in nonsmall cell lung cancer. Ann Thorac Surg 79(1):375–382

Brush J, Boyd K, Chappell F et al. (2011). The value of FDG positron emission tomography/computerised tomography (PET/CT) in pre-operative staging of colorectal cancer: a systematic review and economic evaluation. Health Technol Assess 15(35): 1–192, iii-iv

Cheson BD, Pfistner B, Juweid ME et al (2007) Revised response criteria for malignant lymphoma. J Clin Oncol 25(5):579–586

Czernin J, Benz MR, Allen-Auerbach MS (2010) PET/CT imaging: the incremental value of assessing the glucose metabolic phenotype and the structure of cancers in a single examination. Eur J Radiol 73(3):470–480

De Santis M, Becherer A, Bokemeyer C et al (2004) 2-^{18}fluoro-deoxy-D-glucose positron emission tomography is a reliable predictor for viable tumor in postchemotherapy seminoma: an update of the prospective multicentric SEMPET trial. J Clin Oncol 22(6):1034–1039

Delgado-Bolton RC, Fernandez-Perez C, Gonzalez-Mate A et al (2003) Meta-analysis of the performance of ^{18}F-FDG PET in primary tumor detection in unknown primary tumors. J Nucl Med 44(8):1301–1314

Duet M, Hugonnet F, Faraggi M (2010) Role of positron emission tomography (PET) in head and neck cancer. Eur Ann Otorhinolaryngol Head Neck Dis 127(1):40–45

Elstrom R, Guan L, Baker G et al (2003) Utility of FDG-PET scanning in lymphoma by WHO classification. Blood 101(10):3875–3876

Essler M, Link A, Belloni B et al (2011) Prognostic value of [^{18}F]-fluoro-deoxy-glucose PET/CT, S100 or MIA for assessment of cancer-associated mortality in patients with high risk melanoma. PLoS ONE 6(9):e24632

Fischer BM, Mortensen J, Hojgaard L (2001) Positron emission tomography in the diagnosis and staging of lung cancer: a systematic, quantitative review. Lancet Oncol 2(11):659–666

Fletcher C, Uni K, Meteus F (eds) (2002) World Health Organization Classification of Tumors, Pathology and Genetics of Tumors of Soft Tissue and Bone. IARC Press, Lyon

Fletcher JW, Djulbegovic B, Soares HP et al (2008) Recommendations on the use of ^{18}F-FDG PET in oncology. J Nucl Med 49(3):480–508

Forstner R, Sala E, Kinkel K et al (2010) ESUR guidelines: ovarian cancer staging and follow-up. Eur Radiol 20(12):2773–2780

Gould MK, Maclean CC, Kuschner WG et al (2001) Accuracy of positron emission tomography for diagnosis of pulmonary nodules and mass lesions: a meta-analysis. JAMA 285(7):914–924

Gupta T, Master Z, Kannan S et al (2011) Diagnostic performance of post-treatment FDG PET or FDG PET/CT imaging in head and neck cancer: a systematic review and meta-analysis. Eur J Nucl Med Mol Imaging 38(11):2083–2095

Hain SF, O'Doherty MJ, Timothy AR et al (2000) Fluorodeoxyglucose positron emission tomography in the evaluation of germ cell tumours at relapse. Br J Cancer 83(7):863–869

Havrilesky LJ, Kulasingam SL, Matchar DB et al (2005) FDG-PET for management of cervical and ovarian cancer. Gynecol Oncol 97(1):183–191

Herrmann K, Benz MR, Krause BJ et al. (2012) F-18-FDG-PET/CT in evaluating response to therapy in solid tumors: where we are and where we can go. Q J Nucl Med Mol Imaging: in press

Herrmann K, Ott K, Buck AK et al (2007) Imaging gastric cancer with PET and the radiotracers 18F-FLT and 18F-FDG: a comparative analysis. J Nucl Med 48(12):1945–1950

Heusner TA, Kuemmel S, Hahn S et al (2009) Diagnostic value of full-dose FDG PET/CT for axillary lymph node staging in breast cancer patients. Eur J Nucl Med Mol Imaging 36(10):1543–1550

Hooft L, Hoekstra OS, Deville W et al (2001) Diagnostic accuracy of ^{18}F-fluorodeoxyglucose positron emission tomography in the follow-up of papillary or follicular thyroid cancer. J Clin Endocrinol Metab 86(8):3779–3786

Huebner RH, Park KC, Shepherd JE et al (2000) A meta-analysis of the literature for whole-body FDG PET detection of recurrent colorectal cancer. J Nucl Med 41(7):1177–1189

Hutchings M, Barrington SF (2009) PET/CT for therapy response assessment in lymphoma. J Nucl Med 50(Suppl 1):21S–30S

Jadvar H (2011) Prostate cancer: PET with ^{18}F-FDG, ^{18}F- or ^{11}C-acetate, and ^{18}F- or ^{11}C-choline. J Nucl Med 52(1):81–89

Juweid ME, Stroobants S, Hoekstra OS et al (2007) Use of positron emission tomography for response assessment of lymphoma: consensus of the Imaging Subcommittee of International Harmonization Project in Lymphoma. J Clin Oncol 25(5):571–578

Kubicek GJ, Champ C, Fogh S et al (2010) FDG-PET staging and importance of lymph node SUV in head and neck cancer. Head Neck Oncol 2:19

Kwee TC, Kwee RM (2009) Combined FDG-PET/CT for the detection of unknown primary tumors: systematic review and meta-analysis. Eur Radiol 19(3):731–744

Lv YL, Yuan DM, Wang K et al (2011) Diagnostic performance of integrated positron emission tomography/computed tomography for mediastinal lymph node staging in non-small cell lung cancer: a bivariate systematic review and meta-analysis. J Thorac Oncol 6(8):1350–1358

Moog F, Bangerter M, Diederichs CG et al (1998) Extranodal malignant lymphoma: detection with FDG PET versus CT. Radiology 206(2):475–481

Orlando LA, Kulasingam SL, Matchar DB (2004) Meta-analysis: the detection of pancreatic malignancy with positron emission tomography. Aliment Pharmacol Ther 20(10):1063–1070

Patnana M, Bronstein Y, Szklaruk J et al (2011) Multimethod imaging, staging, and spectrum of manifestations of metastatic melanoma. Clin Radiol 66(3):224–236

Reske SN (2009) PET and PET-CT of malignant tumors of the exocrine pancreas. Radiologe 49(2):131–136

Ruf J, Lopez Hanninen E, Oettle H et al (2005) Detection of recurrent pancreatic cancer: comparison of FDG-PET with CT/MRI. Pancreatology 5(2–3):266–272

Rusthoven KE, Koshy M, Paulino AC (2004) The role of fluorodeoxyglucose positron emission tomography in cervical lymph node metastases from an unknown primary tumor. Cancer 101(11):2641–2649

Schick V, Franzius C, Beyna T et al (2008) Diagnostic impact of ^{18}F-FDG PET-CT evaluating solid pancreatic lesions versus endosonography, endoscopic retrograde cholangio-pancreatography with intraductal ultrasonography and abdominal ultrasound. Eur J Nucl Med Mol Imaging 35(10):1775–1785

Schoder H, Herrmann K, Gonen M et al (2005) 2-[^{18}F]fluoro-2-deoxyglucose positron emission tomography for the detection of disease in patients with prostate-specific antigen relapse after radical prostatectomy. Clin Cancer Res 11(13):4761–4769

Schreyogg J, Weller J, Stargardt T et al (2010) Cost-effectiveness of hybrid PET/CT for staging of non-small cell lung cancer. J Nucl Med 51(11):1668–1675

Schwarz JK, Grigsby PW, Dehdashti F et al (2009) The role of ^{18}F-FDG PET in assessing therapy response in cancer of the cervix and ovaries. J Nucl Med 50(Suppl 1):64S–73S

van den Abbeele AD (2008) The lessons of GIST–PET and PET/CT: a new paradigm for imaging. Oncologist 13(Suppl 2):8–13

van Tinteren H, Hoekstra OS, Smit EF et al (2002) Effectiveness of positron emission tomography in the preoperative assessment of patients with suspected non-small-cell lung cancer: the PLUS multicentre randomised trial. Lancet 359(9315):1388–1393

van Vliet EP, Heijenbrok-Kal MH, Hunink MG et al (2008) Staging investigations for oesophageal cancer: a meta-analysis. Br J Cancer 98(3):547–557

van Westreenen HL, Westerterp M, Bossuyt PM et al (2004) Systematic review of the staging performance of ^{18}F-fluorodeoxyglucose positron emission tomography in esophageal cancer. J Clin Oncol 22(18):3805–3812

Viney RC, Boyer MJ, King MT et al (2004) Randomized controlled trial of the role of positron emission tomography in the management of stage I and II non-small-cell lung cancer. J Clin Oncol 22(12):2357–2362

Wahl RL, Jacene H, Kasamon Y et al (2009) From RECIST to PERCIST: Evolving Considerations for PET response criteria in solid tumors. J Nucl Med 50(Suppl 1):122S–150S

Wu LM, Hu JN, Hua J et al (2012) ^{18}F-Fluorodeoxyglucose Positron Emission Tomography to Evaluate Recurrent Gastric Cancer: A systematic review and meta-analysis. J Gastroenterol Hepatol 27(3):472–480

Xie P, Li M, Zhao H et al (2011) ^{18}F-FDG PET or PET-CT to evaluate prognosis for head and neck cancer: a meta-analysis. J Cancer Res Clin Oncol 137(7):1085–1093

Molecular Imaging in Oncology

Egesta Lopci and Stefano Fanti

Abstract

The major application for PET imaging in clinical practice is represented by cancer imaging and ^{18}F-FDG is the most widely employed positron emitter compound. However, some diseases cannot be properly evaluated with this tracer and thus there is the necessity to develop more specific compounds. The last decades were a continuous factory for new radiopharmaceuticals leading to an endless list of PET tracers; however, just some of them guard diagnostic relevance in routine medical practice. This chapter describes a selected list of non-FDG PET tracers, basing on their introduction into and impact on clinical practice.

Contents

E. Lopci
Nuclear Medicine Unit, Humanitas Cancer Center,
Via Manzoni 56, 20089 Rozzano, MI, Italy

S. Fanti (✉)
Nuclear Medicine Department, S. Orsola-Malpighi Hospital,
University of Bologna, Via Massarenti 9, 40138 Bologna, Italy
e-mail: stefano.fanti@aosp.bo.it

O. Schober and B. Riemann (eds.), *Molecular Imaging in Oncology*,
Recent Results in Cancer Research 187, DOI: 10.1007/978-3-642-10853-2_13,

1 Introduction to Non-FDG PET Tracers

Undoubtedly mankind has found a new "Black Death" of modern era in oncologic pathologies. A big leap, however, in medical diagnosis was made with the introduction of molecular imaging, and positron emission tomography (PET and PET/CT) is certainly one of the most rapidly growing and promising areas of molecular imaging application, with large impact on the clinical assessment of different oncologic diseases.

Since its approval by the Food and Drug Administration in 2000, a major breakthrough for PET imaging was represented by the metabolic tracer ^{18}F-Fluorodeoxyglucose (^{18}F-FDG). Up to now more than 90 % of worldwide PET studies are performed using ^{18}F-FDG and its clinical application is extended not only in oncologic, but also in neurologic and cardiologic field.

Although ^{18}F-FDG-PET provides high sensitivity and specificity in the majority of cancers, it remains independently a "nonspecific" tracer. As a glucose analogue it provides functional information on cellular metabolism, and as an oncologic tracer its use is essentially based on the presence of a glucolytic phenotype in malignant cells even in good oxygenation, the so-called Warburg (1956) effect. The phenomenon, however, is not always a characteristic for all sorts of tumours, and some contrarily show a reduced ^{18}F-FDG uptake. In addition this PET tracer cannot differentiate between cells that have a high metabolic rate associated with neoplasia, and those with increased metabolism due to other conditions such as infection, inflammation or even normal physiological uptake.

Many malignancies in fact are poorly imaged by ^{18}F-FDG, starting with prostate cancer (Rohren et al. 2004; Kelloff et al. 2005; Kayani and Groves 2006) and continuing with HCC (Ho et al. 2003), renal cell carcinomas, low-grade sarcomas, low-grade lymphomas, brain tumours or well-differentiated histologies such as neuroendocrine tumours (NET), etc. (Oyama et al. 1999; Dimitrakopoulou-Strauss and Strauss 2003; Kang et al. 2004).

Consequently, development of new radiotracers becomes of utmost importance in clinical practice in order to increase the diagnostic accuracy for PET. In the last two decades many alternative PET tracers have been proposed and evaluated in preclinical and clinical studies, leading to an endless list of radiopharmaceuticals. However, just a limited portrayal is of relevant impact on clinical practice and this chapter aims describing the most significant representatives.

2 Clinical Applications of ^{11}C-Choline

^{11}C-Choline is an oncologic tracer and was at first introduced in PET imaging in 1997 (Hara et al. 1997a) for the detection of brain and prostate cancer. It is a small molecule which is rapidly taken up by cells and, as a precursor for the biosynthesis of phospholipids (phosphatidilcholine), it is integrated into cellular membranes (Zeisel 1981; Pascali et al. 2000). The uptake of ^{11}C-choline is therefore a marker for membrane turnover and metabolism (Vallabhajosula 2007), which is reported to be substantially increased in malignant cells (Podo 1999; Ackerstaff et al. 2001; Sutinen et al. 2003).

^{11}C-Choline is physiologically detected in the salivary glands, liver, kidneys parenchyma and pancreas, only few minutes after the injection (3–5 min) and may show some faint uptake also in the spleen, bone marrow, muscles and bowel. ^{11}C-Choline has a high signal-to-background ratio, is successfully taken up in various tumours, including slowly growing ones, and presents a late urinary excretion which makes it a good tracer for the detection of prostate and bladder cancers (Hara et al. 1997b, 1998; Kotzerke et al. 2000; Picchio et al. 2006).

The main drawbacks of this tracer are related to the short half-life of the radionuclide ^{11}C (T1/2 20 min) and the rapid in vivo oxidation (Vallabhajosula 2007), which led to the development of ^{18}F-labelled choline analogues such as ^{18}F-fluorocholine (FCH) (Cimitan et al. 2006; Degrado et al. 2001; Hara et al. 2002). Not substantially important differences have been detected in between the two tracers, except for the earlier urinary appearance of ^{18}F-fluorocholine, probably due to an incomplete tubular reabsorption (Husarik et al. 2008).

As an oncologic tracer ^{11}C-choline has a potential role in any neoplasia, although in clinical practice it has found a principal application in prostate cancer (Hara et al. 1998; De Jong et al. 2003; Picchio et al. 2003; Krause et al. 2008).

PET imaging with ^{11}C-choline has been proposed to early detect primary prostate cancer, to stage/restage the tumour, but the prevailing utility appears to be the detection of tumour recurrence in case of biochemical relapse (Fanti et al. 2007).

At staging ^{11}C-choline has been utilised prevalently to assess nodal and bone metastasis in prostate cancer patients (Hara et al. 1998; Kotzerke et al. 2000; De Jong et al. 2003; Powles et al. 2007; Schiavina et al. 2008). In fact there are some limitations in purely identifying the primary tumour (T staging), at first related to the difficulty to discriminate between malignant lesions and benign disease (i.e. prostatitis, benign prostatic hyperplasia) (Farsad et al. 2005) and second related to the limited spatial resolution of the method ($\sim$5 mm), leading to a low accuracy in the detection of extracapsular and seminal vesicle extension (Schiavina et al. 2008).

A direct comparison, however, has been made between ^{11}C-choline PET and transrectal ultrasound guided biopsy showing a slightly better sensitivity for PET (66 vs. 61 %) in the detection of primary tumour (reaching 83 % for lesions $\geq$ 5 mm), but a lower specificity (84 vs. 97 %) than biopsy.

When considering the assessment of extraprostatic extension, ^{11}C-choline PET appears significantly less sensitive than the standard of reference (MRI), with a sensitivity of 22 versus 63 % for MRI (Martorana et al. 2006). The same study

group performed also a direct comparison of PET with sextant results of step-section histopathology and found a sensitivity, specificity, and accuracy of 66 %, 81 % and 71 %, respectively (Farsad et al. 2005). A recent paper (Giovacchini et al. 2008), however, discourages the use of ^{11}C-choline-PET in the initial diagnosis and for local staging of prostate cancer.

A more relevant role for ^{11}C-choline PET in staging prostate cancer is reported in selected high risk patients (high levels of PSA or Gleason score, etc.), with the intent to assess extraprostatic metastases. Even with respect to clinical nomograms (Briganti et al. 2006), ^{11}C-choline PET seems to perform better in the detection of nodal metastasis (Schiavina et al. 2008). On a patient-based analysis PET sensitivity and specificity were 60 % and 98 %, respectively, while on a nodal-based analysis, sensitivity was 41 % and specificity 99.8 %.

As reported in literature (De Jong et al. 2002, 2003; Picchio et al. 2003; Yamaguchi et al. 2005; Testa et al. 2007), ^{11}C-choline PET accuracy (sensitivity 80 %; specificity 96 %; accuracy 93 %) is generally better than that of conventional imaging (CI) techniques.

The main application of ^{11}C-choline PET, however, remains the evaluation of prostate cancer relapse in previously treated patients, presenting with rising PSA serum level and negative CI procedures (Castellucci et al. 2009, 2011). The higher sensitivity is seen for the detection of early nodal involvement and secondary bone lesions (Hara et al. 1998; Scattoni et al. 2007; Krause et al. 2008). Since ^{11}C-choline uptake in malignant metastatic cells occurs before bone osteoblastic changes, the method permits the detection of bone lesions even before bone scintigraphy (Picchio et al. 2002; De Jong et al. 2003; Fuccio et al. 2010). On a lesion-based analysis ^{11}C-choline PET shows a sensitivity, specificity and accuracy of 64 %, 90 % and 77 %, respectively (Scattoni et al. 2007). Although with a lower accuracy than for other sites of disease, ^{11}C-choline-PET is useful also in detecting local recurrence (Picchio et al. 2002; De Jong et al. 2003; Breeuwsma et al. 2010).

Despite being the most sensitive examination during restaging, ^{11}C-choline PET still has an imperfect overall detection rate (39–56 %) (Krause et al. 2008; Castellucci et al. 2009), which can be significantly ameliorated by adopting other parameters, such as PSA kinetics. Therefore trigger PSA, PSA velocity and PSA doubling time (Krause et al. 2008; Giovacchini et al. 2008; Castellucci et al. 2009, 2011) contribute in increasing the probability of having positive finding at PET, since they express somehow the malignancy of the disease relapse. The potential role of ^{11}C-choline-PET in restaging contributes consequently in a better assessment of treatment strategies and therefore in patient outcome.

Other oncologies have been successfully studied with ^{11}C-choline PET, starting with the bladder cancer (Hara et al. 1997b; Picchio et al. 2006). Thanks to the late urinary excretion and low background activity, ^{11}C-choline permits a good identification of the primary bladder cancer (sensitivity 96 % for PET vs. 84 % CT) and its proper nodal staging (sensibility and specificity, respectively, 62 % and 100 % for PET vs. 50 % and 75 % for CT) (Picchio et al. 2006).

Brain tumours too are an interesting indication for ^{11}C-choline PET (Hara et al. 2003), which, in very limited studies, have shown a potentially equal or slightly better tumour delineating capability, even when compared to a well-established tracers such as ^{11}C-methionine (Narayanan et al. 2002).

Preliminary results show that ^{11}C-choline PET can have a potential role also in multiple myeloma. In fact it seems to detect more myelomatous lesions than ^{18}F-FDG PET, although the difference between the two tracers is not reported to be statistically significant in terms of mean number of lesions (Tian et al. 2004; Nanni et al. 2007a, b).

At last, its fluorinated analogue has been recently utilised with success in imaging HCC (Talbot et al. 2006, 2010; Yamamoto et al. 2008a), but further data are probably needed to fully assess its application in this neoplasia.

Despite the potentialities of this tracer in detecting many malignancy, ^{11}C-choline and its fluorinated analogues, at present find a proper use in clinical practice mainly in prostate cancer patients (Fig. 1).

3 Clinical Applications of ^{18}F-DOPA

^{18}F-DOPA (^{18}F-dihydroxy-phenylalanine) is a positron emitter compound applied in clinical practice since the 1980s (Garnett et al. 1983; Firnau et al. 1984) as a marker for the basal ganglia dopamine production (Whal and Nahmias 1997). It is the fluorinated form of L-DOPA, which represents the immediate precursor of dopamine (Lovenberg et al. 1962), a central nervous system (CNS) neurotransmitter predominantly found in the nigrostriatal region and related to neurodegenerative and movement disorders such as Parkinson's Disease (PD) (Agid et al. 1990). Unlike dopamine, L-DOPA is actively transported through the blood–brain barrier, then converted into dopamine by the action of L-aromatic amino-acid decarboxylase (Lovenberg et al. 1962) and at last stored in intraneuronal vesicles, ready to be released in the various dopaminergic pathways including the striatal presynaptic space.

The objective of the in vivo detection of dopaminergic degeneration in PD by the means of ^{18}F-DOPA is related to the early diagnosis and monitoring of disease progression (Leenders et al. 1990; Eidelberg 1992; Sawle 1993). The method has in fact demonstrated a high sensitivity and specificity in the diagnosis of PD, ranging from 91–100 % and 90–100 %, respectively (Eshuis et al. 2009), although some papers report a paradoxical up-regulation of decarboxylase activity and consequently a possibly increased trapping of ^{18}F-DOPA in the presynaptic vesicles during the earlier stages of the disease (Ito et al. 1999; Lee et al. 2000).

Main drawbacks, however, of the method are related to the need of a cyclotron-based radiopharmacy and the relatively complicated synthesis of ^{18}F-DOPA (De Vries et al. 1999). The commercial presence of other valid alternatives such as ^{123}I-FP-CIT SPECT, a marker of the pre-synaptic dopamine transporter expression (Goodman et al. 1997), directly correlated to PD alterations and disease stage,

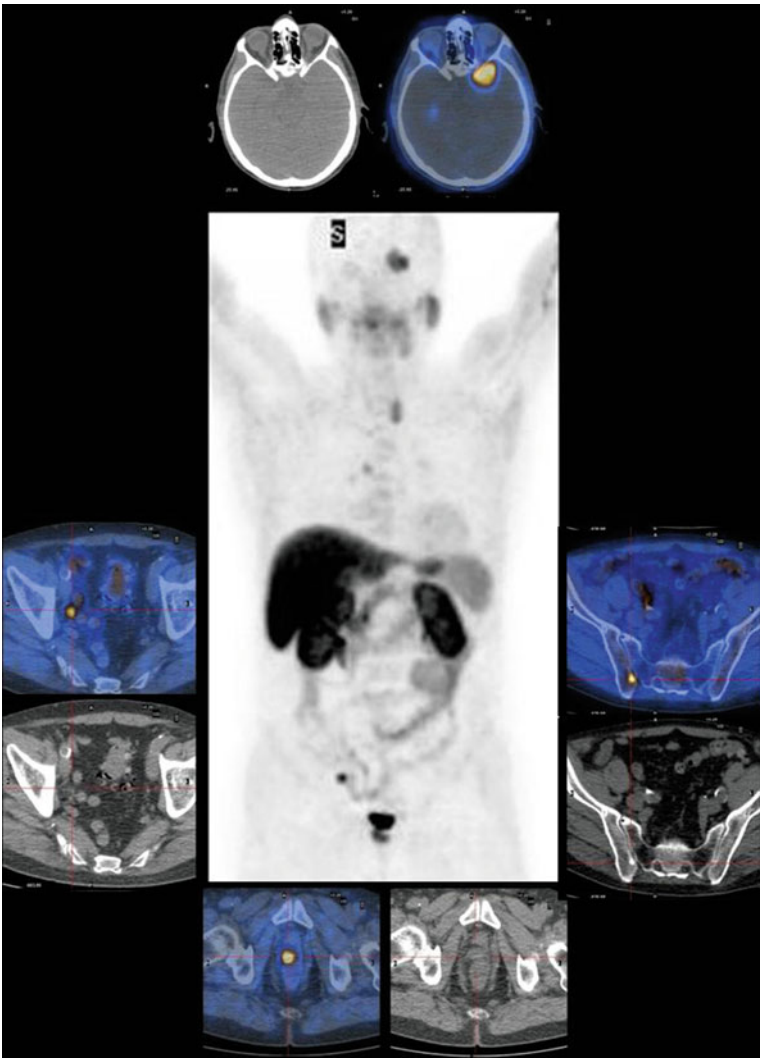

Fig. 1 MIP image of ^{11}C-choline PET/CT(*central part of the figure*), with transversal images of single pathologic findings; local recurrence (*inferior view*); imaging bone lesion (*right sided view*); nodal involvement (*left sided view*); brain lesion (*superior view*)

with similar features to the ^{18}F-DOPA diagnostic value (Eshuis et al. 2006, 2009), makes this latter one not of routine use in clinical practice, despite the unquestionable advantages over ^{123}I-FP-CIT in terms of length of the procedure and image quality.

A mechanism similar to the above-mentioned one, characterised by active uptake and decarboxylation of amines precursors, is noticed also in other brain regions and in extracranial tissues, giving way to the possibility of ^{18}F-DOPA to be

used in the detection of pathological situation such as brain tumours (Heiss et al. 1996), neural crest derived neoplasms (Hoegerle et al. 2001a) and pancreatic islets hyperfunction (i.e. primary hyperinsulinism) (Hardy et al. 2007a).

In oncology, ^{18}F-DOPA has been initially proposed as a marker for melanomas (Dimitrakopoulou-Strauss et al. 2001), thanks to the ability of neural crest derived tumours, now defined as NET, to accumulate and decarboxylate L-DOPA as precursor of dopamine. The amine precursor uptake and decarboxylation (APUD) concept was introduced in 1969 (Pearse 1969) and consequently the known increased activity of L-DOPA decarboxylase in NET (Gazdar et al. 1988; Becherer et al. 2004) permitted their visualisation through positron emitters. The first PET compound, however, was ^{11}C-labelled DOPA used by Ahlström et al. (1995) for NET imaging.

At present ^{18}F-DOPA PET is a well-assessed procedure in the detection of primary and metastatic NET (carcinoids, gastroenteropancreatic tumours, glomus tumour, medullary thyroid cancer, small cell lung cancer, neuroblastoma, paraganglioma, pheochromocytoma, etc.) (Hoegerle et al. 2001a, b, 2002, 2003; Gourgiotis et al. 2003; Jacob et al. 2003; Nanni and Fanti 2007). Its diagnostic accuracy is reported higher than the other CI techniques including CT/MRI, ^{123}I-MIBG and ^{111}In-Octreoscan (Becherer et al. 2004; Imani et al. 2009; Fiebrich et al. 2009). However, the group of neoplasms which mostly benefit from ^{18}F-DOPA imaging are of NET associated with excessive catecholamine release (sensitivity of 73–90 %) (Fiebrich et al. 2009) and particularly pheochromocytomas (sensitivity, 85 %; specificity, 100 %; accuracy, 92 %) (Imani et al. 2009) (Fig. 2). PET imaging with ^{18}F-DOPA, compared to the other radionuclide methods, has in addition a better spatial resolution ($\sim$5 mm vs. 10–15 mm) and a higher signal-to-background ratio, with physiological uptake of the tracer situated only in the basal ganglia, bile ducts, gallbladder, adrenals and excretory tract (Hoegerle et al. 2001a, b). To further improve the method, and in particular to reduce the high renal excretion of the tracer, oral premedication with carbidopa (decarboxylase inhibitor) is suggested to block the aromatic amino acid decarboxylase enzyme (Langsteger et al. 2006). This leads to a 6-fold decreased renal excretion while the tumour uptake increased 3-fold, hence improving the visualisation of NET (Eriksson et al. 2002).

When comparing ^{18}F-DOPA to other PET tracers, such as the ^{68}Ga-labelled somatostatin analogs, whose rationale is based on the well-known overexpression of somatostatin receptors in NET (Reubi 2004), the latter ones show a sightly better accuracy (Ambrosini et al. 2008, 2009).

However, the substantially different pathways of the two kind of tracers suggest a more likely complementary function in the detection of NET sites, in accordance with the natural heterogeneity and development history of these neoplasms.

Another important application of ^{18}F-DOPA is the identification of hyperinsulinism in infants. Otonkoski et al. (2003) were the first to suggest a possible use of ^{18}F-DOPA in congenital hyperinsulinism, based on the fact that several studies showed that normal pancreatic β-cells take up L-DOPA (Lindstrom and Shelin 1986; Borelli et al. 1997).

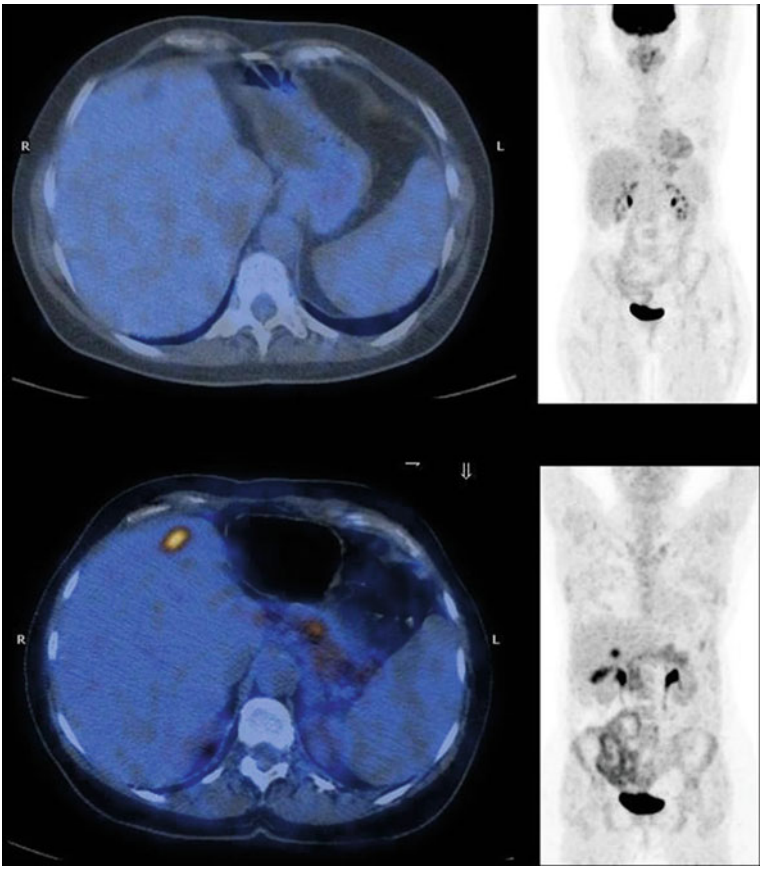

Fig. 2 MIP images of ^{18}F-FDG PET/CT (*upper image*) and ^{18}F-DOPA PET/CT (*lower image*), with transversal views demonstrating a single small liver metastasis derived from a previously operated intestinal carcinoid visible only on the ^{18}F-DOPA images and undetectable on the ^{18}F-FDG images

The preliminary results were very encouraging, and the accuracy of this technique seems to range from 96 to 100 % for the diagnosis of diffused disease and for the localisation of focal lesions (Hardy et al. 2007a). In subsequent studies the diagnosis of focal or diffuse hyperinsulinism was possible in 88 %, with ^{18}F-DOPA scans diagnosing 75 % of focal cases and correctly identifying all sites of disease (Hardy et al. 2007b).

Very recently, a new application of ^{18}F-DOPA in children has been investigated, and this concerns neuroblastoma (Piccardo et al. 2012). The results are quite encouraging and are worthy assessed in larger study population.

At last, ^{18}F-DOPA PET has also been used for the detection of brain tumours (Heiss et al. 1996) and for the localisation of the parathyroid adenoma in patients affected by primary hyperparathyroidism, but incomplete or negative results are incompatible with a possible eventual clinical application (Lange-Nolde et al. 2006).

Despite its promising potentiality for oncological applications in clinical practice, ^{18}F-DOPA PET at the moment, still finds a major field of application only in movement disorders (Nanni and Fanti 2007) and in imaging NET (Becherer et al. 2004; Imani et al. 2009; Fiebrich et al. 2009).

4 Clinical Applications of ^{11}C-Methionine

^{11}C-Methionine is the radiolabelled variant of the essential aminoacid methionine, used as a surrogate marker for the protein metabolism of tumour cells. The precise mechanism of uptake is not fully clear, but methionine is known to be needed for protein synthesis and involved in crucial pathways leading to polyamine synthesis, all reactions accelerated in malignant cells (Hoffman 1984). Its uptake reflects increased amino acid transport and is related to cellular proliferative activity (Hatazawa et al. 1989).

Since the first report of Comar et al. (1976) on L-methyl-^{11}C-methionine, documented as potential agent in imaging different malignancies like brain, lung, lymphoma, breast, pelvic, prostate, melanoma and head and neck tumours (Leskinen-Kallio et al. 1990, 1991, 1992; Lapela et al. 1994; Nunez et al. 2002), much attention has been paid to this amino acid and its ^{11}C-labelled forms (Cook et al. 1999; Groves et al. 2007).

At present the principal clinical application of ^{11}C-methionine PET concerns CNS tumours. Brain has a physiologically intense uptake of ^{18}F-FDG, because glucose is the main metabolic substrate for CNS, and consequently it is very difficult to distinguish malignant lesions in the contest of a hypermetabolic background (Kim et al. 2005; Van Laere et al. 2005). Both high-grade and low-grade tumours may be obscured by adjacent activity or confused with other benign lesions such as infection, infarction or hemorrhage (Wong et al. 2002; Weber et al. 1997; Oriuchi et al. 1996; Ricci et al. 1998). CI methods too, including CT and especially MRI, apart from providing excellent anatomical information with a 65–100 % sensitivity, are deficient in differentiating tumours from other non-pathological findings, as well as tumour grades and volumes (Wong et al. 2002; Gumprecht et al. 2007).

^{11}C-Methionine in contrast is not physiologically taken up by brain and benign conditions such as fibrosis, necrosis or edema are, in the same way, imaged as cold areas in PET (Hustinx et al. 2005; Hatazawa et al. 1989; Derlon et al. 1989). On the contrary, malignant lesions present an increased ^{11}C-methionine uptake due to an increased protein metabolism and increased vascular permeability (Ogawa et al. 1993; Sasaki et al. 1998; Kaschten et al. 1998; Sato et al. 1999; Pirotte et al. 2004; Torii et al. 2005; Van Laere et al. 2005; Borbély et al. 2006). Because of its high contrast the method seems to allow the identification of low- and high-grade lesions and provides an initial prognostic value (Huang et al. 2005; Kato et al. 2008). In fact ^{11}C-methionine uptake and tumour-to-normal brain tissue ratios are reported to correlate with patient prognosis, Ki-67 expression and proliferating cell nuclear antigen (PCNA) expression (Kim et al. 2005; Nariai et al. 2005; Terakawa et al. 2008).

The use, however, of ^{11}C-methionine in grading tumours is yet controversial; whereas some authors report a correlation between tracer uptake and glioma grade (Kameyama et al. 1990), others have not demonstrated any significant differences in uptake between gliomas grade I and II, or III and IV, respectively, although ^{11}C-methionine uptake directly correlates with microvessel density (Kracht et al. 2003).

Overall sensitivity of ^{11}C-methionine PET for gliomas is estimated around 89 %, with a specificity of almost 100 %, but with lower figures in low-grade tumours (65–85 %) (Herholz et al. 1998; Braun et al. 2002; Chung et al. 2002) (Fig. 3). Other intracranial tumours too can have a high ^{11}C-methionine uptake including pituitary adenomas, ependimomas, lymphomas or brain metastases. A recent study performed on 80 patients with brain tumours documented a sensitivity, specificity and accuracy for ^{11}C-methionine of 88, 80 and 86 %. In addition in 50 % of the cases the PET findings had a direct impact on the therapeutic patient management (Yamane et al. 2009).

^{11}C-Methionine PET has a potential use in stereotactic brain biopsy too, especially in distinguishing neoplastic sites from necrotic areas, which are neither easily detectable by MRI nor ^{18}F-FDG-PET (Goldman et al. 1997).

The better tumour delineation of ^{11}C-methionine PET is applied in clinical radiotherapy planning (Nuutinen et al. 2000; Grosu et al. 2005). Both in high-grade and low-grade malignant gliomas, the gross tumour volume defined by ^{11}C-methionine is reported to be more precise than that defined by MRI. The difference in accuracy becomes highly relevant in post-therapeutic lesions, when CI fails to distinguish between residual disease and post-treatment alterations (Nuutinen et al. 2000).

The post-treatment evaluation is in fact the main clinical application for ^{11}C-methionine PET, thanks to its capability of differentiating recurrent brain tumours from radiation necrosis (Lilja et al. 1989; Ogawa et al. 1991; Tsuyuguchi et al. 2003). The sensitivity, specificity and accuracy of ^{11}C-methionine PET in detecting tumour recurrence range from 78–100 %, 60–100 % and about 82 %, respectively (Tsuyuguchi et al. 2003, 2004). False positive cases, however, can be related to ^{11}C-methionine uptake as a consequence of acute inflammation, ischemic stroke with reperfusion, etc., but not in chronic inflammatory or radiogenic lesions (Iwai et al. 2001; Kracht et al. 2003; Tsuyuguchi et al. 2004).

In addition, ^{11}C-methionine PET has been successfully applied in certain non-oncological fields, such as the diagnostic work-up of patients with hyperparathyroidism, although the diagnostic accuracy of PET in this case is not universally considered superior to that of conventional nuclear medicine examination based on ^{99m}Tc-Sestamibi (Rubello et al. 2006; Herrmann et al. 2009). In fact Tang et al. (2008) report a better performance of ^{11}C-metionine with a sensitivity of 92 % for adenomas and 68 % for hyperplasia, towards 95 % and 59 %, respectively for ^{99m}Tc-SESTAMIBI scintigraphy. Other authors demonstrate an inferior sensitivity of ^{11}C-methionine PET in primary hyperparathyroidism, with respect to ultrasonography and scintigraphy (Herrmann et al. 2009), but a superior accuracy in detecting secondary hyperparathyroidism in patients with renal failure and hypercalcemia (Rubello et al. 2006).

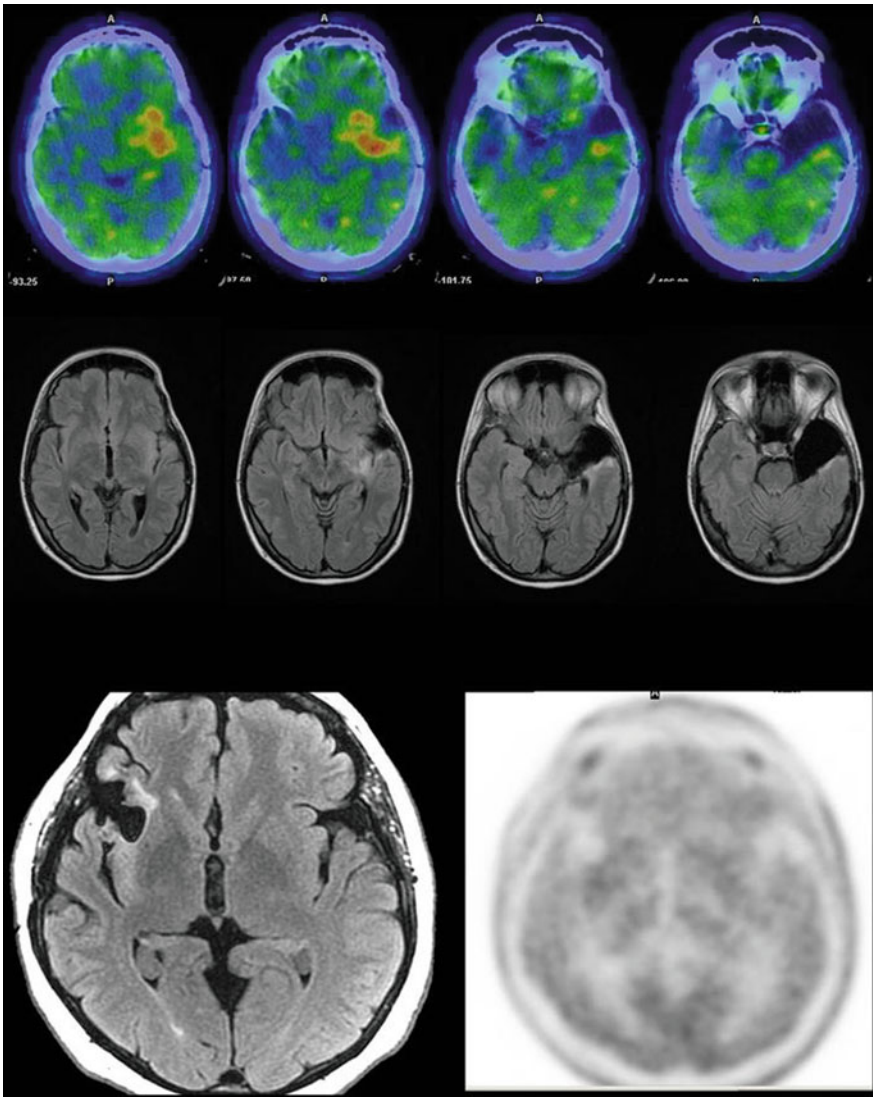

Fig. 3 Transversal images of ^{11}C-methionine PET/CT referred to the corresponding T1-weighted MRI; (*upper study*) perilesional recurrence at the level of surgical cratere, both at the MRI (*inferior views*) and ^{11}C-methionine (*superior views*); (*lower study*) no pathologic uptake of ^{11}C-methionine (*right sided view*) in the suspected right fronto-temporal lesion described at MRI (*left sided view*)

Despite the earlier attempts to define the accuracy of ^{11}C-methionine also in other malignancies such as lymphoma, lung, ovarian, head and neck tumours etc., much more studies are required in order to properly assess the vast potentialities of this promising oncologic tracer.

5 ^{11}C-Acetate

^{11}C-Acetate was proposed as a PET compound almost 3 decades ago, for tracing regional blood flow, cardiac physiology or tissue lipogenesis (Allan et al. 1980, 1981). Once injected, ^{11}C-acetate is rapidly cleared from the bloodstream and activated within the cells into ^{11}C-acetyl-CoA (Howard and Howard 1975). This activation may happen in the cytosol, like in cells with high lipogenic activity such as liver, salivary glands, spleen and also many cancers (Luong et al. 2000; Swinnen et al. 2003; Vallabhajosula 2007), or may happen within the mitochondria, where ^{11}C-acetyl-CoA enters the tricarboxylic acid (TCA) cycle, used for either catabolic or anabolic purpose (Mittendorfer et al. 1998; Chen et al. 2004; Sörensen et al. 2006).

The first pathway leads to the synthesis of cholesterol and fatty acids, which are then incorporated into cell membranes (Howard and Howard 1975), while the second one, in normal cells and myocardium, leads to complete oxidation of ^{11}C-acetyl-CoA to $^{11}C\text{-}CO_2$ and H_2O (Krebs 1948).

This background suggested the use of ^{11}C-acetate as a PET tracer for studies on myocardial blood flow and oxidative metabolism (Sörensen et al. 2006; Rigo et al. 1990), as well as for visualising certain tumours in which ^{18}F-FDG PET is of limited use such as prostate cancer, hepatocarcinoma, etc. (Oyama et al. 2002, 2003; Ho et al. 2003).

In fact, tumours show an increased uptake of ^{11}C-acetate thanks to the above-mentioned mechanisms, on one hand the TCA cycle and the augmented energetic and anabolic needs (lipids or amino acids, etc.), on the other hand the documented overexpression of fatty acid synthetase (Swinnen et al. 2003) entrapping ^{11}C-acetyl-CoA and incorporating it into cellular membranes, important for tumour growth and metastasis (Ponde et al. 2003; Sun et al. 2007; Soloviev et al. 2008). This was already documented in meningioma, glioma, nasopharyngeal carcinoma, lymphoma, nonsmall cell cancer, colon cancer, renal cell cancer, prostate and ovarian cancer (Liu 2000; Dimitrakopoulou-Strauss and Strauss 2003).

Based on the relative success of other fluorinated PET compounds, ^{18}F-fluoroacetate was proposed as a surrogate marker of acetate retention in cancer (Nanni et al. 2007a, Matthies et al. 2004; Ponde et al. 2007). Compared to ^{11}C-acetate, ^{18}F-fluoroacetate seems to be of uncertain utility with respect to the measurement of regional blood flow, cardiac physiology or tissue lipogenesis (Lindhe et al. 2009).

In tumour imaging, ^{11}C-acetate is mainly used for prostate cancer (Dimitrakopoulou-Strauss and Strauss 2003), but it is also applied in patients with hepatocellular carcinoma (HCC) (Ho et al. 2003, 2007 and Delbeke and Pinson 2003), renal cell carcinoma (Shreve et al. 1995), and, despite of limited experience, in gliomas (Liu et al. 2006; Yamamoto et al. 2008b).

^{11}C-Acetate PET/CT has got a higher sensitivity in patients suffering from HCC (83–87 %) as compared to that of ^{18}F-FDG-PET (40–47 %) (Ho et al. 2007, Hwang et al. 2009). These data are not surprising, as it is already known that HCC is one of the those tumours that may exhibit a glycolysis similar to or even lower than that of normal liver parenchyma and therefore may escape detection (Iwata et al. 2000;

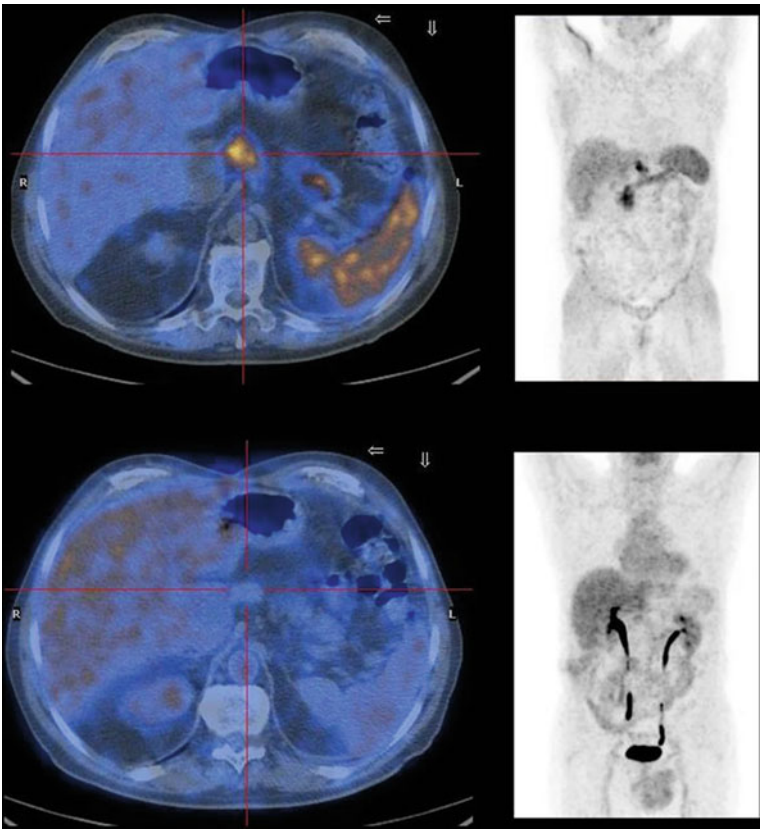

Fig. 4 MIP images of a nodal recurrence of HCC studied with ^{11}C-acetate PET/CT (*upper view*) and ^{18}F-FDG PET/CT (*lower view*); FDG-PET shows no pathology uptake, while acetate-PET clearly detects nodal involvement

Ho et al. 2003). In combination, however, the two PET-studies may show a complementary role: when primary HCC has a low ^{18}F-FDG uptake, there is an avid ^{11}C-acetate uptake, and vice versa (Ho et al. 2007, Hwang et al. 2009) (Fig. 4).

In prostate cancer the low oxidative metabolism and high lipid synthesis seems to be the main cause for ^{11}C-acetate uptake (Yoshimoto et al. 2001) leading to its use for diagnosis (Chierichetti et al. 2005), staging/restaging (Soloviev et al. 2008) and detection of recurrence in biochemical relapse (Oyama et al. 2003; Albrecht et al. 2007). According to the literature, the tracer is sensitive in the detection of primary tumour (Oyama et al. 2002) with good accuracy in N- and M-staging, and in the detection of disease relapse (Kotzerke et al. 2002; Oyama et al. 2003). The clinical applications of ^{11}C-acetate match with those of ^{11}C-choline PET, and, although the latter is more widely used as PET compound, the two tracers seem to yield almost identical results in patients with prostate cancer (Nanni et al. 2007a; Morris and Scher 2007).

6 Clinical Applications of ^{18}F-FLT

^{18}F-3′-deoxy-3′-^{18}F-fluorothymidine (^{18}F-FLT) is the fluorinated analogue of thymidine, one of the four DNA bases, introduced as a PET tracer for measuring tissue and tumour proliferation in 1998 (Shields et al. 1998; Groves et al. 2007).

The rationale of using thymidine analogues is based on the knowledge that this pyrimidine base is rapidly incorporated into newly synthesised DNA, and this led to the first attempts in the 1980s to utilise the native form labelled with ^{11}C (^{11}C-thymidine) for the evaluation of DNA synthesis in vivo (Martiat et al. 1988; Wells et al. 2002). The carbon labelled tracer, however, turned out not suitable for routine clinical use due to the short half-life of ^{11}C and the rapid in vivo degradation of ^{11}C-thymidine. Therefore ^{18}F-FLT, which derives from the cytostatic drug azidovudine (AZT), was preferred for this purpose (Shields et al. 1998).

Despite following the natural pathway of thymidine, ^{18}F-FLT is trapped in cells after phosphorylation by thymidine kinase 1, but it is not or only marginally incorporated into the growing DNA chain (< 2 %) (Been et al. 2004; Buck et al. 2005; Reske and Deisenhofer 2006). This leads to the conclusion that ^{18}F-FLT uptake is not a direct representative of DNA synthesis, but rather of cellular S-phase (Barthel et al. 2005; Buck et al. 2005).

Recently a significant correlation has been reported between this tracer uptake and cellular proliferation in various malignant tumours such as lung cancer, breast cancer, colorectal cancer, gliomas, sarcomas and lymphomas (Buck et al. 2002, 2005, 2008; Chen et al. 2005a; Francis et al. 2003; Kenny et al. 2005; Leyton et al. 2005), also with respect to the proliferation fraction in biopsied tissues as indicated by Ki-67 immunohistochemistry (Buck et al. 2002, 2005; Vesselle et al. 2002).

^{18}F-FLT-PET yields images of high contrast, with good tumour-to-background ratios. Physiological uptake of ^{18}F-FLT is noticed in the bone marrow, due to elevated cell proliferation, in the liver, secondary to hepatic glucuronidation, and in the urinary tract, as part of the renal clearance of the tracer (Shields 2006). According to this pattern of distribution, these areas represent the main limits of the method with respect to imaging accuracy.

In malignant lymphomas, both aggressive and indolent subtypes are reported to show ^{18}F-FLT uptake, with an excellent overall sensitivity up to 100 %. Similar results are reported in non-small cell lung cancer, with a sensitivity of up to 90 % (Buck et al. 2005). However, the detection rate decreases markedly when considering lymphogenic spread (53 %) and distant metastases (67 %), resulting in a lower accuracy of ^{18}F-FLT-PET in tumour staging (Dittman et al. 2003; Cobben et al. 2004; Buck et al. 2005).

In colorectal cancer too, both ^{18}F-FLT and ^{18}F-FDG PET showed a good visualisation of the primary tumours, however, only 34 % of liver metastases were detected with ^{18}F-FLT versus 97 % with ^{18}F-FDG (Francis et al. 2003).

^{18}F-FLT uptake has also been investigated in brain tumours, where its uptake correlates better with the Ki-67 proliferation index and results in a higher accuracy in the detection of recurrent brain tumours when compared with ^{18}F-FDG-PET (Chen et al. 2005a).

The most promising application, however, appears to be monitoring of therapeutic response with ^{18}F-FLT-PET. In animal models of fibrosarcoma and lymphoma (Barthel et al. 2003; Buck et al. 2004), and in preliminary studies in primary breast tumours and metastases, when compared to ^{18}F-FDG, ^{18}F-FLT showed a more significant decrease in uptake after treatment (Barthel et al. 2003; Pio et al. 2006; Leyton et al. 2005).

Generally the mean ^{18}F-FLT uptake in tumours is reported to be significantly lower when compared to the respective ^{18}F-FDG uptake (Buck et al. 2005). Overall ^{18}F-FLT-PET appears to be less accurate in tumour detection than ^{18}F-FDG-PET, however, as a proliferation tracer, ^{18}F-FLT is more specific than ^{18}F-FDG and therefore, the principal role of this tracer can be assessed in monitoring treatment response in the clinical setting.

7 ^{18}F-FET

Tyrosine was radiolabelled and introduced for PET imaging for the first time in 1989 (Coenen et al. 1989). As an amino acid it follows the protein synthesis pathways and therefore its uptake reflects the metabolism of malignant cells too (Wienhard et al. 1991).

Among the possible radiolabelled forms, ^{18}F-fluoroethyltyrosine (^{18}F-FET) yields the most promising results (Fedorova et al. 2009). It is not incorporated into proteins, but despite that ^{18}F-FET PET shows high accuracy in the diagnostics of cerebral gliomas and extracranial squamous cell carcinomas, probably due to intracellular trapping secondary to increased amino acid transport within the cells (Wester et al. 1999; Heiss et al. 1999; Langen et al. 2006).

^{18}F-FET exhibits high in vivo stability, low uptake in inflammatory tissue and suitable uptake kinetics for clinical imaging (Kaim et al. 2002; Prante et al. 2007). In addition it can be produced with high efficiency and therefore it offers the opportunity of commercial distribution via a satellite concept like ^{18}F-FDG (Langen et al. 2006; Stadlbauer et al. 2008).

Several studies have demonstrated the benefit of ^{18}F-FET PET for the management of patients with gliomas in terms of differential diagnosis and grading (Pauleit et al. 2005; Weckesser et al. 2005; Floeth et al. 2007), prediction of prognosis (Floeth et al. 2007), monitoring of therapy response (Pöpperl et al. 2005), radiotherapy planning (Weber et al. 2008) and detection and diagnosis of tumor recurrence (Pöpperl et al. 2004, 2006; Rachinger et al. 2005), with a sensitivity and specificity of 96 % and 53 %, respectively in the detection of tumour tissue (Pauleit et al. 2005). In non-neoplastic brain lesions, however, an increase in ^{18}F-FET uptake may indicate reactive astrocytosis (Salber et al. 2006, 2007).

^{18}F-FET PET has also demonstrated a good sensitivity and specificity in head and neck cancers of 75 % and 95 %, respectively, with an overall accuracy of 90 % (Pauleit et al. 2006). When comparing, however, the diagnostic value with that of ^{18}F-FDG-PET, the latter is more accurate, but ^{18}F-FET uptake yields a better differentiation of tumour tissue from inflammatory disease (Pauleit et al. 2006).

Due to the high accuracy of further well-established PET tracers, such as ^{18}F-FDG or ^{11}C-methionine ^{18}F-FET PET plays only a marginal role in clinical routine.

8 ^{18}F-Fluoride

^{18}F-Fluoride represents the simplest fluorinated radiopharmaceutical adopted in PET imaging. The rationale for its utilisation in bone imaging, started in the 1960s (Blau et al. 1962), is the same as compared to diphosphonates and is based on the physiological absorption of fluoroderivates in the bone matrix as fluoroapatite (Volker et al. 1940; Vallabhajosula 2007). As such, it is a tracer that indicates osteoblastic metabolism.

When compared to the γ-emitter ^{99m}Tc-phosphonates, ^{18}F-fluoride benefits from several advantages related to faster extraction from blood pool (Langsteger et al. 2006), higher capillary permeability and significantly higher pathologic-to-normal bone fluoride uptake (Blake et al. 2001). It has in fact a blood to bone clearance of almost 100 %, almost that of ^{99m}Tc-methylenediphosphonate (^{99m}Tc-MDP), and imaging is practically instantaneously available after ^{18}F-fluoride administration (Langsteger et al. 2006; Groves et al. 2007).

In addition, the method has shown an increased diagnostic sensitivity for bone lesions as compared with ^{99m}Tc-diphosphonates, thanks to the better spatial resolution provided by PET/CT technology (Vallabhajosula 2007).

^{18}F-Fluoride bone uptake has been reported in both sclerotic and lytic metastases (Schiepers et al. 1997; Even-Sapir et al. 2004) and there is a documented evidence that the diagnostic accuracy of ^{18}F-fluoride-PET is better than that of ^{99m}Tc-MDP scintigraphy for detecting bone metastases in several cancers such as lung, prostate and breast cancer (Schirrmeinster et al. 2001; Hetzel et al. 2003; Even-Sapir et al. 2006; Groves et al. 2007). In an investigation of patients with prostate cancer (Even-Sapir et al. 2004, 2006) ^{18}F-fluoride PET/CT, detected bone metastases with a sensitivity and specificity of 100 %, whereas ^{99m}Tc-MDP scintigraphy had a sensitivity and a specificity of 92 % and 82 %, respectively (Groves et al. 2007).

The main limit, however, for this tracer is the fact that as a bone agent ^{18}F-fluoride cannot be considered as tumour-specific. Similar to ^{99m}Tc-diphosphonates it may also be taken up in benign pathologies and nonmalignant orthopaedic problems (Vallabhajosula 2007).

The favourable imaging performance, however, and the clinical utility of ^{18}F-fluoride PET (Grant et al. 2008), compared with ^{99m}Tc-diphosphonate scintigraphy, support the potential use of ^{18}F-fluoride as a routine bone imaging agent.

9 Clinical Applications of PET Tracers for Hypoxia

A major challenge in treating tumours is related to the low level of malignant tissue oxygenation (Tannock and Guttman 1981; Brown 1999). Response to therapy is strongly determined by this fact and it is already reported that acquired resistance to chemo- or radio-therapy, as well as probability for precocious relapse are largely influenced by the fraction of hypoxic tissue in the tumour (Crabtree and Cramer 1933; Gray et al. 1953; Lewis and Welch 2001; Lewis et al. 2001; Piert et al. 2005).

The classic method to directly assess tumour hypoxia is rather invasive and difficult (Cater and Silver 1960; Krause et al. 2008), therefore leading the consequent development of indirect methods of measurement. ^{18}F-Fluoromisonidazole (^{18}F-FMISO) was the first PET tracer for mapping the in vivo tissue oxygenation (Rasey et al. 1987, 1996; Koh et al. 1992). When ^{18}F-FMISO encounters hypoxic environment, it is reduced and bound to intracellular macromolecules, preventing the usual back-diffusion occurring in normal oxygenation conditions. (Caldwell et al. 1995; Cher et al. 2006; Groves et al. 2007).

^{18}F-FMISO-PET has been able to monitor hypoxia in the hearts of patients with myocardial ischaemia (Vallabhajosula 2007), in lung cancer (Koh et al. 1995), in sarcomas (Rajendran et al. 2003), in brain and head and neck cancer (Ng et al. 2003; Hicks et al. 2005; Rajendran et al. 2004), demonstrating a good correlation between ^{18}F-FMISO uptake and poor outcome to radiation and chemotherapy.

However, the tracer has some limitations related to the presence of high normal liver uptake and urinary excretion, but the most important drawbacks are the absent uptake of tracer in necrotic tissue and the modest signal-to-noise ratio, leading to unfavourable imaging characteristics.

Similar in concept to ^{18}F-FMISO, but with better imaging qualities, are the more recently introduced hypoxic tracers, such as ^{18}F-fluoroazomycin arabinozide (^{18}F-FAZA) (Piert et al. 2005) and ^{18}F-fluoronitroimidazole (^{18}F-EF5) (Komar et al. 2008).

In addition, ^{64}Cu-methylthiosemicarbazone (^{64}Cu-ATSM) appears to be rather promising for imaging tumour hypoxia with PET (Padhani 2006). The mechanism of retention is largely attributed to the low oxygen tensions and the altered redox environment of hypoxic tumours (Padhani 2006). This results in an optimal signal-to-background ratio, with absent ^{64}Cu-ATSM in normal tissue and almost exclusive uptake in the hypoxic areas.

Physiologic distribution of the tracer is characterised by an elevated uptake in the liver, to a minor degree in the kidneys and, on delayed acquisitions, within the intestine secondary to biliary excretion (Laforest et al. 2005).

At present several preclinical and clinical studies have evaluated and validated the use of ^{64}Cu-ATSM for imaging hypoxia in tumours and other tissues (Fujibayashi et al. 1997; Dearling et al. 1998a, b, 2002; Lewis et al. 1999, 2001; Maurer et al. 2002).

This is the case for lung and cervical cancers (Dehdashti et al. 2003a, b), where the ^{64}Cu-ATSM uptake was a good predictor of patient outcome, by discriminating those likely to respond to therapy from non-responders (Takahashi et al. 2000). However, much more needs still to be investigated.

10 Clinical Applications of PET Tracers for Angiogenesis

Angiogenesis represents one of the key processes in tumour progression, therefore many efforts have been made to identify antiangiogenic molecules and design antiangiogenic strategies for cancer treatment (Cai et al. 2006, 2008; Folkman 2007; Kerbel and Folkman 2002).

Principally there are two different angiogenesis related molecular targets that have been mostly studied, one is integrin ($\alpha_v\beta_3$) and the second is vascular endothelial growth factor receptor (Cai et al. 2008).

Integrins are a family of adhesion molecules actively involved in tumour angiogenesis and metastasis (Hood et al. 2002; Hynes 2002). Among them is integrin $\alpha_v\beta_3$, which binds to arginine-glycine-aspartic acid (RGD), and is known to be significantly upregulated on tumour vasculature but not on quiescent endothelium (Hood et al. 2002). Molecular imaging tracers containing RGD peptide have been promptly radiolabelled with numerous PET nuclides (^{18}F, ^{64}Cu, ^{68}Ga) for non-invasive monitoring of tumour angiogenesis via integrin $\alpha_v\beta_3$ expression (Chen et al. 2005b; Beer et al. 2006; Cai et al. 2008).

The other mechanism involved in the modulation of angiogenesis is VEGF/VEGFR signalling pathway, significant in both normal and pathologic vasculature development (Ferrara 2002, 2005).

At present seven subtypes of VEGF ad two different endothelium-specific receptors, VEGFR-1 and VEGFR-2, are known (Hicklin and Ellis 2005). There seems to be worst prognosis when a VEGF/VEGFR overexpression is documented (Ferrara 2004), therefore VEGFR-targeted molecular imaging can serve as a new paradigm for assessing the efficacy of antiangiogenic therapeutics and patients outcome. For this purpose PET imaging of VEGFR has been reported over the past several years (Cai et al. 2008).

Many antiagiogenetic drugs have up to now been introduced for tumour treatment, like bevacizumab, sunitinib, sorafenib, etc., demonstrating therapeutic efficacy in several solid cancers (Brandi et al. 2008; Prior et al. 2009; Lyrdal et al. 2009). However, this sort of molecular targeted therapy is not adequate in all patients. The main reason for imaging application in this field relies primarily on the possibility to precociously detect cancer patients who will benefit from a targeted antiangiogenic therapy.

Encouraging results are already reported on several radiopharmaceuticals, such as RGD radiolabelled peptides (^{18}F-Galacto-RGD, ^{68}Ga-NOTA-RGD, etc.) (Jeong et al. 2008; Schnell et al. 2009) and VEGF radiolabelled tracers (^{64}Cu-DOTA-VEGF) (Cai et al. 2006).

Further studies are, however, required, but the undoubtable fascination derived from this subject, makes us optimistic about an exponential increase of targeted therapy development and, consequently, in a parallel application of molecular PET imaging.

References

Ackerstaff E, Pflug BR, Nelson JB et al (2001) Detection of increased choline compounds with proton nuclear magnetic resonance spectroscopy subsequent to malignant transformation of human prostatic epithelial cells. Cancer Res 61:3599–3603

Agid Y, Graybiel AM, Ruberg M, et al (1990) The efficacy of levodopa treatment declines in the course of Parkinson's disease: do nondopaminergic lesions play a role? Adv Neurol 53:83–100

Ahlström H, Eriksson B, Bergstrom M et al (1995) Pancreatic neuroendocrine tumors: diagnosis with PET. Radiology 195:333–337

Albrecht S, Buchegger F, Soloviev D et al (2007) ^{11}CC-Acetate PET in the early evaluation of prostate cancer recurrence. Eur J Nucl Med Mol Imaging 34:185–196

Allan RM, Pike VW, Maseri A et al (1981) Myocardial metabolism of ^{11}C-acetate: experimental and patient studies. Circulation 64(Suppl IV) IV 75

Allan RM, Selwyn AP, Pike VW et al (1980) In vivo experimental and clinical studies of normal and ischemic myocardium using ^{11}C-acetate. Circulation 62(Suppl III) III-74

Ambrosini V, Marzola MC, Rubello D, Fanti S (2010) ^{68}Ga-somatostatin analogues PET and ^{18}F-DOPA PET in medullary thyroid carcinoma. Eur J Nucl Med Mol Imaging 37(1):46–48

Ambrosini V, Tomassetti P, Castellucci P et al (2008) Comparison between ^{68}Ga-DOTA-NOC and ^{18}F-DOPA PET for the detection of gastro-entero-pancreatic and lung neuro-endocrine tumours. Eur J Nucl Med Mol Imaging 35(8):1431–1438

Barthel H, Cleij MC, Collingridge DR et al (2003) 3′-Deoxy-3′-[^{18}F]fluorothymidine as a new marker for monitoring tumor response to antiproliferative therapy in vivo with positron emission tomography. Cancer Res 63:3791–3798

Barthel H, Perumal M, Latigo J et al (2005) The uptake of 3′-deoxy-3′-[^{18}F]fluorothymidine into L178Y tumours in vivo is dependent on thymidine kinase 1 protein levels. Eur J Nucl Med Mol Imaging 32(3):257–263

Becherer A, Szabó M, Karanikas G et al (2004) Imaging of advanced neuroendocrine tumors with ^{18}F-FDOPA PET. J Nucl Med 45(7):1161–1167

Been LB, Suurmeijer AJH, Cobben DCP et al (2004) [^{18}F] FLT-PET in oncology: current status and opportunities. Eur J Nucl Med Mol Imaging 31:1659–1672

Beer AJ, Haubner R, Sarbia M et al (2006) Positron emission tomography using [^{18}F]galacto-RGD identifies the level of integrin $\alpha_v\beta_3$ expression in man. Clin Cancer Res 12:3942–3949

Blake GM, Park-Holohan SJ, Cook GJ et al (2001) Quantitative studies of bone with the use of ^{18}F-fluoride and ^{99m}Tc-methylene diphosphonate. Semin Nucl Med 31:28–49

Blau M, Nagler W, Bender MA (1962) A new isotope for bone scanning. J Nucl Med 3:332–334

Borbély K, Nyáry I, Tóth M et al (2006) Optimization of semi-quantification in metabolic PET studies with ^{18}F-fluorodeoxyglucose and ^{11}C-methionine in the determination of malignancy of gliomas. J Neurol Sci 15:85–94

Borelli MI, Villar MJ, Orezzoli A et al (1997) Presence of DOPA decarboxylase and its localisation in adult rat pancreatic islet cells. Diabetes Metab 23:161–163

Brandi G, Nannini M, Pantaleo MA et al (2008) Molecular imaging suggests efficacy of bevacizumab beyond the second line in advanced colorectal cancer patients. Chemotherapy 54(6):421–424

Braun V, Dempf S, Weller R et al (2002) Cranial neuronavigation with direct integration of ^{11}C methionine positron emission tomography (PET) data—results of a pilot study in 32 surgical cases. Acta Neurochir 144:777–782

Breeuwsma AJ, Pruim J, Van den Bergh AC et al (2010) Detection of local, regional, and distant recurrence in patients with PSA relapse after external-beam radiotherapy using ^{11}C-Choline positron emission tomography. Int J Radiat Oncol Biol Phys 77:160–164

Briganti A, Chun FK-H, Salonia A et al (2006) Validation of a nomogram predicting the probability of lymph node invasion among patients undergoing radical prostatectomy and an extended pelvic lymphadenectomy. Eur Urol 49:1019–1027

Brown JM (1999) The hypoxic cell: A target for selective cancer therapy—Eighteenth Bruce F. Cain Memorial Award Lecture. Cancer Res 59:5863–5870

Buck AK, Herrmann K, Buschenfelde CM et al (2008) Imaging bone and soft tissue tumors with the proliferation marker [^{18}F]fluorothymidine. Clin Cancer Res 14:2970–2977

Buck AK, Hetzel M, Schirrmeister H et al (2005) Clinical relevance of imaging proliferative activity in lung nodules. Eur J Nucl Med Mol Imaging 32:525–533

Buck AK, Schirrmeister H, Hetzel M et al (2002) 3-Deoxy-3-[^{18}F]fluorothymidine-positron emission tomography for noninvasive assessment of proliferation in pulmonary nodules. Cancer Res 62:3331–3334

Buck AK, Vogg ATJ, Glatting G et al (2004) [^{18}F]FLT for monitoring response to antiproliferative therapy in a mouse lymphoma xenotransplant model. J Nucl Med 45:434

Cai W, Chen K, Mohamedali KA et al (2006) PET of vascular endothelial growth factor receptor expression. J Nucl Med 47:2048–2056

Cai W, Gambhir SS, Chen X (2008) Chapter 7. Molecular imaging of tumor vasculature. Methods Enzymol 445:141–176

Caldwell JH, Revenaugh JR, Martin GV et al (1995) Comparison of fluorine-18-fluorodeoxyglucose and tritiated fluoromisonidazole uptake during low-flow ischemia. J Nucl Med 36:1633–1638

Castellucci P, Fuccio C, Nanni C et al (2009) Influence of trigger PSA and PSA kinetics on ^{11}C-choline PET/CT detection rate in patients with biochemical relapse after radical prostatectomy. J Nucl Med 50:1394–1400

Castellucci P, Fuccio C, Rubello D et al (2011) Is there a role for ^{11}C-choline PET/CT in the early detection of metastatic disease in surgically treated prostate cancer patients with a mild PSA increase < 1.5 ng/ml? Eur J Nucl Med Mol Imaging 38:55–63

Cater DB, Silver IA (1960) Quantitative measurements of oxygen tension in normal tissues and in tumors of patients before and after radiotherapy. Acta Radiol 53:233–256

Chen S, Ho C, Feng D et al (2004) Tracer kinetic modeling of ^{11}C-acetate applied in the liver with positron emission tomography. IEEE Trans Med Imaging 23:426–432

Chen W, Cloughesy T, Kamdar N et al (2005a) Imaging proliferation in brain tumors with ^{18}F-FLT PET: comparison with ^{18}F-FDG. J Nucl Med 46(6):945–952

Chen X, Sievers E, Hou Y et al (2005b) Integrin $\alpha_v\beta_3$-targeted imaging of lung cancer. Neoplasia 7:271–279

Cimitan M, Bortolus R, Morassut S et al (2006) [^{18}F]fluorocholine PET/CT imaging for the detection of recurrent prostate cancer at PSA relapse: experience in 100 consecutive patients. Eur J Nucl Med Mol Imaging 33:1387–1398

Cher LM, Murone C, Lawrentschuck N et al (2006) Correlation of hypoxic cell fraction and angiogenesis with glucose metabolic rate in gliomas using ^{18}F-fluoromisonidazole, ^{18}F-FDG PET, and immunohistochemical studies. J Nucl Med 47:410–418

Chierichetti F, Lessi G, Bissoli S et al (2005) Preliminary experience with ^{11}C-acetate and PET/CT in prostate cancer. J Nucl Med (Suppl 2):46

Chung JK, Kim YK, Kim SK et al (2002) Usefulness of ^{11}C-methionine PET in the evaluation of brain lesions that are hypo- or isometabolic on ^{18}F-FDG PET. Eur J Nucl Med Mol Imaging 29:176–182

Cobben DC, Elsinga PH, Hoekstra HJ et al (2004) Is ^{18}F-3′-fluoro-3′-deoxy-L-thymidine useful for the staging and restaging of non-small cell lung cancer? J Nucl Med 45:1677–1682

Coenen HH, Kling P, Stocklin G (1989) Cerebral metabolism of L-[2-^{18}F]fluorotyrosine, a new PET tracer of protein synthesis. J Nucl Med 30:1367–1372

Comar D, Cartron JC, Maziere M et al (1976) Labelling and metabolism of methionine-methyl-^{11}C. Eur J Nucl Med 1:11–14

Cook GJ, Maisey MN, Fogelman I (1999) Normal variants, artefacts and interpretative pitfalls in PET imaging with ^{18}-fluoro-2-deoxyglucose and carbon-11 methionine. Eur J Nucl Med 26:1363–1378

Crabtree HG, Cramer W (1933). The action of radium on cancer cells I and II. Some factors determining the susceptibility of cancer cells to radium. Proc R Soc Ser B 113:238–250

De Jong I, Pruim J, Elsinga PH et al (2003) ^{11}C-choline positron emission tomography for the evaluation after treatment of localized prostate cancer. Eur Urol 44:32–38

De Jong IJ, Pruim J, Elsinga PH et al (2002) Visualization of bladder cancer using ^{11}C-choline PET: first clinical experience. Eur J Nucl Med 29:1283–1288

De Vries EFJ, Luurtsema G, Brussermann M et al (1999) Fully automated synthesis module for the high yield one-pot preparation of 6-[^{18}F]fluoro-L-DOPA. Appl Radiat Isot 51:389–394

Dearling JL, Lewis JS, Mullen GE et al (2002) Copper bis(thiosemicarbazone) complexes as hypoxia imaging agents: structure-activity relationships. J Biol Inorg Chem 7:249–259

Dearling JLD, Lewis JS, Mullen GE et al (1998a) Design of hypoxia-targeting radiopharmaceuticals: selective uptake of copper-64 complexes in hypoxic cells in vitro. Eur J Nucl Med 25:788–792

Dearling JLJ, Lewis JS, Welch MJ et al (1998b) Redox-active complexes for imaging hypoxic tissues: structure-activity relationships in copper(II)bis(thiosemicarbazone) complexes. Chem Commun 22:2531–2533

DeGrado TR, Coleman RE, Wang S et al (2001) Synthesis and evaluation of ^{18}F labeled choline as an oncologic tracer for positron emission tomography: initial findings in prostate cancer. Cancer Res 61:110–117

Dehdashti F, Grigsby PW, Mintun MA et al (2003a) Assessing tumor hypoxia in cervical cancer by positron emission tomography with ^{60}Cu-ATSM: relationship to therapeutic response—a preliminary report. Int J Radiat Oncol Biol Phys 55:1233–1238

Dehdashti F, Mintun MA, Lewis JS et al (2003b) In vivo assesment of tumor hypoxia in lung cancer with ^{60}Cu-ATSM. Eur J Nucl Med Mol Imaging 30:844–850

Delbeke D, Pinson CW (2003) ^{11}C-acetate: a new tracer for the evaluation of hepatocellular carcinoma. J Nucl Med 44:222–223

Derlon JM, Bourdet C, Bustany P et al (1989) [^{11}C]L-methionine uptake in gliomas. Neurosurgery 25:720–728

Dimitrakopoulou-Strauss A, Strauss LG, Burger C (2001) Quantitative PET studies in pretreated melanoma patients: a comparison of 6-[^{18}F]fluoro-L-dopa with ^{18}F-FDG and water using compartment and noncompartment analysis. J Nucl Med 42:248–256

Dimitrakopoulou-Strauss A, Strauss LG (2003) PET imaging of prostate cancer with ^{11}C-acetate. J Nucl Med 44:556–558

Dittman H, Dohmen BM, Paulsen F et al (2003) [^{18}F]FLT PET for diagnosis and staging of thoracic tumours. Eur J Nucl Med Mol Imaging 30:1407–1412

Eidelberg D (1992) Positron emission tomography studies in parkinsonism. Neurol Clin 10:421–433

Eriksson B, Bergstrom M, Sundin A et al (2002) The role of PET in localization of neuroendocrine and adrenocortical tumors. Ann NY Acad Sci 970:159–169

Eshuis SA, Jager PLÛ, Maguire RP et al (2009) Direct comparison of FP-CIT SPECT and F-DOPA PET in patients with Parkinson's disease and healthy controls. Eur J Nucl Med Mol Imaging 36:454–462

Eshuis SA, Maguire RP, Leenders KL et al (2006) Comparison of FP-CIT SPECT with F-DOPA PET in patients with de novo and advanced Parkinson's disease. Eur J Nucl Med Mol Imaging 33:200–209

Even-Sapir E, Metser U, Flusser G et al (2004) Assessment of malignant skeletal disease with ^{18}F-fluoride PET/CT. J Nucl Med 45:272–278

Even-Sapir E, Metser U, Mishani E et al (2006) The detection of bone metastases in patients with high-risk prostate cancer: ^{99m}Tc-MDP planar bone scintigraphy, single- and multi-field-of-view SPECT, ^{18}F-fluoride PET, and ^{18}F-fluoride PET/CT. J Nucl Med 47:287–297

Fanti S, Nanni C, Ambrosini V et al (2007) PET in genitourinary tract cancers. Q J Nucl Med Mol Imaging. 51:260–271

Farsad M, Schiavina R, Castellucci P et al (2005) Detection and localization of prostate cancer: correlation of ^{11}C-choline PET/CT with histopathologic step-section analysis. J Nucl Med 46:1642–1649

Fedorova OS, Kuznetsova OF, Shatik SV et al (2009) ^{18}F-labeled tyrosine derivatives: synthesis and experimental studies on accumulation in tumors and abscesses. Bioorg Khim 35:334–343

Ferrara N (2002) VEGF and the quest for tumour angiogenesis factors. Nat Rev Cancer 2:795–803

Ferrara N (2004) Vascular endothelial growth factor: Basic science and clinical progress. Endocr Rev 25:581–611

Ferrara N (2005) The role of VEGF in the regulation of physiological and pathological angiogenesis. EXS 94:209–231

Fiebrich HB, Brouwers AH, Kerstens MN et al (2009) 6-[F-18]Fluoro-L-dihydroxyphenylalanine positron emission tomography is superior to conventional imaging with ^{123}I-metaiodobenzylguanidine scintigraphy, computer tomography, and magnetic resonance imaging in localizing tumors causing catecholamine excess. J Clin Endocrinol Metab 94:3922–3930

Firnau G, Chiakal R, Garnett ES (1984) Aromatic radiofluorination with ^{18}F fluorine gas: 6-[^{18}F]fluoro-L-dopa. J Nucl Med 25:1228–1233

Floeth FW, Pauleit D, Sabel M et al (2007) Prognostic value of O-(2-^{18}F-fluoroethyl)-L-tyrosine PET and MRI in low-grade glioma. J Nucl Med 48:519–527

Folkman J (2007) Angiogenesis: An organizing principle for drug discovery? Nat Rev Drug Discov 6:273–286

Francis DL, Visvikis D, Costa DC et al (2003) Potential impact of [^{18}F]3′-deoxy-3′-fluorothymidine versus [^{18}F]fluoro-2-deoxy-D-glucose in positron emission tomography for colorectal cancer. Eur J Nucl Med Mol Imaging 30:988–994

Fujibayashi Y, Taniuchi H, Yonekura Y et al (1997) Copper-62-ATSM: A new hypoxia imaging agent with high membrane permeability and low redox potential. J Nucl Med 38:1155–1160

Fuccio C, Castellucci P, Schiavina R et al (2010) Role of ^{11}C-choline PET/CT in the restaging of prostate cancer patients showing a single lesion on bone scintigraphy. Ann Nucl Med 24:485–492

Garnett ES, Firnau G, Nahmias C (1983) Dopamine visualized in the basal ganglia of living man. Nature 305:137–138

Gazdar AF, Helman LJ, Israel MA et al (1988) Expression of neuroendocrine cell markers L-dopa decarboxylase, chromogranin A, and dense core granules in human tumors of endocrine and nonendocrine origin. Cancer Res 48:4078–4082

Giovacchini G, Picchio M, Coradeschi E et al (2008) [^{11}C]choline uptake with PET/CT for the initial diagnosis of prostate cancer: relation to PSA levels, tumour stage and anti-androgenic therapy. Eur J Nucl Med Mol Imaging 35:1065–1073

Goldman S, Levivier M, Pirotte B et al (1997) Regional methionine and glucose uptake in high-grade gliomas: a comparative study on PET-guided stereotactic biopsy. J Nucl Med 38:1459–1462

Goodman MM, Keil R, Shoup TM et al (1997) Fluorine-18-FPCT: a PET radiotracer for imaging dopamine transporters. J Nucl Med 38:119–126

Gourgiotis l, Sarlis NJ, Reynolds JC et al (2003) Localization of medullary thyroid carcinoma metastasis in a multiple endocrine neoplasia type 2A patient by 6-[^{18}F]-Fluorodopamine positron emission tomography J Clin Endocrinol Metab 88:637–641

Grant FD, Fahey FH, Packard AB et al (2008) Skeletal PET with ^{18}F-fluoride: applying new technology to an old tracer. J Nucl Med 49:68–78

Gray LH, Conger AD, Ebert M et al (1953) Concentration of oxygen dissolved in tissues at the time of irradiation as a factor in radiotherapy. Br J Radiol 26:638–648

Grosu AL, Weber WA, Riedel E et al (2005) L-(methyl-^{11}C) methionine positron emission tomography for target delineation in resected high-grade gliomas before radiotherapy. Int J Radiat Oncol Biol Phys 63:64–74

Groves AM, Win Th, Ben Haim S et al (2007) Non-[^{18}F]FDG PET in clinical oncology. Lancet Oncol 8:822–830

Gumprecht H, Grosu AL, Souvatsoqlou M et al (2007) ^{11}C-Methionine positron emission tomography for preoperative evaluation of suggestive low-grade gliomas. Zentralbl Neurochir 68:19–23

Hara T, Yuasa M, Yoshida H (1997a) Automated synthesis of fluorine-18 labeled choline analogue: 2-fluoroethyl- dimethyl-2-oxyethylammonium. J Nucl Med 38:44

Hara T, Kosada N, Kondo T et al (1997b) Imaging of brain tumor, lung cancer, esophageal cancer, colon cancer, prostate cancer and bladder cancer with (C-11)choline. J Nucl Med 38:250

Hara T, Kosaka N, Kishi H (1998) PET imaging of prostate cancer using carbon-11-choline. J Nucl Med 39:990–995

Hara T, Kosaka N, Kishi H (2002) Development of [^{18}F]-Fluoroethylcholine for cancer imaging with PET: Synthesis, biochemistry, and prostate cancer imaging. J Nucl Med 43:187–199

Hara T, Kondo T, Hara T et al (2003) Use of ^{18}F-choline and ^{11}C-choline as contrast agents in positron emission tomography imaging-guided stereotactic biopsy sampling of gliomas. J Neurosurg 99:474–479

Hardy O, Hernandez-Pampaloni M, Saffer JR et al (2007a) Diagnosis and localization of focal congenital hyperinsulinism by ^{18}F-fluorodopa PET scan. J Pediatr 150:140–145

Hardy OT, Hernandez-Pampaloni M, Saffer JR et al (2007b) Accuracy of [^{18}F]fluorodopa positron emission tomography for diagnosing and localizing focal congenital hyperinsulinism. J Clin Endocrinol Metab 92:4706–4711

Hatazawa J, Ishiwata K, Itoh M et al (1989) Quantitative evaluation of L-[methyl-C-11]methionine uptake in tumor using positron emission tomography. J Nucl Med 30:1809–1813

Heiss P, Mayer S, Herz M et al (1999) Investigation of transport mechanism and uptake kinetics of O-(2-^{18}F-fluoroethyl)-L-tyrosine in vitro and in vivo. J Nucl Med 40:1367–1373

Heiss WD, Wienhard K, Wagner R et al (1996) F-Dopa as an amino acid tracer to detect brain tumours. J Nucl Med 37:1180–1182

Herholz K, Hölzer T, Bauer B et al (1998) ^{11}C-methionine PET for differential diagnosis of low-grade gliomas. Neurology 50:1316–1322

Herrmann K, Takei T, Kanegae K et al (2009) Clinical value and limitations of ^{11}C-methionine PET for detection and localization of suspected parathyroid adenomas. Mol Imaging Biol 11:356–363

Hetzel M, Arslandemir C, Konig HH et al (2003) F-18 NaF PET for detection of bone metastases in lung cancer: accuracy, costeff ectiveness, and impact on patient management. J Bone Miner Res 18:2206–2214

Hicklin DJ, Ellis LM (2005) Role of the vascular endothelial growth factor pathway in tumor growth and angiogenesis. J Clin Oncol 23:1011–1027

Hicks RJ, Rischin D, Fisher R et al (2005) Utility of FMISO PET in advanced head and neck cancer treated with chemoradiation incorporating a hypoxia-targeting chemotherapy agent. Eur J Nucl Med Mol Imaging 32:1384–1391

Ho CL, Chen S, Yeung DW et al (2007) Dual-tracer PET/CT imaging in evaluation of metastatic hepatocellular carcinoma. J Nucl Med 48:902–909

Ho CL, Yu SC, Yeung DW (2003) ^{11}C-acetate PET imaging in hepatocellular carcinoma and other liver masses. J Nucl Med 44:213–221

Hoegerle S, Altehoefer C, Ghanem N et al (2001a) Whole body ^{18}F-DOPA PET for detection of gastrointestinal carcinoid tumors. Radiology 220:373–380

Hoegerle S, Altehoefer C, Ghanem N et al (2001b) ^{18}F-DOPA positron emission tomography for tumour detection in patients with medullary thyroid carcinoma and elevated calcitonin levels. Eur J Nucl Med 28:64–71

Hoegerle S, Ghanem N, Altehoefer C et al (2003) ^{18}F-DOPA positron emission tomography for the detection of glomus tumours. Eur J Nucl Med Mol Imaging 30:689–694

Hoegerle S, Nitzsche E, Altehoefer C et al (2002) Pheochromocytomas: detection with ^{18}F DOPA whole body PET—initial results. Radiology 222:507–512

Hoffman RM (1984) Altered methionine metabolism, DNA methylation and oncogenic expression in carcinogenesis. Biochem Biophys Acta 738:49–87
Hood JD, Bednarski M, Frausto R, et al (2002) Tumor regression by targeted gene delivery to neovasculature. Science 296:2404–2407
Howard BV, Howard WJ (1975) Lipids in normal and tumor cells in culture. Prog Biochem Pharmacol 10:135–166
Huang MC, Shih MH, Chung WY et al (2005) Malignancy of intracerebral lesions evaluated with ^{11}C-methionine- PET. J Clin Neurosci 12:775–780
Husarik DB, Miralbell R, Dubs M et al (2008) Evaluation of [^{18}F]-choline PET/CT for staging and restaging of prostate cancer. Eur J Nucl Med Mol Imaging 35:253–263
Hustinx R, Pourdehnad M, Kaschten B et al (2005) PET imaging for differentiating recurrent brain tumours from radiation necrosis. Radiol Clin North Am 43:35–47
Hynes RO (2002) Integrins: bidirectional, allosteric signaling machines. Cell 110:673–687
Hwang KH, Choi DJ, Lee SY et al (2009) Evaluation of patients with hepatocellular carcinomas using [^{11}C]acetate and [^{18}F]FDG PET/CT: a preliminary study. Appl Radiat Isot 67:1195–1198
Imani F, Agopian VG, Auerbach MS et al (2009) ^{18}F-FDOPA PET and PET/CT accurately localize pheochromocytomas. J Nucl Med 50:513–519
Ito Y, Fujita M, Shimada S et al (1999) Comparison between the decrease of dopamine transporter and that of L-DOPA uptake for detection of early to advanced stage of Parkinson's disease in animal models. Synapse 31:178–185
Iwai Y, Yamanaka K, Oda J et al (2001) Tracer accumulation in radiation necrosis of the brain after thallium-201 SPECT and [^{11}C]methionine PET: case report. Neurol Med Chir (Tokyo) 41:415–418
Iwata Y, Shiomi S, Sasaki N et al (2000) Clinical usefulness of positron emission tomography with fluorine-18-fluorodeoxyglucose in the diagnosis of liver tumors. Ann Nucl Med 14:121–126
Jacob T, Grahek D, Younsi N et al (2003) Positron emission tomography with [^{18}F]FDOPA and [^{18}F]FDG in the imaging of small cell lung carcinoma: preliminary results. Eur J Nucl Med Mol Imaging 30:1266–1269
Jeong JM, Hong MK, Chang YS et al (2008) Preparation of a promising angiogenesis PET imaging agent: 68 Ga-labeled c(RGDyK)-isothiocyanatobenzyl-1,4,7-triazacyclononane-1,4,7-triacetic acid and feasibility studies in mice. J Nucl Med 49:830–836
Kaim AH, Weber B, Kurrer MO et al (2002) ^{18}F-FDG and ^{18}F-FET uptake in experimental soft tissue infection. Eur J Nucl Med Mol Imaging. 29:648–654
Kameyama M, Shirane R, Itoh J et al (1990) The accumulation of ^{11}C-methionine in cerebral glioma patients studied with PET. Acta Neurochir (Wien) 104:8–12
Kang DE, White RL Jr, Zuger JH et al (2004) Clinical use of fluorodeoxyglucose F 18 positron emission tomography for detection of renal cell carcinoma. J Urol 171:1806–1809
Kaschten B, Stevenaert A, Sadzot B et al (1998) Preoperative evaluation of 54 gliomas by PET with fluorine-18-fluorodeoxyglucose and/or carbon-11-methionine. J Nucl Med 39:778–785
Kato TJ, Shinoda N, Oka K et al (2008) Analysis of ^{11}C-methionine uptake in low-grade gliomas and correlation with proliferative activity. Am J Neuroradiol 29:1867–1871
Kayani I, Groves AM (2006) ^{18}F-fluorodeoxyglucose PET/CT in cancer imaging. Clin Med 6:240–244
Kelloff GJ, Hoffman JM, Johnson B et al (2005) Progress and promise of FDG-PET imaging for cancer patient management and drug development. Clin Cancer Res 11:2785–2808
Kenny LM, Vigushin DM, Al-Nahhas A et al (2005) Quantification of cellular proliferation in tumor and normal tissues of patients with breast cancer by [^{18}F]fluorothymidine-positron emission tomography imaging: evaluation of analytical methods. Cancer Res 65:10104–10112
Kerbel R, Folkman J (2002) Clinical translation of angiogenesis inhibitors. Nat Rev Cancer 2:727–739
Kim S, Chung JK, Im SH et al (2005) ^{11}C-methionine PET as a prognostic marker in patients with glioma: comparison with ^{18}F-FDG PET. Eur J Nucl Med Mol Imaging 32:52–59
Koh WJ, Bergman KS, Rasey JS et al (1995) Evaluation of oxygenation status during fractionated radiotherapy in human nonsmall cell lung cancers using [F-18]fluoromisonidazole positron emission tomography. Int J Radiat Oncol Biol Phys 33:391–398

Koh W-J, Rasey JS, Evans ML (1992) Imaging of hypoxia in human tumors with [F-18]fluoromisonidazole. Int J Radiat Oncol Biol Phys 22:199–212

Komar G, Seppaenen M, Eskola O et al (2008) ^{18}F-EF5: a new PET tracer for imaging hypoxia in head and neck cancer. J Nucl Med 49:1944–1951

Kotzerke J, Prang J, Neumaier B et al (2000) Experience with carbon-11 choline positron emission tomography in prostate carcinoma. Eur J Nucl Med 27:1415–1419

Kotzerke J, Volkmer BJ, Neumaier B et al (2002) Carbon-11 acetate positron emission tomography can detect local recurrence of prostate cancer. Eur J Nucl Med 29:1380–1384

Kracht LW, Friese M, Herholz K et al (2003) Methyl-[^{11}C]-lmethionine uptake as measured by positron emission tomography correlates to microvessel density in patients with glioma. Eur J Nucl Med Mol Imaging 30:868–873

Krause BJ, Souvatzoglou M, Tincel M et al (2008) The detection rate of ^{11}C choline PET/TC depends on the serum PSA-value in patients with biochemical recurrence of prostate cancer. Eur J Nucl Med Mol Imaging 35:18–23

Krebs HA (1948) The tricarboxylic acid cycle. Harvey Lect Ser 44:165–99

Laforest R, Dehdashti F, Lewis J et al (2005) Dosimetry of $^{60/61/62/64}$Cu-ATSM: a hypoxia imaging agent for PET. Eur J Nucl Med Mol Imaging. 32:764–770

Langen KJ, Hamacher K, Weckesser M et al (2006) O-(2-[^{18}F]fluoroethyl)-L-tyrosine: uptake mechanisms and clinical applications. Nucl Med Biol 33:287–294

Lange-Nolde A, Zajic T, Slawik M et al (2006) PET with ^{18}F-DOPA in the imaging of parathyroid adenoma in patients with primary hyperparathyroidism. A pilot study. Nuklearmedizin. 45:193–196

Langsteger W, Heinisch M, Fogelman I (2006) The role of fluorodeoxyglucose, ^{18}F-dihydroxyphenylalanine, ^{18}F-choline, and ^{18}F-fluoride in bone imaging with emphasis on prostate and breast. Semin Nucl Med 36:73–92

Lapela M, Leskinen-Kallio S, Varpula M et al (1994) Imaging of uterine carcinoma by carbon-11-methionine and PET. J Nucl Med 35:1618–1623

Lee CS, Samii A, Sossi V et al (2000) In vivo positron emission tomographic evidence for compensatory changes in presynaptic dopaminergic nerve terminals in Parkinson's disease. Ann Neurol 47:493–503

Leenders KL, Salmon EP, Tyrrell P et al (1990) The nigro-striatal dopaminergic system assessed in vivo by positron emission tomography in healthy volunteer subjects and patients with Parkinson's disease. Arch Neurol 47:1290–1298

Leskinen-Kallio S, Minn H, Joensuu H (1990) PET and [^{11}C]methionine in assessment of response in non-Hodgkin lymphoma. Lancet 336:1188

Leskinen-Kallio S, Någren K, Lehikoinen P et al (1992) Carbon-11-methionine and PET is an effective method to image head and neck cancer. J Nucl Med 33:691–695

Leskinen-Kallio S, Någren K, Lehikoinen P et al (1991) Uptake of ^{11}C-methionine in breast cancer studied by PET. An association with the size of S-phase fraction. Br J Cancer 64:1121–1124

Lewis JS, McCarthy DW, McCarthy TJ et al (1999) Evaluation of ^{64}Cu-ATSM in vivo and in vitro in a hypoxic tumor model. J Nucl Med 40:177–183

Lewis JS, Welch MJ (2001) PET imaging of hypoxia. Q J Nucl Med 45:183–188

Lewis JS, Sharp TL, Laforest R et al (2001) Tumor uptake of copper-diacetyl-bis(N4-methylthiosemicarbazone): effect of changes in tissue oxygenation. J Nucl Med 42:655–661

Leyton J, Latigo J, Perumal M et al (2005) Early detection of tumor response to chemotherapy by 3′-deoxy-3′-[^{18}F]fluorothymidine positron emission tomography: the effect of cisplatin on the fibrosarcoma tumor model in vivo. Cancer Res 65:4202–4210

Lilja A, Lundqvist H, Olsson Y et al (1989) Positron emission tomography and computed tomography in differential diagnosis between recurrent or residual glioma and treatment-induced brain lesions. Acta Radiol 30:121–128

Lindhe Ö, Sun A, Ulin J et al (2009) [^{18}F]Fluoroacetate is not a functional analogue of [^{11}C]acetate in normal physiology. Eur J Nucl Med Mol Imaging 36:1453–1459

Lindstrom P, Sehlin J (1986) Aromatic amino acids and pancreatic islet function: a comparison of L-tryptophan and L-5-hydroxytryptophan. Mol Cell Endocrinol 48:121–126

Liu RS, Chang CP, Chu LS et al (2006) PET imaging of brain astrocytoma with 1-^{11}C-acetate. Eur J Nucl Med Mol Imaging 33:420–427

Liu RS (2000) Clinical application of (C-11)acetate in oncology. Clin Positron Imaging 3:185

Lovenberg W, Weissbach H, Undenfriend S (1962) Aromatic L-amino acid decarboxylase. J Biol Chem 237:89–93

Luong A, Hannah VC, Brown MS et al (2000) Molecular characterization of human acetyl-CoA synthetase, an enzyme regulated by sterol regulatory element-binding proteins. J Biol Chem 275:26458–26466

Lyrdal D, Boijsen M, Suurküla M et al (2009) Evaluation of sorafenib treatment in metastatic renal cell carcinoma with 2-fluoro-2-deoxyglucose positron emission tomography and computed tomography. Nucl Med Commun 30:519–524

Martiat P, Ferrant A, Labar D et al (1988) In vivo measurement of carbon-11 thymidine uptake in non-Hodgkin's lymphoma using positron emission tomography. J Nucl Med 29:1633–1637

Martorana G, Schiavina R, Corti B et al (2006) ^{11}C-choline positron emission tomography/computerized tomography for tumor localization of primary prostate cancer in comparison with 12-core biopsy. J Urol 176:954–960, discussion 960

Matthies A, Ezziddin S, Ulrich EM et al (2004) Imaging of prostate cancer metastases with ^{18}Ffluoroacetate using PET/CT. Eur J Nucl Med Mol Imaging 31:797

Maurer RI, Blower PJ, Dilworth JR et al (2002) Studies on the mechanism of hypoxic selectivity in copper bis(thiosemicarbazone) radiopharmaceuticals. J Med Chem 45:1420–1431

Mittendorfer B, Sidossis LS, Walser E et al (1998) Regional acetate kinetics and oxidation in human volunteers. Am J Physiol 274(6 Pt 1):E978–E983

Morris MJ, Scher HI (2007) ^{11}C-acetate PET imaging in prostate cancer. Eur J Nucl Med Mol Imaging 34:181–184

Nanni C Fanti S (2007) ^{18}F-DOPA PET and PET/CT. J Nucl Med 48:1577–1579

Nanni C, Castellucci P, Farsad M et al (2007a) ^{11}C/^{18}F-choline PET or ^{11}C/^{18}F-acetate PET in prostate cancer: may a choice be recommended? Eur J Nucl Med Mol Imaging 34:1704–1705

Nanni C, Zamagni E, Cavo M et al (2007b) ^{11}C-choline vs. ^{18}F-FDG PET/CT in assessing bone involvement in patients with multiple myeloma. World J Surg Oncol 5:68

Narayanan TK, Said S, Mukherjee J et al (2002) A comparative study on the uptake and incorporation of radiolabeled methionine, choline and fluorodeoxyglucose in human astrocytoma. Mol Imaging Biol 4:147–156

Nariai T, Tanaka Y, Wakimoto H et al (2005) Usefulness of L-[methyl-^{11}C] methionine-positron emission tomography as a biological monitoring tool in the treatment of glioma. J Neurosurg 103:498–507

Ng P, Rajendran JG, Schwartz DL et al (2003) Can [F-18] fluoromisonidazole PET imaging predict treatment response in head and neck cancer? J Nucl Med 44:128

Nunez R, Macapinlac H, Yeung HWD et al (2002) Combined ^{18}F-FDG and ^{11}C-methionine PET scans in patients with newly progressive metastatic prostate cancer. J Nucl Med 43:46–55

Nuutinen J, Sonninen P, Lehikoinen P et al (2000) Radiotherapy treatment planning and long-term follow-up with [^{11}C]methionine PET in patients with low-grade astrocytoma. Int J Radiat Oncol Biol Phys 48:43–52

Ogawa T, Kanno I, Shishido F et al (1991) Clinical value of PET with ^{18}F-fluorodeoxyglucose and L-methyl-^{11}C-methionine for diagnosis of recurrent brain tumor and radiation injury. Acta Radiol 32:197–202

Ogawa T, Shishido F, Kanno I et al (1993) Cerebral gliomas: evaluation with methionine-PET. Radiology 186:45–53

Oriuchi N, Tomiyoshi K, Inoue T et al (1996) Independent thallium-201 accumulation and fluorine-18-fluorodeoxyglucose metabolism in glioma. J Nucl Med 37:457–462

Otonkoski T, Veijola R, Huopio H et al (2003) Diagnosis of focal persistent hyperinsulinism of infancy with ^{18}F-fluoro-L-DOPA PET. Program of the 42nd annual meeting of the European Society for Paediatric Endocrinology (ESPE), Ljubljana, Slovenia, 2 (abstract 5.09)

Oyama N, Akino H, Kanamaru H et al (2002) ^{11}C-acetate PET imaging of prostate cancer. J Nucl Med 43:181–186

Oyama N, Akino H, Suzuki Y et al (1999) The increased accumulation of [^{18}F]fluorodeoxyglucose in untreated prostate cancer. Jpn J Clin Oncol 29:623–629

Oyama N, Miller TR, Dehdashti F et al (2003) ^{11}C-acetate PET imaging of prostate cancer: detection of recurrent disease at PSA relapse. J Nucl Med 44:556–558

Padhani A (2006) PET imaging of tumour hypoxia. Cancer Imaging 6:S117–S121

Pascali C, Bogni A, Iwata R et al (2000) [^{11}C]Methylation on a C18 Sep-Pak cartridge: a convenient way to produce [N-methyl-^{11}C]choline. J Label Comput Radiopharm43:195–203

Pauleit D, Floeth F, Hamacher K et al (2005) O-(2-[^{18}F]Fluoroethyl)-L-tyrosine PET combined with MRI improves the diagnostic assessment of cerebral gliomas. Brain 128:678–687

Pauleit D, Zimmermann A, Stoffels G et al (2006) ^{18}F-FET PET compared with ^{18}F-FDG PET and CT in patients with head and neck cancer. J Nucl Med 47:256–261

Pearse AG (1969) The cytochemistry and ultrastructure of polypeptide hormone-producing cells of the APUD series and the embryologic, physiologic and pathologic implications of the concept. J Histochem Cytochem 17:303–313

Piccardo A, Lopci E, Conte M et al (2012) Comparison of ^{18}F-dopa PET/CT and ^{123}I-MIBG scintigraphy in stage 3 and 4 neuroblastoma: a pilot study. Eur J Nucl Med Mol Imaging 39:57–71

Picchio M, Landoni C, Messa C et al (2002) Positive ^{11}C-choline and negative [^{18}F]FDG with positron emission tomography in recurrence of prostate cancer. AJR Am J Roentgenol 179:482–484

Picchio M, Messa C, Landoni C et al (2003) Value of [^{11}C]choline positron emission tomography for re-staging prostate cancer: a comparison with [^{18}F]fluorodeoxyglucose positron emission tomography. J Urol 169:1337–1340

Picchio M, Treiber U, Beer AJ et al (2006) Value of ^{11}C-choline PET and contrast-enhanced CT for staging of bladder cancer: correlation with histopathologic findings. J Nucl Med 47:938-44

Piert M, Machulla HJ, Picchio M et al (2005) Hypoxia-specific tumor imaging with ^{18}F-fluoroazomycin arabinoside. J Nucl Med 46:106–113

Pio BS, Park CK, Pietras R, et al (2006) Usefulness of 3'-[F-^{18}]fluoro-3'-deoxythymidine with positron emission tomography in predicting breast cancer response to therapy. Mol Imagin Biol 8:36–42

Pirotte B, Goldman S, Massager N et al (2004) Comparison of ^{18}F-FDG and ^{11}C-methionine for PET-guided stereotactic brain biopsy of gliomas. J Nucl Med 45:1293–1298

Podo F (1999) Tumor phospholipid metabolism. NMR Biomed 12:413–414

Ponde DE, Dence CS, Oyama N et al (2007) ^{18}F-fluoroacetate: a potential acetate analog for prostate tumor imaging—in vivo evaluation of ^{18}F-fluoroacetate versus ^{11}C-acetate. J Nucl Med 48:420–428

Ponde DE, Oyama N, Dence CS et al (2003) [^{18}F]-Fluoroacetate, an analogue of C-11 acetate for tumor imaging. J Nucl Med 44:296

Pöpperl G, Goldbrunner R, Gildehaus FJ et al (2005) O-(2-[^{18}F]Fluoroethyl)-L-tyrosine PET for monitoring the effects of convection-enhanced delivery of paclitaxel in patients with recurrent glioblastoma. Eur J Nucl Med Mol Imaging 32:1018–1025

Pöpperl G, Gotz C, Rachinger W et al (2004) Value of O-(2-[^{18}F]fluoroethyl)-L-tyrosine PET for the diagnosis of recurrent glioma. Eur J Nucl Med Mol Imaging 31:1464–1470

Pöpperl G, Kreth FW, Herms J et al (2006) Analysis of ^{18}F-FET PET for grading of recurrent gliomas: is evaluation of uptake kinetics superior to standard methods? J Nucl Med 47:393–403

Powles T, Murray I, Brock C et al (2007) Molecular positron emission tomography and PET/CT imaging in urological malignancies. Eur Urol 51:1511–1521

Prante O, Blaser D, Maschauer S et al (2007) In vitro characterization of the thyroidal uptake of O-(2-[^{18}F]fluoroethyl)-L-tyrosine. Nucl Med Biol 34:305–314

Prior JO, Montemurro M, Orcurto MV et al (2009) Early prediction of response to sunitinib after imatinib failure by ^{18}F-fluorodeoxyglucose positron emission tomography in patients with gastrointestinal stromal tumor. J Clin Oncol 27:439–445

Rachinger W, Goetz C, Pöpperl G et al (2005) Positron emission tomography with O-(2-[^{18}F]fluoroethyl)-L-tyrosine versus magnetic resonance imaging in the diagnosis of recurrent gliomas. Neurosurgery 57:505–511

Rajendran JG, Mankoff DA, O'Sullivan F et al (2004) Hypoxia and glucose metabolism in malignant tumors: evaluation by [^{18}F]fluoromisonidazole and [^{18}F]fluorodeoxyglucose positron emission tomography imaging. Clin Cancer Res 10:2245–2252

Rajendran JG, Wilson DC, Conrad EU et al (2003) ^{18}F-FMISO and ^{18}F-FDG PET imaging in soft tissue sarcomas: correlation of hypoxia, metabolism and VEGF expression. Eur J Nucl Med Mol Imaging 30:695–704

Rasey J, Koh W, Evans M et al (1996) Quantifying regional hypoxia in human tumors with positron emission tomography of [^{18}F]fluoromisonidazole: a pretherapy study of 37 patients. Int J Radiat Oncol Biol Phys 24:417–428

Rasey JS, Grunbaum Z, Magee S et al (1987) Characterization of radiolabeled fluoromisonidazole as a probe for hypoxic cells. Radiat Res 111:292–304

Reske SN, Deisenhofer S (2006) Is 3′-deoxy-3′-^{18}F-fluorothymidine a better marker for tumour response than ^{18}F-fluorodeoxyglucose? Eur J Nucl Med Mol Imaging 33:S38–S43

Reubi JC (2004) Somatostatin and other peptide receptors as tools for tumor diagnosis and treatment. Neuroendocrinology 80(Suppl 1):51–56

Ricci PE, Karis JP, Heiserman JE et al (1998) Differentiating recurrent tumor from radiation necrosis: time for re-evaluation of positron emission tomography? AJNR 19:407–413

Rigo P, De Landsheere C, Melon P et al (1990) Imaging of myocardial metabolism by positron emission tomography. Cardiovasc Drugs Ther 4(Suppl 4):847–851

Rohren EM, Turkington TG, Coleman RE (2004) Clinical applications of PET in oncology. Radiology 231:305–332

Rubello D, Fanti S, Nanni C et al (2006) ^{11}C-methionine PET/TC in ^{99m}Tc-sestamibi negative hyperparathyroidism in patients with renal failure on chronic haemodialysis. Eur J Nucl Med Mol Imaging 33:453–459

Salber D, Stoffels G, Paulet D, et al (2006) Differential uptake of [^{18}F]FT and [^{3}H]L-methionine in focal ischemia. Nucl Med Biol 33:1029–1035

Salber D, Stoffels G, Paulet D, et al (2007) Differential uptake of O-(2-^{18}F-fluoroethyl)-Ltyrosine, L-^{3}H-methionine, and ^{3}H-deoxyglucose in brain abscesses. J Nucl Med 2007 48:2056–2062

Sasaki M, Kuwabara Y, Yoshida T et al (1998) A comparative study of thallium-201 SPET, carbon-11 methionine PET and fluorine-18 fluorodeoxyglucose PET for the differentiation of astrocytic tumours. Eur J Nucl Med 25:1261–1269

Sato N, Suzuki M, Kuwata N et al (1999) Evaluation of the malignancy of glioma using ^{11}C-methionine positron emission tomography and proliferating cell nuclear antigen staining. Neurosurg Rev 22:210–214

Sawle GV (1993) The detection of pre-clinical Parkinson's disease: what is the role of positron emission tomography? Mov Disord 8:271–277

Scattoni V, Picchio M, Suardi N et al (2007) Detection of lymph-node metastases with integrated [^{11}C]choline PET/CT in patients with PSA failure after radical retropubic prostatectomy: results confirmed by open pelvic-retroperitoneal lymphadenectomy. Eur Urol 52:423–429

Schiavina R, Scattoni V, Castellucci P et al (2008) ^{11}C-choline positron emission tomography/computerized tomography for preoperative lymph-node staging in intermediate-risk and high-risk prostate cancer: comparison with clinical staging nomograms. Eur Urol 54:392–401

Schiepers C, Nuytes J, Bormans G et al (1997) Fluoride kinetics of the axial skeleton measured in vivo with fluorine-18-fluoride PET. J Nucl Med 38:1970–1976

Schirrmeinster H, Glatting G, Hetzel J et al (2001) Prospective evaluation of the clinical value of planar bone scans, SPECT, and ^{18}F-labeled NaF PET in newly diagnosed lung cancer. J Nucl Med 42:1800–1804

Schnell O, Krebs B, Carlsen J et al (2009) Imaging of integrin $\alpha_v\beta_3$ expression in patients with malignant glioma by [^{18}F] Galacto-RGD positron emission tomography. Neuro Oncol 11:861–870

Shields AF, Grierson JR, Dohmen BM et al (1998) Imaging proliferation in vivo with [^{18}F]FLT and positron emission tomography. Nat Med 4:1334–1336

Shields AF (2006) Positron emission tomography measurement of tumor metabolism and growth: its expanding role in oncology. Mol Imaging Biol 8:141–150

Shreve P, Chiao PC, Humes HD et al (1995) Carbon-11-acetate PET imaging in renal disease. J Nucl Med 36:1595–1601

Soloviev D, Fini A, Chierichetti F et al (2008) PET imaging with ^{11}C-acetate in prostate cancer: a biochemical, radiochemical and clinical perspective. Eur J Nucl Med Mol Imaging 35:942–949

Sörensen J, Andrén B, Blomquist G et al (2006) The central circulation in congestive heart failure non-invasively evaluated with dynamic positron emission tomography. Clin Physiol Funct Imaging 26:171–177

Stadlbauer A, Prante O, Nimsky C et al (2008): Metabolic imaging of cerebral gliomas: spatial correlation of changes in O-(2-^{18}F-fluoroethyl)-L-tyrosine PET and proton magnetic resonance spectroscopic imaging. J Nucl Med 49:721–729

Sun A, Sörensen J, Karlsson M et al (2007) 1-[^{11}C]-acetate PET imaging in head and neck cancer—a comparison with ^{18}F-FDG-PET: implications for staging and radiotherapy planning. Eur J Nucl Med Mol Imaging 34:651–657

Sutinen E, Nurmi M, Roivainen A et al (2003) Kinetics of [^{11}C]choline uptake in prostate cancer: a PET study. Eur J Nucl Med Mol Imaging 31:317–324

Swinnen JV, Van Veldhoven PP, Timmermans L et al (2003) Fatty acid synthase drives the synthesis of phospholipids partitioning into detergent-resistant membrane microdomains. Biochem Biophys Res Commun 302:898–903

Takahashi N, Fujibayashi Y, Yonekura Y et al (2000) Evaluation of ^{62}Cu labeled diacetyl-bis(N4-methylthiosemicarbazone) as a hypoxic tissue tracer in patients with lung cancer. Ann Nucl Med 14:323–328

Talbot JN, Gutman F, Fartoux L et al (2006) PET/CT in patients with hepatocellular carcinoma using [^{18}F]fluorocholine: preliminary comparison with [^{18}F]FDG PET/CT. Eur J Nucl Med Mol Imaging 33:1285–1289

Talbot JN, Fartoux L, Balogova S et al (2010) Detection of hepatocellular carcinoma with PET/CT: a prospective comparison of ^{18}F-fluorocholine and ^{18}F-FDG in patients with cirrohosis or chronic liver disease. J Nucl Med 51:1699–1706

Tang BN, Moreno-reyes R, Blocket D et al (2008) Accurate preoperative localization of pathological parathyroid glands using ^{11}C-methionine PET/TC. Contrast Media Mol Imaging 3:157–163

Tannock I, Guttman P (1981) Responses of Chinese hamster ovary cells to anticancer drugs under aerobic and hypoxic conditions. Br J Cancer 42:245–248

Terakawa Y, Tsuyuguchi1 N, Iwai Y et al (2008) Diagnostic accuracy of ^{11}C-methionine PET for differentiation of recurrent brain tumors from radiation necrosis after radiotherapy. J Nucl Med 49:694–699

Testa C, Schiavina R, Lodi R et al (2007) Prostate cancer: sextant localization with MR imaging, MR spectroscopy, and ^{11}C-choline PET/CT. Radiology 244:797–806

Tian M, Zhang H, Higuchi T et al (2004) Oncological diagnosis using ^{11}C-choline-positron emission tomography in comparison with 2-deoxy-2-[^{18}F]fluoro-D-glucose-positron emission tomography. Mol Imaging Biol 6:172–179

Torii K, Tsuyuguchi N, Kawabe J et al (2005) Correlation of amino-acid uptake using methionine PET and histological classifications in various gliomas. Ann Nucl Med 19:677–683

Tsuyuguchi N, Sunada I, Iwai Y et al (2003) Methionine positron emission tomography of recurrent metastatic brain tumor and radiation necrosis after stereotactic radiosurgery: is a differential diagnosis possible? J Neurosurg 98:1056–1064

Tsuyuguchi N, Takami T, Sunada I et al (2004) Methionine positron emission tomography for differentiation of recurrent brain tumor and radiation necrosis after stereotactic radiosurgery—in malignant glioma. Ann Nucl Med 18:291–296

Vallabhajosula S (2007) ^{18}F-labeled positron emission tomographic radiopharmaceuticals in oncology: an overview of radiochemistry and mechanisms of tumor localization. Semin Nucl Med 37:400–419

Van Laere K, Ceyssens S, Van Calenbergh F et al (2005) Direct comparison of ^{18}F-FDG and ^{11}C-methionine PET in suspected recurrence of glioma: sensitivity, inter-observer variability and prognostic value. Eur J Nucl Med Mol Imaging 32:39–51

Vesselle H, Grierson J, Muzi M et al (2002) In vivo validation of 3′deoxy-3′-[^{18}F]fluorothymidine ([^{18}F]FLT) as a proliferation imaging tracer in humans: correlation of [^{18}F]FLT uptake by positron emission tomography with Ki-67 immunohistochemistry and flow cytometry in human lung tumors. Clin Cancer Res 8:3315–3323

Volker JF et al (1940) The absorption of fluorides by enamel, dentin, bone, and hydroxyapatite as shown by the radioactive isotope. J Biol Chem 134:543–548

Warburg O (1956) On the origin of cancer cells. Science 123:309–314

Weber DC, Zilli T, Buchegger F et al (2008) [^{18}F]Fluoroethyltyrosine-positron emission tomography-guided radiotherapy for high-grade glioma. Radiat Oncol 3:44

Weber W, Bartenstein P, Gross MW et al (1997) Fluorine-18-FDG PET and iodine-123-IMT SPECT in the evaluation of brain tumors. J Nucl Med 38:802–808

Weckesser M, Langen KJ, Rickert CH et al (2005) O-(2-[^{18}F]Fluorethyl)-L-tyrosine PET in the clinical evaluation of primary brain tumours. Eur J Nucl Med Mol Imaging. 32:422–429

Wells P, Gunn RN, Alison M et al (2002) Assessment of proliferation in vivo using 2-[^{11}C]thymidine positron emission tomography in advanced intra-abdominal malignancies. Cancer Res 62:5698–5702

Wester HJ, Herz M, Weber W et al (1999) Synthesis and radiopharmacology of O-(2-^{18}F-fluoroethyl)-L-tyrosine for tumor imaging. J Nucl Med 40:205–212

Whal L, Nahmias C (1997) Modeling of fluorine-18-6-fluoro-L-Dopa in humans. J Nucl Med 37:432–437

Wienhard K, Herholz K, Coenen HH et al (1991) Increased amino acid transport into brain tumors measured by PET of L-(2-^{18}F)fluorotyrosine (see comments). J Nucl Med 32:1338–1346

Wong TZ, Van der Westhuizen GJ, Coleman RE (2002) Positron emission tomography imaging of brain tumours. Neuroimaging Clin N Am 12:615–626

Yamaguchi T, Lee J, Uemura H et al (2005) Prostate cancer: a comparative study of ^{11}C-choline PET and MR imaging combined with proton MR spectroscopy. Eur J Nucl Med Mol Imaging 32:742–748

Yamamoto Y, Nishiyama Y, Kameyama R et al (2008a) Detection of hepatocellular carcinoma using ^{11}C-choline PET: comparison with ^{18}-F-FDG PET. J Nucl Med 49:1245–1248

Yamamoto Y, Nishiyama Y, Kimura N et al (2008b) ^{11}C-acetate PET in the evaluation of brain glioma: comparison with ^{11}C-methionine and ^{18}F-FDG-PET. Mol Imaging Biol 10:281–287

Yamane T, Sakamoto S, Senda M (2009) Clinical impact of ^{11}C-methionine PET on expected management of patients with brain neoplasm. Eur J Nucl Med Mol Imaging, Nov 14

Yoshimoto M, Waki A, Yonekura Y et al (2001) Characterization of acetate metabolism in tumor cells in relation to cell proliferation: acetate metabolism in tumor cells. Nucl Med Biol 28:117–122

Zeisel SH (1981) Dietary choline: biochemistry, physiology and pharmacology. Annu Rev Nutr 1:95–121

Part IV
Future Challenges

Future Challenges of Multimodality Imaging

Montserrat Estorch and Ignasi Carrio

Abstract

During the last decade, positron emission tomography/computed tomography (PET/CT) and single-photon emission computed tomography/computed tomography (SPECT/CT) have procured advances in research and clinical application of fusion imaging. The recent introduction of systems that combine PET and MRI opens new horizons for multimodality molecular imaging. These systems offer simultaneous morphologic, functional, and molecular information of a living system. Moreover, other combinations of anatomic and functional imaging modalities (for example CT and MRI or PET and optical imaging) are emerging, holding promise in basic medical research or in clinical medicine. These developments are paralleled by advances in the field of biomolecules and particles, to provide new agents useful for more than one imaging modality and to facilitate the study of the same target by different imaging devices. In the near future PET/MRI may emerge as a new powerful multimodality technique in clinical oncology, offering considerable potential for imaging applications beyond correlation of functional and anatomic images. Future developments should include the simultaneous acquisition of multifunctional data such as PET tracer uptake, MR spectroscopy, or fMRI along with high-resolution anatomic MRI.

Contents

M. Estorch (✉) · I. Carrio
Nuclear Medicine Department, Hospital Sant Pau, Barcelona, Spain
e-mail: icarrio@santpau.cat

O. Schober and B. Riemann (eds.), *Molecular Imaging in Oncology*,
Recent Results in Cancer Research 187, DOI: 10.1007/978-3-642-10853-2_14,

1 Introduction

To understand genetics of cancer and its proliferative nature remains the main objective of current cancer research. Improved knowledge of cancer pathogenesis results in an array of biomarkers to be used for diagnosis and treatment of the disease. Molecular imaging is the visualization, characterization and measurement of biological processes at the molecular and cellular levels in a living system. Molecular imaging techniques using radiotracers allow the demonstration of functional or phenotypic changes associated with pathology in vivo, and the characterization of both genotypic and phenotypic tumoral signatures.

During the last 10 years, positron emission tomography/computed tomography (PET/CT) and single-photon emission computed tomography/computed tomography (SPECT/CT) have procured advances in research and clinical application of fusion imaging unthinkable before, with simultaneous development of quantitative methods to measure absolute concentration of radiotracers related to the severity and/or progression of cancer.

The recent introduction of systems that combine PET and MRI is opening new horizons for multimodality molecular imaging to acquire simultaneously morphologic, functional, and molecular information of a living system. Moreover, other combinations of anatomic and functional imaging modalities (for example CT and MRI or PET and optical imaging) are emerging, holding promise in basic medical research or in clinical medicine. These developments are paralleled by advances in the field of biomolecules and particles, to provide new agents useful for more than one imaging modality and to facilitate the study of the same target by different imaging devices.

2 Technology and Probe Design

During the last 10 years, the introduction of multimodality systems combining CT with SPECT and PET has changed significantly the capabilities of stand-alone SPECT and PET. Fused functional and anatomic images have gained wide acceptance, becoming a powerful clinical tool, especially in oncology. With multimodality imaging as the current paradigm, present research efforts are focused on the integration of MRI with PET and SPECT (Patton et al. 2009).

2.1 SPECT/CT

New technologies have improved the performance of SPECT and SPECT/CT beyond the technology invented by Hal Anger in 1957 (Anger 1957). The initial primary goal of simultaneous SPECT and CT studies was to facilitate lesion localization and attenuation correction. Recently, with the implementation of diagnostic CT, clinical information from SPECT/CT has been significantly improved. In consequence, guidelines of clinical practice need to be adapted and clinical protocols for staging and restaging of cancer should incorporate SPECT/CT when necessary to facilitate precise diagnosis and to reduce patient radiation burden.

Involuntary motions because of cardiac contraction, respiration, or bowel movement are common technical problems encountered in SPECT/CT. Respiratory motion results in inaccuracy of attenuation correction for lung tumors because of eventual misregistration between emission and transmission data. Considerable research efforts are addressed to develop methods for correction of respiratory motion effects, such as external or internal devices that make possible to estimate respiratory motion gating emission data and the adequate matching to CT cine data, or the use of modeling motion and matching of CT data from a single CT and a respiratory gated emission study. Future developments should provide automated correction with minimal radiation dose. On the other hand, the role of attenuation correction in SPECT/CT for oncologic applications is not fully established, with a relatively small number of studies comparing the diagnostic accuracy of attenuated and non-attenuated SPECT images.

In future, silicon photodiode or solid-state materials incorporated to detectors may replace photomultiplier tube technology, improving spatial and energy resolutions, and increasing stability with a more compact size (Despres et al. 2007). Development of these new technologies, will improve overall performance and cost-effectiveness of future SPECT/CT equipment.

2.2 PET/CT

The introduction of combined PET/CT in 2001 opened a new era in the field of nuclear and molecular imaging, improving the sensitivity and specificity of clinical PET, and facilitating clinical acceptance and implementation of multimodality imaging (Beyer et al. 2000). Compared with two separated systems, the combination of PET and CT into a single gantry has provided the paradigm for multimodality imaging, and has improved and simplified clinical management of patients. PET/CT is now a critical component of diagnosis and treatment management of oncologic disease.

Continuing advances in PET technology include detectors with improved spatial resolution, increased axial field-of-view (aFOV) with subsequent improvement of sensitivity, faster and more efficient iterative reconstruction algorithms, and improved signal-to-noise by incorporating time-of-flight (TOF) information. Motion-free gated imaging is offered for specific applications, such to plan appropriate fields of radiotherapy.

The introduction of lutetium oxyorthosilicate, as faster scintillator than bismuth germinates, improves the count rate capability of PET scanners. The increased light output allows improved spatial resolution and energy resolution with reduction of scatter fraction. The dead-time of system is also decreased allowing reduction of the coincidence window and implementation of TOF. The increased aFOV offers an increase of sensitivity that improves spatial resolution. Moreover, increased aFOV procures fewer acquisition positions taking more advantage of the radiation emitted from the patient. The development of new PET image reconstruction algorithms broadens the point spread function or High-Definition PET or HD-PET and results in improved intrinsic resolution and uniformity throughout the FOV (Panin et al. 2006).

As it happens in SPECT/CT, motion between or during PET/CT studies may pose a technical problem, with remaining uncertainties in the registration process. The correction of respiratory motion effects, that may result in inaccuracy in attenuation correction for lung tumors, represents a challenge for PET/CT. Methods to reduce the effect of respiratory motion include breath hold during treatment, "gating" in which the beam is turned on or off in synchrony with the respiratory cycle and "tracking" in which the beam follows the tumor based on imaging technology (Bundschuh et al. 2008; Cheng et al. 2009; Chang et al. 2010). However, at present, the optimal approach that provides automated correction with minimal radiation dose has yet to be demonstrated.

Accurate definition of the boundaries of active disease is of clinical relevance in guiding biopsy sites and in planning surgery and radiotherapy fields. PET/CT studies facilitate the correct anatomical delineation of ^{18}F-FDG uptake optimizing biopsy and improving the planning of surgical procedures (Goerres et al. 2005). The better delineation of tumor tissue by PET/CT has supported the implementation of this multimodality system in radiation therapy planning of various tumors as non-small cell lung carcinomas, head and neck tumors, and lymphoma (Faria et al. 2008; Guido et al. 2009).

2.3 SPECT/MRI and PET/MRI

Since few years, numerous working prototypes of PET/MRI systems have been described and introduced (Catana et al. 2008; Judenhofer et al. 2008; Schlemmer et al. 2008). The combination of SPECT and PET with MRI can be important in areas where this technique is the preferred anatomic imaging modality. There are clear synergies between these modalities in areas where, beyond anatomic landmarking, MRI can detect organ-specific abnormalities and pathologies by spectroscopic quantification of concentrations of molecules. Moreover, the expected radiation dose for SPECT and PET/MRI is significantly less than that for SPECT and PET/CT, which may be of particular importance in oncologic patients that are followed with multiple studies to monitor disease progression and response to therapy.

A potential limitation of MRI in multimodality imaging systems is that this technique does not provide adequate information for attenuation correction of emission studies, being a challenge to separate air and bone, and to measure the variations of density in the lung. Attenuation correction based on MRI is an active

area of research, and its developments will be key for future clinical applications of PET/MRI (Hofmann et al. 2008; Zaidi 2007).

To integrate SPECT and PET with MRI is a technical challenge because these systems can interfere each other. At present, several prototypes have been designed and are at various stages of development (Raylman et al. 2006; Woody et al. 2007). Even if to merge the hardware of SPECT or PET and MRI into a single device is limited by space, the principal challenge derives from conventional PET detectors based on photomultiplier tubes (PMTs), which do not operate properly in presence of the magnetic field of MRI. The consequent mutual interference between both image modalities needs to be reduced at maximum to provide high quality studies, as much PET as MRI. PET systems can interfere with MRI systems degrading the homogeneity of magnetic and radiofrequency fields resulting in a loss of image quality with presence of artifacts. On the other hand, the strong external magnetic field of MRI systems can interfere with PET systems deflecting the normal trajectory of electrons into the PMTs, and the radiofrequency field and the gradient system pulses can affect the electronic of PET producing artifacts on image. To solve mutual interference between PET and MRI, light fibers coupled to the scintillation crystals of PET detectors have been used, with only the MRI elements remaining in the magnetic field and directing the scintillations out this field through light fibers. Scintillation crystals produce several distortion and artifacts on MRI image, due to their different magnetic susceptibilities compared with human tissue. The replacement of photomultipliers tubes by solid-state scintillation detectors has been proposed and is being developed (Townsend 2008). These detectors, based on avalanche photodiodes, have the advantage that to be insensitive to magnetic fields and can be directly connected to the scintillation crystal block within the magnetic field using a short 1–2 mm light guide. In this way, light loss is minimized and the conversion of light to electronic signals takes place inside the MRI system, avoiding the use of optical fibers. Another advantage of avalanche photodiodes is that these are smaller than PMTs allowing a design with a fully integrated PET. This design has the advantages that no metallic components are placed directly in the MRI field of view and that the short light guides loss less light. At present, the design of compact systems using solid-state light detectors and based on superconducting magnet (split magnet) or on field cycling MRI, is a challenging task (Cherry et al. 2008). Certainly, new fully integrated PET/MR systems, eventually coupled to SPECT will be developed and become available in the near future.

3 Tracers

Tumors are hypermetabolic and may be distinguished from nonmalignant tissue by their elevated glucose metabolism. ^{18}F-FDG is a nonspecific tracer for detecting malignant tumors employed for PET imaging and quantification of glucose metabolism in vivo. The standardized uptake value (SUV) is a simple semi-quantitative method widely used to standardize the ^{18}F-FDG uptake. The presence or absence of ^{18}F-FDG accumulation is used to characterize CT findings in multimodality imaging of cancer patients using PET/CT (Bar-Shalom et al. 2003; Gerth et al. 2007; Czernin et al. 2007; la Fougère et al. 2006; Raanani et al. 2006).

In parallel to the technological advances in PET/CT, positron emitter labeled radiopharmaceuticals beyond ^{18}F-FDG are in continuing development, from isotopes such as ^{124}I to highly specific compounds such as ^{68}Ga-DOTATOC. ^{124}I has favorable conditions as much for dosimetry as for quality of images. Its half-life of 4.2 days allows imaging over some biological half-lives of iodine accumulation in thyroid cancer metastases. In consequence, iodine accumulation in lesions even in the submillimeter range, may be detected because of lower background activity (Freudenbersg et al. 2008), with assessment of tumor volumes and adequate dosimetric calculations (Jentzen et al. 2008a, b). As example of highly specific tracer, ^{68}Ga-DOTATOC binds to somatotropin receptors, which are frequently overexpressed in neuroendocrine tumors that may be clinically active even when having very little dimensions. Therefore, their early detection represents an important clinical challenge (Buchmann et al. 2007). Other tracers available for PET/CT, such as as choline labeled with ^{11}C or ^{18}F for prostate cancer, may be less specific. These radiopharmaceuticals are inhomogeneously distributed in the background and may shows some nonspecific binding in the intestine, being the tumor specific binding only moderate (Bouchelouche and Oehr 2008).

New PET compounds for multimodality imaging include those capable to target specific key biologic processes in oncogenesis, such as proliferation (^{18}F-3-fluoro-3-deoxy-L-thymidine [^{18}F-FLT]), hypoxia (^{18}F-fluoromisonidazole [^{18}F-FMISO] and ^{18}F-fluoroazomycin arabinoside [^{18}F-FAZA]), angiogenesis (^{18}F-galacto-arginine-glycine-aspartic acid [^{18}F-galacto-RGD]), and apoptosis (^{124}I- or ^{64}Cu-Annexin V). Imaging of these biologic targets is expected to provide meaningful information for the selection and monitoring of targeted therapy in individual cancer patients, facilitating personalized treatment of the disease.

^{18}F-FMISO is a highly stable radiopharmaceutical directly derived from misonidazole and is the most extensively studied PET agent for hypoxia mapping. ^{18}F-FMISO shows high accumulation in hypoxic tissue which is proportional to the hypoxic fraction of the tumor. PET/CT using ^{18}F-FMISO offers the possibility of in vivo mapping of regional tumor hypoxia, identifying patients who may benefit from changes in their therapeutic regimen because hypoxia has been identified as a major adverse prognostic factor for tumor progression and for resistance to anticancer treatment. In addition, such mapping of hypoxia can be used to guide intensity-modulated radiotherapy (Rajendran et al. 2003; Hicks et al. 2005). At present, assessment of therapy response with hypoxia tracers is still experimental.

The thymidine analog ^{18}F-FLT, derived from the cytostatic drug azidovudine, has been suggested for noninvasive assessment of proliferation and more specific tumor imaging than ^{18}F-FDG. This tracer is stable in vitro and accumulates in proliferating tissues and malignant tumors (Shields et al. 1998; Wells et al. 2002). However, at present the uptake mechanism of ^{18}F-FLT is only partially understood, and the influence of membrane transporters and various nucleoside-metabolizing enzymes remains to be determined. Preliminary data have described a significant correlation between tumoral proliferation and ^{18}F-FLT uptake in various malignant tumors, suggesting that ^{18}F-FLT could be used for therapeutic monitoring in various clinical settings (Salskov et al. 2007; Bading and Shields 2008). Clinical trials are needed to further validate ^{18}F-FLT as a marker for therapy response.

Table 1 PET tracers of ^{18}F: Biochemical process, mechanisms of uptake and localization

Radiotracer	Biochemical Process	Mechanism of uptake and localization
^{18}F-FDG	Glucose metabolism	Facilitate diffusion via glucose transporters Substrate for hexokinase in glucose metabolism
^{18}F-Fluoride	Bone metabolism	Incorporation in the hydroxyapatite crystals in bone
^{18}F-Fluorocholine	Membrane synthesis	Substrate for choline kinase in choline metabolism
^{18}F-Fluoroacetate	Lipid synthesis	Acetate is activated to acetyl-CoA in both the cytosol and mitochondria by acetyl-CoA synthetase
^{18}F-Fluorothymidine	DNA synthesis	Substrate for thymidine kinase in DNA synthesis and reflects tumor cell proliferation rate
^{18}F-FMISO	Hypoxia	Intracellular reduction and binding
^{18}F-FES	Receptor binding	Specific binding to estrogen receptors in breast cancer
^{18}F-FDOPA ^{18}F-FMT ^{18}F-FCCA	AA transport and protein synthesis	Precursor for the synthesis of dopamine Transport into the cells involves amino acid carrier protein Intracellular trapping involves protein synthesis or transmethylation
^{18}F-FB-E[c(RGDyK)]2	Angiogenesis	Integrin receptors on endotelial cells of neovasculature
^{18}F-Oligonucleotide ^{18}F-FHBG	Gene expression	In vivo hybridization with mRNA Substrate to herpes virus thymidine kinase

At present, one of the primary goals in cancer research is to increase the knowledge on genetics of cancer and its proliferative nature. Along this line, non-somatostatin receptors biomarkers overexpressed on the surface of malignant cell have been explored. These are VPAC receptors, a family of 3G protein-coupled receptors located on the plasma membrane of tumor cells that mediate the biological action of vasoactive intestinal peptide (VIP) and pituitary adenylate cyclase activating polypeptide (PACAP). These receptors are present on several common tumors, as breast, prostate, bladder, and colon, and VIP and PACAP can be labeled with ^{99m}Tc and also with ^{64}Cu, with opportunities to image these oncologic diseases early and specifically in the future (Germano et al. 2004; Schulz et al. 2004).

Another exciting and challenging goal in cancer research is the possibility to target intracellular biomarkers for diagnostic application. It has been demonstrated that oncogene expression of tumoral cells is different from their normal cohorts. Targeting specific oncogene mRNAs copies with ^{99m}Tc and ^{64}Cu for SPECT or PET in dividing cells may permit imaging of oncogene expression in several tumors. This technique could be also useful to monitor effectiveness of therapy, with assessment of the upregulation or downregulation of oncogene mRNA copies

Table 2 PET tracers of positron-emitting radionuclides non-^{18}F: Biochemical process, mechanisms of uptake and localization

Radiotracer	Biochemical Process	Mechanism of uptake and localization
^{15}O-Water	Blood flow/perfusion	Freely diffusible across membranes
^{11}C-Choline	Membrane synthesis	Substrate for choline kinase in choline metabolism
^{11}C-Thymidine	DNA synthesis	Substrate for thymidine kinase in DNA synthesis and reflects tumor cell proliferation rate
^{68}Ga-DOTATOC	Receptor binding	Specific binding to somatostatin receptor (SSTR-II)
^{68}Ga-DOTANOC		Specific binding to somatostatin receptor (SSTR-II, III, V)
^{11}C-L-methionine	AA transport and protein synthesis	Transport into the cells involves amino acid carrier protein Intracellular trapping involves protein synthesis or transmethylation
^{124}I-^{64}Cu-^{88}Y-Labeled Antibodies	Binding to tumor antigens	Specific binding to tumor associated antigenic binding sites
^{124}I-^{64}Cu-Annexin V	Apoptosis	Specific binding to phosphatidylserine on cell membrane

and of proliferative tumoral status after treatment (Lendvai et al. 2009; Chakrabarti et al. 2005, 2007; Tian et al. 2004, 2005, 2007).

Molecular biology is rapidly progressing and offering new opportunities to molecular imaging. In the future, by use of new imaging probes it may be possible to determine cellular transcription in a cell or its rate of proliferation, predicting its susceptibility for cancer. At present, studies have examined the utility to assess tumor suppressor gene p53 transcription in a cell or to determine the expression of Ki-67 protein as proliferative index of tumoral cells (Shah et al. 2009; Tan et al. 2005). Currently, therapeutic approaches are focused to block the division of cells, even if these approaches do not discriminate between normal and cancerous cells. To increase cell specificity, antisense technology has emerged. It is based on the sequence-specific binding of an antisense oligonucleotide to target RNA, preventing the oncogene mRNA translation, and modulating the oncogene expression involved in the pathogenesis of oncologic diseases (Lendvai et al. 2009; Hersey et al. 2009). However, at present there are still some challenges to be resolved, as in vivo stability, sequence length, and poor uptake in malignant cells. Moreover, the high costs of targeted therapy approaches and the considerable toxic side-effects are important obstacles for to overcome. Major challenges of new targeted therapy approaches comprise the identification of the correct concentration of

therapeutic agent and its dose schedule, the selection of patients suitable to benefit from treatment, and the assessment of the response of the tumor to therapy (Bennett and Swayze 2010). There are opportunities for targeted molecular multimodality imaging to help in all those challenges and to offer new means for non-invasive assessment of cancer biology.

Main existing PET tracers of ^{18}F and of other positron-emitting radionuclides available for multimodality molecular imaging and their biochemical process, mechanism of uptake and localization are respectively shown in Tables 1 and 2.

4 Optical Imaging

Optical techniques allow imaging of fluorescently tagged living cells in three dimensions with a high sensitivity down to the single-molecule level, with high submicrometric spatial resolution and with temporal resolution in the order of a millisecond. However, these techniques have limited penetration depth of light in living tissue, while the commonly used organic fluorophores and genetically encoded fluorescent proteins are often insufficiently bright and stable. Moreover, the toxic radicals and photoproducts generated prevent long-term in vivo imaging.

At present, advances in nanotechnology offer a vast array of artificial particulate systems capable of targeting different cells in vivo. The most desirable property of such nanoparticles is multifunctionality, containing both therapeutic components and multimodality imaging labels for efficient, specific in vivo delivery of drugs and for accurate quantitative assessment of the therapeutic efficacy noninvasively over time. Described nanoparticles are of several natures and include quantum dots, colloidal gold, superparamagnetic iron-oxide crystals, dendrimers, polymeric micelles and liposomes, nanotubes, nanowires, nanoshells, and others (Kirui et al. 2010; Hu et al. 2009; Bentolila et al. 2009). Molecules, such as peptides, proteins, and antibodies can be attached to these nanoparticles to perform PET, SPECT, MRI, ultrasound as well as optical imaging. Research on nanoparticles is focused on optimization of biocompatibility, in vivo kinetics, targeting efficacy, toxicity, and cost-effectiveness. These new nanoparticles and derived imaging probes will need to be translated into clinical applications.

Bioluminescence imaging is related to the light produced by the enzymatic reaction of a luciferase enzyme with its substrate. The most frequent luciferase enzyme used is the firefly (Photinus pyralis) luciferase. It is commonly used for preclinical cellular and molecular imaging in small animals. At present, bioluminescence imaging is a powerful tool to assess mechanisms of disease and to promote drug development in preclinical models. On the other hand, fluorescence imaging is obtained from a target fluorescent molecule that is excited by an external light of appropriate wavelength. This process is followed by release of longer-wavelength, lower-energy light as signal for imaging. Targets for fluorescence imaging may be endogenous molecules, as collagen or hemoglobin, fluorescent proteins or optical contrast agents that can be used for cellular and molecular imaging in small animal models. Both optical techniques have been used to assay pharmacodynamics of therapeutic agents in vivo, establishing dosing parameters to guide initial clinical trials, and eventual clinical applications

(Erickson et al. 2010). Future challenges include the improvement and development of new near-infrared spectroscopic methods useful for to identify cancer biomarkers and to retrospectively determine if benign and malignant lesions could be distinguished by using these methods (Kukreti et al. 2010).

Prototype instruments for optical/PET and optical/SPECT in small animals are under development in research laboratories (Peter and Semmler 2006; Vu et al. 2006). Hybridizing nuclear medicine and optical imaging systems can serve as a translational platform between the widely used bioluminescent or fluorescent techniques in small animal models, and the nuclear radiotracer medicine assays in human (Cherry 2004). The same rationale can be applied to optical imaging and MRI, localizing any significant and little optical signal on high-resolution 3D structural imaging. A promising line lies on the development of handheld-based optical imaging devices for the purpose of in vivo clinical studies, in particular in minimally invasive surgical environments. At present, there are new devices for in vivo clinical studies with demonstrated ability to perform fast 2D imaging and to detect a fluorescent target within a heterogeneous tissue-mimicking background as well as real human tissue (Erickson et al. 2010).

5 Future and Conclusions

Molecular imaging employing multimodality systems will strongly influence the practice of medicine in the next generations. Specific imaging biomarkers will be developed to enable physicians to ensure better strategies of patient management, to stratify cancer, and to perform personalized medicine. Smarter devices, coupling different imaging modalities, with higher spatial resolution and greater sensitivity will be developed, allowing the visualization of a cluster of cells in vivo. These smart devices will use smart probes to target specific biologic phenomena that will provide a true early diagnosis and will drive the design of therapy and the assessment of its effectiveness.

Even if PET/CT with ^{18}F-FDG for tumor imaging will ultimately replace SPECT/CT, advances in SPECT instrumentation, CT technology, and development of radiotracers have the potential to advance SPECT/CT beyond its current level of performance. The horizon for SPECT/CT imaging lies in the development of new tumor-specific agents that can improve oncologic clinical diagnostic and therapeutic applications.

In the near future PET/MRI may emerges as a new powerful multimodality technique in clinical oncology, offering considerable potential for imaging applications beyond simply correlation of functional and anatomic images. Future developments should include the simultaneous acquisition of multifunctional data, such as PET tracer uptake, MR spectroscopy, or fMRI along with high-resolution anatomic MRI.

The use of imaging as a surrogate endpoint requires demonstration of a significant relationship between imaging results and clinical outcome. Cooperation with the pharmaceutical and the instrumentation industry is needed to foster prospective randomized multicenter trials that are mandatory to demonstrate the relationship between appropriate use of multimodality imaging and better patient outcomes.

References

Anger HO (1957) Scintillation camera. Rev Sci Instrum 29:27–33

Bading JR, Shields AF (2008) Imaging of cell proliferation: status and prospects. J Nucl Med 49:64S–80S

Bar-Shalom R, Yefremov N, Guralnik L et al (2003) Clinical performance of PET/CT in evaluation of cancer: additional value for diagnostic imaging and patient management. J Nucl Med 44:1200–1209

Bennett CF, Swayze EE (2010) RNA targeting therapeutics: molecular mechanisms of antisense oligonucleotides as a therapeutic platform. Annu Rev Pharmacol Toxicol 50:259–293

Bentolila LA, Ebenstein Y, Weiss S (2009) Quantum dots for in vivo small-animal imaging. J Nucl Med 50:493–496

Beyer T, Townsend DW, Brun T et al (2000) A combined PET/CT scanner for clinical oncology. J Nucl Med 41:1369–1379

Bouchelouche K, Oehr P (2008) Positron emission tomography and positron emission tomography/computerized tomography of urological malignancies: An update review. J Urol 179:34–45

Buchmann I, Henze M, Engelbrecht S et al (2007) Comparison of ^{68}Ga-DOTATOC PET and ^{111}In-DTPAOC (Octreoscan) SPECT in patients with neuroendocrine tumours. Eur J Nucl Med Mol Imaging 34:1617–1626

Bundschuh R, Martínez-Möller A, Essler M et al (2008) Local motion correction for lung tumours in PET/CT—First results. Eur J Nucl Med Mol Imaging 35:1981–1988

Catana C, Procissi D, Wu YB et al (2008) Simultaneous in vivo positron emission tomography and magnetic resonance imaging. Proc Natl Acad Sci USA 105:3705–3710

Chakrabarti A, Aruva MR, Sajankila SP (2005) Synthesis of novel peptide nucleic acid-peptide chimera for non-invasive imaging of cancer. Nucleosides Nucleotides Nucleic Acids 24:409–414

Chakrabarti A, Zhang K, Aruva MR et al (2007) Radiohybridization PET imaging of KRAS G12D mRNA expression in human pancreas cancer xenografts with [^{64}Cu]DO3A-peptide nucleic acid-peptide nanoparticles. Cancer Biol Ther 6:948–956

Chang G, Chang T, Pan T, Clark JW Jr, Mawlawi OR (2010) Implementation of an automated respiratory amplitude gating technique for PET/CT: clinical evaluation. J Nucl Med 51:16–24

Cheng NM, Yu CT, Ho KC, Wu YC, Liu YC, Wang CW, Yen TC (2009) Respiration-averaged CT for attenuation correction in non-small-cell lung cancer. Eur J Nucl Med Mol Imaging 36:607–615

Cherry SR (2004) In vivo molecular and genomic imaging: new challenges for imaging physics. Phys Med Biol 49:R13–R48

Cherry SR, Louie AY, Jacobs RE (2008) The integration of positron emission tomography with magnetic resonance imaging. Proc IEEE 96:416–438

Czernin J, Allen-Auerbach M, Schelbert HR (2007) Improvements in cancer staging with PET/CT: literature-based evidence as of september 2006. J Nucl Med 48:78S–88S

Despres P, Funk T, Shah KS et al (2007) Monte Carlo simulations of compact gamma cameras based on avalanche photodiodes. Phys Med Biol 52:3057–3074

Erickson SJ, Ge J, Sanchez A, Godavarty A (2010) Two-dimensional fast surface imaging using a handheld optical device: in vitro and in vivo fluorescence studies. Transl Oncol 3:16–22

Faria SL, Menard S, Devic S, Sirois C, Souhami L, Lisbona R, Freeman CR (2008) Impact of FDG-PET/CT on radiotherapy volume delineation in non-small-cell lung cancer and correlation of imaging stage with pathologic findings. Int J Radiat Oncol Biol Phys 70:1035–1038

Freudenberg LS, Antoch G, Frilling A et al (2008) Combined metabolic and morphologic imaging in thyroid carcinoma patients with elevated serum thyroglobulin and negative cervical ultrasonography: role of ^{124}I-PET/CT and FDG-PET. Eur J Nucl Med Mol Imaging 35:950–977

Germano PM, Le SV, Oh DS et al (2004) Differential coupling of PAC1 SV1 splice variant of human colonic tumors to the activation of intracellular cAMP but not intracellular Ca^{2+} does not activate tumor proliferation. J Mol Neurosci 22:83–92

Gerth HU, Juergens KU, Dirksen U et al (2007) Significant benefit of multimodal imaging: PET/CT compared with PET alone in staging and follow-up of patients with Ewing tumors. J Nucl Med 48:1932–1939

Goerres GW, Stupp R, Barghouth G et al (2005) The value of PET, CT and in-line PET/CT in patients with gastrointestinal stromal tumours: long-term outcome of treatment with imatinib mesylate. Eur J Nucl Med Mol Imaging 32:153–162

Guido A, Fuccio L, Rombi B, Castellucci P, Cecconi A, Bunkheila F, Fuccio C, Spezi E, Angelini AL, Barbieri E (2009) Combined ^{18}F-FDG-PET/CT imaging in radiotherapy target delineation for head-and-neck cancer. Int J Radiat Oncol Biol Phys 73:759–763

Hersey P, Bastholt L, Chiarion-Sileni V, Cinat G, Dummer R, Eggermont AM, Espinosa E, Hauschild A, Quirt I, Robert C, Schadendorf D (2009) Small molecules and targeted therapies in distant metastatic disease. Ann Oncol 20:(Suppl6) vi35–40

Hicks RJ, Rischin D, Fisher R et al (2005) Utility of FMISO PET in advanced head and neck cancer treated with chemoradiation incorporating a hypoxia-targeting chemotherapy agent. Eur J Nucl Med Mol Imaging 32:1384–1391

Hofmann M, Steinke F, Scheel V et al (2008) MRI-based attenuation correction for PET/MRI: a novel approach combining pattern recognition and atlas registration. J Nucl Med 49:1875–1883

Hu R, Yong K-T, Roy I, Ding H, He S, Prasad PN (2009) Metallic nanostructures as localized plasmon resonance enhanced scattering probes for multiplex dark field targeted imaging of cancer cells. J Phys Chem C Nanomater Interfaces 113:2676–2684

Jentzen W, Freudenberg L, Eising EG et al (2008a) Optimized ^{124}I PET dosimetry protocol for radioiodine therapy of differentiated thyroid cancer. J Nucl Med 49:1017–1023

Jentzen W, Weise R, Kupferschläger J et al (2008b) Iodine-^{124} PET dosimetry in differentiated thyroid cancer: recovery coefficient in 2D and 3D modes for PET(/CT) systems. Eur J Nucl Med Mol Imaging 35:611–623

Judenhofer MS, Wehrl HF, Newport DF et al (2008) Simultaneous PET-MRI: a new approach for functional and morphological imaging. Nat Med 14:459–465

Kirui DK, Rey DA, Batt CA (2010) Gold hybrid nanoparticles for targeted phototherapy and cancer imaging. Nanotechnology 21:1–10

Kukreti S, Cerussi AE, Tanamai W, Hsiang D, Tromberg BJ, Gratton E (2010) Characterization of metabolic differences between benign and malignant tumors: high-spectral-resolution diffuse optical spectroscopy. Radiology 254:277–284

la Fougère C, Hundt W, Bröckel N et al (2006) Value of PET/CT versus PET and CT performed as separate investigations in patients with Hodgkin's disease and non-Hodgkin's lymphoma. Eur J Nucl Med Mol Imaging 33:1417–1425

Lendvai G, Estrada S, Bergström M (2009) Radiolabelled oligonucleotides for imaging of gene expression with PET. Curr Med Chem 16:4445–4461

Panin VY, Kehren F, Michel C et al (2006) Fully 3-D PET reconstruction with system matrix derived from point source measurements. IEEE Trans Med Imaging 25:907–921

Patton JA, Townsend DW, Hutton BF (2009) Hybrid imaging technology: from dreams and vision to clinical devices. Semin Nucl Med 39:247–263

Peter J, Semmler W (2006) Performance investigation of a dual-modality SPECT/optical small animal imager. Eur J Nucl Med Mol Imaging 33:S117–S117

Raanani P, Shasha Y, Perry C et al (2006) Is CT scan still necessary for staging in Hodgkin and non-Hodgkin lymphoma patients in the PET/CT era? Ann Oncol 17:117–122

Rajendran JG, Wilson DC, Conrad EU et al (2003) [^{18}F-]FMISO and [^{18}F-]FDG PET imaging in soft tissue sarcomas: correlation of hypoxia, metabolism and VEGF expression. Eur J Nucl Med Mol Imaging 30:695–704

Raylman RR, Majewski S, Lemieux SK et al (2006) Simultaneous MRI and PET imaging of a rat brain. Phys Med Biol 51:6371–6379

Salskov A, Tammisetti VS, Grierson J, Vesselle H (2007) FLT: measuring tumor cell proliferation in vivo with positron emission tomography and 3'-deoxy-3'-[^{18}F]fluorothymidine. Semin Nucl Med 37:429–439

Schlemmer HPW, Pichler BJ, Schmand M et al (2008) Simultaneous MR/PET imaging of the human brain: feasibility study. Radiology 248:1028–1035

Schulz S, Rocken C, Mawrin C et al (2004) Immunocytochemical identification of VPAC1, VPAC2 and PAC1 receptors in normal and neoplastic human tissues with subtype specific antibodies. Clin Cancer Res 10:8234–8242

Shah C, Miller TW, Wyatt SK, McKinley ET, Olivares MG, Sanchez V, Nolting DD, Buck JR, Zhao P, Ansari MS, Baldwin RM, Gore JC, Schiff R, Arteaga CL, Manning HC (2009) Imaging biomarkers predict response to anti-HER2 (ErbB2) therapy in preclinical models of breast cancer. Clin Cancer Res 15:4712–4721

Shields AF, Grierson JR, Dohmen BM et al (1998) Imaging proliferation in vivo with ^{18}F-FLT and positron emission tomography. Nat Med 4:1334–1336

Tan PH, Bay BH, Yip G et al (2005) Immunohistochemical detection of Ki67 in breast cancer correlates with transcriptional regulation of genes related to apoptosis and cell death. Mod Pathol 18:374–381

Tian X, Aruva MR, Qin W et al (2004) External imaging of CCND1 cancer gene activity in experimental human breast cancer xenografts with ^{99m}Tc-peptide–peptide nucleic acid-peptide chimeras. J Nucl Med 45:2070–2082

Tian X, Aruva MR, Wolfe HR et al (2005) Tumor-targeting peptide-PNA peptide chimeras for imaging overexpressed oncogene mRNAs. Nucleosides Nucleotides Nucleic Acids 24:1085–1091

Tian X, Aruva MR, Zhang K et al (2007) PET imaging of CCND1 mRNA in human MCF7 estrogen receptor positive breast cancer xenografts with oncogene-specific [^{64}Cu] chelator-peptide nucleic acid-IGF1 analog radiohybridization probes. J Nucl Med 48:1699–1707

Townsend DW (2008) Multimodality imaging of structure and function. Phys Med Biol 53:R1–R39

Vu NT, Silverman RW, Chatziioannou AF (2006) Preliminary performance of optical PET (OPET) detectors for the detection of visible light photons. Nucl Instrum Methods 569:563–566

Wells P, Gunn RN, Alison M et al (2002) Assessment of proliferation in vivo using 2-[^{11}C] thymidine positron emission tomography in advanced intra-abdominal malignancies. Cancer Res 62:5698-5702

Woody C, Schlyer D, Vaska P et al (2007) Preliminary studies of a simultaneous PET/MRI scanner based on the RatCAP small animal tomograph. Nucl Instrum Methods A 571:102–105

Zaidi H (2007) Is MR-guided attenuation correction a viable option for dualmodality PET/MR imaging? Radiology 244:639–642